frontiers | Research Topics

Exploration, exploitation, and utilization of coal-measure gas into the future

volume II

Edited by
Mingjun Zou, Chongtao Wei, Reza Rezaee, Junjian Zhang and Zhenzhi Wang

Published in
Frontiers in Earth Science

ISSN 1664-8714
ISBN 978-2-8325-2508-1
DOI 10.3389/978-2-8325-2508-1

About Frontiers

Frontiers is more than just an open access publisher of scholarly articles: it is a pioneering approach to the world of academia, radically improving the way scholarly research is managed. The grand vision of Frontiers is a world where all people have an equal opportunity to seek, share and generate knowledge. Frontiers provides immediate and permanent online open access to all its publications, but this alone is not enough to realize our grand goals.

Frontiers journal series

The Frontiers journal series is a multi-tier and interdisciplinary set of open-access, online journals, promising a paradigm shift from the current review, selection and dissemination processes in academic publishing. All Frontiers journals are driven by researchers for researchers; therefore, they constitute a service to the scholarly community. At the same time, the *Frontiers journal series* operates on a revolutionary invention, the tiered publishing system, initially addressing specific communities of scholars, and gradually climbing up to broader public understanding, thus serving the interests of the lay society, too.

Dedication to quality

Each Frontiers article is a landmark of the highest quality, thanks to genuinely collaborative interactions between authors and review editors, who include some of the world's best academicians. Research must be certified by peers before entering a stream of knowledge that may eventually reach the public - and shape society; therefore, Frontiers only applies the most rigorous and unbiased reviews. Frontiers revolutionizes research publishing by freely delivering the most outstanding research, evaluated with no bias from both the academic and social point of view. By applying the most advanced information technologies, Frontiers is catapulting scholarly publishing into a new generation.

What are Frontiers Research Topics?

Frontiers Research Topics are very popular trademarks of the *Frontiers journals series*: they are collections of at least ten articles, all centered on a particular subject. With their unique mix of varied contributions from Original Research to Review Articles, Frontiers Research Topics unify the most influential researchers, the latest key findings and historical advances in a hot research area.

Find out more on how to host your own Frontiers Research Topic or contribute to one as an author by contacting the Frontiers editorial office: frontiersin.org/about/contact

Exploration, exploitation, and utilization of coal-measure gas into the future: Volume II

Topic editors

Mingjun Zou — North China University of Water Conservancy and Electric Power, China

Chongtao Wei — China University of Mining and Technology, China

Reza Rezaee — Curtin University, Australia

Junjian Zhang — Shandong University of Science and Technology, China

Zhenzhi Wang — Henan Polytechnic University, China

Citation

Zou, M., Wei, C., Rezaee, R., Zhang, J., Wang, Z., eds. (2023). *Exploration, exploitation, and utilization of coal-measure gas into the future: Volume II*. Lausanne: Frontiers Media SA. doi: 10.3389/978-2-8325-2508-1

Table of contents

frontiers | Frontiers in Earth Science

TYPE Editorial
PUBLISHED 09 May 2023
DOI 10.3389/feart.2023.1191521

OPEN ACCESS

EDITED AND REVIEWED BY
Shuai Yin,
Xi'an Shiyou University, China

*CORRESPONDENCE
Mingjun Zou,
zoumingjun2008@163.com

RECEIVED 22 March 2023
ACCEPTED 18 April 2023
PUBLISHED 09 May 2023

CITATION
Zou M, Wang Z and Zhang J (2023), Editorial: Exploration, exploitation, and utilization of coal-measure gas into the future: Volume II.
Front. Earth Sci. 11:1191521.
doi: 10.3389/feart.2023.1191521

Editorial: Exploration, exploitation, and utilization of coal-measure gas into the future: Volume II

Mingjun Zou[1]*, Zhenzhi Wang[2] and Junjian Zhang[3]

[1]College of Geosciences and Engineering, North China University of Water Resources and Electric Power, Zhengzhou, China, [2]School of Resources and Environment, Henan Polytechnic University, Jiaozuo, China, [3]College of Earth Science and Engineering, Shandong University of Science and Technology, Qingdao, China

KEYWORDS

coal-measure gas, shale, coalbed methane, CO_2, sandstone gas

Editorial on the Research Topic
Exploration, exploitation, and utilization of coal-measure gas into the future: Volume II

Introduction

As climate change-being a dire challenge for all mankind-impinges on every continent, the exigencies of reducing greenhouse gas emissions have gained soaring attention around the world (Zou et al., 2022). Scientists have made strides in understanding the pivotality of unconventional energies (Bustin and Clarkson, 1998; Zou et al., 2018), in particular coal-measure gas (e.g., coal-bed methane, shale gas, and tight sandstone gas), for mitigating global warming (Avci et al., 2021). And, great successes have been achieved over the past decades.

The exploration, exploitation and utilization of coal-measure gas concern the majors of physics, geology, engineering, etc, and there are many hot Research Topic presented recently (Dai et al., 2019). Yet less is known about the measures to achieve the net carbon emissions of coal-measure gas, which entails how to identify its occurrence and production, how to determine its transformation technologies, and how to examine the applicability of its CO_2 geological storage conditions.

Coalbed methane

During the past few decades, China has achieved significant success in the exploration, exploitation, and utilization of coalbed methane, especially in the hot areas of Qinshui and Ordos Basins. Jiang et al. analyzed the pore structure characteristics of coal samples by low-temperature liquid-nitrogen adsorption measurements. Du et al. investigated the cleat and micro-fracture morphology and its aperture, distribution of minerals, and matrix/fracture interactions for the coals of different ranks. Jian et al. provided a new model for solid waste treatment of coal mine and green mining. Wang et al. analyzed the coal-forming

environment during mass extinction in the latest Permian. Li et al. studied coalbed methane accumulation, *in situ* stress, and permeability of low-rank coals in a complex structural region. Shao et al. determined the potential of gas resources in the Huanghebei coalfield and analyzed the sedimentary reservoir control mechanism. Bao et al. analyzed the ionic concentrations, hydrogen and oxygen isotopes, dissolved inorganic carbon isotopes and trace elements for water samples from coalbed methane wells. Jiang et al. studied coalbed methane flow characteristics based on fractal bifurcation fracture network model.

Shale and sandstone gas

Ge et al. investigated and evaluated the shale gas resources in Lucaogou Formation, and identified the reservoir performance, preservation conditions, compressibility and gas bearing property of gas bearing shale intervals. Yu et al. analyzed the convergent deformation of the cavern while considering the spatial variability distribution of the elastic modulus for sandstones. Hu et al. studied on influencing factors and mechanism of pore compressibility of tight sandstone reservoir.

CO_2 injection

CO_2 injection is beneficial for unconventional gas recovery, and gas desorption, diffusion, permeation, and production are the entire process during the injection. Niu et al. conducted the anisotropic permeability test and the CO_2 injectivity simulation test, and established the corresponding numerical models. He et al. solved the problem of inaccurate gas content measurement due to the unclear characteristics of rapid gas desorption in 0–10 s, and improved the gas desorption experimental device. Chen et al. indicated that the integrated technology of gas production and CO_2 capture and sequestration in the coal goafs and the abandoned coal mines can improve the energy production efficiency and reservoir space utilization. Chen et al. compared the changes of pore structure and porosity due to the supercritical CO_2 extraction, and discussed the evolution of pore characteristics change with coal rank because of supercritical CO_2 extraction.

Author contributions

MZ wrote the primary paper, ZW and JZ revised the paper. All authors had reviewed the paper.

Funding

The authors wish to acknowledge financial supports of this study by the National Natural Science Foundation of China under Grant Nos. 41702168 and 42202207.

Acknowledgments

We are grateful to all of the authors who responded to our call to participate in the compilation of this Research Topic. Our gratitude is also extended to all reviewers who kindly reviewed one or more of the manuscripts submitted to this Research Topic and provided valuable comments and recommendations.

Conflict of interest

The authors declare that the research was conducted in the absence of any commercial or financial relationships that could be construed as a potential conflict of interest.

Publisher's note

References

Avci, I., Ozarpa, C., and Aydin, M. A. (2021). Mitigating global warming in smart energy grids via energy supply security for critical energy infrastructures. *Int. J. Glob. Warm.* 25 (3/4), 288–305. doi:10.1504/ijgw.2021.10042671

Bustin, R. M., and Clarkson, C. R. (1998). Geological controls on coalbed methane reservoir capacity and gas content. *Int. J. Coal Geol.* 38 (1-2), 3–26. doi:10.1016/s0166-5162(98)00030-5

Dai, J., Qin, S., Hu, G., Ni, Y., Gan, L., Huang, S., et al. (2019). Major progress in the natural gas exploration and development in the past seven decades in China. *Pet. explor. Dev.* 46 (6), 1100–1110. doi:10.1016/s1876-3804(19)60266-1

Zou, M., Wei, S., Huang, Z., Lv, X., and Guo, B. (2018). Simulations on recoverability performances for a coalbed methane field in SE edge of Ordos basin, China. *Fuel* 233, 354–360. doi:10.1016/j.fuel.2018.06.071

Zou, M., Yao, L., Zhang, M., Huang, Z., Xu, R., Ding, Z., et al. (2022). Hydraulic fracture to enhance coalbed methane recovery by using coated ceramsite. *Greenh. Gas. Sci. Technol.* 12 (6), 751–763. doi:10.1002/ghg.2188

frontiers | Frontiers in Earth Science

TYPE Original Research
PUBLISHED 11 November 2022
DOI 10.3389/feart.2022.1051245

OPEN ACCESS

EDITED BY
Mingjun Zou,
North China University of Water Resources and Electric Power, China

REVIEWED BY
Yongqiang Cui,
China University of Petroleum, China
Junbiao Ma,
Taiyuan University of Technology, China

*CORRESPONDENCE
Anfa Chen,
anfa108308@163.com
Xuelong Li,
lixlcumt@126.com

SPECIALTY SECTION
This article was submitted to Economic Geology,
a section of the journal
Frontiers in Earth Science

RECEIVED 22 September 2022
ACCEPTED 24 October 2022
PUBLISHED 11 November 2022

CITATION
Hao J, Chen A, Li X, Bian H, Shi Y, Wang X, Zhao J and Liu H (2022), A case study of pillar extraction techniques based on strip-filling and second-mining method.
Front. Earth Sci. 10:1051245.
doi: 10.3389/feart.2022.1051245

A case study of pillar extraction techniques based on strip-filling and second-mining method

Jian Hao[1,2], Anfa Chen[2]*, Xuelong Li[1,2]*, Hua Bian[3], Yongkui Shi[1,2], Xin Wang[4], Jiali Zhao[1,2] and Haojie Liu[1,2]

[1]Mine Disaster Prevention and Control-Ministry of State Key Laboratory Breeding Base, Shandong University of Science and Technology, Qingdao, China, [2]College of Energy and Mining Engineering, Shandong University of Science and Technology, Qingdao, China, [3]School of Energy and Mining Engineering, China University of Mining and Technology-Beijing, Beijing, China, [4]School of Civil Engineering, Shandong University, Jinan, China

Strip coal pillars caused by strip mining are widely distributed in China. Over time, strip coal pillars are posing more potential hazards as their stability decreases; therefore, it becomes increasingly important to recover coal pillars without damaging the ground surface. In this paper, strip-filling and second-mining technique is adopted to probe into an optimal scheme for mine goafs. Construction waste was one type of the materials used for backfilling, which was taken to underground from the surface with a pumping system. Jisuo Coal Mine of Tengzhou, Shandong province was taken as the object of study. Through theoretical calculation and on-site survey, we set a re-mining scheme to control rock stratum stability, i.e., 8-m-wide backfilling for the first time and 4-m-wide backfilling for the second time; moreover, the ground pressure behavior and subsidence of working surface were monitored and a contour map of surface subsidence was thus mapped. *In-situ* practice indicated that the underground pressure from coal pillars was transmitted to the backfilling materials, the maximum normal stress of which was 5 MPa, so it was sufficient for the backfilling strip to support the weight of overlying strata; the maximum value of roof-to-floor convergence of backfilled mining face is 45 mm, the maximum surface subsidence 44mm, the maximum inclination value 0.65 mm/m, the maximum surface curvature 0.018 mm/m^2, and the maximum horizontal deformation 0.16 mm/m. The filling body in the original goafs plays the role of "pier". By the monitoring data of subsidence, its surface deformation value was less than that of buildings suffering from grade I damage, which verified the feasibility of strip-filling and second-mining scheme. The success in this technique provides reliable technical and theoretical support for mines with similar conditions.

KEYWORDS

second-mining of strip coal pillar, construction waste, backfill material, partial backfilling, subsidence control, field monitoring

Abbreviations: w_z, Backfill widt; σ_t, Unidirectional compressive strength of backfill material; H, The mining depth of working face λ Safety factor; L, Length of working face D_1 The strip width; γ, Average volume density of rock D_2 The backfilling width.

1 Introduction

Strip mining is an effective method for mining coal resources reserved under railways, rivers and buildings (Huang et al., 2014; Du et al., 2019a). For decades, China has mined an enormous amount of coal resources in the eastern and northern regions of China from coal mines with the above conditions. With such method, however, a large number of coal pillars are left underground (Ghasemi et al., 2014). Over the years, coal pillars have been exposed to the risk of instability caused by weathering and rheology, resulting in mine tremors and surface subsidence (An et al., 2016; Raffaldi et al., 2019; Sun D. Q. et al., 2021). In addition, some coal mines in eastern China hardly have any coal resources to recover. Given the current situation, it is of great significance in China not to disrupt the ecology and surrounding environment (Qian et al., 2007; Zou et al., 2018b; Hao et al., 2019; Zhou et al., 2022).

In the past few decades, filling and remining has developed rapidly and has been widely used in underground mines in China (Cao, 2017; Yan et al., 2018; Li et al., 2021; Wang et al., 2022). In this regard, relevant scholars first focused on filling materials (Guo et al., 2007; Mkadmi et al., 2014; Qu et al., 2017; Xuan and Xu, 2017; Zhu et al., 2018). (Mohamed and Li, 2017) presented a numerical study carried out to evaluate the stresses in backfilled stopes overlying, compared with the case of a single isolated backfilled stope, the numerical results show that the stress magnitudes in the overlying backfill are considerably increased due to the excavation of the underlying stope (Mohamed and Li, 2017). Zhu et al. (2020a) used the filling scheme to recover wide coal pillars, investigated the stability of coal pillars, the structural characteristics of the overlying strata and the paste filling technical parameters in coal pillar after strip mining through laboratory test (Zhu et al., 2020a), numerical simulation and physical simulation, and put forward a more feasible filling and remining scheme (Liu et al., 2017; Cao et al., 2018; Jiang et al., 2020; Shao et al., 2021). Luan et al. (2017) introduced a new technique for filling and remining thin coal seams, including the development of filling materials, the design and key technology of the filling system for thin seam working faces (Luan et al., 2017). Tuylu, (2022) studyed fly ash with four different chemical compositions (TFA, SFA, YFA, and CFA) was used as a cement substitute in CPB. By substituting fly ash with different chemical compositions in different proportions, CPB samples were created and their strength was elucidated according to 28, 56, and 90-day curing times (Tuylu, 2022). Sun Q. et al. (2021) used short-strip coal pillar recovery with cemented paste backfill (Sun Q. et al., 2021). They developed a paste filling recovery method for residual room coal pillars and investigated its performance through numerical simulation (Luan et al., 2017; Zhou D. W. et al., 2019; Mu et al., 2019; Liu et al., 2020; Sun Q. et al., 2021; Tuylu, 2022). Mamadou Fall et al. (2007) discussed the stress–strain behaviours of cemented paste backfill (CPB) subjected to uniaxial compression and conventional triaxial tests (Fall et al., 2007). In the mining process, in order to solve the problems of rock stratum movement and solid waste disposal, engineers, technicians and researchers have always adopted the filling and remining method. They have also studied the response of formation to partial backfilling and mining technique (Chen et al., 2010; Du et al., 2019b). It is stated that the partial use of C-Class fly ash instead of cement in paste backfill greatly increases the strength in long-term curing (Benzaazoua et al., 2002; Cihangir et al., 2015; Ercikdi and Yilmaz, 2019). Taking into account different geological conditions, Ning et al. (2021) studied the stress distribution on the floor boundary during open-pit mining and backfill mining above the confined aquifer (Ning et al., 2021). These two mining types were simplified as mechanical problems under different boundary conditions. The stress distribution and floor failure evolution in strip mining and filling replacement mining were studied with an elastic mechanics method (Sun and Wang, 2011; Chang et al., 2014; Sun et al., 2018).

Some scholars adopted FLAC3D numerical simulation to study the sensitivity of the main control factors of surface movement and deformation in strip filling and remining, which has important practical significance for protecting surface structure, reducing ecological damage and realizing green and sustainable development of coal mine (Zhang et al., 2016). Based on the limit equilibrium theory, Zhu et al. (2020) established the calculation formulas for the widths of the crushing zone, plastic zone and elastic zone of different types of composite supports, and proposed the design methods for the safety widths of different types of composite supports, providing a theoretical basis for the stability analysis of composite supports (Zhu et al., 2020b; Zou et al., 2020). Nevertheless, studies regarding the recovery of shallow narrow coal pillars have rarely been reported.

In order to increase the mine life and improve the recovery rate of resources, this paper takes the 16E104, 16E106, and 16E108 working faces of Jisuo Coal Mine as the engineering background, and puts forward and implements a coal pillar remining and disaster pre-control technology for strip goafs. Filling and remining is carried out with a filling material comprised of construction waste as the aggregate, a proprietary three-stage continuous concrete mixing device and a large domestic displacement concrete pump used as the filling power system. This technology allows the recovery of about 500 strip coal pillars with modest surface subsidence. Verification through underground mine pressure monitoring and surface settlement observation reveal that the strip filling bodies can work successfully in place of underground coal pillars without damaging the buildings or the environment, providing an effective method for recovering coal pillars. The strip filling and remining technology is effective in controlling the surface movement and deformation and protecting surface buildings. It also provides useful clues for other mining areas with similar geological and mining technical conditions.

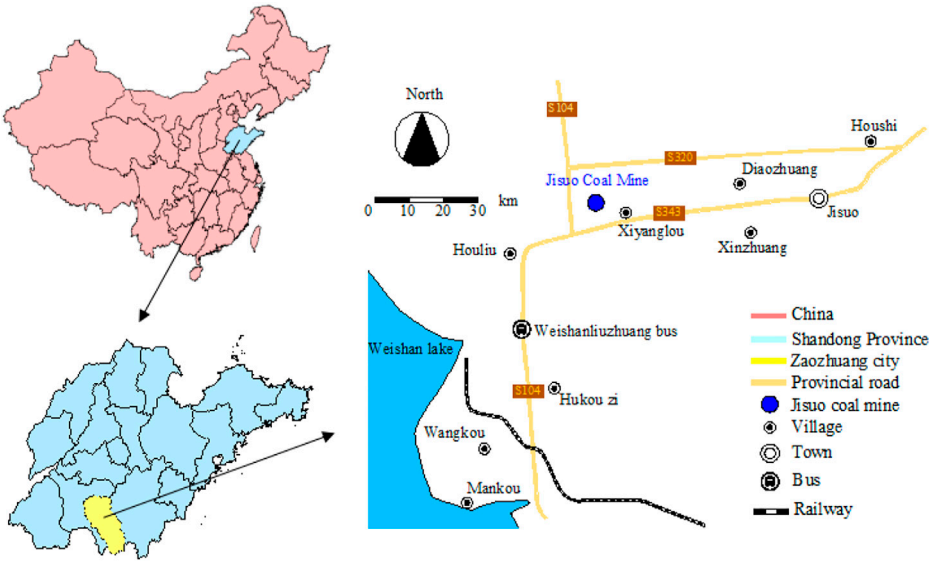

FIGURE 1
Mine location.

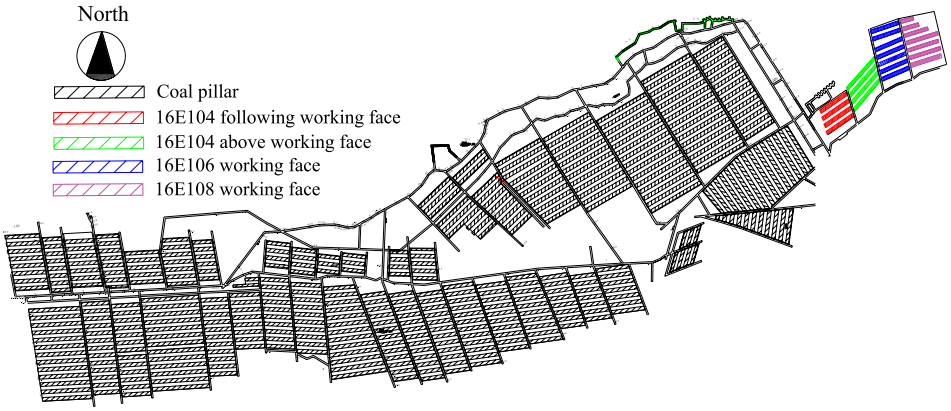

FIGURE 2
Distribution map of the remining pillars in Jisuo Coal Mine.

2 Engineering background

2.1 Mine overview

Jisuo Coal Mine is located at the southern end of Wangchao exploration area of Tengbei coalfield. The mine field is of plain terrain with high population density. Coal under village accounts for more than 80% of the recoverable reserves of the mine. The length of the mine field is about 5.8 km. The average width is about 1.2 km, and the mine field area is about 7.0 km^2. Figure 1 shows the location of the mine.

Since the 1990s, Jisuo Coal Mine has been operating for almost 20 years under the villages by means of strip mining. So far, 655 strips have been mined, and a total of 807,000 tons of coal resources have been recovered. However, 564 strip coal pillars as the support of the overlying strata are still left underground, resulting in a stagnant coal reserve of 717,000 tons. The untapped reserves under the village are about 5.61 million tons, as shown in

10.3389/feart.2022.1051245

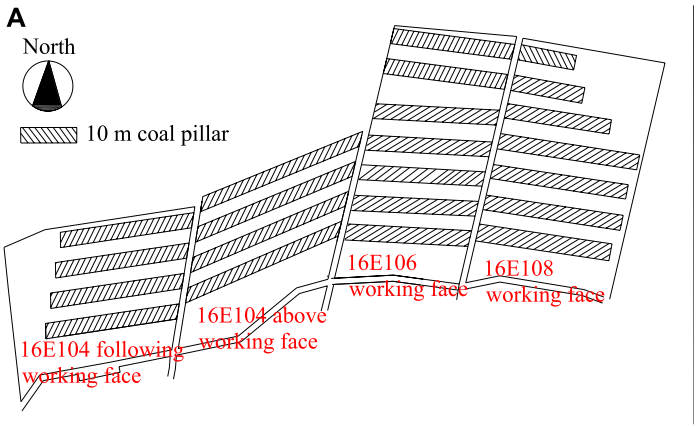

Panel layout of the study site

B

Lithology	Thickness (m)
Limestone (ten)	4.33
No.16 coal	1.21
Sandy mudstone	2.93
Limestone (eleven)	1.70
No.17 coal	0.65
Sandy mudstone	3.10
Mudstone	3.34
No.18 coal (on)	0.50
Siltstone	5.80
No.18 coal (under)	0.60
Limestone (twelve)	4.70
Sandy mudstone	1.60
Limestone (fourteen)	13.10

Coal strata distribution and geological description

FIGURE 3
Panel layout of the study site and coal strata distribution and geological description, **(A)** Panel layout of the study site, **(B)** Coal strata distribution and geological description.

Figure 2. With the depletion of recoverable reserves, the mine is facing the threat of closure and shutdown.

2.2 Overview of working face

In order to investigate the feasibility of remining strip coal pillars, filling remining test was carried out on 16E104, 16E106, and 16E108 working faces. There are no buildings on the ground in this area. Surface subsidence was observed after backfilling to provide basis for the filling and remining of the other areas. The coal seam mined in the test working face is Coal 16, which has an average thickness of 1 m and a dip angle of 5°–10°. Its occurrence is stable or relatively stable, and its thickness variation is insignificant. The coal bed texture is simple and is a comparatively regular coal seam. The average vertical depth of mining is 120 m. The roof is limestone with a thickness of 5.3 m and the floor is mudstone with a thickness of 4.3 m. The length of the working face is 80 m. The original strip mining scheme of the working face was to mine at a 10 m interval in width, leaving

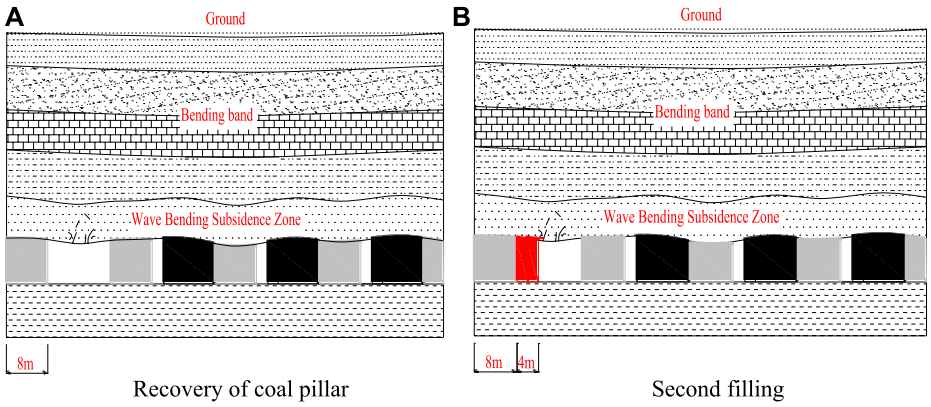

FIGURE 4
Change of direct roof, **(A)** Recovery of coal pillar, **(B)** Second filling.

pillars with equal width. Therefore, there are a large number of 10-m wide coal pillars left. Figure 3 shows the layout of the working face and the histogram of the rock stratum.

3 Filling mechanism, process, and related equipment

3.1 Analysis of filling mechanism

As strip mining (mining at a 10-m-wide interval) was applied before the 16E104, 16E106, and 16E108 working faces were filled, the direct roof above the working face showed a wavy flexual subsidence as a result of the load from the overlying strata while the overlying strata showed flexual subsidence as a result of its own weight (Deng et al., 2016; Zhou N. et al., 2019). As it was quite a long time since the working face was mined, after the first filling, the overlying roof remained the same state as before.

During the first filling, the last filling strip has to cure for 28 days. It takes 1–2 days to fill one single goaf. The working face cannot be remined until 38 days after the filling. Due to previous mining, the direct roof above the coal pillar in the first strip continued to sink flexually, with fine fractures being produced at the same time, but the direct roof in front of the working was not affected significantly, as shown in Figure 4.

After the last strip of coal pillar in the working face had been recovered, the working face has also been filled for the second time. Under the mine pressure, the direct roof above the original strip of coal pillar subsided flexually. The original goaf served as the "pier" due to the existence of the filling body. At the same time, more cracks began to appear inside the direct roof. At the end of the recovery of the working face, the subsidence of the wavy flexual subsidence zone above the working face gradually increased, as shown in Figure 5.

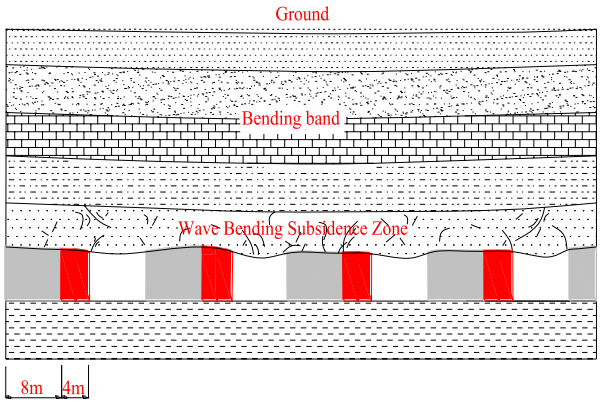

FIGURE 5
Replacement of all coal pillars.

3.2 Filling process

3.2.1 Related parameters

The working faces of Jisuo Coal Mine include 16E104, 16E106 and 16E108, with an average depth of 120 m and an average length of 80 m. The width of the filling body is calculated according to the formula of total weight of overlying strata, as shown in (Eq. 1):

$$w_z = \frac{H \times L \times \gamma}{\sigma_t \times 100}, \quad (1)$$

Where w_z is backfilling width, m; L is length of working face, m; H is the mining depth of working face, m; γ is average volume density of rock, t/m3; σ_t is unidirectional compressive strength of backfill material, MPa.

TABLE 1 Safety factors for different mining schemes.

Filling scheme	Strength of filling material/MPa	The width of the filling/m	Safety factor (λ)
Full filling	5	20	1.6
	5	12	1.0
12 m filled, 8 m left	7.5	12	1.5
	10	12	2.0

In the filling scheme, the final setting strength of the filling body is calculated as 5 MPa, so the support strength per unit area is 5 MPa. The weight of overburden per unit area is 3 MPa, λ=1.6.

As shown in Table 1, increasing the filling width and strength can improve the stability of backfilling, but it also increases the filling cost. With the increase of mining depth, the stability of the strip filling body decreases, thus degrading the adaptability of the mining scheme. Considering the actual situation of the coal mine, the scheme with safety factor of 1.5 is selected for the scheme of "12 m filled 8 m left".

3.2.2 Filling system

1) Top-down filling system for Jisuo Coal Mine, first, the filling process system was installed in locations with suitable distance to the filling face to ensure short distance, low cost and convenient access. Second, filling aggregates, including coal gangue and construction waste, are crushed. Then, coal ash from power plants is utilized to mix well with the coal ganue, construction waste, cement and water with proper proportion in a mixer and stored in the material warehouse. The above processes form the aggregate processing system and paste material preparation system. The paste material conveying system uses a concrete pump to transport the filling material to the underground filling pump through the filling pipeline and to the goaf through the filling pipeline. Filling is operated in two stages: first filling and second filling after the residual coal pillar is recovered. The filling isolation system is composed of formwork and hydraulic pressure prop. The pathway for the filling material to enter into the well is independent from the pathway for coal recovery. The whole filling system can be divided into four parts: an aggregate processing system, a paste material preparation system, a paste material delivery system and a filling isolation system. The backfilling system and the process flow are shown in Figure 6.
2) Underground filling system to prevent the backfill concrete from flowing to other areas, a relatively closed room must be isolated so that the backfill concrete can well contact the roof. In this process, hydraulic pillars and building formwork are used as the frame. Braids are laid inside to form a temporary isolation wall, as shown in Figure 7. In this way, the backfill slurry can be pumped to the isolated backfill area through the pipe.

To avoid serious pipeline blockage caused by filling pump faults and other reasons, a sedimentation tank was installed near the filling station in Jisuo Coal Mine. An emergency treatment ditch was excavated in the filling drilling chamber. Tees were mounted along the filling pipe at intervals to ensure that quick treatment was possible to avoid pipe blockage in case of any power interruption or machine shutdown.

3.2.3 Filling scheme

According to the protection requirements of buildings and the actual mining situation of the mine, in order to ensure that the weight of overburden can be transferred to the "pier" successfully (Tan et al., 2017; Zhang et al., 2017), a filling and remining scheme of mined area (Coal 16) under village was adopted: first filling then mining, then strip remining and strip filling. In this scheme, the preparation for the first filling is to seal the area to be filled with building formwork and hydraulic pillars to prevent slurry leakage, and hang a layer of woven cloth on the inside to form a closed space. Because the coal seam inclination of Jisuo Coal Mine is small, four distribution pipes are evenly arranged in each filling strip to fill from the low end to the high end of the elevation. When the filling body reaches the expected strength, the middle pillar strip is mined, and the strip width is D_1 = 8 m. After the coal pillar strip is completely recovered, the coal pillar is filled for the second time. The filling materials will connect with the initial filling body, serving as an integral filling pillar to support the roof. The backfilling width is D_2 = 4 m.

1) According to the low-to-high direction of floor elevation, all mined-out strips in a working face are filled from north to south, with a filling width of 8 m. With concrete filling pouring in, stress meters are buried to monitor the stress change inside the filling body in real time.
2) There are generally 6–10 mined-out strips in a working face, and each will take 1–2 days to fill, thus in total it will take 15–25 days to fill all cavities in a working face.
3) When the last filling strip in the first working face meets the setting time of 28 days, the mining working face can be

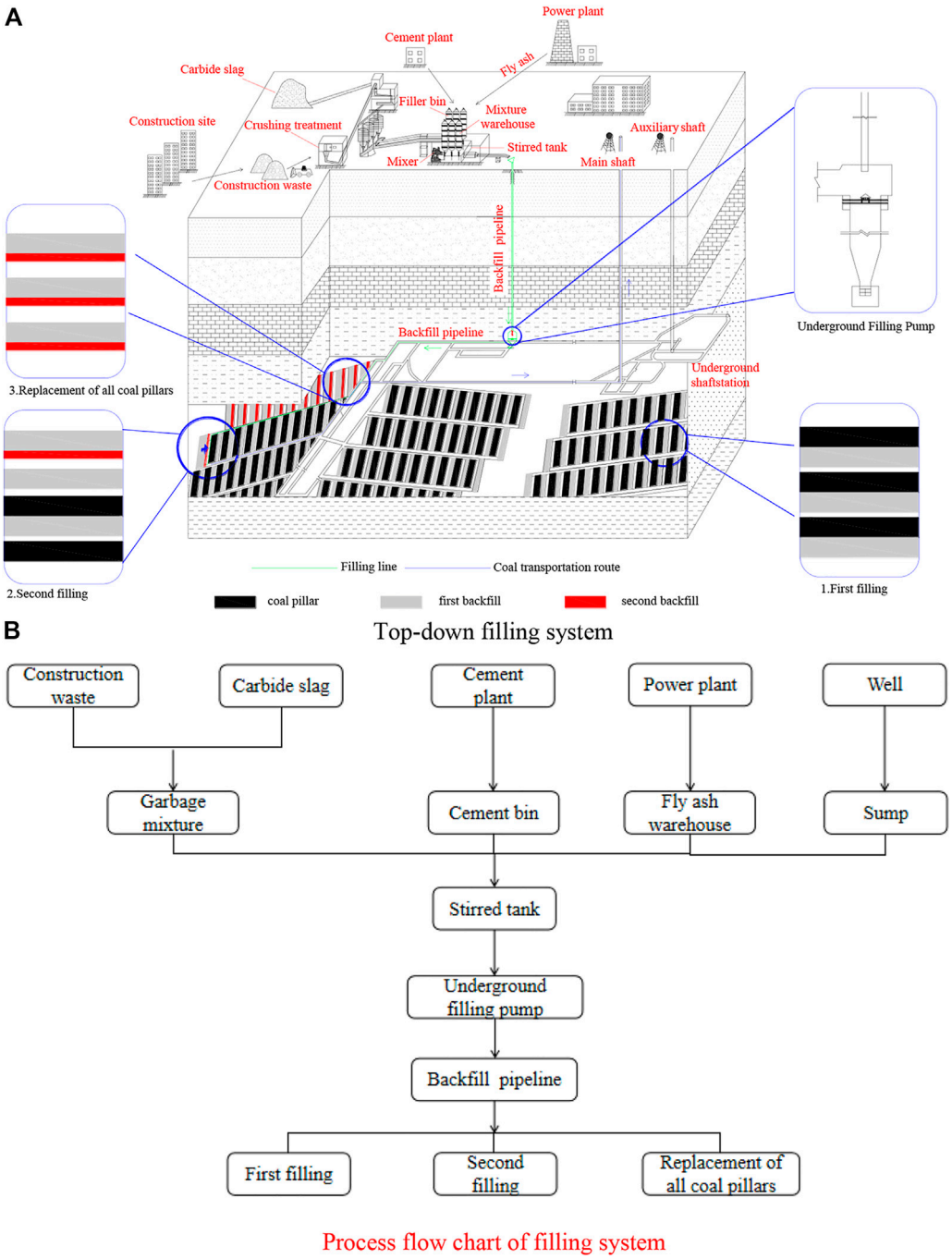

FIGURE 6
Filling system flow chart, **(A)** Top-down filling system, **(B)** Process flow chart of filling system.

arranged according to the low-to-high direction of floor elevation, or from north to south in practice, and the original coal pillar strip can thus be mined. It takes 5–6 days for a coal pillar strip to complete mining. At this time, the second working face has been filled.

4) After the pillar strip mining is completed, the second backfilling shall be carried out in time with a backfilling width of 4 m, and corresponding dynamic monitors shall be arranged to monitor the corresponding variation characteristics of the surrounding rock in the goaf,

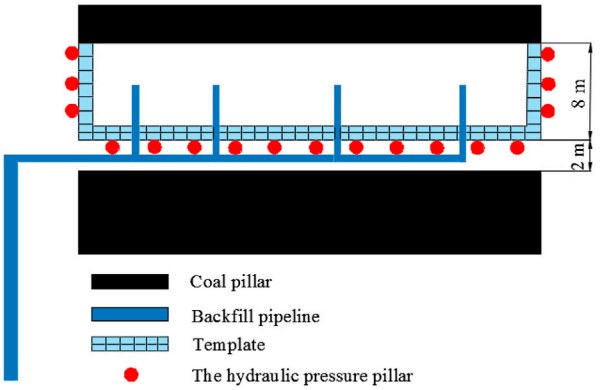

FIGURE 7
Transport diagram of filling paste.

including roof displacement, roof subsidence, bolt/anchor cable stress etc.

5) Generally, five to nine coal pillar strips need to be mined in a working face, thus it takes 25–45 days to complete all mining operations. Therefore, when the last pillar strip mining is completed, the first secondary filling body (4 m-wide filling body) in the first working face and the last primary filling body in the second working face have solidified for more than 28 days. At this time, the northernmost pillar strip of the adjacent second working face can be mined. The strip retreat mining method is adopted, with single hydraulic props and filling strips to support the roof, and full height mining is applied in operation. The filling sequence is shown in Figure 8.

3.2.4 Filling related equipment

3.2.4.1 Aggregate processing system

Aggregate processing mainly includes crushing, iron removal, impurity removal and screening. Construction waste is crushed in two stages by jaw crusher and impact crusher to ensure the particle size and the purity of filled aggregate can meet required standards. Jaw crusher is shown in Figure 9.

3.2.4.2 Paste preparation system

In the process of backfill preparation, firstly, the processed aggregate is screened and subdivided according to the required ratio of backfilling materials. Secondly, it is mixed with fly ash, cementitious materials and water in a required proportion through the mixing system. Paste backfill concrete is thus formed, ready to be used for the next process. The filler bin and water sump are shown in Figure 10.

As shown in Figure 11, fly ash and water are stored in one tank. The mixing plant is a three-stage continuous mixing plant, including three cylindrical devices with spiral stirring apparatus. The mixing plant has the following characteristics: 1) Three machines are installed on the same base to form a three-stage facility which can operate synchronously; 2) The upper machine entrance is square shaped and can be loaded automatically; 3) The intermediate machine is equipped with automatic water supply device; 4) The bottom machine is equipped with automatic raw material feeding and batching devices.

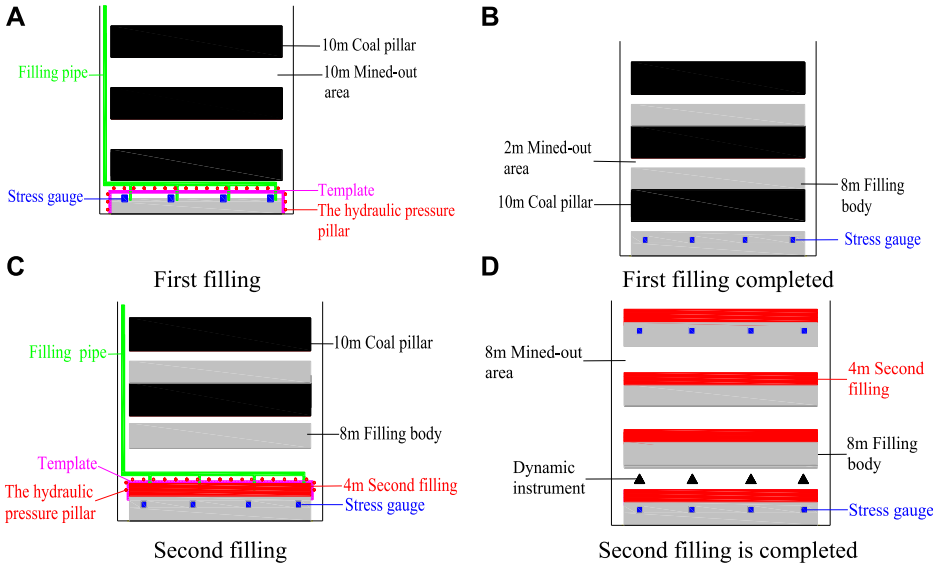

FIGURE 8
Filling sequence diagram, **(A)** First filling, **(B)** First filling completed, **(C)** Second filling, **(D)** Second filling is completed.

FIGURE 9
Jaw crusher.

3.2.4.3 Paste conveying system

The system includes a concrete pump and a pipeline pumping system. The concrete pump is used to deliver the paste concrete to the filling working surface for filling. The mining concrete pump is one of the key equipment for goaf filling and mining, and its actual pumping capacity is not less than 120 m^3/h. HGBS200/14-800 industrial filling pump, a large displacement concrete pump developed by China, is selected for the pumping purpose. The pipeline pumping system consists of filling standpipe, surface pipelines, underground trunk pipeline and underground branch pipeline. Pumping process: The concrete paste is delivered by two surface filling pumps to run through the ground pipes, drill pipes, tunnel pipes, working face pipes, three-way valves and then reach the slurry bin, from which it is pumped into the formwork to fill the goafs.

4 Field monitoring

4.1 Underground monitoring equipment and layout

In order to master the control effect of strip filling and remining, strata movement monitoring was carried out on the underground filling mining face (Li and Aubertin, 2008; Widisinghe and Sivakugan, 2016; Liu et al., 2022). Monitoring indicators include roof displacement and vertical stress of filling body. Devices for filling body stress monitoring and roof dynamic monitoring are shown in Figure 12.

The function of the GYD60 filling body stress gauges are to measure the vertical stress in the backfilling area. Before the first strip filling, they were placed in the designated area, and the related monitoring equipment was also arranged, then filling commenced to cover the stress gauges and the stress data was collected and sent back to the collector through the communication line. The function of the KY-82 roof dynamic instruments is to measure the change of rock stratum displacement, monitor the cumulative subsidence of stope roof, and work with pressure measurement to reflect the characteristics of roof. The dynamic instrument was placed in the strip coal pillar, and space at regular intervals has been prepared to install the dynamic instruments. The observation data were collected on a regular basis.

Three groups of rock movement monitoring equipment were set for each 6 backfills, each containing four KY-82 roof dynamic meters and four GYD60 backfill stress meters. Four stress meters were placed in the filling body built in the first filling, with a length of 80 m and a width of 8 m. The spacing between two stress meters (used to monitor the vertical stress in the backfill body) was 20 m. After the second filling was completed, four roof dynamic instruments were placed in the 8-m-wide goaf to

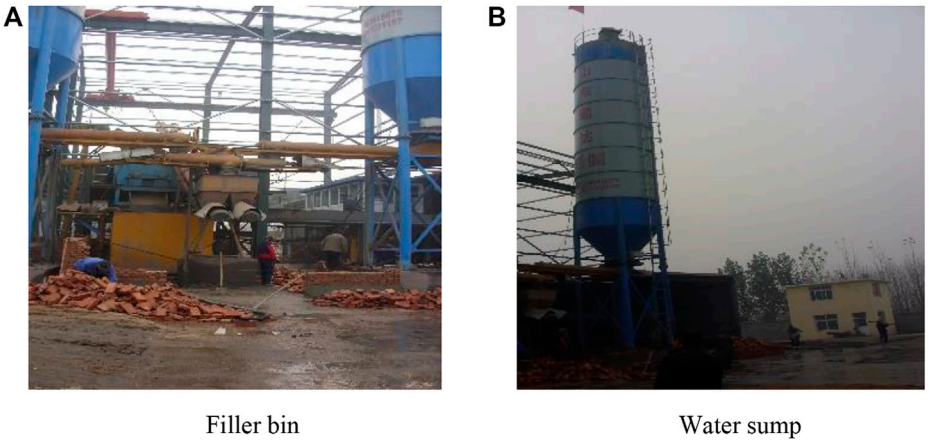

FIGURE 10
Backfill paste and concrete preparation system, **(A)** Filler bin, **(B)** Water sump.

FIGURE 11
Concrete mixing device.

monitor the cumulative subsidence of stope roof, which worked simultaneously with the stress gauges to reflect the roof characteristics. The monitoring equipment layout is shown in Figure 13.

4.2 Surface monitoring content and monitoring point layout

In order to learn the surface subsidence and evaluate the effect of strip filling and re-mining, the surface subsidence observation stations were set up above the 16E104, 16E106, and 16E108 working faces of Jisuo Coal Mine. Monitoring indicators include vertical settlement, surface curvature and horizontal deformation. Observation lines were arranged along the 16E104, 16E106, and 16E108 working faces, and monitoring lines were arranged perpendicular to the 16E106 working face, as shown in Figure 14.

5 Results and discussion

5.1 Response of underground strata to coal pillar recovery

5.1.1 Vertical stress in backfill area

GYD60 stress meters were installed in the filling area in advance to monitor the vertical stress of the filling body (Helinski et al., 2010; Doherty et al., 2015). Three groups of strata movement monitoring equipment were set for every six filling bodies, and each group had four GYD60 stress meters. The monitoring results are shown in Figure 15.

As can be seen from Figure 15A, the horizontal axis shows the number of days after the installation of the stress gauge, the longitudinal axis shows the stress value inside the filling body. The filling body of 1 # station became solidified within 35 days, and the stress change was relatively small. After 35 days, with the mining of coal pillar, the vertical stress in the filling area gradually increased. During the 50–60 days, the stress increased at the fastest speed. This phenomenon had an significant relationship with the distribution of bearing pressure in front of the working face until it reached the maximum value, and the internal stress of the filling body gradually levelled off during the 65–75 days. There were four groups of stress convergence values monitored by 1 # station, which were 4.74 MPa, 4.93 MPa, 5 MPa and 5.27 MPa respectively. As can be seen from Figure 15B, the change rate of the internal stress of the filling body at 2 # station was very small within the first 40 days, and the stress gradually increased during the 40–70 days. The rising rate was the fastest during the

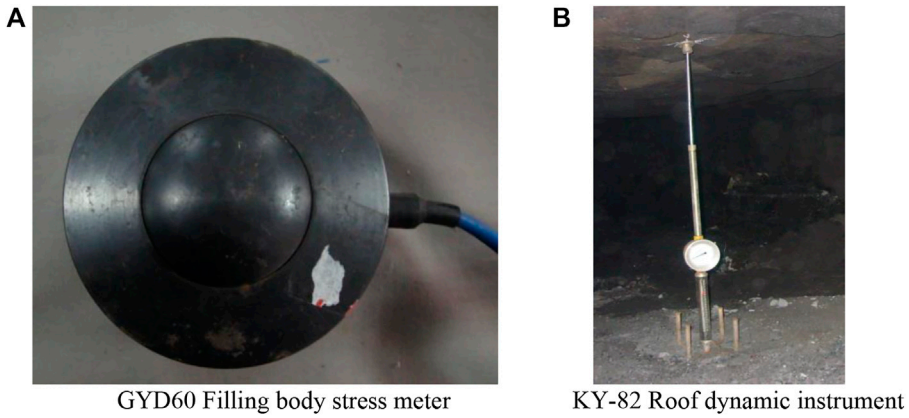

FIGURE 12
Monitoring equipment, **(A)** GYD60 Filling body stress meter, **(B)** KY-82 Roof dynamic instrument.

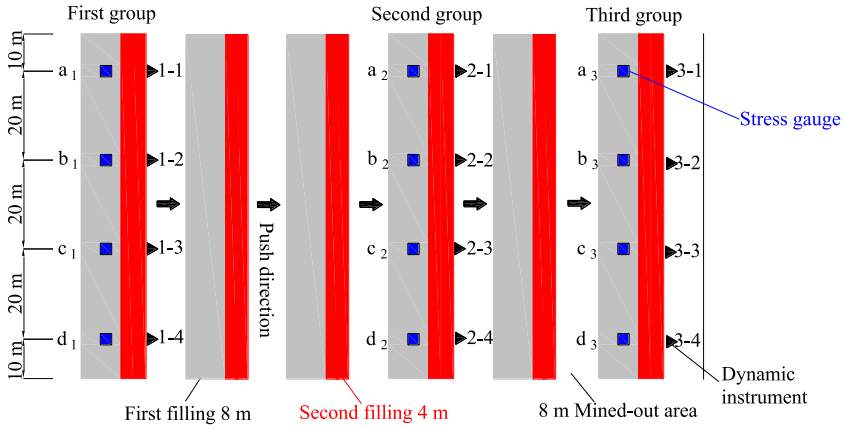

FIGURE 13
Top view of instrument layout.

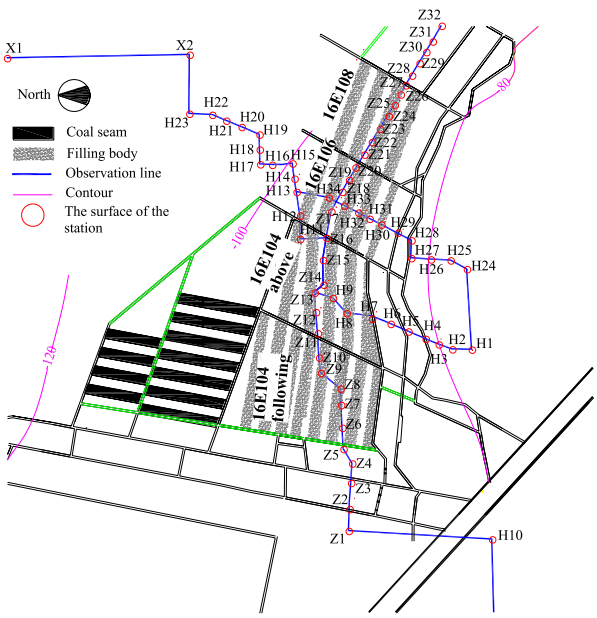

FIGURE 14
Location map of surface stations.

55–65 days, and the stress reached the maximum value on about the 70th day and then gradually became stabilized. There were four groups of stress convergence values monitored by 2 # station, which were 5.04 MPa, 4.95 MPa, 5.54 MPa, and 5.66 MPa respectively. It can be seen from Figure 15C that the increase rate of internal stress in the filling body of 3 # measuring station began to accelerate on the 45th day. With the mining of the working face, the stress increased sharply during 50–70 days, and the stress reached the maximum on about the 70th day. There were four groups of stress convergence values monitored by 3 # station, which were 4.57 MPa, 4.62 MPa, 4.89 MPa and 4.92 MPa respectively.

The variation pattern of vertical stress in coal pillar recovery can thus be seen. With the replacement of coal pillar, the vertical stress increased in varying degrees. The stress change with stoping can be divided into three stages: It was relatively stable at the initial filling stage; stress increased gradually during the 35–45 days due to the occurrence of ground pressure; the stress gradually stabilized during the 65–75 days.

In the early days after the stress meters were installed in the filling body, the vertical stress barely increased, remaining at a stable state. It took about 65–75 days for the vertical stress to stabilize. The mine pressure distributed on the coal pillar can be transmitted smoothly to the filling body, and the filling belt was strong enough to bear the weight of the rock strata.

5.1.2 Monitoring of underground roof dynamic instruments

The displacement meter was used to monitor the roof displacement in the filling area, which could reflect the deformation law and the compression ratio of the filling body. Three groups of rock movement monitoring equipment were set for each 6 filling bodies, and each group was provided with four KY-82 roof dynamic instruments. Based on the monitoring results, the variation pattern of roof displacement was drawn. In these figures, the horizontal axis shows the time span for installing the displacement meters, and the vertical axis shows the underground roof displacement. The variation curve based on the monitoring results of the roof dynamic instrument is shown in Figure 16.

As shown in Figure 16A, by the monitoring results of 1 # station, the slope of curve is higher at first and the deformation rate of roof becomes increasingly faster, indicating that displacement took place between roof and floor; The

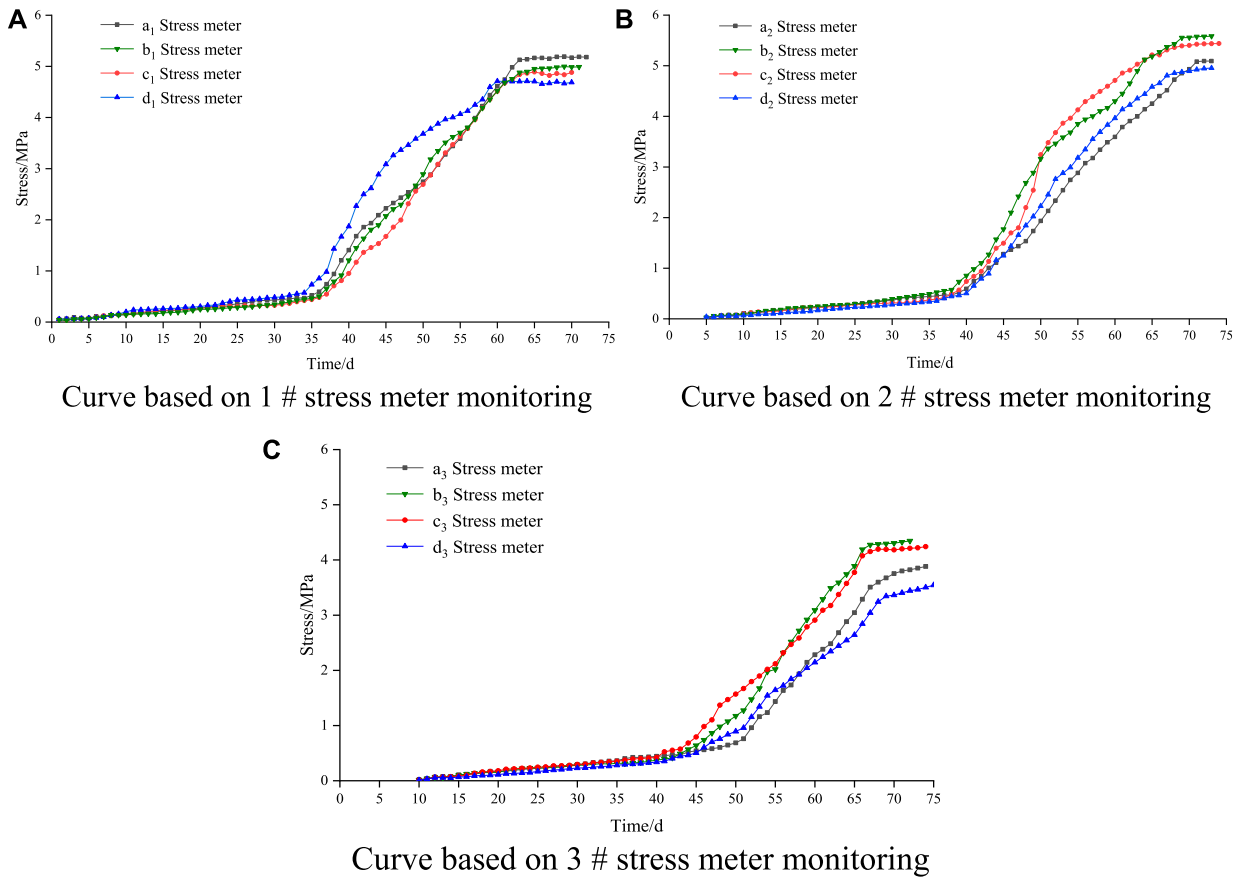

FIGURE 15
Stress evolution law, **(A)** Curve based on 1 # stress meter monitoring, **(B)** Curve based on 2 # stress meter monitoring, **(C)** Curve based on 3 # stress meter monitoring.

deformation of roof was about 50 mm on about the 50th day, and then the slope decreased gradually. After about 70 days, the roof and floor reached a stable state, which was consistent with the vertical stress monitoring results. The abnormal curve of roof subsidence monitored by one to four instruments in 1 # station was due to the development of faults here, and thus the subsidence speed was fast; the changes of other subsidence curves were normal. The maximum roof displacement of the four groups monitored by 1 # station were 52 mm, 51 mm, 53 mm, and 52 mm respectively. The mining height was calculated as 1.21 m, and the average compression ratio of filling body was 4.3%. It can be seen from Figure 16B that the roof deformation monitored by 2 # station has increased significantly from the beginning, and the roof subsidence rate was the largest between the 45th day and 55th day. The roof subsidence levelled off around the 70th day, and the cumulative roof subsidence was 58 mm. The maximum moving amounts of the four groups monitored by 2 # station were 56 mm, 55 mm, 57 mm, and 58 mm respectively. The average compression ratio of the filling body was 47%. It can be seen from Figure 16C that the roof of 3 # station sank slowly from the beginning. With the mining of the working face, the roof subsidence increased gradually from Day 40, and the cumulative roof subsidence was 59 mm on about Day70. The maximum subsidence of the four groups monitored by the 3 # station were 57 mm, 56 mm, 59 mm, and 61 mm respectively. The average compression ratio of the filling body was 48%. After the mined-out area was filled, the roof rock beam became stable and the ground pressure became small, which means the requirement of replacing coal pillar has been met and the overlying strata was effectively controlled.

5.2 Surface response of pillar extraction techniques

Surface deformation were surveyed to evaluate the effect of pillar extraction. The related indicators include the vertical

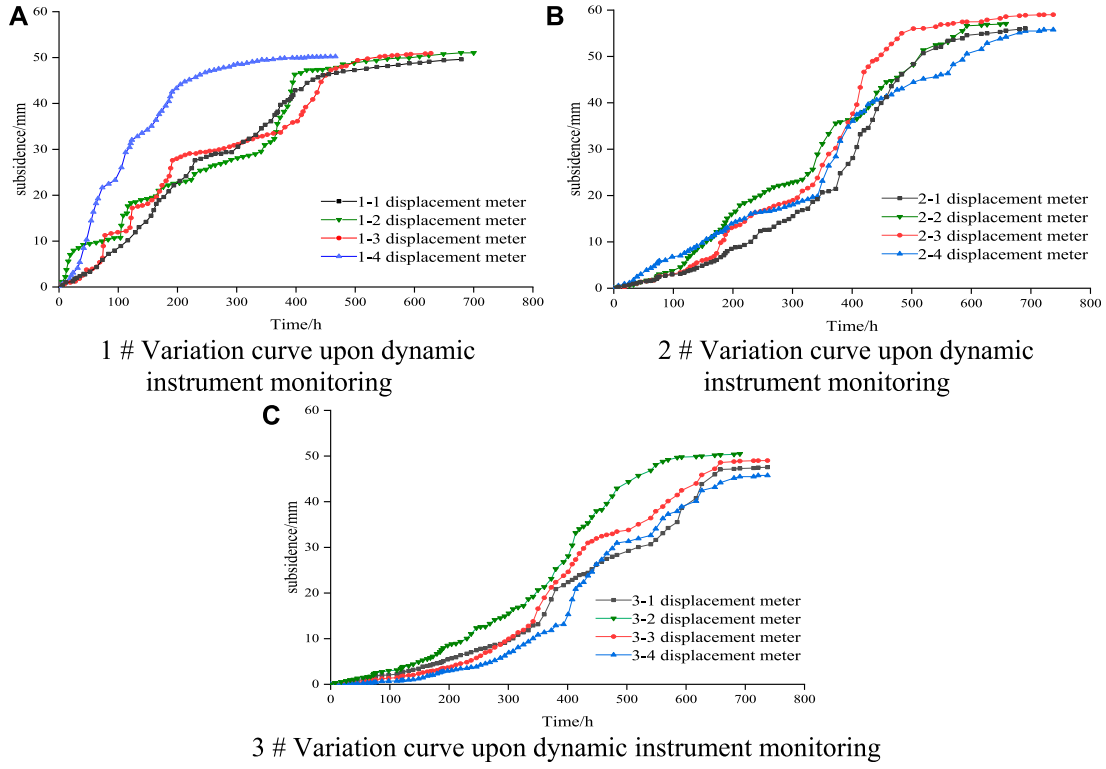

FIGURE 16
Variation curve upon dynamic instrument monitoring, **(A)** 1 # Variation curve upon dynamic instrument monitoring, **(B)** 2 # Variation curve upon dynamic instrument monitoring, **(C)** 3 # Variation curve upon dynamic instrument monitoring.

settlement value, horizontal deformation value and surface curvature. All calculations were performed on the computer using specially designed programs.

5.2.1 Surface subsidence

The point with a subsidence of 10 mm was determined as the boundary point of surface subsidence basin according to the regulations (Chen et al., 2016; Janez et al., 2018). The angular parameters, including the strike boundary angle (59°), the inclined upward boundary angle (62°) and the inclined downward boundary angle (57°) were determined under this geological condition. The contour map of surface subsidence after mining of the test working face was drawn, as shown in Figure 17.

Surface subsidence is the vertical component of the surface movement vector of the main section (Qu et al., 2010). After the coal seam is mined, the stress state of the strata above the goaf is redistributed. With the increase of the goaf, different types of strata collapse and sink one after another until a stable condition is achieved (Guney and Gul, 2018; Zou et al., 2018a; Navid et al., 2019).

As shown in Figure 17, the three working faces of 16E104, 16E106, and 16E108 were adjacent to each other, and the overlying strata activities affected each other during the filling and mining of each working face. The subsidence values of the ground monitoring points at the same distance from the center line of the four working faces were of little difference and showed symmetry. From the initial movement to stability, the subsidence of the monitoring points in the middle of the working face was all greater than that at the boundary of the working face. Taking the monitoring points in the inclined direction of 16E104 working face as an example, after the surface was stable, the maximum subsidence was 50 mm, and the subsidence at the boundary was 14 mm. From the boundary of the working face to the center of the working face, the surface subsidence showed a steady increasing trend. The maximum subsidence in the inclined direction of 16E106 working face was 48 mm; The surface subsidence characteristics of 16E108 working face were similar to those of 16E104 working face. The subsidence increased steadily along the dip direction, and the maximum subsidence was 48 mm. The four working faces gave rise to a subsidence basin through surface subsidence, and the maximum subsidence value was in the center of the working face.

5.2.2 Surface tilt

Detecting surface tilt is one of the main methods of fixed-point observation of surface deformation. Tilt refers to the

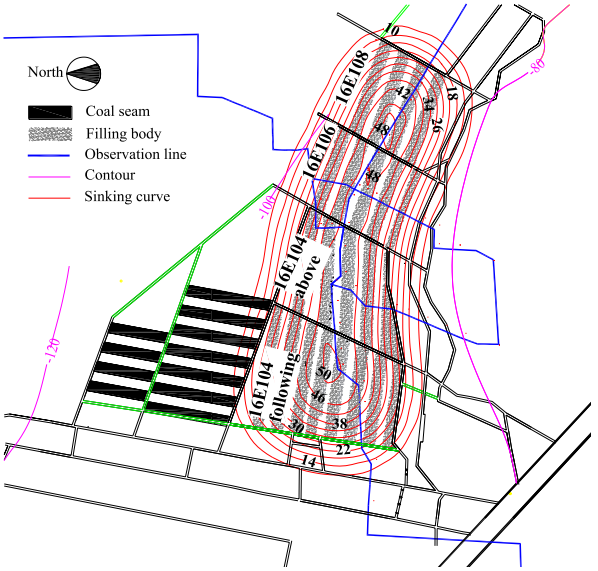

FIGURE 17
Surface subsidence contour map.

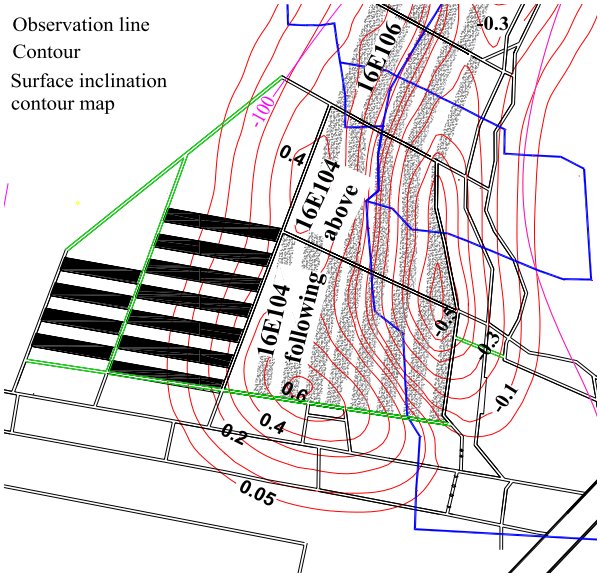

FIGURE 18
Surface tilt contour map.

change of subsidence per unit length of the surface. It mainly measures the relative movement in the vertical direction at a certain point on the surface. Inclination is the first derivative of surface subsidence. There are two groups of inclinations in different directions, the inclination between boundary point and maximum subsidence point has positive value and negative value.

As shown in Figure 18, the three working faces of 16E104,16E106, and 16E108 were adjacent to each other. The working face and its surrounding areas had tilted in different directions with varied degrees. The surface tilt value above the working face was larger than that at the boundary of the working face. The tilt contours in the middle of 16E104 working face and 16E108 working face were denser; On the whole, the surface tilt increased steadily from the boundary to the top of the working face, and the tilt degree increased gradually. The minimum surface tilt value around the three working faces was 0.05 mm/m, and the maximum surface tilt value above the working face was 0.65 mm/m. The surface tilt change was affected by the characteristics of surface subsidence. The surface tilt at the center of the four working faces was larger and the boundary tilt was smaller.

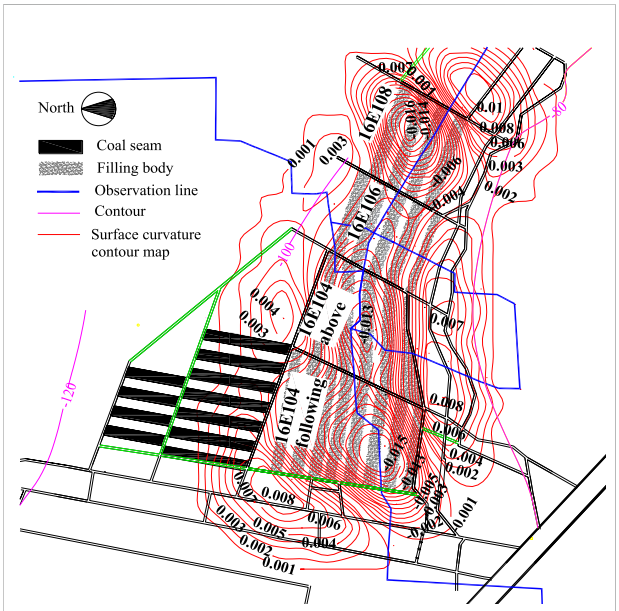

FIGURE 19
Surface curvature contour map.

5.2.3 Surface curvature

Surface curvature represents the degree of surface subsidence and bending, Unit: mm/m^2.

As shown in Figure 19, the three working faces of 16E104, 16E106, and 16E108 were adjacent to each other. The curvature contour at the boundary was denser than that above the working face, indicating that the surface curvature at the boundary was smaller than that above the working face; The greater the subsidence curvature of the curve, the more the subsidence bending will become. Due to the influence of mining, the subsidence curve at the roof of the working face had obvious depression and protrusion near the mining boundary, the

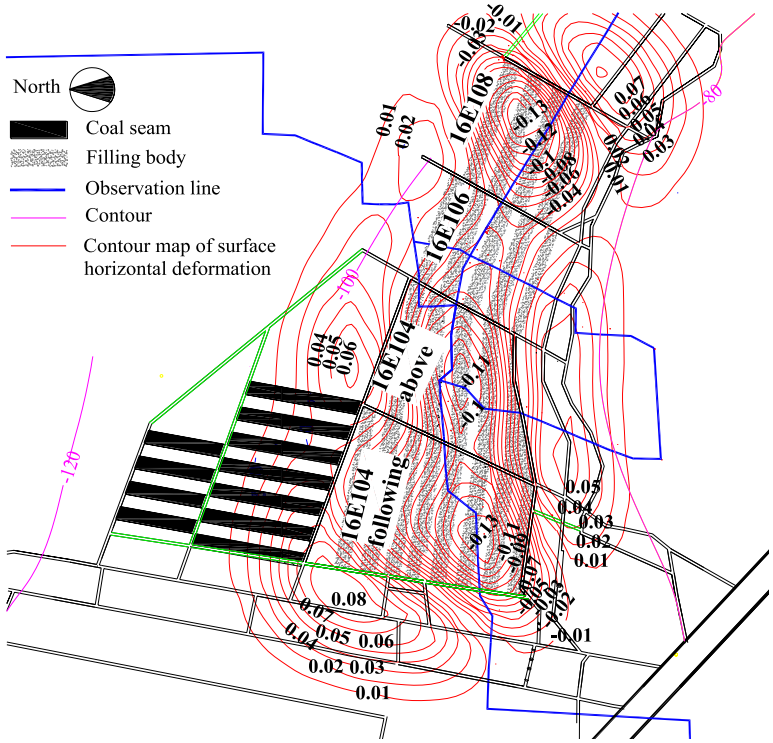

FIGURE 20
Surface horizontal deformation contour map.

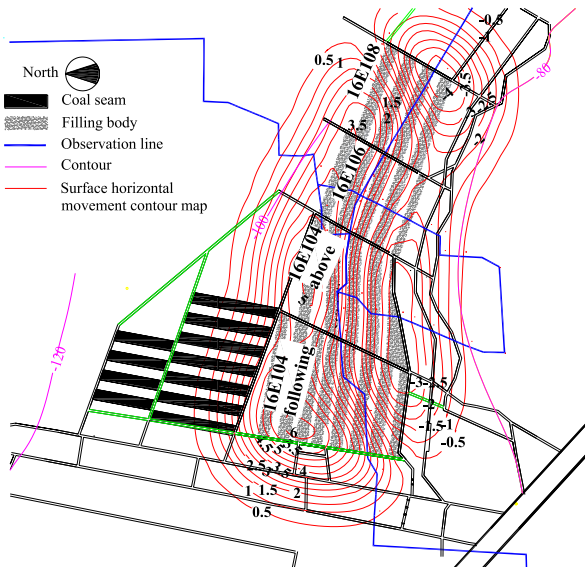

FIGURE 21
Surface horizontal movement contour map.

subsidence curvature of the surrounding rock was less than that of the roof of the goaf, i.e., the roof protruded downward into the goaf, and a subsidence basin was formed on the surface above the goaf.

The maximum curvature of 16E104 working face was 0.015 mm/m^2; The minimum curvature was 0.001 mm/m^2; The maximum curvature of 16E106 working face was 0.013 mm/m^2, the minimum curvature was 0.002 mm/m^2; The maximum curvature of 16E108 working face was 0.018 mm/m^2; The minimum curvature was 0.001 mm/m^2. Among the three working faces, the minimum curvature value was 0.001 mm/m^2 and the maximum curvature value was 0.018 mm/m^2, the variation characteristics of curvature was consistent with the surface subsidence and surface inclination. In conclusion, the filling effect was obvious and the surface subsidence was small.

5.2.4 Surface horizontal deformation

Horizontal deformation represents the change in horizontal movement per unit length, Unit: mm/m. The physical meaning of positive horizontal deformation indicates that the surface is subject to tensile stress, while the physical meaning of negative value indicates the surface is subject to compressive stress.

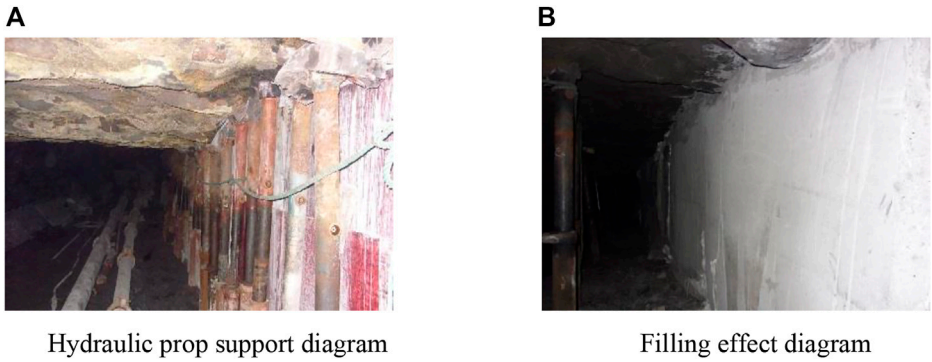

FIGURE 22
Filling support and effect diagram, **(A)** Hydraulic prop support diagram, **(B)** Filling effect diagram.

As shown in Figure 20, the three working faces 16E104, 16E106, and 16E108 were adjacent to each other. Influenced by mining in the working face, the surface showed different degrees of horizontal deformation. Such deformation was relatively large in the south of 16E104 working face and the south of 16E108 working face, but the horizontal deformation of 16E106 working face was relatively small because it was in the middle of the three working faces. In addition, as it sank into a subsidence basin, the surface at the junction of the three working faces was subject to tensile stress, and the maximum horizontal deformation at the junction was 0.08 mm/m; the surface above the working face was subject to compressive stress and the maximum horizontal deformation was 0.16 mm/m.

5.2.5 Surface horizontal displacement

Horizontal movement represents the horizontal component of the surface movement vector, and the variation of horizontal movement and tilt is similar.

As shown in Figure 21, horizontal movement from boundary point to working face increased gradually in three working faces of 16E104, 16E106, and 16E108. Due to the influence of mining, the contour lines of surface horizontal movement above the working face were dense. In the three working faces, the minimum horizontal movement was 0.5 mm and the maximum was 6 mm. As the terrain of the three working faces was relatively flat, from the curve distribution, the strike and inclination of surface movement generally conform to the general subsidence law. The horizontal movement deformation in the middle of 16E104 working face and 16E108 working face had an abrupt change, and the deformation value increased or decreased suddenly.

As mining of the working face proceeded, the surface subsidence gradually increased, and a subsidence basin was formed. According to the surface observation results, the maximum surface subsidence value was 44 mm (H13), and the subsidence at H32, H33, H34, H35, and H36 was 35 mm. By the follow-up observation results, the observation line of surface inclination and strike were gradually stabilized, and the 43 mm observed at point Z17 turned out to be the maximum change value of surface. Taking the subsidence process as a whole, there was no sudden change detected. The surface had continuous subsidence, and the whole subsidence basin fluctuated slightly with a fluctuation about 10 mm. In addition, it was concluded that the maximum surface subsidence after mining in 16E104, 16E106, and 16E108 working faces was 44 mm. The maximum inclination value was 0.65 mm/m; the maximum curvature value was 0.018 mm/m^2; and the maximum horizontal deformation was 0.16 mm/m. All of them were less than the surface deformation value of buildings suffering from grade I damage.

Based on the comprehensive consideration of the deformation value of surface movement, the stability of composite support, social and economic benefits, the strip coal pillar under the village was re-mined, which improved the recovery rate of coal resources, prolonged the service life of the mine and maintained the sustainable development of the mine. Meanwhile, it fundamentally eliminated the hidden dangers of major disasters such as surface collapse and building damage caused by strip coal pillar instability, and ensured the happiness and stability of people's life in the mining area, the harmonious development and long-term stability of society, which was of great practical and far-reaching significance.

In addition, Figure 22A showed the construction of filling formwork at the filling site, which was reinforced by hydraulic props to ensure that the concrete slurry would not leak. Figure 22B showed the effect of the filling body after removing the filling formwork. The filling body was well-structured and well-functioning, with no mechanical damage such as fracture.

6 Conclusion

Taking the strip-filling and second-mining test in Jisuo Coal Mine as an example, this paper verified effectiveness of this

technique by means of monitoring the underground mine pressure and observing the surface settlement. The results show that the strip re-mining technique after backfilling has an ideal effect in controlling surface settlement, effectively solving surface cracks and protecting ecology and surrounding environment.

1) In order to exploit the coal resources reserved under railways, rivers and buildings, a practical technique featuring strip re-mining after filling and disaster pre-control was proposed and implemented. With this technology, the construction waste is used as the aggregate to prepare the backfill material, and the self-developed three-stage continuous concrete mixing device and domestic large displacement concrete pump are used as the backfill power system. The workflow is determined as follows: aggregate processing, slurry preparation, slurry transportation and underground backfilling. The construction waste is used as the filling material to meet the needs of filling and mining. The whole schedule provides a new model for solid waste treatment of coal mine and green mining.
2) Taking Jisuo coal mine as the test object, this paper collected the data, through underground ground pressure monitoring and surface settlement observation, that the maximum stress is 5.27 MPa, the maximum roof subsidence is 59 mm, the maximum surface subsidence after mining is 44 mm, the maximum inclination is 0.65 mm/m, the maximum curvature value is 0.018 mm/m^2 and the maximum horizontal deformation value is 0.16 mm/m. These deformation values did not reach the damage limit of surface buildings, which verified the success of the test scheme.
3) Practice has proved that the application of strip filling re-mining technique in coal mining, especially mines under railways, rivers and buildings, has improved the stress environment of the stope, played a positive role in controlling surface subsidence, and is of great significance to the sustainable development of the ecological environment around the mining area. Therefore, this technology can provide some useful clues for the remining research of foreign coal resources.

Data availability statement

The original contributions presented in the study are included in the article/Supplementary Material, further inquiries can be directed to the corresponding authors.

Author contributions

Conceptualization, JH and AC; methodology, HB; software, XL; formal analysis, YS; resources, XW, JZ, and HL. All authors have read and agreed to the published version of the manuscript.

Funding

The study was financially supported by Taishan Scholars Project, the National Natural Science Foundation of China (Grant Number. 52174121 and 52104204), Natural Science Foundation of Shandong Province (ZR2021QE170).

Acknowledgments

We thank the reviewers for their constructive feedback.

Conflict of interest

The authors declare that the research was conducted in the absence of any commercial or financial relationships that could be construed as a potential conflict of interest.

Publisher's note

All claims expressed in this article are solely those of the authors and do not necessarily represent those of their affiliated organizations, or those of the publisher, the editors and the reviewers. Any product that may be evaluated in this article, or claim that may be made by its manufacturer, is not guaranteed or endorsed by the publisher.

References

An, B. F., Miao, X. X., Zhang, J. X., Ju, F., and Zhou, N. (2016). Overlying strata movement of recovering standing pillars with solid backfilling by physical simulation. *Int. J. Min. Sci. Technol.* 26 (2), 301–307. doi:10.1016/j.ijmst.2015.12.017

Benzaazoua, M., Belem, T., and Bussie`re, B. (2002). Chemical factors that influence the performance of mine sulphidic paste backfill. *Cem. Concr. Res.* 32, 1133–1144. doi:10.1016/s0008-8846(02)00752-4

Cao, W. H., Wang, X. F., Li, P., Zhang, D. S., Sun, C. D., and Qin, D. (2018). Wide strip backfill mining for surface subsidence control and its application in critical mining conditions of a coal mine. *Sustainability* 10 (3), 700. doi:10.3390/su10030700

Cao, Z. Z. (2017). *Study on instability mechanism and rock burst mechanism of coal pillar in roadway filling mining.* China University of Mining and Technology.Beijing, China.

Chang, Q. L., Chen, J. H., Zhou, H. Q., and Bai, J. B. (2014). Implementation of paste backfill mining technology in Chinese coal mines. *Sci. World Journa.* doi:10.1155/2014/821025

Chen, Q. F., Zhou, K. P., and Wang, L. L. (2010). Stress field evolution law of mining environment reconstructing structure with change of filling height. *J. Cent. South Univ. Technol.* 17 (4), 738–743. doi:10.1007/s11771-010-0549-6

Chen, S. J., Wang, H. L., and Wang, H. Y. (2016). Strip coal pillar design based on estimated surface subsidence in eastern China. *Rock Mech. Rock Eng.* 49 (9), 1–10. doi:10.1007/s00603-016-0988-y

Cihangir, F., Ercikdi, B., Kesimal, A., Deveci, H., and Erdemir, F. (2015). Paste backfill of high-sulphide mill tailings using alkali-activated blast furnace slag: Effect of activator nature, concentration and slag properties. *Miner. Eng.* 83, 117–127. doi:10.1016/j.mineng.2015.08.022

Deng, X. J., Zhang, J. X., Kang, T., and Han, X. L. (2016). Strata behavior in extra-thick coal seam mining with upward slicing backfilling technology. *Int. J. Min. Sci. Technol.* 26 (4), 587–592. doi:10.1016/j.ijmst.2016.05.009

Doherty, J. P., Hasan, A., Suazo, G. H., and Fourie, A. (2015). Investigation of some controllable factors that impact the stress state in cemented paste backfill. *Can. Geotech. J.* 52 (12), 1901–1912. doi:10.1139/cgj-2014-0321

Du, X. J., Feng, G. R., Qi, T. Y., Guo, Y., Zhang, Y. J., and Wang, Z. H. (2019a). Failure characteristics of large unconfined cemented gangue backfill structure in partial backfill mining. *Constr. Build. Mater.* 194, 257–265. doi:10.1016/j.conbuildmat.2018.11.038

Du, X. J., Feng, G. R., Zhang, Y. J., Wang, Z., Guo, Y., and Qi, T. (2019b). Bearing mechanism and stability monitoring of cemented gangue fly ash backfill column with stirrups in partial backfill engineering. *Eng. Struct.* 188, 603–612. doi:10.1016/j.engstruct.2019.03.061

Ercikdi, B., and Yilmaz, T. (2019). Strength and microstructure properties of cemented paste backfill; Effect of class-c fly ash . *Dokuz Eylul Univ. Fac. Eng. J. Sci. Eng.* 21 (61), 15–23. doi:10.21205/deufmd.2019216102

Fall, M., Belem, T., Samb, S., and Benzaazoua, M. (2007). Experimental characterization of the stress–strain behaviour of cemented paste backfill in compression. *J. Mat. Sci.* 42 (11), 3914–3922. doi:10.1007/s10853-006-0403-2

Ghasemi, E., Ataei, M., and Shahriar, K. (2014). An intelligent approach to predict pillar sizing in designing room and pillar coal mines. *Int. J. Rock Mech. Min. Sci. (1997).* 65 (75), 86–95. doi:10.1016/j.ijrmms.2013.11.009

Guney, A., and Gul, M. (2018). Analysis of surface subsidence due to longwall mining under weak geological conditions: Turgut basin of Yataan-Mula (Turkey) case study, *Int. J. Min.*, 33. 1–17. doi:10.1080/17480930.2018.1443691

Guo, G. L., Zha, J. F., Wu, B., and Jia, X. G. (2007). Study of "3-step mining"subsidence control in coal mining under buildings. *J. China Univ. Min. Technol.* 17 (3), 316–320. doi:10.1016/s1006-1266(07)60096-0

Hao, J., Shi, Y. K., Lin, J. H., Wang, X., and Xia, H. C. (2019). The effects of backfill mining on strata movement rule and water inrush: A case study. *Processes* 7 (2), 66. doi:10.3390/pr7020066

Helinski, M., Fahey, M., and Fourie, A. (2010). Coupled two-dimensional finite element modelling of mine backfilling with cemented tailings. *Can. Geotech. J.* 47 (11), 1187–1200. doi:10.1139/t10-020

Huang, Y., Tian, F., Wang, Y. J., Wang, M., and Hu, Z. L. (2014). Effect of coal mining onvegetation disturbance and associated carbon loss. *Environ. Earth Sci.* 73 (5), 2329–2342. doi:10.1007/s12665-014-3584-z

Janez, R., Drago, P., and Milivoj, V. (2018). Analysis of dynamic surface subsidence at the underground coal mining site in velenje. Slovenia through Modified Sigmoidal Function. *Minerals* 8 (2), 74. doi:10.3390/min8020074

Jiang, N., Wang, C. X., Pan, H. Y., Yin, D. W., and Ma, J. B. (2020). Modeling study on the influence of the strip filling mining sequence on mining-induced failure. *Energy Sci. Eng.* 8 (6), 2239–2255. doi:10.1002/ese3.660

Li, L., and Aubertin, M. (2008). An improved analytical solution to estimate the stress state in subvertical backfilled stopes. *Can. Geotech. J.* 45 (10), 1487–1496. doi:10.1139/t08-060

Li, X. L., Chen, S. J., and Wang, S. (2021). Study on in situ stress distribution law of the deep mine taking Linyi Mining area as an example. *Adv. Mater. Sci. Eng.* 9 (4), 5594181. doi:10.1155/2021/5594181

Liu, H. Y., Zhang, B. Y., and Li, X. L. (2022). Research on roof damage mechanism and control technology of gob-side entry retaining under close distance gob. *Eng. Fail. Anal.* 138 (5), 106331. doi:10.1016/j.engfailanal.2022.106331

Liu, J. W., Sui, W. H., and Zhao, Q. J. (2017). Environmentally sustainable mining: A case study of intermittent cut-and-fill mining under sand aquifers. *Environ. Earth Sci.* 76 (16). doi:10.1007/s12665-017-6892-2

Liu, S. M., Li, X. L., Wang, D. K., and Zhang, D. (2020). Investigations on the mechanism of the microstructural evolution of different coal ranks under liquid nitrogen cold soaking. *Energy Sources A: Recovery Util. Environ. Eff.*, 1–17. doi:10.1080/15567036.2020.1841856

Luan, H. J., Jiang, Y. J., Lin, H. L., and Wang, Y. H. (2017). A new thin seam backfill mining technology and its application. *Energies* 10 (12), 2023. doi:10.3390/en10122023

Mkadmi, N. E., Aubertin, M., and Li, L. (2014). Effect of drainage and sequential filling on the behavior of backfill in mine stopes. *Can. Geotech. J.* 51 (51), 1–15. doi:10.1139/cgj-2012-0462

Mohamed, A. S, and Li, L (2017). Numerical investigation of the stresses in backfilled stopes overlying a sill mat. *J. Rock Mech. Geotechnical Eng.* 9 (3), 490–501. doi:10.1016/j.jrmge.2017.01.001

Mu, W. Q., Li, L. C., Guo, Z. P., Du, Z. W., and Wang, S. X. (2019). Novel segmented roadside plugging-filling mining method and overlying rock mechanical mechanism analyses. *Energies* 12 (11), 2073. doi:10.3390/en12112073

Navid, H., Ali, M., Misagh, M., Aref, F., and Kamyar, T. (2019). Fuzzy evaluation method for the identification of subsidence susceptibility in an underground mine (case study in Tabas coal mine of Iran). *Nat. Hazards* 99 (2), 797–806. doi:10.1007/s11069-019-03774-2

Ning, S., Zhu, W. B., Yi, X. Y., and Wang, L. L., (2021). Evolution law of floor fracture zone above a confined aquifer using backfill replacement mining technology. *Geofluids*, doi:10.1155/2021/8842021

Qian, M. G., Miao, X. X., and Xu, J. L. (2007). Green mining of coal resources harmonizing with environment. *J. China Coal Soc.* 32 (1), 1–7. doi:10.13225/j.cnki.jccs.2007.01.001

Qu, Q. D., Yao, Q. L., Li, X. H., and Rong, T. Y (2010). Key factors affecting control surface subsidence in backfilling mining. *J. Min. Saf. Eng.* 27 (4), 458–462.

Qu, X. K., Jiang, F. X., Wang, H. T., Zhu, S. T., Zhang, M., Xu, K., et al. (2017). Study on the mechanism of coal seam impact induced by pillar instability in goaf. *J. Min. Saf. Eng.* 34 (6), 1134–1140. doi:10.13545/j.cnki.jmse.2017.06.015

Raffaldi, M. J., Seymour, J. B., Richardson, J., Zahl, E., and Board, M. (2019). Cemented paste backfill geomechanics at a narrow-vein underhand cut-and-fill mine. *Rock Mech. Rock Eng.* 52 (12), 4925–4940. doi:10.1007/s00603-019-01850-4

Shao, X. P., Wang, L., Li, X., Fang, Z. Y., Zhao, B. C., Liu, E. S., et al. (2021). Conversion mechanism of a continuous pressure arch structure in strip filling mining. *Arab. J. Geosci.* 14, 1825. doi:10.1007/s12517-021-07918-2

Sun, D. Q., Wu, Q. L., Li, X. Y., Zhang, Z. M., Xu, X. T., Li, Y., et al. (2021). Sensitivity analysis and numerical simulation study on main controlling factors of surface movement and deformation in strip filling mining under thick unconsolidated layers. *Geofluids* 2021. doi:10.1155/2021/6615937

Sun, Q., Zhou, N., Song, W. J., and Zhao, X. (2021). Risk assessment and prevention of surface subsidence under buildings by cemented paste filling and strip mining methods: a case study. *Adv. Civ. Eng.*. doi:10.1155/2021/9965279

Sun, Q., Zhang, J. X., and Zhou, N. (2018). Study and discussion of short-strip coal pillar recovery with cemented paste backfill. *Int. J. Rock Mech. Min. Sci.* 104, 147–155. doi:10.1016/j.ijrmms.2018.01.031

Sun, X. K., and Wang, W. (2011). Theoretical research on high water material replacement mining the strip coal pillar above confined aquifer. *J. China Coal Soc.* 36 (6), 909–913. doi:10.13225/j.cnki.jccs.2011.06.018

Tan, Y., Guo, W. B., Bai, E. H., Yang, D. M., Xu, G. S., and Yan, H. (2017). Overburden failure induced by instability of coal pillar in strip wongawilli mining. *J. Coal Sci.* 42 (7), 1656–1662. doi:10.13225/j.cnki.jccs.2016.1163

Tuylu, S. (2022). Investigation of the effect of using different fly ash on the mechanical properties in cemented paste backfill. *J. Wuhan. Univ. Technol. -Mat. Sci. Ed.* 37 (4), 620–627. doi:10.1007/s11595-022-2576-1

Wang, S., Li, X. L., and Qin, Q. Z. (2022). Study on surrounding rock control and support stability of Ultra-large height mining face. *Energies* 15 (8), 6811. doi:10.3390/en15186811

Widisinghe, S, and Sivakugan, N, (2016). Vertical stress isobars for silos and square backfilled mine stopes. *Int. J. Geomech.* 16 (2). doi:10.1061/(asce)gm.1943-5622.0000499

Xuan, D. Y., and Xu, J. L. (2017). Longwall surface subsidence control by technology of isolated overburden grout injection. *Int. J. Min. Sci. Technol.* 27, 813–818. doi:10.1016/j.ijmst.2017.07.014

Yan, H., Zhang, J. X., Zhang, S., and Zhou, N. (2018). Physical modeling of the controlled shaft deformation law during the solid backfill mining of ultra-close coal seams. *Bull. Eng. Geol. Environ.* 78, 3741–3754. doi:10.1007/s10064-018-1335-1

Zhang, J. X., Sun, Q., Zhou, N., Jiang, J. Q., Germain, D., and Abro, S. (2016). Research and application of roadway backfill coal mining technology in Western coal mining area. *Arab. J. Geosci.* 9 (10). doi:10.1007/s12517-016-2585-5

Zhang, X. G., Lin, J., Liu, J. X., Li, F., and Pang, Z. Z. (2017). Investigation of hydraulic-mechanical properties of paste backfill containing coal gangue-fly ash and its application in an underground coal mine. *Energies* 10 (9), 1309. doi:10.3390/en10091309

Zhou, D. W., Wu, K., Bai, Z. H., Zhenqi, H., Liang, L., Yuankun, X., et al. (2019). formation and development mechanism of ground crack caused by coal mining: Effects of overlying key strata. *Bull. Eng. Geol. Environ.* 78 (2), 1025–1044. doi:10.1007/s10064-017-1108-2

Zhou, N., Yan, H., Jiang, S. Y., and Sun, Q. (2019). Stability analysis of surrounding rock in paste backfill recovery of residual room pillars. *Sustainability* 11 (2), 478. doi:10.3390/su11020478

Zhou, X. M., Wang, S., and Li, X. L. (2022). Research on theory and technology of floor heave control in semicoal rock roadway: Taking longhu coal mine in Qitaihe mining area as an Example. *Lithosphere* 2022 (11), 3810988. doi:10.2113/2022/3810988

Zhu, Li, Guo, R. F., and Jia, Q. C. (2020). Research on the influence of slurry filling on the stability of floor coal pillars during mining above the room-and-pillar goaf: A case study. *Geofluids* 2020 (1), 1–21. doi:10.1155/2020/8861348

Zhu, W. B., Yu, S. C., Xuan, D. Y., and Shan, Z. J (2018). Experimental study on excavating strip coal pillars using caving zone backfill technology. *Arab. J. Geosci.* 11 (18). doi:10.1007/s12517-018-3914-7

Zhu, X. J., Guo, G. L., Liu, H., Peng, X. N., Yang, X. Y., and Peng, Z. B. (2020). Research on the stability evaluation model of composite support pillar in backfill-strip mining. *Math. Problems Eng.* 2020, 11. doi:10.1155/2020/3138258

Zou, M. J., Liu, Y. Z., and Huang, Z. Q. (2020). Geological control of irreducible water within the coal matrix and its quantified evaluation model. *ACS Omega* 5 (16), 9540–9549

Zou, M. J., Wei, C. T., Zhang, M., and Lv, X. C. (2018a). Quantification of gas and water transfer between coal matrix and cleat network during drainage process. *J. Energy Res. Techn.* 140 (3), 032905-1–9

Zou, M. J., Wei, C. T., Zhang, M., Lv, X. C., and Guo, B. (2018b). Quantification of gas and water transfer between coal matrix and cleat network during drainage process. *Fuel* 233, 354–360

frontiers | Frontiers in Earth Science

TYPE Original Research
PUBLISHED 06 January 2023
DOI 10.3389/feart.2022.1041288

OPEN ACCESS

EDITED BY
Junjian Zhang,
Shandong University of Science and Technology, China

REVIEWED BY
Lei Xue,
Institute of Geology and Geophysics (CAS), China
Yafeng Zhang,
Zhengzhou University of Technology, China

*CORRESPONDENCE
Rui Bai,
215452297@qq.com

SPECIALTY SECTION
This article was submitted to Economic Geology,
a section of the journal
Frontiers in Earth Science

RECEIVED 10 September 2022
ACCEPTED 20 September 2022
PUBLISHED 06 January 2023

CITATION
Yu H, Wang J, Cao L, Bai R and Wang P (2023), Effects of the number of simulation iterations and meshing accuracy in monte-carlo random finite-difference analysis.
Front. Earth Sci. 10:1041288.
doi: 10.3389/feart.2022.1041288

Effects of the number of simulation iterations and meshing accuracy in monte-carlo random finite-difference analysis

Huaichang Yu[1,2], Jialiang Wang[1,2], Li Cao[3], Rui Bai[3]* and Peng Wang[3]

[1]Henan Province Key Laboratory of Rock and Soil Mechanics and Structural Engineering, North China University of Water Resources and Electric Power, Zhengzhou, China, [2]College of Geosciences and Engineering, North China University of Water Resources and Electric Power, Zhengzhou, China, [3]Yunnan Dianzhong Water Diversion Engineering Co., Ltd., Kunming, China

Monte-Carlo random finite-difference analysis (MCRFDA) can incorporate the spatial variability of soil properties into the analysis of geotechnical structures. However, two factors, namely, the fineness of the generated elements (reflected by the number of elements, N_e) and the number of MC simulation iterations, N_{MC}, considerably affect the computational efficiency of this method, creating a barrier to its broad use in real-world engineering problems. Hence, an MCRFDA model of a circular underground cavern is developed in this study. The convergent deformation of the cavern is analyzed while considering the spatial variability distribution of the elastic modulus. Moreover, the effects of N_{MC} and N_e on random FD calculations are investigated. The results show the following. An N_{MC} greater than 500 is desirable for the FD analysis of a conventional structure. For a specific structure, N_e does not have a significant impact on the mean of the simulated values but appreciably affects the standard deviation (SD) of the simulated values, where reducing N_e increases the SD of the simulated values.

KEYWORDS

Monte-Carlo random finite-difference analysis, random field, elastic modulus, cavern deformation, meshing accuracy

1 Introduction

Geotechnical structures are formed from complex and prolonged physical and chemical processes that are responsible for their inherent uncertainties. Phoon and Kulhawy (1999) identified inherent variability, measurement error, and transformation uncertainty as three principal sources of uncertainty in geotechnical parameters. The consideration of the uncertainty of geotechnical parameters has been a major issue in the numerical simulation of geotechnical structures in recent decades. Currently, random variable (RV) and random field (RF) models are commonly used to simulate geotechnical

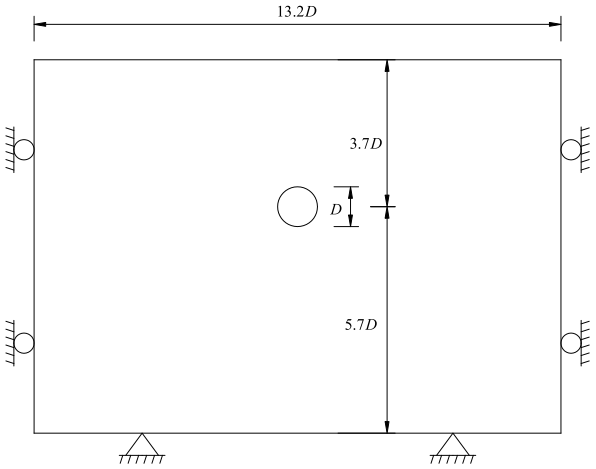

FIGURE 1
Model and boundary diagram.

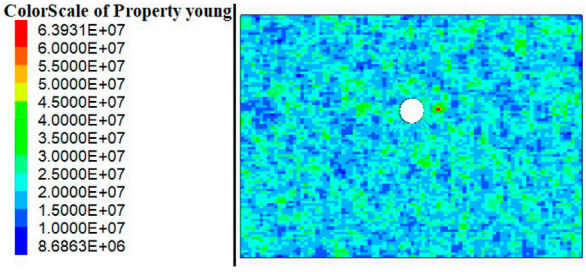

FIGURE 2
Spatial variability distribution of elastic modulus.

structures. RV models describe the uncertainty of geotechnical parameters using RVs that follow a certain probability distribution and evaluate the safety of engineering structures based on the reliability index or failure probability. With a well-defined concept and a simple principle, RV models are extensively used to analyze the reliability of geotechnical structures. Chowdhury and Xu (1993) investigated the reliability of homogeneous and layered inhomogeneous slopes using the RV method. However, RV models also have shortcomings: they simply treat geotechnical structures as homogeneous materials and use the reliability index or failure probability to evaluate the safety of engineering structures. Due to factors such as mineral composition and geological activity, the geotechnical parameters at a specific site vary with the location in space. Because RV models neglect the spatial variability of parameters, they method cannot produce accurate analytical results.

Vanmarcke (1977); Vanmarcke (1983) established a relatively sound RF theory that essentially models the characteristic parameters of a soil mass using an RF that follows a homogeneous normal distribution. On this basis, the RF is discretized into RVs. Subsequently, the reliability of the system is determined through the calculation of a large number of RVs and a statistical analysis of the results. This method is referred to as Monte-Carlo random finite-difference analysis (MCRFDA). Numerous researchers (Christian et al., 1994; El-Ramly et al., 2002; Hicks and Samy, 2002; Baecher and Christian, 20062006; Cassidy et al., 2013; Cho, 2014) have employed this method to analyze the reliability of geotechnical engineering structures. Dou and Wang (Dou and Wang, 2017) constructed a one-dimensional non-stationary random field to represent the saturated permeability coefficient of soil, and studied the stability of infinite slope. Cheng et al. (2016) studied the surface deformation of shield tunnel considering the spatial variability of elastic modulus.

As a reliability calculation method originating from engineering practice, Monte Carlo method is both simple and direct but has disadvantages of large amount of calculation. Cho (2007) used Latin hypercube sampling technology to generate random characteristics of soil mass to reduce the calculation amount of Monte Carlo analysis. Ghanem and Spanos (1991) proposed the spectral expansion method of node random variables to reduce the computational effort. The use of MCRFDA first requires the RF to be discretized. The fineness of discretization depends on the size of the generated elements. Computational accuracy increases as the density of elements increases. Refining elements without limit is, however, not possible in actual calculations, which require a balance to be struck between the fineness of the generated elements and computational efficiency. With respect to the number of simulation iterations, N_{MC}, in MC analysis, a similar balance also needs to be sought between computational accuracy and efficiency. Hence, in this study, we hope to find a balance between these two aims by analyzing a specific model, with the goal of providing a reference for similar problems.

2 Monte-carlo random finite-difference analysis and program realization

The stochastic finite difference method can be divided into two main categories according to the different treatment methods. One is based on analysis to find the relationship between system response and input signal, so as to obtain the law of internal force and deformation of structure and to carry out system reliability analysis. The specific methods include perturbation stochastic finite difference method and Newman stochastic finite difference method. The other is based on statistics, which discretizes the random field into random variables, calculates a large number of random variables and counts the results to obtain the reliability of the system.

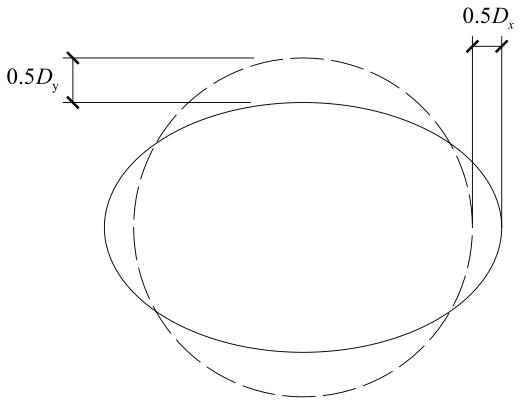

FIGURE 3
Schematic diagram of convergence deformation of cavern.

The main way to achieve this is Monte-Carlo Random Finite Difference Analysis. Monte Carlo stochastic finite difference method is a theoretical framework for analyzing the influence of spatial variability of geotechnical parameters on geotechnical structures by using stochastic fields. It combines stochastic field theory, finite difference method and Monte-Carlo method. The finite difference method replaces the partial derivative of the function on the grid node with the difference quotient, which is simple and intuitive.

In the Uncertainties Analysis of actual geotechnical engineering, random variables in different spatial locations are described by random field method. This process is the discretization of random field. Vanmarcke (1983) clearly pointed out that random finite element analysis must include the discrete process of random field. There are two main ways to discrete the random field: one is to discrete the random field into random field grid, which is called space discretization; the other is abstract discretization, which expands the random field in series, also called spectral decomposition of random field.

Beacher and Ingra (1981) first proposed stochastic analysis method based on center point method, which Kiureghian and Ke (1988) improved. The center point method uses the random field theory to calculate the random variable value $X(u_{io})$ at the centroid of each unit. It considers that the parameters in the unit are constant and equal to the random variable value $X(u_{io})$ at the centroid of the unit:

$$X(u_i) = X(u_{io}). \tag{1}$$

The most criticized point of the center point method is that it assumes that the internal parameters of the cell are completely related, so the calculation accuracy is related to the size of the divided cell. The more closely the cell is divided, the more accurate the calculation result will be. However, when the structure is complex or there are many elements, other discrete methods are difficult to realize. At this time, the advantages of the center point method are particularly prominent.

Based on the studies performed by Cassidy et al. (2013), the covariance matrix decomposition technique is used in this study to generate RFs. The procedure is detailed as follows:

(1) A numerical model of the object of analysis that comprises n elements is established, followed by the extraction of the coordinates of the center of each element.
(2) An autocorrelation function is used to calculate the $\rho(x, y, z)$ of the ith element with respect to all elements (including

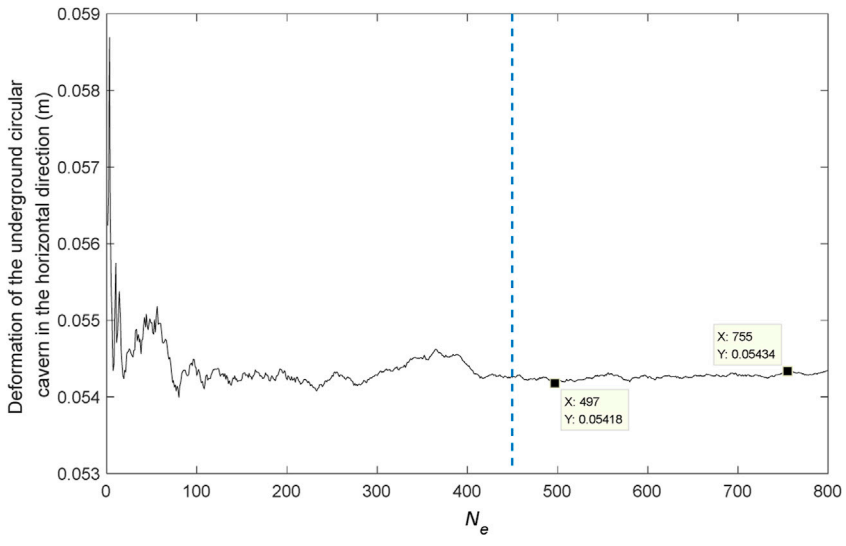

FIGURE 4
The change of horizontal displacement with the number of simulation groups.

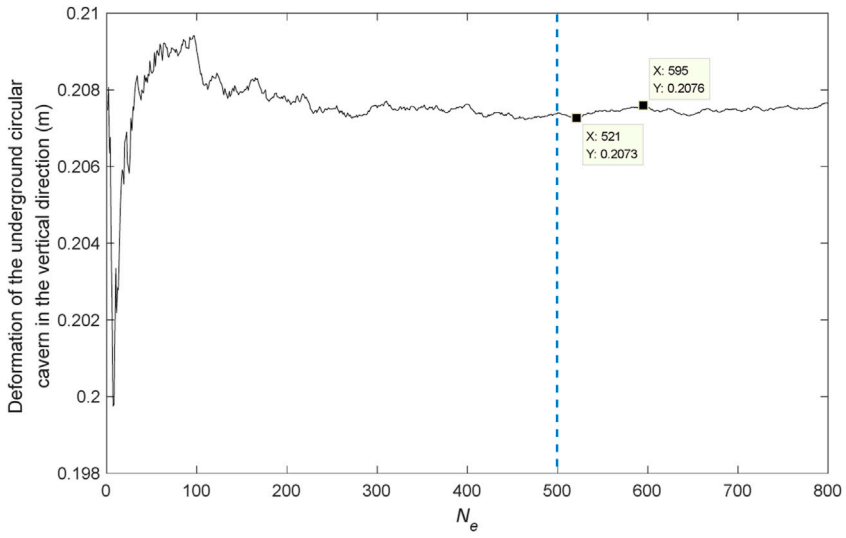

FIGURE 5
The change of vertical displacement with the number of simulation groups.

itself), which yields an nth-order column vector. Subsequently, i is traversed from 1 to n, which produces a matrix, $C_{n\times n}$, comprising n column vectors arranged in i rows. $C_{n\times n}$ is the covariance (autocorrelation) matrix of the model.

$$C_{n\times n} = \begin{bmatrix} \rho_{11} & \rho_{1r} & \rho_{1n} \\ \rho_{r1} & \rho_{rr} & \rho_{rn} \\ \rho_{n1} & \rho_{nr} & \rho_{nn} \end{bmatrix}. \quad (2)$$

(3) The Cholesky decomposition technique is used to decompose $C_{n\times n}$:

$$C_{n\times n} = LU = LL^T, \quad (3)$$

where matrix L^T is the transpose of matrix L.

(4) Y is used to denote the resulting n-dimensional column vector. The elements are independent of each other and generally follow a standard normal distribution. We let

$$Z = sLY + \mu, \quad (4)$$

where Z is a normally distributed RV with a mean of μ and a variance of s^2.

(5) The FISH language is used to assign Z to the corresponding element in the numerical model, generating an MC RF in the Fast Lagrangian Analysis of Continua (FLAC) software. The previous steps are repeated M times to generate all the required MC RFs.

3 Effects of NMC on calculation results

With study Huang et al. (2017) as a reference, a two-dimensional FD model was developed in this study based on a shield subway tunnel in Shanghai. Free, normal displacement-constrained, and fixed boundary conditions were applied to the top (ground surface), sides, and bottom of the model, respectively, as shown in Figure 1.

The FLAC in 3 Dimensions (FLAC3D) numerical analysis software was used to establish a model with 9344 elements, and the tunnel diameter D was set to 6.2 m. To facilitate calculation, the model was set as an elastic constitutive and only considers the condition of complete drying model with a Poisson's ratio (v) of 0.33 and a density of 1800 kg/m^3.

As noted by Fenton and Griffiths (2008), of all soil parameters, elastic modulus E and v are the primary factors affecting soil deformation. Due to its low spatial variability, v is not as important as E in soil deformation analysis. Therefore, only the spatial variability of E generally needs to be considered in the spatial variability analysis of soil deformation. E is assumed to follow a lognormal distribution with a mean of 20 MPa. Variability can be expressed in terms of the coefficient of variation (COV), a dimensionless parameter defined as the ratio of the standard deviation (SD) to the mean. In this study, COV was set to 0.3, and the fluctuation range was set to $\delta_x = \delta_y = 2$ m.

A total of 800 RFs of E were generated. Figure 2 shows the spatial distribution of E formed by one typical RF (different element colors represent different E values).

The equilibrium state was first calculated under the action of self-weight to generate the original *in situ* stress field.

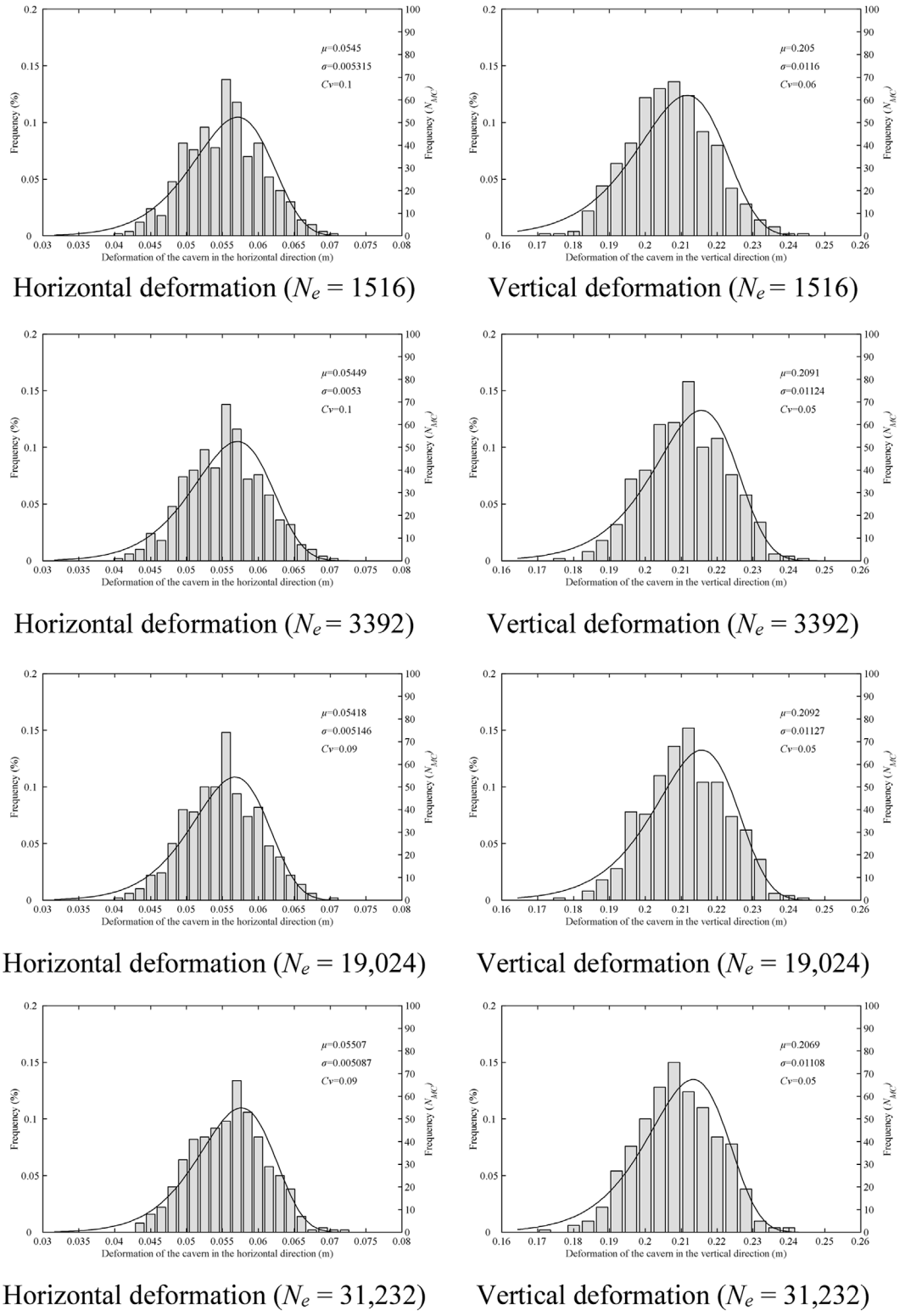

FIGURE 6
Distribution of calculation results using different numbers of elements. Horizontal deformation (N_e = 1516), Vertical deformation (N_e = 1516), Horizontal deformation (N_e = 3392), Vertical deformation (N_e = 3392), Horizontal deformation (N_e = 19,024), Vertical deformation (N_e = 19,024), Horizontal deformation (N_e = 31,232), Vertical deformation (N_e = 31,232).

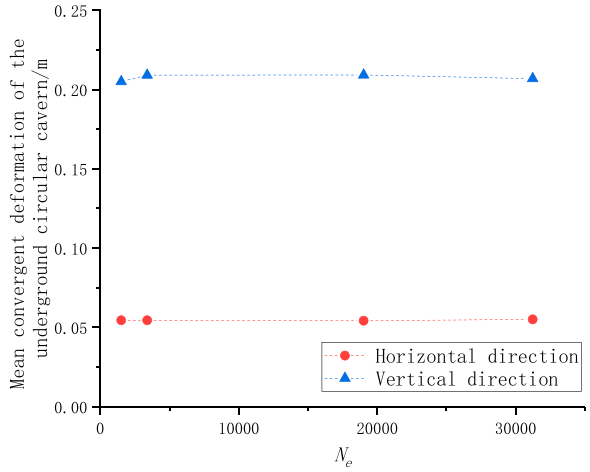

FIGURE 7
Mean value of convergence deformation with different numbers of elements.

Subsequently, the horizontal displacement (D_x) and vertical displacement (D_y) of the contour of the cavern after excavation were calculated, as shown in Figure 3.

In MCRFDA, N_{MC} needs to be determined to produce accurate simulations. Figures 4, 5 show the results for the case examined in this study obtained from calculations based on 800 RFs. After N_{MC} exceeded 450, the maximum and minimum values of the mean horizontal convergent deformation were 54.34 and 54.18 mm, respectively. This difference of 0.2% suggests that the mean horizontal convergence did not change significantly as N_{MC} increased beyond 450. After N_{MC} exceeded 500, the maximum and minimum values of the mean vertical convergent deformation were 207.6 and 207.3 mm, respectively. This difference of 0.1% suggests that the mean vertical convergence did not change significantly as N_{MC} increased beyond 500. Therefore, for the case examined in this study, calculations based on at least 500 RFs are required to ensure a reasonable mean for convergence.

4 Effects of the fineness of the generated elements on calculation results

The model was divided into different numbers of elements, N_e, while keeping its overall dimension and soil parameters unchanged. For each N_e, calculations were performed based on 500 RFs. Figure 6 shows the distribution of the results.

Figures 7, 8 show the variation in the mean and SD of the convergent deformation of the underground circular cavern with N_e, respectively.

As shown in Figure 7, the mean of the simulated values did not change significantly as N_e increased. Therefore, it can be concluded that the conventional element size is sufficient to produce high-accuracy simulations using an accurate numerical simulation model.

As shown in Figure 8, in contrast to the mean convergent deformation, the SD of the convergent deformation in each of the horizontal and vertical directions decreased considerably as N_e increased. At a fixed N_e, the simulated values tended to concentrate toward the mean. This finding may suggest that at a fixed spatial variability, increasing the density of elements

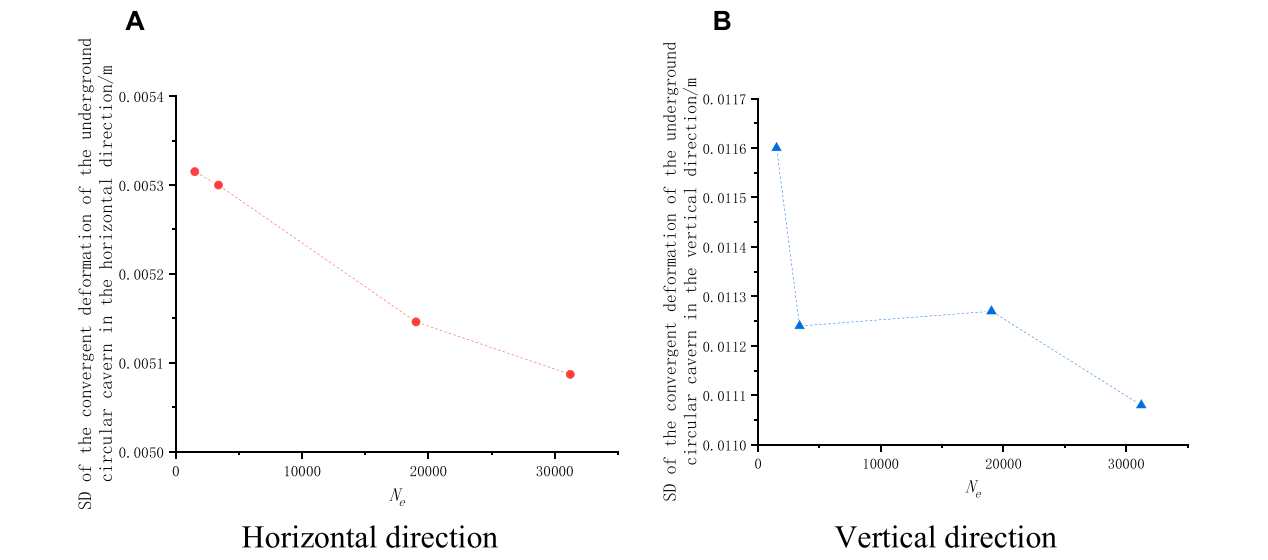

FIGURE 8
Standard deviation of convergence deformation with different numbers of elements. **(A)** Horizontal direction. **(B)** Vertical direction.

can increase the uniformity of the distribution of soil parameters, thus reducing the probability of extreme cases.

5 Conclusion

An MCRFDA model of a circular underground cavern is developed. The convergent deformation of the cavern is analyzed with the consideration of the spatial variability of E. The effects of N_{MC} and N_e on random FD calculations are investigated. The results show the following:

(1) An N_{MC} greater than 500 is desirable for the random FD analysis of a conventional structure.
(2) For a specific structure, N_e does not have a significant impact on the mean of the simulated values but considerably affects the SD of the simulated values. Reducing N_e increases the SD of the simulated values.

Data availability statement

The raw data supporting the conclusions of this article will be made available by the authors, without undue reservation.

Author contributions

All authors contributed to the study conception and design. Material preparation, data collection and analysis were performed by LC, RB, and PW. The first draft of the manuscript was written by HY and JW, and all authors commented on previous versions of the manuscript. All authors read and approved the final manuscript.

Funding

This research was supported by the key science and technology special program of Yunnan province (No. 202102AF080001).

Conflict of interest

Authors LC, RB, and PW were employed by Yunnan Dianzhong Water Diversion Engineering Co., Ltd.

The remaining authors declare that the research was conducted in the absence of any commercial or financial relationships that could be construed as a potential conflict of interest.

Publisher's note

References

Baecher, G. B., and Christian, J. T. (2006, 2006). Geotechnical engineering in the information technology age.The influence of spatial correlation on the performance of Earth structures and foundations, *Geo-Congress*

Beacher, G. B., and Ingra, T. S. (1981). Stochastic FEM in settlement predictions [J]. *J. Geotechnical Eng. Div.* 107 (4), 449–463.

Cassidy, M. J., Uzielli, M., and Tian, Y. H. (2013). Probabilistic combined loading failure envelopes of a strip footing on spatially variable soil. *Comput. Geotech.* 49 (49), 191–205.

Cheng, H. Z., Chen, J., Li, J. B., Hu, Z. F., Li, J. H., and Huang, J. H. (2016). Study on surface deformation induced by shield tunneling based on random field theory. *Chin. J. Rock Mech. Eng.* (S2), 4256–4264. doi:10.13722/j.cnki.jrme.2016.0099

Cho, S. E. (2007). Effects of spatial variability of soil properties on slope stability [J]. *Eng. Geol.* 92 (3-4), 97–109.

Cho, S. E. (2014). Probabilistic stability analysis of rainfall-induced landslides considering spatial variability of permeability. *Eng. Geol.* 171 (8), 11–20.

Chowdhury, R. N., and Xu, D. W. (1993). Rational polynomial technique in lope-reliability analysis. *J. Geotech. Eng.* 119 (12), 1910–1928.

Christian, J. T., Ladd, C. C., and Baecher, G. B. (1994). Reliability applied to slope stability analysis. *ASCE J. Geotech. Eng.* 120 (12), 2180–2207.

Dou, H. Q., and Wang, H. (2017). Probabilistic analysis of spatial variability of saturated hydraulic conductivity on infinite slope based on the non-stationary random field. *China Civ. Eng. J.* (08), 105–113+128. doi:10.15951/j.tmgcxb.2017.08.012

El-Ramly, H., Morgenstern, N. R., and Cruden, D. M. (2002). Probabilistic slope stability analysis for practice. *Can. Geotech. J.* 39 (3), 665–683.

Fenton, G. A., and Griffiths, D. V. (2008). *Risk assessment in geotechnical engineering*. Hoboken, New Jersey, USA: John Wiley & Sons.

Ghanem, R. G., and Spanos, P. D. (1991). Spectral stochastic finite-element formulation for reliability analysis[J]. *J. Eng. Mech.* 117 (10), 2351–2372.

Hicks, M. A., and Samy, K. (2002). Influence of heterogeneity on undrained clay slope stability. *Q. J. Eng. Geol. Hydrogeol.* 35 (1), 41–49.

Huang, H. W., Xiao, L., Zhang, D. M., and Zhang, J. (2017). Influence of spatial variability of soil Young's modulus on tunnel convergence in soft soils. *Eng. Geol.* 228, 357–370.

Kiureghian, A. D., and Ke, J. B. (1988). The stochastic finite element method in structural reliability [J]. *Probabilistic Eng. Mech.* 3 (2), 83–91.

Phoon, K. K., and Kulhawy, F. H. (1999). Characterization of geotechnical variability. *Can. Geotech. J.* 36 (4), 612–624.

Vanmarcke, E. H. (1977). Probabilistic modeling of soil profiles. *ASCE J. Geotech. Eng.* 103 (11), 1227–1246.

Vanmarcke, E. H. (1983). *Random fields: Analysis and synthesis*. Cambridge, MA, USA: MIT Press.

frontiers | Frontiers in Earth Science

TYPE Original Research
PUBLISHED 10 January 2023
DOI 10.3389/feart.2022.1108786

OPEN ACCESS

EDITED BY
Zhenzhi Wang,
Henan Polytechnic University, China

REVIEWED BY
Fei Huang,
Hunan University of Science and Technology, China
Mingyang Wu,
Institute of Rock and Soil Mechanics (CAS), China

*CORRESPONDENCE
Binwei Xia,
xbwei33@cqu.edu.cn

SPECIALTY SECTION
This article was submitted to Economic Geology, a section of the journal Frontiers in Earth Science

RECEIVED 26 November 2022
ACCEPTED 19 December 2022
PUBLISHED 10 January 2023

CITATION
Jiang S, Xia B, Peng J and Zeng T (2023), Study on coalbed methane flow characteristics based on fractal bifurcation fracture network model.
Front. Earth Sci. 10:1108786.
doi: 10.3389/feart.2022.1108786

Study on coalbed methane flow characteristics based on fractal bifurcation fracture network model

Shuzhen Jiang[1,2,3], Binwei Xia[1,2,3]*, Jiansong Peng[1,2,3] and Tai Zeng[1,2,3]

[1]State Key Laboratory of Coal Mine Disaster Dynamics and Control, Chongqing University, Chongqing, China, [2]National and Local Joint Engineering Laboratory of Gas Drainage in Complex Coal Seam, Chongqing University, Chongqing, China, [3]School of Resources and Safety Engineering, Chongqing University, Chongqing, China

The geometric structure and distribution of the fracture network significantly impact the coalbed methane flow characteristics. The indoor optical microscope test is utilized to analyze the distribution and structural characteristics of natural fractures in coal. The results indicate that the fracture network in coal consists primarily of irregular bifurcated fractures, but the influence of the bifurcation fracture network's structural characteristics on permeability remains unclear. Therefore, the fracture network geometric structure characteristic parameters are considered in accordance with the fractal theory, and the analytical formula of the bifurcation fracture network permeability is established. Meanwhile, the bifurcation fracture network geometric model with varied structural parameters is reconstructed using the pixel probability decomposition algorithm. Finally, the influence of the key parameters of the reconstructed bifurcation fracture network on the coal seam permeability is analyzed through numerical simulation. The results indicate that the permeability of the bifurcated fracture network increases with the increase of fracture porosity φf, aperture ratio χ, and proportionality coefficient η, and decreases with the increase of tortuosity fractal dimension DT, bifurcation angle θ, fractal dimension Df, and bifurcation level n. Among them, fracture porosity and proportionality coefficient have the greatest influence on permeability, followed by tortuosity fractal dimension, aperture ratio.

KEYWORDS

fractal geometry, permeability model, bifurcation fracture, structural characteristic, coalbed methane

1 Introduction

Coal bed methane (CBM) is a clean, environmentally friendly high-quality energy source. Efficient exploitation of CBM profoundly impacts the healthy and sustainable development of the world's resources (Li and Jin 2019; Li et al., 2022). The productivity of underground oil and gas reservoirs is mainly determined by a large number of their randomly distributed fractures, and their microstructure and distribution characteristics significantly impact the fluid flow characteristics (Xu et al., 2006; Liu et al., 2015; Wang et al., 2018). At present, researchers still have insufficient understanding, characterization, and model establishment of the structural characteristics of the bifurcation fracture network. It is crucial to study the structural characteristics of the bifurcation fracture networks to accurately construct the permeability model of coal reservoirs and improve the low permeability of coalbed methane.

Studies have shown that bifurcation is the key characteristic of fractures in porous media. Naturally, fracture networks are often interconnected to form multistage bifurcation fracture

networks (Xu et al., 2016). This paper believes that coal, as a typical fractured porous medium, has similar topological structures in its fracture network. Bobaru and Zhang (2015) analyzed the causes of fracture bifurcation and its problem in homogeneous, isotropic materials using the near-dynamic brittle fracture model, such as fracture morphology, bifurcation angle, and branch expansion velocity. The authors pointed out that bifurcation is the normal state of fracture and analyzed the structural characteristics of the bifurcation fracture but did not study the flow characteristics of the fluid in fracture. Through the CT scanning test, Fu et al. (2020) observed that coal samples contained many fractures of different scales, and their structure and distribution characteristics were difficult to describe. Therefore, it was necessary to simplify the structure characteristics reasonably. For example, Jin et al. (2020) and Zhao et al. (2020) used fractal theory to describe the complex microstructure of porous media and eases the modeling of multi-scale microstructures significantly. In addition, some scholars have used a tree-like bifurcation fracture network to characterize the complex fracture network in underground reservoirs. Zhang et al. (2021) compared the fracture network in porous media to a tree-like bifurcation fracture, established the expression of effective thermal conductivity according to the fractal characteristics of pores' diameter and fracture size, and analyzed the influence of microstructure parameters of porous matrix and bifurcation fracture networks on thermal conductivity. Zhu et al. (2021) used tree-like bifurcation fracture networks to characterize fracturing fractures, established a simulation model of tree-like bifurcation fracture networks, and discussed the influence of fracture opening, bifurcation angle, and tortuosity degree on the imbibition of the bifurcation fracture network.

Much work on the structural characteristics of bifurcated fracture networks has been done through theoretical analysis and numerical simulation. Establishing an effective fracture network permeability model is critical to revealing the fluid flow characteristics (Jafari and Babadagli 2016). Miao et al. (2015a), Miao et al. (2015b) takes into account the microstructure parameters of fractures, such as opening, length, dip angle, density, *etc.*, and establishes the fractal permeability model of dual-porosity media. Jin et al. (2017) believe that the fractal behavior of pore networks in natural tight reservoirs has a significant influence on the transport property of the reservoir. They study the relationship between the four fractal dimensions and establish the mathematics to describe the flow of fluid in fractal tight porous media. Li et al. (2021) took into account the influence mechanism of the distribution characteristics of coal surface fracture structure on coal permeability and developed a fractal permeability model for coal and rock. Shi et al. (2022) proposed a fractal permeability model for fractured rocks that comprehensively considered the geometric fracture characteristics and the fluid transport mechanism. The permeability of fractured rock with different geometric parameters and roughness is analyzed. However, their study neglected the connections between fractures and did not consider the influence of the bifurcation structures of the fracture network on fluid seepage. Xu et al. (2008) utilized the dual-domain model to simulate bifurcated fractured porous media, established the fractal analytical expression of permeability, and demonstrated that the fractal dimension of pore distribution has a significant impact on seepage characteristics. Miao et al. (2018) takes into account the aperture ratio, length ratio, branch number, and bifurcation level of fractures and proposes an analytical expression for dimensionless permeability of damaged tree bifurcation networks. Wang and Cheng (2020) established a fractal permeability model of a two-dimensional curved tree fracture network. However, the relationship between the structural parameters of the bifurcation fracture network and permeability is unclear in their study.

In conclusion, the structural parameters of bifurcation fracture networks, the establishment of permeability models, and the quantitative relationship between the structural parameters and permeability need to be studied. Therefore, based on the fractal geometry theory, the geometric structure characteristics of bifurcation fracture networks are considered, and the analytical expression of permeability of bifurcation fracture networks is derived. Afterward, the geometric model of bifurcation fracture networks with different structural characteristics was reconstructed by the pixel probability decomposition algorithm, and the model was imported into COMSOL Multiphysics numerical simulation software. Lastly, the influence of vital geometric parameters on the bifurcation fracture network's permeability is analyzed.

2 Structural characteristics of bifurcation fracture networks

2.1 Sample preparation and experiment introduction

In order to observe and analyze the geometric structure and distribution of the primary fracture networks in coal rocks, several samples were collected from Xichenzhuang Coal Mine, Jincheng city, Shanxi Province, China (Supplementary Figure S1A). Some were processed into 50 mm × 50 mm specimens, and their macroscopic natural fracture networks were observed by stereomicroscope (Supplementary Figure S1B). Due to the wide observation range and large acceptable size of the specimens, many fracture networks can be observed by stereomicroscopes. However, the magnification is limited (≤50x), and most microscopic fracture structures cannot be observed.

In order to more accurately observe the fracture networks' morphology, the rest were processed into irregular samples of about 8 mm for scanning electron microscopy (SEM) observation (Supplementary Figure S1C) to obtain the microstructure of the fracture networks. The scanning electron microscope's accuracy (≤25,000,00x) is much greater than that of the stereographic one, but the observation range is small, and the fracture's structure is limited. Therefore, combining the two can reflect the structural characteristics of coal and rock fracture networks more intuitively and clearly.

2.2 Structural characteristics of the fracture networks

Combining microscope (Supplementary Figure S2) and SEM (Supplementary Figure S2) results, it is observed that the natural fracture network in coal consists primarily of a large number of irregularly curved bifurcate fractures, followed by a limited number of single fractures with poor connectivity. Compared to bifurcate fractures, single ones' contribution to the seepage is minimal; therefore, this paper mainly focuses on the seepage characteristics in the coal-rock bifurcation fracture networks.

2.2.1 Bifurcation and curved characteristics of fracture networks

Studies have shown that fracture networks' tortuosity and bifurcation properties significantly affect the reservoirs' permeability (Yu and Cheng 2002; Xu et al., 2016). The fracture networks' structural features and bifurcation are depicted in Supplementary Figure S2C and Supplementary Figure S3B. In the fracture network, the main fracture usually extends into two branches, and the branches will continue to bifurcate to form lower-level bifurcation fractures. The level of the branch is denoted by k, and the maximum order of the branch is denoted by n. In this study, the angle between two branches of the same level is defined as the bifurcation angle, denoted by θ.

In addition, the fractures' curved nature is usually characterized by tortuosity τ. As depicted in Supplementary Figure S4A, L_t is the bending length of the fracture, L_0 is the linear length of the fracture, and tortuosity is equal to the ratio of the two.

In the figure, a is the fracture opening, h is the fracture depth, and the relationship between L_t and L_0 can be expressed as follows (Yu and Li 2004):

$$L_t(\alpha) = a^{1-D_T} L_0^{D_T} \tag{1}$$

Where D_T is the fractal dimension characterizing the fractures' curved nature, the curvier the fracture, the greater is τ; that is, the greater the value of D_T. When D_T=1, the fracture is linear, with $1<D_T<2$ in two-dimensional space and $1<D_T<3$ in three-dimensional space.

From equation (1), D_T can be calculated by the following equation (Yu and Li, 2004; Yu 2008):

$$D_T = 1 + \frac{Ln\,\tau_{av}}{Ln(L_0/a_{av})} \tag{2}$$

Where τ_{av} is the average tortuosity of fractures; a_{av} Is the average opening of the fracture.

2.2.2 Characteristic relationship between the opening and the length of bifurcation fractures

According to Murray's law inference, in fracture networks with perfect fluid flow, all branched fractures' cross-sectional sum should be greater than the primary fracture, and the main fracture radius of the cubic must approximately be equal to the sum of the cubic bifurcation fractures' radius. Therefore, fractures' aperture will decrease during the bifurcation process illustrated in Supplementary Figure S2, Supplementary Figure S3, and observations. At the same time, through plenty of observations and analysis, it is found that the length of all the fractures in the bifurcation fracture network is always random, and the length of the bifurcation fractures is considered to meet the fractal distribution. In order to deeply analyze the structural characteristics of the bifurcated fracture networks, the length ratio β, the opening ratio χ, and the proportion coefficient η are introduced to represent the relationship between the opening and the length of the bifurcated fracture network:

$$\beta = \frac{l_{k+1}}{l_k} \tag{3}$$

$$\chi = \frac{a_{k+1}}{a_k} \tag{4}$$

$$\eta = \frac{a_k}{l_k} \tag{5}$$

Where β is the length ratio, expressed as the ratio between the length of the secondary fracture and the upper one; χ is the opening ratio, expressed as the ratio of the opening degree of the secondary fracture to the upper one's, and $0<\chi<1$; l_0 and a_0 are the length and the opening of the main fractures, respectively. L_k and a_k (k=0,1..,n) are the length and the opening of the k-level bifurcation fracture, respectively, and the length and opening ratio in the bifurcation fracture networks are considered unchanged (Xu and Yu 2001). η is the proportionality coefficient. For the fracture network satisfying the self-similar distribution, the ratio between the opening and the length of a single fracture is usually between 0.1 and 0.001 (Klimczak et al., 2010; Luo et al., 2021).

3 Fractal permeability model of bifurcation fracture networks

3.1 Fractal characteristics of bifurcation fracture networks

A large number of random fracture networks are often analyzed by fractal geometry, and fractal dimension is often used as a quantitative parameter to characterize the distribution complexity of fracture networks (Miao et al., 2015a). In this study, both the length and opening of the bifurcation fracture network meet the fractal scaling law (Yu and Li 2001; Wu et al., 2021). The total number of bifurcation fracture networks whose main fracture length is greater than or equal to l_0 satisfies the following fractal scaling relation (Liu et al., 2016; Xu et al., 2016):

$$N(\mathrm{L} \geq l_0) = (l_{0\max}/l_0)^{D_f} \tag{6}$$

Where N is the number of bifurcation fracture networks; l_0 is the length of the main fracture; $l_{0\max}$ is the maximum length of the main fracture; D_f is the fractal dimension representing the distribution of fractures, which is usually obtained by the box-counting method, $0<D_f<2$ in two-dimensional space and $0<D_f<3$ in three-dimensional space. In addition, Xu et al. (2016) proved that the fractal dimension of fracture length is equal to the box dimension D_f.

In general, Equation (6) is continuously differentiable. By differentiating l_0, we can obtain:

$$-dN(l_o) = D_f l_{0\max}^{D_f} l_0^{-(D_f+1)} dl_0 \tag{7}$$

3.2 The establishment of the fractal permeability model

Based on the fractal geometry theory and considering the structural characteristics of the fracture network, this paper establishes the permeability model of bifurcation fracture networks. During this process, the adjacent bifurcation fractures' impact on one another is ignored, and the energy loss at the bifurcation is not considered.

The fluid flow in a single fracture is usually described by the cubic law (Miao et al., 2015a; Miao et al., 2015b):

$$q = \frac{a^3 h \Delta P}{12 \mu L_0} \tag{8}$$

where a is the fracture's opening; h is its depth; μ is the hydrodynamic viscosity coefficient; and ΔP is the pressure difference between the two ends of the fracture.

Since fractures are curved in natural conditions, Wang and Cheng (2020) obtained the flow rate in a single curved fracture considering the curved characteristics and combined it with Newton's law of viscosity, satisfying the fractal distribution as follows:

$$q = \int_{(a/2)}^{(a/2)} v dA = 2\int_{0}^{(a/2)} v h d\alpha = \frac{\Delta P a^{2+D_T} h}{2^{1+D_T}\mu L_0^{D_T}(2+D_T)} \tag{9}$$

According to Equation (9), the flow rate of a single k-level fracture is:

$$q_k = \left(\frac{1}{2}\right)^k q = \frac{\Delta P_k a_k^{2+D_T} h}{2^{1+D_T}\mu l_k^{D_T}(2+D_T)} \tag{10}$$

Therefore, the pressure difference between the two ends of the k-level fracture is:

$$\Delta P_k = \frac{q_k 2^{1+D_T}\mu l_k^{D_T}(2+D_T)}{a_k^{2+D_T} h} \tag{11}$$

Ignoring the pressure loss at the bifurcation, the total pressure difference of the whole bifurcation fracture is:

$$\Delta P = \sum_{k=0}^{n} \Delta P_k \tag{12}$$

By substituting Equations 3 and 4 and Equation 5 into Equations 11 and 12, we can obtain:

$$\Delta P = \frac{2^{1+D_T}\mu(2+D_T)q}{h a_0^2 \eta^{D_T}} \frac{1-\left(\frac{\beta^{D_T}}{2\chi^{2+D_T}}\right)^{n+1}}{1-\frac{\beta^{D_T}}{2\chi^{2+D_T}}} \tag{13}$$

Therefore, the total flow rate of a bifurcation fracture is):

$$q_Y = \frac{\Delta P h a_0^2 \eta^{D_T}}{2^{1+D_T}\mu(2+D_T)} \frac{1-\frac{\beta^{D_T}}{2\chi^{2+D_T}}}{1-\left(\frac{\beta^{D_T}}{2\chi^{2+D_T}}\right)^{n+1}} \tag{14}$$

Assuming that the fracture area in each section of the study object is equal, then:

$$\begin{aligned} A_f &= \int_{l_{0\max}}^{l_{0\max}} l_0 a_0 dN(l_0) \\ &= -\int_{l_{0\max}}^{l_{0\max}} h a_0 dN(l_0) \\ &= \frac{\eta D_f}{2-D_f} l_{0\max}^{2D_f-2}\left[1-\left(\frac{l_{0\min}}{l_{0\max}}\right)^{2-D_f}\right] \end{aligned} \tag{15}$$

Therefore,

$$A = A_f / \varphi_f = \frac{\eta D_f}{\varphi_f(2-D_f)} l_{0\max}^{2D_f-2}\left[1-\left(\frac{l_{0\min}}{l_{0\max}}\right)^{2-D_f}\right] \tag{16}$$

where A_f is the fracture area; A is the total area of the study section; and φ_f is the fracture porosity, which is numerically equal to the ratio of A_f to A.

After integrating equation (7) and substituting equation (15), the total flow of the bifurcation fracture network is obtained as follows:

$$\begin{aligned} Q &= \int_{l_{0\max}}^{l_{0\max}} q_Y dN(l_0) \\ &= \frac{\eta^{2-D_f}\Delta P D_f l_{0\max}^{2D_f-3}}{2^{1+D_T}\mu(2+D_T)(3-D_f)} \frac{1-\frac{\beta^{D_T}}{2\chi^{2+D_T}}}{1-\left(\frac{\beta^{D_T}}{2\chi^{2+D_T}}\right)^{n+1}}\left[1-\left(\frac{l_{0\min}}{l_{0\max}}\right)^{3-D_f}\right] \end{aligned} \tag{17}$$

Since $l_{0\min}/L_{0\max}<10^{-2}$ and $0<D_f<2$ stand in two-dimensional space $(l_{0\min}/L_{0\max})^{3-D_f}\approx 0$, Eq. 17 can be simplified as follows.

$$Q = \frac{\eta^{2-D_f}\Delta P D_f l_{0\max}^{2D_f-3}}{2^{1+D_T}\mu(2+D_T)(3-D_f)} \frac{1-\frac{\beta^{D_T}}{2\chi^{2+D_T}}}{1-\left(\frac{\beta^{D_T}}{2\chi^{2+D_T}}\right)^{n+1}} \tag{18}$$

According to the geometric relationship of bifurcation fractures, the equivalent linear length L of the curved bifurcation fracture networks along the flow direction (horizontal) is:

$$L = l_0\left[1+\frac{\sin\theta}{\sqrt{2(1-\cos\theta)}}\frac{\beta(1-\beta^n)}{1-\beta}\right] \tag{19}$$

Therefore, by substituting equations (16) and (18) and (19) into Darcy's law ($k=(Q\mu L)/(A\Delta P)$) for calculation, the analytical expression of bifurcation fracture networks' permeability satisfying the fractal distribution can be obtained as follows:

$$K_f = \frac{\eta^{1+D_T}\varphi_f(2-D_f)}{2^{1+D_T}(2+D_T)(3-D_f)} \frac{1-\frac{\beta^{D_T}}{2\chi^{2+D_T}}}{1-\left(\frac{\beta^{D_T}}{2\chi^{2+D_T}}\right)^{n+1}}\left[1+\frac{\sin\theta}{\sqrt{2[1-\cos\theta]}}\frac{\beta(1-\beta^n)}{1-\beta}\right] \tag{20}$$

3.3 Validity verification of the model

In order to verify the reliability of the fractal permeability model of bifurcation fracture networks in this study, the data in Supplementary Table S1 are put into Expression (20) and compared with the fractal permeability model of fractured porous media proposed by Miao and Yang (2015a). Supplementary Figure S5 shows the comparison results.

In this research, bifurcations and flexural characteristics are accounted for in Equation (20), and the results indicate that Miao et al. overestimated permeability. The reason is that the flexural and bifurcation properties of fractures hinder the seepage of coal seams, which is consistent with the actual situation. The fractal permeability model presented in this paper is therefore more effective.

3.4 Reconstruction of the geometric model of bifurcation fracture network

According to Equation (20), the permeability of the bifurcation fracture network is affected by the geometrical structural characteristics of the fracture, such as the fractal dimension of tortuosity, length and opening ratio, proportionality coefficient, fracture porosity, fractal dimension, bifurcation angle, and bifurcation level. In order to quantitatively describe their relationship with CBM flow characteristics, the complex fracture networks in natural coal seams were simplified for subsequent

modeling analysis. In the past, researchers often used CT imaging to reconstruct the network model (Song et al., 2020; Song et al., 2021; Song et al., 2022) present a novel pore scale modeling on dissociation and transportation mechanism of MH in porous sediments. But the reconstructed model was too complex and not targeted. Therefore, based on the basic theory of the two-dimensional pixel spatial probability decomposition method, this paper used a two-dimensional random fracture network generation program to generate multiple fracture networks with different tortuousness (Xia et al., 2021a; Wu et al., 2021) and rebuilt multiple bifurcation fracture network models with different characteristic parameters.

Multiple fractures with specific statistical characteristics are generated in the two-dimensional pixel space. The growth probability values of the eight growth directions of the fractures to be determined and the tortuosity of the generated random fracture network are shown in Supplementary Table S2. The relevant geometric parameters of the reconstructed bifurcation fracture network model are shown in Supplementary Table S3.

4 Numerical modeling

4.1 Basic assumptions

The flow situation of underground coalbed methane is very complex. In order to make the model converge better, the following assumptions should be made first (Wang et al., 2016; Xia et al., 2021a):

The coal reservoir is simplified as a dual pore medium consisting of matrix and fracture network systems. The transport of coalbed methane mainly occurs in bifurcation fracture networks.

1) The flow of coalbed methane in coal seams meets Darcy's law (single-phase flow);
2) The fluid seepage direction is parallel to the main fracture of the bifurcation fracture;
3) The interaction between fluid flow in fractures and fluid flow in matrix is not taken into account;
4) The seepage field is simulated regardless of the deformation of the coal bed and the surrounding mechanical field.

4.2 Fluid governing equations and boundary conditions

The continuity equation of CBM flow in coal seams can be expressed by Darcy's law combined with mass conservation (Xia et al., 2021b; Ren et al., 2021):

$$\nabla \cdot \left(\rho_g \mathrm{u}\right) = 0,\ \rho_g = \frac{M_g}{RT} \tag{21}$$

$$\mathrm{u} = -\frac{K}{\mu}\nabla P,\ \nabla P = \frac{\Delta P}{L} \tag{22}$$

Where ρ_g is the gas density, Kg/m^3; u is the flow rate, m/s; T is the coal reservoir's temperature, °C; Mg is the gas's molar mass, g/mol; R is the gas constant.

Related parameters of fluid and matrix in the simulation are shown in Supplementary Table S4. The model's boundary conditions are shown in Supplementary Figure S6.

4.3 Parameter analysis and discussion

The reconstructed bifurcation fracture network model was imported into Comsol Multiphysics numerical simulation software, and Equation (20) was solved according to the boundary conditions in Supplementary Figure S6 and relevant parameters in Supplementary Table S4. Afterward, the velocity distribution cloud diagram of coalbed methane in the bifurcation fracture network with different structural characteristic parameters was obtained (Supplementary Figure S7). Then, the flow velocity at the outlet was counted. Subsequently, the permeability value was calculated using Darcy's law.

The simulation results show that the gas velocity in the bifurcation fracture is significantly higher than that of in the matrix, the coalbed methane migration mainly occurs in the bifurcation fracture networks, and the matrix contributes little to the permeability of the coal reservoirs, which is consistent with the previous findings of (Yu and Cheng, 2002; Yu, 2008).

In addition, due to the presence of bifurcation structures in the fracture the velocity of the fluid in the fracture decreases gradually with the occurrence of bifurcation. The gas velocity in the main fracture is significantly higher than that of the secondary fracture, and the higher the bifurcation level is, the smaller the fluid velocity. Therefore, the bifurcation of the fracture has an inhibitory effect on the gas seepage.

4.3.1 Relationship between tortuosity fractal dimension D_T and bifurcation fracture network's permeability K_f

In order to obtain the relationship between the fracture's tortuosity and permeability, other geometric structural parameters were fixed, and the fractal dimension's tortuosity's value was increased from 1.0012 to 1.0548. The structural parameters of 12 bifurcated fracture network models with different tortuosity established in the study are shown in Supplementary Table S3 (Case. I). Supplementary Figure S7A shows the velocity distribution cloud of the bifurcation fracture network model with different tortuosity.

Supplementary Figure S8 compares and analyzes the numerical simulation and the theoretical prediction results of the bifurcated fracture network's permeability as the fractal dimension of tortuosity increases. The results show that the larger the fractal dimension of tortuosity, the smaller the permeability is. The reason is that when the fluid flows in the fracture, the curvier (rough) the fracture wall, the greater the flow resistance, and the longer the fluid flow path is. In addition, the collision between the fluid particles and the convex part of the fracture wall increases the fluid's energy loss, and the seepage velocity of the fluid decreases. This conclusion is consistent with previous research results (e.g., Yu and Cheng 2002; Liu et al., 2015).

4.3.2 Relationship between fracture porosity φf, bifurcation level n, and the bifurcation fracture network's permeability Kf

As observed in Supplementary Figure S9, when the bifurcation level n = 1, 3, and 5, the permeability and fracture porosity both exhibit a stable linear growth relationship, and the difference between the permeability values at the same fracture porosity is very small. Therefore, the permeability of the bifurcation fracture network is almost not affected by the bifurcation level.

In order to determine the quantitative relationship between the fracture porosity and its network permeability, it was increased from

0.0078 to 0.0447, the bifurcation level was increased from 1 to 5, and other structural parameters were not altered. The geometric structural parameters of 10 groups of bifurcation fracture network models with different fracture porosities are shown in Table 3 (Case II). The simulation results are shown in Supplementary Figure S7B.

Supplementary Figure S7B shows that fracture porosity positively correlates with permeability. For example, although the maximum fracture porosity is only increased by less than 0.04, the maximum seepage velocity of the CBM in the bifurcated fracture network is increased from 7.14×10^{-4} (m/s) to 1.15×10^{-2} (m/s) indicating that the fracture porosity plays a vital role in the fracture network's permeability. The study area's fracture porosity, defined as the surface area of the fracture network as a percentage of its total surface area, indicates that the permeability of the fracture network increases with the fracture porosity, i.e., the number of fractures that serve as the main channel for fluid flow. Our results and (Miao et al., 2015a; Miao et al., 2015b) were consistent with (Xu et al., 2016) et al.'s findings.

Supplementary Figure S10 shows the relationship between the fracture porosity φ_f and the fractal dimension D_f of the reconstructed bifurcation fracture network model. The fractal dimension increases exponentially with increasing fracture porosity. The analysis above shows that the fracture porosity of the fracture network has a significant positive impact on the permeability. However, according to Equation (20), the bifurcation fracture network's permeability negatively correlates with the fractal dimension. Therefore, it can be inferred that although the bifurcation fracture network's fractal dimension increases indirectly with increasing the fracture porosity, the impact of the fracture porosity on permeability is much greater than that of the fractal dimension on permeability.

4.1.3 Relationship between bifurcation angle, θ, and bifurcation fracture network's permeability, Kf

Supplementary Figure S7C demonstrates that the seepage velocity within the main fracture appears to be stable. With the occurrence of bifurcation, however, the seepage velocity in the low-level fracture gradually decreases, and the greater the bifurcation angle, the slower the seepage velocity in the secondary fracture at the same level. Additionally, it has been demonstrated that the larger the bifurcation level, the more apparent the change. This is because the angle between the low-level fracture and the main fracture (the direction of fluid flow) becomes closer to vertical as the bifurcation angle increases. Consequently, the fluid flowing through the fracture experiences greater resistance, the local losses at the bifurcation increase, and the fluid seepage velocity decreases. Supplementary Figure S11 compares the simulation results with the theoretically predicted ones of permeability at different bifurcation angles. It can be seen from the figure that the fitting curve of the simulation results is consistent with the theoretically predicted one.

4.1.4 Relationship between the opening ratio χ, the proportion coefficient η. And the permeability Kf of the bifurcation fracture network

In order to determine the influence of the opening ratio and the bifurcation fracture network's proportionality coefficient on permeability, the permeability values with the opening ratio increased from 0.55 to 1.00, and other parameters fixed are obtained when the proportionality coefficient is 0.4, 0.5 and 0.0625, respectively. The geometric structural parameters of the bifurcation fracture network model in the simulation are shown in Supplementary Table S3 (Case. VI), and the simulation results are shown in Supplementary Figure S7D. The result show that as the opening ratio increases, bifurcations in the fracture network fluid flow rate increase. The reason is that the opening ratio indirectly increases the fluid seepage channel.

Supplementary Figure S12 provides a quantitative analysis of the relationship among the three parameters. Under different proportional coefficients, the permeability and the bifurcation fracture network's opening ratio have a non-linear growth relationship with the same growth trend. In addition, the longitudinal comparison reveals that, under similar opening ratio conditions, the greater the proportional coefficients, the greater the permeability of the bifurcation fracture network.

But the influence of the proportionality coefficient is greater than that of the openness ratio. For example, when the scaling coefficient η increases from 0.04 to 0.05, the fracture network's permeability increases from 2.886×10^{-13} m^2 to 1.0274×10^{-12} m^2 when the opening ratio is at χ=0.8. However, when the opening ratio χ is increased by 0.1 with the scaling coefficient η remaining unchanged, the permeability only increases by about 3.5×10^{-13} m^2.

5 Conclusion

1) Based on the fractal geometry theory combined with the bifurcation fracture network's structural parameters, an analytical expression of the bifurcation fracture network's permeability was established. The pixel probability algorithm and mathematical software were then used to reconstruct multiple sets of bifurcation fracture geometric models with distinct structural parameters.
2) The permeability analytical formula (20) was solved using COMSOL Multiphysics numerical simulation software. The simulated result was nearly consistent with the theoretically predicted trend.
3) The fracture flexural and bifurcation properties inhibit the flow of the coalbed methane in the bifurcation fracture network to different degrees. That is, the permeability of the fracture network decreases with the increase of the tortuosity fractal dimension D_T, bifurcation angle θ, and bifurcation level n. The fracture degrees and openings of bifurcation fractures play a prominent role in promoting the coalbed methane's transport. That is, the permeability of bifurcation fracture networks increases with the increase of the fracture porosity φ_f, pore size ratio χ, and proportion coefficient η.
4) The intricate geometric structures of fracture networks significantly influence coalbed methane migrations. According to sensitivity analysis, the degree to which structural parameters of a bifurcation fracture network affect permeability is as follows: $\varphi_f > \eta > D_T > \chi \approx D_f > \theta > n$.

Data availability statement

The original contributions presented in the study are included in the article/Supplementary Material, further inquiries can be directed to the corresponding author.

Author contributions

SJ carried out the experimental and manuscript writing work. BX, JP, TZ offered theoretical guidance and carried out the modification of the manuscript.

Funding

This work was supported by the National Natural Science Foundation of China (Grant No. 51974042), the National Natural Science Foundation of China (Grant No. U19B2009), and the Shanxi Science and Technology Plan Announced Bidding Project (Grant No. 20191101015).

Acknowledgments

I would like to express my gratitude to EditSprings (https://www.editsprings.cn) for the expert linguistic services provided.

Conflict of interest

The authors declare that the research was conducted in the absence of any commercial or financial relationships that could be construed as a potential conflict of interest.

Publisher's note

Supplementary material

The Supplementary Material for this article can be found online at: https://www.frontiersin.org/articles/10.3389/feart.2022.1108786/full#supplementary-material

References

Bobaru, F., and Zhang, G. (2015). Why do cracks branch? A peridynamic investigation of dynamic brittle fracture. *Int. J. Fract.* 196, 59–98. doi:10.1007/s10704-015-0056-8

Fu, Y., Chen, X., and Feng, Z. (2020). Characteristics of coal-rock fractures based on CT scanning and its influence on failure modes. *J. China Coal Soc.* 45, 568–578. doi:10.13225/j.cnki.jccs.2019.0480

Jafari, A., and Babadagli, T. (2016). Estimation of equivalent fracture network permeability using fractal and statistical network properties. *Hydrogeology J.* 24, 1623–1649. doi:10.1016/j.petrol.2012.06.007

Jin, Y., Li, X., Zhao, M., Liu, X., and Li, H. (2017). A mathematical model of fluid flow in tight porous media based on fractal assumptions. *Int. J. Heat Mass Transf.* 108, 1078–1088. doi:10.1016/j.ijheatmasstransfer.2016.12.096

Jin, Y., Wang, C., Liu, S., Quan, W., and Liu, X. (2020). Systematic definition of complexity assembly in fractal porous media. *Fractals* 28, 2050079. doi:10.1142/s0218348x20500796

Klimczak, C., Schultz, R., Parashar, R., and Reeves, D. (2010). Cubic law with aperture-length correlation: Implications for network scale fluid flow. *Hydrogeology J.* 18 (4), 851–862. published online:19 February. doi:10.1007/s10040-009-0572-6

Li, B., Wang, B., Yang, K., Ren, C., Yuan, M., and Xu, J. (2021). Study on fractal characteristics of coal pore fissure structure and permeability model. *Coal Sci. Technol.* 49, 226–231. doi:10.13199/j.cnki.cst.2021.02.026

Li, D., Li, G., and Liu, L. (2022). Present situation and development direction of coalbed methane (gas) exploitation and utilization in Shanxi Province. *Min. Saf. Environ. Prot.* 49, 132–136. doi:10.19835/j.issn.1008-4495.2022.02.024

Li, Y., and Jin, X. (2019). Study on high efficiency coalbed methane exploitation Technology in low permeability coal reservoir. *China Resour. Compr. Util.* 37, 84–86. doi:10.3969/j.issn.1008-9500.2019.02.025

Liu, R., Jiang, Y., Li, B., and Wang, X. (2015). A fractal model for characterizing fluid flow in fractured rock masses based on randomly distributed rock fracture networks. *Comput. Geotechnics* 65, 45–55. doi:10.1016/j.compgeo.2014.11.004

Liu, R., Yu, L., and Jiang, Y. (2016). Fractal analysis of directional permeability of gas shale fracture networks: A numerical study. *J. Nat. Gas Sci. Eng.* 33, 1330–1341. doi:10.1016/j.jngse.2016.05.043

Luo, Y., Xia, B., Li, B., Hu, H., Wu, M., and Ji, K. (2021). Fractal permeability model for dual-porosity media embedded with natural tortuous fractures. *Fuel* 295, 120610. doi:10.1016/j.fuel.2021.120610

Miao, T., Chen, A., Zhang, L., and Yu, B. (2018). A novel fractal model for permeability of damaged tree-like branching networks. *Int. J. Heat. Mass Transf.* 127, 278–285. doi:10.1016/j.ijheatmasstransfer.2018.06.053

Miao, T., Yang, S., Long, Z., and Yu, B. (2015a). Fractal analysis of permeability of dual-porosity media embedded with random fractures. *Int. J. Heat. Mass Transf.* 88, 814–821. doi:10.1016/j.ijheatmasstransfer.2015.05.004

Miao, T., Yu, B., Duan, Y., and Fang, Q. (2015b). A fractal analysis of permeability for fractured rocks. *Int. J. Heat Mass Transf.* 81, 75–80. doi:10.1016/j.ijheatmasstransfer.2014.10.010

Ren, Y., Wei, J., and Zhang, L. (2021). A fractal permeability model for gas transport in the dual-porosity media of the coalbed methane reservoir. *Transp. Porous Media* 140, 511–534. doi:10.1007/s11242-021-01696-x

Shi, D., Li, L., Liu, J., Wu, M., Pan, Y., and Tang, J. (2022). Effect of discrete fractures with or without roughness on seepage characteristics of fractured rocks. *Phys. Fluids* 34 (073611), 073611. doi:10.1063/5.0097025

Song, R., Liu, J., Yang, C., and Sun, S. (2020). Study on the multiphase heat and mass transfer mechanism in the dissociation of methane hydrate in reconstructed real-shape porous sediments. *Energy* 254, 124421. doi:10.1016/j.energy.2022.124421

Song, R., Sun, S., Liu, J., and Yang, C. (2021). Pore scale modeling on dissociation and transportation of methane hydrate in porous sediments. *Energy* 237, 121630. doi:10.1016/j.energy.2021.121630

Song, R., Wang, Y., Tang, Y., Liu, J., and Yang, C. (2022). 3D Printing of natural sandstone at pore scale and comparative analysis on micro-structure and single/two-phase flow properties. *Energy* 261, 125226. doi:10.1016/j.energy.2022.125226

Wang, F., and Cheng, H. (2020). A fractal permeability model for 2D complex tortuous fractured porous media. *J. Petroleum Sci. Eng.* 188, 106938. doi:10.1016/j.petrol.2020.106938

Wang, J., Chen, L., Kang, Q., and Rahman, S. S. (2016). Apparent permeability prediction of organic shale with generalized lattice Boltzmann model considering surface diffusion effect. *Fuel* 181, 478–490. doi:10.1016/j.fuel.2016.05.032

Wang, Z., Pan, J., Hou, Q., Yu, B., Li, M., and Niu, Q. (2018). Anisotropic characteristics of low-rank coal fractures in the Fukang mining area, China. *Fuel* 211, 182–193. doi:10.1016/j.fuel.2017.09.067

Wu, M., Wang, W., Zhang, D., Deng, B., Liu, S., Lu, J., et al. (2021). The pixel crack reconstruction method: From fracture image to crack geological model for fracture evolution simulation. *Constr. Build. Mater.* 273, 121733. doi:10.1016/j.conbuildmat.2020.121733

Xia, B., Luo, Y., Pan, C., Gong, T., Hu, H., and Ji, K. (2021a). Coalbed methane flow characteristics based on fractal geometry and stochastic rough fracture network. *Energy Sources, Part A Recovery, Util. Environ. Eff.*, 1–19 published online:04 Jan. doi:10.1080/15567036.2020.1859015

Xia, B., Luo, Y., Hu, H., and Wu, M. (2021b). Fractal permeability model for a complex tortuous fracture network. *Phys. Fluids* 33, 096605. doi:10.1063/5.0063354

Xu, P., Li, C., Qiu, S., and Sasmito, A. P. (2016). A fractal network model for fractured porous media. *Fractals* 24, 1650018. doi:10.1142/s0218348x16500183

Xu, P., Yu, B., Qiu, S., and Cai, J. (2008). An analysis of the radial flow in the heterogeneous porous media based on fractal and constructal tree networksAn analysis of the radial flow in the heterogeneous porous media based on fractal and constructal tree networks. *Phys. A Stat. Mech. its Appl.* 387, 6471–6483. doi:10.1016/j.physa.2008.08.021

Xu, P., Yu, B., Yun, M., and Zou, M. (2006). Heat conduction in fractal tree-like branched networks. *Int. J. Heat Mass Transf.* 49, 3746–3751. doi:10.1016/j.ijheatmasstransfer.2006.01.033

Yu, B. (2008). Analysis of flow in fractal porous media. *Appl. Mech. Rev.* 61, 50801. doi:10.1115/1.2955849

Yu, B., and Cheng, P. (2002). A fractal permeability model for bi-dispersed porous media. *Int. J. Heat Mass Transf.* 45, 2983–2993. doi:10.1016/s0017-9310(02)00014-5

Yu, B., and Li, J. (2004). A geometry model for tortuosity of flow path in porous media. *Chin. Phys. Lett.* 21, 1569–1571. doi:10.1088/0256-307x/21/8/044

Yu, B., and Li, J. (2001). Some fractal characters of porous media. *Fractals* 09, 365–372. doi:10.1142/s0218348x01000804

Zhang, J., Wang, Y., Lou, G., and Kou, J. (2021). A fractal model for effective thermal conductivity of dual-porosity media with randomly distributed tree-like networks, ". *Fractals* 29, 2150146. doi:10.1142/s0218348x21501462

Zhao, M., Jin, Y., Liu, X., Zheng, J., and Liu, S. (2020). Characterizing the complexity assembly of pore structure in a coal matrix: Principle, methodology, and modeling application. *J. Geophys Res-Sol Ea.* 125, e2020JB020110. doi:10.1029/2020jb020110

Zhu, Z., Song, Z., Shao, Z., Wu, M., and Xu, X. (2021). Simulation of imbibition in porous media with a tree-shaped fracture following the level-set method. *Phys. Fluids* 33 (8), 082109. published online:19 August. doi:10.1063/5.0060519

frontiers | Frontiers in Earth Science

TYPE Original Research
PUBLISHED 10 January 2023
DOI 10.3389/feart.2022.1103286

OPEN ACCESS

EDITED BY
Zhenzhi Wang,
Henan Polytechnic University, China

REVIEWED BY
Kun Zhang,
Henan Polytechnic University, China
Yanjun Meng,
Taiyuan University of Technology, China
Baoxin Zhang,
China University of Mining and Technology, China

*CORRESPONDENCE
Dawei Lv,
lvdawei95@gmail.com

SPECIALTY SECTION
This article was submitted to Economic Geology, a section of the journal Frontiers in Earth Science

RECEIVED 20 November 2022
ACCEPTED 05 December 2022
PUBLISHED 10 January 2023

CITATION
Ge D, Lv D, Yao P, Wen S, Li J and Lei G (2023), Physical property differences of source rocks in the Lucaogou Formation and adsorption ability variation under their influence. *Front. Earth Sci.* 10:1103286. doi: 10.3389/feart.2022.1103286

Physical property differences of source rocks in the Lucaogou Formation and adsorption ability variation under their influence

Dongfeng Ge[1,2], Dawei Lv[1]*, Peng Yao[1], Shupeng Wen[3], Jiahui Li[1] and Guoming Lei[2]

[1]College of Earth Sciences and Engineering, Shandong University of Science and Technology, Qingdao, China, [2]No.9 Geological Party, Xinjiang Bureau of Geological and Mining Resources, Urumqi, China, [3]113 Team of Guizhou Coal Geology Bureau, Guiyang, China, [4]The First Exploration Team of Shandong Province Coal Geology Bureau, Qingdao, China

Shale gas exploration is very important for the China in the further. There are many findings of shale gas in Northwest China, especially in Junggar Basin Permian Lucaogou Formation of the Xinjiang Uygur Autonomous Region. However the basic geological characteristics of Lucaogou Formation is not still clear. In order to solve this problems, Quanzijie shale gas collected from the southern margin of the Junggar Basin is taken as the study area, and shale gas resources are investigated and evaluated using the organic-rich shale section. On this basis, the investigation and evaluation of shale gas resources in the Lucaogou Formation is performed. The reservoir performance, preservation conditions, compressibility, and gas-bearing properties of gas-bearing shale intervals are identified. The results are as follows: The vertical and horizontal lithological and lithofacies variations of the source rocks of the Lucaogou Formation are clarified. This layer is characterized by the upward thinning of grain size and the upward darkening of color in the vertical direction. The layer can be divided into upper and middle-lower sections, with organic shale being most developed in the upper section, and sandstone and dolomite being more developed in the middle and lower area. The main hydrocarbon source rocks are developed in the upper area of the Lucaogou Formation. The total thickness of the hydrocarbon source rocks is 78.12–513.73 m. The lithology is mainly gray-black shale, silty mudstone, and oil shale. The average organic carbon content is 4.86%. The maturity of the organic matter is mainly 0.7–0.8%. The shale reservoirs have a high content of brittle minerals, but the physical properties both of the shale and sandstone reservoirs are poor. These are generally ultra-low porosity and ultra-low permeability reservoirs, in which the oil and gas reservoir space is mainly fractures.

KEYWORDS

Junggar Basin, Lucaogou Formation, shale reservoirs, porosity–permeability, hydrocarbon source rocks

Introduction

In the past few decades, the large-scale commercial development of shale oil and gas has changed the global energy supply structure (Chen et al., 2011; Aljamaan et al., 2017; Tang et al., 2021). The "shale oil and gas revolution" in the United States has turned it from an energy-importing country into an energy-exporting country. China is rich in shale oil and gas resources (Wang et al., 2014; Li et al., 2018; Ju et al., 2019). Continental shale, marine shale, and sea–land transitional shale are widely developed in oil- and gas-bearing basins in the northwest, north, and northeast of China, as well as in Qinghai Tibet and southern regions. This is an important field of unconventional oil and gas exploration and development in China (Gale et al., 2007; Gou., 2017; Gong et al., 2021).

Shale reservoirs are characterized by low porosity and ultra-low permeability (Hou et al., 2018; Javed et al., 2019; Yuan and Rezaee., 2019). Natural fractures are widely developed in shale, which is an important reservoir space and seepage channel of shale reservoirs (Dong et al., 2010; Habina et al., 2017; Guo et al., 2019). This can significantly improve the storage and seepage capacity of shale, affecting the enrichment, preservation conditions, single-well productivity, fracturing, and other development effects of shale oil and gas, and it is an important geological factor to be considered for shale oil and gas development (Yang et al., 2016; Yan et al., 2017; Li et al., 2018; Zhang et al., 2020).

Sets of hydrocarbon source rocks are developed in the southeast margin of Junggar Basin, including Permian, Triassic, Jurassic, Cretaceous, and Paleogene. Among them, the Permian Lucaogou Formation is one of the most important hydrocarbon source rocks, and it is also the stratum with the most potential for oil and gas exploration (Jiao et al., 2014; Hu et al., 2016; Jiang et al., 2019). Until now, several industrial oil wells have been drilled in the Lucaogou Formation. Some scholars have studied the oil-bearing properties, geochemical characteristics, hydrocarbon generation potential, and the mechanisms of the source rocks in this formation. The results show that this set of source rocks is a set of saline and semi-saline lacustrine sediments, with complex and diverse lithology, strong heterogeneity, wide distribution range, and large thickness, which shows good prospects for oil and gas exploration (Li et al., 2015; Liu et al., 2018).

In conclusion, the physical properties of shale reservoirs have become the main controlling factor for shale oil and gas production, and numerous research achievements have been made. However, research on the basic geological (sedimentary facies, reservoir physical properties, etc.) characteristics of shale oil and gas in the southern margin of the Junggar Basin is still insufficient, which seriously restricts the exploration and development of shale oil and gas resources in this area.

In this paper, Quanzijie shale gas collected from the southern margin of the Junggar Basin is taken as the study area, and shale gas resources are investigated and evaluated by using the organic-rich shale section. First, a set of strata is divided into upper and middle–lower sections, the basic characteristics of the source rocks are described in detail, and the shale facies type is identified by using rock type and TOC content. Second, the spatial distribution differences of the hydrocarbon source rocks are studied. Third, the type of organic matter, reservoir physical properties, and pore structure of different rock types and layers are compared, and differences in the organic geochemical characteristics are analyzed. On this basis, the physical property differences of source rocks in the Lucaogou Formation and dynamic variation of free surface energy under their influence is studied. These results can provide a theoretical basis for the efficient development of shale oil and gas in the southern margin of the Junggar Basin.

Geological setting and sample preparation

Geological setting

The tectonic environment of the study area in this paper is located in the eastern segment of the Dahuangshan–Dalongkou reversed turn. Owing to the influence of the Bogda Mountain front thrust belt, a series of tectonic deformations dominated by compressive stress has developed in this study area. Crumpled deformation formed by south to north napping can be seen in the Lucaogou Formation, where hydrocarbon source rocks are developed. This area is located in the east section of the south Junggar thrust belt. Regional and secondary faults are relatively developed. Generally, there are two large folds along the back, namely, the Dalongkou Syncline and the West Dalongkou Anticline. The hydrocarbon source rock horizon in this area is mainly the Lucaogou Formation, which can be mainly divided into the upper and middle-lower sections (Zhao et al., 2017; Qiao et al., 2020).

The upper section of this formation is composed of grayish black carbonaceous shale, silty mudstone, oil shale, and multi-layer dolomitic limestone and marlstone. The lithology of the upper section of the north wing of the Dalongkou Syncline in the area changes continuously, but the sand content in the upper section of the formation is significantly increased near the core of the Dalongkou Syncline and the Bogda Mountain front area in the south wing. The lithology is black-gray argillaceous siltstone, siltstone, and even fine sandstone, and the shale content is lower (Figure 1).

Sample and experimental methods

Shale and sandstone samples were collected from the upper and middle–lower sections of the Lucaogou

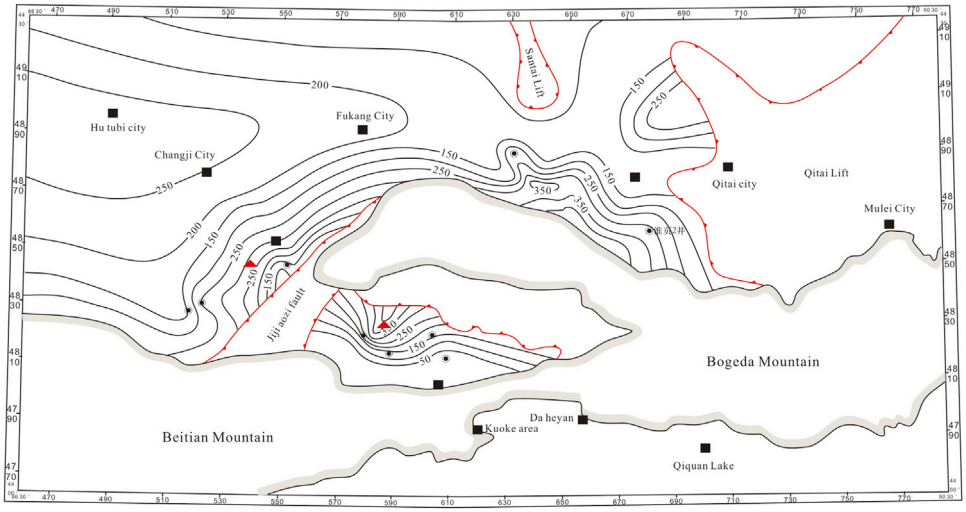

FIGURE 1
Study area, location, columnar drilling, and sampling locations.

Formation for experimental testing. The organic geochemical characteristics and mineral composition of all the samples were analyzed. Then, the morphological characteristics of all the samples were observed by FE-SEM and quantitatively characterized by PCAS software. Subsequently, pore volume, specific surface area, and pore size distribution of the pores were quantitatively studied by N_2 adsorption.

TOC experiments

All the samples were manually selected, manually ground to <60 meshes, and weighed 10 g. According to the national standard (GB/T 19145-2003), they were tested in the Jiangsu Institute of Geology and Mineral Resources Design. In the XRD experiment, the clay test sample was artificially broken into 60–80 meshes, weighing 200 g, and the whole rock test sample was broken into small pieces weighing 30 g, ground completely to <200 meshes, which was completed in Sinopec East China Branch's test center. The instrument used was Ultima IV, and the experiments were conducted according to the industry standard SY/T 5163-2010.

FE-SEM experiment

Small samples were selected after argon ion polishing, after which a Quanta250 scanning electron microscope was used for testing and analysis. The FE-SEM photos taken were quantitatively analyzed by PCAS software, which is a professional software developed by Liu et al. (2011) to identify the micro pore structure in high-resolution SEM photos. This technique has been successfully applied to the quantitative identification of clay mineral micro-fractures and organic-rich shale micro pores.

Isothermal adsorption test

The instrument used in this experiment was a IS-100 high-pressure gas isothermal adsorption and desorption instrument. In strict accordance with the GB/T 19560-2008 Test Method for High Pressure Isothermal Adsorption of Coal, the sample was ground to 60–80 meshes, and a 100-g sample was taken and put it into the vacuum drying oven. The coal sample was dried at 373K for 6 h. Then, the sample was cooled to room temperature and put into the coal sample tank for evacuation. Methane adsorption experiments were carried out at ambient temperature (30°C) and an equilibrium pressure range of 0–15 MPa. The adsorption equilibrium time at each pressure point was greater than 12 h.

Results and discussion

Detailed description and difference comparison of lithofacies types

Outcrop observation and drilling revealed that the typical sedimentary rocks of the Lucaogou Formation (P_3l) in this area are gray shale, oil shale, siltstone with dolomite, limestone lens, and a small amount of sandstone lens. According to the differences in the lithology, sedimentary structure, contents, mineral components, and logging curve of the sediments, the

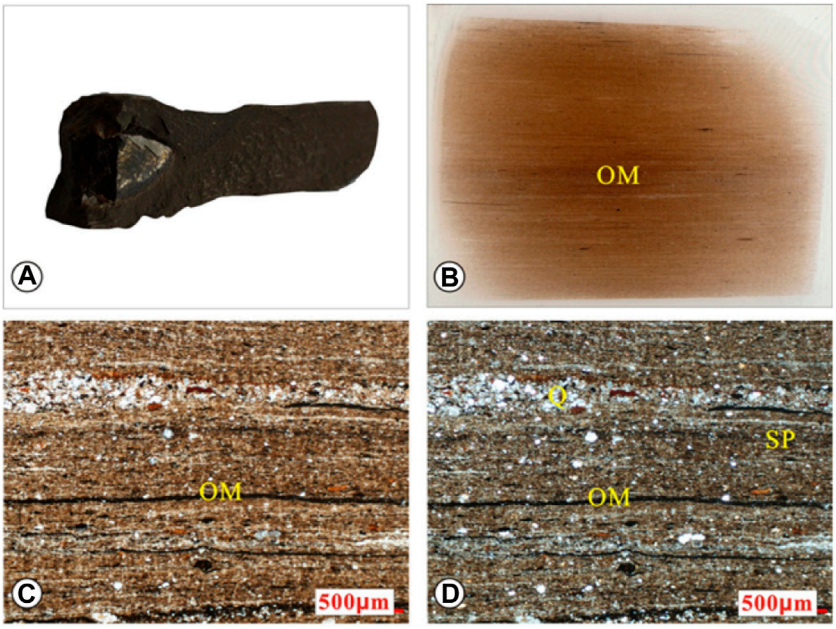

FIGURE 2
Thin section photos of black oil shale samples **(A)**, Asphaltic concretion; **(B–D)** Muddy structure and layered structure can be seen under the microscope.

oil shale of the Lucaogou Formation in the study area is divided into five lithologic facies: black oil shale/shale facies; gray-black/dolomitic mudstone facies; gray-white argillaceous dolomite/limestone facies; gray-white micritic dolomite/micritic limestone facies; and granular limestone/dolomite facies. Among them, black oil shale/shale facies and gray-black calcareous/dolomitic mudstone facies are the main lithofacies types.

Black oil shale/shale facies

Black oil shale/shale facies are the most important lithologic facies in this study area. The main lithology is black/black-brown oil shale and gray-black shale. Many shales are intercalated with siltstone laminae or bands (mm). The siltstone can be seen in the liquefaction deformation structure, which may be turbidite sandstone at the far end of the semi-deep lake. The most intuitive features of this phase are the black color and prominent page structure.

The weathered color of the oil shale is mainly light blue-gray, gray-white, etc. The fresh surface is mainly black. After weathering, it presents an obvious book-like page texture. The fresh rock has thick foliation and common horizontal bedding. It contains fish (ancient cod, complete or fragmented), abundant phyllopods, bivalves, ostracods, and plant fossils preserved *in situ*. There are cubic or globular pseudomorphs of luteite with punctate ferritization and gypsum snowflake crystals (secondary changes) and bitumen-bearing nodules (Figure 2A). In this section, microscopically, the argillaceous structure and the layered structure can be seen (Figure 2).

Lime/dolomitic mudstone facies

Compared with the black oil shale/shale lithologic facies, the most intuitive sign of this facies is grayish black with undeveloped foliation, mostly in a transitional relationship with the black shale facies. The lithology of this lithofacies includes calcareous mudstone, dolomitic mudstone, and silty mudstone. It is mostly mixed with siltstone laminations or bands.

The weathered color of the mudstone is mostly grayish white, brown-gray, and other colors. The fresh surface is grayish black, with a massive structure, and the section is mostly shell-shaped. Lime shales mixed with thin siltstone laminations or bands are common, and liquefaction deformation structures are found in the siltstone (Figure 3).

Spatial distribution differences of the hydrocarbon source rocks

Figure 5 shows that the hydrocarbon source rocks of P_3l in the study area are distributed in the upper section of the Lucaogou Formation vertically. The thickness of the upper section is 185.22–522.72 m. The lithology of the hydrocarbon

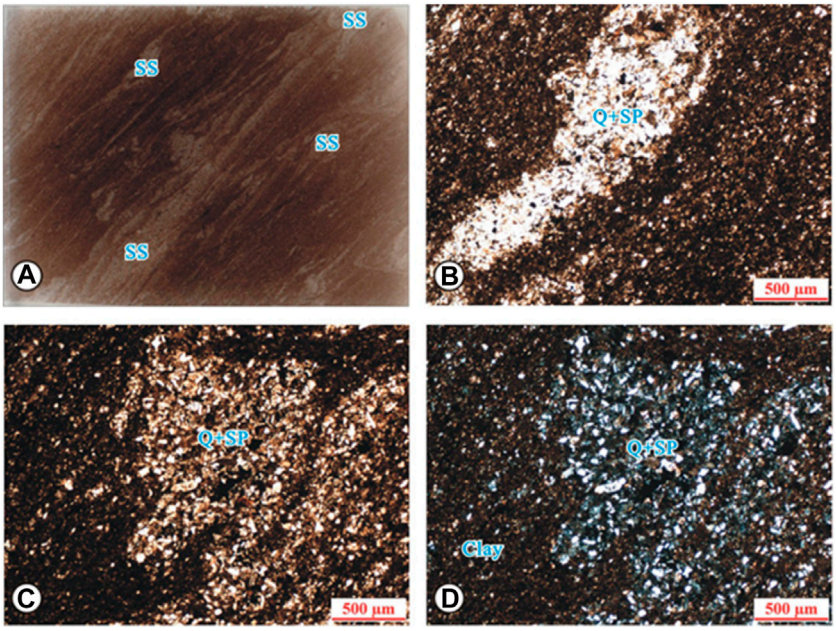

FIGURE 3
Thin section photo of grayish black silty banded dolomitic mudstone rock **(A)**, Lime mudstone; **(B)**, Dolomitic mudstone; **(C)**, Silty mudstone; **(D)**, mudstone rock.

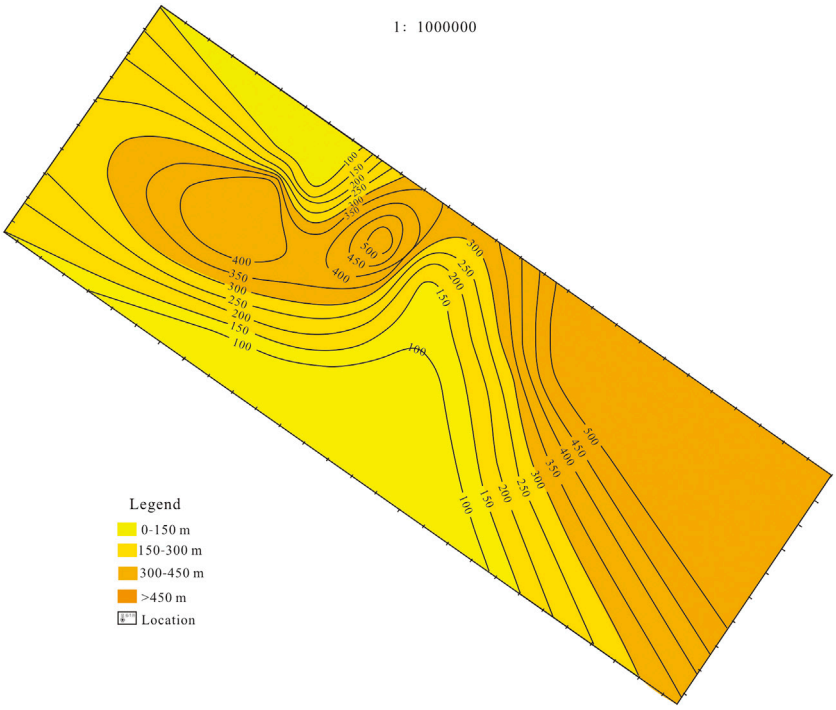

FIGURE 4
Thickness of the hydrocarbon source rocks in the upper part of the Lucaogou Formation.

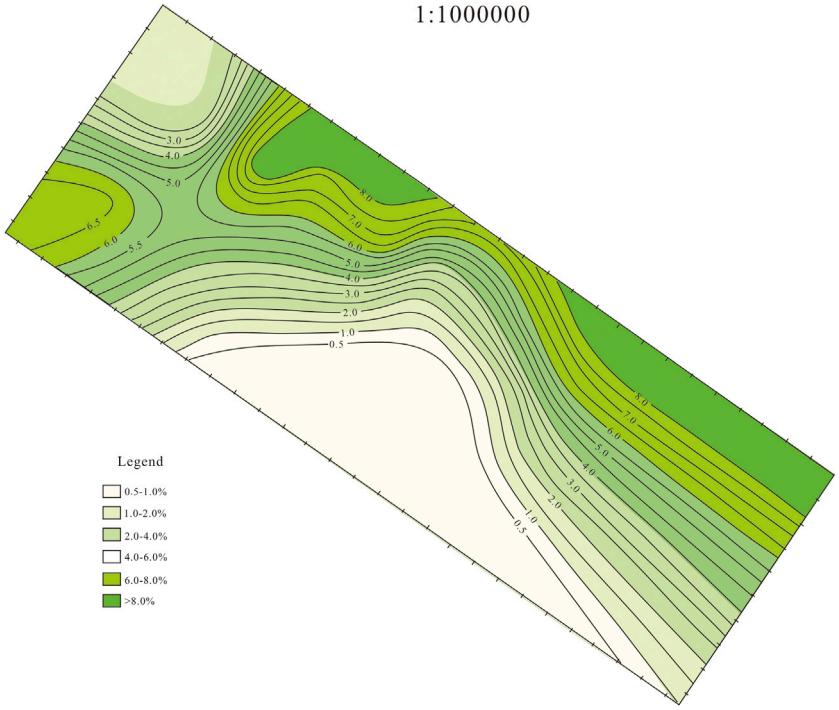

FIGURE 5
Distribution of the TOC content in the source rocks of the Lucaogou Formation.

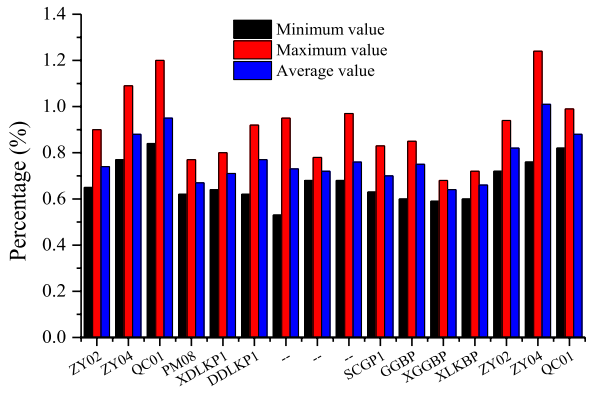

FIGURE 6
Distribution of the TOC content in the source rocks of the samples collected from the Lucaogou Formation.

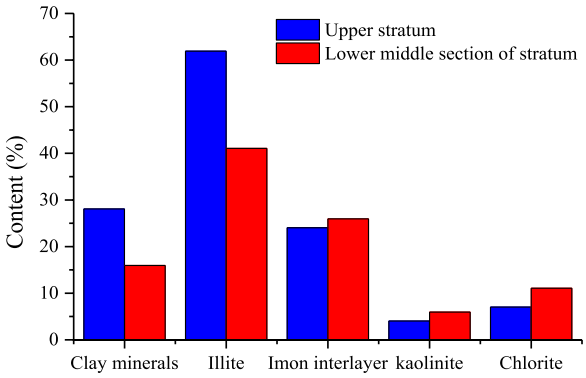

FIGURE 7
Percentage of clay minerals and components in the upper and middle–lower sections.

source rocks is gray-black shale, silty mudstone, and black oil shale. The total thickness of the upper section is 78.12–513.73 m. The proportion of hydrocarbon source rocks in the upper section of the formation is 36%–98%, with an average of 85%. The lithology of the non-hydrocarbon source rocks in the upper section is gray dolomite, argillaceous dolomite, argillaceous siltstone, and a small amount of argillaceous silty limestone, with a total thickness of 2.92–136.46 m, ranging from 1 to 19 layers. The middle-lower section is composed of gray-white silty fine sandstone and dolomitic siltstone, mixed with a thin layer of dark mudstone, and the source rock is not developed.

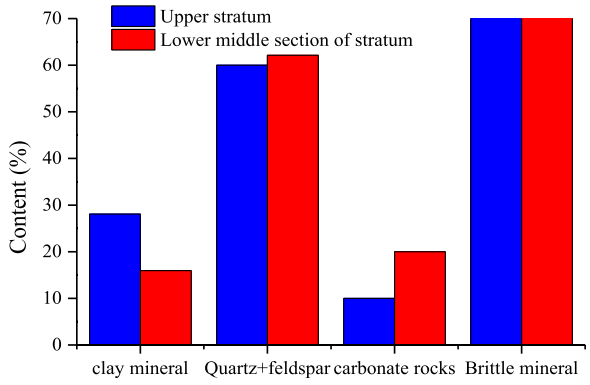

FIGURE 8
Percentage of mineral components in upper and middle–lower samples.

syncline are exposed to the surface, and their thickness is centered around the Xiaolongkou area, showing a trend of gradual thinning around. The core and south wing of the syncline are covered by the Quaternary system. The thickness of the hydrocarbon source rocks controlled by drilling is much smaller than that of the north wing of the syncline. The thickness of the hydrocarbon source rocks changes: in the south wing of the syncline it is less thick than in the core of the syncline, while it is at its thickest in the north wing of the syncline.

In the study area, the thickness variation of the hydrocarbon source rocks in the upper section is larger. The thickness of the hydrocarbon source rocks in the area of Dalongkou–Gangou in the west decreases gradually toward the surrounding area, while the hydrocarbon source rocks in the area of the Quancan 1 Well are

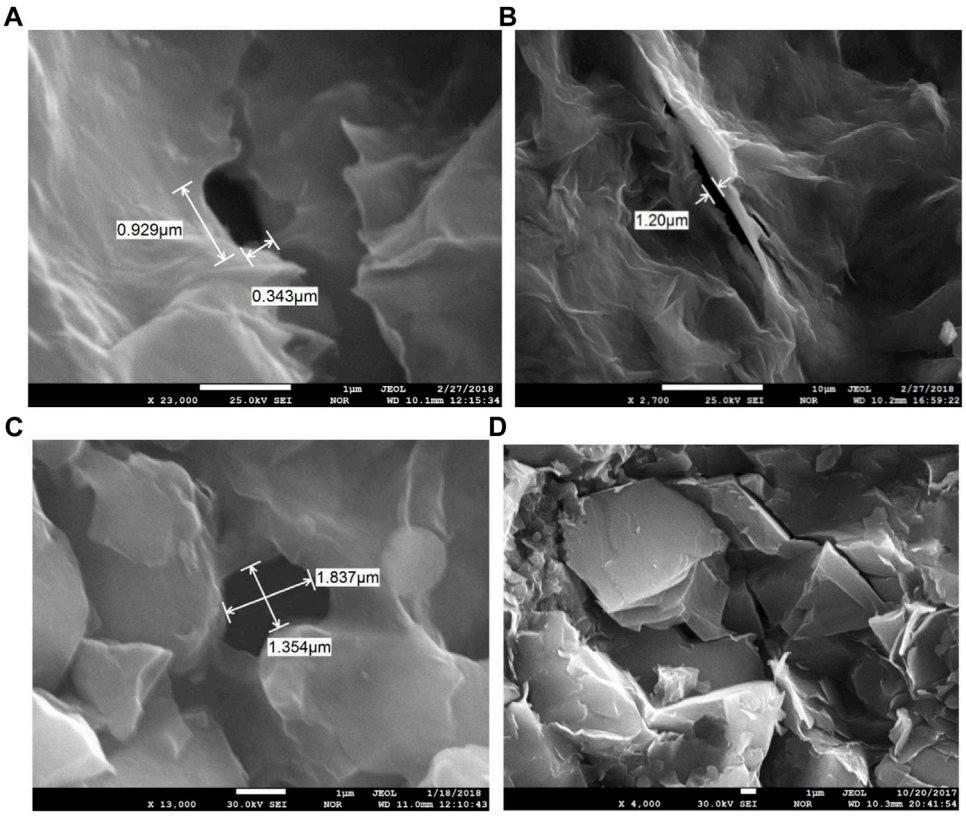

FIGURE 9
Pore type of all samples: **(A)** intergranular pore of shale reservoirs in the upper section; **(B)** intergranular gap of shale reservoirs in the upper section; **(C)** mold pore of sandstone reservoirs in the upper section; **(D)** granular minerals and intergranular microcracks of sandstone reservoirs in the upper section.

The results show that the hydrocarbon source rocks in the upper section are basically distributed around the Dalongkou Syncline. The hydrocarbon source rocks in the north wing of the thinner, and thickness of the hydrocarbon source rocks in the area of Well Qi1 increases gradually toward the northeast (Figure 4).

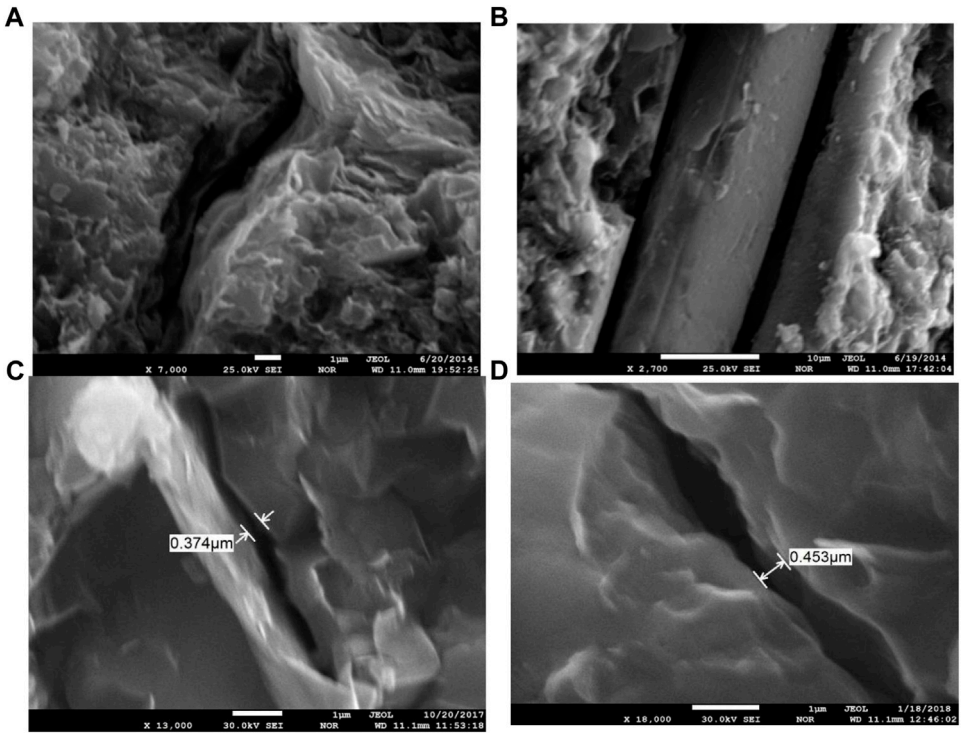

FIGURE 10
Fracture type of all samples: **(A)** dissolution fissure in the upper section; **(B)** straight gap between mineral particles of sandstone in the lower section; **(C)** micro-fracture of sandstone in the upper section; **(D)** micro-fracture of sandstone in the upper section.

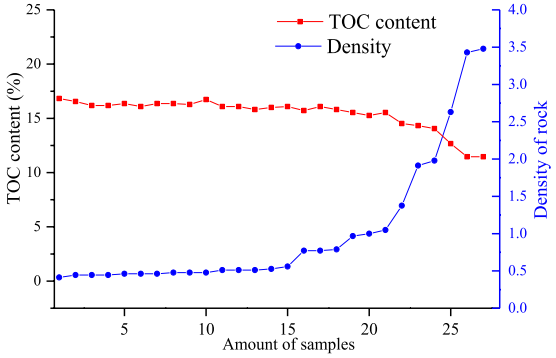

FIGURE 11
Comparison of shale rock density and organic carbon content in the upper part of the Lucaogou Formation.

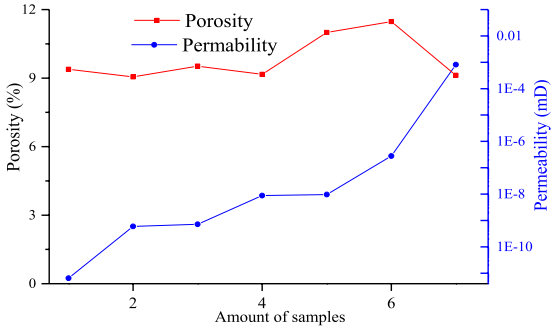

FIGURE 12
Relationship between the porosity and permeability of shale reservoirs in the upper section.

Difference comparison of organic geochemical characteristics

Type of organic matter

The organic macerals of kerogen are mainly sapropel amorphous and humic amorphous. The sapropel formation is composed of sapropel amorphous and algal bodies, with a relative abundance of 0%–86%, with an average of 49.91%. Most of the non-resinous bodies are cuticle and chitin, with a relative abundance of 0%–87%, with an average of 18.91%. The vitrinite consists of structural vitrinite and unstructured vitrinite, with a relative abundance of 5%–79%, with an average of 26.7%.

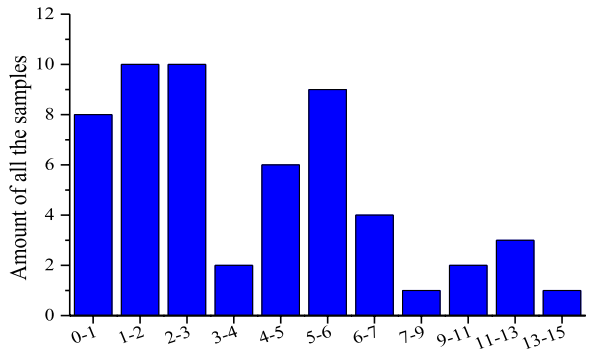

FIGURE 13
Distribution frequency of the specific surface area in different intervals of the upper shale reservoirs.

sapropel humic type. Vertically, hydrocarbon protoliths of the upper section are type II_1, type II_2, and a small amount of type III, while the middle–lower section is dominated by type II_1.

Organic matter content (TOC)

The organic carbon content of the source rocks is generally higher. The surface and drilling revealed that the TOC content is 0.5%–27.48%, with an average of 4.31%. Based on 22 samples of non-hydrocarbon source rocks, the TOC content was found to be 0.06%–0.48%, with an average of 0.33%, and the TOC content of source rock was mainly distributed between 0.6% and 7.0% (Figure 5). According to distribution of the TOC content (Figure 8), the higher TOC value area of the hydrocarbon source rocks is basically distributed around the basin–mountain junction in the north of the study area,

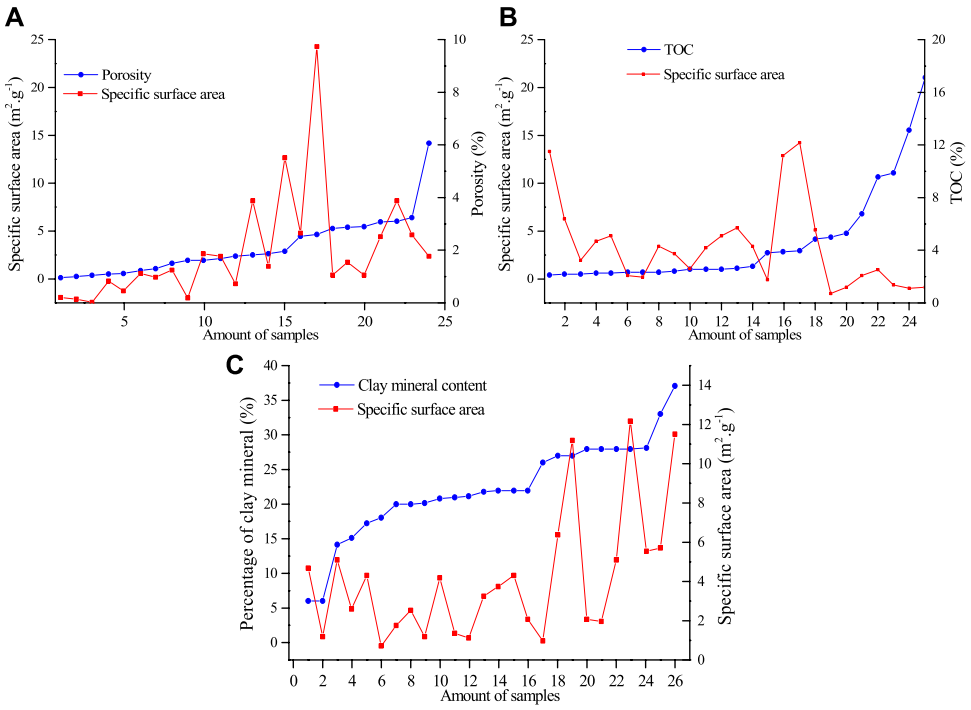

FIGURE 14
Relationship between specific surface area and pore parameter (a, specific surface area vs porosity; b, specific surface area vs TOC; c, specific surface area vs mineral content)

The relative abundance of the inert group is 2%–53%, with an average of 10.48%. The kerogen is light-yellow-brown, with no weak fluorescence, and the kerogen type index is −82 to 81.

The results show that the types of kerogen in the source rocks are type II_1, type II_2, and type III, with few type I. Type II is the main type, accounting for 89% in total. This shows that the main type of kerogen in the survey area is sapropel type, followed by

indicating a decreasing trend from north to south. The higher organic carbon content area is concentrated in the Dalongkou–Gangou area in the west, with an average organic carbon content of more than 6%. The average organic carbon content in the area from Heijiawan to Dongdalongkou is 3%–4%, while the average organic carbon content in the area from Quancan Well 1 to Zhunye Well 4 in the south of the survey area is 0.5%–2%.

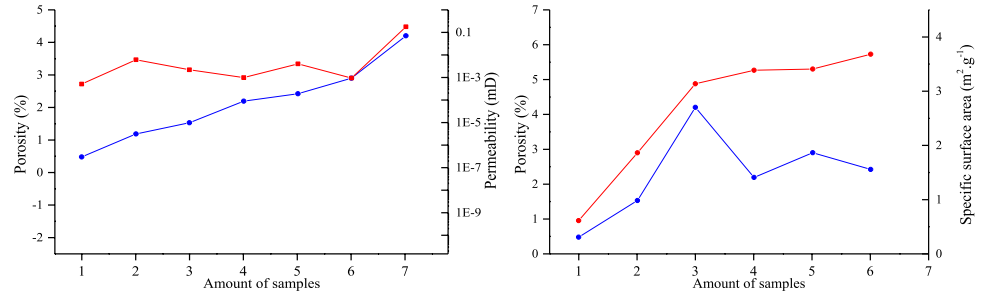

FIGURE 15
Change in the porosity and permeability of the sandstone sample in the upper section. The blue line is porosity and red line is permeability.

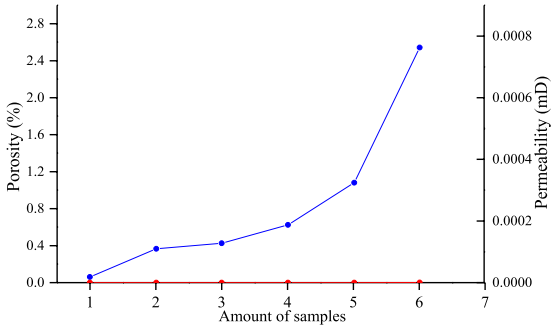

FIGURE 16
Relationship between the porosity and permeability of shale reservoirs in the middle–lower section. The blue line is porosity and red line is permeability.

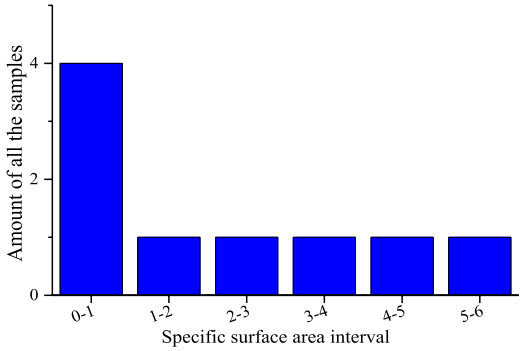

FIGURE 17
Distribution frequency of the specific surface area in different intervals of shale reservoirs in the middle and lower sections.

In conclusion, the hydrocarbon source rock abundance in the north of this study area is better than that in the south. From the tectonic location of the source rocks, the hydrocarbon source rock abundance in the north wing of Dalongkou Syncline is higher than that in the core and south wing of the syncline. This is because the northern area was a deep-water area of the lake basin during the deposition, and the water body gradually became shallow toward the south. Bogda Mountain provided the main material source for the formation of hydrocarbon source rocks in the area during the Lucaogou Formation of the Late Permian, and the TOC content was mainly affected and controlled by the sedimentary environment. The deeper the sediment body, the higher its TOC content will be.

Maturity

The results show that the $R_{o,\ max}$ of the hydrocarbon source rocks is 0.53%–1.24%, with an average of 0.78%. It generally follows normal distribution characteristics. The main body belongs to the mature stage, the second belongs to the lower-maturity stage, and a small amount is distributed in the immature stage, with a low degree of thermal evolution (Figure 6).

Adsorption of reservoirs in the Lucaogou Formation

Petromineralogical characteristics

Clay minerals

The maximum clay mineral content (59%) of the shale reservoir samples in the upper section is slightly higher than the maximum clay content (38%) in the middle and lower sections, while the minimum clay content (4%) is equivalent to that of the samples in the middle and lower sections (3%), and the average clay content (28%) in the upper section is higher than that of the samples in the middle and lower sections (16%). The clay mineral composition of the shale reservoirs in the upper and middle–lower sections is mainly illite, followed by the illite/montmorillonite interbeds, while kaolinite, chlorite, and green/montmorillonite interbeds are relatively small. In the clay composition of the upper section, the average illite content (62%) is significantly higher than average illite content (41%) of the lower–middle section (Figure 7). In both

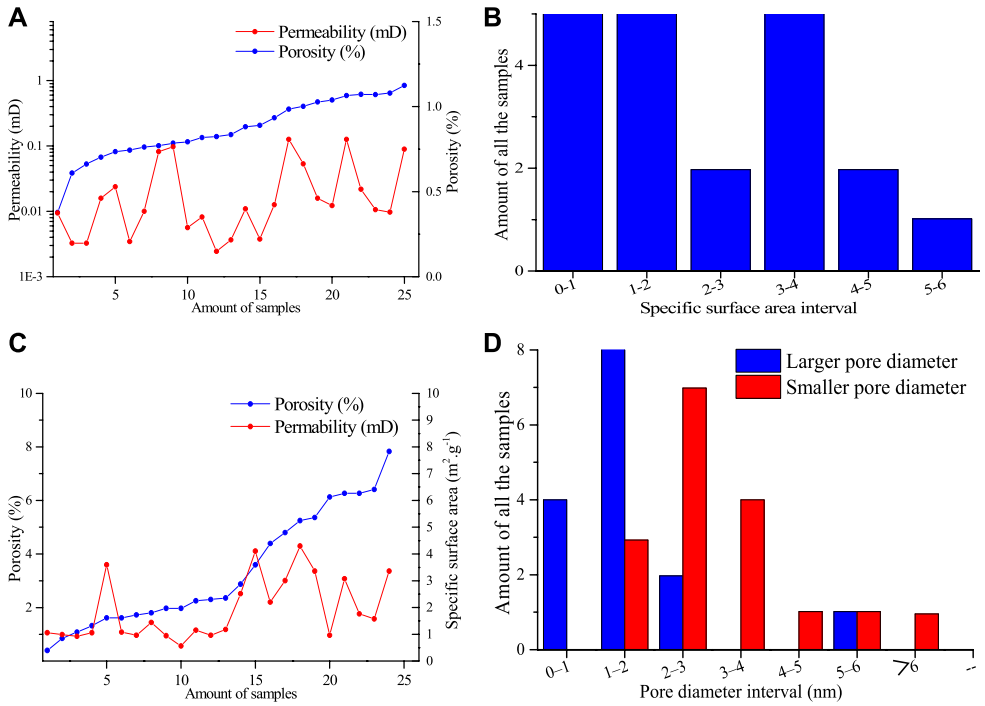

FIGURE 18
Permeability and porosity of sandstone reservoirs in the middle and lower sections/Specific surface area of all the samples in middle-lower section

the upper sample and the middle–lower sample, the illite/montmorillonite interlayer in the clay mineral components decreases with the increase of illite content.

Brittle minerals

The brittle minerals of the upper and lower sections are mainly quartz, feldspar, calcite, and dolomite. Among them, the average content of quartz and feldspar in the upper section (60%) is close to that in the middle–lower section (62%), the average content of carbonate rock (10%) is lower than that in middle–lower section (20%), and the average content of brittle minerals (71%) is lower than that in the middle–lower sample (84%) (Figure 8).

Type of reservoir space

The combination of macro and micro

Based on the core observation and scanning electron microscope results, it can be seen that the reservoir space types of this formation are diverse, mainly including macro-scale fractures and pores, as well as micro-scale pores and fractures.

Pores

The pores are mainly intergranular pores, intragranular pores, intergranular gaps, and mold holes at the micro-scale (Figure 9). All kinds of pores can form good self-sourced oil and gas reservoir spaces.

The fractures include macro-scale fractures, dissolution fractures, sutures and micro-scale fractures, lamina fractures, dissolution fractures, intergranular fractures, and internal fractures of clay minerals (Figure 10). For fluids, fractures play a dual role, which can be both a fluid migration channel and an effective reservoir space. It can not only destroy the oil and gas reservoir, resulting in the loss of oil and gas, but can also improve the reservoir pore connectivity and permeability.

Reservoir physical properties and pore structure

Shale reservoirs in the upper section

The rock density of the shale reservoir has a significant negative correlation with organic carbon content (TOC), that is, low TOC content represents high rock density (Figure 11). Therefore, it can be concluded that rock density logging data can be used to identify carbonaceous shale intervals during drilling.

As shown in Figure 12, permeability tends to increase with the increase of porosity, but the correlation between porosity and permeability is not obvious. On the contrary, some low porosity samples have high permeability values, indicating that their permeability is obviously affected by the micro-fractures. Some

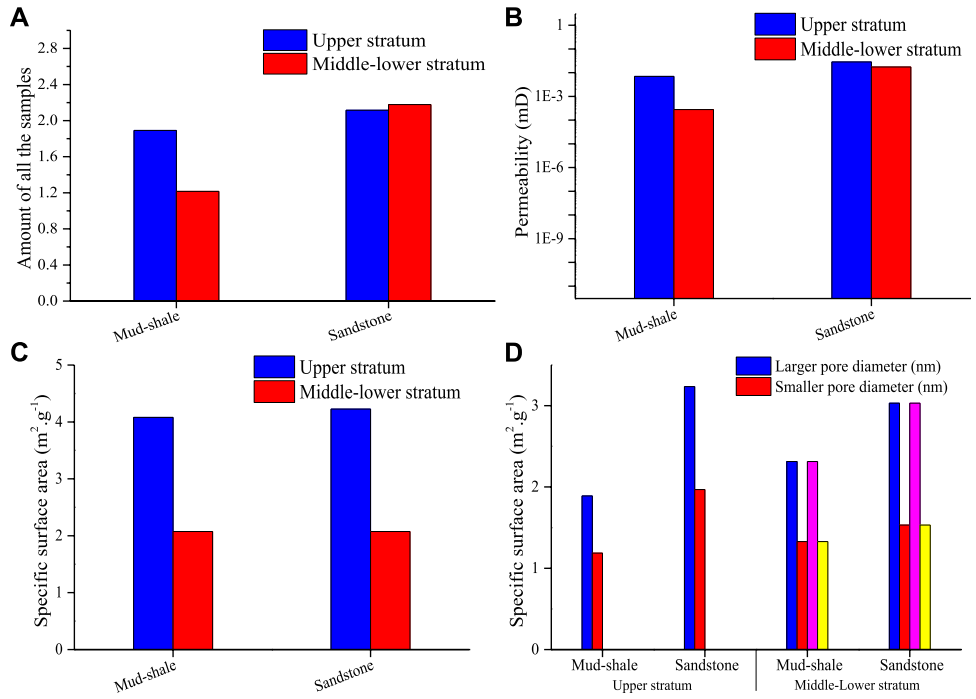

FIGURE 19
Comparison of the petrophysical properties of the upper/middle–lower reservoirs: **(A)** porosity; **(B)** permeability; **(C)** specific surface area; **(D)** specific surface area comparison of different lithology.

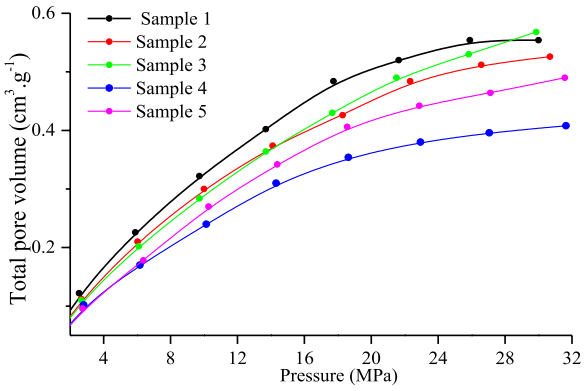

FIGURE 20
Isothermal adsorption simulation experiment curve for Zhunye Well 4.

higher porosity samples have lower permeability values, indicating poor pore connectivity.

The specific surface area test results show that the minimum value of the specific surface area in the upper section is 0.12 m^2/g, the maximum value is 14.2 m^2/g, and the average value is 4.08 m^2/g, mainly distributed in the range of 0–6 m^2/g (Figure 13).

With the increase of the specific surface area, the porosity generally has an upward trend, but the correlation between them is general. The specific surface area is negatively correlated with the percentage of TOC content, and it is approximately positively correlated with the percentage of clay minerals (Figure 14).

Sandstone reservoirs in the upper part of the Lucaogou Formation

Figure 15A shows that permeability tends to increase with the increase of porosity, but the correlation between porosity and permeability is not obvious. On the contrary, some low porosity samples have high permeability values, indicating that their permeability is obviously affected by the micro-fractures in the samples. Figure 15B shows that the minimum and maximum specific surface areas of the sandstone reservoirs in the upper part of Lucaogou Formation are 0.951 and 5.75 m^2/g, respectively, with a main distribution range of 3–6 m^2/g. As the specific surface area increases, the porosity has an overall upward trend.

Shale reservoirs in the middle-–lower section

Figure 16 shows that the permeability tends to increase with the increase of porosity, but the correlation between porosity and permeability is general. This indicates that the minimum specific

surface area of the shale reservoirs in the middle–lower section is 0.162 m^2/g, and the main distribution range is 0–1 m^2/g (Figure 17).

Sandstone reservoirs in the middle-lower section

Figure 18A shows that there is an upward trend with permeability, but the correlation between porosity and permeability is not obvious. On the contrary, lower porosity samples have high permeability values, which indicates that permeability is obviously affected by micro-fractures in the samples. The minimum and maximum specific surface areas of sandstone reservoirs are 5.75 and 2.056 m^2/g, respectively, with a main distribution range of 0–2 m^2/g (Figure 18B). Figure 18C shows that porosity has an overall upward trend with the increase of the specific surface area. Figure 18D shows that the pore diameter interval distributions in the samples which reflect the statics data are effective.

Physical properties of reservoir rocks

Figure 19A shows that the porosity of the shale reservoirs in the upper section is greater than that in the middle–lower section. The porosity of the upper sandstone reservoirs is less than that of lower sandstone reservoirs. The porosity of the sandstone reservoirs is greater than that of shale, and the porosity of the sandstone reservoirs in the middle–lower section is greater than that of mudstone. Figure 19B shows that the permeability of the shale and sandstone reservoirs in the upper section is higher than that in the middle–lower section. The permeability of the sandstone reservoirs is higher than that of shale. Figure 19C shows that the specific surface areas of sandstone and shale are similar, and the specific surface areas in the upper section are larger than those in the middle-lower section. According to the scanning electron microscope statistical analysis results (Figure 19D), the average pore length and diameter of sandstone rocks are larger than that of shale.

Adsorption of hydrocarbon source rocks in the Lucaogou Formation

In this paper, high-temperature isothermal adsorption tests were carried out on 13 samples to characterize the adsorption of organic-rich shale in the study area (Figure 20). The test conditions comprised a laboratory temperature of 30°C, a helium concentration of 99.999%, and a methane concentration of 99.99%. These results show that the average Langmuir volume V_L is 2.93 m^3/t and the average Langmuir pressure P_L is 7.83 MPa. In general, the larger the Langmuir volume, the stronger the adsorption capacity of mudstone. The average Langmuir volume V_L of siltstone fine sandstone is 0.89 m^3/t, which is much smaller than that of mudstone, and the average Langmuir pressure P_L is 14.8 MPa.

Conclusion

In this paper, Quanzijie shale gas collected from the southern margin of the Junggar Basin was taken as the study area, and shale gas resources were investigated and evaluated by using the organic-rich shale section. On this basis, the investigation and evaluation of shale gas resources in the Lucaogou Formation was performed. The reservoir performance, preservation conditions, compressibility, and gas-bearing properties of gas-bearing shale intervals were identified. The results are as follows.

The vertical and horizontal lithological and lithofacies variations of the source rocks of the Lucaogou Formation were clarified. This layer is characterized by the upward thinning of grain size and the upward darkening of color in the vertical direction. The layer can be divided into upper and middle–lower sections; organic shale is most developed in the upper section, and sandstone and dolomite are more developed in the middle–lower section.

The main hydrocarbon source rocks are developed in the upper section of the Lucaogou Formation. The total thickness of the hydrocarbon source rocks is 78.12–513.73 m. The lithology is mainly gray-black shale, silty mudstone, and oil shale. The average organic carbon content is 4.86%. The maturity of the organic matter is mainly 0.7–0.8%. The shale reservoirs have a high content of brittle minerals, but the physical properties both of the shale and sandstone reservoirs are poor. They are generally ultra-low porosity and ultra-low permeability reservoirs, in which the oil and gas reservoir space is mainly fractures.

Data availability statement

The raw data supporting the conclusions of this article will be made available by the authors, without undue reservation.

Author contributions

DG is responsible for writing. DL designed the ideas. PY is responsible for drawing. SW is responsible for analyzing the data. JL is responsible for analyzing the data. GL is responsible for analyzing the data.

Funding

This work was jointly financially supported by the Xinjiang Uygur Autonomous Region Tianshan Talents Training Fund Project (TSYC2021171), Xinjiang Uygur Autonomous Region Science and Technology Talent Training Fund (QN2016YX0643), Xinjiang Uygur Autonomous Region Geological Exploration Fund (N16-2-LQ28), Xinjiang Uygur Autonomous Region Tianshan Talent Training Program (TSYC2021171), Youth Innovation

Team Development Plan of Universities in Shandong Province, and SDUST Research Fund (No. 2018TDJH101).

Conflict of interest

The authors declare that the research was conducted in the absence of any commercial or financial relationships that could be construed as a potential conflict of interest.

Publisher's note

All claims expressed in this article are solely those of the authors and do not necessarily represent those of their affiliated organizations, or those of the publisher, the editors, and the reviewers. Any product that may be evaluated in this article, or claim that may be made by its manufacturer, is not guaranteed or endorsed by the publisher.

References

Aljamaan, H., Al Ismail, M., and Kovscek, A. R. (2017). Experimental investigation and Grand Canonical Monte Carlo simulation of gas shale adsorption from the macro to the nano scale. *J. Nat. Gas Sci. Eng.* 48, 119–137. doi:10.1016/j.jngse.2016.12.024

Chen, S., Zhu, Y., Wang, H., Liu, H., Wei, W., and Fang, J. (2011). Shale gas reservoir characterisation: A typical case in the southern Sichuan Basin of China. *Energy* 36 (11), 6609–6616. doi:10.1016/j.energy.2011.09.001

Dong, J., Hsu, J., Wu, W., Shimamoto, T., Hung, J. H., Yeh, E. C., et al. (2010). Stress-dependence of the permeability and porosity of sandstone and shale from TCDP Hole-A. *Int. J. Rock Mech. Min. Sci.* 47 (7), 1141–1157. doi:10.1016/j.ijrmms.2010.06.019

Gale, J. F. W., Reed, R. M., and Holder, J. (2007). Natural fractures in the Barnett Shale and their importance for hydraulic fracture treatments. *AAPG Bull.* 91 (4), 603–622. doi:10.1306/11010606061

Gong, L., Wang, J., Gao, S., Fu, X., Liu, B., Miao, F., et al. (2021). Characterization, controlling factors and evolution of fracture effectiveness in shale oil reservoirs. *J. Pet. Sci. Eng.* 203 (2), 108655. doi:10.1016/j.petrol.2021.108655

Gou, Q. Y. (2017). Application of fracture prediction technology based on stack front anisotropy in shale reservoir. *China Petrochem.* (3), 26–27. [in chinese].

Guo, X., Huang, Z., Zhao, L., Han, W., Ding, C., Sun, X., et al. (2019). Pore structure and multi-fractal analysis of tight sandstone using MIP, NMR and NMRC methods: A case study from the Kuqa depression, China. *J. Pet. Sci. Eng.* 178, 544–558. doi:10.1016/j.petrol.2019.03.069

Habina, I., Radzik, N., Topór, T., and Krzyzak, A. (2017). Insight into oil and gas-shales compounds signatures in low field 1H NMR and its application in porosity evaluation. *Microporous Mesoporous Mater.* 252, 37–49. doi:10.1016/j.micromeso.2017.05.054

Hou, X., Zhu, Y., and Yao, H. (2018). Coupled accumulation characteristics of Carboniferous-Permian coal measure gases in the Northern Ordos Basin, China. *Arabian J. Geosci.* 11 (7), 156. doi:10.1007/s12517-018-3512-8

Hu, J., Tang, S., and Zhang, S. (2016). Investigation of pore structure and fractal characteristics of the lower Silurian Longmaxi shales in Western Hunan and Hubei Provinces in China. *J. Nat. Gas Sci. Eng.* 28, 522–535. doi:10.1016/j.jngse.2015.12.024

Javed, M. A., Komulainen, S., Daigle, H., Zhang, B., Vaara, J., Zhou, B., et al. (2019). Determination of pore structures and dynamics of fluids in hydrated cements and natural shales by various 1H and 129Xe NMR methods. *Microporous Mesoporous Mater.* 281, 66–74. doi:10.1016/j.micromeso.2019.02.034

Jiang, J., Yang, W., Cheng, Y., Zhao, K., and Zheng, S. (2019). Pore structure characterization of coal particles via MIP, N2 and CO2 adsorption: Effect of coalification on nanopores evolution. *Powder Technol.* 354, 136–148. doi:10.1016/j.powtec.2019.05.080

Jiao, K., Yao, S., Liu, C., Gao, Y., Wu, H., Li, M., et al. (2014). The characterization and quantitative analysis of nanopores in unconventional gas reservoirs utilizing FESEM–FIB and image processing: An example from the lower Silurian Longmaxi Shale, upper Yangtze region, China. *Int. J. Coal Geol.* 128-129, 1–11. doi:10.1016/j.coal.2014.03.004

Ju, W., Wang, J., Fang, H., and Sun, W. (2019). Paleotectonic stress field modeling and prediction of natural fractures in the Lower Silurian Longmaxi shale reservoirs, Nanchuan region, South China. *Mar. Pet. Geol.* 100, 20–30. doi:10.1016/j.marpetgeo.2018.10.052

Li, W., Liu, H., and Song, X. (2015). Multifractal analysis of Hg pore size distributions of tectonically deformed coals. *Int. J. Coal Geol.* 144-145, 138–152. doi:10.1016/j.coal.2015.04.011

Li, Z., Shen, X., Qi, Z., and Hu, R. (2018). Study on the pore structure and fractal characteristics of marine and continental shale based on mercury porosimetry, N_2 adsorption and NMR methods. *J. Nat. Gas Sci. Eng.* 53, 12–21. doi:10.1016/j.jngse.2018.02.027

Liu, C., Shi, B., Zhou, J., and Tang, C. (2011). Quantification and characterization of microporosity by image processing, geometric measurement and statistical methods: Application on SEM images of clay materials. *Appl. Clay Sci.* 54, 97–106. doi:10.1016/j.clay.2011.07.022

Liu, K., Ostadhassan, M., and Kong, L. (2018). Multifractal characteristics of Longmaxi shale pore structures by N2 adsorption: A model comparison. *J. Pet. Sci. Eng.* 168, 330–341. doi:10.1016/j.petrol.2018.04.072

Qiao, J., Zeng, J., Jiang, S., Ma, Y., Feng, S., Xie, H., et al. (2020). Role of pore structure in the percolation and storage capacities of deeply buried sandstone reservoirs: A case study of the Junggar Basin, China. *Mar. Pet. Geol.* 113, 104129–129. doi:10.1016/j.marpetgeo.2019.104129

Tang, Q., Zhou, L., Chen, L., Tan, X., and Wang, G. (2021). Development characteristics of shale lithofacies in the Longmaxi Formation and their main controlling factors in the Changning area, South Sichuan basin, SW China. *Front. Earth Sci.* 9, 775657. doi:10.3389/feart.2021.775657

Wang, Y., Zhu, Y., Chen, S., and Li, W. (2014). Characteristics of the Nanoscale pore structure in northwestern Hunan shale gas reservoirs using field emission scanning electron microscopy, high-pressure mercury intrusion, and gas adsorption. *Energy Fuels* 28 (2), 945–955. doi:10.1021/ef402159e

Yan, G., Wei, C., Song, Y., and Zhang, J. (2017). Pore characteristics of organic-rich shale in the Carboniferous-Permian coal-bearing strata in Qinshui Basin. *Energy Explor. Exploit.* 35 (5), 645–662. doi:10.1177/0144598717709668

Yang, R., He, S., Yi, J., and Hu, Q. (2016). Nano-scale pore structure and fractal dimension of organic-rich Wufeng-Longmaxi shale from Jiaoshiba area, Sichuan Basin: Investigations using FE-SEM, gas adsorption and helium pycnometry. *Mar. Pet. Geol.* 70, 27–45. doi:10.1016/j.marpetgeo.2015.11.019

Yuan, Y., and Rezaee, R. (2019). Fractal analysis of the pore structure for clay bound water and potential gas storage in shales based on NMR and N2 gas adsorption. *J. Pet. Sci. Eng.* 177, 756–765. doi:10.1016/j.petrol.2019.02.082

Zhang, P., Lu, S., Li, J., and Chang, X. (2020). 1D and 2D Nuclear magnetic resonance (NMR) relaxation behaviors of protons in clay, kerogen and oil-bearing shale rocks. *Mar. Pet. Geol.* 114, 104210. doi:10.1016/j.marpetgeo.2019.104210

Zhao, P., Wang, Z., Sun, Z., Cai, J., and Wang, L. (2017). Investigation on the pore structure and multifractal characteristics of tight oil reservoirs using NMR measurements: Permian Lucaogou Formation in Jimusaer Sag, Junggar Basin. *Mar. Pet. Geol.* 86, 1067–1081. doi:10.1016/j.marpetgeo.2017.07.011

frontiers | Frontiers in Earth Science

TYPE Original Research
PUBLISHED 10 January 2023
DOI 10.3389/feart.2022.1047557

OPEN ACCESS

EDITED BY
Mingjun Zou,
North China University of Water Resources and Electric Power, China

REVIEWED BY
Taotao Cao,
Hunan University of Science and Technology, China
Teng Li,
Xi'an Shiyou University, China

*CORRESPONDENCE
Wei Jiang,
jiangwei3q@163.com

SPECIALTY SECTION
This article was submitted to Economic Geology, a section of the journal Frontiers in Earth Science

RECEIVED 18 September 2022
ACCEPTED 23 September 2022
PUBLISHED 10 January 2023

CITATION
Jiang W, Zhou Y, Wu C and Du M (2023), Fractal characteristics and theirs influence on methane adsorption in high-rank coals with NMR.
Front. Earth Sci. 10:1047557.
doi: 10.3389/feart.2022.1047557

Fractal characteristics and theirs influence on methane adsorption in high-rank coals with NMR

Wei Jiang[1,2,3]*, Ying Zhou[1,2], Caifang Wu[3] and Mingyang Du[1,2,3]

[1]School of Earth Sciences and Engineering, Suzhou University, Suzhou, China, [2]National Engineering Research Center of Coal Mine Water Hazard Controlling, Anhui, China, [3]School of Resource and Geoscience, China University of Mining and Technology, Xuzhou, China

To further understand the pore structure characteristics and their effect on CH_4 adsorption capacity for high-rank coals. Based on 11 fresh coal samples from the Zhina coalfield of South China. We analyzed the pore structure characteristics of coal samples by low-temperature liquid-nitrogen adsorption (LP-N_2A) measurements. On the basis of nuclear magnetic resonance (NMR), we obtained the fractal dimensions of different types of pores by the new model, studied the relationship between the fractal dimensions, and the characteristic parameters of coals (composition and pore characteristics) and discussed the influence of the fractal dimensions on CH_4 adsorption. The results show that according to LP-N_2A isotherms, all coals can be classified into three types. The micropores provide the largest proportion of the specific surface area (SSA) of coals. Two fractal dimensions, D_a (adsorption pore) and D_s (seepage pore), ranged from 2.471 to 2.805 and from 2.812 to 2.976, which were acquired in the saturated water condition by NMR. Furthermore, D_a and D_s have different correlations with ash yield, carbon contents, moisture, SSA and irreducible fluid porosity. The coal composition and pore parameters have much greater control over fractal dimensions. Moreover, the different fractal dimensions have different influences on methane adsorption. With the increase of D_a, the methane adsorption capacity is enhanced, but it is weakened with the increase of D_s. The high-rank coals have more SSA with higher D_a and provide more adsorption sites for CH_4. Langmuir pressure P_L has different correlations with fractal dimensions. D_a decreases with the increase of P_L. The adsorption velocity is faster with higher D_a. Thus, the fractal dimensions are the comprehensive reflection of differences among the physical properties of coal and are able to show the effect of coal properties on methane adsorption fully.

KEYWORDS

nuclear magnetic resonance, fractal dimension, coalbed methane, adsorption, coal pore structure

1 Introduction

Coal is a complex and heterogeneous porous medium. Its internal pore surface area is much larger than its external surface area which can be neglected. The pore surface with strong adsorption ability is the primary storage and migration of coalbed methane (CBM) (Alexeev, 1977; Meyers, 1982). The structure and developmental features of pores perform a significant control function in adsorption capacity, desorption capacity and permeability of coal reservoirs, which directly affects the exploration efficiency of CBM. Meanwhile, the unstable CBM production is influenced by the complex features of pore-fracture, buried depth of coal seam and geothermal dynamics (Johnson and Flores, 1998; Saboorian-Jooybari, 2016; Zhao et al., 2019). Thus, it is a great significance to characterize coal reservoirs by researching the storage capacity and migration mechanism of pores in coal reservoirs (Dullien, 1991).

At present, defining the coal pore system, there are various classifications of qualitative descriptions of pores in coal reservoirs (Hodot, 1966; Sing, 1982; Fu et al., 2005; Cai et al., 2013a). Based on gas adsorption–desorption, Hodot's classification (Hodot, 1966) is widely used. The pores are divided into four types: micropores (less than 10 nm), transition pores (10–100 nm), mesopores (100–1000 nm) and macropores (more than 1,000 nm). Pores (less than 100 nm) are adsorption pores which play a crucial role in CBM adsorption and diffusion pores (Cai et al., 2013b). In the present study, the pore characteristics of coal reservoir are studied by many methods and technologies, such as mercury intrusion porosimetry (MIP) (Gao et al., 2018; Ju et al., 2018), scanning electron microscopy (SEM) (Shan et al., 2015; Li et al., 2020a), N_2 adsorption-desorption and CO_2 gas adsorption (Acevedo and Barriocanal, 2015; Li et al., 2019; Nie et al., 2020), atomic force microscope (AFM) (Pan et al., 2015), small-angle X-ray scattering (SAXS) (Ferro et al., 2012; Coetzee et al., 2015; Liu and He, 2017) and nuclear magnetic resonance (NMR) (Lee and Lee, 2013; Li et al., 2017). The result shows that the pore structure of coal has a fractal feature within a certain scale range (Fu et al., 2005; Shi et al., 2006; Yao et al., 2009; Liu et al., 2015; Peng et al., 2017). However, these technical methods may cause the decrease of pore diameter, the damage of coal matrix system and the loss of some important details of coal reservoir (Yao and Liu, 2012). NMR is an efficient experimental method to study the pore properties of coal reservoirs. The NMR technique is widely applied in petrophysical features, shapes, sizes and porosity of pores, because of its rapid, accurate and high-resolution characteristics. NMR T_2 cutoff value (T_{2C}) is an important parameter for irreducible water saturation calculation, pore size distribution (PSD) and permeability prediction. Ge et al. (2014) studied the influential factors of T_{2C} and proposed the predicating model for T_{2C} value by multiple linear regressions of multifractal parameters. Yao et al. (2010) designed the NMR experiments of 100% water-saturated and irreducible water coal samples, respectively. Results show that the relaxation times corresponding to the adsorption-pore (< 100 nm), seepage-pore (> 100 nm) and fracture are 0.5–2.5 ms, 20–50 ms and >100 ms, respectively. Meanwhile, the NMR-based permeability model is built on the basis of the data of calculated irreducible and producible porosities. Zheng et al. (2020) divided T_2 cutoffs into two types: the absolute irreducible fluid T_2 cutoffs (T_{2C1}) and absolute movable fluid T_2 cutoff (T_{2C2}); Based on the dual T_2 cutoffs model, the pore fluid typing of coal is divided into three types: absolute irreducible fluid ($T_2 < T_{2C1}$), partial movable fluid ($T_{2C1} < T_2 < T_{2C2}$) and absolute movable fluid ($T_2 > T_{2C2}$).

Because of the complexity and anisotropy of the pore structure of the coal reservoir, it is difficult to give an accurate description by the traditional geometrical method and is unable to measure by fixed scale. The fractal theory is an effective method to quantitatively describe pore structure features (Song et al., 2013; Wang et al., 2013). Based on the isotherms of N_2 gas adsorption/desorption, adopting the fractal Frenkel–Halsey–Hill (FHH) method, the fractal dimensions D_1 and D_2, which represent the irregularity of pore surface and heterogeneity of pore structure, are obtained (Yao et al., 2008). Coupled with CH_4 isotherm adsorption experiments, D_1 has more significant influence than D_2 on adsorption capacity (Li et al., 2015). Song et al. (2017) analyzed the fractal characteristics of nanopores in tectonically deformed coals on the basis of mercury intrusion and N_2/CO_2 gas adsorption experiments. They found that the fractal dimension (<8 nm) has an important role in the adsorption capacity. Additionally, previous researchers have found that the NMR fractal theory is used to study the pore-fracture characteristics of coal (Li et al., 2013; Sun et al., 2015; Ouyang et al., 2016). Based on the NMR T_2 spectrum, the fractal dimensions are divided into D_1(adsorption pores) and D_2(seepage pores). D_2 has a significant influence on the permeability of the coal reservoir (Chen et al., 2018). Zhou et al. (2016) calculated the adsorption space fractal (D_{NMRA}), seepage space fractal (D_{NMRS}) and moveable fluid space fractal (D_{NMRM}) in low-rank coals, respectively. They demonstrated the model between permeability and D_{NMRM}. With MIP and NMR methods, MIP and NMR permeability were estimated by the modified Kozeny-Carman Equation and movable porosity-permeability model, respectively (Li et al., 2020b). Zhou et al. (2022) proposed a novel model by the low-field NMR and obtained the fractal dimensions of accessible, inaccessible and total pores, respectively. Nevertheless, the correlation between CH_4 adsorption capacity and NMR fractal dimensions of coals has not been sufficiently researched.

In this paper, we collect 11 coal samples from the Zhina coalfield of South China and carry out the experiment analyses to investigate the characteristics of pores and coal adsorption by the LP-N_2A, NMR and CH_4 isotherm adsorption methods. According to the experimental data and results analysis, we

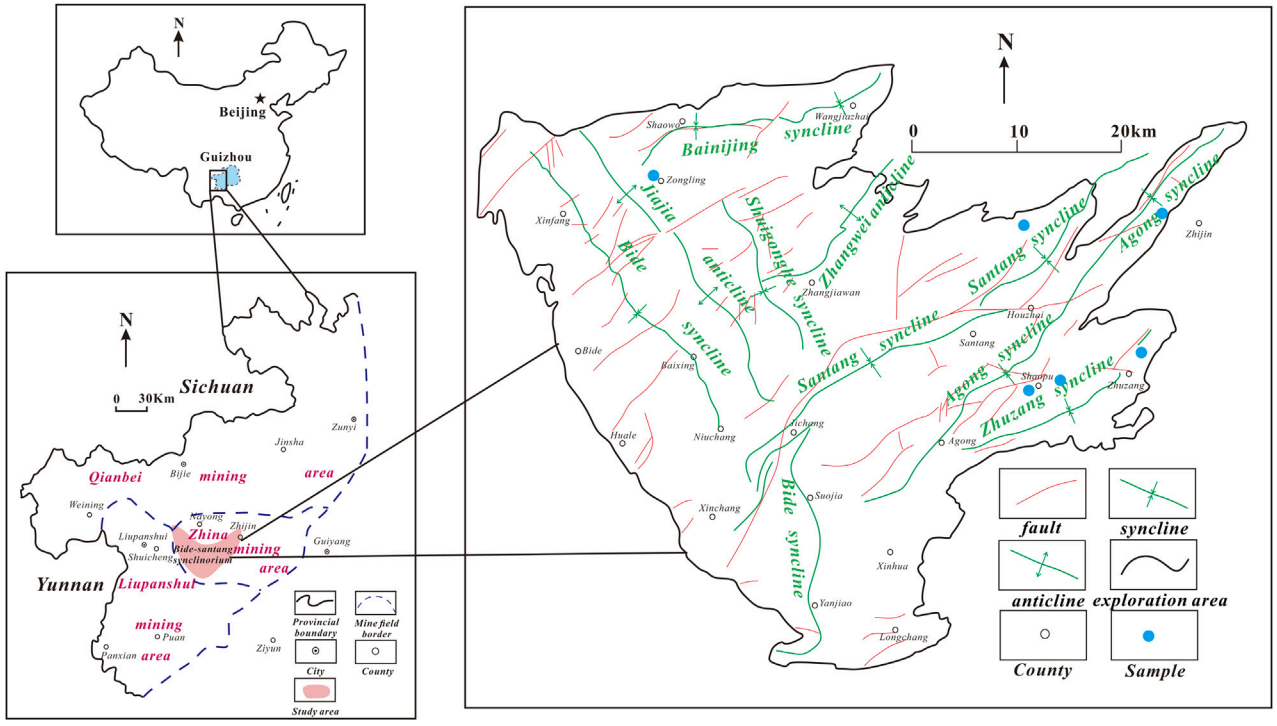

FIGURE 1
Location map showing the distribution of sampling points in the Bide-Santang Basin, China (modified from Yang et al., 2014, 2019).

analyze the pore characteristics of coal samples, calculate the fractal dimensions of different pore types, and study the relationships between CH_4 adsorption capacity and fractal dimensions.

2 Materials and methods

2.1 Sampling

Eleven samples were collected from the Bide-Santang Basin, which is a CBM reservoir of multiple coal seams in the Zhina coalfield, Guizhou Province (Figure 1). Zhina coalfield, located in western Guizhou Province, is the largest anthracite coal occurrence area in China. The coal-bearing strata of the Bide-Santang Basin are the Longtan and Changxing formations of Upper Permian, with a formation thickness of 300–450 m. In the upper Permian, the coal-bearing formation was mainly developed at continental, continental-marine transitional and shallow marine sedimentary facies. Multiple coal-bearing strata formed during this period due to frequent sea transgression and regression. Tectonic activities during the Yanshan and Himalayan formed large synclines and synclinoria, which became important structures controlling coal in the region (Yang et al., 2019). The gas content of coal seam of in Longtan Formation is generally high. The average gas content is 10–15.78 m^3/t. The reservoir pressure is 2.95–11.59 MPa. The *in-situ* permeability of coal reservoir is low, and its average value is 0.14 mD (Cheng et al., 2021). Table 1 shows the collected samples and their locations. All the samples whose size was 30 cm×30cm×30 cm were wrapped with plastic wrap according to the Chinese Standard (GB/T 19,222–2003) and quickly packed. The grind and screening of samples were completed in the laboratory after sampling. According to GB/T6948-2008 and GB/T212–2008, samples (less than 0.200 mm in particle diameter) were selected for proximate analysis and maximum vitrinite reflectance.

2.2 CH4 isotherm adsorption experiments

Experiments were performed at the China petroleum exploration and development research institute Langfang branch using TerraTek Isothermal Adsorption and Desorption Experimental System (IS–300), according to Chinese standard (GB/T 19,560–2008). The sensitivity of the temperature sensor and pressure sensor is 0.3 C and 0.001°MPa, respectively. All the

TABLE 1 Coal analysis results for samples.

Sample ID	Vitrinite reflectance ($R_{o,max}$ %)	Coal-bearing strata	Proximate analysis(%)[a]			
			M_{ad}	V_{daf}	A_{ad}	FC_{ad}
X-1	2.30	longtan formation	0.52	12.0	25.16	62.81
X-2	3.21	longtan formation	1.66	6.70	7.83	88.65
X-3	3.32	longtan formation	1.25	5.48	13.68	85.28
X-4	3.02	longtan formation	1.08	6.95	11.15	81.03
X-5	3.40	longtan formation	1.55	6.21	14.56	82.56
Y-1	2.60	changxing formation	0.42	11.17	15.07	72.8
Y-2	2.74	longtan formation	1.14	11.37	18.76	70.48
Y-3	2.90	longtan formation	0.68	7.56	16.87	79.52
Y-4	2.70	longtan formation	0.70	8.82	12.16	77.36
Y-5	3.11	longtan formation	0.83	7.50	11.87	79.86
Y-6	2.86	longtan formation	0.94	8.08	9.95	80.82

Note: The approximate content of fixed carbon (FC_{ad}), ash (A_{ad}) and moisture (M) are from the air-dried basis of samples; V_{daf} is volatile matter content from the dry ash-free basis of samples.

coal samples were broken, smashed and screened to a size range of 0.18–0.25 mm. Then, the moisture-equilibrium treatment of 200 g samples was carried out. The screened experimental samples were put in an incubator with oversaturated K_2SO_4 solution. The samples were weighed every other 24 h until the quality change was below 2 percent of their weight. The experimental temperature was 30°C, and the experimental pressure range was 0–13 MPa. The time of adsorption equilibrium kept above 12 h.

2.3 LP-N_2A and NMR measurement

LPN_2A was performed for the 11 coal samples using a Micromeritics ASAP 2000 surface area measurement. First, the coal samples were ground into a size range of 0.25–0.40 mm. Approximately 5 g of coal particles was placed in a vacuum oven and degassed at 105 C for 12 h to remove air, free moisture and other impurities. Then, degassed samples were exposed to N_2 with purity greater than 99.99% at a temperature of 77.3°K. The range of relative pressure (P/P_0) was from 0.01 to 0.995. Moreover, the Brunauer–Emmett–Teller (BET), Barrett–Joyner–Halenda (BJH) and density functional theory (DFT) models were applied to evaluate the specific surface area (SSA), pore volume (PV) and PSD, respectively (Brunauer et al., 1938; Barrett et al., 1951; Geerlings et al., 2003).

NMR measurement was performed at SGS Unconventional Petroleum Technical Testing Limited Company, following specifications of surveys SY/T 6490-2007. Firstly, several horizontal cylindrical core plugs with a diameter of 2.5 cm were drilled; Secondly, all core plugs were placed in a drying oven until drying to constant weight, then saturated with 100% saturated standard brine for 24 h; Thirdly, core plugs were placed in the probe of low magnetic field resonance core analyzer to test the transverse relaxation time T_2 and worked out relaxation time spectrum of T_2 by inversion. Finally, core plugs were placed in a centrifuge to dehydrate, and the centrifugal pressure was 200°psia.

2.4 Fractal theory based on NMR

Lots of papers have extensively reported the fractal dimensions of NMR (Zhang et al., 2007; Wang et al., 2011; Zhang and Weller, 2014). The fractal dimensions of NMR are obtained from the NMR data of the irreducible water and saturated water by establishing the equation of fractal dimension of coal pores (Ouyang et al., 2016; Zhou et al., 2018), But the low correlation coefficient of fractal makes these methods unsuitable for obtaining quantitative heterogeneity for porous media. We calculated the fractal dimension of pores by the new model (Zhou et al., 2022).

The critical characteristic of fractal targets in nature is self-affinity of dimension and can be quantified by a power-law function (Lai et al., 2018).

$$N(r) \propto r^{-D} \tag{1}$$

Where r is the pore size for rock, D is the fractal dimension, $N(r)$ is the number of objects whose sizes are greater than the size.

The pore size distribution could be directly related to the distribution of NMR T_2 relaxation time (Daigle and Johnson, 2016). The formula can be expressed as

$$\frac{1}{T_2} = F_s \frac{\rho}{r} \tag{2}$$

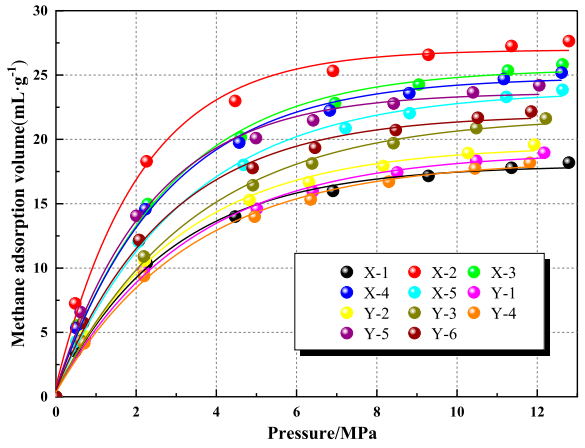

FIGURE 2
Results of methane adsorption test and the fitting Langmuir curves.

If the coal structure is a tube, then Fs = 2; Fs = 3 for spherical; ρ is the strength of transverse relaxation;

The signal amplitude at the T_{2i} relaxation time is a function of the number of protons, corresponding to the pore volume of pore radius r_i (Dillinger and Esteban, 2014). The total PV (V_p , %) represents the sum of the signal amplitudes from minimum to maximum T_2 values, then V_p can be expressed as

$$V_p = \sum_{i=1}^{n} V_{pi} \tag{3}$$

Where V_{p1} and V_{pn} are the signal amplitude at the minimum and maximum T_2 value, respectively. V_{pi} corresponds to the signal amplitude at T_{2i} value.

The pore morphology of coal samples is assumed to be spherical, then the number of pores with a specified size r_i can be given by

$$N_i = \frac{V_{pi}}{\frac{4}{3}\pi r_i^3} = \frac{V_{pi}}{36\pi(\rho T_{2i})^3} \tag{4}$$

Therefore, the number of pores whose pore size is larger than r_i is expressed as

$$N(r) = \sum_{j}^{n} N_i = \sum_{j}^{n} \frac{V_{pi}}{\frac{4}{3}\pi r_i^3} \tag{5}$$

Where $j = i + 1$

By combining Equations 1, 2, and 5:

$$N(r) = \frac{V_{pi}}{36\pi(\rho T_{2i})^3} \propto (3\rho T_{2i})^{-D} \tag{6}$$

Using logarithms for Eq. 6, is revised as

$$\log\left(\sum_{j}^{n} \frac{V_{pi}}{(T_{2i})}\right) + \log\frac{1}{A} = -D\log B - D\log(T_{2i}) \tag{7}$$

Where $A = 36\pi\rho^3$ and $= 3\rho$. $-DlogB$ and $log(1/A)$ are the constants. The fractal dimension can be obtained by the slope of the optimal fit line in the log–log plot of pore number $N(r)$ against pore radius (T_2) .

3 Results

3.1 Coal rank, coal component and CH_4 adsorption analysis results

As seen from Table 1, the maximum vitrinite reflectance of coals ranges from 2.30 to 3.40%, which belongs to high-rank coal. Moisture contents of coals increase from 0.52 to 1.66%, ash yields of coals increase from 7.83 to 25.16%, carbon contents of coals reduce from 88.65 to 62.81% and volatile matter contents of most samples increase from 5.48 to 12.00%. The composition of coal samples is complicated, and each component concentration has the noticeable differences. Most of the coal samples are

TABLE 2 Fitting results of methane adsorption test.

Sample ID	Langmuir volume (m^3/t)	Langmuir pressure (MPa)	Equilibrium moisture (wt%)	Correlation coefficients R^2
X-1	21.65	2.45	4.58	0.9972
X-2	31.04	1.57	6.05	0.9695
X-3	30.76	2.42	5.37	0.9973
X-4	29.86	2.34	5.45	0.9975
X-5	29.48	2.98	4.86	0.9976
Y-1	23.82	3.14	5.07	0.9972
Y-2	24.17	2.82	4.25	0.9971
Y-3	27.56	3.34	6.03	0.9980
Y-4	23.24	3.26	3.60	0.9977
Y-5	28.27	2.03	4.80	0.9955
Y-6	26.83	2.50	2.99	0.9966

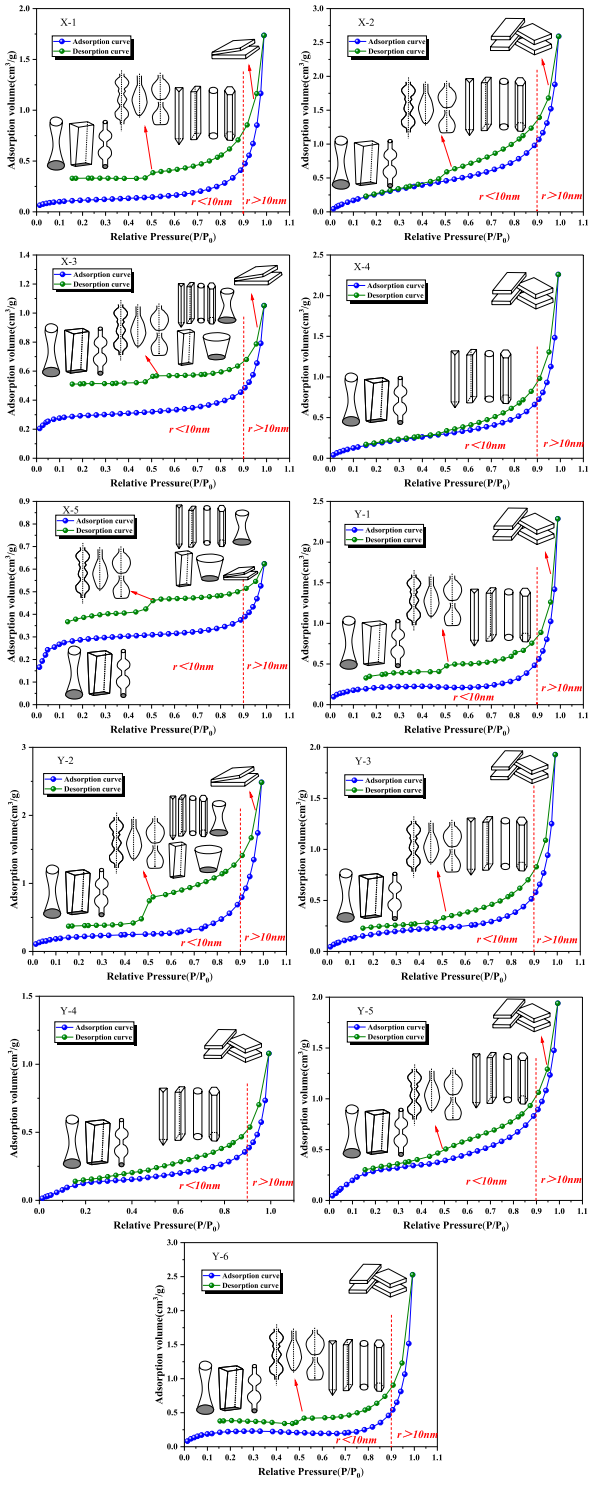

FIGURE 3
N_2 adsorption/desorption isotherms of all the samples.

low–middle ash coal. Vitrinite is the dominant maceral composition for all coal samples.

The results of the methane adsorption experiment of each coal sample are shown in Figure 2. The experimental results are fitted by the Langmuir equation:

$$V = \frac{V_L * P}{(P_L + P)} \tag{8}$$

Where P is the pressure, MPa; V is the absorption at the pressure P, m^3/t; V_L is the Langmuir volume, m^3/t; P_L is the Langmuir pressure, MPa.

The fitted results are shown in Table 2. The degree of the fitting is high by the Langmuir equation about the methane adsorption curves of all coal samples. The Langmuir volume ranges from 21.65 ml/g to 31.04 ml/g, and the Langmuir pressure ranges from 1.57°MPa to 3.34 MPa. It shows that the adsorption capacity of different coal samples has the certain difference. But methane adsorption of coal samples has a different growth rate with increasing pressure. Methane adsorption of some coal samples increases rapidly at low pressure but flattens at high pressure. Yet methane adsorption of some other coal samples increases slowly (Li et al., 2013). For example, the methane adsorption of coal sample X-2 is about 17.4 ml/g at 2 MPa pressure, but that of coal sample X-3 is only about 13.9 ml/g at the same pressure. Although their V_L has little difference, the methane adsorption at low pressure differs greatly. This illustrates that the ease of their methane adsorption is different. Coal sample X-2 is easy to adsorb methane, but coal sample X-3 is the opposite. In the process of coalbed gas production, the adsorbing methane of coal sample X-2 is difficult to desorb, but coal sample X-3 is not.

3.2 LP-N_2A isotherms and pore structure characteristics

The characteristic differences of adsorption and desorption isotherms of coal samples represent the development of different types of pores (Yang et al., 2014). For porous media, the LP-N_2A curves may be grouped into six types and hysteresis loops may be divided into four types (Sing, 1985). Figure 3 shows the LP-N_2A isotherms for 11 coal samples. The LP-N_2A isotherms of coals have remarkable differences. Based on the classification scheme proposed by De Boer (De Boer, 1958) and IUPAC (IUPAC, 1982), all coal samples can be classified as three types (A, B, and C) by the characteristics of LP-N_2A isotherms.

Type A is for X-2, X-4, Y-3, Y-4 and Y-6 samples. When $p/p_0 < 0.8$, the adsorption curves increase slowly. The adsorption curves increase rapidly at p/p_0 approaching 1.0. There are inconspicuous hysteresis loops and no inflection points at $0.4 < p/p_0 < 1.0$. But the adsorption and desorption curves nearly overlap at $p/p_0 < 0.4$. The adsorption volume is small at $p/p_0 < 0.4$. At this stage, the pores consist mainly of impermeable pores closed at one end. When $0.4 < p/p_0 < 0.9$,

TABLE 3 Pore characteristics of all the samples based on N_2 adsorption/desorption analysis.

Sample ID	SSA(m^2/g)	PV (cm^3/g)	Average PD (nm)	PV-N_2 (cm^3/g)		SSA-N_2 (m^2/g)		Hysteresis loop types
				<10 nm	>10 nm	<10 nm	>10 nm	
X-1	0.407	0.0027	26.4	0.00045	0.0023	0.236	0.171	B
X-2	1.277	0.0038	12.5	0.0012	0.0026	1.013	0.264	A
X-3	0.989	0.0013	6.6	0.00044	0.00086	0.911	0.078	C
X-4	0.805	0.0035	17.4	0.00082	0.00268	0.577	0.228	A
X-5	0.980	0.0010	3.9	0.00055	0.00045	0.949	0.031	C
Y-1	0.761	0.0035	18.6	0.00053	0.00298	0.514	0.247	B
Y-2	0.657	0.0032	19.5	0.00069	0.00251	0.447	0.210	B
Y-3	0.925	0.0039	16.8	0.00081	0.00309	0.649	0.276	A
Y-4	0.519	0.0017	12.8	0.00048	0.00122	0.399	0.120	A
Y-5	1.037	0.0030	11.6	0.0012	0.00183	0.856	0.181	A
Y-6	0.841	0.0040	18.6	0.00062	0.00338	0.584	0.257	B

TABLE 4 NMR porosity of coal samples.

Sample No.	Irreducible fluid porosity (%)	Moveable fluid porosity (%)	Total porosity (%)
X-1	2.11	1.54	3.65
X-2	5.77	1.48	7.25
X-3	5.02	1.64	6.66
X-4	5.96	1.73	7.69
X-5	4.91	1.24	6.15
Y-1	3.96	1.42	5.38
Y-2	2.89	1.58	4.47
Y-3	4.54	1.02	5.56
Y-4	4.43	1.15	5.58
Y-5	4.62	1.19	5.81
Y-6	4.78	1.51	7.29

the pore was dominated by cylindrical pores with openings at both ends. Due to the obvious adsorption hysteresis loops and the rapid rise of the adsorption curve, the pores are mainly open parallel plate pores at $0.9 < p/p_0 < 1.0$. This shows that the transition pores, mesopores and some micropores of samples have good connectivity. The samples (e.g., X-1, Y-1, Y-2 and Y-6) belong to type B. Their adsorption curves increase steadily at $p/p_0 < 0.8$ and then increase significantly and rapidly at $0.8 < p/p_0 < 1.0$. It is different from type A in that it has a wide hysteresis loop at $0.5 < p/p_0 < 1.0$. When $p/p_0 < 0.4$, most of the pores are impermeable pores closed at one end. But their adsorption and desorption branches have no overlap at $p/p_0 < 0.5$, which is thought to be due to pore swelling and chemical interactions of gas and coal pore surface (Sun et al., 2015; Li et al., 2018). The hysteresis loop indicates that the pores are mainly open cylinder pores at $0.4 < p/p_0 < 0.9$. The desorption curve has an inflection point at a relative pressure of approximately 0.5, which reacts to the presence of thin neck and ink bottle pores. When $0.9 < p/p_0 < 1.0$, the pore types are also open parallel plate pores. Moreover, type C is for X-3 and X-5 samples. The pore types are similar to type B and type C at $p/p_0 < 0.4$, but the hysteresis loop is also not completely closed. When $0.4 < p/p_0 < 0.9$, the appearance of wide hysteresis loops indicates that the pores are mainly composed of open pores, including cylinder pores and wedge pores. The desorption curve has a sharp inflection point at p/p_0 of 0.5, which indicates the presence of a large number of fine bottleneck and ink bottle pores. When $0.9 < p/p_0 < 1.0$, type C differs from other types in having few plate-shaped pores.

The LPN_2GA test results are shown in Table 3. The SSA and PV of coal samples are obviously different. The SSA and

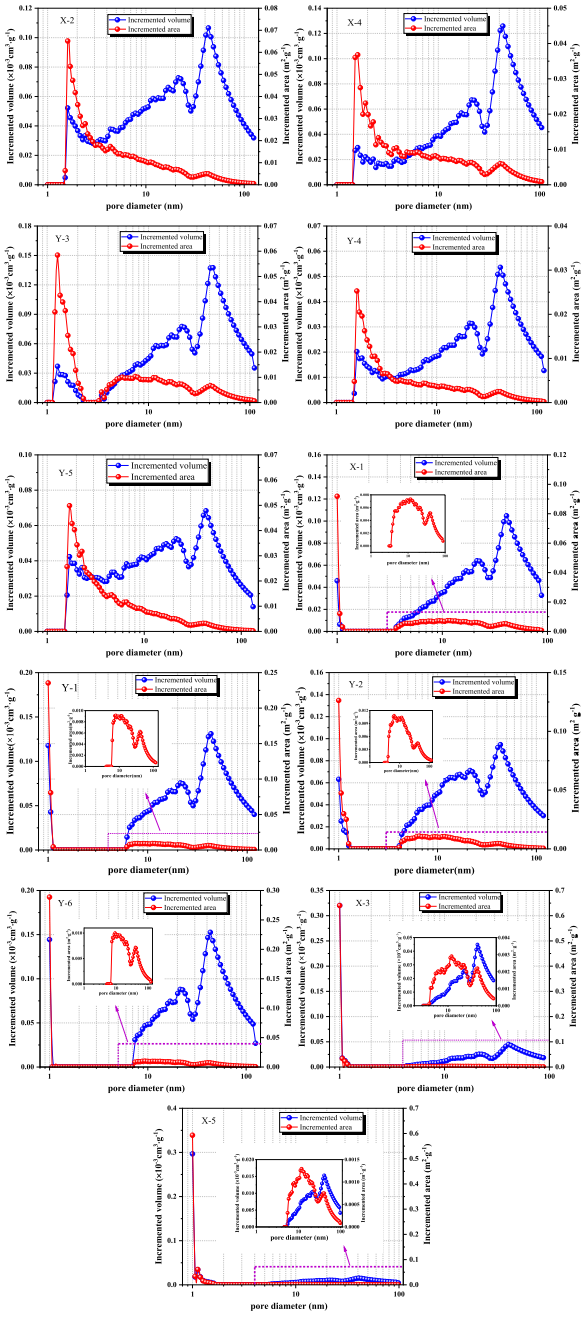

FIGURE 4
The distribution of incremental PV and SSA with LPN$_2$GA. (X-2, X-4, Y-3, Y-4 and Y-5) Type A, (X-1, Y-1, Y-2 and Y-6) Type B, and (X-3 and X-5) Type C.

PV range from 0.407 to 1.277 m^2/g and 0.001–0.004 cm^3/g, respectively. The PSD of the PV and SSA in different types of coal samples is shown in Figure 4. The SSA distribution curves suggest that all coal samples exhibit unimodality with the main peak at ~1 nm, indicating that the SSA of coal samples is more concentrated in micropores (the SSA for < 10 nm and > 10 nm

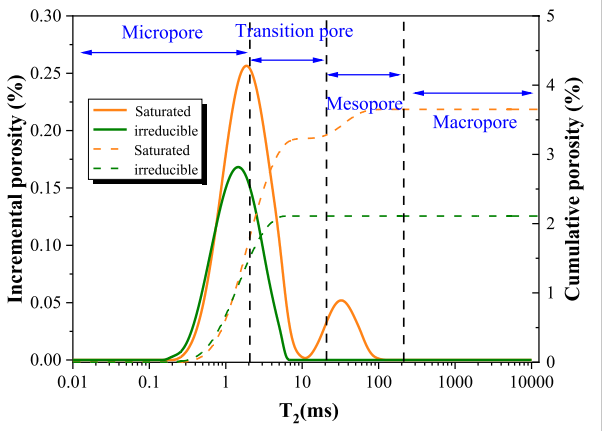

FIGURE 5
NMR T_2 distribution of X-1 coal sample in the saturated water condition and the irreducible water condition.

is 0.236–1.013°m^2/g and 0.031–0.276°m^2/g, respectively). Compared with type A, the SSA of type B/C pores is generally undeveloped at > 3 nm. Except for samples X-3 and X-5, the PV distribution shows obvious multimodality in which the peaks of the overall samples are at ~1, ~20 and ~50 nm. The PV for < 10 nm and > 10 nm is 4.4×10-4-1.2×10–3°cm^3/g and 4.5×10-4-3.38×10–3°cm^3/g, respectively, indicating that the pores for > 10 nm provide most of the pore volume. Meanwhile, the micropores of type C provide the largest proportion of PV and SSA. Mainly because of the increasing metamorphic degree of coals, the loss of oxygen functional groups and side chains is accompanied by the significant improvement in the degree of aromatization and the increasing and orderly arrangement of aromatic ring layers in the molecular structure of coal, which results in the decrease of larger pores and the increase of smaller pores (Li et al., 2017).

3.3 Pore size distribution of NMR

Previous researches (Cai et al., 2013a; Li et al., 2013) found that T_2 can reflect the PV/size distribution in the saturated water, but cannot provide absolute full-scale PSD. There are two methods to obtain full-scale PSD by NMR measurement, namely centrifugation test and surface relaxation method.

According to the relationship between different centrifugal forces and centrifugal pore radius (Washburn equation), the pore radius r corresponding to the T_2 cutoff value can be obtained at the optimal centrifugal pressure. Yao et al. (2010) propose the centrifugal experiment method of full-

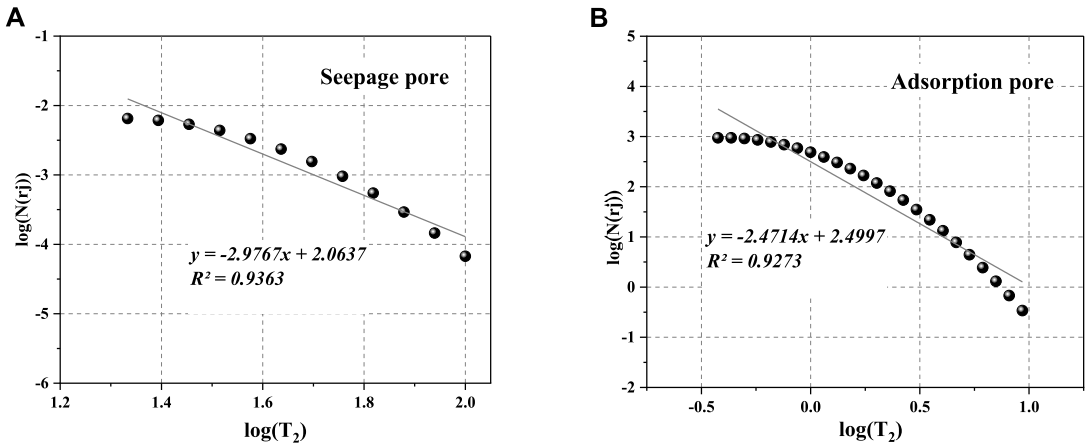

FIGURE 6
The double-logarithm relationship of different pores between log(T_2) vs. log($N(rj)$) for Sample X-1. **(A)** The double-logarithm relationship of seepage pore, **(B)** The double-logarithm relationship of adsorption pore.

TABLE 5 The fractal dimension and correlation coefficient of different pores from NMR data.

Sample No.	D_a	R^2	D_s	R^2
X-1	2.471	0.93	2.976	0.94
X-2	2.805	0.89	2.814	0.91
X-3	2.68	0.91	2.843	0.86
X-4	2.738	0.90	2.819	0.85
X-5	2.612	0.92	-	-
Y-1	2.522	0.98	2.904	0.93
Y-2	2.579	0.92	2.869	0.85
Y-3	2.545	0.88	2.926	0.98
Y-4	2.497	0.88	2.957	0.98
Y-5	2.605	0.91	2.863	0.99
Y-6	2.755	0.89	2.812	0.96

scale PSD of coal reservoir by NMR T_2 cutoff value. The formula can be expressed as

$$r_{ci} = r*T_{2i}/T_{2c} \quad (9)$$

Where r_{ci} (nm) is a pore size corresponding to a relaxation time T_{2i} (ms), T_{2c} is a relaxation time threshold, r (nm) is the pore size corresponding to the T_{2c} and r is about 100 nm.

It is worth noting that there are still some movable fluids in the sample when $T_2 < T_{2C}$. Thus, the centrifugal experiment method is inapplicable. Then, Zheng et al., 2019 proposed a surface relaxation method to calculate the surface relaxivity of different coals, which are 2.1 μm/s, 3.0 μm/s and 1.6 μm/s for low-, medium-, and high-rank coal, respectively.

The pore of coal can be divided into micropores, transition pores, mesopores, and macropores. Micropores and transition pores belong to adsorption pores, mesopores and macropores belong to seepage pores. According to Eq. 2, the T_2 spectrum of coal samples is divided into four parts, corresponding to <2.08 ms, 2.08–20.8 ms, 20.8–208 ms, > 208 ms, and representing different pores: micropore, transition pore, mesopore, macropore, respectively (Figure 5). We also calculated the cumulative porosity in two conditions. The cumulative porosity of other coal samples is given in Table 4. The irreducible and moveable fluid porosity range from 2.11% to 5.96% and 1.02%–1.73%, respectively.

3.4 Characteristics of fractal dimensions in NMR

The fractal dimension of pore structure can be obtained from the slope of the equation by the linear fitting data of $\log(N(r_j))$ and $\log(T_2)$. The linear correlation coefficient for sample X-1 is greater than 0.92, indicating that the adsorption and seepage pore structures of samples can be characterized by the fractal geometry theory (Figure 6). D_a and D_s represent the fractal dimensions of adsorption and seepage pores under the condition of saturated water, respectively. The fractal dimension results of all samples

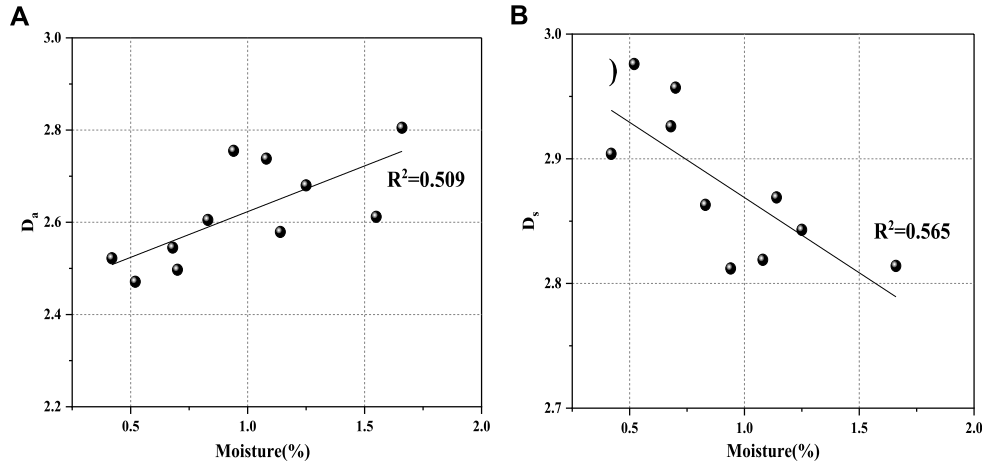

FIGURE 7
Collection between fractal dimensions (D_a and D_s) and moisture content.

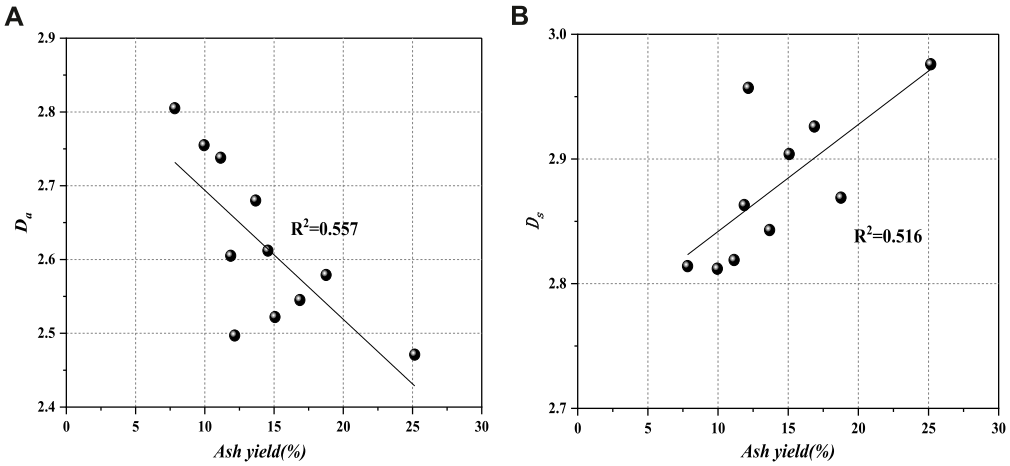

FIGURE 8
Collection between fractal dimensions (D_a and D_s) and ash yield. **(A)** Relationship between D_a and ash yield, **(B)** Relationship between D_s and ash yield.

are listed in Table 5. Generally, the fractal dimension D is between 2 and 3. When fractal dimension D is 2, the pore surface is smooth. When fractal dimension D is 3, the pore surface is rough (Zhang and Weller, 2014). The more complicated rock surface is, the larger D is (Mandelbrot and Benoit, 1998). The ranges of D_a and D_s vary from 2.471 to 2.805 and from 2.812 to 2.976, with the average of 2.619 and 2.878, respectively. Because the relaxation time of the seepage pore is not detected for sample X-5, the fractal dimension of the seepage pore is missing. The fractal dimension D_a is less than D_s, indicating that seepage pores are more complex than adsorption pores in all samples.

4 Discussions

Due to the complex physical properties of coal, the methane adsorption capacity of the coal is affected by many factors, such as coal composition, pore characteristics and so on (Lin et al., 2021). Fractal represents the complexity of coal samples and can be used as a combination of comprehensive factors. However, most previous studies focused on the relationship between the coal permeability and fractal dimension by NMR, so this study mainly discussed the influence of fractal characteristics on methane adsorption capacity for high-rank coals.

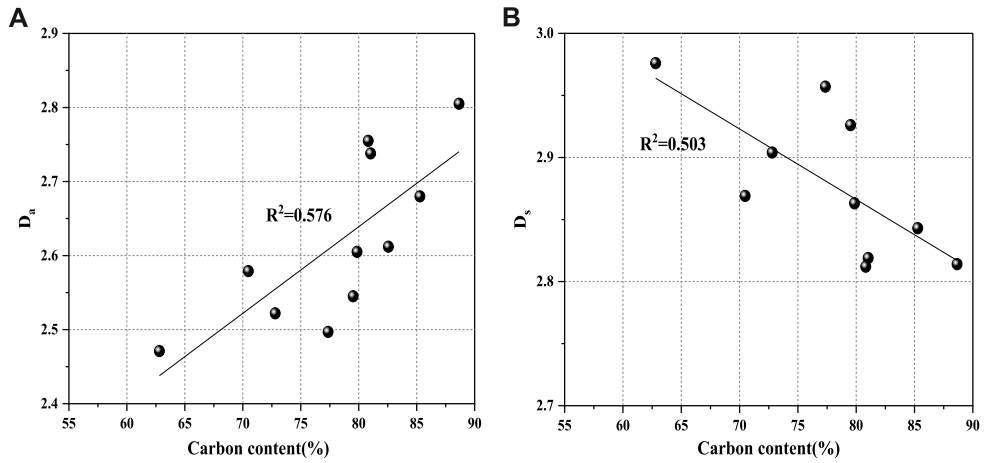

FIGURE 9
Collection between fractal dimensions (D_a and D_s) and carbon content. **(A)** Relationship between D_a and carbon content, **(B)** Relationship between D_s and carbon content.

4.1 Relationships between composition and fractal dimensions of coals

In order to solve the effect of coal composition on fractal characteristics of different coal pore structures by NMR, all correlations between coal compositional parameters and fractal dimensions are shown in Figures 7–9, and the data on coal composition is listed in Table 1.

Figure 7 shows the relationships between moisture contents and fractal dimensions of coals. With the increase of moisture content, fractal dimension D_s decreases (Figure 7B). Yet fractal dimension D_a increases with increasing moisture content (Figure 7A). It means that the fractal dimensions D_a and D_s are greatly influenced by moisture content.

The moisture of coal reservoirs includes free water from seepage pore and irreducible water from adsorption pore. Moisture change in coal is influenced by coal rank. The volume of seepage pore is reduced by compression with the rising of coal rank, but the volume of adsorption pore increases (Yao, et al., 2008). The volume of the adsorption pore increases and that of the seepage pore decreases with the increase of moisture content of high-rank coals, and the surface of the adsorption pore may be influenced by gas-liquid interfacial tension. As a result, the adsorption pore is more complicated, and the seepage pore is more homogeneous (Li et al., 2015).

The relationships between the ash yield and the four fractal dimensions of coals are shown in Figure 8. Ash yield of coals is negatively correlated with D_a (Figure 8A), and positively correlated with D_s (Figure 8B). The mineral content of coal is reflected indirectly by ash yield. If ash yield is high, mineral content is high. With increasing ash yield, adsorption pores may be more homogeneous by filling minerals, which can lead to the decreased fractal dimension D_a. But D_s has a positive correlation with the ash yield of coals. The main reasons are as follows. On the one hand, with increasing ash yield, some seepage pores are partially filled with ash, leading to more heterogeneous structure of seepage pores, and greater fractal dimensions. On the other hand, the newly generated mineral pores lead to enhancing the heterogeneity of seepage pores (Yao et al., 2008; Liu and Wu, 2016).

Figure 9 showsthe relationships between carbon contents and fractal dimensions of coals. With the increase of carbon content, the fractal dimension D_a increases and D_s decreases. We conclude that because of devolatilization and/or oxidation, the high carbon coal usually has low water content and ash yield in the coalification process. In this case, decreasing moisture content and ash yield may have caused the increase of D_a and the decrease of D_s. Meanwhile, the volume and percentage of seepage pores are reducing in coals with increasing carbon contents, which leads to more homogeneous structure of seepage pores.

4.2 Relationships between porosity and fractal dimensions of coals

Figure 10 shows the line relationship between pore structure parameters and fractal dimensions (D_a and D_s). The fractal dimension D_a has a positive linear correlation with the total SSA and SSA of micropore, indicating that

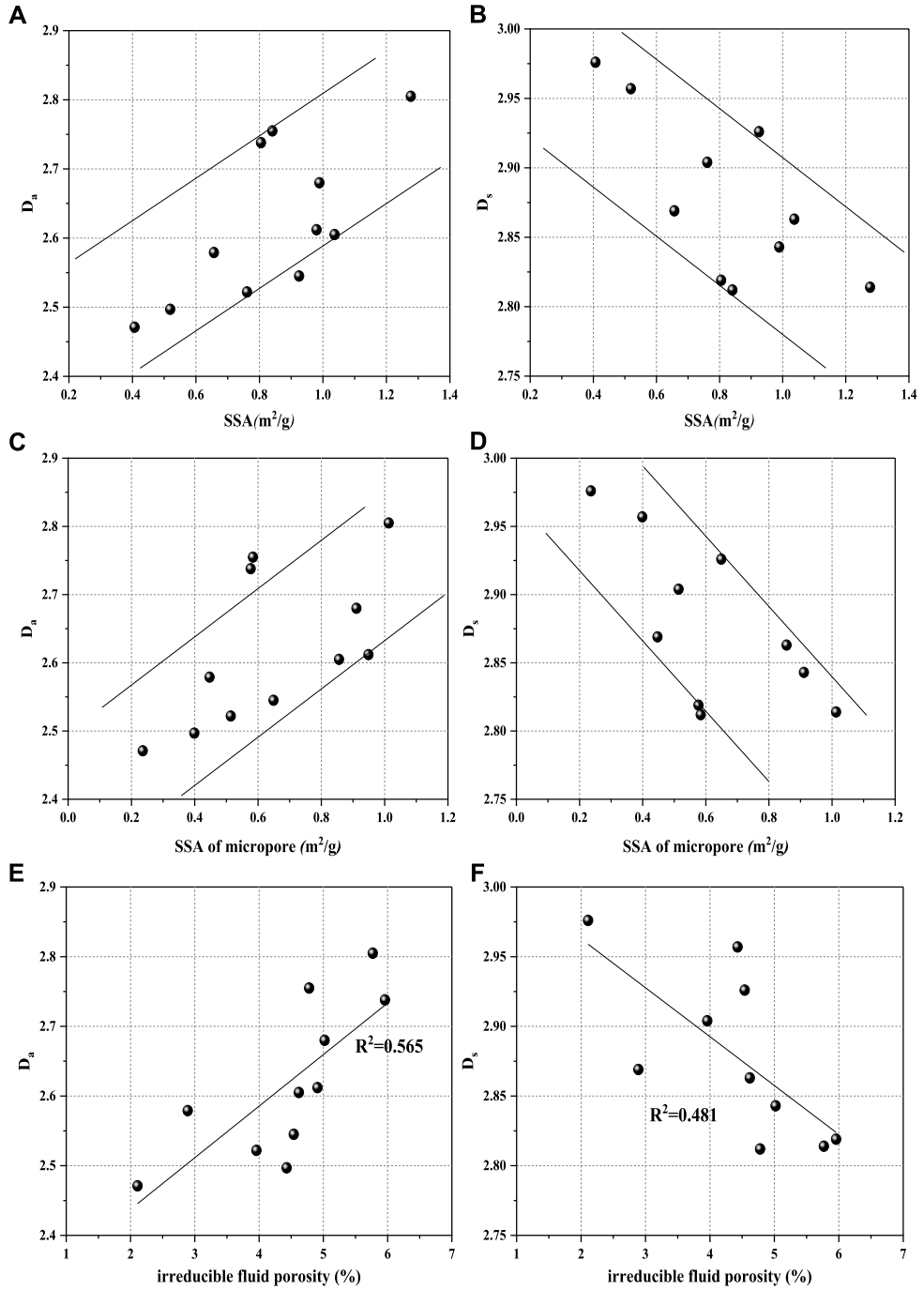

FIGURE 10
Collection between fractal dimension and pore structure. **(A** and **B)** Relationship between fractal dimensions and SSA, **(C** and **D)** Relationship between fractal dimensions and SSA of micropore, **(E** and **F)** Relationship between fractal dimensions and porosity.

high-rank coals with higher total SSA and micropore SSA have higher D_a values (Figure 10A, Figure 10C). This means that the total surface area is mainly provided by micropores for high-rank coals. The higher the total SSA is, the higher the micropore percentage will be, resulting in more complexity of the adsorption pore structure. With the increase of total SSA and micropore SSA, D_s gradually decreases, indicating that the higher the total SSA of high-rank coals is, the smaller the content of seepage pores is, leading to more heterogeneous structure of

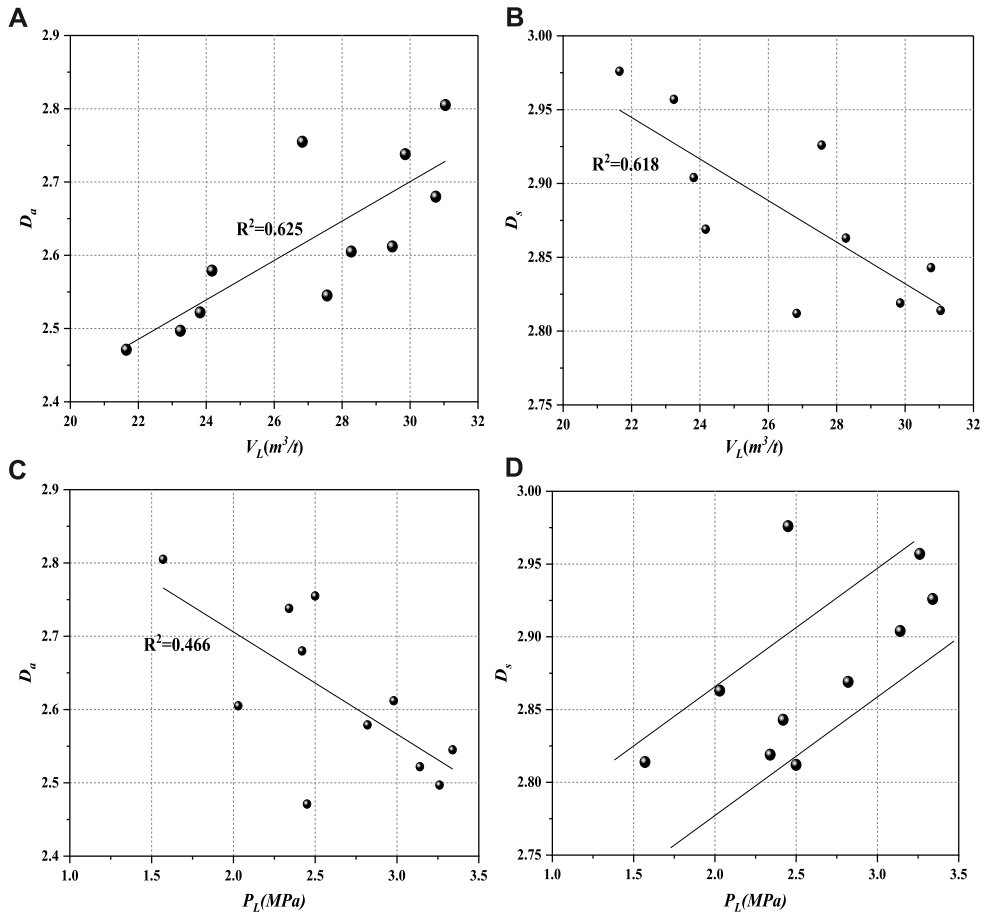

FIGURE 11
Effect of fractal dimensions on methane adsorption. **(A, B)** Relationship between fractal dimensions and V_L, **(B)** Relationship between fractal dimensions and P_L.

seepage pores (Figure 10B, Figure 10D). To further reveal the correlation between fractal dimensions and pore structure characteristics, more information is needed. Table 3 shows the parameters including the total porosity, moveable fluid porosity and irreducible fluid porosity, which are obtained from NMR experimental analysis. The D_a has a positive correlation with the irreducible fluid porosity (Figure 10E). In contrast, The fractal dimensions D_s has a negative correlation with the irreducible fluid porosity (Figure 10F). This means that with increasing irreducible fluid porosity, the volume and percentage of adsorption pores are increasing, which leads to the increase of SSA, more complicated structure of adsorption pores and more heterogeneous structure of seepage pores for high-rank coals. Therefore, they may result in relatively high CH_4 adsorption capacity of coals with higher D_a and less D_s value.

4.3 Relationship between coal adsorption capacity and fractal dimension

The influence of fractal dimensions of different coal samples on V_L and P_L is shown in Figure 11. As shown in Figure 11A and Figure 11B, V_L gradually increases with the increase of D_a, which illustrates that the ultimate adsorption capacity of coal samples is gradually enhanced. V_L has a positive linear correlation with D_a. However, V_L has a negative correlation with D_s, which means that the increase of the D_s value results in a decrease in CH_4 adsorption capacity. The analysis shows that D_a and D_s reflect the fractal feature of adsorption and seepage pores, respectively. As is well-known, the adsorption pore has the primary influence on the adsorption capacity of coal. On the one hand, the higher D_a value represents more SSA of high-rank coals which provide more adsorption sites for CH_4, so the high-rank coals have stronger adsorption capacity with higher D_a. On the other

hand, with the increase of D_s value, the high-rank coals have stronger heterogeneity of seepage pore structure, fewer adsorption sites for CH_4 and higher capillary condensation on pore surfaces, which leads to the reduction of CH_4 adsorption. Above all, the fractal dimension D_a affects on CH_4 adsorption capacity greater than D_s.

In the Langmuir equation, P_L, which reflects the adsorption capacity of coal at the low-pressure stage, represents the adsorption pressure when the adsorption volume of CH_4 gets to half of V_L. The influence of the fractal dimensions D_a and D_s on P_L is shown in Figure 11C and Figure 11D. As can be seen from the figures, The D_a value is negatively correlated with P_L. The CH_4 adsorption velocity of coal samples is increasing. According to the volume filling theory of micropores (Carrott et al., 1987), the micropores with the adsorption potential of significant superposition can reach saturation of adsorption capacity at lower pressure, and the adsorption energy has a close relationship with the surface of the micropores. With the increase of D_a value, the percentage and surface of micropores will increase, which causes the increase of CH_4 adsorption velocity for high-rank coals. However, there is a positive correlation between P_L and D_s. With the increase of D_s, the percentage of seepage pores will increase and the surface of micropores will decrease. So the CH_4 adsorption velocity decreases with higher D_s value for high-rank coals. Therefore, the fractal dimension D_a has an important influence on P_L.

Since the physical properties of coal are complicated, the difference in fractal dimensions of coal samples is caused by multiple factors, such as the content of each component in coal, pore size distribution, and so on. The above factors result in the heterogeneity of coal surface and structure, which will influence the methane adsorption capacity of coal. Thus, the fractal dimensions are the comprehensive reflection of differences among the physical properties of coal and are able to show the effect of coal properties on methane adsorption fully.

5 Conclusion

1. According to the characteristics of LP-N_2A isotherms, all coal samples can be classified into three types. The SSA distribution curves exhibit unimodality with the main peak at ~1 nm for all coal samples, indicating that the SSA of high-rank coals is more concentrated in micropores. The PV distribution shows obvious multimodality for most coal samples, and the peaks are at ~1, ~20 and ~50 nm. The pores for > 10 nm provide most of the pore volume. Meanwhile, the micropores of type C provide the largest proportion of PV and SSA.
2. We divide the T_2 spectrum of coal samples into four parts by the surface relaxivity of high-rank coal. Meanwhile, the fractal dimensions of different pore types are obtained from the slope of the equation by the linear fitting data of $\log(N(r_j))$ and $\log(T_2)$. The average values of D_a and D_s are 2.619 and 2.878, respectively.
3. The composition and pore parameters of coals have much greater control over fractal dimensions. The fractal dimension D_a has a negative correlation with ash yield and moisture content, and a positive correlation with carbon content. The fractal dimension D_s has a positive correlation with ash yield and moisture content, and a negative correlation with carbon content. The high-rank coals with higher D_a value have the more complicated structure of adsorption pores with higher SSA and irreducible fluid porosity, which results in relatively high CH_4 adsorption capacity of coals.
4. The different fractal dimensions have varying effects on methane adsorption. With the increase of fractal dimension D_a, V_L increased and P_L decreased, which illustrates that the CH_4 adsorption capacity and velocity are gradually enhanced for high-rank coals. Compared with Da, Ds has the opposite effect on the CH_4 adsorption capacity and velocity of high-rank coals. Thus, the fractal dimensions of different pore types, which are calculated based on NMR, are able to show the effect of coal properties on CH_4 adsorption fully.

Data availability statement

The original contributions presented in the study are included in the article/Supplementary Material, further inquiries can be directed to the corresponding author.

Author contributions

WJ: laboratory experiments and data analysis; YZ: manuscript preparation; CW: manuscript review; and MD: sample collection.

Funding

This study was financially supported by the start-up fund for doctoral research of Suzhou University (No.2019jb16), Scientific research platform project of Suzhou University (2021XJPT54) and College Students' innovation and entrepreneurship training program of Suzhou University (KYLXYBXM22-070).

Conflict of interest

The authors declare that the research was conducted in the absence of any commercial or financial relationships that could be construed as a potential conflict of interest.

Publisher's note

References

Acevedo, B., and Barriocanal, C. (2015). Texture and surface chemistry of activated carbons obtained from tyre wastes. *Fuel Process. Technol.* 134, 275–283. doi:10.1016/j.fuproc.2015.02.009

Alexeev, A. D., Vasilenko, T., and Ulyanova, E. (1977). Closed porosity in fossil coals. *Fuel* 78, 635–638. doi:10.1016/s0016-2361(98)00198-7

Barrett, E. P., Joyner, L. G., and Halenda, P. P. (1951). The determination of pore volume and area distributions in porous substances. I. computations from nitrogen isotherms. *J. Am. Chem. Soc.* 73, 373–380. doi:10.1021/ja01145a126

Brunauer, S., Emmett, S., and Teller, E. J. (1938). Adsorption of gases in multi-molecular layers. *J. Am. Chem. Soc.* 60 (2), 309–319. doi:10.1021/ja01269a023

Cai, Y., Liu, D., Pan, Z., Yao, Y., Li, J., and Qiu, Y. (2013b). Pore structure and its impact on CH_4 adsorption capacity and flow capability of bituminous and subbituminous coals from northeast China. *Fuel* 103, 258–268. doi:10.1016/j.fuel.2012.06.055

Cai, Y., Liu, D., Pan, Z., Yao, Y., and Qiu, Y. (2013a). Petrophysical characterization of Chinese coal cores with heat treatment by nuclear magnetic resonance. *Fuel* 108 (11), 292–302. doi:10.1016/j.fuel.2013.02.031

Carrott, P., Roberts, R. A., and Sing, K. (1987). Adsorption of nitrogen by porous and non-porous carbons. *Carbon* 25 (1), 59–68. doi:10.1016/0008-6223(87)90040-6

Chen, Y., Liu, D., and Gan, Q. (2018). Insights into fractal characteristics of pores in different rank coals by nuclear magnetic resonance (NMR). *Arab. J. Geosci.* 11 (19), 578. doi:10.1007/s12517-018-3943-2

Cheng, Y. Y., Cheng, Z. L., Li, S., Chen, S. D., and Guo, T. (2021). Characteristics of coalbed methane accumulation in Bide-Santang syncline, Western Guizhou and favorable sector. *Geol. Bull. China* 40 (7), 1140–1148.

Coetzee, G. H., Sakurovs, R., Neomagus, W., Hein, J. P., Everson, R. C., Mathews, J. P., et al. (2015). Pore development during gasification of South African inertinite-rich chars evaluated using small angle X-ray scattering. *Carbon* 95, 250–260. doi:10.1016/j.carbon.2015.08.030

Daigle, H., and Johnson, A. (2016). Combining mercury intrusion and nuclear magnetic resonance measurements using percolation theory. *Transp. Porous Media* 111, 669–679. doi:10.1007/s11242-015-0619-1

De Boer, J. H. (1958). *The shape of capillaries*. Landon: Butterworth.

Dillinger, A., and Esteban, L. (2014). Experimental evaluation of reservoir quality in Mesozoic formations of the Perth Basin (Western Australia) by using a laboratory low field nuclear magnetic resonance. *Mar. Petroleum Geol.* 57, 455–469. doi:10.1016/j.marpetgeo.2014.06.010

Dullien, F. A. L. (1991). *Porous media fluid transport and pore structure*. Massachusetts, United States: Academic Press.

Ferro, N. D., Delmas, P., Duwig, C., Simonetti, G., and Morari, F. (2012). Coupling X-ray microtomography and mercury intrusion porosimetry to quantify aggregate structures of a cambisol under different fertilisation treatments. *Soil Tillage Res.* 119, 13–21. doi:10.1016/j.still.2011.12.001

Fu, X. H., Qin, Y., Zhang, W. H., Wei, C. T., and Zhou, R. F. (2005). Fractal classification and natural classification of coal pore structure based on migration of coalbed methane. *Chin. Sci. Bull.* 50, 66–71. doi:10.1007/bf03184085

Gao, Sh., Wang, L., Gao, J., and Zhang, R. (2018). Experimental study on pore structures of hard coal with different metamorphic grade based on fractal theory. *Coal Sci. Tech.* 46 (8), 93–100. doi:10.13199/j.cnki.cst.2018.08.015

Ge, X., Fan, Y., Zhu, X., Chen, Y., and Li, R. (2014). Determination of nuclear magnetic resonance T_2 cutoff value based on multifractal theory-An application in sandstone with complex pore structure. *Geophysics* 80 (1), 11–21. doi:10.1190/geo2014-0140.1

Geerlings, P., Proft, F. D., and Langenaeker, W. (2003). Conceptual density functional theory. *Chem. Rev.* 103 (29), 1793–1874. doi:10.1021/cr990029p

Hodot, B. B. (1966). *Outburst of coal and coalbed gas*. Beijing: China Industry Press.

IUPAC (1982). Reporting physisorption data for gas/solid systems with special reference to the determination of surface area and porosity. *Pure Appl. Chem.* 54 (11), 2201–2218. doi:10.1351/pac198557040603

Johnson, R. C., and Flores, R. M. (1998). Developmental geology of coalbed methane from shallow to deep in Rocky Mountain basins and in Cook inlet Matanuska basin, Alaska, USA and Canada. *Int. J. Coal Geol.* 35 (1), 241–282. doi:10.1016/s0166-5162(97)00016-5

Ju, Y., Sun, Y., Tan, J., Bu, H., Han, K., Li, X., et al. (2018). The composition, pore structure characterization and deformation mechanism of coal-bearing shales from tectonically altered Coalfields in Eastern China. *Fuel* 234, 626–642. doi:10.1016/j.fuel.2018.06.116

Lai, J., Wang, G., Fan, Z., Zhou, Z., Chen, J., and Wang, S. (2018). Fractal analysis of tight shaly sandstones using nuclear magnetic resonance measurements. *Am. Assoc. Pet. Geol. Bull.* 102 (2), 175–193. doi:10.1306/0425171609817007

Lee, B. H., and Lee, S. K. (2013). Effects of specific surface area and porosity on cube counting fractal dimension, lacunarity, configurational entropy, and permeability of model porous networks: Random packing simulations and NMR micro-imaging study. *J. Hydrology* 496, 122–141. doi:10.1016/j.jhydrol.2013.05.014

Li, P., L., Zhang, X., and Zhang, S. (2018). Structures and fractal characteristics of pores in low volatile bituminous deformed coals by low-temperature N_2 adsorption after different solvents treatments. *Fuel* 224, 661–675. doi:10.1016/j.fuel.2018.03.067

Li, X., Kang, Y., and Haghighi, M. (2017). Investigation of pore size distributions of coals with different structures by nuclear magnetic resonance (NMR) and mercury intrusion porosimetry (MIP). *Measurement* 116, 122–128. doi:10.1016/j.measurement.2017.10.059

Li, Y., Yang, J., Pan, Z., and Tong, W. (2020a). Nanoscale pore structure and mechanical property analysis of coal: An insight combining AFM and SEM images. *Fuel* 260, 116352. doi:10.1016/j.fuel.2019.116352

Li, Z., Hao, Z., Pang, Y., and Gao, Y. (2015). Fractal dimensions of coal and their influence on methane adsorption. *J. China Coal Soc.* 40 (4), 863–869. doi:10.13225/j.cnki.jccs.2014.3022

Li, Z., Liu, D., Cai, Y., and Si, G. (2020b). Evaluation of coal petrophysics incorporating fractal characteristics by mercury intrusion porosimetry and low-field NMR. *Fuel (Lond).* 263, 116802. doi:10.1016/j.fuel.2019.116802

Li, Z., Liu, D., Cai, Y., and Teng, J. (2019). Adsorption pore structure and its fractal characteristics of coals by N_2 adsorption/desorption and FESEM image analyses. *Fuel* 257, 116031. doi:10.1016/j.fuel.2019.116031

Li, Z. W., Lin, B. Q., Hao, Z. Y., and Gao, Y. B. (2013). Characteristics of pore size distribution of coal and its impacts on gas adsorption. *J. China Univ. Min. Technol.* 42 (6), 1047–1053. doi:10.13247/j.cnki.jcumt.2013.06.025

Lin, Y., Qin, Y., and Duan, Z. (2021). Pore structure, adsorptivity and influencing factors of high-volatile bituminous coal rich in inertinite. *Fuel* 293, 120418. doi:10.1016/j.fuel.2021.120418

Liu, H. H., Sang, S. X., Liu, S. Q., and Zhu, Q. P. (2015). Growth characteristics and genetic types of pores and fractures in a high-rank coal reservoir of the southern Qinshui basin. *Ore Geol. Rev.* 64, 140–151. doi:10.1016/j.oregeorev.2014.06.018

Liu, S., and Wu, C. (2016). Study on fractal characteristics of different scales pore coal reservoir in Bide-Santang Basin. *Coal Sci. Technol.* 44 (2), 33–38. doi:10.13199/j.cnki.cst.2016.02.006

Liu, X. F., and He, X. Q. (2017). Effect of pore characteristics on coalbed methane adsorption in middle-high rank coals. *Adsorption* 23 (1), 3–12. doi:10.1007/s10450-016-9811-z

Mandelbrot, B. B., and Benoit, B. (1998). The fractal geometry of nature. *Am. J. Phys.* 51 (3), 286–287. doi:10.1119/1.13295

Meyers, R. A. (1982). *Coal structure*. New York: Academic Press.

Nie, B., Lun, J., Wang, K., and Shen, J. (2020). Three-dimensional characterization of open and closed coal nanopores based on a multi-scale analysis including CO2 adsorption, mercury intrusion, low-temperature nitrogen adsorption, and small-angle X-ray scattering. *Energy Sci. Eng.* 8, 2086–2099. doi:10.1002/ese3.649

Ouyang, Z., Liu, D., Cai, Y., and Yao, Y. (2016). Fractal analysis on heterogeneity of pore-fractures in middle-high rank coals with NMR. *Energy fuels.* 30, 5449–5458. doi:10.1021/acs.energyfuels.6b00563

Pan, J., Zhu, H., Hou, Q., Wang, H., and Wang, S. (2015). Macromolecular and pore structures of Chinese tectonically deformed coal studied by atomic force microscopy. *Fuel* 139, 94–101. doi:10.1016/j.fuel.2014.08.039

Peng, C., Zou, C., Yang, Y., Zhang, G., and Wang, W. (2017). Fractal analysis of high rank coal from southeast Qinshui basin by using gas adsorption and mercury porosimetry. *J. Petroleum Sci. Eng.* 156, 235–249. doi:10.1016/j.petrol.2017.06.001

Saboorian-Jooybari, H. (2016). New analytical formulas for prediction of gas-liquid relative permeabilities through fractures-Part I: Incompressible flow. *J. Nat. Gas Sci. Eng.* 30, 604–615. doi:10.1016/j.jngse.2016.02.002

Shan, C., Zhang, T., Guo, J., Zhang, Z., and Yang, Y. (2015). Characterization of the micropore systems in the high-rank coal reservoirs of the southern Sichuan Basin, China. *Am. Assoc. Pet. Geol. Bull.* 99 (11), 2099–2119. doi:10.1306/07061514240

Shi, Y. M., Zhang, Y. G., Yong, H. E., Zheng, H. F., Lu, W. Z., and Zheng, H. J. (2006). The study of flow units using fractal and fractal dimension methods of capillary pressure curve. *Earth Sci. Front.* 13 (3), 129–134.

Sing, K. S. W. (1982). Reporting physisorption data for gas/solid systems with special reference to the determination of surface area and porosity (Provisional). *Pure Appl. Chem.* 54 (11), 2201–2218. doi:10.1351/pac198254112201

Sing, K. S. W. (1985). Reporting physisorption data for gas/solid systems with special reference to the determination of surface area and porosity (Recommendations 1984). *Pure Appl. Chem.* 57, 603–619. doi:10.1351/pac198557040603

Song, X. X., Tang, Y. G., Wei, L. I., Wang, S. Q., and Yang, M. X. (2013). Fractral characteristics of adsorption pores of tectonic coal from Zhongliangshan southern coalmine. *J. China Coal Soc.* 38 (1), 134–139. doi:10.13225/j.cnki.jccs.2013.01.002

Song, Y., Jiang, B., and Liu, J. (2017). Nanopore structural characteristics and their impact on methane adsorption and diffusion in low to medium tectonically deformed coals: Case study in the huaibei coal field. *Energy fuels.* 31 (7), 6711–6723. doi:10.1021/acs.energyfuels.7b00512

Sun, W., Feng, Y., Jiang, C., and Chu, W. (2015). Fractal characterization and methane adsorption features of coal particles taken from shallow and deep coalmine layers. *Fuel* 155, 7–13. doi:10.1016/j.fuel.2015.03.083

Wang, C., Jiang, C. F., and Wei, C. (2013). Fractral dimension of coals and analysis of its influencing factors. *J. China Univ. Min. Technol.* 42 (6), 1009–1014. doi:10.13247/j.cnki.jcumt.2013.06.020

Wang, L. G., Jesus, M., and Salazar, J. (2011). Effects of surfactant-emulsified oil-based mud on borehole resistivity measurements. *SPE J.* 16 (3), 608–624. doi:10.2118/109946-pa

Yang, Z., Qin, Y., Wang, G. X., and An, H. (2014). Investigation on coal seam gas formation of multi-coalbed reservoir in Bide-Santang Basin Southwest China. *Arab. J. Geosci.* 8, 5439–5448. doi:10.1007/s12517-014-1640-3

Yang, Z., Qin, Y., Yi, T., Tang, J., Zhang, Z., and Wu, C. (2019). Analysis of multi-coalbed CBM development methods in Western Guizhou, China. *Geosci. J.* 23, 315–325. doi:10.1007/s12303-018-0037-9

Yao, Y., and Liu, D. (2012). Comparison of low-field NMR and mercury intrusion porosimetry in characterizing pore size distributions of coals. *Fuel* 95 (1), 152–158. doi:10.1016/j.fuel.2011.12.039

Yao, Y., Liu, D., Tang, D., Tang, S., and Huang, W. (2008). Fractal characterization of adsorption-pores of coals from North China: An investigation on CH_4 adsorption capacity of coals. *Int. J. Coal Geol.* 73, 27–42. doi:10.1016/j.coal.2007.07.003

Yao, Y., Liu, D., Tang, D., Tang, S., Huang, W., Liu, Z., et al. (2009). Fractal characterization of seepage-pores of coals from China: An investigation on permeability of coals. *Comput. Geosci.* 35 (6), 1159–1166. doi:10.1016/j.cageo.2008.09.005

Yao, Y., Liu, D., Yao, C., Tang, D., Tang, S., and Huang, W. (2010). Petrophysical characterization of coals by low-field nuclear magnetic resonance (NMR). *Fuel* 89 (7), 1371–1380. doi:10.1016/j.fuel.2009.11.005

Zhang, C., Chen, Z., and Zhang, Z. (2007). Fractal characteristics of reservoir rock pore structure based on NMR T_2 distribution. *J. Oil Gas Technol.* 29 (4), 80–86.

Zhang, Z., and Weller, A. (2014). Fractal dimension of pore-space geometry of an Eocene sandstone formation. *Geophysics* 79 (6), 377–387. doi:10.1190/geo2014-0143.1

Zhao, D., Guo, Y., Wang, G., and Mao, X. (2019). Characterizing nanoscale pores and its structure in coal: Experimental investigation. *Energy Explor. Exploitation* 37 (4), 1320–1347. doi:10.1177/0144598719831397

Zheng, S., Yao, Y., Elsworth, D., and Liu, Y. (2020). A novel pore size classification method of coals: Investigation based on NMR relaxation. *J. Nat. Gas Sci. Eng.* 81, 103466. doi:10.1016/j.jngse.2020.103466

Zheng, S., Yao, Y., Liu, D., Cai, Y., Liu, Y., and Li, X. (2019). Nuclear magnetic resonance T_2 cutoffs of coals: A novel method by multifractal analysis theory. *Fuel* 241, 715–724. doi:10.1016/j.fuel.2018.12.044

Zhou, S., Liu, D., Cai, Y., and Yao, Y. (2016). Fractal characterization of pore–fracture in low-rank coals using a low-field NMR relaxation method. *Fuel* 181, 218–226. doi:10.1016/j.fuel.2016.04.119

Zhou, S., Liu, D., Karpyn, T., and Yao, Y. (2018). Effect of coalification jumps on petrophysical properties of various metamorphic coals from different coalfields in China. *J. Nat. Gas Sci. Eng.* 60, 63–76. doi:10.1016/j.jngse.2018.10.004

Zhou, S., Wang, H., Jiang, S., Yan, D., Guoqing, L., Zhang, Z., et al. (2022). A novel approach to obtain fractal dimension in coals by LFNMR: Insights from the T_2 peak and T_2 geometric mean. *J. Energy Eng.* 148 (3), 0000827. doi:10.1061/(asce)ey.1943-7897.0000827

frontiers | Frontiers in Earth Science

TYPE Original Research
PUBLISHED 16 January 2023
DOI 10.3389/feart.2022.1053142

OPEN ACCESS

EDITED BY
Junjian Zhang,
Shandong University of Science and Technology, China

REVIEWED BY
Zhen Lou,
China University of Mining and Technology, China
Yanyan Chen,
Research Institute of Petroleum Exploration and Development (RIPED), China

*CORRESPONDENCE
Hong-qing Cui,
hqcui@hpu.edu.cn
Hang Zhang,
381537341@qq.com

SPECIALTY SECTION
This article was submitted to Economic Geology, a section of the journal Frontiers in Earth Science

RECEIVED 25 September 2022
ACCEPTED 04 November 2022
PUBLISHED 16 January 2023

CITATION
He X, Cui H-q, Zhang H, Wang Z-z, Wang Z-h and Shi G-s (2023), Experimental study and weighting analysis of factors influencing gas desorption.
Front. Earth Sci. 10:1053142.
doi: 10.3389/feart.2022.1053142

Experimental study and weighting analysis of factors influencing gas desorption

Xin He[1], Hong-qing Cui[1,2]*, Hang Zhang[1]*, Zhen-zhi Wang[3], Ze-hua Wang[1] and Guang-shan Shi[1]

[1]School of Safety Science and Engineering, Henan Polytechnic University, Jiaozuo, Henan, China, [2]State Key Laboratory Cultivation Base for Gas Geology and Gas Control of Henan Province, Jiaozuo, Henan, China, [3]School of Resources and Geoscience, China University of Mining and Technology, Xuzhou, Jiangsu, China

Gas is one of the necessary contributing factors for coal and gas outburst accidents, and the gas desorbed in coal is the energy carrier in the outburst process. The study of gas desorption laws is the premise and basis for gas content determination and gas accident prevention. To solve the problem of inaccurate gas content measurement due to the unclear characteristics of rapid gas desorption in 0–10 s, the gas desorption experimental device was improved, the influence factors of gas desorption were studied experimentally, and a comprehensive analysis method was proposed based on the gas desorption rate, gas desorption efficiency, initial gas desorption amount and total desorbed gas. The experiment analysed five factors that affected gas desorption, including the degree of metamorphism, type of failure, particle size, pressure and temperature. The results show that there is a monotonically decreasing power function relationship between the initial gas desorption rate and time and a monotonically increasing logarithmic function relationship between the gas desorption amount and time; the curve has a limit value. The gas desorption amount is large in 0–10 s and increases slowly afterwards. Among the factors affecting gas desorption, their importance decreases in the order of pressure > metamorphism > particle size > failure type > temperature. This study is of great practical value for the calculation of gas losses in gas content determination, and the resulting gas desorption laws are of great importance in guiding gas control work.

KEYWORDS

gas content, gas desorption, weighting analysis, gas pressure, metamorphism, particle size

1 Introduction

Excavation activities in coal mines cause the formation stress balance to be destroyed, thereby increasing the gas potential energy. Gas can be desorbed from the coal body and flooded into the mining tunnel in a very short period of time. The exposed coal is in a state of stress unloading. Under the dual action of *in situ* stress and gas, the coal is crumpled and damaged, resulting in the relaxation of pores and fissures. The diffusion resistance of

free gas is reduced, and it continuously flows into the roadway, causing hidden dangers to production (Hao et al., 2000). The accurate determination of gas content is difficult but it is a crucial factor in coal mine production and is the premise of resource utilization and disaster prevention (Zhang, 2009; Wang et al., 2018; Wang et al., 2018b). To predict the risk of gas-related disasters, it is necessary to timely and accurately measure the initial gas release velocity and gas content.

The initial velocity of gas release (ΔP) is an important index for evaluating the risk of coal and gas outbursts in China (with $\Delta P \geq 10$ as the critical value). ΔP is an empirical value, and it is not accurate to use the same index under different metamorphism, pressure, temperature and other conditions (Zhang, 2006); this indicator represents the amount of gas emission in 10–60 s after atmospheric pressure adsorption but cannot reflect the instantaneous emission characteristics and actual attenuation changes of gas when different blocks are exposed. However, the instantaneous desorption and release of gas is the basic reason for the complex occurrence conditions and prominent dangers of coal gas (Fu and Yang, 2008). It is also the basis for coal seam gas content determination and outburst risk prediction (Jia and Chen, 2009; Jiang et al., 2009).

Therefore, the accurate determination of gas content and initial gas release velocity cannot be separated from the study of gas desorption laws. Previous researchers have performed much research on gas desorption, but there is a lack of research on gas release in the first 0–10 s and its influencing factors.

2 Experimental design

The desorption of gas in coal particles is a complex dynamic and hydrodynamic process. In the original state, the adsorbed gas, on the surface of the coal matrix or in the micropores, and the free gas in the fracture system are in a relative dynamic equilibrium. When the environmental factors around the tectonic coal change or under the action of vibration (Wang et al., 2021), the increased kinetic energy of the gas molecules is sufficient to overcome the gravitational effect of the adsorption potential well on the surface of the coal body; then, the adsorbed gas becomes free, and the adsorbed gas will be desorbed again.

The desorption of gas from coal is a complex process. First, the gas is desorbed from the adsorption state on the surface of the coal body into a free state (Wang et al., 2021b) and then desorbed from the coal body. To analyse the law of gas desorption under different conditions, based on the Langmuir adsorption model, the experimental equipment is improved, and the experimental conditions are established.

2.1 Experimental setup

The "Method for Determination of Methane Adsorption Capacity of Coal (High Pressure Volumetric Method)" (Ministry of coal industry of the people's Republic of China, 1997) was adopted, and the experimental device was improved, which consisted of 7 units of aeration, air extraction, temperature control, adsorption, desorption, desorption rate measurement, and communication auxiliary (Table 1).

The principle of the test device is shown in Figure 1.

2.2 Sample preparation

Coal samples were collected at the excavation face of the Changcun Mine in the Lu'an Mining Area and the Zouzhuang Mine in the Huaibei Mining Area. The coal was sampled from the newly disclosed coal, and its firmness coefficient and initial gas release velocity were determined. Later, it was transferred to the laboratory for sample preparation. A total of 30 coal samples with different degrees of metamorphism, failure types and particle sizes were prepared, the gas parameters were measured, and industrial analysis was performed. The characteristics of the experimental samples are shown in Table 2.

2.3 Experimental steps

2.3.1 Parameter design

A large number of studies have shown that gas desorption is controlled by the degree of coal metamorphism (Grażyna and Kinga, 1998; Zhang, 2018), the type of failure (Xie, 2014; Wang et al., 2020), particle size (Wang, 2018; Tu et al., 2022), equilibrium pressure (Li et al., 2018; Li et al., 2021), temperature (Liu, 2011; Li et al., 2022), moisture (Xiao, 2010; Zhang, 2011; Chen et al., 2013; Wang et al., 2018c), electromagnetic field (Xu et al., 2003; Li and Lei, 2012; Zhao and Deng, 2022) and so on.

Group 0 was selected as the control group, and 10 groups of experiments were designed with metamorphic degree, failure type, particle size, pressure and temperature as variables. To explore the influence of the metamorphic degree on gas desorption, gas coal with a low metamorphic degree was selected as Group 1. Geological structure is an important factor for the occurrence of coal and gas outbursts. Tectonic action will change the physical structure and chemical properties of coal, and the failure type of a coal body is an index used to measure the impact of tectonic action. Tectonic coal has the characteristics of low strength, poor cohesiveness, looseness and even pulverization after being damaged by extrusion deformation and shear crumpling. Therefore, structural coal from the same mining area is selected as Group 2 to study the influence of failure type on gas desorption. For primary structure coal, the smaller the particle size is, the larger the specific surface area. Group 3 is the experimental group of coal gas desorption with different particle sizes. According to the Langmuir adsorption model, pressure and temperature are important factors affecting the

TABLE 1 Unit equipment list of gas desorption experimental device.

Unit	Component	Technical parameter
Pneumatic unit	① Gas tank	Concentration 99.9%, Pressure 13 MPa
Extraction unit	② Vacuum gauge	Control range 1.0×10^{5}–1.0×10^{-1}Pa
		Control accuracy ±1%
	③ Vacuum pump	Ultimate vacuum 6.7×10^{-2}Pa
Temperature control unit	④ Super constant temperature water bath	Temperature range +5 ~ +95°C, constant temperature fluctuation
Adsorption unit	⑨ Coal sample tank	Volume≤150 ml, pressure≤10 MPa
	⑩ Pressure gauge	Range 0–16 MPa, minimum scale 0.1 MPa
Desorption unit	⑤ Graduated cylinder	Range 60 L, minimum scale 10 ml
	⑤ Desorption tube	Range 1000 ml, scale 4 ml, Range 500 ml, scale 2 ml
Desorption rate measurement unit	⑥ Gas mass flowmeter	Response time ≤1 s, differential pressure range 0.05–0.3 MPa
	⑦ Desorber	Automatic valve opening and closing
	⑧ Computer	data acquisition software
Auxiliary units	⑪ Four-way valve	Drying box; valve etc,.
	⑫ Three-way valve	
	⑬ Globe valve	
	⑭ Ball valve	

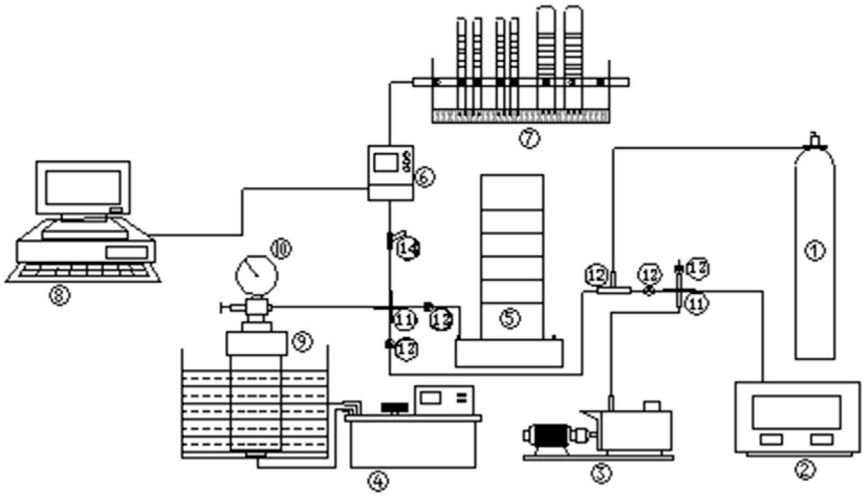

FIGURE 1
Principle picture of experimental device studying gas (CBM) desorption feature of tectonically coal.

adsorption and desorption of gas on the coal surface. In China, the identification of coal and gas outbursts is based on the gas pressure (≤0.74 MPa), and the minimum experimental pressure is 0.5 MPa. Five groups of desorption experiments with different pressures are designed with an increasing interval of 0.5 MPa. According to the practice of production and the geothermal studies, the formation temperature of coal seams in China is mostly 21°C–37°C, so desorption experiments of 20°C, 30°C, and 40°C at different temperatures are designed. Due to the limitations of the experimental setup, influencing factors such as water content and the presence of an electromagnetic field were not tested. The experimental variables and parameters are shown in Table 3.

2.3.2 Operation steps

The experimental operation process is divided into 7 steps:

Step 1: Put the experimental coal sample into the drying oven for 4 h, remove the moisture in the coal, and seal it after removal from the oven.

TABLE 2 Characteristics of experimental coal samples.

	Changcun mine in Lu'an mining area	Changcun mine in Lu'an mining area	Zuzhuang mine in huaibei mining area	Zuzhuang mine in huaibei mining area
Metamorphism degree	lean coal	lean coal	gas coal	gas coal
Type of damage	Type I~II	Type III~IV	Type II	Type IV~V
Robustness factor (f)	0.70	0.21	0.69	0.16
Initial velocity of gas release ($\triangle P$)	5	14	4	10
Adsorption constants a ($cm^3 \cdot g^{-1}$)	32.238	32.334	20.648	20.554
b (MPa^{-1})	0.684	0.770	0.414	0.347
Apparent density ($g \cdot cm^{-3}$)	1.38	1.42	1.18	1.23
Real density ($g \cdot cm^{-3}$)	1.42	1.47	1.29	1.35
Moisture of coal M_{ad} (%)	1.13	1.40	1.45	1.98
Ash content of coal A_{ad} (%)	9.52	12.37	12.67	19.28
Volatile matter of coal V_{ad} (%)	13.43	13.60	37.02	38.58

TABLE 3 Experimental parameters and variable design.

Number	Metamorphism degree	Damage type	Particle size (mm)	Pressure (MPa)	Temperature (°C)
Group 0	High	Type II	1.0–3.0	1.00	30
Group 1	Low	Type II	1.0–3.0	1.00	30
Group 2	High	Type IV	1.0–3.0	1.00	30
Group 3	High	Type II	0.5–1.0	1.00	30
Group 4	High	Type II	1.0–3.0	0.50	30
Group 5	High	Type II	1.0–3.0	1.50	30
Group 6	High	Type II	1.0–3.0	2.00	30
Group 7	High	Type II	1.0–3.0	2.50	30
Group 8	High	Type II	1.0–3.0	1.00	20
Group 9	High	Type II	1.0–3.0	1.00	40

Step 2: Load the cooled experimental coal sample into the coal sample tank and weigh it. Fill it as much as possible to reduce dead space.

Step 3: Tighten the coal sample tank and connect it to the experimental system to check the hermeticity of the system.

Step 4: Turn on the constant temperature water bath and set the experimental temperature.

Step 5: Vacuum the gas adsorption unit until the vacuum gauge shows 10 Pa. Once this value is reached, stop vacuuming.

Step 6: Close the connection between the gas adsorption unit and the vacuum pumping unit, open the gas charging unit and the gas adsorption unit, and fill the coal sample tank with pure CH_4 gas so that the gas in the coal sample tank reaches 1.2 times the design pressure. Once this is achieved, stop charging. Observe the change of the pressure gauge, and after the pressure gauge drops to the design pressure, fill the coal sample tank with pure gas. After more than 36–60 h of adsorption, the pressure in the coal sample tank will reach the experimental design adsorption equilibrium pressure.

Step 7: After the gas pressure in the coal sample tank reaches the design pressure for 6 h, turn on the flowmeter and stabilize it for more than 0.5 h. At the same time, prepare a stopwatch, and record the initial scale of the graduated cylinder, laboratory temperature and atmospheric pressure. When starting desorption, first open the desorption valve of the coal sample tank. Open the stop valve connecting the coal sample tank and the large cylinder, and when the pressure gauge of the coal sample tank drops to zero, close the stop valve connecting the coal sample tank and the large cylinder, and open the coal sample

TABLE 4 Comparison of gas desorption characteristic values.

Number	V_0 [mL/(g·s)]		T_{180} [ml/g]		E_{480} [s]		T_{480} [ml/g]		E_{180} [min]	
	Measured value	Ratio	Measured value	Ratio	Measured value	Ratio	Measured value	Ratio	Measured value	Ratio
Group 0	4.83	1	1.99	1	68	1	6.28	1	198	1
Group 1	2.53	0.52	0.95	0.48	122	1.79	5.81	0.93	204	1.03
Group 2	7.22	1.49	3.01	1.51	77	1.13	8.01	1.28	121	0.61
Group 3	7.83	1.62	2.42	1.22	92	1.35	10.53	1.68	170	0.86
Group 4	2.05	0.42	1.09	0.55	102	1.50	5.39	0.86	216	1.09
Group 5	8.33	1.72	2.93	1.47	65	0.96	10.22	1.63	182	0.92
Group 6	12.32	2.55	3.25	1.63	68	1.00	12.69	2.02	191	0.96
Group 7	15.14	3.13	3.46	1.74	70	1.03	12.98	2.07	173	0.87
Group 8	4.53	0.94	2.05	1.03	70	1.03	6.78	1.08	201	1.02
Group 9	4.77	0.99	1.76	0.88	79	1.16	6.50	1.04	189	0.95

tank ball valves connected to the small and large measuring tubes. The gas mass flowmeter starts to collect data automatically. The stopwatch starts timing and the data reading of the desorption amount both start when the ball valve is opened.

2.3.3 Experiment records and readings

1) 0–10 s, read the desorption amount every 1 s, counting 10 times;
2) 10–90 s, read the desorption amount every 2 s, counting 40 times in total;
3) 90–180 s, read the desorption amount every 5 s, counting 18 times in total;
4) 180–600 s, read the desorption amount every 10 s, counting 42 times in total;
5) 10–30 min, read the gas desorption amount every 1 min, counting 20 times;
6) 30–120 min, read the gas desorption amount every 5 min, counting 18 times in total;
7) 120–360 min, read the desorption amount every 10 min, counting 24 times in total;
8) After 6 h, read the gas desorption amount every 1 h until the reading no longer changes.

3 Experimental results and discussion

3.1 Experimental results

The results of 10 groups of gas desorption experiments under different conditions were counted, including the initial rate of gas desorption (V_0), initial gas desorption capacity (T_{180}), initial gas desorption efficiency (E_{180}), total gas desorption (T_{480}), and total gas desorption efficiency (E_{480}). The ratio of gas desorption characteristic values of the experimental groups to that of control Group 0 was calculated under different experimental conditions (Table 4). Among them, desorption efficiency refers to the time required for gas desorption to reach 80% of the total amount of desorption.

3.1.1 Experimental results of group 0

The experimental conditions for Group 0: meager lean coal, primary structural coal (Type II), particle size 1.0–3.0 mm, pressure 1.00 MPa and temperature 30°C (Figure 2). Group 0 was selected as the control group, the gas desorption conditions under different experimental conditions were compared, and then the influence of various factors on the gas desorption rate and amount were analysed.

3.1.2 Experimental results of group 1

The experimental conditions for Group 1: gas coal, primary structural coal (Type II), particle size 1.0–3.0 mm, pressure 1.00 MPa and temperature 30°C (Figure 3).

3.1.3 Experimental results of group 2

The experimental conditions for Group 2: meagre lean coal, tectonic coal (Type IV), particle size 1.0–3.0 mm, pressure 1.00 MPa and temperature 30°C (Figure 4).

3.1.4 Experimental results of group 3

The experimental conditions for Group 3: meagre lean coal, primary structural coal (Type II), particle size 0.5–1.0 mm, pressure 1.00 MPa and temperature 30°C (Figure 5).

3.1.5 Experimental results of groups 4, 5, 6, and 7

To explore the influence of pressure on the gas desorption law, experimental Groups 4, 5, 6, and 7 were designed to conduct a comparative analysis of gas desorption under experimental pressures of 0.50, 1.50, 2.00 and 2.50 MPa, respectively, with meagre lean coal, primary structural coal, and particle sizes of 1.0–3.0 mm at 30°C. The results of the experiment are shown in Figure 6.

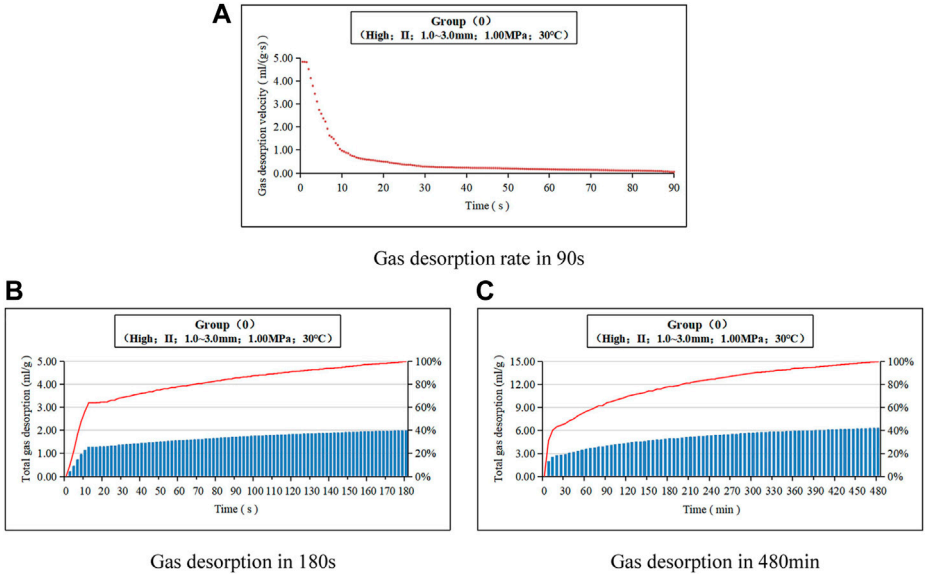

FIGURE 2
Gas desorption law diagram (Group 0).

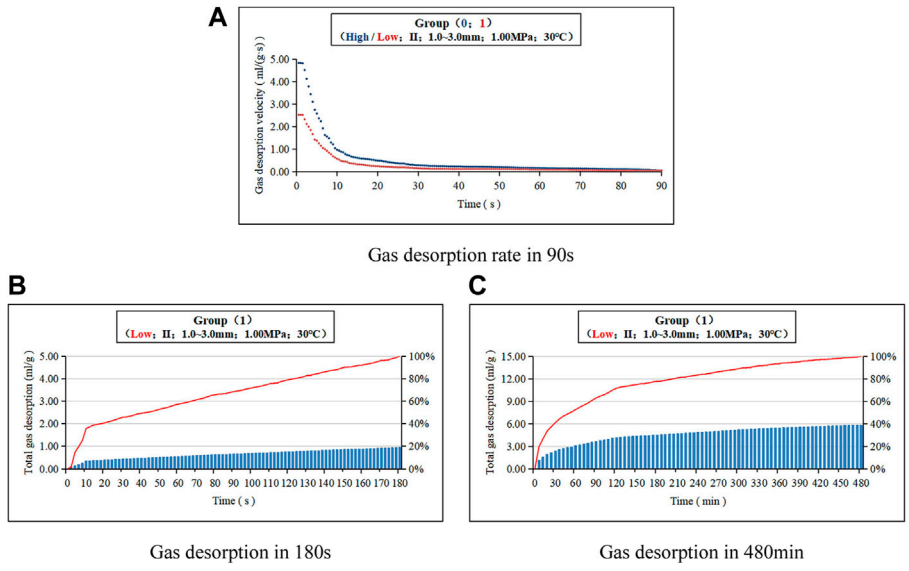

FIGURE 3
Gas desorption law diagram (Group 1).

3.1.6 Experimental results of groups 8 and 9

To explore the influence of temperature on the gas desorption law, experimental Groups 8 and 9 were designed to conduct a comparative analysis of gas desorption at 20°C and 40°C, respectively, under the conditions of meagre lean coal, primary structural coal, and particle sizes of 1.0–3.0 mm with a pressure of 1.0 MPa. The results of the experiment are shown in Figure 7.

3.2 Discussion of the influencing factors of gas desorption

The rate of gas desorption in 90 s, the amount of gas desorption in 180 s and the total amount of gas desorption in 480 min were analysed through 10 groups of experimental studies on gas desorption under different conditions. The

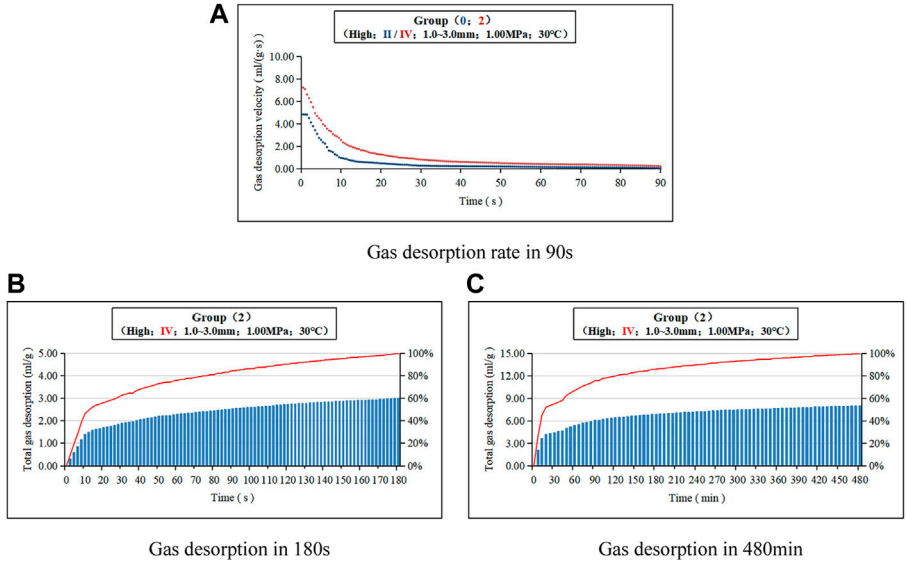

FIGURE 4
Gas desorption law diagram (Group 2).

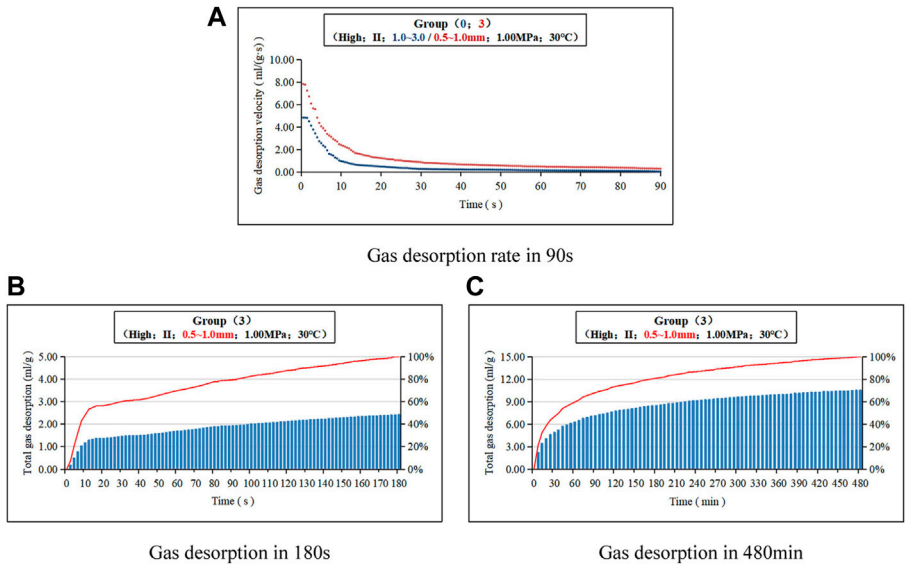

FIGURE 5
Gas desorption law diagram (Group 3).

function curve and correlation coefficient of the experimental results are shown in Table 5.

3.2.1 Influence of the metamorphism degree on gas desorption

Studies have shown that the effect of the degree of metamorphism on the gas desorption rate is mainly controlled by the pore and fracture system in the coal body (Li, 2011). The adsorption and desorption capacity of coal depends on the pore structure and specific surface area of coal.

Table 6 (Li and Si, 2004; Zhang et al., 2006; Tang and Wang, 2010) shows that with the increase in the degree of metamorphism, the micropores and small pores in the coal increase, the specific surface area increases, and the adsorption capacity increases (Zhang, 2006; Zhang, 2009).

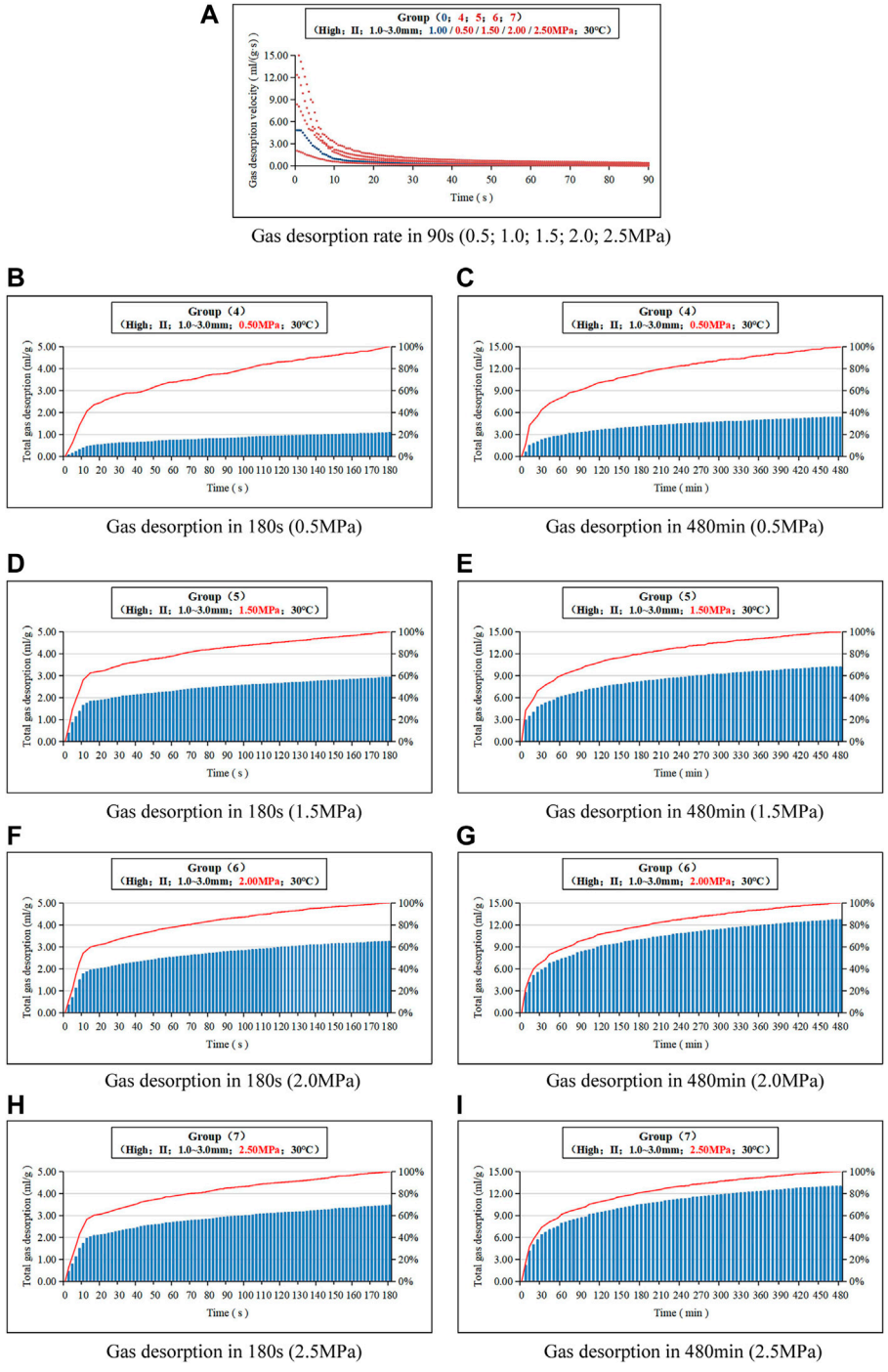

FIGURE 6
Gas desorption law diagram (Group 4,5,6,7).

1) According to Figure 3A, we find that as the degree of metamorphism increases, the initial gas desorption rate increases significantly. The initial gas desorption rate of lean coal is 1.91 times that of gas coal.

2) Comparing Figure 2B and Figure 3B, we can see that the difference in the gas desorption amount within 10 s is obvious. The gas desorption amount of meagre lean coal reaches more than 60%, while that of the gas coal is less than

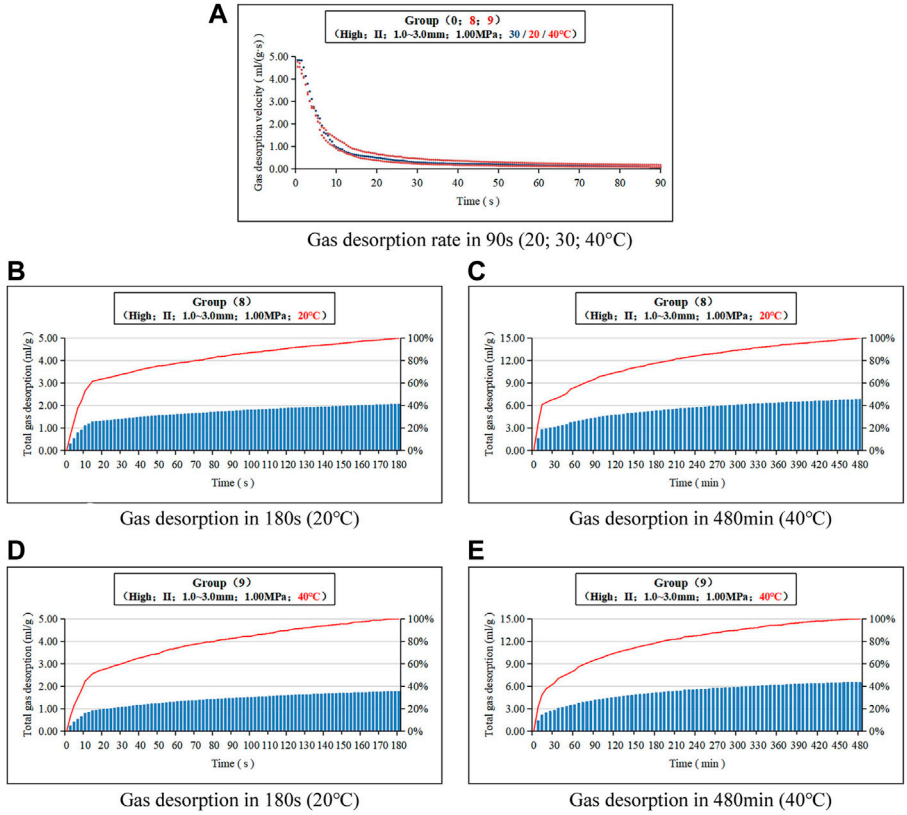

FIGURE 7
Influence law of temperature on gas desorption (Group 8,9).

TABLE 5 Gas desorption curve of characteristic.

Number	V_t		T_{180}		T_{480}	
	Fitting function	R^2	Fitting function	R^2	Fitting function	R^2
Group 0	$V_{t\text{-}0}$=9.360 $t^{-1.000}$	0.968	$T_{180\text{-}0}$=0.193ln(t) + 0.127	0.957	$T_{480\text{-}0}$=0.206ln(t) + 0.083	0.988
Group 1	$V_{t\text{-}1}$=4.809 $t^{-0.981}$	0.966	$T_{180\text{-}1}$=0.233·ln(t)$^-$0.162	0.938	$T_{480\text{-}1}$=0.225·ln(t) + 0.008	0.998
Group 2	$V_{t\text{-}2}$=14.513 $t^{-0.852}$	0.966	$T_{180\text{-}2}$=0.216·ln(t) + 0.021	0.993	$T_{480\text{-}2}$=0.185·ln(t) + 0.207	0.968
Group 3	$V_{t\text{-}3}$=12.779 $t^{-0.789}$	0.979	$T_{180\text{-}3}$=0.210·ln(t) + 0.016	0.968	$T_{480\text{-}3}$=0.211·ln(t) + 0.084	0.996
Group 4	$V_{t\text{-}4}$=5.942 $t^{-1.072}$	0.866	$T_{180\text{-}4}$=0.229·ln(t)$^-$0.085	0.984	$T_{480\text{-}4}$=0.224·ln(t) + 0.002	0.997
Group 5	$V_{t\text{-}5}$=13.926 $t^{-0.868}$	0.977	$T_{180\text{-}5}$=0.189·ln(t) + 0.141	0.969	$T_{480\text{-}5}$=0.204·ln(t) + 0.102	0.995
Group 6	$V_{t\text{-}6}$=16.645 $t^{-0.968}$	0.963	$T_{180\text{-}6}$=0.202·ln(t) + 0.093	0.977	$T_{480\text{-}6}$=0.212·ln(t) + 0.069	0.997
Group 7	$V_{t\text{-}7}$=22.340 $t^{-0.884}$	0.983	$T_{180\text{-}7}$=0.200·ln(t) + 0.090	0.980	$T_{480\text{-}7}$=0.213·ln(t) + 0.077	0.995
Group 8	$V_{t\text{-}8}$=8.412 $t^{-1.037}$	0.979	$T_{180\text{-}8}$=0.194·ln(t) + 0.116	0.975	$T_{480\text{-}8}$=0.210·ln(t) + 0.068	0.990
Group 9	$V_{t\text{-}9}$=7.686 $t^{-0.829}$	0.982	$T_{180\text{-}9}$=0.217·ln(t) + 0.006	0.994	$T_{480\text{-}9}$=0.221·ln(t) + 0.031	0.997

40%. With the increase in the degree of metamorphism, the initial (180 s) gas desorption capacity increases significantly: $T_{180\text{-}0}$ is 1.99 ml/g, $T_{180\text{-}1}$ is 0.95 ml/g, and the initial gas desorption capacity of lean coal is 2.09 times that of gas coal.

3) Comparing Figure 2C and Figure 3C, it can be seen that the initial gas desorption efficiencies of coals with different metamorphic degrees are higher. With the prolongation of desorption time, the desorption rate becomes slow, and the

TABLE 6 Relationship between metamorphism degree and coal pore development.

Metamorphism degree	Micropore, small hole		Medium hole, large hole	
	Development	Pore volume ratio	Development	Pore volume ratio
Low	No development	20% on average	Developing	46% on average
Medium	Less development	<50%	More development	38% on average
High	Developing	>50%	Less developed	<10%

total amount of desorption increases slowly. The total amount of gas desorption in 480 min is similar, approximately 6.0 ml/g.

4) In the early stage of gas desorption, the time required for the gas desorption volume of Group 1 to reach 80% is 122 s, which is much longer than Group 0 at 68 s. In the whole process of gas desorption, it took approximately 200 min for both groups to reach 80%. The analysis shows that the amount of gas desorption differs greatly in the early stage of gas desorption in coal with different metamorphic degrees, the pores and fissures in coal with high metamorphic degrees are well developed, and the gas adsorption and desorption capacity is strong.

3.2.2 Influence of the failure types on gas desorption

The desorption rate of coal gas is closely related to its damage degree. In the same mining area, the same coal seam, and the same location, the measurement of the initial gas release velocity (ΔP) of samples with different damage degrees and types shows that with the increase in the damage degree, the initial gas release velocity increases, that is, the gas desorption rate increases.

The pore-fracture system of tectonic coal is fully developed, and the rich internal surface area gives a strong gas adsorption capacity, but the low strength of the coal makes it easy to close microcracks under high pressure conditions and form "coal bricks", thus sealing a large amount of high-energy gas (Zhang and Zhang, 2005). Wang Chaojie et al. studied the pressure gradient on the coal surface and the gas expansion energy generated during tectonic coal desorption (Wang et al., 2021c), establishing the evolution law of key gas parameters during the initial desorption process.

1) According to Figure 4A, the initial gas desorption rate of Type IV coal is significantly higher than that of Type II, and $V_{0\text{-}2}$ is 7.22 ml/(gs). The initial rate of gas desorption from tectonic coal is 1.49 times that of primary structural coal; the difference in desorption rate is mainly in the first 30 s. With the extension of desorption time, the gas desorption rate of coal with different failure types tends to be equal.
2) Comparing Figures 2B,C and Figures 4B,C, the gas resolution of Type IV coal in the same mine and coal seam is significantly higher than that of Type II coal, and the more serious the damage of the coal body is, the larger the amount of gas desorption will be; the $T_{180\text{-}3}$ of Type IV coal is 3.01 ml/g, which is 1.51 times that of Type II coal, and the $T_{480\text{-}3}$ is 8.01 ml/g, which is 1.28 times that of Type II coal.
3) In the early stage of gas desorption, the time needed for the gas desorption of Group 2 to reach 80% was 77 s, which was almost the same as that of Group 0. However, in the whole process of gas desorption, it only takes 121 min for the desorption amount of Group 2 to reach 80%, which is far less than that of Group 0. This indicates that the initial gas desorption rate of Type IV coal is high, but the decay is faster, and the variation in gas desorption velocity in Type IV coal is greater per unit time. The gas desorption of tectonic coal can be divided into two different processes: first, a part of the methane adsorbed on the outer surface of coal and the surface of open large pores can communicate with the surrounding environment, and methane directly exchanges with the environment to produce desorption. Second, the other part of the adsorbed methane on the internal pore surface of coal must undergo a diffusion process to exchange with the environment and produce desorption. Surface adsorption and desorption can be completed instantaneously, while the diffusion process is relatively slow, so the desorption speed of structural coal is faster.

3.2.3 Influence of the particle size on gas desorption

There is a correlation between the coal failure type and the coal particle size on the gas desorption law. The experimental results show that the gas desorption rate is highly sensitive to the particle size of the coal sample. The larger the particle size is, the greater the distance of gas diffusion and flow, the greater the resistance, and the smaller the desorption rate and the desorption amount; the smaller the particle size is, the shorter the distance of gas diffusion and migration, and the larger the desorption rate and the desorption amount; and the effect of particle size on gas desorption has a limit value. When the limit particle size is reached, the desorption rate no longer changes with the particle size. Li et al. (2019) established a mathematical expression for the desorption index K_1, believing that the smaller the particle size of the drill cuttings is, the more significant the desorption performance.

TABLE 7 Correlation analysis table of influencing factors of gas desorption.

	R_R	R_E	R_I	R_T	R
Metamorphism degree	1.91	1.79	2.09	1.08	7.72
Failure type	1.50	1.13	1.51	1.28	3.28
Particle size	1.62	1.35	1.22	1.68	4.48
Pressure	2.44	1.15	1.67	1.72	8.06
Temperature	1.04	1.10	1.08	1.06	1.31

The analysis shows that in the case of the natural exposure of coal mining, among the factors affecting gas desorption, the order of significance is pressure > metamorphism > particle size > failure type > temperature.

1) According to Figure 5A, as the particle size decreases, the initial gas desorption rate increases: $V_{0\text{-}3}$ is 7.83 ml/(gs). The initial gas desorption rate of coal with particle sizes of 0.5–1.0 mm is 1.62 times that of coal with particle sizes of 1.0–3.0 mm.
2) Comparing Figure 2B and Figure 5B, there is little difference in the total amount of gas desorption in 180 s for coal with different particle sizes. The desorption capacity of small particle size coal is only 0.42 ml/g more than that of large particle size coal.
3) Comparing Figure 2C and Figure 5C, it can be seen that the gas desorption capacity of coal with a particle size of 0.5–1.0 mm in 480 min is significantly higher, which is 10.53 ml/g, 1.68 times higher than that of coal with a particle size of 1.0–3.0 mm.
4) The experimental results also show that the desorption amount of coals with different failure types is very different, even if the particle size is the same, that is, the initial gas desorption increase rate of Type II coal (primary structured coal) is significantly higher than that of Type IV coal (tectonic coal).

3.2.4 Influence of the pressure on gas desorption

The gas adsorption equilibrium pressure is an important factor affecting the gas desorption law. It not only characterizes the gas content in coal but also provides the energy required for gas desorption and diffusion. The gas desorption rate and desorption amount of the same coal sample increased with increasing gas adsorption equilibrium pressure in the same time period.

1) According to Figure 6A, with the increase in adsorption equilibrium pressure, the initial rate of gas desorption increases continuously. Pressure has a particularly significant effect on the gas desorption rate at the initial stage (within 10 s), and the desorption rate does not change much in 10–90 s.
2) Comparing Figure 2B and Figures 6B,D,F,H, it can be seen that with the increase in adsorption equilibrium pressure, the initial gas desorption amount increases continuously. The effect of pressure on the initial gas desorption rate and desorption amount is significant.
3) Comparing Figure 2C and Figures 6C,E,G,I, it can be seen that with the increase of adsorption equilibrium pressure, the total amount of gas desorption also increases, $T_{480\text{-}4}$ is 5.39 ml/g, $T_{480\text{-}0}$ is 6.28 ml/g, $T_{480\text{-}5}$ is 10.22 ml/g, $T_{480\text{-}6}$ is 12.69 ml/g, $T_{480\text{-}7}$ is 12.98 ml/g, and with the increase of pressure, the time for gas desorption to reach more than 80% is gradually shortened.
4) Furthermore, the gas desorption rate and desorption amount of Type IV coal (tectonic coal) increase faster with pressure. At the same time, with the increase in adsorption equilibrium pressure, the gas desorption rate of Type IV coal decays faster and tends to be stable after 10 s.
5) The effect of pressure on gas desorption is mainly to increase the ability of coal particles to adsorb gas. The increase in the gas concentration gradient in the coal changes the stress state of the coal particles, and the increase in pore stress mainly changes the shape of the coal particle pores, making the elastic deformation of coal significant and improving the gas desorption rate. The intuitive response is that as the pressure increases, the gas desorption rate of coal particles increases. The effect of pressure on gas desorption is obvious, regardless of the desorption amount, desorption rate, desorption efficiency and so on.

3.2.5 Influence of the temperature on gas desorption

Some studies suggest that with increasing temperature, the ability of coal to adsorb gas gradually decreases (Kim, 1977; Fails, 1996). However, Krooss et al. (2002) believed that when the gas adsorption equilibrium pressure was higher than a certain value, the gas adsorption isotherm curves of coal at different temperatures would appear to cross; when the gas adsorption equilibrium pressure was higher than the pressure at the cross point, with increasing temperature, the adsorption amount under the same pressure also increased. From the perspective of gas expansion energy, Li et al. (2022) found that with increasing desorption time, the degree of linear correlation between gas expansion energy, desorption rate and desorption amount decreased.

Gas adsorption by coal is an exothermic process, and gas desorption is an endothermic process. Temperature has a great influence on gas desorption. The higher the temperature is, the higher the ability of gas molecules to desorb from the pores and surface of coal, and the easier it is for gas to be desorbed from the coal body to become free gas. The amount of gas desorbed per unit time and the amount of gas desorbed cumulatively in the same time period are also larger. Therefore, temperature is an important factor affecting the law of coal gas desorption.

1) According to Figure 7A, the gas desorption rate does not change significantly, and the desorption rate of Type IV coal (tectonic coal) only slightly varies with temperature. In the initial stage (within 30 s), the gas desorption rate decays rapidly at 20°C, but the gas desorption rate decays slowly at 40°C.
2) Comparing Figures 2B,C and Figures 7B–E, the effect of temperature change on the total amount of gas desorption is almost the same, but its increment over time is different. Initial

amount of gas desorption followed the order T_{180} (20°C) > T_{180} (30°C) > T_{180} (40°C), while the total amount of gas desorption followed the order T_{480} (20°C) > T_{480} (40°C) > T_{480} (30°C). The analysis indicated that with increasing temperature, the gas content adsorbed in the coal body decreased correspondingly.

3.3 Tradeoff analysis of the influencing factors for gas desorption

Some scholars have performed a considerable amount of research on the influencing factors of gas desorption, and they have differing opinions on which is the single dominating factor. However, there are few studies on the weight analysis of each factor. Structural deformation has a very important effect on the particle size and adsorption/desorption properties of coal, and deformation can promote gas desorption, which increases as the deformation increases (Li et al., 2022). Through regression analysis, some scholars believe that the influence sensitivity order of gas desorption is pressure > temperature > particle size > moisture > moulding pressure (Wang et al., 2019).

In this paper, the coal property factors (metamorphic degree, failure type, particle size) and environmental factors (pressure, temperature) are experimentally studied. To weigh the sensitivity of each factor, the *R*-value method is proposed, which combines four indicators: gas desorption rate, gas desorption efficiency, initial gas desorption volume and total gas desorption.

$$R = R_R \cdot R_E \cdot R_I \cdot R_T$$

R_R----The degree of influence on the gas desorption rate.

$$R_R = \overline{Max(V_n, V_0)/Min(V_n, V_0)}$$

R_E----The degree of influence on the gas desorption efficiency.

$$R_E = \overline{Max(E_n, E_0)/Min(E_n, E_0)}$$

R_I----The degree of influence on the initial gas desorption amount.

$$R_I = \overline{Max(T_{180-n}, T_{180-0})/Min(T_{180-n}, T_{180-0})}$$

R_T----The degree of influence on the total gas desorption.

$$R_T = \overline{Max(T_{480-n}, T_{480-0})/Min(T_{480-n}, T_{480-0})}$$

The results of the correlation analysis are shown in Table 7.

4 Conclusion

1) Under different experimental conditions, there is a monotonically decreasing power function relationship between the initial gas desorption rate and time, that is, V_t=a t - b (a, b are regression constants). There is a monotonically increasing logarithmic function relationship between the gas desorption amount and time, namely, T_t=$a$ln(t) + b (a, b are regression constants), and the curve has a limit value.
2) In the initial stage of gas desorption (0–180 s), the gas desorption amount is very large in 0–10 s, and then the gas desorption amount increases slowly, while the desorption rate is almost uniform. From the perspective of the entire gas desorption process, the gas desorption amount increases rapidly in 0–30 min, and the gradient of the increase in gas desorption amount decreases in 30–180 min; at 180 min, the gas desorption amount is approximately 80% of the total desorption. When the desorption time is longer than 180 min, the gas desorption amount basically stablizes.
3) The weight of the following factors affecting gas resolution is listed as follows: pressure > degree of metamorphism > particle size > type of failure > temperature. If the coal is subjected to strong structural extrusion and shearing during the formation process, the coal is broken and pulverized, and abundant micropores and inner surfaces are formed. These microcracks easily accumulate free gas. However, coal with high pressure, serious damage, and the poor mechanical strength of powdery or mylonitic coal is beneficial to the rapid desorption and release of gas within 0–10 s in the initial stage of gas desorption, and the risk of gas outburst is high.

Data availability statement

The datasets presented in this study can be found in online repositories. The names of the repository/repositories and accession numbers can be found in the article/Supplementary Material.

Author contributions

All authors listed have made a substantial, direct, and intellectual contribution to the work and approved it for publication. XH: Experiment, Data curation, Formal analysis, Writing—original draft. H-qC: Conceptulization, Funding acquisition, Supervision. HZ: Conceptualization, Experiment. Z-zW: Supervision. Z-hW: Data curation. G-sS: Modify, Correction.

Funding

This work was supported by the National Scientific Foundation of China (41372160) and plan support for key scientific research projects of colleges and universities in Henan Province (20B620001).

Conflict of interest

The authors declare that the research was conducted in the absence of any commercial or financial relationships that could be construed as a potential conflict of interest.

Publisher's note

References

Chen, X. J., Cheng, Y. P., He, T., and Li, X. (2013). Water injection impact on gas diffusion characteristic of coal. *J. Min. Saf. Eng.* 03, 443–448. doi:10.13210/j.cst.2013.03.024

Fails, T. G. (1996). Coalbed methane potential of some Variscan foredeep basins. *Geol. Soc. Lond. Spec. Publ.* 109 (1), 13–26. doi:10.1144/gsl.sp.1996.109.01.02

Fu, X. W. J., and Yang, T. H. (2008). Gas irradiation feature of tectonic coal. *J. China coal Soc.* 07, 775–779. doi:10.3321/j.issn:0253-9993.2008.07.011

Grażyna, C. S., and Kinga, B. (1998). The effect of coal metamorphism on methane desorption. *Fuel (Lond).* 6, 645–648. doi:10.1016/S0016-2361(97)00177-4

Hao, J. S., Yuan, C. F., and Zhang, Z. X. (2000). The tectonic coal and its effects on coal and gas outburst. *J. Jiaozuo Inst. Technol.* 06, 403–406. doi:10.3969/j.issn.1673-9787.2000.06.001

Jia, D. X., and Chen, X. J. (2009). Test and research on gas desorption law of intensive failed coal. *Coal Sci. Technol.* 06, 64–66. doi:10.13199/j.cst.2009.06.69.jiadx.025

Jiang, B., Qin, Y., Ju, Y. W., Wang, J. L., and Li, M. (2009). The coupling mechanism of the evolution of chemical structure with the characteristics of gas of tectonic coals. *Earth Sci. Front.* 02, 262–271. doi:10.3321/j.issn:1005-2321.2009.02.020

Kim, A. G. (1977). *Estimating methane content of bituminous coalbeds from adsorption data*. Pittsburgh, PA: United States Department of the Interior, Bureau of Mines, 8245.

Krooss, B. M., Bergen, F. V., Gensterblum, Y., Siemons, N., Pagnier, H. J. M., and David, P. (2002). High-pressure methane and carbon dioxide adsorption on dry and moisture-equilibrated Pennsylvanian coals. *Int. J. Coal Geol.* 51 (2), 69–92. doi:10.1016/S0166-5162(02)00078-2

Li, C. W., and Lei, D. J. (2012). Experimental research of the influence of static electric field on the characteristics of coal gas emission. *J. China Coal Soc.* 06, 28–30. doi:10.13225/j.cnki.jccs.2012.06.019

Li, C. W., Xue, H. L., Hu, P., Guan, C., and Liu, W. B. (2018). Effect of stress on the diffusion kinetics of methane during gas desorption in coal matrix under different equilibrium pressures. *J. Geophys. Eng.* 15 (3), 841–851. doi:10.1088/1742-2140/aaa8ad

Li, L., Sun, Z. G., Wang, F. K., and Zhang, K. Z. (2019). Study on the gas desorption law and indicator influencing factors of fixed-size coal samples. *Sci. Rep.* 9 (1), 17134. doi:10.1038/s41598-019-53211-4

Li, S. G., Bai, Y., Lin, H. F., Yan, M., Long, H., and Guo, D. D. (2021). Effect of N2/CO2 injection pressure on CH4 desorption in gas-bearing coal rock. *Nat. Gas. Ind.* 03, 80–89. doi:10.3787/j.issn.1000-0976.2021.03.009

Li, X. S., Ju, Y. W., Song, Y., Yan, Z. F., and Li, Q. G. (2022a). Particle size and internal structure of deformed coal: Microstructure and adsorption/desorption characteristics of CO2 and CH4. *Front. Earth Sci. (Lausanne).* 10, 876196. doi:10.3389/feart.2022.876196

Li, X. W., Wang, C. J., Chen, Y. J., and Li, H. N. (2022b). Influence of temperature on gas desorption characterization in the whole process from coals and its application analysis on outburst risk prediction. *Fuel* 321, 124021. doi:10.1016/J.FUEL.2022.124021

Li, X. Y., and Si, S. L. (2004). Coalbed gas desorption characteristics of coal reservoir in China. *Coal Geol. Explor.* 03, 27–29. doi:10.3969/j.issn.1001-1986.2004.03.009

Li, Y. B. (2011). Experimental study on initial stage features of gas desorption of tectonic coal. *Master's thesis*. China: Henan Polytechnic University.

Liu, Y. W. (2011). Study on gas emission rules, mechanism and dynamic model from coal particle. *Doctoral dissertation*. China: Henan Polytechnic University.

Ministry of coal industry of the people's Republic of China (1997). *Method for the determination of methane sorption on coal (high pressure volumetric method)*. China: China Standard Publishing House.

Tang, D. Z., and Wang, W. (2010). *Control mechanism of coal reservoir physical properties and prediction method of favorable reservoi*. Beijing: Science Press.

Tu, Q. Y., Cheng, Y. P., Xue, S., and Ren, T. (2022). Effect of particle size on gas energy release for tectonic coal during outburst process. *Fuel* 307, 121888. doi:10.1016/J.FUEL.2021.121888

Wang, C. J., Li, X. W., Xu, C. H., Chen, Y. J., Tang, Z. X., Zhang, C., et al. (2021a). Dynamic characterization during gas initial desorption of coal particles and its influence on the initiation of coal and gas outbursts. *Processes* 9 (7), 1101. doi:10.3390/PR9071101

Wang, C. J., Yang, S. Q., Li, J. H., Li, X. W., and Jiang, C. L. (2018a). Influence of coal moisture on initial gas desorption and gas-release energy characteristics. *Fuel* 232, 351–361. doi:10.1016/j.fuel.2018.06.006

Wang, F. K., Liang, Y. P., Li, X. D., Li, L., Li, J. G., and Chen, Y. L. (2019). Orthogonal experimental study on multifactor conditions for gas desorption in coal. *Adv. Civ. Eng.* 2019, 1–12. doi:10.1155/2019/3028721

Wang, Y. L. (2018). Experimental study on gas desorption and initial velocity of gas dispersion in low permeability and outburst coal seam in Guizhou. *Master's thesis*. China: Guizhou University.

Wang, Z. Y., Cheng, Y. P., Wang, L., Zhou, H. X., He, X. X., Yi, M. H., et al. (2020). Characterization of pore structure and the gas diffusion properties of tectonic and intact coal: Implications for lost gas calculation. *Process Saf. Environ. Prot.* 135, 12–21. doi:10.1016/j.psep.2019.12.020

Wang, Z. Z., Fu, X. H., Deng, Z., and Pan, J. N. (2021b). Investigation of adsorption-desorption, induced strains and permeability evolution during N2-ECBM recovery. *Nat. Resour. Res.* 30 (5), 3717–3734. doi:10.1007/s11053-021-09884-8

Wang, Z. Z., Fu, X. H., Hao, M., Li, G. F., Pan, J. N., Niu, Q. H., et al. (2021c). Experimental insights into the adsorption-desorption of CH4/N2 and induced strain for medium-rank coals. *J. Petroleum Sci. Eng.* 204, 108705. doi:10.1016/j.petrol.2021.108705

Wang, Z. Z., Pan, J. N., Hou, Q. L., Niu, Q. H., Tian, J. J., Wang, H. C., et al. (2018b). Changes in the anisotropic permeability of low-rank coal under varying effective stress in Fukang mining area, China. *Fuel* 234, 1481–1497. doi:10.1016/j.fuel.2018.08.013

Wang, Z. Z., Pan, J. N., Hou, Q. L., Yu, B. S., Li, M., and Niu, Q. H. (2018c). Anisotropic characteristics of low-rank coal fractures in the Fukang mining area, China. *Fuel* 211, 182–193. doi:10.1016/j.fuel.2017.09.067

Xiao, Z. G. (2010). Experimental study and application of inhibitory effect on gas desorption of coal seam injected with water. *Doctoral dissertation*. China: Henan Polytechnic University.

Xie, X. X. (2014). Experimental study on gas loss quantity of tecnonic coal. *Master's thesis*. China: Henan Polytechnic University.

Xu, K., Liu, M. J., and Liu, Y. W. (2003). Study of the adsorption and desorption (surface modification) in alternative electronic field. *Coal Geol. Explor.* 03, 23–26. doi:10.1007/s11769-003-0003-x

Zhang, G. H. (2011). Experimental study of external solution invasion impact on gas desorption about coal with gas. *Doctoral dissertation*. China: Liaoning Technical University.

Zhang, Q. (2018). Influence of metamorphic grade on gas adsorption/desorption characteristics of outburst coal. *Master's thesis*. China: China University of Mining and Technology.

Zhang, X. M., Han, B. S., and Li, J. W. (2006). CBM storage character of lignite and gas content estimate method. *Coal Geol. Explor.* 34, 28–30. doi:10.3969/j.issn.1001-1986.2006.03.008

Zhang, Y. G. (2006). Evolution of deformed coal and process of coal mechanochemistry. *Doctoral dissertation*. China: Taiyuan university of technology.

Zhang, Z. M. (2009). *Gas Geology*. Xuzhou: China University of Mining and Technology Press, 167–284.

Zhang, Z. M., and Zhang, Y. G. (2005). *Gas geological law and gas prediction[M]*. Beijing: China Coal Industry Publishing House, 23–31.

Zhao, F. J., and Deng, Q. G. (2022). Effect of electromagnetic field on coal seepage characteristics. *Arab. J. Geosci.* 15 (9), 806. doi:10.1007/S12517-022-09997-1

frontiers | Frontiers in Earth Science

TYPE Original Research
PUBLISHED 16 January 2023
DOI 10.3389/feart.2022.1076076

OPEN ACCESS

EDITED BY
Mingjun Zou,
North China University of Water Resources and Electric Power, China

REVIEWED BY
Xin Li,
Xinjiang University, China
Haihai Hou,
Liaoning Technical University, China
Niu Qinghe,
Shijiazhuang Tiedao University, China

*CORRESPONDENCE
Meng Li,
limeng@hpu.edu.cn

SPECIALTY SECTION
This article was submitted to Economic Geology, a section of the journal Frontiers in Earth Science

RECEIVED 21 October 2022
ACCEPTED 04 November 2022
PUBLISHED 16 January 2023

CITATION
Li M, Li M, Pan J, Gao D and Cao Y (2023), Coalbed methane accumulation, in-situ stress, and permeability of coal reservoirs in a complex structural region (Fukang area) of the southern Junggar Basin, China. *Front. Earth Sci.* 10:1076076. doi: 10.3389/feart.2022.1076076

Coalbed methane accumulation, in-situ stress, and permeability of coal reservoirs in a complex structural region (Fukang area) of the southern Junggar Basin, China

Meng Li[1,2]*, Mingjie Li[1,2], Jienan Pan[1,2], Di Gao[1,2] and Yunxing Cao[1,2]

[1]School of Resources and Environment, Henan Polytechnic University, Jiaozuo, China, [2]Collaborative Innovation Center of Coalbed Methane and Shale Gas for Central Plains Economic Region, Henan, Jiaozuo, China

The enrichment of coalbed methane (CBM), *in-situ* stress field, and permeability are three key factors that are decisive to effective CBM exploration. The southern Junggar Basin is the third large CBM basin in China but is also known for the occurrence of complex geological structures. In this study, we take the Fukang area of the southern Junggar Basin as an example, coalbed methane accumulation and permeability, and their geological controls were analyzed based on the determination of geological structures, *in-situ* stress, gas content, permeability, hydrology and coal properties. The results indicate that gas contents of the Fukang coal reservoirs are controlled by structural framework and burial depth, and high-to-ultra-high thickness of coals has a slightly positive effect on gas contents. Perennial water flow (e.g., the Baiyanghe River) favors gas accumulation by forming a hydraulic stagnant zone in deep reservoirs, but can also draw down gas contents by persistent transportation of dissolved gases to ground surfaces. Widely developed burnt rocks and sufficient groundwater recharge make microbial gases an important gas source in addition to thermogenic gases. The *in-situ* stress field of the Fukang area (700–1,500 m) is dominated by a normal stress regime, characterized by vertical stress > maximum horizontal stress > minor horizontal stress. Stress ratios, including lateral stress coefficient, natural stress ratios, and horizontal principal stress ratio are all included in the stress envelopes of China. Permeability in the Fukang area is prominently partitioned into two distinct groups, one group of low permeability (0.001–0.350 mD) and the other group of high permeability (0.988–16.640 mD). The low group of permeability is significantly formulated by depth-dependent stress variations, and the high group of permeability is controlled by the relatively high structural curvatures in the core parts of synclines and the distance to the syncline core. Meanwhile, coal deformation and varying dip angles intensify the heterogeneity and anisotropy of permeability in the Fukang area. These findings will promote the CBM recovery process in China and improve our understanding of the

interaction between geological conditions and reservoir parameters and in complex structural regions.

KEYWORDS

gas content, permeability, *in-situ* stress, burnt rocks, hydrogeology, structural curvature, coal deformation

1 Introduction

Recovery of coalbed methane (CBM) from coal seams can not only benefit mining safety, reduce greenhouse gas emissions, and also increase clean energy supply (Karacan et al., 2011; Moore, 2012). In the Junggar Basin, the CBM resources have been estimated at 3.83 trillion cubic meters, which is the third largest CBM basin in China after the Qinshui Basin and Ordos Basin (Fu et al., 2016; Ou et al., 2018; Yu and Wang, 2020). Exploration of CBM in the Junggar Basin has made significant progress in recent years, among which the Fukang area of the southern Junggar Basin is one of the most successful and typical representatives. The previous investigation demonstrated that coal seam gas-in-place (GIP) resources in the Fukang area are about 682×10^8 m^3, which account for more than twenty percent of the known CBM resources in the southern Junggar Basin (Yang et al., 2005; Ou et al., 2018). The highest daily gas production of vertical wells in China, 27,896 m^3, was archived and gas production has reached 100 million cubic meters annually in this area (Cao et al., 2012; Zhang B et al., 2021). However, before the massive CBM development of this area, coal mining safety issues once seriously threatened coal mining activities in this area because of the coal-and-gas-outburst risks. About 83 workers were killed in the coal-and-gas-outburst accident at the Qimei No.2 mine in 2005 (Yin, 2009), and among the 29 coal mines in the Fukang area, 13 of them are outburst-prone coal mines (Figure 1). Despite the abundant CBM resources, severe coal mining safety situation, and active CBM exploration activities in the Fukang area, complex geological conditions, like, complicated tectonic structures, varying *in-situ* stress, large dip angle, occurrence of deformed coals and widely-developed burnt rocks all make this area a special CBM development case and has aroused great interests among researchers. Understanding how these factors control gas accumulation and permeability, which are critical to CBM exploration and development, is urgent to be solved.

Sedimentology, organic geochemistry, and petroleum and gas potential of Jurassic coal measures in the Junggar Basin, NW China were firstly investigated by Graham et al. (1990), Hendrix et al. (1992) and Chen et al. (1998). Recently, diverse databases have been reported on the geology and reservoir properties of coal reservoirs in the complex structural regions of the southern Junggar Basin. In terms of gas enrichment and origin, Fu et al. (2016), Ou et al. (2018), and Yu and Wang (2020) evaluated the CBM potential of the southern Junggar Basin. Zhi et al. (2013), Fu et al. (2019), Fu et al. (2021) and Wang et al. (2022) investigated the origin and distribution of coalbed gas in the Jurassic coal reservoirs from different parts of the southern Junggar Basin by isotopic and compositional analysis. Several enrichment patterns were further proposed by Li et al. (2018) and Hou et al. (2021). In the aspect of coal properties, Wang et al. (2018) and Zhang T et al. (2021) studied the permeability anisotropy of high-dipping coals from the southern Junggar Basin based on laboratory experiments and numerical simulations. Li et al. (2019) and Fu et al. (2020) reported several datasets of *in-situ* stress from the eastern part of the southern Junggar Basin and discussed vertical permeability trends. Zhou et al. (2016) and Li et al. (2017) conducted experimental studies on the pore structure characteristics of coals in the southern Junggar Basin. Meanwhile, Kang et al. (2020, 2022) studied the in-seam variation of permeability and coal structures through analysis of geophysical Logging in the western Fukang area, southern Junggar Basin.

Although significant contributions have been made by previous researchers, these published studies were mostly experimental research or investigations based on unilateral production data, and important issues concerning gas accumulation and permeability, and their geological controls from tectonic structures, *in-situ* stress, hydrology, burnt rocks, and coal deformation in the complex structural region are thus far poorly understood due to a lack of sufficient data. In this study, we take the Fukang area of the southern Junggar Basin as an example, 55 datasets of field-measured gas contents, 141 datasets of permeability by injection/fall-off well tests, eight datasets of *in-situ* stress by multi-cycle hydraulic fracturing tests, 11 datasets of gas composition were determined, combined with observation and statistics of tectonic structures, fractures/macro-fractures, burnt rocks, coal macerals, and hydrological conditions, we hope to address important issues mentioned above, and further the understanding of gas accumulation and heterogeneity of permeability of the steep-dipping coals in complex structural regions. This work will contribute to the CBM exploration of the southern Junggar Basin, northwestern China, and other CBM basins with complex geological structures.

2 Geological setting

2.1 Tectonic background

The Fukang area is located in the eastern part of the southern Junggar Basin, with an East-West extension of

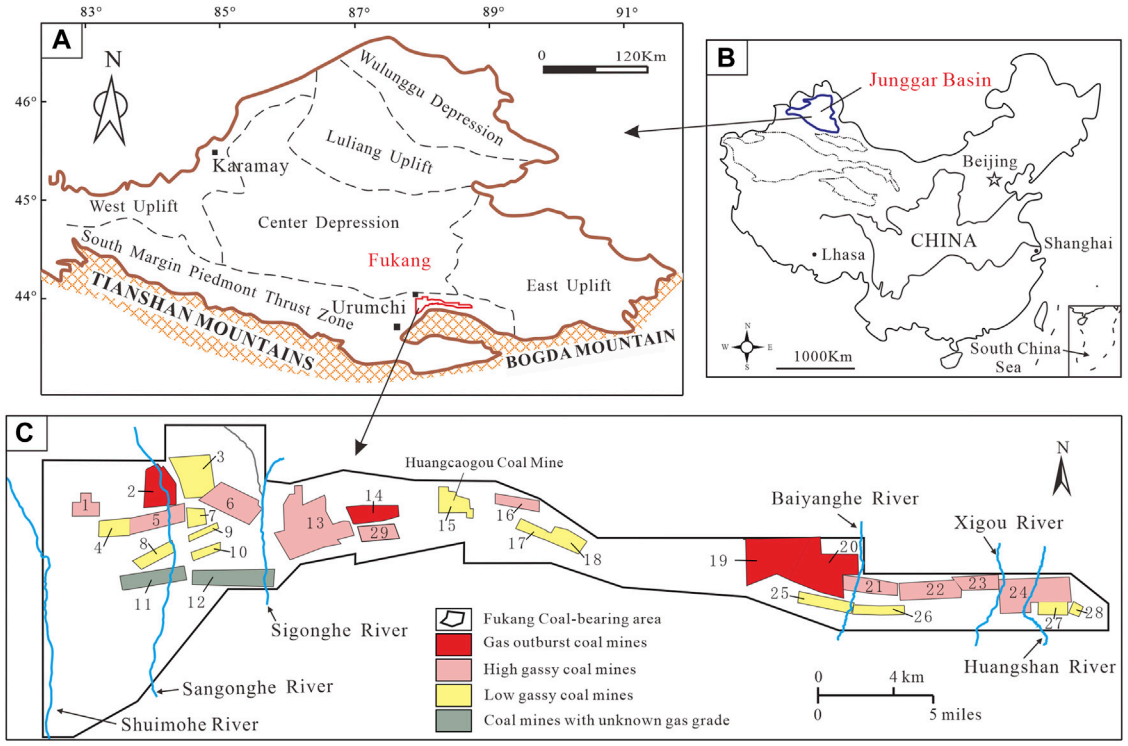

FIGURE 1
(A)-Geographical location of the Junggar Basin. China. **(B)**-Tectonic units of the southern Junggar Basin and location of the Fukang area. **(C)**-Distribution of major coal mines and its potential of coal-and-gas outburst in the Fukang area. (1-Mopangou mine, 2- Qimei No. 2 mine, 3-Dingjiawan mine, 4-Gangou mine, 5-Xinshiji mine, 6-Qimei No. 1 mine, 7-Taipingtan mine, 8-Guangyuan mine, 9-Liuyun mine, 10-Sangongjianjiang mine, 11-Tianchi No. 1 mine, 12-Tianchi No. 3 mine, 13-Wugongmine, 14-Xiaohuangshanmine, 15-Huangcaogou mine, 16-Jinlong mine, 17-Xinlong mine, 18-Kanglong mine, 19-Shizhuanggou mine, 20-Quanshuigoumine, 21-Dahuangshan No. 3 mine, 22-Xigou No. 1 mine, 23-Xigou No. 2 mine, 24-Dahuangshan No. 1 mine, 25-Jintai No. 1 mine, 26-Jintai No. 2 mine, 27-Dongfengfusheng mine, 28-Dahuangshan mine, 29-Choumeigou mine).

57 km and a North-South extension of 3–15 km (Figure 1). The total coal-bearing area is approximately 310 km^2. The Fukang area is tectonically situated in the eastern portion of the south margin piedmont thrust zone of the Junggar Basin (also known as North Bogda Mountain Thrust Zone; Hu et al., 2010; Wu, 1989), and is characterized by a series of compressional synclines and anticlines sandwiched by the two approximately parallel boundary faults, including the Fukang Reverse Fault to the north and the Yaomoshan Reverse Fault to the south. Abundant secondary reverse faults that strike south and southeast are present in these folds and are cut by a series of strike-slip faults (Figure 2; Yang and Tian, 2011; Yin, 2009).

Fault and fold intensity generally increase westward, with the most intense folds and faults occurring at the central portion of the Fukang area, that is, the arcuate structural zone. Compressional thrust from the south by the Bogda Mountain has resulted in large formation dipping angles in the Fukang area, averaging greater than 40°. Coal-bearing strata in the north limbs of these synclines dip towards the south or southeast with an angle of 20°–55°, whereas for strata in the south limbs, the dip is generally 30°–85°NW, or even reverses (Figure 2).

2.2 Coal-bearing sequences and coal seams

Coal-bearing sequences were deposited along the southern Junggar Basin due to tectonic extension and subsidence during the Early and Middle Jurassic, when warm and humid climates were developed (Graham et al., 1990; Carroll et al., 2010; Hou et al., 2022a). The Lower and Middle Jurassic coal-bearing sequences of the southern Junggar Basin have a total thickness of about 2000 m (~6,600 ft). In the Fukang area, coal measures consist of the Lower Jurassic Badaowan Formation and Sangonghe Formation, and the overlying Xishanyao Formation of the Middle Jurassic (Figure 3). The

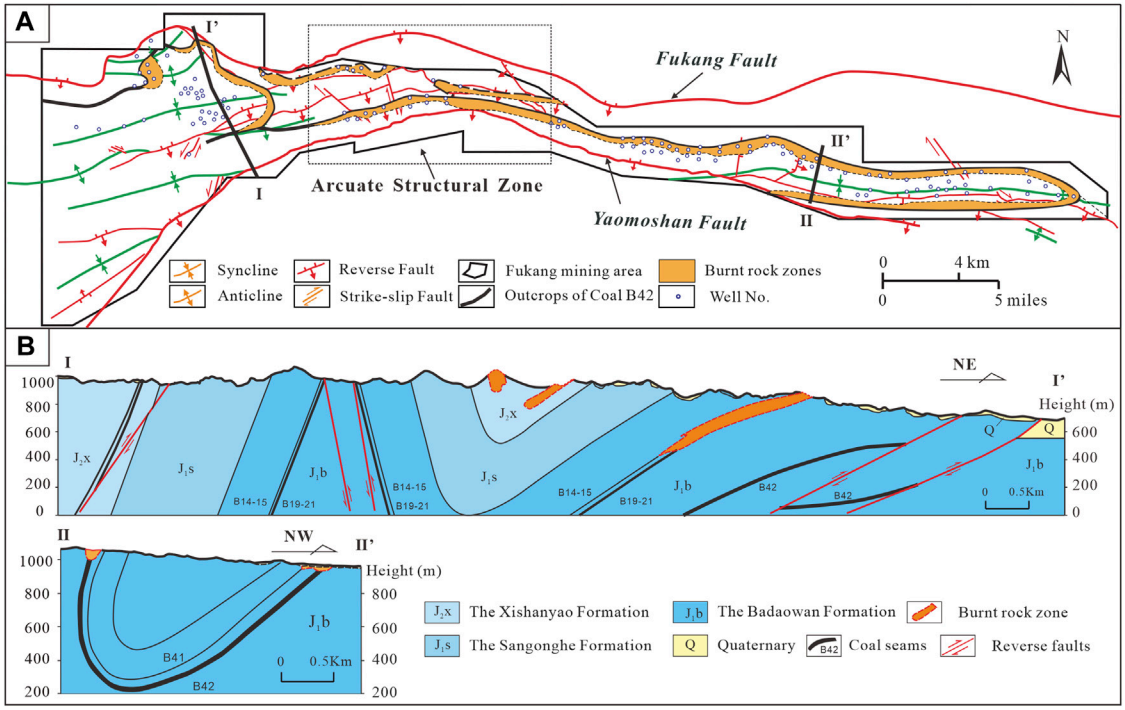

FIGURE 2
Structure outline map **(A)** and two cross-sections **(B)** of the Fukang area showing the occurrences of major faults, folds and coal seams, and distribution of burnt rock zones.

Badaowan Formation is characterized by thick coal seams interbedded with coarse-grained clastic rocks, which were deposited in fluvial deltaic and lacustrine environments (Hendrix et al., 1992; Hou et al., 2020). The younger Sangonghe Formation is typically composed of mudstones, siltstones, medium-to-coarse sandstones, and conglomerates, deposited on the alluvial and flood plains. The Xishanyao Formation consists of sandstones, siltstones, mudstones, and thick coal seams, which are of fluvial-deltaic origin (Hendrix et al., 1992; Hou et al., 2022b).

The Badaowan and Xishanyao formations are the major coal-bearing strata in the study area. Up to 44 coal seams, namely, Nos. B44 to B1, from bottom to top, occur in the Badaowan Formation. The Xishanyao Formation includes 45 coal seams, namely, Nos. X45 to X1 from bottom to top. Due to differential erosion, the Xishanyao Formation is only residual to the west of the Sigonghe River in the study area. Considering the stability and depth of coal as well as coal reservoir properties, gas exploration, and production, by now, were dominantly targeted in the Badaowan Formation in the Fukang area.

Due to the widespread outcropping of coal seams and extremely hot and dry weather of northwestern China, spontaneous combustion of coals occurred frequently in the shallow part of the Fukang area, which led to the formation of coke, and hard, tight, porous burnt rocks which constitute the burnt rock zones in the shallow subsurface area (Figure 4A). Burnt rock zones were frequently developed in the Fukang area and have a strong ability for water storage. In the west part, burnt rock zones are distributed in the limb portion of the Fukang Syncline and the axis portion of the South Fukang Anticline with a width of 30–120 m and a depth of 50–250 m. In the east part, burnt rock zones occur along the north coal outcrops with a width of 30–170 m and with a depth of 250–590 m (Figures 2, 5, 6).

2.3 Characteristics of coal reservoirs

The major coal seams of the Badaowan Formation for coalbed methane exploration are Nos. B14-B15, B19-B21, B39, B41, B42, B43, and B44 coals, of which No. B42 coal is the most stable and continuous seam and has been given priority for fracturing and recovery (Figure 3). But all these major seams are thick (3.5–8.0 m) to ultra-thick (greater than 8 m) coals, with an average accumulated thickness of 76.76m, and are widespread in the entire study area. Nos. B14-15, B19-21, B42, and B44 coal seams are ultra-thick coal and have average thicknesses of 19.48, 8.22, 16.54, and 16.33 m respectively. Nos. B39, B41, and B43 coals are thick coal seams, with an average thickness of 5.60, 5.18, and 5.41 m respectively. The thickness of the No.

10.3389/feart.2022.1076076

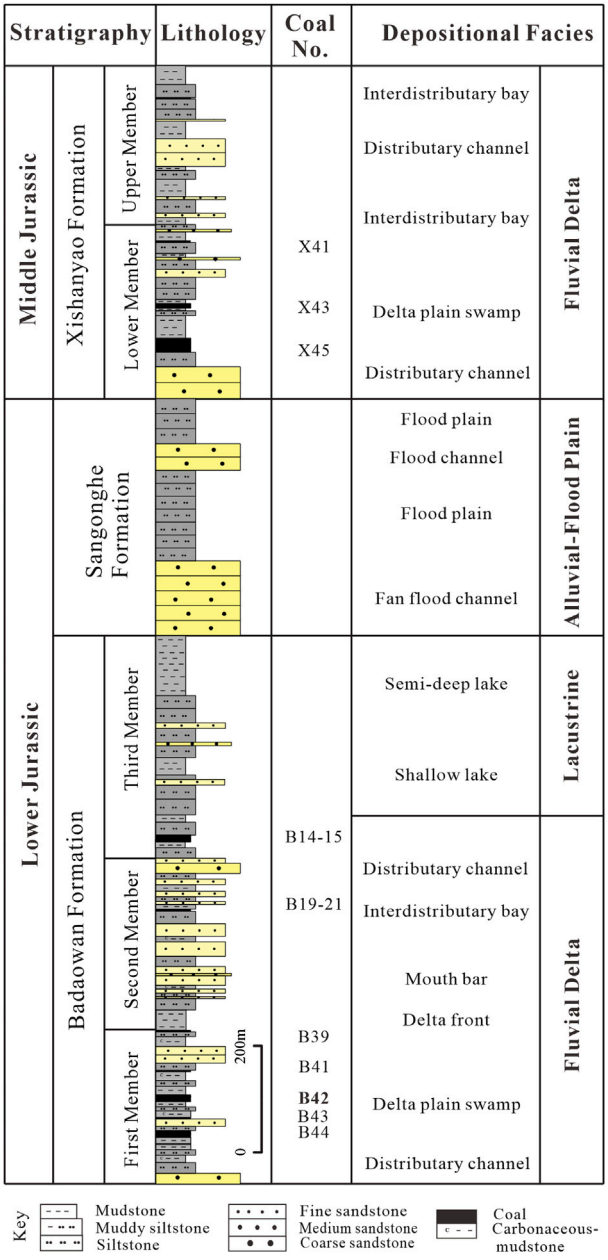

FIGURE 3
Stratigraphic column of the Lower-Middle Jurassic coal-bearing sequences in the Fukang area, southern Junggar Basin, China.

B42 coal ranges between 3.5 and 51.0 m, with an average thickness of 18.5 m. A prominent increasing trend of coal thickness of Coal B42 is recognized (from less than 6.0 to 51.0 m), with coals thicker than 30 m (depocenter) situated in the west part of the study area (Figure 5). Meanwhile, economic coals of the Xishanyao Formation include Nos. X41, X43, and X45 coals with thicknesses averaging 6.74, 18.00, and 33.24 m respectively.

Taking coal No. B42 and X45 as examples, burial depths of coal reservoirs of the Badaowan and Xishanyao Formations were illustrated in Figure 5B and Figure 6B. The burial depth of the Badaowan Formation ranges from zero to about 2000 m (0–6,562 ft) and generally increases towards the south and west, and that of the Xishanyao Formation ranges from zero to about 1000 m. Both burial depths of these two coal measures reach the maximum at the syncline axis portion.

The rank of coals in the Fukang area is dominated by high-volatile C-D bituminous with vitrinite reflectance (Ro) ranging from 0.54% to 0.72%. The macro-lithotype is represented by semi-bright and bright coals. Coal macerals are dominantly composed of vitrinite (ranging from 51.70% to 96.03%) and inertinite (ranging from 0.39% to 45.20%). Exinite is rare and shows a range from 0.1% to 4.94%. The inorganic components of coals consist of carbonate minerals, clay minerals, and pyrites (Supplementary Table S1).

3 Samples and methods

A series of coal cores and blocks were obtained from CBM exploration boreholes as well as underground coal mines in the Fukang area, southern Junggar Basin. Observation of tectonic structures, burnt rocks, fractures, coal deformation, and determination of *in-situ* stress, gas content, and permeability were conducted in the field, while coal composition, vitrinite reflectance, and coalbed gas composition were determined based on collected samples in the laboratory. Vitrinite reflectance measurements were made using a Zeiss microscope with a ×40 oil immersion objective by the national standard of 'Method of determining microscopically the reflectance of vitrinite in coal' (GB/T 6948-2008). Maceral analyses of the samples were made using a point counter by the Chinese National Standard of 'Determination of maceral group composition and minerals in coal' (GB/T 8899-2013). The minimum number of points counted is 500 and the amounts of organic and mineral components determined from point-counting are given as volume percent. Gas contents were determined using the 'direct method', according to the Chinese National Standard of 'Method of determining coalbed gas content' (GB/T 19559-2008). A total of 11 gas samples from field CBM wells in the Fukang area were collected directly from the wellhead. All these gas samples were quantified volumetrically and analyzed for gas composition (CH_4, CO_2, N_2, C_2H_6, and longer-chain hydrocarbons) based on the Chinese National Standard of 'Analysis of natural gas composition-gas chromatography' (GB/T 13610-2014).

The injection/fall-off well test and *in-situ* stress measurements were conducted for the determination of reservoir properties after well completion and before production. The injection/fall-off well test in this study was performed according to the Chinese National Standard of

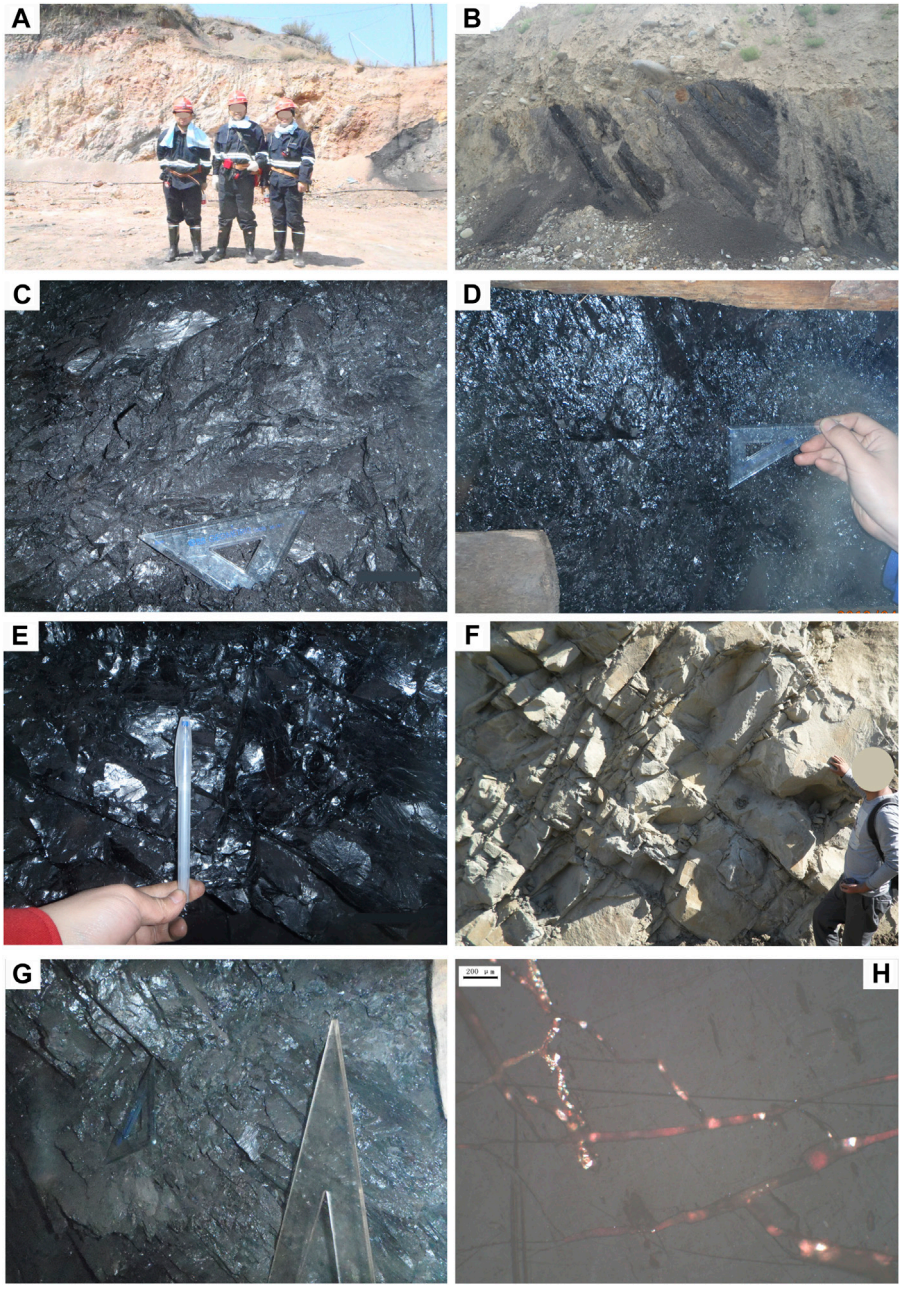

FIGURE 4
Tectonically deformed coals, coal fractures and coal macerals in the Fukang area. **(A)**-Burnt rocks in the Qimei No.1 coal mine. **(B)**-Coal seam outcrops in the western Fukang area. **(C)**-Strong-brittle cataclastic coal in the Huangcaogou mine. **(D)**-Strong-ductile granulated coal in the Wugong mine. **(E,G)**-High-frequency fractures developed in coals from the Jintai No.1 mine **(E)** and Sangongjianjiang mine **(G)**. **(F)**-Well-developed macrofractures at outcrops from Qimei No. 1 mine. **(H)**- Interconnected fractures under microscope of coals from the Qimei No.2 mine.).

'The method of injection/falloff well test for coalbed methane well' (GB/T 24504-2009). Through the injection/fall-off well test process, reservoir parameters including reservoir pressure, permeability, and geothermal status were recorded and calculated. To ensure the accuracy of the data, the well test data in this work were primarily analyzed using the semi-log and log-log curves and were further verified using historical matching pressure curves as discussed by Hopkins et al. (1998). After the injection/fall-off well test, the *in-situ* stress measurements were carried out using multi-cycle hydraulic fracturing tests based on

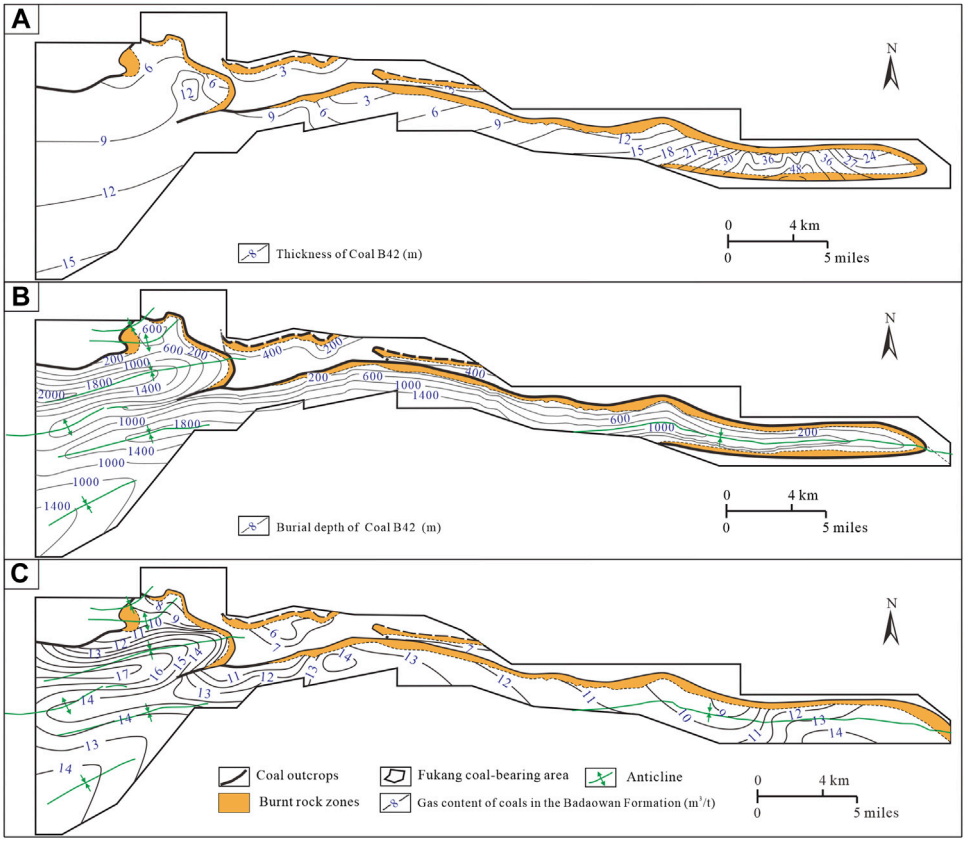

FIGURE 5
Thickness **(A)**, burial depth **(B)** and gas content **(C)** of the Coal B42 of the Badaowan Formation in the Fukang area.

the Chinese Earthquake Industry Standard (DB/T14-2000). To ensure the data are representative and comparable, the measurement of *in-situ* stress was performed for four cycles. During the *in-situ* stress measurement, the balance pressure that can just keep the fracture open is called closing pressure (P_c) and is considered to be equal to the minimum horizontal principal stress (σ_h) (Haimson and Fairhurst, 1970; Haimson and Cornet, 2003),

$$\sigma_h = P_c \tag{1}$$

At the moment a coal seam cracks, because the liquid cannot be timely supplemented, the pressure will greatly decrease; therefore, the critical pressure value recorded by the electric pressure gauge is the breakdown pressure (P_f) of coal seams. According to the theory of elastic mechanics, the maximum horizontal principal stress (σ_H) can be expressed as

$$\sigma_H = 3P_c - P_f - P_o + T \tag{2}$$

where P_f is the breakdown pressure, MPa; P_o is the reservoir pressure, MPa; and T is the tensile strength of coal or rock, MPa.

The vertical stress can be estimated according to the weight of overlying rock as discussed by Hoek and Brown (1980) who combined 116 *in situ* stress test results worldwide and established the prediction formulas of vertical stress (σ_v) as Eq. 3.

$$\sigma_v = 3\gamma D \approx 0.027D \tag{3}$$

where γ is the bulk density of rock in kN/m^3, and D is depth in m.

4 Results

4.1 Gas content

To investigate the gas accumulation of the Fukang coals, the lateral distribution of gas content of the total coal measures in the Badaowan Formation has been illustrated in Figure 5C. Gas contents of coal reservoirs from the Badaowan Formation show a great variation, ranging from about 0.29 to 16.64 m^3/t with an average of 8.15 m^3/t (Supplementary Table S1). Gas contents of the Badaowan Formation are typically greater in the western Fukang area, mostly ranging from 10 to 17 m^3/t, while that of the central and eastern Fukang area is generally from 8 to 14 m^3/t. Variations of gas contents in the Fukang area show clear variation with structure. High gas contents are dominantly

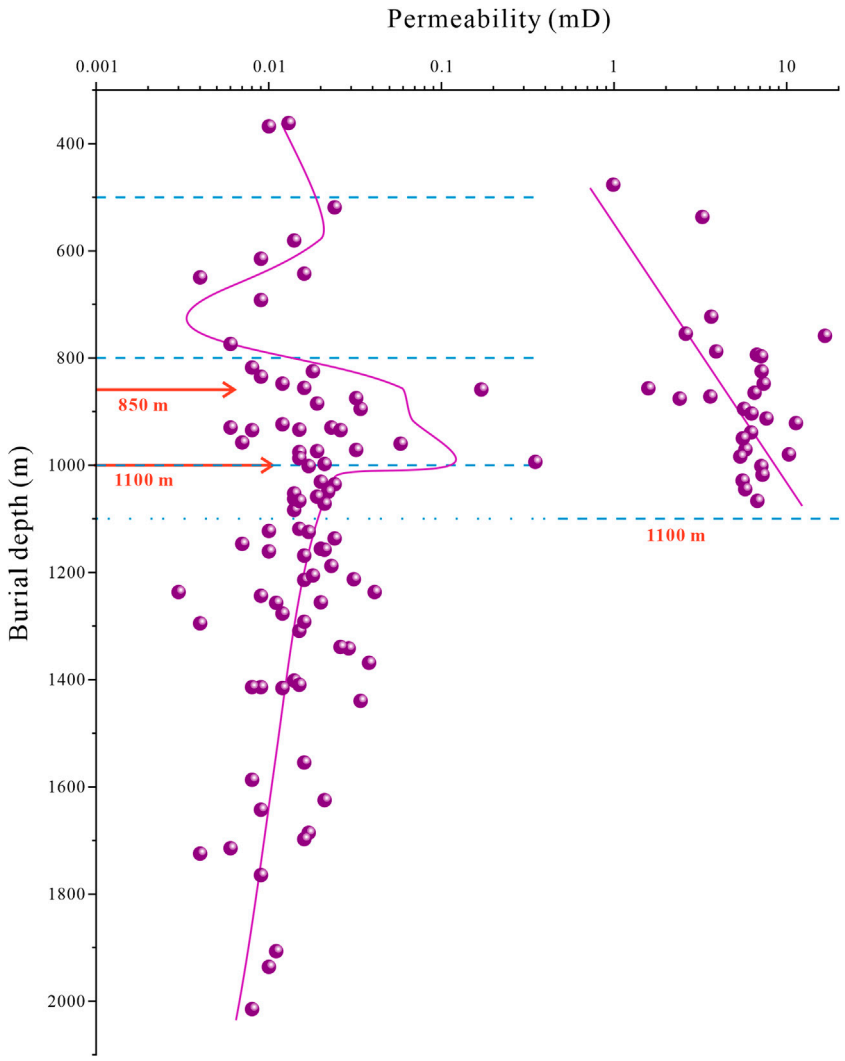

FIGURE 6
Vertical variation of permeability with burial depth.

found in the axis portion of synclines where the burial depths increased dramatically due to the high dip angle of coal seams in the limb portion of the synclines. For example, the highest gas content occurs around the axis portion of the Fukang Syncline, ranging from 14 to 17 m^3/t (Figure 5C). These areas include the Guangyuan mine, Liuyun mine, Sangongjianjiang mine, and Qimei No.1 mine. Meanwhile, the gas content of coal seams adjacent to the outcrop or burnt rock zones generally has gas contents less than 8 m^3/t.

4.2 Permeability

Permeability is a critical control of effective and economical coalbed methane production (Pan et al., 2010; Anggara et al., 2016; Niu et al., 2021). Previous studies illuminated that the permeability of low-to-medium-rank coals is generally favorable despite a high degree of heterogeneity (Wang et al., 2009; Li et al., 2017). The maximum permeability of 16.640 mD was found in the Qimei No.1 mine where the maximum daily gas production of 2.7 × 10^4 m^3/d was achieved in the Fukang area, southern Junggar Basin. On the whole, permeability in the Fukang area shows a high degree of dispersity and is prominently partitioned into two distinct groups behaving different trends with burial depth, one group of high permeability (0.988–16.640 mD) and the other group of low permeability (0.001–0.350 mD) (Figure 6; Supplementary Table S2). In the high permeability group, a positive co-relationship between permeability and depth was found where permeability increases from 1 mD to over 10 mD. However, this group of high permeability only exists

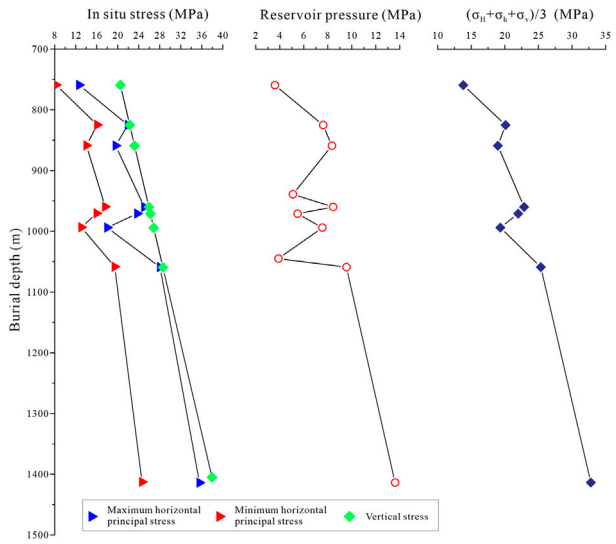

FIGURE 7
Variation of *in-situ* stresses, reservoir pressure and average total stress with depth.

at burial depths shallower than 1,100 m. In the low permeability group, permeability shows different variations as burial depth increases. At depths shallower than 500 m, permeability is generally stable at around 0.01–0.02 mD. From depths of 500–800 m, permeability begins to decrease with depths, and down to an extremely low value (0.004 mD) at depth of around 750 m. From depths of 800–1,000 m, permeability shows an evident increase, and shifts to a relatively high value 'plateau' (≥0.01 mD). Between this high permeability interval, two levels of relatively high permeability occur at depths of 850 and 1,000 m. For coal reservoirs deeper than 1,100 m, permeability shows great dispersion, but a gradually deteriorated trend was found through this strata range, and permeability reduces to extremely low at the deeper reservoirs (0.001 mD ~ 0.01 mD) (Figure 6). In addition, permeability also shows a high degree of variation in the horizontal direction due to different reservoir properties around the Fukang area. Permeability is typically high in the axis portion of the Fukang Syncline and Huangshan Syncline (Figure 7), where permeability is mostly greater than 1 mD even for some deep coal seams (depth > 1000 m).

4.3 *In situ* stress field

With Eqs 1–3, *in-situ* stress of eight datasets were derived from depths between 700 and 1,500 m in the Fukang area, southern Junggar Basin (Supplementary Table S3). The vertical principal stress (σ_v) ranges from 20.49 to 38.18 MPa with an average of 27.04 MPa. The maximum horizontal principal stress (σ_H) is mainly from 12.66 to 35.57 MPa with an average of 23.28 MPa, and its stress gradient is 1.67–2.66 MPa/100 m. The minimum horizontal principal stress (σ_h) is 8.26–24.67 MPa with an average of 16.22 MPa. By an arithmetic average of the maximum horizontal principal stress, minimum horizontal principal stress, and vertical stress, the total average *in-situ* stress (σ_{av}) of the Fukang area was calculated, which is from 13.80 to 32.81 MPa, averaging 22.18 MPa (Figure 8). Compared with the magnitudes of *in situ* stress of the eastern Ordos Basin where σ_{av} is 19.81 MPa, the southern Qinshui Basin where σ_{av} is 18.92 MPa and the western Guizhou where σ_{av} is 15.79 MPa(Meng et al., 2011; Zhao et al., 2016; Chen et al., 2017; Chen et al., 2018), the *in-situ* stress of the Fukang area, southern Junggar Basin is relatively high, which may result from the intense tectonic activities during the Yanshan and Himalaya movements (Li et al., 2019; Fu et al., 2020).

Vertically, the maximum and minimum horizontal principal stresses, and the vertical principal stress are all positively correlated with buried depth with varying trends at specific burial depths. The maximum principal stress and minimum principal stress markedly decrease at depths of 750 m, 850 m, and 1,000 m, while varying trends of vertical stress with depth do not change. The average *in-situ* stress (σ_{av}) also shows evident decreases at depth of 850 and 1,000 m, which means the *in-situ* stress at these levels are relatively low, and this is well coincident with the relatively low values of reservoir pressure between 850 and 1,050 m. It is reasonable to conclude that it is the relatively low *in-situ* stress that contributes to the low

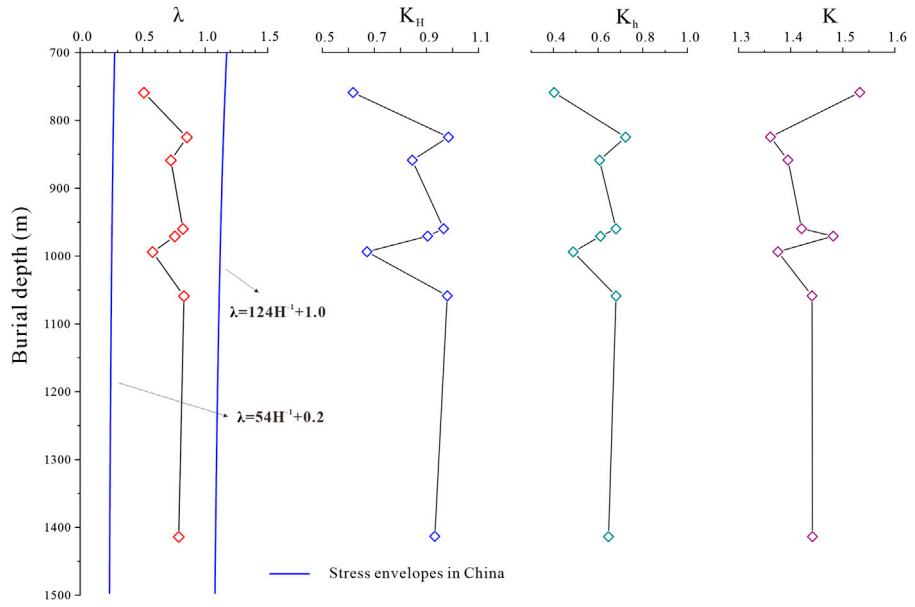

FIGURE 8
Variation of principal stress ratios with depth.

reservoir pressure at these levels. On the whole, the measured results show that the *in-situ* stress of the Fukang area is characterized by $\sigma_v > \sigma_H > \sigma_h$, revealing a normal stress regime (Anderson, 1951; Hoek and Brown, 1980). Although the tectonic structure of the southern Junggar Basin is dominated by a series of thrust fault systems, the current *in-situ* stress regime of the Fukang area, at least from depths of 700–1,500 m, is advantageous for normal faulting activity and indicates an extension zone which is favorable for developing high permeability.

To characterize the variation of *in situ* stress field, several stress ratios, including lateral stress coefficient (λ) and natural stress ratios (K_H and K_h) were introduced (Brown and Hoek, 1978; Hoek and Brown, 1980). The lateral stress coefficient is defined as the ratio of average horizontal principal stress to vertical stress, expressed as

$$\lambda = \frac{\sigma_H + \sigma_h}{2\sigma_v} \quad (4)$$

The natural stress ratios (K_H, K_h) are defined as the effect of tectonic movement on the stress and can be expressed as

$$K_H = \frac{\sigma_H}{\sigma_v} \quad (5)$$

$$K_h = \frac{\sigma_h}{\sigma_v} \quad (6)$$

And the horizontal principal stress ratio (K) reflects the degree of anisotropy of the horizontal stress, expressed as

$$K = \frac{\sigma_H}{\sigma_h} \quad (7)$$

The lateral pressure coefficient (λ) is an effective parameter to characterize the *in-situ* stress distribution characteristics. The lateral pressure coefficient (λ) of coal reservoirs (700–1,500 m) in the Fukang area is in the range of 0.51–0.85, with an average of 0.72, and all the lateral pressure coefficients are included between the *in-situ* stress envelopes of China (Figure 9) (Zhao et al., 2016). Overall, λ is lower than 1, which means that the Fukang CBM reservoirs are dominated by overburden stress. At depths of 750–825 m, λ shows a remarkable increase from 0.51 to 0.85, indicating a vertical-stress-dominated stress regime. From depths >825 m, λ is relatively high (averaging 0.8), except for two levels of low values at 850 and 1000 m, indicating that horizontal stresses begin to play an important role at depths >825 m despite fluctuations of stress field at specific depths. The value of σ_H/σ_v ranges from 0.62 to 0.98 with an average of 0.85, and that of σ_h/σ_v is from 0.40 to 0.72 (average of 0.60). The horizontal principal stress ratio (K) ranges from 1.36 to 1.53, with an average of 1.45, indicating relatively low variation of *in-situ* stress in the horizontal direction (Figure 9).

5 Discussions

5.1 Influencing factors of gas accumulation

5.1.1 Coal thickness and sealing performance

The dissipation of coalbed methane is dominated by diffusion, deriving from differential concentration between

two points (Fick, 1995; Pillalamarry et al., 2011; Fu et al., 2019). Concerning *Fick's Law* and *Principle of Mass Balance*, as coal thickness increases, the time lasting for achieving the median concentration when diffusion is terminated will be lengthened accordingly (Fick, 1995; Pillalamarry et al., 2011). In the Fukang area, a slightly positive correlation between coal thickness and gas contents was revealed which indicates a high resource potential due to the ultra-thickness of the Fukang CBM reservoirs (Figure 10A). Meanwhile, CBM reservoirs are known as 'self-generation and self-accumulation' reservoirs, a well-sealed surrounding condition will undoubtedly improve gas accumulation. The roof of coals in the study area is dominated by mudstones, carbonaceous mudstones, siltstones, and muddy siltstones. Hou et al. (2021) analyzed the surrounding rock condition of coal reservoirs in the middle section of the southern Junggar Basin and subdivided it into four types. The surrounding rocks of the Fukang coals can be classified as Type III and IV which are mainly developed in the distributary bay of the lower deltaic plain and deep-water facies. This indicates a good reservoir sealing performance, and is in favor of the development of high gas content. However, intensely occurring faults increase the likelihood of gas escape through these discontinuous gaps of coal seams. But no evidence shows faults have enhanced gas escaping from coal seams by comparing tectonic structures in Figure 2 and variations of gas contents in Figure 5C, probably due to the compressional properties of the

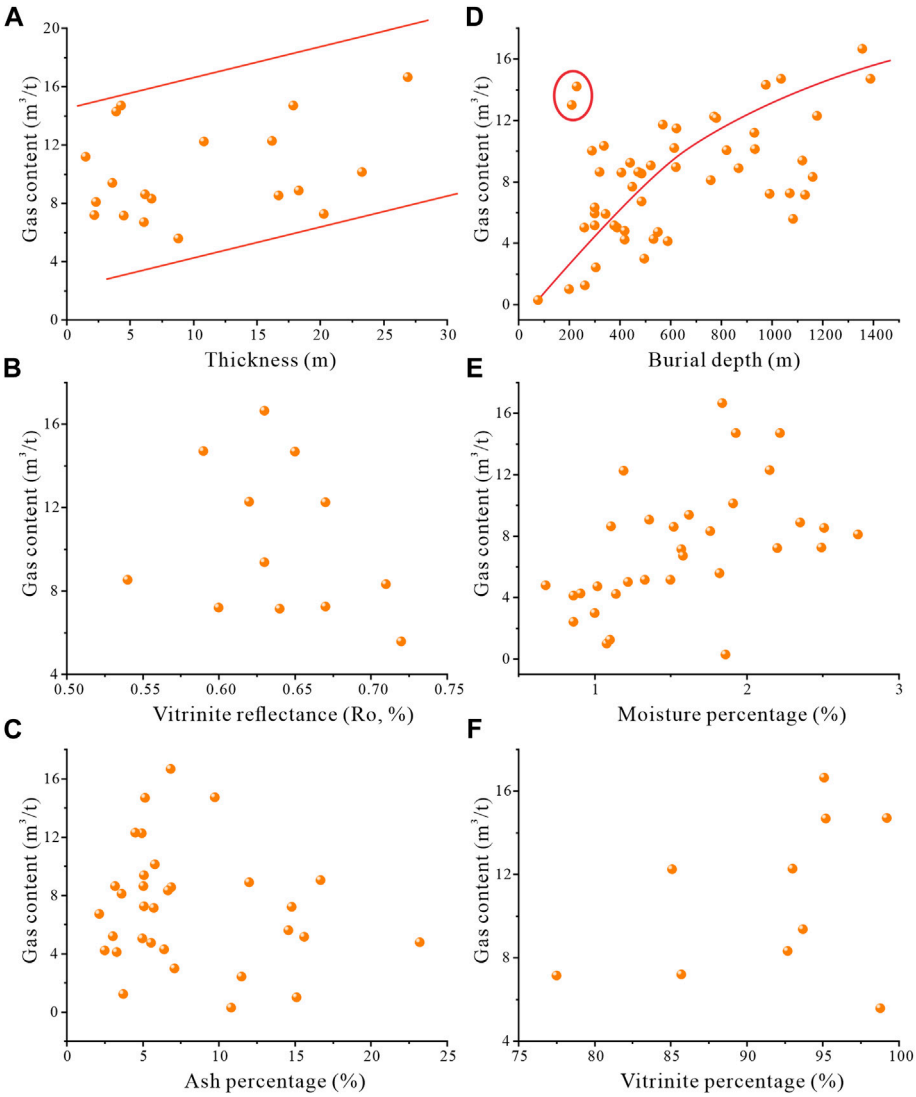

FIGURE 9
Correlations of gas content with coal thickness **(A)**, vitrinite reflectance **(B)**, ash percentage **(C)**, burial depth **(D)**, moisture percentage **(E)**, and vitrinite percentage **(F)**.

occurring reverse faults in the southern Junggar Basin. In addition, steep coal seams in the Fukang area with large dip angles (30°–85°, even reverse) and associated fractures are possible factors that are unfavorable for the preservation of coalbed methane. Decreasing gas contents adjacent to coal outcrops dominatingly resulted from the high dipping properties of coal measures.

5.1.2 Tectonic structure and burial depth

Burial depth has been proven to have a profound effect on gas accumulation which can be summarized into three aspects, 1) reservoir pressure generally increases as deepening burial depth, and gas storage capacity at deep coal reservoirs can be enhanced due to the dominance of adsorption over desorption at high pressures (Faiz et al., 2007; Scott et al., 2007; Xu et al., 2021). 2) gas flow can be limited due to the generally weakened permeability of coal reservoirs in deep positions (as discussed in 4.2), and the increasing distance of gas diffusion and escaping from deep coals to the ground surface is beneficial to gas accumulation (Bustin and Clarkson, 1998; Palmer and John, 1998; Yao et al., 2013; Kang et al., 2020). 3)However, with further increases in depth, temperature increases and will account for more free, soluble gases due to elevated desorption capacity beyond adsorption at high temperatures (Liu et al., 2013; Kang et al., 2018; Fu et al., 2019). As a result, the occurrence of more free, soluble gases adds the chance of gas leakage which might override the positive effects of increased pressures in deep coal reservoirs. As shown in Figure 10B, the gas content of the Fukang coals is positively related to burial depth, but the rate of gas content increase with depth is gradually reduced from depth deeper than 800 m, which might result from the increasing negative effect of elevated temperature. In general, at depths shallower than 600 m gas contents are mainly lower than 8 m^3/t, and at depths greater

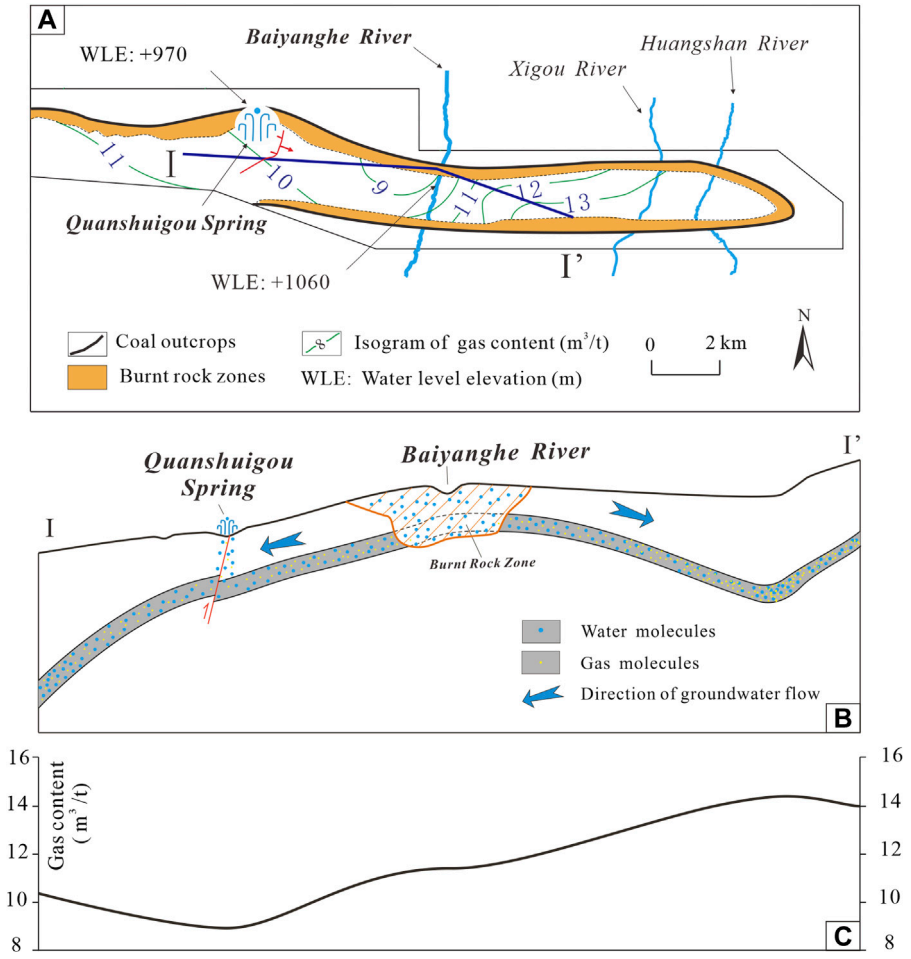

FIGURE 10
Gas accumulation model showing the effect of burnt rock zone, hydrology, biogenic gas formation and coal seam structures on gas contents. **(A)**-Contour map of gas content showing the distribution of geological factors. **(B)**-Diagram of section I-I' in diagram **(A)** showing migration of coalbed methane and formation water controlled by hydrogeology and tectonic structures. **(C)**-Variation of gas content in section I-I'.

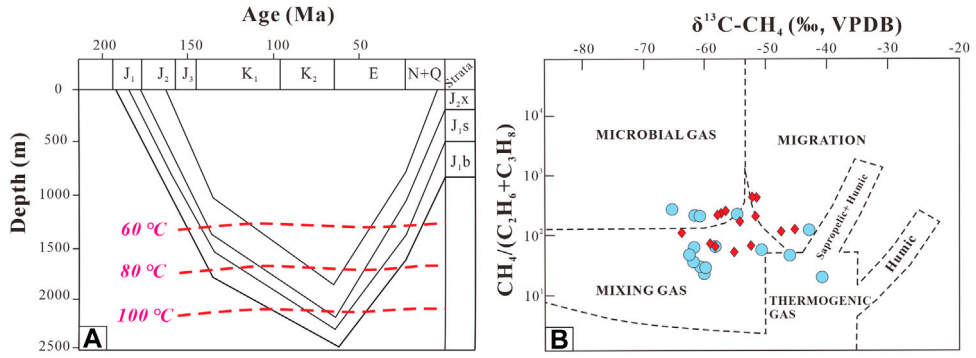

FIGURE 11
(A) Burial history of the southern Junggar Basin, showing basin wide subsidence during the Jurassic-Cretaceous, and Late Cretaceous-Quaternary uplift (modified after Wang et al., 2009). **(B)** Genetic characterization of coalbed methane from the southern Junggar Basin using $\delta^{13}C(CH_4)$ versus hydrocarbon index $[CH_4/(C_2H_6+C_3H_8)]$. Data of blue circles are from Zhi et al. (2013) and that of red diamonds are from Wang et al. (2022). Compositional fields are from Whiticar (1999).

than 600 m gas contents are mostly over 8 m^3/t. However, behind the positive trend between gas content and burial depth, their covariation behaves a large scatter, from which we can infer that combined effects from the three different aspects mentioned above might coexist in the Fukang area. Interestingly, there are two erratic dots at depth of around 250 m in Figure 10B, which exhibit extremely high gas contents (14.21 and 13.00 m^3/t, respectively). Concerning the high gas content at such a shallow burial depth, late-stage biogenic gases might occur in these positions which have been confirmed in literature in the southern Junggar Basin (Hu et al., 2010; Zhi et al., 2013; Wang et al., 2022), and will be discussed in the following section. As a result, late-stage biogenic gases might also contribute to the scatter correlation between gas content and burial depths.

5.1.3 Hydrogeology and burnt rocks

Regional structures and basin hydrodynamics can significantly affect the gas generation and accumulation in coal reservoirs (Bustin and Clarkson, 1998; Pashin, 2010; Gentzis, 2013; Li et al., 2022; Wang et al., 2022). In the Fukang area, groundwater recharges are dominated by glacial melt-water runoff from the Bogda Mountain perennial snow areas, and burnt rock hydrops in the burnt rock zones (Li et al., 2018). Both glacial melt-water runoff and burnt rock hydrops flow down into the deep Jurassic aquifers. Burnt rocks are characteristic of porous fissures which can naturally connect coal outcrops and aquifers in the deep strata (Figures 4A,B). Glacial melt-water runoffs generally flow from south to north and across the coal outcrops, which include the Shuimohe, Sangonghe, Sigonghe, Baiyanghe, and Xigou Rivers in the Fukang area (Figure 1). Worth to note, perennial water flow only exists at the Baiyanghe River which has an average discharge rate of 2.50 m^3/s and a clear flow direction. The Baiyanghe River (water level at +1,060 m) normally occurs as a watershed and forms the groundwater recharge source of the Fukang coal reservoirs (Figure 11). On the west side of the Baiyanghe River, groundwater moves from west to east, through the Baiyanghe River, to burnt rock hydrops, and eventually to the Quanshuigou Springwater outlet (water level at +970 m). In these areas, continuous water flow can transport dissolved coalbed gases away from coal reservoirs to the groundwater, and ultimately to the ground surface. After hundreds of thousands of years of persistent gas loss, gas content can be drawdown to relatively low. For instance, gas content to the west of the Baiyanghe River is generally lower than 10 m^3/t (Figure 11). On the east side of the Baiyanghe River, groundwater flows from east to west, through the Baiyanghe River, to aquifers in the deep part, where a hydraulic stagnant zone was formed. Overpressure in the deep stagnant zone and opposite-direction transportation of water flow compared to gas migration in coal reservoirs can significantly prevent upward gas escaping and favor gas accumulation. As a result, relatively high gas content is developed to the east of the Baiyanghe River, for instance, gas content in the Xigou No.1 and Xigou No.2 mines is generally greater than 11 m^3/t.

5.1.4 External factors

Coal rank and composition are two factors controlling the potential of gas generation (Scott et al., 2007; Yao et al., 2013). However, no clear correlation between gas content and maceral component and coal rank (vitrinite reflectance) was discovered (Figures 10B–F). this may probably result from the narrow range of coal rank, and vitrinite-dominant composition or their effects on gas accumulation were covered by other effects from the factors mentioned above.

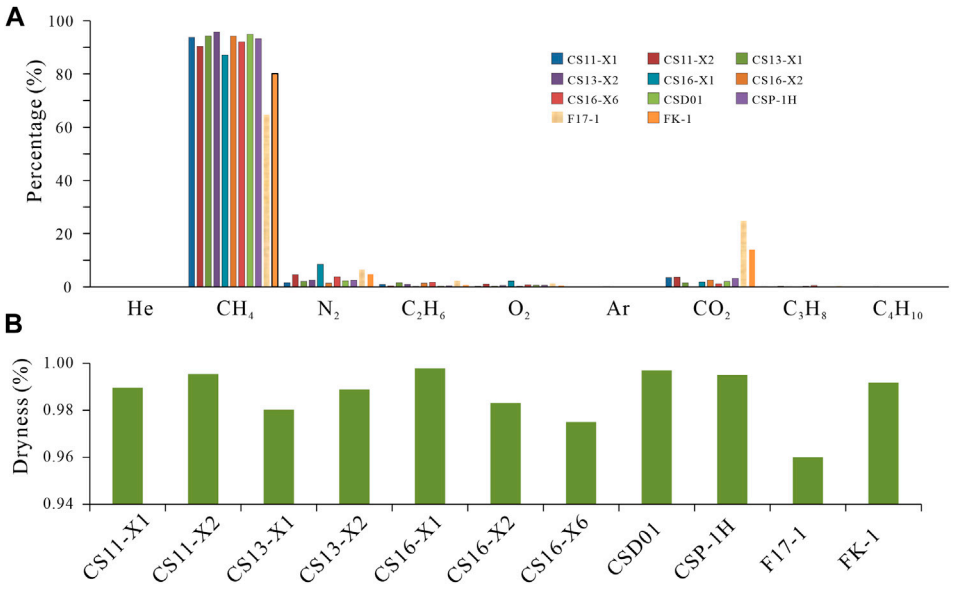

FIGURE 12
Composition **(A)** and dryness **(B)** of coalbed gases in the Fukang area.

5.2 Origins of coalbed methane

The Lower-Middle Jurassic coal-bearing succession in the Fukang area reached its maximum burial depth in the Late Cretaceous when the first coalification event took place, and maximum vitrinite reflectance reached about 0.8% at that age. After the Late Cretaceous, the coal sequences were continuously uplifted and coalification ceased (Chen et al., 1998; Zhi et al., 2013) (Figure 12A). due to differential burial depth, the vitrinite reflectance of the Fukang coals is from 0.54% to 0.72%, which indicates a thermogenic stage of coalbed gas generation. In addition, components of coalbed gases from the desorption of drilling coal cores were determined, which include CH_4, N_2, CO_2, C_2H_6, C_3H_8, C_4H_{10}, Ar, and He (Figure 13). The percentage of methane ranges from 89.16 to 95.78%, and that of carbon dioxide ranges from 0.04% to 24.71%. Air dryness of well extracted gases shows $C_1/C_{1\text{-}5}$ ranges from 0.96 to 1.00, indicating a coal-type, dry gas. These characteristics of coalbed gases further manifest that thermogenic coalbed gases from the Fukang coal reservoirs are mainly thermal degrading gases (Graham et al., 1990; Rice, 1993; Whiticar, 1999).

Recently, carbon isotopic analyses were conducted in the southern Junggar Basin by several researchers. The isotopic composition of methane from the southern Junggar Basin indicated that methane $\delta^{13}C$ value ranges between −41.9‰ and −64.6‰ (Figure 12B) (Hu et al., 2010; Zhi et al., 2013; Wang et al., 2022). In general, thermogenic methane has $\delta^{13}C$ values higher than −55‰ and biogenic methane has values lower than −60‰ because of preferential depleted carbon consumption by methanogens (Whiticar, 1996, 1999; Rice et al., 2008). The Intermediate carbon isotopic value has been interpreted to be a mixture of coexisting biogenic and thermogenic gases (Hu et al., 2010; Fu et al., 2021; Zhang B et al., 2021; Wang et al., 2022). Biogenic gases in the study area have been demonstrated to be dominated by second-stage biogenic gases and a combined microbial pathway of methane generation via both CO_2 reduction and acetate fermentation was proposed by Wang et al. (2022). Fu et al. (2021) pointed out that CO_2 reduction is the main pathway for generating microbial gas based on the identification of bacterial and archaeal16s rRNA genes in formation water (Fu et al., 2021). What is worth noting is that burnt rocks are widely developed around coal outcrops in the Fukang area and other places of the southern Junggar Basin. Freshwater abundant in microorganisms can be easily transported to the deep coal reservoirs through these porous burnt rocks. Coal reservoirs beneath the burnt rock zones, where sufficient groundwater supply exists, can make microbial gases formation for a persistent long period, and high gas content reservoir 'sweet spots' can be developed. High gas content (greater than 13 m^3/t) and methane concentration in the Choumeigou mine confirm the contribution of burnt rocks to gas accumulation in the Fukang area. Wang et al. (2022) further demonstrated that microbial gas is mainly present at depths <800 m, while thermogenic gas primarily occurs at buried depths greater than 1,000 m, and a mixture of the two was present at buried depths of 800–1,000 m. As a result, analyses of widespread burnt rocks and regional hydrodynamic conditions along coal outcrops could be an effective way to

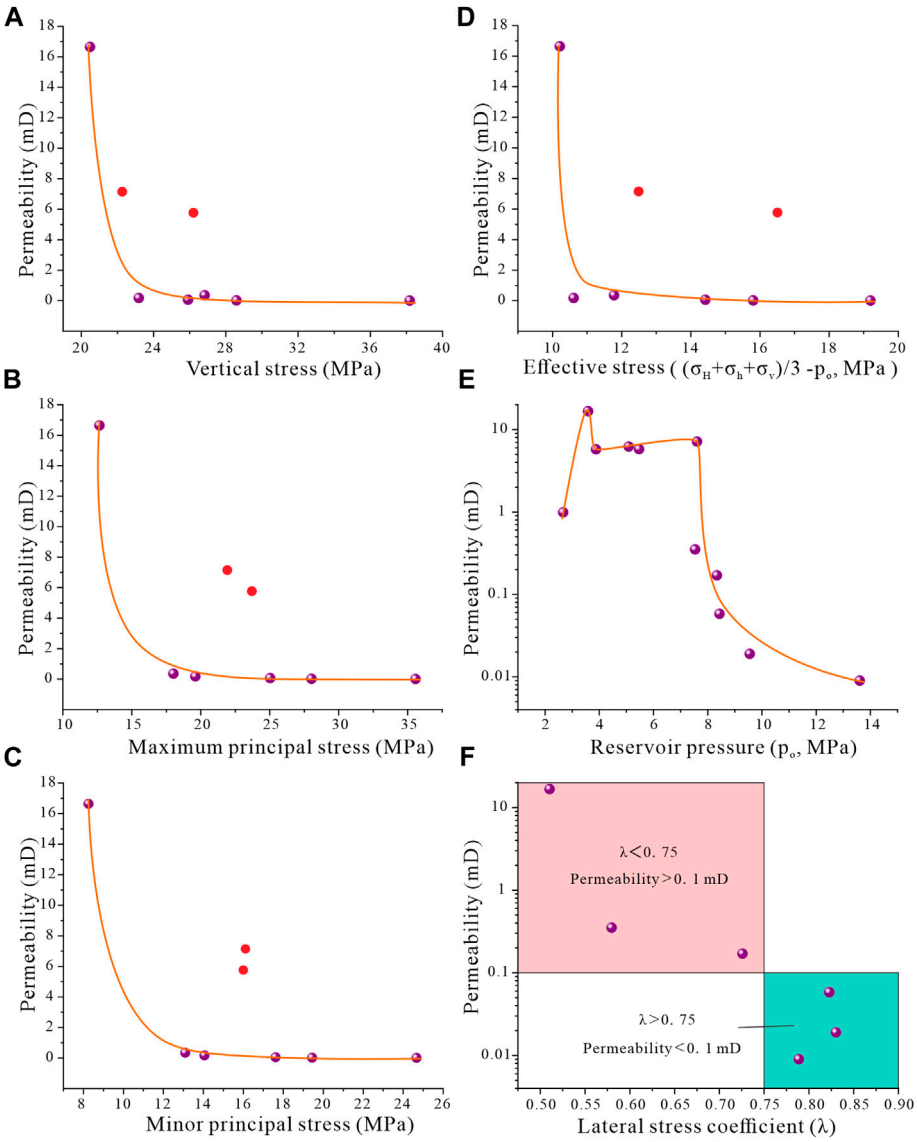

FIGURE 13
Diagram showing influences of in-situ stress field **(A–C)**, effective stress **(D)**, reservoir pressure **(E)**, and lateral stress coefficient **(F)** on permeability.

determine areas with enriched coalbed methane in the southern Junggar Basin.

5.3 Influencing factors of permeability

5.3.1 Fractures/macro-fractures

Naturally occurring fractures in coal are deemed to be the single most important physical attribute governing gas flow in CBM reservoirs (Bustin, 1997; Zhou et al., 2016; Wang et al., 2018; Niu et al., 2022). Fractures are very developed in the Fukang coals, which is consistent with the published cognition that high-density of fractures are generally formed in low-to-medium-rank coals (Dawson and Esterle, 2010; Moore, 2012; Wang et al., 2018). Field observation shows the density of face cleats in the Fukang area ranges from 7 to 49 in every 5 cm while that of butt cleats are from 8 to 29 in every 5 cm (Figure 4H). In addition to these millimeter-centimeter-scale cleats, macro-fractures with magnitude from several centimeters to tens of meters can be obviously found at outcrops in the Fukang area (Figure 4F). Macro-fractures can cut through more than one type of coal sublayers or the whole coal seams. The well-developed

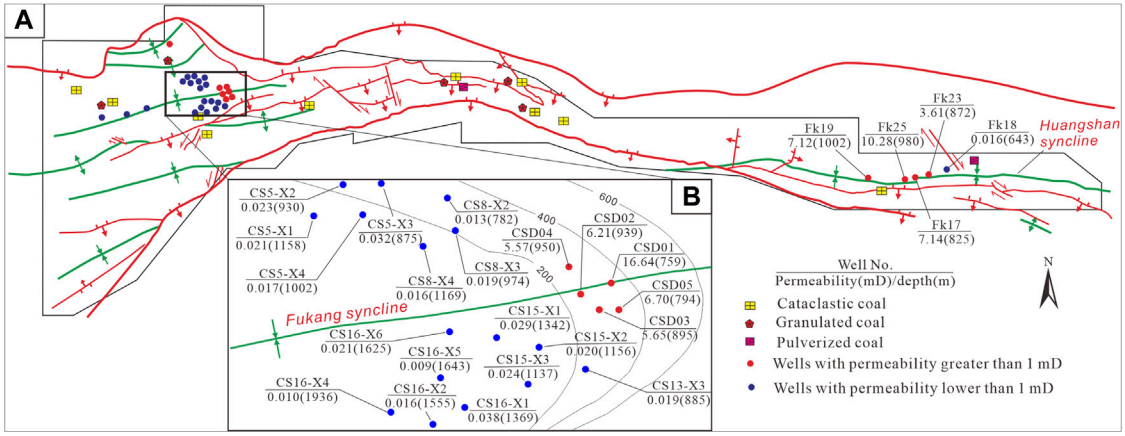

FIGURE 14
(A) Diagram showing distribution of deformed coals and measured permeability of Coal B42 from coalbed methane wells. **(B)** Enlargement of diagram **(A)** at the core part of the Fukang Syncline.

fractures in the Fukang coals of the southern Junggar Basin are partly due to the semi-bright and bright coal (vitrinite group) dominated coal composition on the one hand, and the relatively high intense tectonic stress condition (before present) also has a profound effect on the formation of fractures. Although high-frequency fractures are revealed in the Fukang area, but one thing should bear in mind that all the measurements of fractures are not at the *in-situ* status of geo-stress and depth anymore. The apertures and interconnectedness of the original fractures could be extraordinarily different from the measured fractures. So, *in-situ* permeability determination should be conducted based on analyses of *in-situ* stress, depths, and other external effects. And this appropriately explains why the permeability of the Fukang coals in the southern Junggar Basin exhibit a high range from 0.001 to 16.640 mD despite the high-frequency fractures.

5.3.2 *In-situ* stress

Coal reservoir permeability is basically controlled by fractures and its connectivity, and *in-situ* stress field, but will be dynamically regulated by changing effective stress, matrix shrinkage, and gas slippage during the depletion of CBM wells (Smyth and Buckley, 1993; Pan and Connell, 2011; Chen et al., 2018; Niu et al., 2021; Zhang T et al., 2021). Magnitude, heterogeneity, and anisotropy of initial permeability before CBM production generally determine the potential production rate of CBM wells and have become the core of exploring CBM 'sweet spots' and optimizing CBM well types. Based on measurement of *in-situ* stress and permeability, the influence of *in-situ* stress on the magnitude and heterogeneity of permeability was analyzed. Considering the hydraulic fracturing method adopted in this work cannot be used to derive *in-situ* stress orientation, therefore, the effect of *in-situ* stress on the anisotropy of coal permeability is not included in this paper.

Figures 14A–C shows the relationship between principal stress and permeability. As increases in vertical stress, and maximum and minimum horizontal principal stress, the corresponding permeability perform exponential decline except for two erratic dots (discussed in the following section). Many studies pointed out it was the effective stress that fundamentally formulates the magnitude of permeability (Palmer, 2009; Meng et al., 2011; Liu and Harpalani, 2013). To further quantify the influence of effective *in-situ* stress on permeability, we take the average total *in-situ* stress minus reservoir pressure (P_o) as effective *in-situ* stress (EIS), expressed as,

$$EIS = \frac{\sigma_v + \sigma_H + \sigma_h}{3} - P_o \quad (8)$$

An exponential decline of permeability with increases in effective stress was discovered in the Fukang area (Figure 14D), which is also verified by the cases from the Qinshui Basin, Ordos Basin, western Guizhou province in China, and other basins of the globe (Jasinge et al., 2011; Meng et al., 2011; Chen et al., 2017; Chen et al., 2018). In the Fukang area, when EIS <11 MPa, permeability dramatically reduces from 16.64 to 0.17 mD with the increase of EIS, which reconfirms the significant effect of effective stress on the permeability of coal reservoirs. When EIS >11MPa, permeability declines to extremely low, mostly below 0.2 mD, which means the major fracture systems in coal seams tend to be closed under high effective stress.

Furthermore, distinct varying trends between lateral stress ratio (λ) and permeability were analyzed here. As shown in

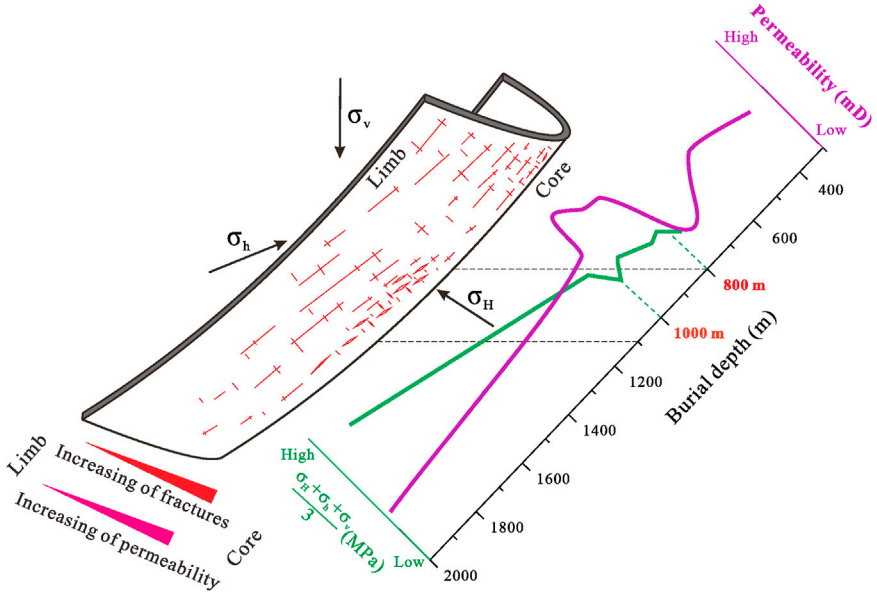

FIGURE 15
Permeability variation model showing the combined effects of *in-situ* stresses and coal structures on permeability in the Fukang area, southern Junggar Basin.

Figure 14F, where $\lambda < 0.75$, permeability is generally greater than 0.1 mD, but when $\lambda > 0.75$, permeability is lower than 0.1 mD. The lateral stress ratio actually reflects the change of the *in-situ* stress regime, when $\lambda < 0.75$, the horizontal stresses are relatively low as vertical stress dominates the *in-situ* stress field, and low stress in the horizontal direction favors the development of relatively high permeability. When $\lambda > 0.75$, the *in-situ* stress from both the horizontal and vertical directions are tending to converge, and the consistency of *in-situ* stress from three directions in a normal faulting stress regime enhanced the compression and closures of fractures in coal reservoirs, which resulted in the relatively low permeability. In addition, the relationship between coal permeability and reservoir pressure was plotted in Figure 14E. When reservoir pressure is low (2–8 MPa), permeability is relatively high (≥1 mD), however, when reservoir pressure is >8 MPa, permeability decreases rapidly to less than 0.2 mD. As shown in Figure 8, low reservoir pressures (2–8 MPa) generally distribute at depths shallower than 1,100 m where the total *in-situ* stress is low. As a result, it can be inferred that it is the low *in-situ* stress (EIS), not the low reservoir pressure, that eventually accounts for the relatively high permeability in the shallower coal seams (<1,100 m).

At the same time, as mentioned above, permeability can be partitioned into two separate groups with distinct relationships with depths, and the low group of permeability performs a distinct variation trend with depth. Associated with vertical variation of *in-situ* stress field, the co-relationship between depth-dependent *in-situ* stress field and permeability was discussed here. At shallower coal reservoirs (depths <500 m), *in-situ* stress measurements in major Chinese coal basins have revealed that *in-situ* stress field at this depth range is dominated by tectonic compression, and the major principal stress normally exhibits the trend of $\sigma_H > \sigma_h > \sigma_v$ (Chen et al., 2017; Chen et al., 2018; Li et al., 2019). As a result, the reverse faulting stress regime reflected by the principal stress field is decisive to the low permeability at depths shallower than 500 m (0.01–0.02 mD) (Figures 6, 8). When coal reservoirs go deeper, *in-situ* stress in the Fukang area shifts to the regime of $\sigma_v > \sigma_H > \sigma_h$, and is dominated by gravitational loading but with distinctive variation of stress field as shown in Figure 8. At depths of 500–800 m, with deepening coal reservoirs, *in-situ* stress increase gradually, and a decreasing trend of permeability with depth were found at this depth range. Then, as burial depth increases, horizontal stress behaves a prominent decline at depths of 800–1,000 m, especially at levels of 850 and 1,000 m, this causes the effective stress acted on coal seams to attenuate, as a result, a relatively high permeability 'plateau' was developed. Finally, as depth increases to deeper than 1,000 m, the *in-situ* stress regime transfers to the normal increasing stress field and persists to decrease with depth, so a persistent decline of permeability was discovered at depths below 1,000 m. Therefore, the variation of permeability of the low permeability group with depths actually reflects the co-

variation between depth-dependent stress field change and permeability.

5.3.3 Geometry and attitude of coal seams

As a layered energy reservoir, the geometry and attitude of coal seams also have a great impact on permeability. The frequency of fractures, apertures, interconnectedness, and orientation of fractures can be quite different in different parts of the coal seams, and all these factors can significantly influence the heterogeneity and anisotropy of reservoir properties. The Fukang area of the southern Junggar Basin is characterized by intense tectonic structures as shown in Figure 2, and varying strike and dip angles shaped the complex attitude and frequently changing morphology of coal seams. Kang et al. (2022) calculated the structural curvature of coal seams in the western Fukang block, which ranges from 0.0001 to 0.005 and can be classified as high structural curvature as discussed by Shen et al. (2010). It is worth noting that in the core parts of folds, where high structural curvature occurs, extraordinary high-frequency fractures and favorable apertures have been developed due to the relatively tensile stress regime (Figures 4E,G; Figure 15). The distribution of measured permeability from CBM wells shows a remarkable increase of permeability in CBM wells in the core parts of synclines compared to that in the lime parts of synclines (Figure 7). Measured permeability from CBM wells in the core parts of synclines is mainly greater than 1 mD, while that in the lime parts of synclines is mostly lower than 0.1 mD. Moreover, the closer to the core of synclines, the higher permeability is prone to be developed. The highest permeability (16.64 mD) has been discovered in the CBM well CSD-01 which is located just at the core of the Fukang syncline. So, it is not difficult to infer that the high group of permeability in Figure 6 represents measured permeability from CBM wells proximal to the fold core, and the correlation between permeability and depths reflects the covariation between measured permeability and the distance from the operating well to the core of the corresponding folds. Additionally, these high permeability dots erratically exhibited in Figures 14A–D are from CBM well CSD03 and Fk17 with permeability of 5.76 mD and 7.14 mD respectively. It can be seen in Figure 14 that both of these two wells are distributed at the core part of the major synclines in the Fukang area, actually, it is the high structural curvature of coal seams that accounts for the high permeability in these coal reservoirs.

Furthermore, the dip angle of the Fukang coal has a high range from 20° to 90°, or even reverse. The orientation of fractures/cleats in coal seams, and the stress and strain of coal reservoirs vary with dip angle changes, and this can significantly increase the anisotropy of permeability. Zhang B et al. (2021) demonstrated that the rate of permeability decrease had a tendency of first decrease and then increase with dip angle gradually increased from 0° to 90°. This will increase the difficulty of permeability prediction and upgrade the uncertainty of optimization of sweet pot for CBM exploration. However, detailed field observations and measurements of fractures and microfracture at outcrops and underground coal mines will help determine the heterogeneity and anisotropy of permeability. Statistical analysis of macro-fractures in the western Fukang area shows that a group of macro-fractures along the strike are more developed than another group of macro-fractures perpendicular to the strata strike, which indicates prevailing permeability will be developed along the strike, and fracturing in the Fukang area should be conducted along this direction.

5.3.4 Coal deformation

Tectonic deformation can lead to obvious alteration of pore-fracture systems in coal reservoirs, and can significantly change the seepage capacity of gas flow (Karacan and Okandan, 2000; Li et al., 2003; Li et al., 2021). Deformation of coal structure in a brittle or cataclastic manner can enhance permeability by the magnitude of 3–8 times above the surrounding reservoir (Li and Ogawa, 2001; Jiang et al., 2010). This kind of relatively weak deformation tends to open up existing cleat apertures and increase their interconnectedness, thus increasing permeability (Kang et al., 2022; Li et al., 2003; Pan et al., 2015). On the contrary, in sheared coals behave in a more ductile or mylonitic manner, permeability has been demonstrated to be dramatically deteriorated (Li and Ogawa, 2001; Li et al., 2021). With mylonitic deformation, the coals tend to be tightly compressed and cleat apertures collapse (Li et al., 2003). These types of shear zones have also been related to a high risk of coal and gas outbursts during mining activities (Li et al., 2016; Pan et al., 2019).

In the Fukang area, tectonic deformation is widely recognized at both outcrops and heading stopes in underground mines. Tectonically deformed coals in this area can be subdivided into cataclastic coals (Deformation in a cataclastic manner), as well as granulated and pulverized coals (Deformation in ductile and mylonitic manners). All three types of deformed coals are dominantly distributed in the central part of the Fukang area, as known as the arcuate structural zone, that is to the west of the Kanglong coal mine and to the east of the Wugong coal mine (Figures 4C,D, 7). In these places, intense tectonic movement and high shearing stress resulted in the high occurrences and intensity of coal deformation. Kang et al. (2022) evaluated in-seam variation of coal structures in the western Fukang area by logging data analyses and found that the whole thick coal seams in the western Fukang area are vertically composed of 5–10 sublayers with different coal structures, and tectonically deformed coals are mainly developed in the lower-middle part of coal seams (Kang et al., 2022). Although the occurrence of cataclastic coals can improve the aperture of fractures/cleats and enhance gas flow in coal seams, unevenly distributed granulated and pulverized coals can profoundly decrease the interconnectedness of fractures/cleats and hinder gas flow. For instance, at the Qimei No.2 mine where granulated coals were developed, extremely low permeability (0.023 mD) was

discovered at CBM well CX5-X2, and a serious coal-and-gas-outburst occurred in 2005. Overall, the development of deformed coals has a profound effect on the permeability heterogeneity of coal reservoirs, which increases the difficulty of coalbed methane stimulation and recovery and increase the ever-existing risk of coal-and-gas-outburst during the underground mining in the Fukang area. CBM exploration and exploitation in the Fukang area should avoid these places where deformed coals were reported.

6 Conclusion

1) Structural framework and burial depth generally control gas contents of coal reservoirs in the Fukang area. Gas contents increase with deepening burial depth, but the rate of gas content increase with depth is gradually reduced due to enhanced negative effects from increased temperature beyond the positive effects from increased pressures in deep coal reservoirs. The high-to-ultra-high thickness of coal reservoirs has a slightly positive effect on gas content.
2) Perennial water flow of the Baiyanghe River is in favor of gas accumulation to the east part of the Baiyanghe River by forming a hydraulic stagnant zone in the deep coal reservoirs. But gas contents can be drawdown by persistent transportation of dissolved coalbed gases to ground surfaces (Quanshuigou Springwater outlet) to the west of the Baiyanghe River. Meanwhile, widely developed burnt rocks make groundwater easily access the deep coal reservoirs, and abundant microorganisms transported to the deep coal reservoirs facilitate the generation of late-stage microbial gases, which, together with thermal degrading gases, account for the origin of coalbed gases in the Fukang area.
3) The *in-situ* stress field of the Fukang area is characterized by vertical stress (σ_v) > maximum horizontal stress (σ_H) > minor horizontal stress (σ_h), indicating a normal stress regime. The maximum principal stress, minimum principal stress, and vertical stress generally increase with depth, but the maximum and minimum principal stress show an evident decline at depths of 850 and 1,000 m. All the stress ratios, including lateral stress coefficient (λ), natural stress ratios (K_H and K_h), and horizontal principal stress ratio (K) are included in the *in-situ* stress envelopes of China.
4) Permeability in the Fukang area shows a high degree of dispersity, ranging from 0.001 to 16.640 mD, and is prominently partitioned into two distinct groups, one group of high permeability (0.988–16.640 mD) and the other group of low permeability (0.001–0.350 mD). The low group of permeability is prominently formulated by depth-dependent stress field change. At depths of 500–800 m, permeability gradually decreases with increasing *in-situ* stress as burial depth deepens. From 800 to 1000 m, horizontal principal stresses behaved a prominent decline which contribute to a relatively high permeability 'plateau'. At depths deeper than 1,000 m, a persistent decline of permeability occurs with deepening burial depth. For the high group of permeability, relatively high structural curvature in the core parts of synclines, and the distance to the syncline core significantly dominate permeability in the Fukang area.
5) Furthermore, permeability shows exponential decline with increasing effective *in-situ* stress and lateral stress ratio (λ) has a profound effect on permeability. When $\lambda < 0.75$, permeability is generally greater than 0.1 mD while permeability is lower than 0.1 mD when $\lambda > 0.75$. Frequently occurring deformed coals increase the difficulty of coalbed methane stimulation and recovery. High-ranging dip angle of the Fukang coal seams can dramatically increase the anisotropy of permeability. Analysis of the attitude of fractures/macro-fractures will favor the determination of preferred fracturing orientation and optimizing CBM well types.

Data availability statement

All data discussed in the paper will be made available in the Supplementary Material, further inquiries can be directed to the corresponding author.

Author contributions

ML and MiL are responsible for writing original manuscript. JP and YC are responsible for copyright and revising the manuscript. DG is responsible for drawing figures and data arrangement. DG and MiL is responsible for basic data and maps. ML, DG, and MiL are responsible for field and lab work.

Funding

This research was funded by the National Natural Science Foundation of China (No. 41502108, 41772162), China Postdoctoral Science Foundation (No. 2016T90667) and the Key Research Project of Universities of Henan Province (No. 20A170008).

Acknowledgments

We are grateful to Xuesong Yang from the Xinjiang Cleanseed New Energy Company for the help of field work and data collection and Yawen Wu and He Zhou from Henan Polytechnic University for the analysis of gas contents. Professor Jiangfeng Chen from Henan Polytechnic University is thanked for supplying the hydrogeological data.

Conflict of interest

The authors declare that the research was conducted in the absence of any commercial or financial relationships that could be construed as a potential conflict of interest.

Publisher's note

All claims expressed in this article are solely those of the authors and do not necessarily represent those of their affiliated organizations, or those of the publisher, the editors and the reviewers. Any product that may be evaluated in this article, or claim that may be made by its manufacturer, is not guaranteed or endorsed by the publisher.

Supplementary material

The Supplementary Material for this article can be found online at: https://www.frontiersin.org/articles/10.3389/feart.2022.1076076/full#supplementary-material

References

Anderson, E. M. (1951). *The dynamics of faulting and dyke formation with applications to britain*. Second edition ed. Oliver and Boyd, Edinburgh.

Anggara, F., Sasaki, K., and Sugai, Y. (2016). The correlation between coal swelling and permeability during CO2 sequestration: A case study using kushiro low rank coals. *Int. J. Coal Geol.* 166, 62–70. doi:10.1016/j.coal.2016.08.020

Brown, E. T., and Hoek, E. (1978). Trends in relationships between measured *in-situ* stresses and depth. *Int. J. Rock Mech. Min. Sci. Geomechanics Abstr.* 15, 211–215. doi:10.1016/0148-9062(78)91227-5

Bustin, R. M., and Clarkson, C. R. (1998). Geological controls on coalbed methane reservoir capacity and gas content. *Int. J. Coal Geol.* 38, 3–26. doi:10.1016/s0166-5162(98)00030-5

Bustin, R. M. (1997). Importance of fabric and composition on the stress sensitivity of permeability in some coals, northern sydney basin, Australia: Relevance to coalbed methane exploitation. *AAPG Bull.* 81, 1894–1908.

Cao, Y., Yang, X., He, M., Tian, l., and Shi, b. (2012). *Evaluation and development technology of pilot Project selection for coalbed methane in low-rank coals of the Fukang mining area, Xinjiang uygur autonomous region*. Xinjiang Cleanseed New Energy Co., Ltd and Henan Polytechnic University, Jiaozuo, China 118.

Carroll, A. R., Graham, S. A., and Smith, M. E. (2010). Walled sedimentary basins of China. *Basin Res.* 22, 17–32. doi:10.1111/j.1365-2117.2009.00458.x

Chen, J., Zhao, C., Wang, Z., He, z., and Qin, Y. (1998). Organic geochemical characteristics of oil, gas and source rocks of Jurassic coal measures in Northwestern China. *Geol. Rev.* 44, 149–158.doi:10.1016/j.jnggs.2019.11.003

Chen, S., Tang, D., Tao, S., Xu, H., Li, S., Zhao, J., et al. (2017). *In-situ* stress measurements and stress distribution characteristics of coal reservoirs in major coalfields in China: Implication for coalbed methane (CBM) development. *Int. J. Coal Geol.* 182, 66–84. doi:10.1016/j.coal.2017.09.009

Chen, S., Tang, D., Tao, S., Xu, H., Zhao, J., Fu, H., et al. (2018). *In-situ* stress, stress-dependent permeability, pore pressure and gas-bearing system in multiple coal seams in the Panguan area, Western Guizhou, China. *J. Nat. Gas Sci. Eng.* 49, 110–122. doi:10.1016/j.jngse.2017.10.009

Dawson, G. K. W., and Esterle, J. S. (2010). Controls on coal cleat spacing. *Int. J. Coal Geol.* 82, 213–218. doi:10.1016/j.coal.2009.10.004

Faiz, M., Saghafi, A., Sherwood, N., and Wang, I. (2007). The influence of petrological properties and burial history on coal seam methane reservoir characterisation, Sydney Basin, Australia. *Int. J. Coal Geol.* 70, 193–208. doi:10.1016/j.coal.2006.02.012

Fick, A. (1995). On liquid diffusion. *J. Memb. Sci.* 100, 33–38. doi:10.1016/0376-7388(94)00230-v

Fu, H., Tang, D., Pan, Z., Yan, D., Yang, S., Zhuang, X., et al. (2019). A study of hydrogeology and its effect on coalbed methane enrichment in the southern Junggar Basin, China. *Am. Assoc. Pet. Geol. Bull.* 103, 189–213. doi:10.1306/06071817190

Fu, H., Tang, D., Xu, H., Xu, T., Chen, B., Hu, P., et al. (2016). Geological characteristics and CBM exploration potential evaluation: A case study in the middle of the southern Junggar Basin, NW China. *J. Nat. Gas Sci. Eng.* 30, 557–570. doi:10.1016/j.jngse.2016.02.024

Fu, H., Yan, D., Yang, S., Wang, X., Wang, G., Zhuang, X., et al. (2021). A study of the gas-water characteristics and their implications for the coalbed methane accumulation modes in the Southern Junggar Basin, China. *Am. Assoc. Pet. Geol. Bull.* 105, 189–221. doi:10.1306/02282018273

Fu, H., Yan, D., Yang, S., Wang, X., Zhang, Z., and Sun, M. (2020). Characteristics of *in situ* stress and its influence on coalbed methane development: A case study in the eastern part of the southern Junggar Basin, NW China. *Energy Sci. Eng.* 8, 515–529. doi:10.1002/ese3.533

Gentzis, T. (2013). Coalbed methane potential of the Paleocene Fort Union coals in south-central Wyoming, USA. *Int. J. Coal Geol.* 108, 27–34. doi:10.1016/j.coal.2012.06.003

Graham, S. A., Brassell, S., Carroll, A. R., Xiao, X., Demaison, G., Mcknight, C. L., et al. (1990). Characteristics of selected petroleum source rocks, xianjiang uygur autonomous region, northwest China. *AAPG Bull.* 74, 493–512.

Haimson, B. C., and Cornet, F. H. (2003). ISRM suggested methods for rock stress estimation—Part 3: Hydraulic fracturing (HF) and/or hydraulic testing of pre-existing fractures (HTPF). *Int. J. Rock Mech. Min. Sci. (1997).* 40, 1011–1020. doi:10.1016/j.ijrmms.2003.08.002

Haimson, B., and Fairhurst, C. (1970). "*In-situ* stress determination at great depth by means of hydraulic fracturing," in *Rock mechanics - theory and practice*. Editor W. H. Somerton (Amer. Inst. Mining Eng.), New York, NY, USA 559–584.

Hendrix, M. S., Graham, S. A., Carroll, A. R., Sobel, E. R., Mcknight, C. L., Schulein, B. J., et al. (1992). Sedimentary record and climatic implications of recurrent deformation in the Tian Shan: Evidence from Mesozoic strata of the north Tarim, south Junggar, and Turpan basins, northwest China. *Geol. Soc. Am. Bull.* 104, 53–79. doi:10.1130/0016-7606(1992)104<0053:sracio>2.3.co;2

Hoek, E., and Brown, E. T. (1980). *Underground excavations in rock*. CRC Press London, UK.doi:10.1201/9781482288926

Hopkins, C. W., Frantz, J. H., Flumerfelt, R. W., and Spivey, J. P. (1998). Pitfalls of injection/falloff testing in coalbed methane reservoirs. SPE permian basin oil and gas recovery conference. Midland, TX, USA (Society of Petroleum Engineers). 9–24.

Hou, H. H., Shao, L. Y., Tang, Y., Li, Y. N., Liang, G. D., Xin, Y. L., et al. (2020). Coal seam correlation in terrestrial basins by sequence stratigraphy and its implications for palaeoclimate and palaeoenvironment evolution. *J. Earth Sci-China*, 1–24. doi:10.1007/s12583-020-1069-4

Hou, H., Liang, G., Shao, L., Tang, Y., and Mu, G. (2021). Coalbed methane enrichment model of low-rank coals in multi-coals superimposed regions: A case study in the middle section of southern Junggar Basin. *Front. Earth Sci.* 15, 256–271. doi:10.1007/s11707-021-0917-6

Hou, H., Shao, L., Li, Y., Liu, L., Liang, G., Zhang, W., et al. (2022a). Effect of paleoclimate and paleoenvironment on organic matter accumulation in lacustrine shale: Constraints from lithofacies and element geochemistry in the northern Qaidam Basin, NW China. *J. Petroleum Sci. Eng.* 208, 109350. doi:10.1016/j.petrol.2021.109350

Hou, H., Shao, L., Liang, G., Tang, Y., Zhang, H., and Zhang, J. (2022b). Repeated wildfires in the middle jurassic Xishanyao formation (aalenian and bajocian ages) in northwestern China. *Acta Geol. Sin.* 96, 1752–1763. doi:10.1111/1755-6724.14912

Hu, G., Zhang, S., Li, J., Li, J., and Han, Z. (2010). The origin of natural gas in the Hutubi gas field, Southern Junggar Foreland Sub-basin, NW China. *Int. J. Coal Geol.* 84, 301–310. doi:10.1016/j.coal.2010.10.009

Jasinge, D., Ranjith, P. G., and Choi, S. K. (2011). Effects of effective stress changes on permeability of latrobe valley Brown coal. *Fuel* 90, 1292–1300. doi:10.1016/j.fuel.2010.10.053

Jiang, B., Qu, Z., Wang, G. G. X., and Li, M. (2010). Effects of structural deformation on formation of coalbed methane reservoirs in Huaibei coalfield, China. *Int. J. Coal Geol.* 82, 175–183. doi:10.1016/j.coal.2009.12.011

Kang, J., Fu, X., Elsworth, D., and Liang, S. (2020). Vertical heterogeneity of permeability and gas content of ultra-high-thickness coalbed methane reservoirs in the southern margin of the Junggar Basin and its influence on gas production. *J. Nat. Gas Sci. Eng.* 81, 103455. doi:10.1016/j.jngse.2020.103455

Kang, J., Fu, X., Gao, L., and Liang, S. (2018). Production profile characteristics of large dip angle coal reservoir and its impact on coalbed methane production: A case study on the Fukang west block, southern Junggar Basin, China. *J. Petroleum Sci. Eng.* 171, 99–114. doi:10.1016/j.petrol.2018.07.044

Kang, J., Fu, X., Shen, J., Liang, S., Chen, H., and Shang, F. (2022). Characterization of coal structure of high-thickness coal reservoir using geophysical logging: A case study in southern Junggar Basin, Xinjiang, northwest China. *Natural Resources Research.* 31, 929–951, doi:10.1007/s11053-022-10018-x

Karacan, C. Ö., and Okandan, E. (2000). Fracture/cleat analysis of coals from Zonguldak Basin (northwestern Turkey) relative to the potential of coalbed methane production. *Int. J. Coal Geol.* 44, 109–125. doi:10.1016/s0166-5162(00)00004-5

Karacan, C. Ö., Ruiz, F. A., Cotè, M., and Phipps, S. (2011). Coal mine methane: A review of capture and utilization practices with benefits to mining safety and to greenhouse gas reduction. *Int. J. Coal Geol.* 86, 121–156. doi:10.1016/j.coal.2011.02.009

Li, G., Yan, D., Zhuang, X., Zhang, Z., and Fu, H. (2019). Implications of the pore pressure and *in situ* stress for the coalbed methane exploration in the southern Junggar Basin, China. *Eng. Geol.* 262, 105305. doi:10.1016/j.enggeo.2019.105305

Li, H., and Ogawa, Y. (2001). Pore structure of sheared coals and related coalbed methane. *Environ. Geol.* 40, 1455–1461. doi:10.1007/s002540100339

Li, H., Ogawa, Y., and Shimada, S. (2003). Mechanism of methane flow through sheared coals and its role on methane recovery☆. *Fuel* 82, 1271–1279. doi:10.1016/s0016-2361(03)00020-6

Li, J., Pan, D., Cui, R., Ding, E., Zhang, W., and Hu, M. (2016). Prediction of tectonically deformed coal based on lithologic seismic information. *J. Geophys. Eng.* 13, 116–122. doi:10.1088/1742-2132/13/1/116

Li, L., Liu, D., Cai, Y., Wang, Y., and Jia, Q. (2021). Coal structure and its implications for coalbed methane exploitation: A review. *Energy fuels.* 35, 86–110. doi:10.1021/acs.energyfuels.0c03309

Li, W., Li, X., Zhao, S., Li, J., Lu, S., Liu, Y., et al. (2022). Evaluation on carbon isotope fractionation and gas-in-place content based on pressure-holding coring technique. *Fuel* 315, 123243. doi:10.1016/j.fuel.2022.123243

Li, X., Fu, X., Yang, X., Ge, Y., and Quan, F. (2018). Coalbed methane accumulation and dissipation patterns: A case study of the Junggar Basin, NW China. *J. Asian Earth Sci.* 160, 13–26. doi:10.1016/j.jseaes.2018.04.003

Li, Y., Zhang, C., Tang, D., Gan, Q., Niu, X., Wang, K., et al. (2017). Coal pore size distributions controlled by the coalification process: An experimental study of coals from the Junggar, Ordos and Qinshui basins in China. *Fuel* 206, 352–363. doi:10.1016/j.fuel.2017.06.028

Liu, A., Fu, X., Wang, K., An, H., and Wang, G. (2013). Investigation of coalbed methane potential in low-rank coal reservoirs - free and soluble gas contents. *Fuel* 112, 14–22. doi:10.1016/j.fuel.2013.05.032

Liu, S., and Harpalani, S. (2013). Permeability prediction of coalbed methane reservoirs during primary depletion. *Int. J. Coal Geol.* 113, 1–10. doi:10.1016/j.coal.2013.03.010

Meng, Z., Zhang, J., and Wang, R. (2011). *In-situ* stress, pore pressure and stress-dependent permeability in the Southern Qinshui Basin. *Int. J. Rock Mech. Min. Sci. (1997).* 48, 122–131. doi:10.1016/j.ijrmms.2010.10.003

Moore, T. A. (2012). Coalbed methane: A review. *Int. J. Coal Geol.* 101, 36–81. doi:10.1016/j.coal.2012.05.011

Niu, Q., Cao, L., Sang, S., Wang, W., Zhou, X., Yuan, W., et al. (2021). Experimental study on the softening effect and mechanism of anthracite with CO2 injection. *Int. J. Rock Mech. Min. Sci. (1997).* 138, 104614. doi:10.1016/j.ijrmms.2021.104614

Niu, Q., Wang, Q., Wang, W., Chang, J., Chen, M., Wang, H., et al. (2022). Responses of multi-scale microstructures, physical-mechanical and hydraulic characteristics of roof rocks caused by the supercritical CO2-water-rock reaction. *Energy* 238, 121727. doi:10.1016/j.energy.2021.121727

Ou, C., Li, C., Zhi, D., Xue, L., and Yang, S. (2018). Coupling accumulation model with gas-bearing features to evaluate low-rank coalbed methane resource potential in the southern Junggar Basin, China. *Am. Assoc. Pet. Geol. Bull.* 102, 153–174. doi:10.1306/03231715171

Palmer, I., and John, M. (1998). How permeability depends on stress and pore pressure in coalbeds: A new model. *SPE Reserv. Eval. Eng.* 1, 539–544. doi:10.2118/52607-pa

Palmer, I. (2009). Permeability changes in coal: Analytical modeling. *Int. J. Coal Geol.* 77, 119–126. doi:10.1016/j.coal.2008.09.006

Pan, J., Lv, M., Hou, Q., Han, Y., and Wang, K. (2019). Coal microcrystalline structural changes related to methane adsorption/desorption. *Fuel* 239, 13–23. doi:10.1016/j.fuel.2018.10.155

Pan, J., Zhu, H., Hou, Q., Wang, H., and Wang, S. (2015). Macromolecular and pore structures of Chinese tectonically deformed coal studied by atomic force microscopy. *Fuel* 139, 94–101. doi:10.1016/j.fuel.2014.08.039

Pan, Z., Connell, L. D., and Camilleri, M. (2010). Laboratory characterisation of coal reservoir permeability for primary and enhanced coalbed methane recovery. *Int. J. Coal Geol.* 82, 252–261. doi:10.1016/j.coal.2009.10.019

Pan, Z., and Connell, L. D. (2011). Modelling of anisotropic coal swelling and its impact on permeability behaviour for primary and enhanced coalbed methane recovery. *Int. J. Coal Geol.* 85, 257–267. doi:10.1016/j.coal.2010.12.003

Pashin, J. C. (2010). Variable gas saturation in coalbed methane reservoirs of the Black Warrior Basin: Implications for exploration and production. *Int. J. Coal Geol.* 82, 135–146. doi:10.1016/j.coal.2009.10.017

Pillalamarry, M., Harpalani, S., and Liu, S. (2011). Gas diffusion behavior of coal and its impact on production from coalbed methane reservoirs. *Int. J. Coal Geol.* 86, 342–348. doi:10.1016/j.coal.2011.03.007

Rice, C. A., Flores, R. M., Stricker, G. D., and Ellis, M. S. (2008). Chemical and stable isotopic evidence for water/rock interaction and biogenic origin of coalbed methane, Fort Union Formation, Powder River Basin, Wyoming and Montana U.S.A. *Int. J. Coal Geol.* 76, 76–85. doi:10.1016/j.coal.2008.05.002

Rice, D. D. (1993). Composition and origins of coalbed gas, 159–184. *SG 38: Hydrocarbons from coal.* U.S. Department of Energy Office of Scientific and Technical Information USA

Scott, S., Anderson, B., Crosdale, P. J., Dingwall, J., and Leblang, G. (2007). Coal petrology and coal seam gas contents of the Walloon Subgroup -Surat Basin, Queensland, Australia. *Int. J. Coal Geol.* 70, 209–222. doi:10.1016/j.coal.2006.04.010

Smyth, M., and Buckley, M. J. (1993). Statistical analysis of the microlithotype sequences in the Bulli Seam, Australia, and relevance to permeability for coal gas. *Int. J. Coal Geol.* 22, 167–187. doi:10.1016/0166-5162(93)90025-6

Wang, B., Li, J., Zhang, Y., Wang, H., Liu, H., Li, G., et al. (2009). Geological characteristics of low rank coalbed methane, China. *Petroleum Explor. Dev.* 36, 30–34. doi:10.1016/s1876-3804(09)60108-7

Wang, Q., Xu, H., Tang, D., Yang, S., Wang, G., Ren, P., et al. (2022). Indication of origin and distribution of coalbed gas from stable isotopes of gas and coproduced water in Fukang area of Junggar Basin, China. *Am. Assoc. Pet. Geol. Bull.* 106, 387–407. doi:10.1306/09152120028

Wang, Z., Pan, J., Hou, Q., Niu, Q., Tian, J., Wang, H., et al. (2018). Changes in the anisotropic permeability of low-rank coal under varying effective stress in Fukang mining area, China. *Fuel* 234, 1481–1497. doi:10.1016/j.fuel.2018.08.013

Whiticar, M. J. (1999). Carbon and hydrogen isotope systematics of bacterial formation and oxidation of methane. *Chem. Geol.* 161, 291–314. doi:10.1016/s0009-2541(99)00092-3

Whiticar, M. J. (1996). Stable isotope geochemistry of coals, humic kerogens and related natural gases. *Int. J. Coal Geol.* 32, 191–215. doi:10.1016/s0166-5162(96)00042-0

Wu, Q. (1989). Structural evolution and prospects of Junggar Basin. *Xinjiang Geol.* 4, 1–19.

Xu, C., Yang, G., Wang, K., and Fu, Q. (2021). Uneven stress and permeability variation of mining-disturbed coal seam for targeted CBM drainage: A case study in Baode coal mine eastern Ordos Basin China, 289. 119911: .*Fuel* doi:10.1016/j.fuel.2020.119911

Yang, Q., Liu, D. M., Huang, W. H., Che, Y., Hu, B. L., and Wei, Y. J. (2005). *Coalbed methane geology and resources comprehensive evaluation in northwest China*. Beijing, China: Geological Publication House.

Yang, S., and Tian, J. (2011). Characteristics of CBM reservoir in eastern part of Junggar Basin. *China Coalbed Methane* 8, 21–23.

Yao, Y., Liu, D., and Qiu, Y. (2013). Variable gas content, saturation, and accumulation characteristics of Weibei coalbed methane pilot-production field

in the southeastern Ordos Basin, China. *Am. Assoc. Pet. Geol. Bull.* 97, 1371–1393. doi:10.1306/02131312123

Yin, H. (2009). Prospect of exploration of CBM resources in Fukang coal mining area in Xinjiang and recommendations on its development. *China Coalbed Methane* 6, 16–18.

Yu, Y., and Wang, Y. (2020). Characteristics of low-rank coal reservoir and exploration potential in Junggar Basin: New frontier of low-rank CBM exploration in China. *J. Pet. Explor. Prod. Technol.* 10, 2207–2223. doi:10.1007/s13202-020-00923-3

Zhang, B., Deng, Z., Fu, X., and Yin, K. (2021). A study on three-phase gas content in coal reservoirs and coalbed methane-water differential distribution in the western Fukang mining area, Xinjiang, China. *ACS Omega* 6, 3999–4012. doi:10.1021/acsomega.0c05930

Zhang, T., Tao, S., Tang, D., Tang, S., Xu, H., Zhang, A., et al. (2021). Permeability anisotropy in high dip angle coal seam: A case study of southern Junggar Basin. *Nat. Resour. Res.* 30, 2273–2286. doi:10.1007/s11053-021-09831-7

Zhao, J., Tang, D., Xu, H., Li, Y., Li, S., Tao, S., et al. (2016). Characteristic of *in situ* stress and its control on the coalbed methane reservoir permeability in the eastern margin of the Ordos Basin, China. *Rock Mech. Rock Eng.* 49, 3307–3322. doi:10.1007/s00603-016-0969-1

Zhi, D., Xue, l., Wang, Y., Ou, C., Peng, W., Yang, D., et al. (2013). *Coalbed methane resource and exploration potential in Junggar Basin*. Beijing, China: Petroleum Industry Press.

Zhou, S., Liu, D., Cai, Y., and Yao, Y. (2016). Gas sorption and flow capabilities of lignite, subbituminous and high-volatile bituminous coals in the Southern Junggar Basin, NW China. *J. Nat. Gas Sci. Eng.* 34, 6–21. doi:10.1016/j.jngse.2016.06.039

frontiers | Frontiers in Earth Science

TYPE Original Research
PUBLISHED 16 January 2023
DOI 10.3389/feart.2022.1048042

OPEN ACCESS

EDITED BY
Zhenzhi Wang,
Henan Polytechnic University, China

REVIEWED BY
Chong Xu,
Guizhou Education University, China
Bing Jia,
Henan University of Urban Construction, China
Yanjun Meng,
Taiyuan University of Technology, China

*CORRESPONDENCE
Zhigang Du,
gangduzhi@163.com

†These authors have contributed equally to this work and share first authorship

SPECIALTY SECTION
This article was submitted to Economic Geology, a section of the journal Frontiers in Earth Science

RECEIVED 19 September 2022
ACCEPTED 20 October 2022
PUBLISHED 16 January 2023

CITATION
Huang Q, Du Z, Liu H, Niu Q, Fang H, Yang J and Lou M (2023), Investigation of cleat and micro-fracture and its aperture distribution in the coals of different ranks in North China: Relative to reservoir permeability.
Front. Earth Sci. 10:1048042.
doi: 10.3389/feart.2022.1048042

Investigation of cleat and micro-fracture and its aperture distribution in the coals of different ranks in North China: Relative to reservoir permeability

Qiang Huang[1†], Zhigang Du[1,2*†], Hewu Liu[3], Qinghe Niu[4], Huihuang Fang[3], Jinyang Yang[1] and Minghang Lou[1]

[1]School of Civil Engineering, Luoyang Institute of Science and Technology, Luoyang, China, [2]Yima Coal Corporation, Henan Energy Group Corporation, Sanmenxia, China, [3]School of Earth and Environment, Anhui University of Science and Technology, Huainan, China, [4]State Key Laboratory of Mechanical Behavior and System Safety of Traffic Engineering Structures, Shijiazhuang Tiedao University, Shijiazhuang, China

The apertures of cleats and micro-fractures in coal play an important role in the permeability of the coal bed. In this study, optical microscopy and scanning electron microscopy were used to investigate the morphology of cleats and micro-fractures and their apertures, distribution of minerals, and matrix/fracture interactions. The neighboring mineralized and unmineralized cleats suggest the possibility of multi-stage evolutionary processes of cleat formation during the coalification process. The micro-fracture distribution of coals is closely related to their components, including organic macerals and inorganic minerals. Micro-fractures are prone to developing at the junction surface of organic macerals or the surface of organic and inorganic minerals. A mineral-genetic micro-fracture can be classified as an intra-crystal micro-fracture, an extra-crystal micro-scale fracture, or a grain-edge micro-scale fracture. Compared with the low- and middle-ranking coals, cleat and micro-scale fractures in high-ranking coal are usually filled with carbonate minerals and clay minerals. Statistical analysis reveals that the aperture distribution of cleat and micro-fracture in coal shows a log-normal distribution. The aperture of cleat and micro-fracture shows a decreasing trend with increase in coal rank. For low-ranking coal, cleats contribute more to the permeability than micro-fractures. However, for the middle- and high-ranking coals, the contribution of cleats and micro-fractures to the coal reservoir permeability will be close. As the rank of coal increases, the degree of cleat contribution to reservoir permeability decreases, while the degree of micro-fracture contributing to the reservoir permeability increases. Possible reasons for the extremely low reservoir permeability in China may be the following: 1) subsurface cleats and micro-fractures close their apertures significantly due to the *in situ* geo-stress or 2) cleats and micro-fractures have better permeability in the geological history, which makes the precipitation of minerals decrease the coal reservoir permeability. Therefore, the acid solvent (e.g., HAc, HCl, and HF) added to the drilling or hydraulic fracturing fluid or the geo-stress relief technologies may be an effective way of enlarging the cleat or micro-fracture aperture and enhance the reservoir permeability for coalbed methane production.

KEYWORDS
coal, cleat, micro-fracture, permeability, statistical analysis

Introduction

In coal, fractures form the primary seepage passage for coalbed methane (CBM) migration out of the coalbed, which plays an essential role in the successful production of CBM (Heriawan and Koike, 2015; Weniger et al., 2016; Zhang et al., 2016; Shi et al., 2018; Wang et al., 2018; Wang et al., 2021; Du et al., 2022). At present, enhanced measures commonly used in the development of CBM production, including the technology of hydraulic fracturing or foam fracturing, are primarily intended to create fracture channels or fracture networks in the coalbed.

Due to the importance of fractures in coal, scholars have performed extensive investigations into the fracture attributes, including the aperture, appearance, extension, and distribution characteristics. Usually, cleats refer to systematic fractures in coal beds since miners adopted the term in the early 19th century (Kendall and Briggs, 1933). In all the factors that can affect the gas transport of CBM production, the permeability of cleat systems has the most influence (Niu et al., 2021; Du et al., 2022). Pan et al. (2014) noted that cleats are usually restricted to a single lithotype, while fractures can cross different lithotypes. Cleat apertures between 4 μm and 50 μm may be optimal for CBM production, based on the San Juan Basin coals. Larger apertures may lead to high permeability as well as high water production, which is detrimental to economic production (Scott, 2002). Sapiie et al. (2014) applied 2D and 1D methods to determine the distributions of cleat spacing and found a power-law relationship in Indonesian coal cleats. Cleat apertures in the subsurface are smaller than in unstressed surface samples, but core samples at the surface approximate the aperture.

With the development of advanced testing technology, the contribution of micro-fracture to the permeability of coalbed has attracted the attention of many scholars. Gamson et al. (1993) studied the low- and middle-ranking coals in the Bowen Basin, Australia. They defined micro-fractures in the coal as those that are invisible to the naked eye and that have an aperture of 0.05–20 μm and micro-permeability. Karacan and Okandan (2000) studied middle-ranking coal in the Zonguldak Basin of Turkey and found that the micro-fractures often communicate with the cleats in the coal. Yao et al. (2010) studied mass samples (including low-, middle-, and high-ranking coals) in North China and found that the micro-fracture density in the coal is closely related to the rank of the coal. Gong et al. (2010) used CT image analysis technology and found that the micro-fracture aperture in the coal can reach 182.62 μm. Kumar et al. (2011) proposed using microwave energy to induce fractures and increase cleat apertures in coal. Mohamad and Katsuaki (2015)studied low-ranking coal in Indonesia and concluded that the micro-fracture development in coal is closely related to the mineral components. Taking coals suffering from different degrees of geological deformation, Du et al. (2019) examined the permeability of cleats and micro-fractures in the coal using statistical methods and found that the permeability of the cleat (about 1–100 mD) was much larger than that of the micro-fracture (about 0.01–1 mD).

On the whole, earlier works have conducted a wide range of research studies on fractures in coal. In addition to the study of cleats, research on micro-fractures is increasingly active in recent years. Quantitative approaches have been used to express the relationship between coal fractures and permeability. In the classical permeability parallel-plate fracture model, the permeability of the coal can be written as follows:

$$k = \frac{(84.4 \times 10^5)x^3}{s}, \quad (1)$$

where k is fracture permeability (D), x is the aperture of the fracture between two fracture surfaces (cm), and s is the fracture space. This relationship indicates that the fracture aperture, x, has a significant influence on permeability, as it is raised to the third power of the permeability.

A better understanding of the cleat and the micro-fracture structure, especially the aperture, is essential for evaluating the permeability of the coal reservoir and the economic aspects of CBM exploration and exploitation (Nalendra et al., 2020). At present, the distribution of fracture apertures and their effects on fluid flow in the rock are attracting more attention, but little work has focused on this issue in coal (Yang et al., 2012; Rutqvist et al., 2018; Brixel, 2020). This study seeks to provide a further understanding of the fracture attribute of coal and its permeability. The experiment samples were prepared in the way described by Du et al. (2019). The cleat and micro-fracture characteristics and their aperture distribution to the coal reservoir permeability are investigated for coals of different ranks in North China. The implications of this for the CBM exploration and exploitation are also discussed.

Materials and methods

Sample collection

In this study, 50 coal samples were collected. The locations of the samples are shown in Figure 1. These include low-ranking coal from the Shendong mining area of Shaanxi Province, middle-ranking coal from the Pingdingshan mining area of Henan Province and high-ranking coal from the Qinshui Basin of Shanxi Province.

Basic coal analyses, including vitrinite reflectance measurements, petrographic composition analysis, mineral

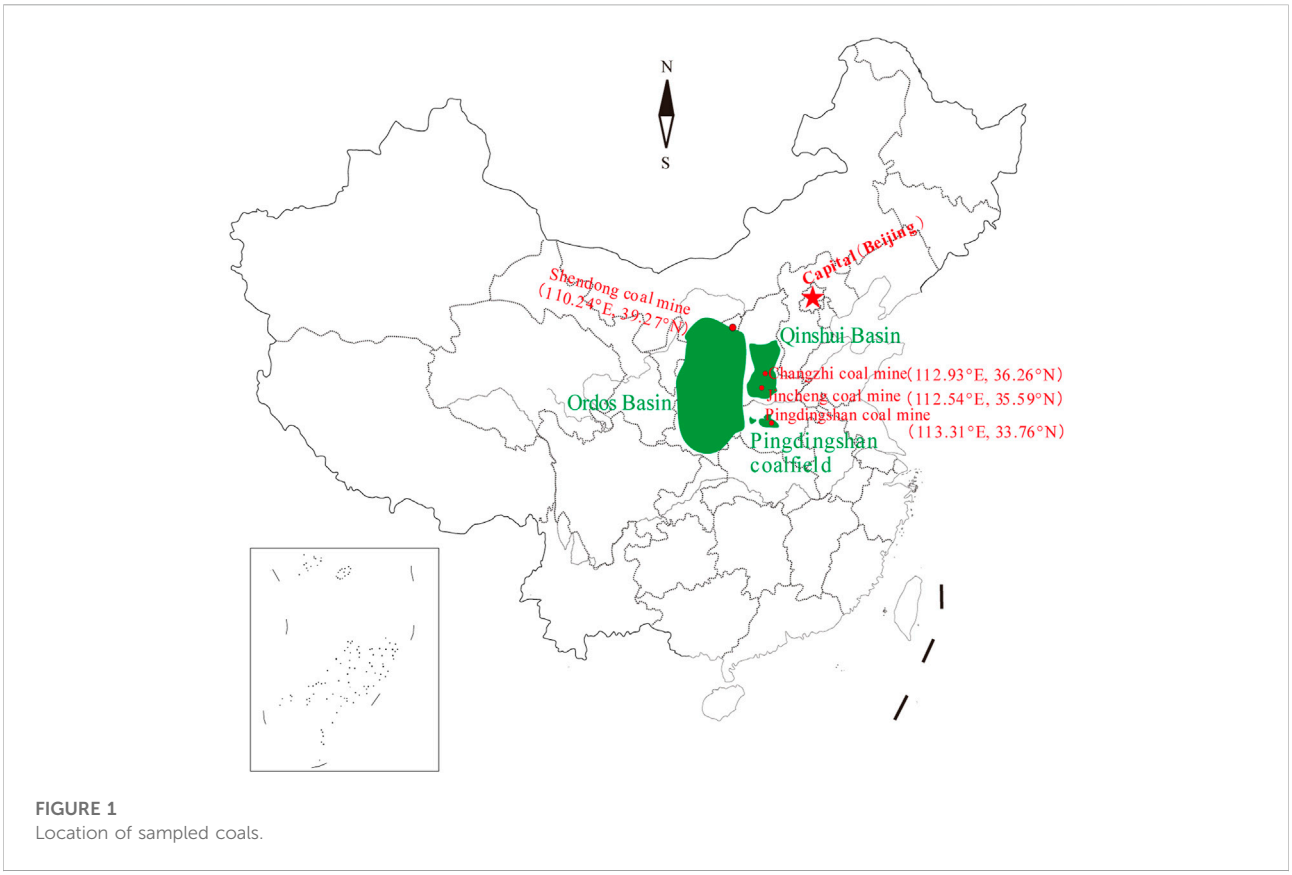

FIGURE 1
Location of sampled coals.

matter, micro-fracture frequency, and orientation determination, were performed for all these samples by using the standard methods described in the previous research (Li et al., 2015; Du et al., 2019). These methods are here briefly described. The coal blocks were crushed, and polished sections were prepared for vitrinite reflectance determination (with 500 points) and petrographic composition analysis. Chemical compositions of mineral matter were determined using SEM-EDS on naturally broken surfaces. The original micro-fracture frequency was investigated using optical microscopy.

The collected coal samples were assigned designations, as follows: Shendong sample (SD), Pingdingshan sample (PDS), and Qinshui sample (QS). In terms of coal quality (Table 1), the sulfur content in the SD and PDS samples was higher than in the QS sample. In the petrographic composition (Table 2), all of the coals mainly consisted of vitrinite maceral. A comparison shows that there was more inertinite maceral in the PDS sample. The coals were typically richer in vitrinite than inertinite macerals, with more than 80% vitrinite and 10–20% inertinite in most of the samples studied. Liptinite was usually present as only a small fraction (0–3.4%) of the macerals in three of the coals (samples B1, B3, and B4), while the others had no liptinite. The ash yield of the coals varied from 4.34% to 17.44%, and fixed carbon varied from 75.06 to 85.94%.

Sample preparation

Studies of fractures in coal have been performed with sample preparation randomly or arbitrarily by small particle samples. Due to the arbitrariness of the sample preparation, there are no reference standards to systematically classify micro-scale fractures in the coal. Cleat as endogenous fractures, formed during the process of coalification, has good continuity, and face cleat (long fracture) and butt cleat (short fracture) can be clearly distinguished in a hand specimen (Figure 2). Therefore, taking the direction of the cleat in the coal as a positioning standard, an oriented sample was prepared.

Fractures at the edge of the sample are considered damage-induced and were not used in the analysis. To minimize these fractures, the non-destructive method of a diamond wire cutting machine was used. The collected coal samples were prepared as follows: first, the oriented block samples (width 50 mm × length 80 mm × thickness 10–15 mm) were cut from the collected samples with the diamond wire cutting machine along the direction of the face cleat and butt cleat (Figure 3). The cutting speed of the diamond wire cutting machine was 0.02 m/s. The oriented samples (width 1 × length 1 × thickness 0.5 cm) were also

TABLE 1 Coal quality data of the sampled coals.

Sample	Proximate analysis (wt%, adb)				Element analysis (%)					Density 10^3 kg/m^3
	M_{ad}	A_d	V_{daf}	FC_{ad}	$S_{t.d}$	O_{daf}	C_{daf}	H_{daf}	N_{daf}	
SD	13.90	7.69	39.64	47.94	0.79	20.30	73.18	4.48	1.18	1.52
PDS	1.01	6.10	16.63	77.49	0.40	3.40	90.51	4.39	1.27	1.31
QS	1.47	8.51	5.93	84.09	0.39	4.42	90.77	3.74	0.64	1.44

TABLE 2 Petrographic composition data of the sampled coals.

Sample	Formation	$R_{o,max}$ %	Petrographic analysis (vol.%, mmf)			
			Vitrinite vol.%	Liptinite vol.%	Inertinite vol.%	Mineral vol.%
SD	Middle-lower Jurassic (J_2y)	0.56	80	1	7	12
PDS	Lower Permian (P_1sh)	1.32	74	0	19	7
QS	Lower Permian (P_1sh)	2.75	93	0	2.0	5

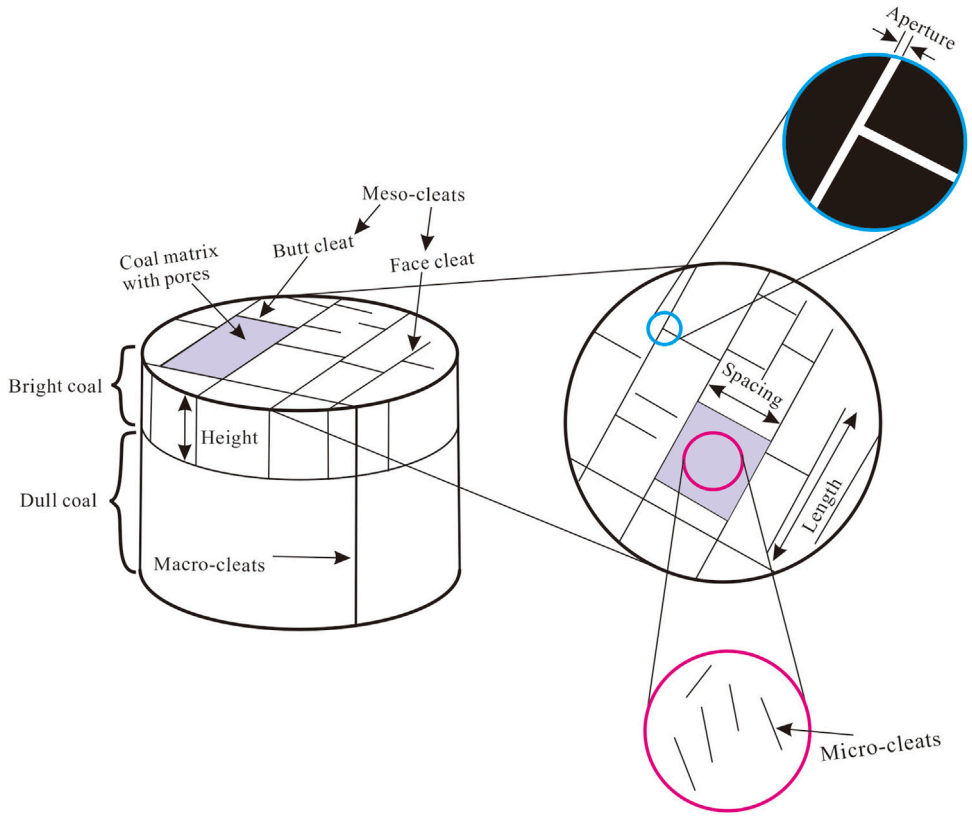

FIGURE 2
Fracture patterns in the coal (revised from Laubach et al., 1998).

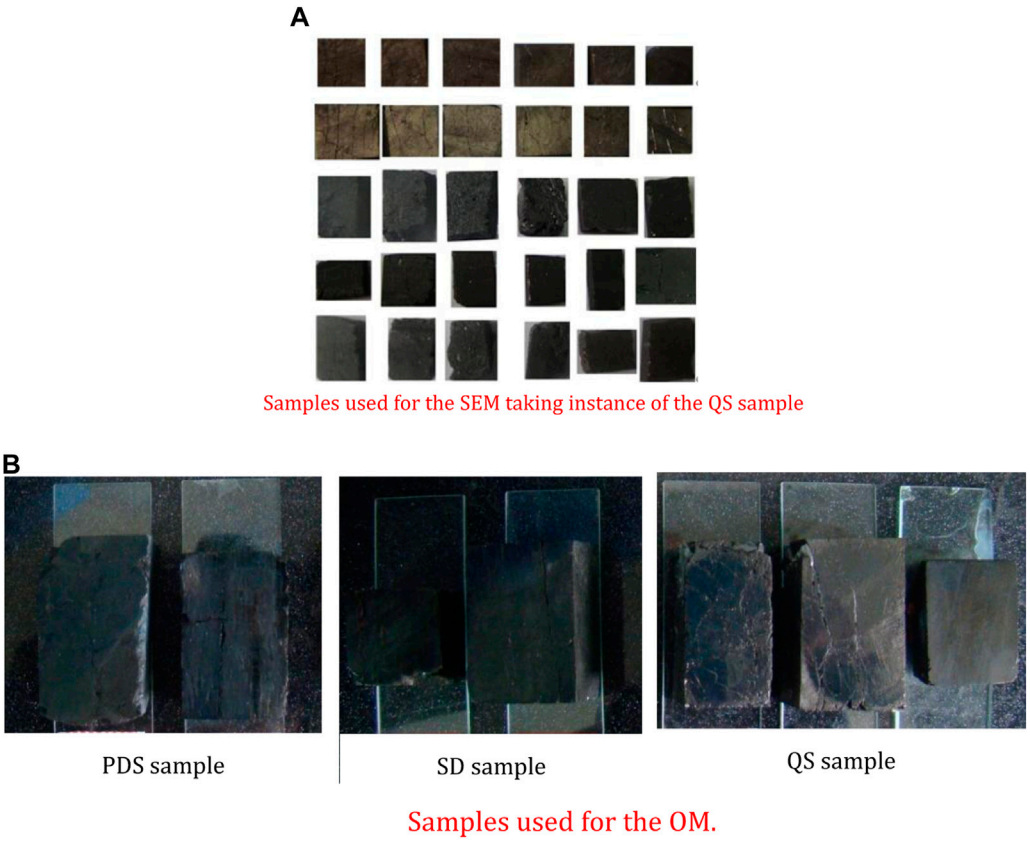

FIGURE 3
Prepared oriented coal samples.

prepared. Then, these samples were gold coated (Figure 3A) and polished (Figure 3B) for study by scanning electron microscopy (SEM) and optical microscopy (OM).

To interpret the coal micro-structure, oriented block samples are the best method of examining a small, specific part of a given sample in three dimensions: 1) the face cleat, 2) the butt cleat, and 3) the bedding. The major advantages of using this technique are that it allows observation of 1) coal micro-structure in three dimensions and therefore provides information on the shape, size, and cross-sectional area of the micro-structures and their bearings to the face and butt cleat and bedding; 2) fracture aperture, orientation, and continuity; and 3) the distribution of the micro-fracture and its relationship to the pore or cleat.

Apparatus and methods

In this study, the combined methods of OM and SEM were adopted. The OM method can be used to observe the micro-fractures in the coal. Its model is Leica DM4 P with a magnification of eyepiece 10× and a magnification of objective lens of 5×, 10×, 20×, 50×, and 100×. Then, with the eyepiece and the objective lens, a maximum magnification of 1000× imaging can be achieved. In addition, the SEM method was also adopted to study the fractures in coal. Its model is Quanta 250 with a function of magnification imaging of 1 million times. This can be taken to observe the nano-fracture in coal. An X-ray energy spectrometer is attached to this instrument, which helps recognize the minerals.

In the results section of this study, frequency diagrams of the cleat and micro-fracture aperture are compared between coals of different ranks. The fracture aperture, which contributes to the permeability of the coal reservoir, can be fitted to an appropriate probability distribution. In the case of a coal fracture aperture, several probability distributions are available to describe such data; they vary significantly in mathematical complexity and the number of parameters that require fitting. Minitab® 17, for instance, has over 20 distributions that can be readily tested. The log-normal distribution of fracture aperture of rock was previously reported by Snow (1968). According to the results

10.3389/feart.2022.1048042

TABLE 3 Probability distributions analyzed in the present work.

Distribution	Probability distribution function	Cumulative distribution function	Skewness	Kurtosis
Normal $x \sim N(\mu, \sigma^2)$	$P(x) = \frac{1}{\sqrt{2\pi}\sigma} exp\left[-\frac{(x-\mu)^2}{2\sigma^2}\right]$	$t = x^{\lambda} \text{for} \lambda \neq 0$ $C(x) = \int_0^x \frac{1}{\sqrt{2\pi}\sigma} exp\left[-\frac{(t-\mu)^2}{2\sigma^2}\right]dt$	$\nu_{1-N} = E[(x - E(x))^3]/(D(x))^{3/2}$	$\nu_{2-N} = E[(x - E(x))^4]/(\sigma(x))^{3/2}t$
Log-normal $Ln(x) \sim N(\mu, \sigma^2)$	$P(x) = \frac{1}{\sqrt{2\pi}\sigma} exp\left[-\frac{(\ln x-\mu)^2}{2\sigma^2}\right]$	$C(x) = \int_0^{\ln x} \frac{1}{\sqrt{2\pi}\sigma} exp\left[-\frac{(t-\mu)^2}{2\sigma^2}\right]dt$	$\nu_{1-L} = E[(Ln(x) - E(Ln(x)))^3]/(D(Ln(x)))^{3/2}$	$\nu_{2-L} = E[(Ln(x) - E(Ln(x)))^4]/(\sigma(Ln(x)))^{3/2}$
Square root $\sqrt{x} \sim N(\mu, \sigma^2)$	$P(x) = \frac{1}{\sqrt{2\pi}\sigma} exp\left[-\frac{(\sqrt{x}-\mu)^2}{2\sigma^2}\right]$	$C(x) = \int_0^{\sqrt{x}} \frac{1}{\sqrt{2\pi}\sigma} exp\left[-\frac{(t-\mu)^2}{2\sigma^2}\right]dt$	$\nu_{1-S} = E[(\sqrt{x} - E(\sqrt{x}))^3]/(D(\sqrt{x}))^{3/2}$	$\nu_{2-S} = E[(\sqrt{x} - E(\sqrt{x}))^4]/(\sigma(\sqrt{x}))^{3/2}t$

from the rock, the normal, logarithmic normal, and square root distributions were selected. The distributions and their transformations are listed in Table 3. All of these are two-parameter distributions, although some have three-parameter versions as well. The maximum likelihood method was used to estimate these parameters.

Results and discussion

Cleats and micro-structures in coals

Cleats commonly show little shear offset and are, therefore, opening-mode fractures (Solano et al., 2007; Sapiie et al., 2014). Previous studies of coals using scanning electron microscopy (SEM) show a range of micro-structures between the micro-pores and the cleat system. To characterize cleats and micro-structures in coals (Figure 4), a line is placed perpendicular to the cleat or micro-fracture direction. Fracture aperture is determined from the opposite fracture plane in this way.

The occurrence of nanometer-sized pores or cavities (209.2 to 456.8 nm) on the cleat suggests that it is a gas drainage passage in the transmissibility of methane from the coal matrix to the cleat. Among cleats in coal, the face cleat is the most conspicuous fracture seen in the hand specimen and penetrates the coal at right angles to the bedding. The butt cleat, in comparison, is less pervasive and is confined to areas between the face cleats and typically penetrates the coal at right angles to the face cleat and bedding. Both the face and butt cleats commonly occur as orthogonal sets, oriented perpendicular to the bedding. Characteristically, face and butt cleats are of a planar shape, varying in vertical extent or height (L-5 mm) and width (0.1–2 mm), and are usually spaced 0.3–2 mm apart. In all of the coals examined, cleats are infilled with clays, quartz, or calcite, offering little porosity and permeability, which will be discussed in detail as follows.

A cleat network can be simply classified into two orthogonal fractures (face and butt cleats). Both face and butt cleats are oriented perpendicular to bedding, but butt cleats usually abut against face cleats. Thus, face cleats are through-going, while butt cleats end at intersections with face cleats. Cleats form in response to the physical and chemical processes during coalification. Fracture growth modeling shows that this orthogonal relationship can arise under biaxial extension (Olson et al., 2009), a circumstance that can accompany the conditions under which cleats form. Laubach et al. (1998) gave a thorough review of the origins of cleats as well as a discussion of cleat-forming mechanisms. The coupling action of the fluid pressure and *in situ* stress determines the development of cleats and micro-fractures in the coal, which is also related to the coal types, rank, maceral, and coal thickness.

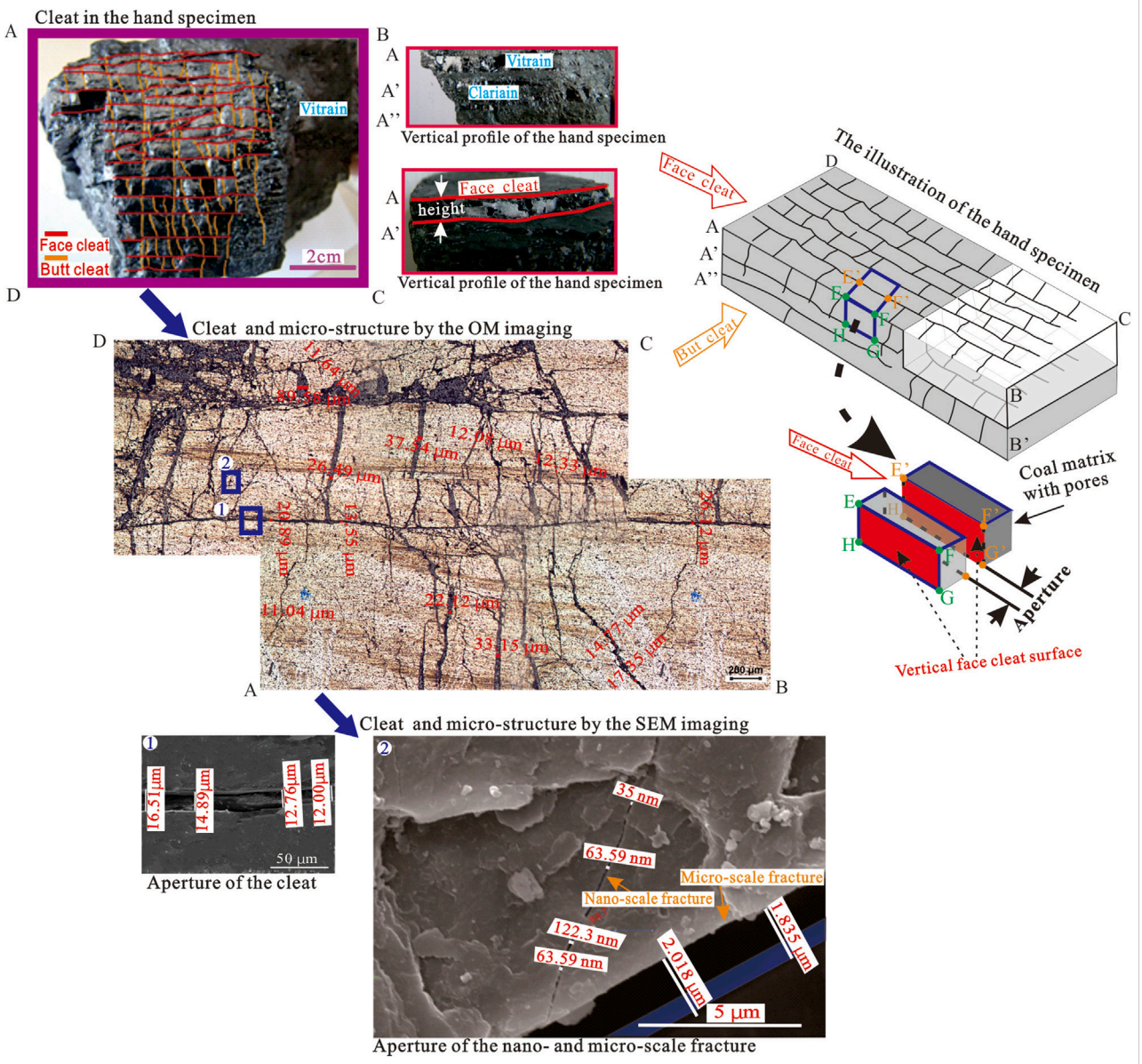

FIGURE 4
Cleats and micro-structures in coal.

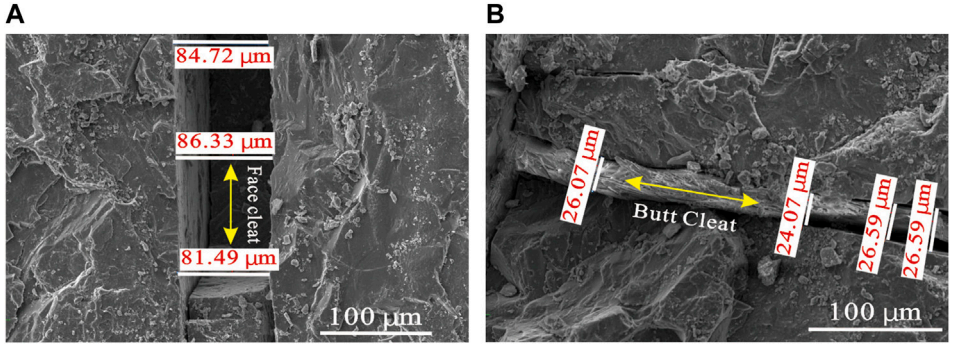

FIGURE 5
Mineralized face cleat and butt cleat: **(A)**, face cleat; **(B)** butt cleat.

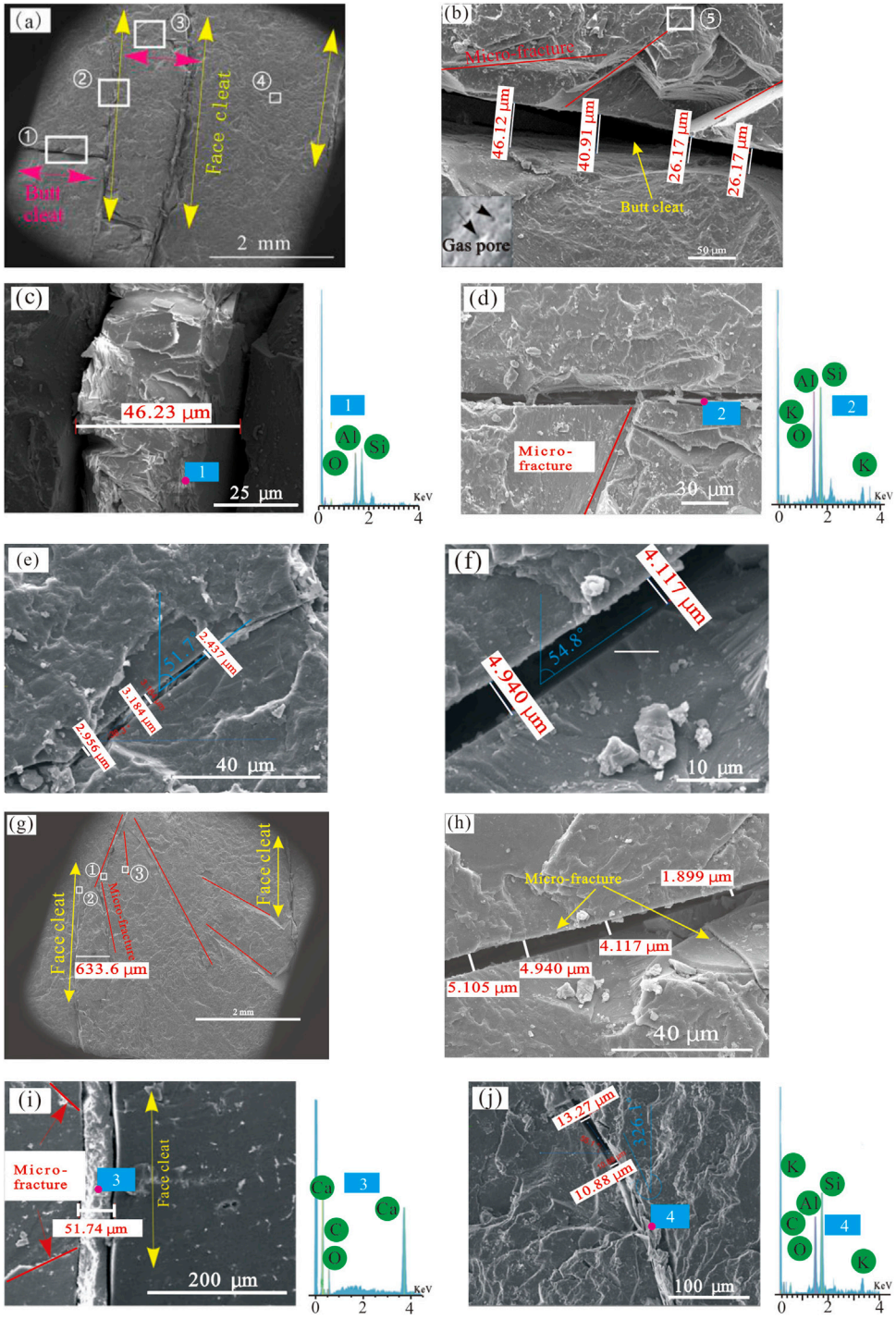

FIGURE 6
Cleat and micro-fractures in the coal: **(a)**, face cleat and butt cleat; **(b)**, enlarged view of point 1 in Figure 6(a); **(c)**, enlarged view of point 2 in Figure 6(a); **(d)**, enlarged view of point 3 in Figure 6(a); **(e)**, enlarged view of point 4 in Figure 6(a); **(f)**, enlarged view of point 5 in Figure 6(b); **(g)**, face cleat and micro-fracture; **(h)**, enlarged view of point 1 in Figure 6(g); **(i)**, enlarged view of point 2 in Figure 6(g); **(j)** enlarged view of point 3 in Figure 6(g).

Cleat and micro-fractures related to the inorganic non-metallic mineral

Figures 5A,B show the mineralized face cleat and butt cleat in the QS sample, respectively. From a genetic perspective, the mineral matter in coal, similar to the organic matter, is a product of the processes associated with coal formation, as well as changes in subsurface fluids and other aspects of sediment diagenesis (Golab et al., 2013). Cleat minerals are not intimately associated with coal, unlike detrital and early diagenetic (syngenetic) minerals. The occurrence of cleat minerals is of great importance for determining the evolution of the pore fluids and the age of the cleat itself. Cleat minerals may form due to several different processes, and the formation and migration of CBM and other hydrocarbons generated during or after coalification may also be related to mineralization (Ward, 2002, 2016). Tectonism and geothermal activity can produce hydrothermal fluids, which can result in epigenetic mineralization and alteration of diagenetic minerals within coals (Saxby, 2000; Dai et al., 2014). At least, the mineralized cleats imply that cleats had better fluid conductivity during geological history, which is beneficial for the infiltration and migration of mineralized fluids and the precipitation of minerals in the stressed cleats. This further indicates that although cleat apertures in the subsurface are smaller than in unstressed surface samples, core samples at the surface approximate the apertures (Weniger et al., 2016).

Figure 6 shows the cleat and micro-fractures related to the inorganic non-metalic mineral. The minerals in the fractures were analyzed using an X-ray energy spectrometer attached to the SEM microscope. Figure 6A presents the overview of the orthogonal face cleat and butt cleat. Figure 6B shows the non-mineralized butt cleat, where several micro-fractures exist in communication with the cleats, and the micro-pores exist on the cleat surface; Figure 6C shows the mineralized face cleat. In this situation, the adjacently mineralized and unmineralized cleats suggest a multi-stage evolutionary process for cleat formation and fluid migration during coalification. The face cleat and butt cleat in Figures 6C,D are filled with kaolinite and illite, respectively. Regarding the genesis of minerals in the coal fractures, Spears and Caswell (1986) proposed that the precipitation of sulfides first occurs at an early stage of coalification. As the coalification progressed, quartz and clay minerals precipitated one after another. Finally, the clay mineral precipitates. The adjacent cleats are filled with two different minerals, which further indicates the multi-stage evolutionary characteristic of the cleat formation and fluid migration in its geological history.

From the results, it can be observed that the original fractures normally exist as two sets: one set of fractures is almost parallel to the bedding layer plane, and these fractures are most likely hydraulic fractures which by definition form *via* a different mechanism that is unrelated to cleats. The second set of fractures is closely perpendicular to the bedding plane, which is probably cleats. The coexistence of unmineralized and mineralized fractures in the coal means that the coal seam underwent structural deformation before chemical precipitation by hydrodynamics. However, many of the open fractures originate from structural deformations during coalification. The coal-bearing basin of North China underwent three-stage orogeny. Non-sealing faults and folds with axial striking NNE–SSW and near N–S are common, which were formed by the NW–SE compressional stresses during the Jurassic–Cretaceous Yanshanian Orogeny. After undergoing Indosinian orogeny, Yanshanian orogeny, and Himalayan orogeny, many tensile faults formed during these tectonic movements.

Two mechanisms are related to the origin of coal micro-fractures: coalification and post-coalification. Coalification is the origin of endogenous micro-fractures (endo-microfracture). By contrast, the post-coalification resulting from the extraneous stress deformation induces the formation of exogenous micro-fractures (exo-microfracture). Endo-microfracture was distinctly distinguished from the exo-microfracture in the frequency and morphology of the investigated coals. As shown in Figures 6E,J, the endo-microfracture is commonly characterized by the isolated distribution, whereas the exo-microfracture is characterized by the brittle fracturing appearance such as the dendritic (Figure 6B), step-shaped (Figure 6D), filamentous (Figure 6F), and turtleback (Figure 6H) textures. More importantly, in terms of the permeability contribution, the frequency of the micro-fractures, their morphology, the connectivity of the network, and the degree of mineral filling are important controls on coal permeability. This shows that most endo-microfractures are mineralized. By contrast, most exo-microfractures are unmineralized and randomly developed by high anisotropy within the coal. The different characteristics between exo-microfracture and endo-microfracture are responsible for their different effects on coal permeability. The endo-microfracture is commonly formed within certain macerals as a result of peat formation and coalification. Based on the results of coal macerals, coal lithotype, and coal facies analyses, it was found that these factors are strongly correlated to the development of endo-microfractures. For the endo-microfractures to form, two primary preconditions must be fulfilled for coal macerals or lithotypes: the high gas generation yield together with poor gas diffusibility (Yao and Liu, 2009).

Micro-fractures related to the inorganic metallic mineral

Coal consists of a variety of inorganic constituents (minerals and nonmineral inorganics) that are broadly referred to as

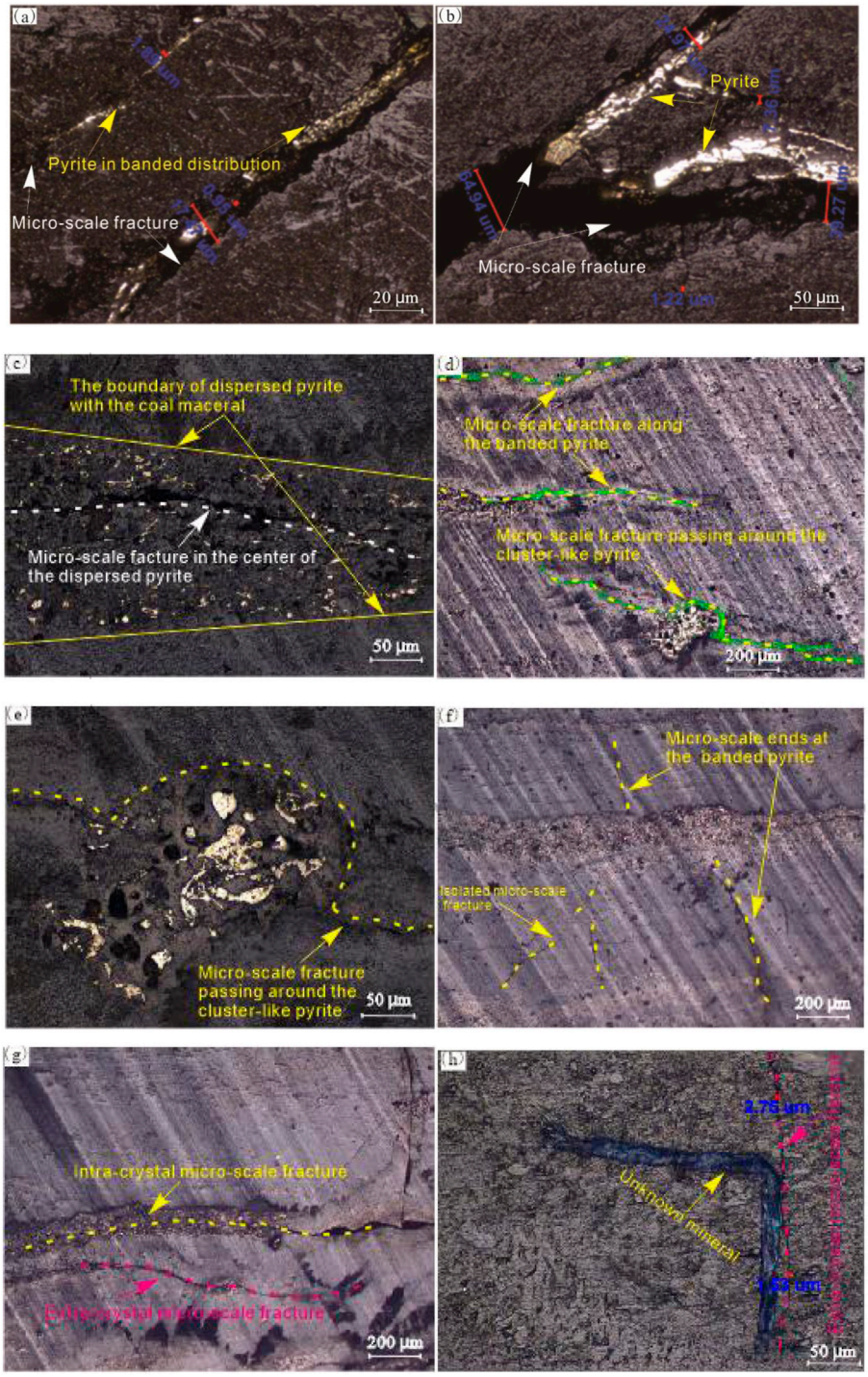

FIGURE 7
Micro-fractures to the inorganic metallic mineral: **(A)**, micro-fractures extending along the banded pyrite; **(B)**, micro-fractures bifurcated by the adjacent banded pyrite; **(C)**, micro-fractures extending along the center of the dispersed pyrite; **(D)**, micro-scale fractures extending around the edge of the cluster-like pyrite particles; **(E)**, 200-fold magnification of the Figure 7D; **(F)**, micro-fractures extending perpendicular to the banded pyrite; **(G)**, micro-fractures extending along the center of the banded pyrite; **(H)**, micro-fractures extending along with the banded mineral (unknown mineral).

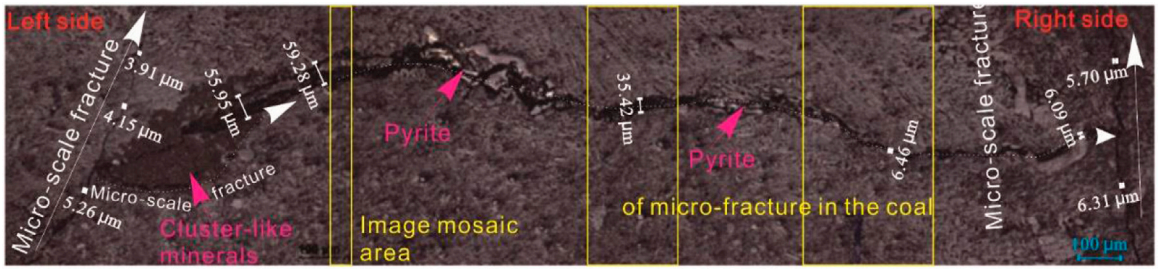

FIGURE 8
Propagation mode of micro-fracture in the coal.

mineral matter (Ward, 2002). It has been found that the extension modes of micro-fractures in coal are closely related to the occurrence of minerals. The presence of mineral matter may alter the way an induced fracture propagates through coal seams, as can the presence of pre-existing fractures. The induced fracture modes depend on the heterogeneity of the coal and the arrangement of the pre-existing macroscopic mineral bands, as well as the underground stresses. Thus, it is of great importance to study the mineral occurrence and its impact on fracture generation for CBM production.

Mineral-related micro-fractures can be classified into three types: intra-crystal micro-fractures (i.e., micro-fractures that completely developed within the mineral crystal particles), extra-crystal micro-fractures (i.e., micro-fractures that developed in the coal matrix and terminated in the mineral band or along with the mineral band), and grain edge micro-fracture (i.e., micro-fractures that developed along the edge of the particle). The mentioned three types of micro-scale fractures have been observed in the coals of SD-1, SD-2, PDS-1, and PDS-2, and their formation mechanisms were intimately associated with the occurrence form of pyrite in the coal.

Figure 7A shows the micro-fractures extending along the banded pyrite. Figure 7B shows the micro-fractures are bifurcated in the adjacent banded pyrite. Figure 7C shows the micro-fractures extending along the center of dispersed pyrite. Figure 7D shows the micro-scale fractures extending around the edge of the cluster-like pyrite particles. Figure 7E represents a 200-fold magnification of the marquee in Figure 7D to show the trace trajectory of micro-fracture development. Figure 7F shows the micro-fractures extending along the direction perpendicular to the banded pyrite. Figure 7G shows the micro-fractures extending along the center of the banded pyrite. Figure 7H shows the micro-fractures outside the crystal, and it extends along with the banded mineral (unknown mineral). Figure 8 shows the micro-fractures in the SD-1 samples. From the left view to the right view: first, the micro-fracture bifurcates at the edge of the cluster-like minerals and extends around this mineral and then extends along with the banded pyrite, eventually ending and being crossed by the vertically developed micro-fracture on the right side. The endo-microfractures are commonly formed by the processes of generation, accumulation, and centralized-release of gas from coal (Yao and Liu, 2009).

For coal, the organic compositions primarily include vitrinite maceral, liptinite maceral, and inertinite maceral. Among these, the vitrinite maceral and the liptinite maceral are brittle, whereas the inertinite maceral is somewhat ductile (Permana et al., 2013).By contrast, the mechanical properties of the organic micro-components are weaker relative to the inorganic components. The presence of inorganic micro-components in coal can cause mechanical differences between the interface of organic and inorganic components, which will make the interface boundary prone to fracturing (Li et al., 2015).

In mechanical properties, Young's modulus of pyrite is between 15 GPa and 30 GPa by the atomic force microscope contact probe testing (Cui et al., 2013). This is significantly higher than that of the coal matrix. For the pyrite present in the coal, it will improve the brittleness of the coal and affect the occurrence form of micro-fractures in the coal. At the boundary of coal maceral and pyrite, due to the differential elastic stiffness, tensile stress is formed within the pyrite particles. This finally induces the intergranular micro-fractures to be formed (Moustafa et al., 2004). In addition, due to the density difference between coal maceral and inorganic minerals, the cohesion of coal drops significantly, which makes the micro-fractures grow and extend along with the interface of coal maceral and inorganic minerals.

Micro-fractures related to the organic coal maceral

Bright coals with an abundance of brittle and fracture-prone vitrinite can become the host of many fractured flow paths during seam deformation. This makes bright coals more permeable than dull ones, which could result in more fracture-filling minerals when hydrothermal fluids or brine water flows through the seam (Permana et al., 2013). The micro-fracture development shows selectivity to the coal maceral, where the vitrinite maceral has a higher micro-fracture density for the coal, and the micro-

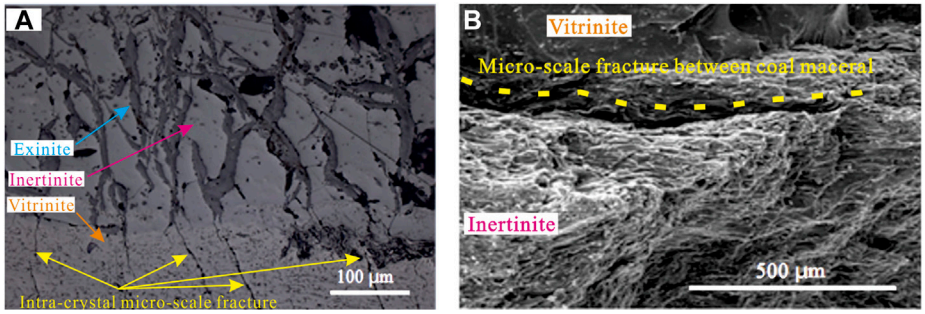

FIGURE 9
Micro-fractures developed in the coal maceral: **(A)**, vitrinite maceral; **(B)**, inertinite macerals.

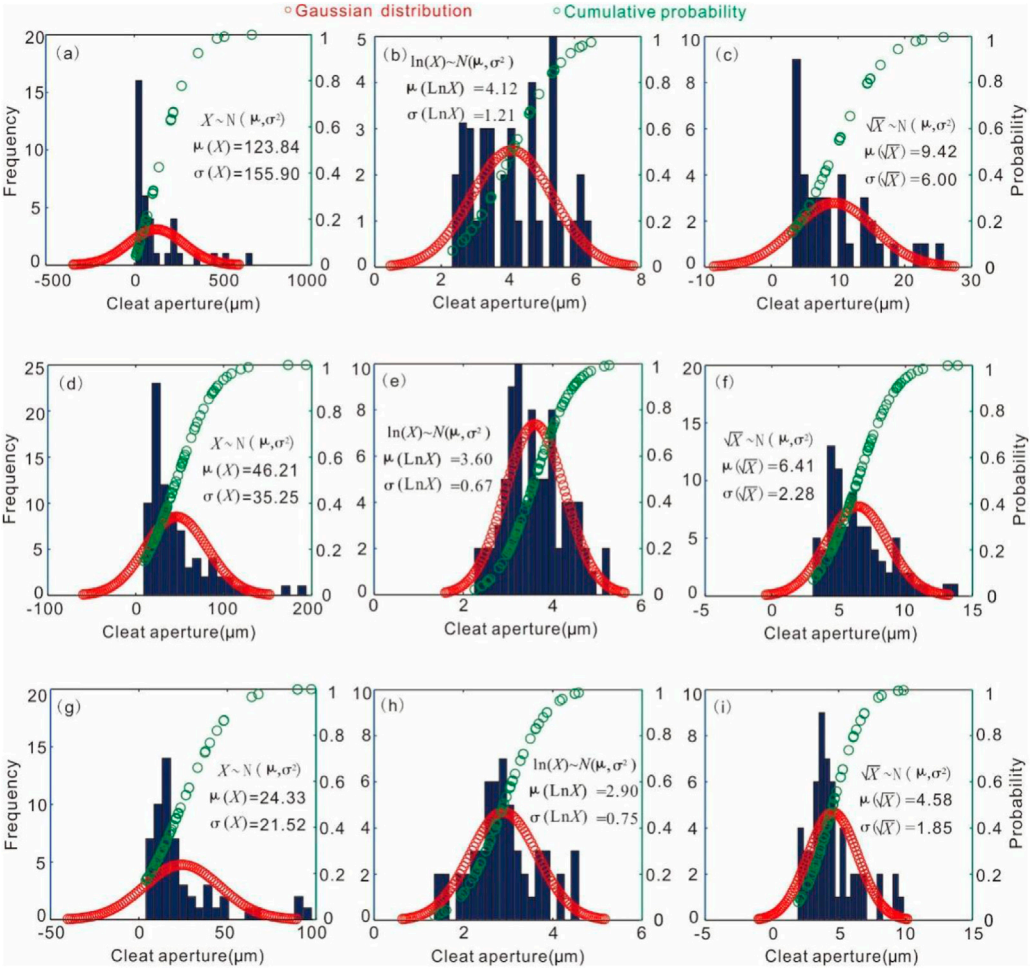

FIGURE 10
Cleat aperture distribution for the coals with different ranks: **(A–C)**, low-ranking coal; **(D–F)**, middle-ranking coal; **(G–I)**, high-ranking coal.

TABLE 4 Summary of fracture aperture goodness-of-fit statistics of coal with different ranks.

Fracture type	Coal sample	Statistical analysis	Expected aperture (μm)		Skewness (*S*)	Kurtosis (*K*)	Confidence	Interval probability		Quartile	Abundance
			Mean	Interval				P_1^{Cf}	P_2^{Cf}		
Cleat	Low-ranking coal	$x \sim N(\mu, \sigma^2)$	123.84	71.86–175.82	1.91	6.18	0.95	43.9%	87.1%	206.78	4–7 (5 cm)
		$Ln(x) \sim N(\mu, \sigma^2)$	4.12	3.72–4.53	0.28	1.89	0.95	65.5%	90.3%	206.43	
		$\sqrt{x} \sim N(\mu, \sigma^2)$	9.42	7.42–11.42	1.07	3.30	0.95	53.8%	90.6%	206.78	
	Middle-ranking coal	$x \sim N(\mu, \sigma^2)$	27.30	23.17–31.43	1.64	5.78	0.95	100%	100%	35.23	5–14 (5 cm)
		$Ln(x) \sim N(\mu, \sigma^2)$	3.11	2.98–3.25	0.35	2.40	0.95	100%	100%	35.16	
		$\sqrt{x} \sim N(\mu, \sigma^2)$	4.97	4.62–5.33	0.95	3.44	0.95	100%	100%	35.23	
	High-ranking coal	$x \sim N(\mu, \sigma^2)$	24.32	18.51–30.14	1.96	6.40	0.95	100%	100%	27.78	4–10 (5 cm)
		$Ln(x) \sim N(\mu, \sigma^2)$	2.90	2.69–3.10	0.27	2.86	0.95	99.8%	100%	27.66	
		$\sqrt{x} \sim N(\mu, \sigma^2)$	4.58	4.08–5.09	1.20	4.08	0.95	99.8%	100%	27.77	
Micro-fracture	Low-ranking coal	$x \sim N(\mu, \sigma^2)$	5.38	3.93–6.83	3.58	17.57	0.95	47.6%	99.1%	5.30	3–9 (200 μm)
		$Ln(x) \sim N(\mu, \sigma^2)$	1.33	1.14–1.51	0.51	3.63	0.95	63.9%	98.3%	5.30	
		$\sqrt{x} \sim N(\mu, \sigma^2)$	2.11	1.88–2.34	2.06	8.53	0.95	55.2	99.3%	5.30	
	Middle-ranking coal	$x \sim N(\mu, \sigma^2)$	4.37	3.62–5.11	1.73	6.46	0.95	56.6%	100%	6.10	4–11 (200 μm)
		$Ln(x) \sim N(\mu, \sigma^2)$	1.06	0.86–1.27	−0.97	4.55	0.95	70.1%	96.9%	6.10	
		$Ln(x+1) \sim N(\mu, \sigma^2)$	1.46	1.34–1.60	0.10	2.62	0.95	69.0%	99.2%	6.10	
		$\sqrt{x} \sim N(\mu, \sigma^2)$	1.91	1.74–2.08	0.61	3.29	0.95	65.0%	99.8%	6.11	
	High-ranking coal	$x \sim N(\mu, \sigma^2)$	4.22	3.27–5.17	4.08	23.62	0.95	56.1%	100%	5.51	3–7 (200 μm)
		$Ln(x) \sim N(\mu, \sigma^2)$	0.97	0.78–1.17	−0.91	5.50	0.95	72.7%	97.3%	5.50	
		$Ln(x+1) \sim N(\mu, \sigma^2)$	1.40	1.28–1.52	0.57	3.90	0.95	72.2%	99.3%	5.50	
		$\sqrt{x} \sim N(\mu, \sigma^2)$	1.83	1.66–2.01	1.68	8.25	0.95	66.7%	99.8%	5.50	

For cleats, P_1^{Cf} and P_2^{Cf} are the probability of aperture sizes less than 100 μm and 300 μm, respectively; for micro-fractures, P_1^{Mf} and P_2^{Mf} are the probability of aperture sizes less than 5 μm and 20 μm, respectively. Determination for the goodness-of-fit statistics model of aperture size distribution depending on whose kurtosis deviates little from value of *K*=3 and skewness deviates little from value of S=0.

10.3389/feart.2022.1048042

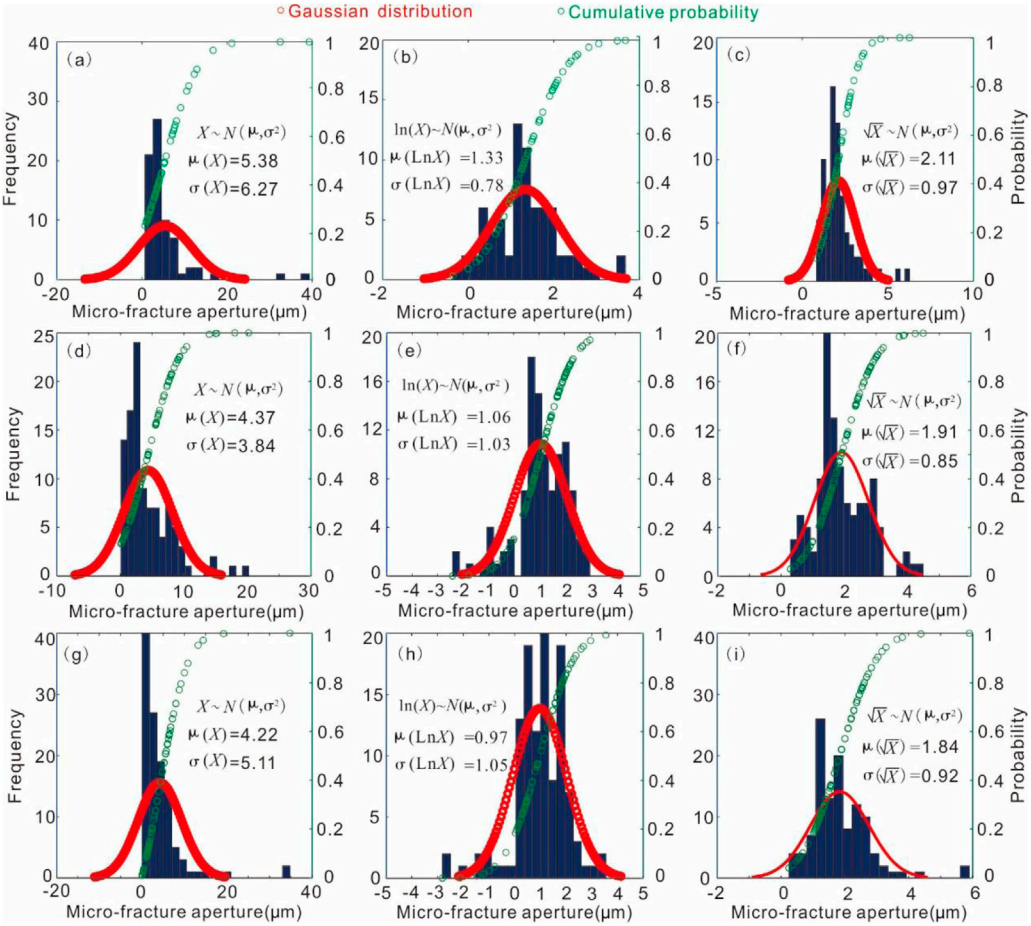

FIGURE 11
Micro-fracture aperture distribution for the coals with different ranks: **(A–C)**, low-ranking coal; **(D–F)**, middle-ranking coal; **(G–I)**, high-ranking coal.

fractures in the vitrinite maceral are interrupted at the location of their intersections to the liptinite and inertinite macerals (Figure 9A). Micro-fractures are prone to being formed along with the interface of coal maceral (Figure 9B).

For lignite of a low coal ranking, there is no self-generating high-pressure fluid. With the increase in metamorphic degree, especially in the middle-rank coal, there is more fluid in the coal pores. This decreases the liquid phase and increases the gas phase. Meanwhile, the porosity of coal decreases with the increase of metamorphic degree and the pore structure deteriorates, which hinders fluid expulsion out of the coal pores. Thus, the capillary pressure due to the existing gas-liquid two-phase fluid in the coal pores produces the local high pressure in the coal. This phenomenon forms a better choice for the vitrinite maceral, which has a high abundance of organic matter and a high potential for hydrocarbon generation. Consequently, vitrinite maceral carries more micro-fractures and endogenous fractures.

Statistical analysis of cleat and micro-fracture aperture and their permeabilities

Aperture distribution of cleat and micro-fracture

Figure 10 plots the aperture distribution for the cleat aperture of coals with different ranks. Figures 10A–C present the aperture frequency *versus* the normal distribution, the log-normal distribution, and the square root-normal distribution for the low-rank coal, respectively. Similarly, Figures 10D–F and Figures 10G–I plot the aperture frequency of cleat for the middle-rank coal and the high-rank coal, respectively. The statistical cylindrical diagram displays the aperture distributions of the cleat in the coal of different ranks are somewhat skewed. The determination

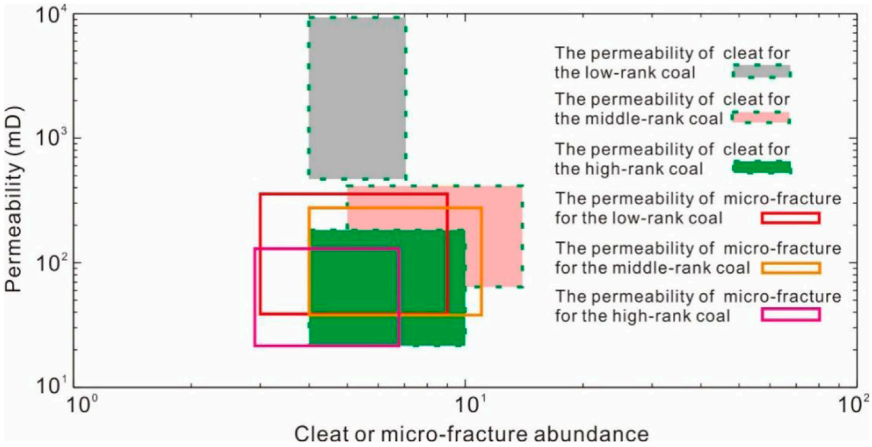

FIGURE 12
Permeability of cleat and micro-fracture for the coals of different ranks based on Weniger et al. (2016).

of the goodness-of-fit statistics model of aperture size distribution depends on four parameters as the mean value (μ), standard deviation (σ), kurtosis coefficient (K), and skewness coefficient (S). For the mean value (μ) and the standard deviation (σ) in the normal distribution and the square root-normal distribution cylindrical diagram, the cleat aperture will be negative for its two standard deviations from the mean value. Furthermore, their kurtosis coefficients and skewness coefficients deviate more from the value of K=3 and S=0, which constitute a standard for meeting a standard normal distribution (Table 4). This shows that the lognormal distribution can better descript the cleat aperture attribute, which is similar to the distribution law of fractures found in the rock (Snow, 1968). Comparingthe statistical results, cleat aperture attributes are further examined to determine the relationship between cleat aperture and coal rank. The statistical results show that the cleat apertures of low-, middle-, and high-ranking coals range from 41.26 to 92.76 μm, 19.69 to 25.79 μm, and 14.73 to 22.19 μm, respectively. Most cleat apertures are smaller than 300 μm. With the increase in coal ranking, the cleat aperture presents a decreasing trend.

Figure 11 plots the aperture distribution for the micro-fracture aperture field of coals with different ranks. Figure 11A plots aperture frequency *versus* the normal distribution of micro-fracture aperture size for low-ranking coal; and Figure 11B plots aperture frequency *versus* the lognormal distribution of micro-fracture aperture size for low-ranking coal. Figure 11C plots aperture frequency *versus* the square root-normal distribution of micro-fracture aperture size for low-ranking coal. As such, Figures 11D–F and Figures 11G–I plot the corresponding aperture frequency for middle-ranking coal and high-ranking coal, respectively. The aperture size of the micro-fracture is lower than that of the cleat by approximately an order of magnitude, and the aperture distributions are also somewhat skewed. The statistical cylindrical diagram shows that the log-normal distribution can best describe the micro-fracture aperture attribute. Determination from the skewness coefficient, data in the middle-rank coal and the high-rank coal appear to be square root-normally distributed. Actually, due to the nano-scale fracture present in the coal (88.2, 89.0, 171.2, 322.7, 400.1, 427.8, 515.8, and 639.5 nm in middle-ranking coal and 63, 230.5, 285.8, 305.6, 368.4, 456.8, 610, 630, and 712.4 nm in high-ranking coal), with an aperture size of less than 1 μm (i.e., 1000 nm) and this leads to the occurrence of negative skewness for the log-normal distribution in the unit of microns. As the data were treated as $Ln(x+1) \sim N(\mu, \sigma^2)$, the goodness-of-fit statistics of micro-fracture aperture attribute by the lognormal distribution was achieved.

Permeability of cleat and micro-fracture

Though cleat and micro-fracture apertures in the subsurface are smaller than in unstressed surface samples, they can approximate the aperture (Weniger et al., 2016). On the assumption that the cleat and micro-fracture are unmineralized and parallel each other, the permeability of cleat and micro-fracture for the coal of different ranks is evaluated from the measured abundance and apertures according to Eq. 1, as shown in Figure 12. It can be seen that the permeability of cleats for the low-, middle-, and high-ranking coal are 474–9440, 64o406, and 22o184 mD, respectively. The permeability of micro-fracture for the low-, middle-, and high-ranking coal are 39–353, 38–275, and 22–134 mD, respectively. Generally, for low-ranking coal, due to the differential aperture size, the cleat contributes more to the reservoir permeability than micro-fractures. For middle- and high-ranking coals, the contributions of cleats and micro-fractures to the coal reservoir permeability are similar. With the increase of coal rank, the cleat in the roles of contributing to the

reservoir permeability decreases, whereas the contribution of the micro-fracture to the reservoir permeability increases.

In the field, evaluated from the well test, the reservoir permeability of low-ranking coal in the Powder River Basin, America, falls at 10 to 1000 mD, that of low-ranking coal in the Surat Basin, Australia, falls at 1 to 1600 mD, that of middle- and high-ranking coals in the Bowen Basin, Australia, falls in 1–500 mD, and that of high-ranking coal in the Qinshui Basin, China, falls at 20–1.76 mD (Long et al., 2014; Kang et al., 2017). Generally, the *in situ* coal reservoir permeability for Australia and America is comparable with statistically evaluated permeability in Figure 12, with a difference of about an order of magnitude. However, the *in situ* coal reservoir permeability of China is lower than that of Australia and America by approximately 1–3 orders of magnitude. According to Tang (2001), due to the strong orogeny, the minimum geo-stress for the coal basin in China is close to the maximum geo-stress in Australia and America. Among possible reasons for the extremely low permeability of coal reservoirs in China are two aspects: 1) the subsurface cleat and micro-fracture close their apertures significantly due to the much larger geo-stress, which reduces the contribution of cleat and micro-fracture to the coal reservoir permeability; 2) the subsurface cleat and micro-fracture have better permeability for the hydrothermal fluids in the geological history, which is beneficial to the precipitation of minerals in the stressed cleat and micro-fracture and thereby the decreased coal reservoir permeability.

Implications of cleat and micro-fracture to the field CBM exploration and exploitation

Cleat and micro-fracture apertures in conjunction with spacing and degree of mineralization define the permeability of coal reservoirs. To stimulate gas production, hydraulic fracturing is a means of creating more fractures for fluid flow, which includes newly created fractures and increased sizes of openings of the existing ones. The mineral in the coal can change the mechanical and petrophysical features of the coal seam, which determines the growth of created fractures. In addition, the mineral matter in coal, especially the massive clay minerals and carbonate minerals, is a significant aspect in the design and selection of fluids for drilling and hydraulic fracturing. Nowadays, acid treatment is extensively used in sandstone reservoirs to remove the formation damage (Shuchart and Gdanski, 1996; Taylor et al., 2005; Yang et al., 2012; Zhang et al., 2017). In terms of the common mineral occurrences in cleats and micro-fractures in coal, acid solvents such as HAc, HCl, and HF at a certain concentration can be added to the drilling or hydraulic fracturing fluid to remove the minerals and enhance the reservoir permeability. Meanwhile, geo-stress relief technologies may be also an effective way of enlarging the cleat or micro-fracture aperture for enhancing the coal reservoir permeability (Du et al., 2022).

Conclusion

1) The neighboring mineralized and unmineralized cleats suggest multi-stage evolution processes for cleat formation during the process of coalification. The micro-fracture distribution of coals is closely related to their components, including organic macerals and inorganic minerals. Generally, micro-fractures have a high density in the vitrinite maceral and develop more at the junction surface of organic macerals or the surface between the organic and inorganic minerals. The formation mechanism of mineral-genetic micro-fractures can be classified as intra-crystal micro-fractures, extra-crystal micro-fractures, and grain edge micro-fractures. Compared with the low- and middle-ranking coals, cleats and micro-fractures in high-ranking coal are usually filled with carbonate minerals and clay minerals.
2) Statistical analysis reveals that the aperture distribution of cleats and micro-fractures in coal meets a log-normal distribution. The aperture of cleat and micro-fracture in the coal shows a decreasing trend with the increase of coal rank. Given the assumptions that the cleat and micro-fracture are unmineralized and parallel each other, the permeability of cleats for the low-, middle-, and high-ranking coals is 474–9440 mD, 64 to 406 mD, and 22 to 184 mD, and the permeability of micro-fractures for the low-, middle-, and high-ranking coals is 39–353 mD, 38 to 275 mD, and 22 to 134 mD, respectively. For the low-ranking coal, cleat contributes more to the reservoir permeability than micro-fractures do. For the middle- and high-ranking coal, the contribution of cleat and micro-fracture to the coal reservoir permeability will be close. With the increase in coal ranking, the degree of cleat contributing to reservoir permeability decreases, whereas that of micro-fractures contributing to the reservoir permeability increases.
3) Among the possible reasons for the extremely low permeability of coal reservoirs in China may be two aspects: one is that the subsurface cleats and micro-fractures close their apertures significantly due to the *in situ* geo-stress; the other is that subsurface cleats and micro-fractures have better permeability for the hydrothermal fluids in the geological history, which increases the precipitation of minerals in the cleat and micro-fracture and then decreases the coal reservoir permeability.

4) Regarding the mineral presenting in the cleat and micro-fracture of coal, acid solvents (e.g., HAc, HCl, and HF) can be added to the drilling or hydraulic fracturing fluid to remove the minerals for enhancing the reservoir permeability. In addition, the geo-stress relief technologies may also be an effective way to improve the coal reservoir permeability for CBM production.

Data availability statement

The original contributions presented in the study are included in the article/Supplementary Material; further inquiries can be directed to the corresponding author.

Author contributions

QH and ZD were responsible for the experiments and the writing of this manuscript. HL, QN, and HF helped create the figures for this paper. JY and ML provided language help. Each author has contributed to this manuscript.

Funding

This study has been sponsored financially by the Natural Science Foundation of Henan Province (Project no. 222300420242), the Science and Technology Development Project of Luoyang (Project no. 2101025A), the Heluo Young Talent Lifting Project of Society and Technology Association of Luoyang (Project no. 2022HLTJ06), the Science and Technology Innovation Leading Talent Project of Zhongyuan (Project no. 214200510030), and the Key Research and Development Project of Henan Province (Project no. 221111321500).

Acknowledgments

We are grateful to the reviewers for their suggestions for improving this paper.

Conflict of interest

ZD was employed by Yima Coal Corporation, Henan Energy Group Corporation.

The remaining authors declare that the research was conducted in the absence of any commercial or financial relationships that could be construed as a potential conflict of interest.

Publisher's note

References

Brixel, B. (2020). *Fluid flow in sparse fracture systems, prior to and after fault slip (PhD thesis)*. Zürich: ETH Zürich.

Cui, J. W., Zhu, R. K., Wu, S. T., and Bai, B. (2013). The role of pyrite in shale organic matter enrichment, hydrocarbon generation and expulsion and shale oil accumulation. *Geol. Rev.* 59, 783–784.

Dai, S. F., Luo, Y., Seredin, V. V., Ward, C. R., Hower, J. C., Zhao, L., et al. (2014). Revisiting the late Permian coal from the Huayingshan, Sichuan, southwestern China: enrichment and occurrence modes of minerals and trace elements. *Int. J. Coal Geol.* 122, 110–128. doi:10.1016/j.coal.2013.12.016

Du, Z. G., Tao, Y. W., Zhang, X. D., Ding, W. X., and Huang, Q. (2022). CBM exploration: permeability of coal owing to cleat and connected fracture. *Energy Explor. Exploitation* 40 (1), 38–56. doi:10.1177/01445987211057195

Du, Z. G., Zhang, X. D., Huang, Q., Zhang, S., and Wang, C. (2019). Investigation of coal pore and fracture distributions and their contributions to coal reservoir permeability in the Changzhi block, middle-southern Qinshui Basin, North China. *Arab. J. Geosci.* 12, 505–519. doi:10.1007/s12517-019-4665-9

Gamson, P. D., Beamish, B. B., and Johnson, D. P. (1993). Coal microstructure and micropermeability and their effects on natural gas recovery. *Fuel* 72, 87–99. doi:10.1016/0016-2361(93)90381-b

Golab, A., Ward, C. R., Permana, A., Lennox, P., and Botha, P. (2013). Highresolution three-dimensional imaging of coal using microfocus Xray computed tomography, with special reference to modes of mineral occurrence. *Int. J. Coal Geol.* 113, 97–108. doi:10.1016/j.coal.2012.04.011

Gong, W. L., An, L. Q., Zhao, H. Y., and Mao, L. T. (2010). Multiple scale characterization of CT image for coal rank fractures based on image description. *Rock Soil Mech.* 31, 371–381.

Heriawan, M. N., and Koike, K. (2015). Coal quality related to microfractures identified by CT image analysis. *Int. J. Coal Geol.* 140, 97–110. doi:10.1016/j.coal.2015.02.001

Kang, Y. S., Sun, L. Z., Zhang, B., Jiao, G. U., Jian, Y. E., jiang, S., et al. (2017). The controlling factors of coalbed reservoir Permeability and CBM development strategy in China. *Geol. Rev.* 63 (5), 1401–1418.

Karacan, C., and Okandan, E. (2000). Fracture/cleat analysis of coals from Zonguldak Basin (northwestern Turkey) relative to the potential of coalbed methane production. *Int. J. Coal Geol.* 44, 109–125. doi:10.1016/s0166-5162(00)00004-5

Kendall, P. F., and Briggs, H. (1933). XIII.—the Formation of rock joints and the cleat of coal. *Proc. R. Soc. Edinb.* 53, 164–187. doi:10.1017/s037016460001556x

Kumar, H., Lester, E., Kingman, S., Bourne, R., Avila, C., Jones, A., et al. (2011). Inducing fractures and increasing cleat apertures in a bituminous coal under isotropic stress via application of microwave energy. *Int. J. Coal Geol.* 88 (1), 75–82. doi:10.1016/j.coal.2011.07.007

Laubach, S. E., Marrett, R. A., Olson, J. E., and Scott, A. R. (1998). Characteristics and origins of coal cleat: a review. *Int. J. Coal Geol.* 35, 175–207. doi:10.1016/s0166-5162(97)00012-8

Li, C. C., Liu, D. M., Pan, Z. J., and Pan, Z. J. (2015). Mineral occurrence and its impact on fracture generation in selected Qinshui Basin coals: An experimental perspective. *Int. J. Coal Geol.* 150-151, 35–50. doi:10.1016/j.coal.2015.08.006

Long, S. X., Ye, L. Q., and Chen, C. F. (2014). Comparison and enlightenment of coalbed methane geology at home and abroad. *QilGas Geo* 35 (5), 696–703.

Mohamad, N. H., and Katsuaki, K. (2015). Coal quality related to microfractures identified by CT image analysis. *Int. J. Coal Geol.* 140, 97–110. doi:10.1016/j.coal.2015.02.001

Moustafa, E. O., Tang, C. A., and Zhang, Z. (2004). Scanning of essential minerals in granite electron microscope study on the microfracture behavior. *Geo. Resour.* 13, 129–136.

Nalendra, J. S., Edy, S., and Dyah, H. E. W. (2020). "Coal properties and cleat attributes at TanjungEnim coalfield in south palembang sub-basin, south sumatra," in AIP Conference Proceedings, 2nd International Conference on Earth Science, Mineral, and Energy, China, 08 July, 2020.

Niu, Q. H., Wang, Q. Z., Wang, W., Chang, J. F., Chen, M. Y., Wang, H. C., et al. (2021). Responses of multi-scale microstructures, physical-mechanical and hydraulic characteristics of roof rocks caused by the supercritical CO_2-water-rock reaction. *Energy* 238, 121727. doi:10.1016/j.energy.2021.121727

Olson, J. E., Laubach, S. E., and Lander, R. H. (2009). Natural fracture characterization in tight gas sandstones: Integrating mechanics and diagenesis. *Am. Assoc. Pet. Geol. Bull.* 93 (11), 1535–1549. doi:10.1306/08110909100

Pan, J. N., Wang, H. C., Wang, K., and Niu, Q. (2014). Relationship of fractures in coal with lithotype and thickness of coal lithotype. *Geomech. Eng.* 6 (6), 613–624. doi:10.12989/gae.2014.6.6.613

Permana, A., Ward, C. R., Li, Z., and Gurba, L. W. (2013). Distribution and origin of minerals in high-rank coals of the south walker creek area, Bowen Basin, Australia. *Int. J. Coal Geol.* 116-117, 185–207. doi:10.1016/j.coal.2013.03.001

Rutqvist, J., Figueiredo, B., Hu, M., and Tsang, C. F. (2018). "Continuum modeling of hydraulic fracturing in complex fractured rock masses," in *Hydraulic fracture modeling* (Netherland: Elsevier), 195–217.

Sapiie, B., Rifiyanto, A., and Perdana, L. A. (2014). "Cleats analysis and CBM potential of the barito basin, south kalimantan, Indonesia," in AAPG International Conference & Exhibition, Istanbul, Turkey, September 14-17.

Saxby, J. D. (2000). "Minerals in coal," in *Organic matter and mineralisation: Thermal alteration, hydrocarbon generation and role in metallogenesis*. Editors M. Mastalerz and M. Glikson (New York: Kluwer Academic Publishers), 314–328.

Scott, A. R. (2002). Hydrogeologic factors affecting gas content distribution in coal beds. *Int. J. Coal Geol.* 50 (1-4), 363–387. doi:10.1016/s0166-5162(02)00135-0

Shi, X. H., Pan, J. N., Hou, Q. L., Jin, Y., Wang, Z. Z., Niu, Q. H., et al. (2018). Micrometer-scale fractures in coal related to coal rank based on micro-CT scanning and fractal theory. *Fuel* 212, 162–172. doi:10.1016/j.fuel.2017.09.115

Shuchart, C. E., and Gdanski, R. D. (1996). "Improved success in acid stimulation with a new organic-HF system," in Presented at European Petroleum Conference, Milan, Italy, Oct 22-24.

Snow, D. T. (1968). Rock fracture spacings, openings, and porosities. *J. Soil Mech. Found. Div.* 94, 73–91. doi:10.1061/jsfeaq.0001097

Solano, W., Mastalerz, M., and Schimmelmann, A. (2007). Cleats and their relation to geologic lineaments and coalbed methane potential in Pennsylvanian coals in Indiana. *Int. J. Coal Geol.* 72, 187–208. doi:10.1016/j.coal.2007.02.004

Spears, D. A., and Caswell, S. A. (1986). Mineral matter in coals: cleat minerals and their origin in some coals from the english midlands. *Int. J. Coal Geol.* 6, 107–125. doi:10.1016/0166-5162(86)90015-7

Tang, S. H. (2001). Probe into the influence factors on permeability of coal reservoirs. *Coal Geo. China.* 13 (1), 28–31.

Taylor, K. C., Al-Katheeri, M. I., Nasr-EI-Din, H. A., and Aramco, S. (2005). Development and field application of a new measurement technique for organic acid additives in stimulation fluids. *SPE J.* 10, 152–160. doi:10.2118/85081-pa

Wang, Z., Fu, X., Hao, M., Li, G., Pan, J., Niu, Q., et al. (2021). Experimental insights into the adsorption-desorption of CH_4/N_2 and induced strain for medium-rank coals. *J. Pet. Sci. Eng.* 204, 108705. doi:10.1016/j.petrol.2021.108705

Wang, Z., Pan, J., Hou, Q., Yu, B., Li, M., and Niu, Q. (2018). Anisotropic characteristics of low-rank coal fractures in the Fukang mining area, China. *Fuel* 211, 182–193. doi:10.1016/j.fuel.2017.09.067

Ward, C. R. (2002). Analysis and significance of mineral matter in coal seams. *Int. J. Coal Geol.* 50, 135–168. doi:10.1016/s0166-5162(02)00117-9

Ward, C. R. (2016). Analysis, origin and significance of mineral matter in coal: an updated review. *Int. J. Coal Geol.* 165, 1–27. doi:10.1016/j.coal.2016.07.014

Weniger, S., Weniger, P., and Littke, R. (2016). Characterizing coal cleats from optical measurements for CBM evaluation. *Int. J. Coal Geol.* 154-155, 176–192. doi:10.1016/j.coal.2015.12.005

Yang, F., Nasr-EI-Din, H. A., and Al-Harbi, B. M. (2012). "Acidizing sandstone reservoirs using HF and formic acids," in Presented at the SPE International Symposium and Exhibition on Formation Damage Control, Lafayette, Louisiana, Feb 15-17.

Yao, Y. B., Liu, D. M., Cai, Y. D., and Li, J. Q. (2010). Advanced characterization of pores and fractures in coals by nuclear magnetic resonance and X-ray computed tomography. *Sci.Sinic. Terr.* 40, 1598–1607. doi:10.1007/s11430-010-0057-4

Yao, Y. B., and Liu, D. M. (2009). Microscopic characteristics of microfractures in coals: An Investigation into permeability of coal. *Procedia Earth Planet. Sci.* 1, 903–910. doi:10.1016/j.proeps.2009.09.140

Zhang, X. D., Yu, K. K., Zhang, S., and Du, Z. G. (2017). Change mechanism in surface properties of treated tectonic coal by different acids. *Coal Convers.* 40, 1–7.

Zhang, Y. H., Xu, X. M., Lebedev, M., Sarmadivaleh, M., Lglauer, S., and Iglauer, S. (2016). Multi-scale x-ray computed tomography analysis of coal microstructure and permeability changes as a function of effective stress. *Int. J. Coal Geol.* 165, 149–156. doi:10.1016/j.coal.2016.08.016

frontiers | Frontiers in Earth Science

TYPE Original Research
PUBLISHED 18 January 2023
DOI 10.3389/feart.2022.1057831

OPEN ACCESS

EDITED BY
Mingjun Zou,
North China University of Water Resources and Electric Power, China

REVIEWED BY
Haihai Hou,
Liaoning Technical University, China
Jun Shen,
China University of Geosciences Wuhan, China
Dongdong Wang,
Shandong University of Science and Technology, China

*CORRESPONDENCE
Juan Wang,
66676872@qq.com

SPECIALTY SECTION
This article was submitted to Economic Geology, a section of the journal Frontiers in Earth Science

RECEIVED 30 September 2022
ACCEPTED 31 October 2022
PUBLISHED 18 January 2023

CITATION
Wang J, Shao L, Yan Z and Wang X (2023), The coal-forming environment during mass extinction in the latest permian: Evidence from geochemistry of rare Earth elements.
Front. Earth Sci. 10:1057831.
doi: 10.3389/feart.2022.1057831

The coal-forming environment during mass extinction in the latest permian: Evidence from geochemistry of rare Earth elements

Juan Wang[1,2,3]*, Longyi Shao[2], Zhiming Yan[2] and Xuetian Wang[2]

[1]School of Resources and Environment, Henan Polytechnic University, Jiaozuo, China, [2]State Key Laboratory of Coal Resources and Safe Mining, College of Geoscience and Surveying Engineering, China University of Mining and Technology (Beijing), Beijing, China, [3]Collaborative Innovation Center of Coal Work Safety and Clean High Efficiency Utilization, Jiaozuo, China

The C_1 coal of Latest Permian during mass extinction in eastern Yunnan was studied to reveal the terrestrial paleoenvironment and influence of geological events on coal-formation during mass extinction. An analysis of Rare Earth Elements (REEs) was conducted on the C_1 coal from the Yantang Mine of Xuanwei, eastern Yunnan Province, which was deposited during the latest Permian. A total of 24 samples from coals, partings, roofs and floors from the C_1 coal were taken from the fresh face in the underground mine. The results of the REEs analysis indicated that the total REE content (∑REE) in the C_1 coal varies from 23.99 μg/g to 267.94 μg/g, averaged 122.69 μg/g. The C_1 coal is enriched in light REE (LREE) relative to heavy REE (HREE), signifying the fractionation between LREE and HREE. Most samples of the coal seam C_1 are depleted in Eu in various degrees and slightly depleted in Ce, especially two partings in sub-seams B_1 and B_3 which show the significant negative Eu anomalies. The geochemical characteristics of REE reveal that the C_1 coal was deposited in a weak oxidation environment; the sedimentary environment was turbulent during the middle-later stage of coal-forming process; the C_1 coal was affected by the basalt clastic materials from the Khangdian Oldland and acidic synsedimentary volcanic ash in the coal-forming period. The geochemical characteristics of Tonsteins in C_1 coal are similar to those of marine Permian-Triassic boundary (PTB) volcanic ash layers in South China, which are both derived from the felsic volcanism caused by the closure of the Paleo-Tethys at the southwestern margin of the South China. Furthermore, the C_1 coal was also affected by the eruption of Siberian large igneous province (SLIP) in the early stage.

KEYWORDS

the latest Permian, rare Earth elements, coal-forming environment, volcanism, eastern Yunnan

1 Introduction

Rare Earth elements (REEs) present relatively stable chemical properties as well as a high degree of uniformity, and are easily preserved in a geologic body after sedimentation. The information about the sediment provenance that REEs carry is not easy to lose and is little affected by metamorphism. Therefore, REEs have been used as powerful geochemical indicators to reflect provenance compositions and changes, and provide geochemical evidences for the formation and evolution of coal seams (Wang et al., 2008; Xie et al., 2014; Arbuzov et al., 2018). At present, many studies on REEs in coals have been focusing on the characteristics of contents and the spatial distribution, occurrence, distribution pattern, provenance analysis and primary sedimentary environment of coals (Hao et al., 2004; Ren et al., 2006; Wu et al., 2013; Liu et al., 2015; Munir et al., 2018; Hedin et al., 2019; Ulrich et al., 2019). However, fewer studies have focused on the relationships between the geochemical characteristics of REEs and special geological events.

End-Permian time is one of the most important critical transition in geological history, and the largest mass extinction occurred at the Permian-Triassic transition (Wang et al., 2018; Guo et al., 2022). As the last coal deposited at the end Permian, the C_1 coal recorded the terrestrial paleoenvironment changes during mass extinction (Wang et al., 2018), the geochemical characteristics of C_1 coal may be closely related to the event. The geochemical characteristics of trace elements other than REEs have been studied by Shao et al. (2015), and they proposed that enriched elements mainly derived from continental weathering of the Emeishan basalt, synsedimentary volcanic ashes and medium-low temperature hydrothermal fluid. REEs, however, are more reliable tracers to reveal provenance and paleoenvironment, and can better constrain the environment and biological evolution events (Tian et al., 2014). In this paper, systematic REEs geochemical analyses of the latest Permian C_1 coal in Xuanwei county have been conducted, combined with previous research results about major and trace elements in C_1 coal to accurately trace the provenance change during the coal forming (Shao et al., 2015), reveal the sedimentary environment and tectonic background of coal forming, and discuss a series of geological events occurred on land during the mass extinction at the latest Permian, especially the effects of volcanic activities on coal-formation.

2 Geological setting

Xuanwei County is located in the eastern Yunnan Province and adjacent to the west Guizhou Province (Figure 1), which was tectonically located in the western part of the South China cratonic basin during the Late Permian (Shao et al., 2013). The siliciclastic sediments in this area were supplied predominantly by the Khangdian Oldland to the west. Meanwhile a long-term gradual easterly transgression throughout Late Permian provided sufficient accommodation space for the development of this important latest Permian coal province (Wang et al., 2011; Shao et al., 2013). The C_1 coal is widely distributed in eastern Yunnan, mainly located in

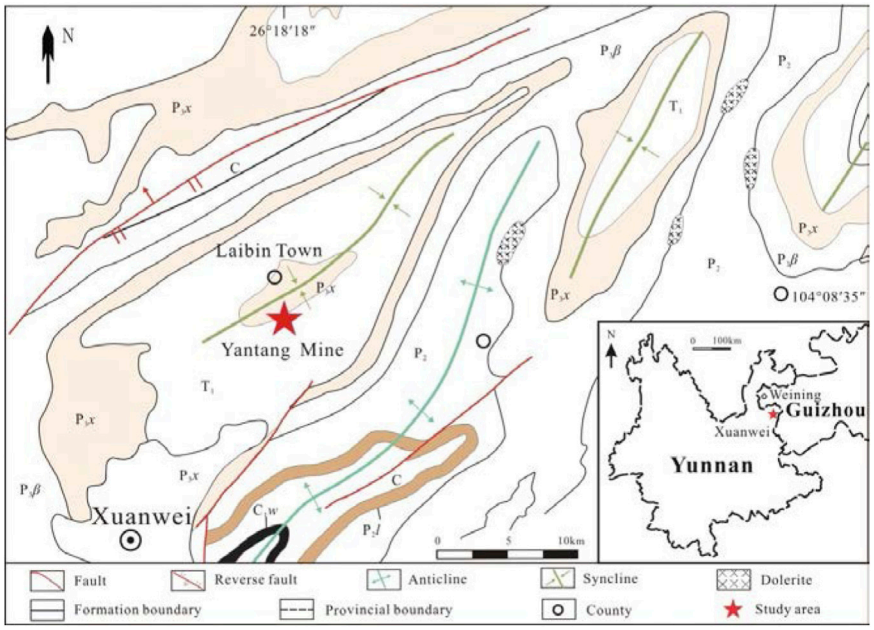

FIGURE 1
Location of the Yantang mine, Laibin Town, Xuanwei county, Yunnan Province (cited from Wang et al., 2018).

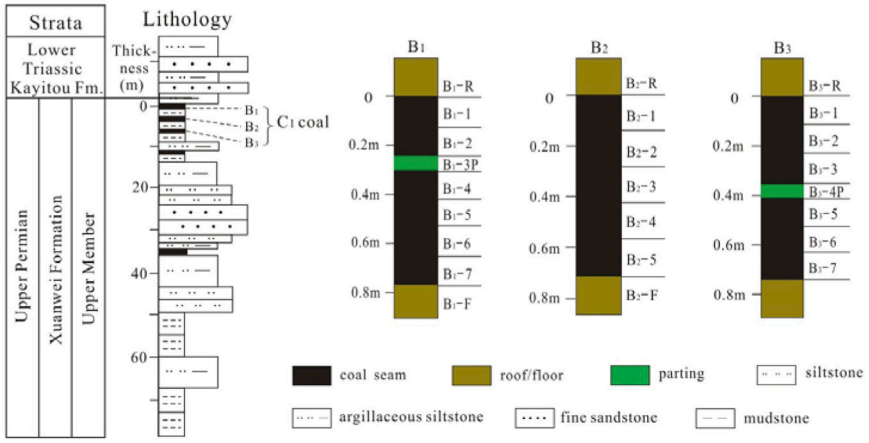

FIGURE 2
The stratigraphic section of mineable coal seam and sampling horizons of the Yantang Mine.

Xuanwei, Fuyuan and Weining areas, and lied in the uppermost portion of the Xuanwei Formation of Late Permian. The Xuanwei Formation unconformably underlaid by the Emeishan Basalt, and is conformably overlaid by the Kayitou Formation of Early Triassic (Figure 2). In the Xuanwei area, this formation consists mainly of grey fine-grained sandstone, siltstone and mudstone, some volcanic ash beds, and numerous coal seams including the C_1 coal seam at its top (Wang et al., 2012). The Xuanwei Formation of Late Permian is mostly made of continental fluvial deposits (Wang et al., 2011).

TABLE 1 Partial proximate analysis, sulfur contents and vitrinite reflectance in coals from the Yantang Mine in Xuanwei, Yunnan (%).

No.	M_{ad}	A_d	V_d	$S_{t,d}$	$S_{s,d}$	$S_{p,d}$	$S_{o,d}$	R^o_{av}
B_1-1	1.86	63.36	12.13	0.24	0.03	0.18	0.03	1.28
B_1-2	0.90	48.21	14.15	0.12	0.01	0.10	0.01	1.26
B_1-4	1.12	28.32	20.30	0.10	bdl	0.07	0.03	1.37
B_1-5	1.16	40.29	16.91	0.06	bdl	0.05	0.01	1.31
B_1-6	0.91	32.11	16.95	0.17	bdl	0.16	0.01	1.24
B_1-7	0.93	27.54	19.65	0.07	bdl	0.03	0.04	1.27
B_2-1	1.16	37.01	17.53	0.38	0.02	0.30	0.06	1.19
B_2-2	0.96	23.06	20.93	0.22	0.02	0.19	0.01	1.25
B_2-3	0.94	61.32	9.68	0.19	0.01	0.17	0.01	nd
B_2-4	0.80	32.10	19.62	0.64	0.02	0.34	0.28	1.27
B_2-5	0.81	25.37	20.71	0.13	0.01	0.12	bdl	1.33
B_3-1	0.78	40.23	16.24	0.10	bdl	0.06	0.04	nd
B_3-2	0.31	27.55	19.66	0.10	0.01	0.03	0.06	nd
B_3-3	0.88	45.71	17.71	0.11	0.01	0.02	0.08	nd
B_3-5	0.99	17.80	24.94	0.10	0.01	bdl	0.09	nd
B_3-6	0.41	16.88	26.30	0.11	0.02	0.01	0.08	nd
B_3-7	0.25	22.43	27.16	0.11	0.02	0.02	0.07	nd

M, moisture; A, ash yield; V, volatile content; ad, air dry basis; d, dry basis; St, total sulfur; Ss, sulfate sulfur; Sp, pyritic sulfur; So, organic sulfur; Roav, average vitrinite reflectance. All data in Table 1 comes from Shao et al., 2015.

3 Sampling and experimental methods

3.1 Sample description and basic data

Samples were collected from the Yantang Mine of Laibin Town, Xuanwei County, and the coal seam C_1 is the only minable seam in this mine which included three sub-seams B_1, B_2, and B_3 in descending order. Within the sub-seam B_1 and B_3, a 5 cm-thick Tonstein (kaolinite claystone altered from volcanic ash) layer exists (Figure 2). The total of 24 collected coal-seam channel samples including coal, Tonstein, roof and floor, were taken from the fresh face of the underground mine. The sampling site was located at N 26°18′18″ and E 104°08′35″ and the samples were collected with a vertical spacing of about 10 cm. All samples collected were at least 1 kg in weight and were immediately stored in plastic bags to ensure as little contamination as possible. The method of sample collection followed the Chinese National Standard for Collecting Channel Samples GB/T 482-2008.

The partial proximate analysis, sulfur contents and vitrinite reflectance of C_1 coal are presented in Table 1. The analytical data show that all samples are bituminous coal with a medium-high ash yield, ultralow total sulfur content and low-medium volatile content. According to coal ash classification (GB/T 15224.1–94), the coal samples B_1-1 and B_2-3 are classified as mixture of coal and mudstone since their ash yields exceeds 50%. Therefore, these are not included in the discussion of the C_1 coal in the present paper.

TABLE 2 REE contents of the late permian coal seam samples from the Yantang Mine, Xuanwei, Yunnan (μg/g).

No.	La	Ce	Pr	Nd	Sm	Eu	Gd	Tb	Dy	Ho	Er	Tm	Yb	Lu
B_1-R	68.80	126.00	15.50	61.50	8.46	2.00	7.77	1.60	10.10	2.01	6.09	1.02	5.62	0.75
B_1-1	26.20	48.70	5.32	20.20	2.49	0.52	1.99	0.53	3.42	0.77	2.27	0.60	2.28	0.30
B_1-2	29.70	62.70	7.67	29.50	5.96	0.95	5.02	0.76	3.95	0.75	1.94	0.33	1.96	0.30
B_1-3P	60.00	117.00	13.50	51.40	10.20	1.71	10.60	2.42	14.90	2.98	9.81	1.52	10.70	1.67
B_1-4	35.90	80.50	10.00	42.90	9.00	1.49	9.61	2.10	11.20	2.26	6.52	0.99	5.65	0.86
B_1-5	33.30	65.65	7.77	30.10	5.58	0.87	4.73	0.76	3.91	0.83	2.62	0.44	2.76	0.48
B_1-6	12.70	24.90	3.03	12.80	2.38	0.48	2.82	0.53	2.53	0.50	1.44	0.23	1.49	0.26
B_1-7	4.61	9.30	1.25	5.21	2.01	0.57	4.58	1.34	9.26	2.01	6.15	1.00	5.52	0.96
B_1-F	72.60	167.00	21.80	88.20	15.40	2.49	10.50	1.68	7.97	1.66	5.18	1.00	6.54	1.06
B_2-R	48.80	92.60	9.11	32.00	5.35	0.97	4.80	1.01	6.59	1.29	3.96	0.72	4.48	0.71
B_2-1	41.90	94.40	11.40	44.40	7.63	1.60	6.37	0.93	4.62	0.85	2.55	0.48	2.54	0.42
B_2-2	3.17	6.09	0.86	3.93	1.09	0.32	1.85	0.42	2.54	0.47	1.40	0.22	1.39	0.24
B_2-3	21.50	51.50	6.63	25.30	5.28	1.02	3.90	0.67	3.38	0.70	2.25	0.42	2.44	0.41
B_2-4	71.00	114.00	12.40	48.00	7.03	1.61	5.30	0.80	3.64	0.53	1.51	0.21	1.27	0.21
B_2-5	3.62	7.85	1.12	5.62	1.88	0.70	3.05	0.77	4.46	0.90	2.65	0.43	2.14	0.33
B_2-F	50.40	96.90	10.70	34.50	7.15	2.47	9.07	1.83	10.90	1.90	5.63	0.87	5.36	0.78
B_3-R	98.20	178.00	24.10	97.50	15.70	3.31	11.10	2.11	10.30	2.75	7.26	1.01	6.53	1.02
B_3-1	7.59	17.50	1.41	5.57	1.02	0.26	0.96	0.19	1.12	0.25	0.69	0.11	0.81	0.11
B_3-2	11.80	21.50	2.39	9.47	1.97	0.34	1.88	0.34	1.62	0.39	0.99	0.19	1.24	0.16
B_3-3	17.40	33.10	3.69	13.90	3.66	0.58	3.08	0.60	3.60	0.83	2.03	0.36	2.62	0.40
B_3-4P	32.40	61.90	7.17	26.80	5.81	0.47	4.79	1.13	7.52	1.85	5.71	1.16	8.32	1.16
B_3-5	13.90	27.30	3.60	14.80	4.30	0.93	3.77	0.69	4.40	0.93	2.47	0.39	2.34	0.34
B_3-6	21.60	37.60	4.92	21.70	6.05	1.51	5.72	1.12	8.18	2.00	4.85	0.71	5.13	0.71
B_3-7	50.90	106.00	15.70	58.70	12.30	3.04	8.91	1.23	5.05	0.83	2.47	0.32	2.16	0.33

3.2 Analytical methods

The bulk samples were air-dried, crushed, ground to less than 200-mesh and dried for 2 h in a drying oven at 105°C~110°C. The samples were then preprocessed by low-temperature airproof acid digestion, whose detailed procedure is described hereafter. An accurately weighed sample of 0.0500 g was mixed with 1 ml of HF, 3 ml of HNO_3 and 1 ml of $HClO_4$ in a dedicated 25 ml digestion vessel. After the cap assembles were sealed, the vessel was put into a low-temperature electric warming plate for heating at 125°C for 24 h. Finally, the residue was dissolved with 1% HNO_3 and then transferred to a 50 ml volumetric flask. The prepared samples were then determined for their REE compositions using the inductively coupled-plasma mass spectrometry (ICP-MS) (Finnigan MAT), with the relative analysis error of ±5%, according to the "GB/T 14506.30–2010". The REEs testing was performed at the Analytical Laboratory of Beijing Research Institute of Uranium Geology. The final results were reported as the μg/g in coal with a dry basis for each sample.

4 Results

The contents of REEs and other trace elements in the C_1 coal obtained by ICP-MS analysis are presented in Tables 2, 3. The total REE content (∑REE) in C_1 coals (excluding roof, floor and Tonstein) varies from 23.99 μg/g to 267.94 μg/g, averaged 122.69 μg/g, which is slightly lower than that of average Chinese coal with 135.89 μg/g (Dai et al., 2012). Compared with the Late Permian coal in the adjacent area, the average ∑REE in C_1 coal is slightly lower than that of Yueliangtian coals from Panxian county, western Guizhou (136 μg/g, marine and continental transitional environment, cited from Wang et al., 2017), but higher than that of continental coals from Shizong county and Fuyuan county in eastern Yunnan (101 μg/g and 105.9 μg/g, respectively, cited from Wang et al., 2017 and Wang et al., 2012). The ∑REE of the roof and floor strata ranges from 212.39 μg/g to 458.89 μg/g, averaged 326.01 μg/g, which is 2.65 times of that of coal, indicating that the total amount of REEs in mudstone is significantly higher than that of coal. However, there is not significant vertical variation of REE contents among benches of individual coal seam, as seen from Figure 3.

TABLE 3 The REE and elements data of the late permian coal seam samples from the Yantang Mine, Xuanwei, Yunnan.

Sample No.	∑REE (μg/g)	HREE (μg/g)	LREE (μg/g)	L/H	$(La/Yb)_N$	δEu	δCe	Ce_{anom}	Al/Ti
B_1-R	317.22	34.96	282.26	8.07	7.27	0.84	0.80	−0.067	6.05
B_1-1	115.59	12.16	103.43	8.51	6.82	0.80	0.86	−0.050	15.61
B_1-2	151.48	15.00	136.48	9.10	9.00	0.59	0.87	−0.015	25.95
B_1-3P	308.41	54.60	253.81	4.65	3.33	0.56	0.86	−0.037	42.62
B_1-4	218.97	39.18	179.79	4.59	3.77	0.55	0.89	−0.006	41.39
B_1-5	159.78	16.52	143.27	8.67	7.16	0.57	0.85	−0.036	15.04
B_1-6	66.09	9.80	56.29	5.75	5.06	0.63	0.84	−0.048	16.61
B_1-7	53.77	30.82	22.95	0.74	0.50	0.64	0.81	−0.046	18.22
B_1-F	403.08	35.59	367.49	10.33	6.59	0.67	0.88	0.003	38.88
B_2-R	212.39	23.56	188.83	8.02	6.47	0.65	0.92	−0.030	24.47
B_2-1	220.10	18.77	201.33	10.73	9.79	0.78	0.90	0.008	27.30
B_2-2	23.99	8.53	15.46	1.81	1.35	0.76	0.77	−0.077	31.33
B_2-3	125.39	14.16	111.23	7.86	5.23	0.77	0.90	0.024	9.45
B_2-4	267.52	13.48	254.04	18.85	33.19	0.90	0.80	−0.104	15.17
B_2-5	35.52	14.73	20.79	1.41	1.00	1.00	0.81	−0.050	20.45
B_2-F	238.46	42.08	416.81	9.91	8.93	1.05	0.87	−0.027	7.82
B_3-R	458.89	4.23	33.35	7.88	5.57	0.86	0.76	−0.081	8.53
B_3-1	37.58	6.81	47.47	6.97	5.65	0.88	1.12	0.047	11.25
B_3-2	54.28	13.53	72.33	5.35	3.94	0.61	0.84	−0.061	18.73
B_3-3	85.85	31.64	134.55	4.25	2.31	0.59	0.86	−0.042	23.68
B_3-4P	166.19	15.33	64.83	4.23	3.53	0.30	0.85	−0.043	62.95
B_3-5	80.16	28.42	93.38	3.29	2.50	0.79	0.80	−0.052	18.67
B_3-6	121.80	21.30	246.64	11.58	13.99	0.88	0.76	−0.099	13.19
B_3-7	267.94	12.16	103.43	8.51	6.82	0.99	0.78	−0.035	5.14

Chondritic values by Herrmann are used for normalization with the modification of REEs (Hao et al., 2004); ∑REE=LREE+HREE; LREE=La+Ce+Pr+Nd+Sm+Eu; HREE=Gd+Tb+Dy+Ho+Er+Tm+Yb+Lu; L/H=LREE/HREE; $(La/Yb)_N = La_N/Yb_N$; $\delta Eu = Eu_N/(Sm_N \times Gd_N)^{1/2}$; $\delta Ce = Ce_N/(La_N \times Pr_N)^{1/2}$;N stands for chondrite normalization; Data of Ti and Al are cited from Shao et al., 2015.

The REEs contents of chondrites were taken from Herrmann (Hao et al., 2004) and the chondrite-normalized REE distribution patterns of all samples from the seam C_1 are showed in Figure 3. All of the curves show a certain slope and are tilted to the right. The curves of Light REE (LREE) are slightly sloping compared with Heavy REE (HREE). The samples from seam B_1 and B_3 show a similar distribution trend respectively, while the curves of samples from seam B_2 are haphazard. The $(La/Yb)_N$ ratios of all samples change from 0.50 to 33.19, with an average value of 6.73, indicating that LREE were significantly enriched relative to HREE. This is consistent with all other studies which reveal the predominance of the LREE relative to HREE.

Most samples of the C_1 coal are depleted in Eu at various degrees, with δEu values ranging from 0.55 to 1.00 for an average of 0.74, and with a peak negative value (0.30) appearing in Tonstein B_3-4. The δCe value of C_1 coals show slightly negative or free anomalies, ranging from 0.76 to 1.12, averaged 0.85.

The REE patterns may be subsequently altered to a variable extent by post-depositional, diagenetic exchange or surface weathering (Zeng et al., 2001; Blake et al., 2017). As a special organic sedimentary rock, coal may also be affected by the above-mentioned factors during the coal-forming process, which could affect REEs fractionation and enrichment. For instance, δCe value easily changes due to diagenesis, which then leads to a significantly positive correlation between δCe and δEu, a significantly negative correlation between δCe and $(Dy/Sm)_N$, and a significantly positive correlation between δCe and ∑REE (Shields et al., 2001; Zeng et al., 2011; Qu et al., 2018). To confirm the influence of diagenesis on samples from seam C_1, the above three correlation coefficients are calculated as -0.10, 0.15 and 0.18, respectively (Figure 4). The correlation values are not significant, showing that diagenesis has very little influence on the Ce anomaly in the C_1 coal. In consideration of this result, the Ce anomaly is regarded to reflect the characteristics of the terrestrial environment during sedimentary period as it represents the information of the original samples.

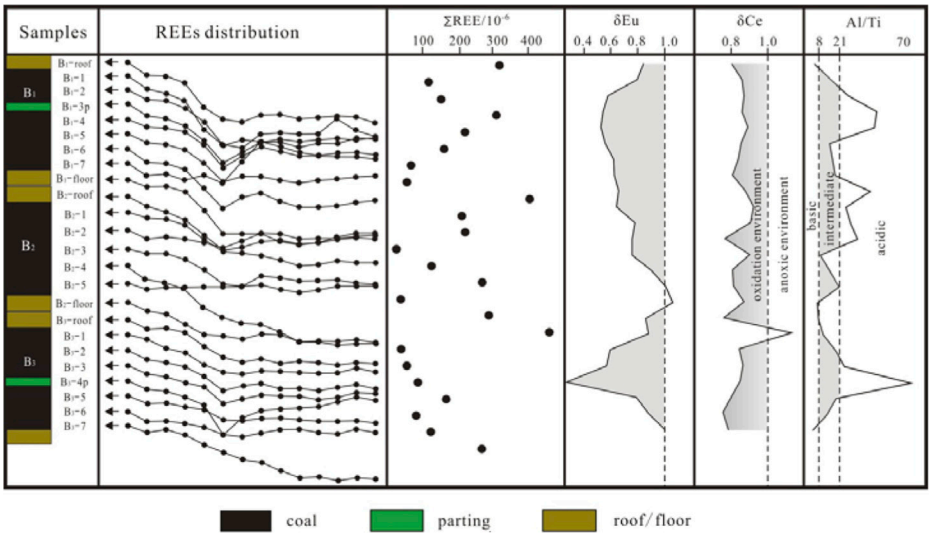

FIGURE 3
Stratigraphic distribution of patterns of ∑REE, δEu, δCe and Zr/Hf in all coal samples from Yantang Mine, Xuanwei, Yunnan.

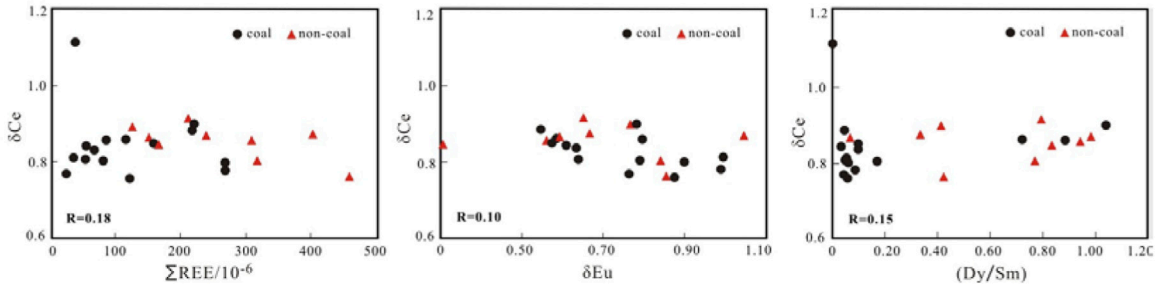

FIGURE 4
δCe correlate with δEu, $(Dy/Sm)_N$ and ∑REE in the C_1 coal of Yantang Mine, Xuanwei, Yunnan.

5 Discussion

5.1 Sedimentary environment

Ce anomaly is an effective redox indicator, which can be used to analyze sedimentary environment and paleo-water medium conditions. The δCe greater than 1 indicates a reducing condition, while that less than 1 reflects a more oxidizing condition (Qu et al., 2018). In general, the negative Ce anomaly indicates the marine sedimentary environment, while the mafic basalt has slightly positive or free Ce anomaly (Zhao et al., 2019; Wang et al., 2020). The δCe of samples from the seam C_1 are mostly between 0.76 and 0.92, averaged 0.84, indicating a slightly negative Ce anomaly (Table 3 and Figure 3), which is significantly different from the REE characteristics of seawater (Qu et al., 2018; Huang et al., 2019). Therefore, the influence of sea water can be excluded. The above discussion of δCe in samples from seam C_1 suggested that the coal-forming peatland was affected by the input of basic basalt clastic materials from the Khangdian Oldland, and the coalforming peatland was in weak oxidation environment.

In addition, Ce_{anom} is also widely used in the identification of paleoredox conditions. The Ce_{anom} is greater than 0 indicates water hypoxia, while that less than 0 reflects oxidized water (Tian et al., 2018). Most Ce_{anom} of samples from seam C_1 are less than 0 (Table 2), indicating the weak oxidation environment of coal-forming peatland. Only a few samples in seam B_2 have Ce_{anom} greater than 0, indicating that peatland oxidation and reduction environments alternate during coalforming, suggesting a turbulent coal-forming environment.

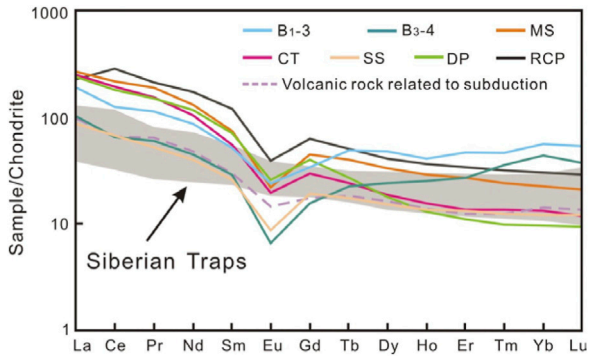

FIGURE 5
Chondrite-normalized REE patterns of the tonsteins in the C_1 coal, PTB volcanic ashes and subduction-related rock.

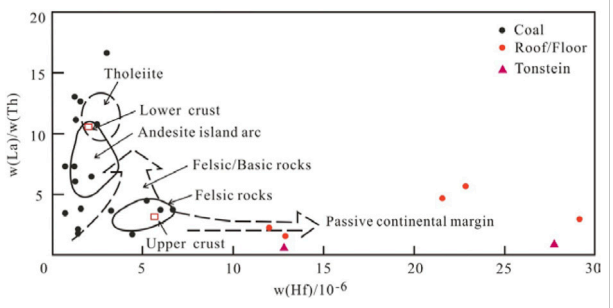

FIGURE 6
w(La)/*w*(Th)—*w*(Hf) discrimination diagram for provenance attribute Data of Zr and Hf are cited from Shao et al. (2015).

5.2 The character of volcanic ash

Eu anomaly is inherited from the source rock, and as such Eu is generally recognized as an indicator of the nature of provenances. Basalt shows mostly no negative Eu anomaly, while granite and other acidic rocks present obvious negative Eu anomaly (Chen et al., 1990; Wang et al., 2019). Since the main provenance area of the coal-bearing basin in the study area is basalt (and its weathering and alteration products) originating from Khangdian Oldland, there should be no Eu anomaly in the C_1 coal samples. However, most coal bench samples of the C_1 seam are depleted in Eu at various degrees (Figure 3 and Table 2), except those at the roofs and floors and their vicinity. According to the sedimentary sequence of the C_1 coal, the bottom coal of seam B_3 that was first deposited has no Eu anomaly, and then the degree of negative Eu anomaly increases gradually upward, and reaches the maximum value of the whole coal seam rapidly at Tonstein B_3-4 (δEu is 0.30), and then decreases rapidly upward. There was no Eu anomaly in the floor and bottom coal of the sub-seam B_2 which deposited followed by the sub-seam B_1, and the degree of negative Eu anomaly increased slowly from the bottom of sub-seam B_2 upward to sub-seam B_1 (B_1-4) and Tonstein (B_1-3), reaching the maximum Eu negative anomaly, and then the Eu negative anomaly decreased rapidly. The Eu negative anomaly degree of Tonstein B_1-3 is significantly lower than that of B_3-4, which may be caused by the input of acidic volcanic materials, and acidic volcanic activities are more intense during the B_3 coal-forming period.

The Al in normal igneous rocks resides mostly in feldspars and the Ti in mafic minerals. Therefore, the Al/Ti ratio is an important parameter to determine the parent rock composition. Generally, basic rock with a Al/Ti ratio of 3–8 and intermediate rock with a Al/Ti ratio of 8–21, 21–70 indicate acidic rock (Hayashi et al., 1997). The Al/Ti ratio of Tonstein B_1-3 and B_3-4 is 42.62 and 62.95, respectively, whereas that of most coals is between 9.45 and 41.39 (Table 3). Integration of δEu and Al/Ti ratios suggest that there were twice significantly acidic volcanic activities during coal-forming (Figure 7A).

Tonstein is the preserved "relic" of volcanic activity, the δEu with 0.56 and 0.30 of Tonstein B_1-3 and B_3-4 are very close to that of five typical PTB ash beds in South China (He et al., 2014; Tan et al., 2019), so it is inferred that the two volcanic activities are the same provenance with those indicated by the PTB volcanic ash layer in South China. Furthermore, the similar shaped curves and negative Eu anomaly indicate that the Tonsteins and ash beds have the same REE origin from volcanic rocks related to plate subduction (Siberian Traps) (Widiatama et al., 2021) (Figure 5).

5.3 Source and tectonic background of the C_1 coal

REEs have special geochemical characteristics, and are stable during weathering, erosion, transportation, deposition and early diagenesis. Therefore, the REEs have been used to infer the material source of sediments (Bai et al., 2015; Tian et al., 2018; Qu et al., 2018). The different chondrite-normalized patterns of sub-seam B_1, B_2 and B_3 (Figure 3) show different coal-forming process. With few exceptions, the distribution curves of REEs in the first deposited sub-seam B_3 are most similar, indicating the stable and single provenance. The distribution curves and abundance of REEs in samples from the sub-seam B_2 have more variability than sub-seam B_3. In addition, Ce_{anom} of samples reflected that the oxidation and reduction environment appeared alternately during coal-forming of sub-seam B_2. All of the above results indicate that the sedimentary environment of peat swamp was relatively turbulent and the provenance was unstable during this period. The distribution curves of REEs in the latest sub-seam B_1 are slightly different. Besides, the abundance of ∑REE in top coal suddenly decreases, inferred that the input of terrigenous substances replaces the paleoplant, and finally leads to the termination of coal-forming process.

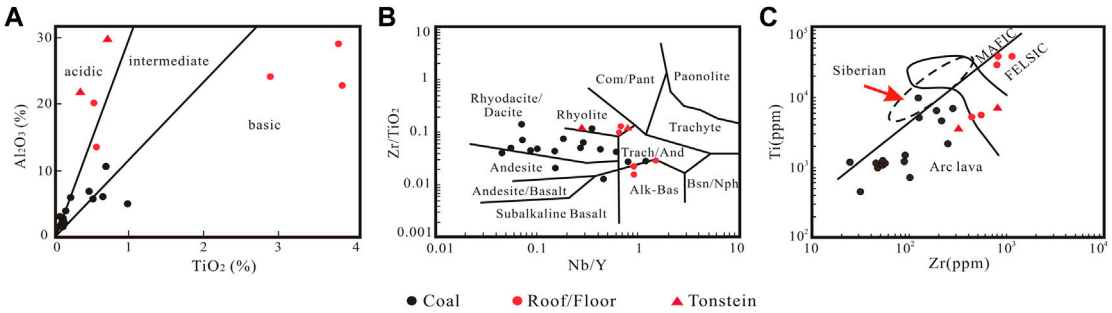

FIGURE 7
(A) Zr versus Ti diagram (modified from He et al., 2014), **(B)** plots of mass fractions of Al_2O_3 *versus* TiO_2, and **(C)** Zr/TiO_2 versus Nb/Y diagram (modified from He et al., 2014).

Diagrams of *w*(La)/*w*(Th)—*w*(Hf) is commonly used to discriminate the source rocks and tectonic setting (Bai et al., 2015; Qu et al., 2018). The result shows that coals from the seam C_1 are from multiple sources, such as tholeiite, andesite island arc, felsic and basic rocks (Figure 6). Tonsteins, seam roofs and floors are plotted mainly into the felsic and basic rocks area (Figure 6). All samples from the seam C_1 are deposited in the passive continental margin.

Tonsteins in the seam C_1 classify as acidic rock on the Al_2O_3 *versus* TiO_2 and diagram of Nb/Y—Zr/TiO_2 (Figures 7A,B), and Tonsteins originate from felsic magmatic arc.

Integration of dispersion of coal samples plotted in above diagrams and variation of distribution curves of REEs, it can be inferred that the provenance of C_1 coal is complex and influenced by the input of basalt and acidic volcanic ash during coal-forming process (Figures 3, 6, 7). Concretely, the roofs and floors originated from the basalt clastic materials of the KhangDian Oldland, while the Tonstein layer is derived from the acidic synsedimentary volcanic ash. Based on the dual influence of volcanism and basic basalt clastic material, the source rocks of the coal seam C_1 show basic, intermediate and acidic (Figure 7A).

5.4 The relationship between coal formation and volcanic activity

During the Permian-Triassic, the Paleo-Tethys along a subduction zone between the South China and Indochina cratons closed gradually, and Indochina Plate moved rapidly northward and collided with other plates, consequently felsic volcanic activities were extraordinarily active(Cawood, 2005; Wang et al., 2019; Zhao et al., 2019) (Figure 8A). During one eruption, dust nanoparticles can travel thousands of kilometers through the stratosphere and affect all areas of the Earth for years (Ermolin et al., 2018). The volcanic ash falling to South China was altered in different sedimentary environments to form kaolinite, illite or illite/smectite, such as Tonsteins interbedded in C_1 coal from Xuanwei area and five typical marine PTB sections in South China (Figures 8B,C) (He et al., 2014; Wang et al., 2018). Multiple volcanic claystone beds are widely developed in South China, which become more frequent and thicker towards southwest margin of Yangtze, indicating that the source of PTB tuff and volcanic claystone is in the southwest margin of the Yangtze Plate (Sun et al., 2013; Wang et al., 2022). Recently, previous studies on the source of PTB volcanic ash in South China have shown that, the PTB volcanism occurred near southwest South China and their adjacent convergent continental margin due to the closure of Paleo-Tethys. Furthermore, volcanic ash derived from subduction-zone arc between South China and Indochina cratons, which is not the trigger of PTB mass extinction due to limited eruption (Isozaki et al., 2007; Zhao et al., 2013; He et al., 2014; Wang et al., 2018; Wang et al., 2019; Zhao et al., 2019; Hou et al., 2020).

The age of Tonstein (252.0 ±2.3 Ma, Wang et al., 2018) of the sub-seam B_1 overlaps with age of granite (235–252 Ma, Ma et al., 2019) as evidence of subduction-zone, and Xuanwei area is immediately adjacent to the continental magmatic arc of the southwest margin of the South China at the End-Permian (Wang et al., 2018). By comparing REE patterns of two Tonsteins, five typical PTB volcanic ash layers, volcanic rocks related to subduction and Siberian traps (Figure 5) (He et al., 2014; Liu et al., 2015), it is found that the distribution curves of the first three are very similar, except the last one, mainly due to the absence of negative Eu anomaly. In addition, the REE patterns of Tonsteins are slightly different from those of PTB volcanic ash layers, such as little fractionation of LREE and HREE and flatter distribution curve, which may be caused by the volcanic ash falling in different sedimentary environments. Tonsteins were deposited in continental fluvial sedimentary environment, and the input of terrigenous materials tends to flatten the distribution curves of REE, which is different from the marine PTB volcanic

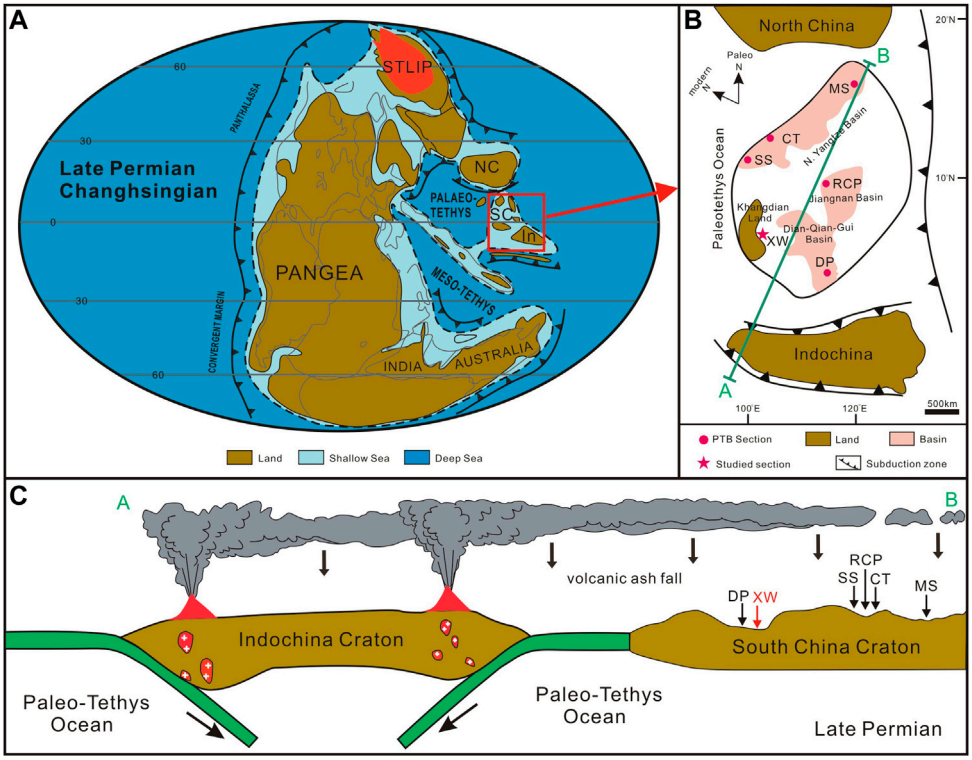

FIGURE 8
(A) Global paleogeography at late permian (Changhsingian) (modified from Metcalfe, 2013; Wang et al., 2019); **(B)** Potential volcanic ash source areas and inferred direction of ash transport (A→B) in South China and Indochina area during late permian (modified from Wang et al., et al., 2018; Zhao et al., 2019); **(C)** Composite cross-section of Late Permian South China and Indochina Craton, showing subduction of the Paleo-Tethys Plate beneath the Indochina Craton margin (modified from Wang et al., 2018; Zhao et al., 2019). Abbreviations in A: STLIP-Siberian Traps Large Province; NC-North China; SC-South China; In-Indochina Craton; B: DP-Dongpan, XW-Xuanwei, SS-Shangsi, RCP-Rencunping, CT-Chaotian, MS-Meishan.

ashes (Liu et al., 2018). The diagrams of Al_2O_3-TiO_2, Nb/Y-Zr/TiO_2 and Zr-Ti (Figure 7) also confirmed that the two layers of Tonstein derived from volcanic magmatic arc and were acidic, which was different from the basic SLIP (Kamo et al., 2003). Therefore, it was inferred that Tonsteins in the C_1 coal were from felsic volcanism of the End-Permian, rather than SLIP.

Significantly, the bottommost coal sample B_3-7, which has been plotted in the SLIP area (Figure 7C), and its δEu of 0.99, Al/Ti of 5.14, REE pattern curve and diagram of *w*(La)/*w*(Th)-*w*(Hf) and Zr-Ti, indicating that it has been affected by basic basalts. It is further confirmed that C_1 coal was influenced by SLIP in its early stage. Compared with Indochina craton, SLIP and eastern Yunnan Province are more far apart. However, the SLIP is known as the largest continental volcanic event since Phanerozoic, and volcanic ash nanoparticles can transport to worldwide. With the overlap between constraint on SLIP eruption and C_1 coal forming, therefore it can be inferred that the C_1 coal was affected by SLIP in the early stage of coal forming.

6 Conclusion

The C_1 coal from Xuanwei County, Yunnan Province contains two layers of Tonstein. REEs, several major and trace elements data indicate the following:

(1) The total REE content of the C_1 coal ranges from 23.99 to 267.94 μg/g, averaged 122.69 μg/g. C_1 coal samples are enriched in LREE relative to HREE and show significant fractionation between LREE and HREE. Most samples including coals, Tonsteins, roofs and floors present varying degrees of negative Eu anomaly, especially two Tonsteins in sub-seam B_1 and B_3 with the significant negative Eu anomalies. Most samples of the seam C_1 are slightly depleted in Ce.
(2) The C_1 coal-forming peatland was affected by the input of basic basalt clastic materials from Khangdian Oldland and acidic volcanic ash. The C_1 coal was deposited in a weak oxidation environment, and experienced turbulent

environment during the middle and later stage of coal-forming period.

(3) The geochemical characteristics of Tonsteins in the C_1 coal are similar to those of the marine PTB volcanic ash layers in South China, which are both derived from the felsic volcanism caused by the closure of the Paleo-Tethys at the southwestern margin of the South China. Furthermore, the C_1 coal was also affected by the eruption of SLIP in the early stage.

Data availability statement

The original contributions presented in the study are included in the article/supplementary material, further inquiries can be directed to the corresponding author.

Author contributions

JW searched the literature; JW and LS analyzed the data and wrote the paper; ZY and XW collected samples and performed the experiments.

Funding

This work is supported by the National Natural Science Foundation of China (No. 41602123 and 41572090), and the Fundamental Research Funds for the Universities of Henan Province (No. NSFRF220401).

Conflict of interest

The authors declare that the research was conducted in the absence of any commercial or financial relationships that could be construed as a potential conflict of interest.

Publisher's note

All claims expressed in this article are solely those of the authors and do not necessarily represent those of their affiliated organizations, or those of the publisher, the editors and the reviewers. Any product that may be evaluated in this article, or claim that may be made by its manufacturer, is not guaranteed or endorsed by the publisher.

References

Arbuzov, S. I., Maslov, S. G., Finkelman, R. B., Mezhibor, A. M., Ilenok, S. S., Blokhin, M. G., et al. (2018), Modes of occurrence of rare Earth elements in peat from Western Siberia Rare Earth and major element geochemistry of Eocene fine-grained sediments in oil shale- and coal-bearing layers of the Meihe Basin, Northeast China. *J. Asian Earth Sci. of Geochemical Exploration* 184, 4089–48101 97

Blake, J. M., Peters, S. C., and Johannesson, K. H. (2017). Application of REE geochemical signatures for mesozoic sedimentprovenance to the gettysburg basin, Pennsylvania. *Sediment. Geol.* 349, 103–111. doi:10.1016/j.sedgeo.2016.12.009

Cawood, P. A. (2005). Terra australis orogen: Rodinia breakup and development of the pacific and iapetus margins of gondwana during the neoproterozoic and paleozoic. *Earth. Sci. Rev.* 69, 249–279. doi:10.1016/j.earscirev.2004.09.001

Chen, D. Q., and Chen, G. (1990). *Practical geochemistry of rare earth elements*. Beijing: Metallurgical Industry Press, 228–230. (in Chinese).

Dai, S. F., Ren, D. Y., Chou, C. L., Finkelman, R. B., Seredin, V. V., and Zhou, Y. P. (2012). Geochemistry of trace elements in Chinese coals: A review of abundances, genetic types, impacts on human health, and industrial utilization. *Int. J. Coal Geol.* 94 (3), 3–21. doi:10.1016/j.coal.2011.02.003

Ermolin, M. S., Fedotov, P. S., Malik, N. A., and Karandashev, V. K. (2018). Nanoparticles of volcanic ash as a carrier for toxic elements on the global scale. *Chemosphere* 200, 16–22. doi:10.1016/j.chemosphere.2018.02.089

Guo, B. Q., Gao, D., Guo, H. L., Liu, J. G., Wang, J. H., and Shi, Y. (2022). Geochemistry of the Permian–Triassic boundary strata in the southwest margin of the North China Craton: Provenance and tectonic implications. *Geol. J.*,23 1–14. doi:10.1002/gj.4558

Hao, L. B., and Qi, C. M. (2004). *Principles of geochemistry*, 2. Beijing: Geological Press, 54–55. (in Chinese)., pp.

Hayashi, K. I., Fujisawa, H., Holland, H. D., and Ohmoto, H. (1997). Geochemistry of ~1.9 Ga sedimentary rocks from northeastern Labrador, Canada. *Geochimica Cosmochimica Acta* 61 (19), 4115–4137. doi:10.1016/s0016-7037(97)00214-7

He, B., Zhong, Y. T., Xu, Y. G., and Li, H. X. (2014). Triggers of permo-triassic boundary mass extinction in South China: The siberian traps or paleo-tethys ignimbrite flare-up? *Lithos* 204, 258–267. doi:10.1016/j.lithos.2014.05.011

Hedin, B. C., Capo, R., Stewart, B. W., Hedin, R. S., Lopano, C. L., and Stuckman, M. Y. (2019). The evaluation of critical rare Earth element (REE) enriched treatment solids from coal mine drainage passive treatment systems. *Int. J. Coal Geol.* 208, 54–64. doi:10.1016/j.coal.2019.04.007

Hou, H. H., Shao, L. Y., Tang, Y., Li, Y. N., Liang, G. D., Xin, Y. L., et al. (2020). Coal seam correlation in terrestrial basins by sequence stratigraphy and its implications for palaeoclimate and palaeoenvironment evolution. *J. Earth Sci.*, 1–24.

Huang, Q. H., Bai, X. F., Wang, H., Cheng, H. G., and Zhu, Z. Y. (2019). Geochemical characteristics and geological significance of trace elements and rare Earth elements in carbonate rocks at Middle-Upper Permian boundary in Linxi area, Inner Mongolia. *Glob. Geol.* 38 (3), 611–622.

Isozaki, Y., Shimizu, N., Yao, J. X., Ji, Z. S., and Matsuda, T. (2007). End-Permian extinction and volcanism-induced environmental stress: The Permian-Triassic boundary interval of lower-slope facies at Chaotian, South China. *Palaeogeogr. Palaeoclimatol. Palaeoecol.* 252, 218–238. doi:10.1016/j.palaeo.2006.11.051

Kamo, S. L., Czamanske, G. K., Amelin, Y., Fedorenko, V. A., Davis, D. W., and Trofimov, V. R. (2003). Rapid eruption of Siberian flood-volcanic rocks and evidence for coincidence with the Permian-Triassic boundary and mass extinction at 251 Ma. *Earth Planet. Sci. Lett.* 214, 75–91. doi:10.1016/s0012-821x(03)00347-9

Liu, D. N., Zhou, A. C., and Chang, Z. G. (2015). Geochemistry characteristics of major and rare Earth elements in No.8 raw and weathered coal from Taiyuan Formation of Datong coalfield. *J. China Coal Soc.* 40 (2), 422–430. (in Chines, with English abstract).

Liu, Q. Q., Chi, Q. H., Wang, X. Q., Zhou, J., Liu, H. L., Liu, D. S., et al. (2018). Distribution and influencing factors of rare Earth elements in carbonate rocks along three continental-scale transects in eastern China. *Earth Sci. Front.* 25 (4), 99–115. (in Chines, with English abstract).

Ma, X. H., Chen, C. J., Zhao, J. X., Qiao, S. L., and Zhou, Z. H. (2019). Late permian intermediate and felsic intrusions in the eastern central asian orogenic belt: Final-stage magmatic record of paleo-asian oceanic subduction? *Lithos* 326-327, 265–278. doi:10.1016/j.lithos.2018.12.022

Metcalfe, I. (2013). Gondwana dispersion and Asian accretion: Tectonic and palaeogeographic evolution of eastern Tethys. *J. Asian Earth Sci.* 66, 1–33. doi:10.1016/j.jseaes.2012.12.020

Munir, M. A. M., Liu, G. J., Yousaf, B., Ali, M. U., Abbas, Q., and Ullah, H. (2018). Enrichment of Bi-Be-Mo-Cd-Pb-Nb-Ga, REEs and Y in the permian coals of the huainan coalfield, anhui, China. *Ore Geol. Rev.* 95, 431–455. doi:10.1016/j.oregeorev.2018.02.037

Qu, X. R., Li, J., Sun, C. R., Zhang, Q. H., Tang, S. H., and Wei, J. G. (2018). Geochemistry characteristics of rare Earth elements in the late Paleozoic black shale from eastern Ordos Basin. *J. China Coal Soc.* 43 (4), 1083–1093. (in Chinese, with English abstract).

Ren, D. Y., Zhao, F. H., Dai, S. F., Zhang, J. Y., and Luo, K. L. (2006). *Trace element geochemistry of coal*. Beijing: Science Press, 321–334. (in Chinese).

Shao, L. Y., Gao, C. X., Zhang, C., Wang, H., Guo, L. J., and Gao, C. H. (2013). Sequence-palaeogeography and coal accumulation of late permian in southwestern China [J]. *Acta sedimentol. sin.* 31 (5), 856–866. (in Chinese, with English abstract).

Shao, L. Y., Wang, J., Hou, H. H., Zhang, M. Q., Wang, H., Spiro, B., et al. (2015). Geochemistry of the C_1 coal of latest permian during mass extinction in Xuanwei, yunnan. *Acta Geol. sin.* 89 (1), 163–179. (in Chinese, with English abstract).

Shields, G., and Stille, P. (2001). Diagenetic constraints on the use of cerium anomalies as palaeoseawater redox proxies: An isotopic and REE study of Cambrian phosphorites. *Chem. Geol.* 175 (1-2), 29–48. doi:10.1016/s0009-2541(00)00362-4

Sun, Y. D. (2013). *Coupling climatic and biodiversity changes with volcanisms during the Palaeozoic-Mesozoic upheavals in South China*. Wuhan: China University of Geosciences PhD thesis. (in Chinese with English abstract).

Tan, C., Yuan, X. J., Yu, B. S., Liu, C., Li, W., and Cui, J. W. (2019). Geochemical characteristics and paleoclimatic implications of the upper permian and middle-lower triassic strata in southern ordos basin. *GEOSCIENCE* 33 (3), 615–628. (in Chinese with English abstract).

Tian, X. L., Luo, K. L., Wang, S. B., and Ni, R. X. (2014). Geochemical characteristics of trace elements and rare Earth elements during the Cryogenian-Ediacaran transition in Yangtze Gorges area. *J. Palaeogeogr.* 16 (4), 483–502. (in Chinese, with English abstract).

Ulrich, M., Cathelineau, M., Munoz, M., Boiron, M. C., Teitler, Y., and Karpoff, A. M. (2019). The relative distribution of critical (Sc, REE) and transition metals (Ni, Co, Cr, Mn, V) in some Ni-laterite deposits of New Caledonia. *J. Geochem. Explor.* 197, 93–113. doi:10.1016/j.gexplo.2018.11.017

Wang, H., Shao, L. Y., Hao, L. M., Zhang, P. F., Glasspool, I. J., Wheeley, J. R., et al. (2011). Sedimentology and sequence stratigraphy of the Lopingian (Late Permian) coal measures in southwestern China. *Int. J. Coal Geol.* 85, 168–183. doi:10.1016/j.coal.2010.11.003

Wang, H., Shao, L. Y., Newton, R. J., Bottrell, S. H., Wignall, P. B., and Large, D. J. (2012). Records of terrestrial sulfur deposition from the latest Permian coals in SW China. *Chem. Geol.* 292-293, 18–24. doi:10.1016/j.chemgeo.2011.11.005

Wang, J., Shao, L. Y., Wang, H., Spiro, B., and Large, D. (2018). SHRIMP zircon U-Pb ages from coal beds across the Permian-Triassic boundary, eastern Yunnan, southwestern China. *J. Palaeogeogr.* 7 (2), 117–129. doi:10.1016/j.jop.2018.01.002

Wang, P. P. (2017). *Enrichment and differentiation mechanism of minerals and trace elements in the Late Permian coals from eastern Yunnan and western Guizhou Province*. Beijing: China University of Mining and Technology PhD thesis. (in Chinese, with English abstract).

Wang, Q., and Yang, R. D. (2008). Tracing study on REEs of coal measure in late permian in bijie city, Guizhou province, China. *J. Chin. rare earth Soc.* 26 (1), 102–107. (in Chinese, with English abstract).

Wang, T., Zhu, X. M., Dong, Y. L., Chen, H. H., Su, B., Liu, Y., et al. (2020). Trace elements as paleo sedimentary environment indicators: A case study of the paleogene anjihaihe formation in the northwestern junggar basin. *Acta Geol. Sin.* 94 (12), 3830–3851. (in Chinese with English abstract).

Wang, X. B., Dai, S. F., Chou, C. L., Zhang, M. Q., Wang, J. M., Song, X. L., et al. (2012). Mineralogy and geochemistry of late permian coals from the taoshuping mine, yunnan province, China: Evidences for the sources of minerals. *Int. J. Coal Geol.* 96-97, 49–59. doi:10.1016/j.coal.2012.03.004

Wang, X. D., Cawood, P. A., Zhao, L. S., Chen, Z. Q., Lyu, Z. Y., and Ma, B. (2019). Convergent continental margin volcanic source for ash beds at the Permian-Triassic boundary, South China: Constraints from trace elements and Hfisotopes. *Palaeogeogr. Palaeoclimatol. Palaeoecol.* 519, 154–165. doi:10.1016/j.palaeo.2018.02.011

Wang, Y., Cao, J., Zhang, B. L., Liao, Z. W., Zhang, B., Liu, J. C., et al. (2022). Genesis of the wangpo bed in the sichuan basin: Formation by eruptions of the emeishan large igneous province. *Palaeogeogr. Palaeoclimatol. Palaeoecol.* 2022 (594), 110935. doi:10.1016/j.palaeo.2022.110935

Widiatama, A. J., Natalia, H. C., Ikhram, R., Santy, L. D., Wahyudiono, J., Wiguna, L. R. S., et al. (2021). Pedaro formation, equivalent of plover sandstone at savu island, outer banda arc. *IOP Conf. Ser. Earth Environ. Sci.* 882 (1), 012052–012044. doi:10.1088/1755-1315/851/1/012052

Wu, D., Sun, R. Y., and Liu, G. J. (2013). Characterization of REE geochemistry of the permian coals from the zhuji coal mine. *Huainan Coalf. its Geol. Implic. Acta Geol. sinica* 87 (8), 1158–1166. in Chinese, with English abstract.

Xie, Y. Y., Meng, J., and Guo, L. F. (2014). REE geochemistry of modern eolian dust deposits in Harbin city, Heilongjiang province, China: Implications for provenance. *Catena* 123, 70–78. doi:10.1016/j.catena.2014.07.008

Zeng, J. W., Xu, R., and Gong, Y. M. (2011). Hydrothermal activities and seawater acidification in the Late Devonian F-F transition: Evidence from geochemistry of rare Earth elements. *Sci. China Earth Sci.* 54, 540–549. (in Chinese, with English abstract). doi:10.1007/s11430-011-4171-8

Zhao, L. S., Chen, Z. Q., Algeo, T. J., Chen, J. B., Chen, Y. L., Tong, J. N., et al. (2013). Rare Earth element patterns in conodont albid crowns: Evidence for massive inputs of volcanic ash during the latest Permian biocrisis? *Glob. Planet. Change* 105, 135–151. doi:10.1016/j.gloplacha.2012.09.001

Zhao, T. Y., Algeo, T. J., Feng, Q. L., Zi, J. W., and Xu, G. Z. (2019). Tracing the provenance of volcanic ash in Permian-Triassic boundary strata, South China: Constraints from inherited and syn-depositional magmatic zircons. *Palaeogeogr. Palaeoclimatol. Palaeoecol.* 516, 190–202. doi:10.1016/j.palaeo.2018.12.002

frontiers | Frontiers in Earth Science

TYPE Original Research
PUBLISHED 19 January 2023
DOI 10.3389/feart.2023.1122040

OPEN ACCESS

EDITED BY
Zhenzhi Wang,
Henan Polytechnic University, China

REVIEWED BY
Rui Li,
Chongqing University, China
Jinhai Zhao,
Shandong University of Science and Technology, China

*CORRESPONDENCE
Run Chen,
chenrun@cumt.edu.cn

SPECIALTY SECTION
This article was submitted to Economic Geology, a section of the journal Frontiers in Earth Science

RECEIVED 12 December 2022
ACCEPTED 05 January 2023
PUBLISHED 19 January 2023

CITATION
Chen R, Bao Y, Lv F, Chen F, Hu K and Zhang Y (2023), Coal measure energy production and the reservoir space utilization in China under carbon neutral target.
Front. Earth Sci. 11:1122040.
doi: 10.3389/feart.2023.1122040

Coal measure energy production and the reservoir space utilization in China under carbon neutral target

Run Chen[1,2]*, Yunxia Bao[1,3], Fengrong Lv[3], Fu Chen[4], Kunpeng Hu[3] and Yajun Zhang[3]

[1]Jiangsu Key Laboratory of Coal-Based Greenhouse Gas Control and Utilization, Xuzhou, China, [2]Carbon Neutrality Institute, China University of Mining and Technology, Xuzhou, China, [3]School of Resources and Geosciences, China University of Mining and Technology, Xuzhou, China, [4]School of Public Administration, Hohai University, Nanjing, China

Coal measure energy production and reservoir space utilization are both important for energy security and can assist in achieving carbon neutrality. Coal measure energy production and reservoir utilization are therefore of scientific significance. This study focuses on the security of coal supply by discussing the possible technical approaches of combining low-carbon mining of coal measure resources and coal reservoir space utilization. Our study found that 1) the integration of underground coal gasification and carbon capture and sequestration (UCG-CCS) is an effective technology to improve energy efficiency and achieve the carbon neutral target in China; 2) CO_2-enhanced coalbed methane (CO_2-ECBM) recovery is an important way to reduce CO_2 emissions during coalbed methane recovery; and 3) the integrated technology of solid waste filling (WF), coal bioconversion (CB), gas production (GP), and CO_2 capture and sequestration (CCS) in coal goafs and abandoned coal mines can improve the energy production efficiency and reservoir space utilization and reduce geological disasters due to surface subsidence. These integrated technologies will become increasingly important for coal measure energy production and efficient reservoir space utilization as they will provide scientific theory and technical support to achieve carbon neutrality.

KEYWORDS

carbon neutral target, CO_2 sequestration, reservoir space utilization, UCG-CCS, WF-CB-GP-CCS

1 Introduction

China is richly endowed with coal but has fewer oil and gas resources. Coal production and consumption account for a high proportion of China's energy production and consumption (Zou et al., 2021a; Chen et al., 2021; Xie et al., 2021). The total primary energy production in China increased from 628 million tons of standard coal in 1980 to 4.08 billion tons of standard coal in 2020, and the total energy consumption increased from 517 million tons of standard coal to 4.98 billion tons of standard coal over the same period (Figure 1). The Chinese gross domestic product (GDP) rapidly increased from 367.87 billion yuan to 101,598.62 billion yuan (National Bureau of Statistics of China, 2021; Zou et al., 2021b). The rapid development of China's economy has been supported by the increased consumption of energy. The increased energy output also caused a large increase in greenhouse gas emissions, such as CO_2 (Dong et al., 2014; Yang et al., 2020). In 2020 alone, China's energy-related CO_2 emissions were about 9.9 billion tons, accounting for 30.9% of the global total carbon emissions and ranking first in the world

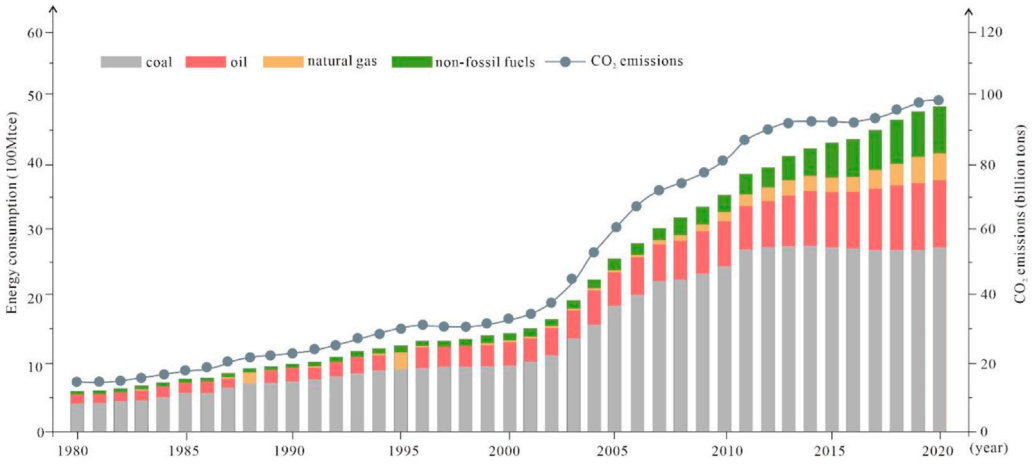

FIGURE 1
Trends of energy consumption and CO_2 emissions in China from 1980 to 2020.

(Zhang et al., 2021). Against this background, even if the proportions of natural gas and renewable energy could be increased to reduce the carbon-intensive power supply, the development of renewable energy will not outpace the price and security advantages of coal-fired power (Hecking, 2016; Fan & Chen, 2018; Zhang et al., 2018). China's *14th Five-Year Plan (2021–2025) and the Outline of Long-term Goals for 2035* specifically stated the following: "We will formulate an action plan to peak carbon emissions by 2030, improve the system of controlling both the total amount and intensity of energy consumption, and promote the clean, efficient and safe use of fossil energy such as coal."

To keep the global temperature rise within 1.5°C, as proposed in the *Paris Agreement*, net-zero global CO_2 emissions, where there is a balance between man-made removal and man-made emissions, must be achieved by 2050. This is known as "carbon neutrality" (Chen et al., 2021). Global climate catastrophes are becoming more and more severe. Achieving this goal is regarded as the key to climate security and the survival of humanity (Zhang et al., 2021). By the end of 2020, 127 countries and regions had put forward their carbon neutrality targets, with some having set timetables for restricting or banning the use of fossil energy (Chen et al., 2021). At the General Debate of the 75th Session of the United Nations General Assembly, President Xi Jinping of the People's Republic of China promised that the CO_2 emissions will achieve peak before 2030, and carbon neutrality will be achieved before 2060.

Coal measure energies, which include coal, coalbed methane, coal measure gas, and shale gas, are the main current sources of energy in China. The production of coal measure energies and the utilization of their reservoir spaces are important for achieving the carbon peak and carbon neutrality targets in China. Over the past few decades, significant progress has been made in the exploration and production of coal measure energies.

For a long time, coal mining rates were low in China, being affected by the resource conditions, the state of mining technologies, and resource management. The resource recovery rate of a state-owned coal mine was generally about 50%, while the resource recovery rate of locally administered state and township-individual coal mines with relatively poor conditions was only about 20%–30% (State Administration of Coal Mine Safety, 2002). From 1949 to 2014, the total amount of residual coal in China was 126.644 billion tons. These included state-owned, local state-owned, and township-individual coal mines at 26.93 billion tons, 20.198 billion tons, and 78.87 billion tons, respectively (Huang et al., 2014). The main obstacle was how to improve the coal mining rate.

In contrast, the volumes of coal goafs totaled 13.836 billion m^3 in China by the end of 2016. These coal goafs led to frequent mining disasters such as land subsidence, and it is estimated that the volume of coal goafs in China will reach 23.452 billion m^3 by 2030 (Xie, 2018). Challenges that must be addressed in coal goaf mining are how to efficiently use the underground space and reduce coal goaf mining disasters.

Coal measure gas in China has the characteristics of "three low and one high" (low pressure, low permeability, low saturation, and high content) due to the complex geological conditions that often complicate coal measure gas production (Lv et al., 2011). Improving the recovery of coal measure gas is a key problem to overcome. Only a few technologies can simultaneously exploit coal measure energy and optimally use coal reservoir space. Coal measure energy production must be increased to reach China's carbon neutral target, and the reservoir space utilization must be optimized. To meet the demand for clean and green mining against the background of future carbon neutrality, this study considers these two technologies comprehensively by focusing on coal measure energy production and reservoir space utilization from theory and practice.

2 Theoretical basics

2.1 Principle of underground coal gasification (UCG)

Underground coal gasification, which involves *in situ* coal gasification, is the controlled burning of coal under *in situ* conditions (Figure 2). The thermal and chemical reaction of the solid organic matter in the coal generates mixed gases during controlled burning. These gases can be converted into various fuels

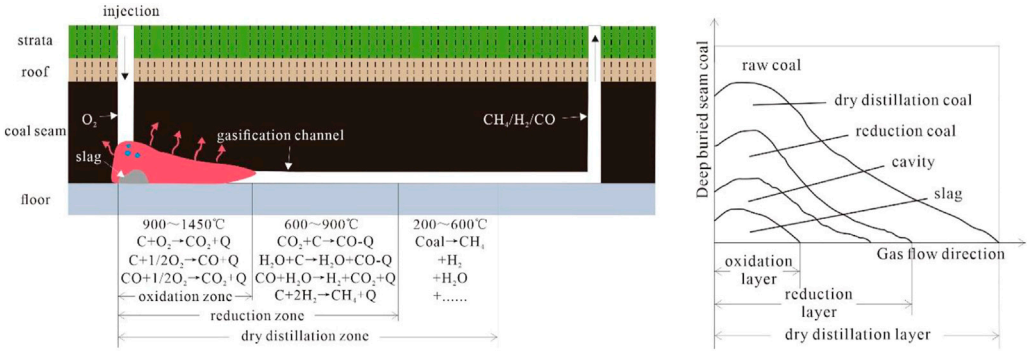

FIGURE 2
Principles of UCG and the gasification reaction zone diagram.

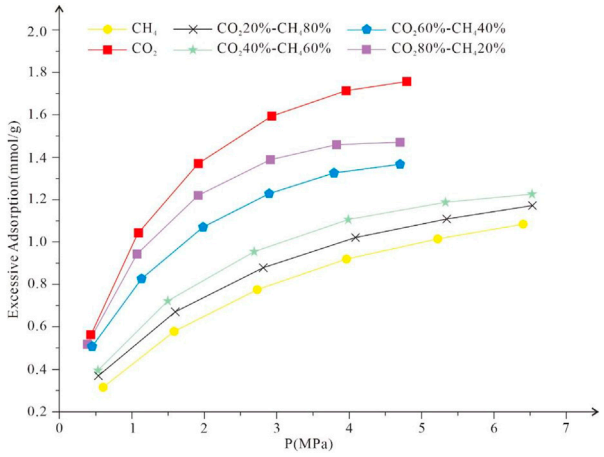

FIGURE 3
Curves of gas isothermal adsorption on coal.

or raw materials after ground classification, such as natural gas for power generation, carbon monoxide, and hydrogen for synthetic ethanol. UCG is a relatively new technology for the clean utilization of coal and the production of chemical raw materials (Blinderman, 2017; Perkins, 2018). UCG has a high coal recovery rate (up to 85%) and can be generated at a low economic cost. It also has a limited environmental impact with almost no groundwater pollution risk. Since it is an unstaffed form of underground coal mining, it has a higher worker safety performance, especially for some thin coal seams, deep high gas coal seams, abandoned coal seams, and marginal unminable coal seams. However, its application can be restricted by the coal quality, hydrogeology, and other limitations (Qin et al., 2019).

The ash content of the slag in the oxidation zone is 94.9%, with a small amount of unburned carbon after UCG (Ma, et al., 2019). The volatile content of the residue in the reduction zone is lower than that of the residue in the dry distillation zone, and the fixed carbon content is slightly higher than that in the dry distillation zone. From the temperature and the reaction of the coal seam, the coal seam first undergoes drying and distillation and then undergoes gasification at a higher temperature, making the volatile content of the residual in the reduction zone lower and the fixed carbon content higher. The results show that the residues in the reduction zone and the dry distillation zone contain a small amount of O and S atoms.

Principle of CO_2 sequestration and enhanced coalbed methane (CO_2-ECBM) recovery

Decades ago, researchers found significant differences in the adsorption capacities of gases in coal and shale (Figure 3). Generally, CO_2 absorbs better on coal and shale than methane under the same conditions (Liu et al., 2010). Therefore, scientists proposed simultaneous CO_2 sequestration and enhanced CBM and shale gas recovery in the same geological formation. Later, due to the demand for greenhouse gas emission reduction, CO_2 sequestration in coal measure strata and enhanced coal measure gas recovery were favored.

Principles of biogas and coal bioconversion (CB)

Biogas is generated by microbial fermentation of organic substances under anerobic conditions. Biogas is generally generated in marshy areas. People often see marshes, sewage ditches, or cesspools emitting biogas bubbles. During biogas generation, human and livestock manure, straw, sewage, and other organic substances are fermented under anerobic (oxygen-free) conditions in a closed biogas tank, where biogas fermentation microorganisms decompose and transform the organic material to biogas. Methanation of the organic substrates under anerobic conditions is thought to occur in four generally accepted stages (Figure 4). The pathways of biogas are acetic acid fermentation and CO_2 reduction:

$$\text{Acetic acid fermentation} \quad CH_3COOH \rightarrow CH_4 + CO_2. \quad (1)$$

$$CO_2 \text{ reduction} \quad CO_2 + 4H_2 \rightarrow CH_4 + 2H_2O. \quad (2)$$

Coal measure gas is an unconventional natural gas. There are two types of coal measure gas: thermal and biological. Biogenic coal measure gas, similar to biogas, is formed through the synergic degradation of organic matter by microbial communities in a coal

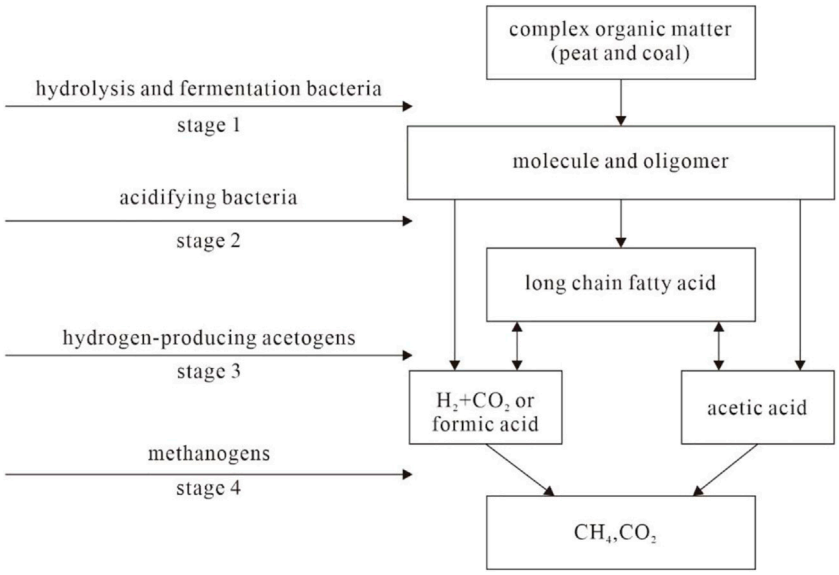

FIGURE 4
Four stages of organic substrate methanation under anerobic conditions.

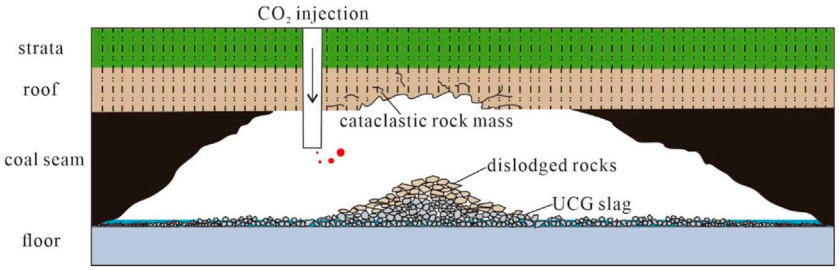

FIGURE 5
Schematic diagram of CO_2 sequestration in the UCG space.

seam. Due to the theory of biogenesis, coal bioconversion has been receiving more attention as a clean coal utilization technology (Zhang et al., 2017; Zhao et al., 2022).

3 Integration of technologies and their applications

The energy composition and carbon neutralization target in China requires that coal measure energy should be produced effectively, with low carbon emissions, and that the reservoir space should be utilized effectively. Therefore, several integrated technologies were proposed to exploit coal measure energy and efficiently use the reservoir space.

3.1 Coal mining and reservoir space utilization

With continuous economic development, China's demand for energy is on the rise. Most of the easily exploitable shallow coal seams have already been mined out. Traditional deep coal seam mining methods not only increase energy consumption and pollute the environment but also have a low recovery rate. After mining, it is difficult to use the residual coal reservoir space. Efficient technology is urgently needed to mine underground coal and ensure the rational utilization of the mined reservoir space to reduce disasters caused by surface subsidence. Therefore, we propose a technology that integrates UCG and CCS. In this integrated technology, combustible gas is provided by UCG, after which CO_2 is captured and sequestrated in the residual UCG reservoir space.

Previous studies show that the coal reservoir space consists of UCG slag, the cavity, reduction coal, dry distillation coal, and raw coal after UCG, distributed outward along the gasification channel after UCG was implemented (Figure 5). There are significant differences in the material composition of the gasification slag in the three zones (Akbarzadeh & Chalatrunyk, 2014; Bhaskaran et al., 2015; Howaniec, 2016; Liu et al., 2018). As shown in Figure 2, Oxidation zone, reduction zone and dry distillzaiton zone. These factors cause significant differences in the CO_2 sequestration paths of the three zones of the

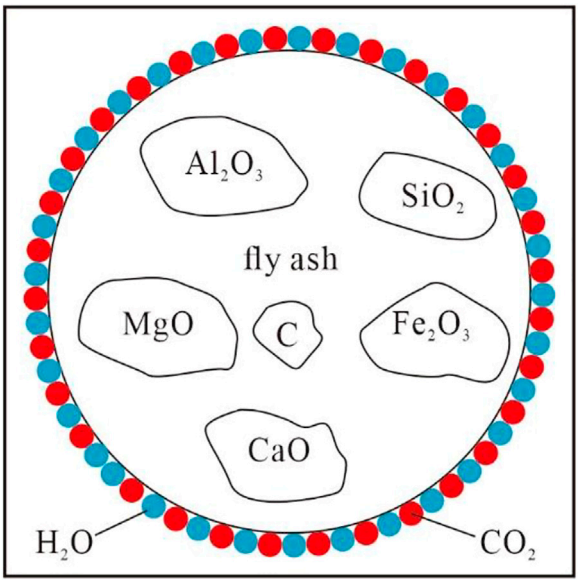

FIGURE 6
Schematic diagram of the CO_2 reaction with alkaline oxides.

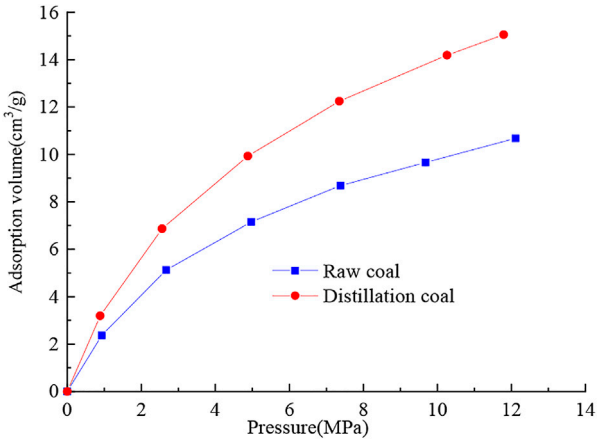

FIGURE 7
Methane adsorption isotherm of the raw and distillation coals.

UCG space. Slag is mainly composed of alkaline oxides, silica, and a small amount of residue carbon. This means that CO_2 sequestration on the slag surface occurs mainly *via* chemical reactions and/or CO_2 adsorption on residual carbon (Figure 6). The chemical reactions that sequestrate CO_2 are as follows:

$$Ca^{2+} + CO_3^{2-} \rightarrow CaCO_3, \quad (3)$$

$$Mg^{2+} + CO_3^{2-} \rightarrow MgCO_3, \quad (4)$$

$$Fe^{2+} + CO_3^{2-} \rightarrow FeCO_3. \quad (5)$$

The substances in dry distillation coal are dominated by organic matter and a small amount of morphologically transformed minerals. After high-temperature baking during coal gasification, dry distillation coal has a stronger gas adsorption capacity than raw coal and can, therefore, sequestrate more CO_2 (Figure 7). The composition of reduced coal is between that of slag and dry distillation coal. CO_2 sequestration in dry distillation coal mainly occurs *via* adsorption and mineralization.

The integrated technology of UCG and CCS is efficient for mining coal resources, and the UCG space can also be used effectively while at the same time providing a new pathway for geological CO_2 sequestration.

3.2 Coal measure gas production and its reservoir space utilization

Coal measure gas recovery is limited because the coal measure reservoirs have the "three low" (low pressure, low permeability, and low saturation) characteristics. Many researchers have suggested CO_2-enhanced coalbed methane recovery to make up for the defect of the reservoir and to reduce CO_2 atmospheric emissions during peak CO_2 emissions (Clarkson & Bustin, 2000; Mukherjee & Misra, 2018). The integrated technology that we suggest is simultaneous coal measure gas production and CO_2 sequestration. A schematic of this integrated technology is shown in Figure 8.

Thermodynamic calculations indicate that the maximum density of CO_2 is 500–700 kg/m^3 under the reservoir temperature and pressures characteristic of a depth of 800–1000 m (Orr, 2009). Supercritical carbon dioxide (SC-CO_2) has both acidic and supercritical solvent characteristics. Therefore, it is both easy to have a series of complex interactions between SC-CO_2 and some inorganic minerals and to extract small organic molecular substances from the coal, which changes its pore structure, adsorption, and permeability.

A weak acidic system is formed after CO_2 has been injected into the coal measure strata. Under these conditions, carbonate minerals (such as calcite, siderite, and dolomite) in coal are prone to dissolution, precipitation, and carbonation, while clay minerals may undergo carbonation (Chen &Qin, 2012; Harvey et al., 2013; Du et al., 2018). The chemical reactions for the carbonate mineral dissolution are as follows:

$$CaCO_3(s) + H^+ \leftrightarrow Ca^{2+} + HCO_3^-. \quad (6)$$

$$CaCO_3(s) + CO_2 + H_2O \leftrightarrow Ca^{2+} + 2HCO_3^-. \quad (7)$$

$$CaCO_3(s) + H_2O \leftrightarrow Ca^{2+} + HCO_3^- + OH^-. \quad (8)$$

$$Al_2Si_2O_5(OH)_4(s) + 6CO_2 + 5H_2O \leftrightarrow 2Al^{3+} + 2H_4SiO_4 + 6HCO_3^-. \quad (9)$$

The interaction between the CO_2 and the carbonate and clay minerals affects the pore structure, adsorption capacity, and permeability of coal measure reservoirs, which in turn affects the CO_2 injectability, sequestration capacity, and stability during the processing of enhanced coal measure gas recovery and CO_2 sequestration (Chen & Qin, 2012). The interaction between the CO_2 and carbonate minerals and/or clay minerals enlarges the pore size and increases the number of pores, which increases the pores' special surface and increases the methane adsorption ability (Chen et al., 2017a). Carbonate minerals (calcite, dolomite, *etc.*) dissolved after the reaction of CO_2-H_2O increase the permeability of the coal seam (Zhang et al., 2015).

Previous studies have shown that supercritical CO_2 extracted small and medium molecular substances that change the physical properties of coal, especially its adsorption and permeability characteristics. The

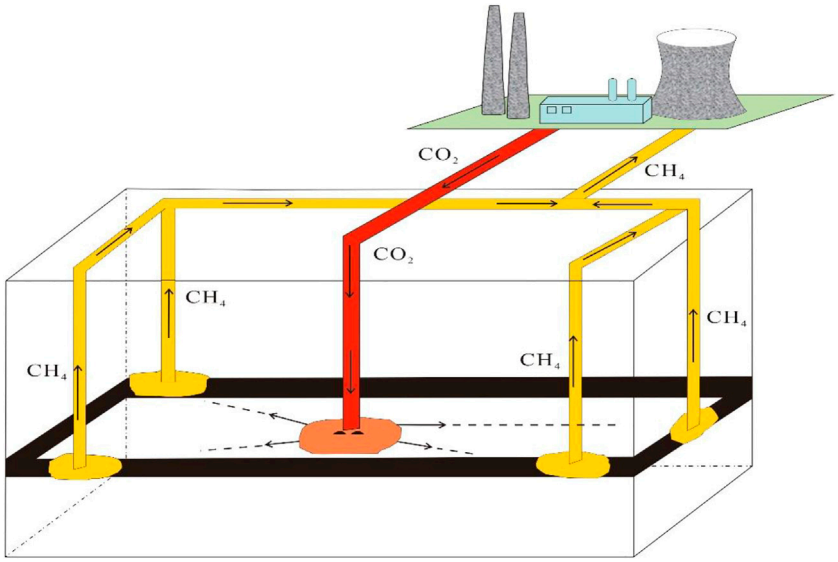

FIGURE 8
Schematic diagram of CO_2 sequestration and enhanced coal measure gas recovery.

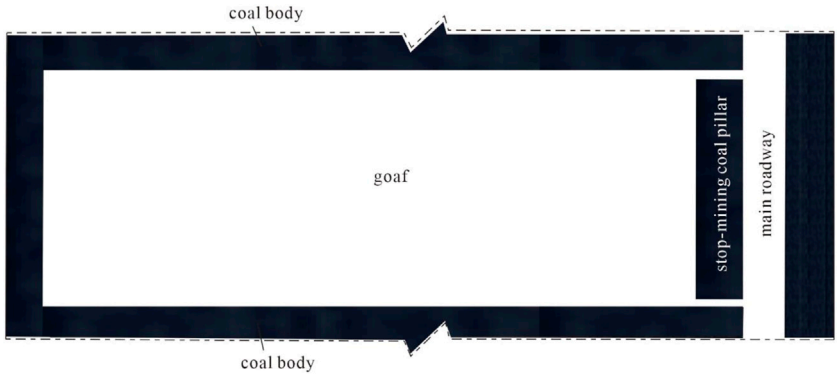

FIGURE 9
Schematic diagram of the coal goaf.

adsorption of coal was enhanced at the low-rank stage and weakened at the high-rank stage, which generally enhanced the recovery of coal measure gas and improved CO_2 geological sequestration (Chen et al., 2017b; Chen et al., 2018).

These studies have proved that CO_2-ECBM is an important extraction method to improve coal measure gas production, reduce CO_2 atmospheric emissions, and effectively utilize the coal measure reservoir space.

3.3 Gas production and the utilization of the coal goaf space and abandoned coal mine space

Previous studies have identified the presence of large volumes of coal measure gas in coal goafs and abandoned coal mines (Han, 2003; Meng et al., 2016). Coal mining in these strata can easily crack and collapse the overlying strata (Wang et al., 2022). Random stacking of coal gangue and disposal of domestic garbage cause land waste and environmental pollution (Wang, 2006; Jin et al., 2014). An integrated technology of gas production (GP), waste filling (WF), coal bioconversion (CB), and CO_2 sequestration, based on the principles of biogas and biogenic coal measure gas, is proposed for the coal goafs and abandoned coal mines.

This paper uses the coal goaf as an example to illustrate the coal measure energy production and its reservoir space utilization. First, pipes are laid in the roof strata of the coal goaf for grouting and gas extraction after mining the coal. Figure 9 shows a schematic diagram of the coal goaf. Second, the coal goaf is infilled with solid wastes such as coal, gangue, and domestic garbage. Third, the coal goaf is closed to inject a solution of microorganisms and nutrients into the goaf. Fourth, CO_2 is injected into the coal goaf after a period of gas extraction to sequestrate the CO_2.

The feasibility of the integrated technology has been confirmed by research studies. After mining the coal seam, coal measure gas

accumulates in the coal goaf through the micro-fissures due to induced pressure differences caused by the mining disturbance (Liu, 2011; Sun, 2014; Yin et al., 2014; Wang et al., 2022). After filling the goaf with domestic garbage and gangue, the coal goaf space is used effectively with WF, and the organic matter in the domestic garbage, the gangue, and the coal is bioconverted to gas by the microorganisms under the anerobic conditions in the goaf (Lin et al., 2006; Rathi et al., 2015; Ritter et al., 2015). Accumulated and bio-converted gases provide sufficient gas resources for extraction. Meanwhile, the mesopore-specific surface area and the pore volume are decreased after coal–gangue–domestic garbage bioconversion, while the micropore-specific surface area increases as the pore volume decreases. After bioconversion, the gas adsorption capacities are increased (Zhang et al., 2017; Wang et al., 2021), which means that the residues can sequestrate more CO_2 in the goaf. The changes in the pore structure and gas adsorption enhance both CO_2 sequestration in the coal measure strata and coal measure gas recovery. Therefore, the WF-CB-GP-CCS technology is suitable for energy production and reservoir space utilization in coal goafs and abandoned coal mines.

4 Conclusion

The principles of UCG, CO_2-ECBM, biogas generation and CO_2 sequestration are used against the background of carbon neutrality that integrates the concepts of coal measure energy production and reservoir space utilization. This study found that 1) the integrated UCG-CCS technology can ensure better energy exploitation and reservoir space utilization in minable coal seams. 2) The integrated CO_2-ECBM is especially appropriate for coal measure gas exploitation and reservoir space utilization in unminable coal seams. 3) The integrated WF-CB-GP-CCS technology can be adopted for both energy production and effective reservoir space utilization in coal goafs and abandoned coal mines. These integrated technologies will become an important tool for coal measure energy production and reservoir space utilization and provide scientific theory and technical support for achieving the carbon neutrality target.

Data availability statement

The original contributions presented in the study are included in the article/Supplementary Material. Further inquiries can be directed to the corresponding author.

Author contributions

RC and FC designed the facilities; YB, FL, KH, and YZ compiled the data and plotted the graphs; RC and FC writed original draft and reviewed; RC provided feedback to the manuscript.

Funding

The authors gratefully acknowledge the financial support from the Fundamental Research Funds for the Central Universities (2019XKQYMS24).

Conflict of interest

The authors declare that the research was conducted in the absence of any commercial or financial relationships that could be construed as a potential conflict of interest.

Publisher's note

All claims expressed in this article are solely those of the authors and do not necessarily represent those of their affiliated organizations, or those of the publisher, the editors, and the reviewers. Any product that may be evaluated in this article, or claim that may be made by its manufacturer, is not guaranteed or endorsed by the publisher.

References

Akbarzadeh, H., and Chalaturnyk, R. J. (2014). Structural changes in coal at elevated temperature pertinent to underground coal gasification: A review. *Int. J. Coal Geol.* 131, 126–146. doi:10.1016/j.coal.2014.06.009

Bhaskaran, S., Samdani, G., Aghalayam, P., Ganesh, A., Singh, R., Sapru, R., et al. (2015). Experimental studies on spalling characteristics of Indian lignite coal in context of underground coal gasification. *Fuel* 154, 326–337. doi:10.1016/j.fuel.2015.03.066

Blinderman, M. S. (2017). Application of the exergy UCG technology in international UCG projects[C/OL]//2017 institute of physics (IOP) conference series: Proceedings of workshop on challenges and opportunities of underground coal gasification. *Inst. Phys. Publ.* 76 (1), 012009. doi:10.1088/1755-1315/76/1/012009

Chen, F., Yu, H. C., Bian, Z. F., and Yin, D. Y. (2021). How to handle the crisis of coal industry in China under the vision of carbon neutrality. *J. China Coal Soc.* 46 (06), 1808–1820. doi:10.31035/cg2021083

Chen, R., and Qin, Y. (2012). Fluid-solid coupling between supercritical CO_2 and minerals in coal and geological significances. *Coal Sci. Technol.* 40 (10), 17–21. doi:10.1021/acs.energyfuels.7b02650

Chen, R., Qin, Y., Wei, C. T., Wang, L., Wang, Y., and Zhang, P. (2017b). Changes in pore structure of coal associated with Sc-CO_2 extraction during CO_2-ECBM. *Appl. Sci.* 7 (9), 931. doi:10.3390/app7090931

Chen, R., Wang, Y. Y., Qin, Y., Wang, L., Wei, C., and Zhang, P. (2017a). New discovery on supercritical CO_2-H_2O treated coal: Pore structure and methane adsorption. *Acta Geol. Sin. Engl. Ed.* 91 (4), 1509–1510. doi:10.1111/1755-6724.13385

Chen, R., Zhang, P. F., Qin, Y., Wei, C. T., and Wang, L. L. (2018). New discovery on methane adsorption change of coal due to Sc-CO_2 extraction during CO_2-ECBM. *Acta Geol. Sin. Ed.* 92 (6), 2438–2439. doi:10.1111/1755-6724.13741

Clarkson, C. R., and Bustin, R. M. (2000). Binary gas adsorption/desorption isotherms: Effect of moisture and coal composition upon carbon dioxide selectivity over methane. *Int. J. Coal Geol.* 42 (4), 241–271. doi:10.1016/s0166-5162(99)00032-4

Dong, W., and Yang, Y. (2014). Exploitation of mineral resource and its influence on regional development and urban evolution in Xinjiang, China. *J. Geogr. Sci.* 24 (6), 1131–1146. doi:10.1007/s11442-014-1143-x

Du, Y., Sang, S. X., Wang, W., Liu, S., Wang, T., and Fang, H. (2018). Experimental study of the reactions of supercritical CO_2 and minerals in high-rank coal under formation conditions. *Energy & Fuels* 32 (2), 1115–1125. doi:10.1021/acs.energyfuels.7b02650

Fan, M., and Chen, L. (2018). Spatial characteristics of land uses and ecological compensations based on payment for ecosystem services model from 2000 to 2015 in Sichuan Province, China. *Ecol. Inf.* 50, 162–183. doi:10.1016/j.ecoinf.2019.01.001

Han, B. (2003). *Xi'an*. Shaanxi, China: Xi'an Branch of China Coal Institute.Study on evaluation method of CBM resource development potential in abandoned mines

Harvey, O. R., Qafoku, N. P., Cantrell, K. J., Lee, G., Amonette, J. E., and Brown, C. F. (2013). Geochemical implications of gas leakage associated with geologic CO_2 storage-a qualitative review. *Environ. Sci. Technol.* 47 (1), 23–36. doi:10.1021/es3029457

Hecking, H. (2016). Twenty-first century, the century of coal? CO_2 prices to curb coal demand. *Oxf. Rev. Econ. Policy* 32 (2), 260–281. doi:10.1093/oxrep/grw011

Howaniec, N. (2016). The effects of pressure on coal chars porous structure development. *Fuel* 172, 118–123. doi:10.1016/j.fuel.2016.01.028

Huang, W. G. (2014). *Study on comprehensive evaluation and stable production technology for underground gasification of residue coal*. Xuzhou, China: China University of Mining and Technology.

Jin, H., Wu, F., and Zhu, M. (2014). Mineral characteristics of coal gangue from liupanshui in guizhou province. *Chin. J. Process Eng.* 14 (1), 151–156.

Lin, C. M., Li, Y. L., and Qi, B. W. (2006). Research status and exploration potential of biogenic gas of the article. *J. Pala.* 8, 317–330. doi:10.1016/j.ngib.2019.01.001

Liu, S., Qi, C., Jiang, Z., Zhang, Y., Niu, M., Li, Y., et al. (2018). Mineralogy and geochemistry of ash and slag from coal gasification in China: A review. *Int. Geol. Rev.* 60 (5), 717–735. doi:10.1080/00206814.2017.1287013

Liu, Y. W., Su, Z. L., and Fang, H. B. (2010). Review on CBM desorption/adsorption mechanism. *Well Test.* 19 (6), 37–44. doi:10.11885/j.issn.1674-5086

Lv, Y., Tang, D., Xu, H., and Tao, S. (2011). CO_2 sequestration enhancing coalbed methane recovery. *Environ. Sci. Technol.* 34 (5), 95–99.

Ma, A. L., Chen, L. J., and Xu, B. (2019). Study on physicochemical properties of "three zone" residues during underground coal gasification. *Coal Sci. Technol.* 47 (11), 217–223.

Meng, Z. P., Shi, X. C., Tian, Y. D., and Li, C. (2016). Evaluation model of CBM resources in abandoned coal mine and its application. *J. China Coal Soc.* 41 (3), 537–544.

Mukherjee, M., and Misra, S. (2018). A review of experimental research on Enhanced Coal Bed Methane (ECBM) recovery via CO_2 sequestration. *Earth-Science Rev.* 179, 392–410. doi:10.1016/j.earscirev.2018.02.018

National Bureau of Statistics of China (2021). *China statistical yearbook 1978-2020*. Beijing, China: China Statistics Press.

Orr, F. M. (2009). Onshore geologic storage of CO_2. *Science* 325 (5948), 1656–1658. doi:10.1126/science.1175677

Perkins, G. (2018). Underground coal gasification-part I: Field demonstrations and process performance. *Prog. Energy Combust. Sci.* 67, 158–187. doi:10.1016/j.pecs.2018.02.004

Qin, Y., Wang, Z. T., and Han, L. (2019). Geological problems in underground coal gasification. *J. China Coal Soc.* 44 (8), 2516–2530.

Rathi, R., Priya, A., Vohra, M., Lavania, M., Lal, B., and Sarma, P. M. (2015). Development of a microbial process for methane generation from bituminous coal at thermophilic conditions. *Int. J. Coal Geol.* 147-148, 25–34. doi:10.1016/j.coal.2015.06.004

Ritter, D. J., Vinson, D. S., Barnhart, E. P., Akob, D. M., Fields, M. W., Cunningham, A. B., et al. (2015). Enhanced microbial coalbed methane generation: A review of research, commercial activity, and remaining challenges. *Int. J. Coal Geol.* 146, 28–41. doi:10.1016/j.coal.2015.04.013

State Administration of Coal Mine Safety (2020). *China coal industry yearbook 2002*. Beijing, China: Coal Industry Press.

Sun, H. D. (2014). *Study on distribution and evaluation methodology of CBM (coal mine gas) resources in coal resource depleting mine*. Xuzhou, China: China University of Mining and Technology.

Sun, Y. N. (2011). *The research on the law of methane gas flow and the structure of interspaces in surrounding rock of coal goaf*. Fuxin, China: Liaoning Technical University.

Wang, A., Shao, P., and Wang, Q. (2021). Biogenic gas generation effects on anthracite molecular structure and pore structure. *Front. Earth Sci.* 15 (2), 272–282. doi:10.1007/s11707-021-0925-6

Wang, J. C., Yang, Z. B., and Qin, Y. (2022). Research status and prospects of secondary enrichment and accumulation of residual coalbed methane resources in abandoned mines. *Coal Geol. Explor.* 50 (4), 35–44.

Wang, X. F. (2006). *Study on hydrodynamic law of trace element pollution in coal gangue leaching*. Wuhan, China: Huazhong University of Science and Technology.

Xie, H. P., Gao, M. Z., and Liu, J. Z. (2018). Research on exploitation and volume estimation of underground space in coal mines. *J. China Coal Soc.* 43 (6), 1484–1503.

Xie, H. P., Ren, S. H., and Xie, Y. C. (2021). Development opportunities of the coal industry towards the goal of carbon neutrality. *J. China Coal Soc.* 46 (6), 1808–1820.

Yang, Y., Yu, H. Y., Lu, G., Wang, L. m., Zhao, Y., and Hao, L. s. (2020). Interview on the unprecedented changes of energy geopolitics and national energy security. *J. Nat. Resour.* 35 (11), 2803–2820. doi:10.31497/zrzyxb.20201119

Yin, Z. S., Sang, S. X., and Zhou, X. Z. (2014). Study on migration and enrichment regularities of CBM in exhausted coal resource. *Wells Special Oil Gas Reserv.* 21 (5), 48–51.

Zhang, L. L., Long, R. Y., and Chen, H. (2018). Carbon emission reduction potential of urban rail transit in China based on electricity consumption structure. *Resour. Conservation Recycl.* 142, 113–121. doi:10.1016/j.resconrec.2018.11.019

Zhang, R., Liu, S. M., Bahadur, J., Elsworth, D., Wang, Y., Hu, G., et al. (2017). Changes in pore structure of coal caused by coal-to-gas bioconversion. *Sci. Rep.* 7, 3840. doi:10.1038/s41598-017-04110-z

Zhang, W. Y., Ni, X. M., and Wang, Y. B. (2015). Variation of coal permeability after injection carbon dioxide reactions with minerals in coal. *J. China Coal Soc.* 40 (5), 1087–1092.

Zhang, Y. S., Dong, D., Xiao, Y., Wang, T., and Wang, J. (2021). Current status and trends in energy production, consumption, and storage under carbon neutrality conditions in China. *China Sci. Bull* 66, 4466–4476. doi:10.1360/tb-2021-0797

Zhao, W. Z., Su, X. B., Xia, D. P., Hou, S., Wang, Q., and Zhou, Y. (2022). Enhanced coalbed methane recovery by the modification of coal reservoir under the supercritical CO_2 extraction and anaerobic digestion. *Energy* 259, 124914. doi:10.1016/j.energy.2022.124914

Zou, C. N., He, D. B., and Jia, C. Y. (2021b). Connotation and pathway of world energy transition and its significance for carbon neutral. *Acta Pet. Sin.* 42 (2), 233–247.

Zou, C. N., Xue, H. Q., and Xiong, B. (2021a). Connotation, innovation and vision of "carbon neutral". *Nat. Gas. Ind.* 41 (8), 46–57.

frontiers | Frontiers in Earth Science

TYPE Original Research
PUBLISHED 19 January 2023
DOI 10.3389/feart.2022.1042477

OPEN ACCESS

EDITED BY
Zhenzhi Wang,
Henan Polytechnic University, China

REVIEWED BY
Zhang Kun,
Anhui University of Science and Technology, China
Haichao Wang,
Xinjiang University, China

*CORRESPONDENCE
Wei Wang,
wangweiuuu@163.com
Qinghe Niu,
qinghniu@163.com

†PRESENT ADDRESS
Qizhi Wang,
School of Civil Engineering, Hebei University of Science and Technology, Shijiazhuang, China

SPECIALTY SECTION
This article was submitted to Economic Geology,
a section of the journal
Frontiers in Earth Science

RECEIVED 12 September 2022
ACCEPTED 20 October 2022
PUBLISHED 19 January 2023

CITATION
Niu Q, Hu M, Leng B, He X, Su W, Wang W, Wang Q, Chang J, Ji Z and Qi X (2023), Experimental and numerical model of anisotropic permeability and CO_2 injectivity of coal during CO_2 enhanced coalbed methane recovery process.
Front. Earth Sci. 10:1042477.
doi: 10.3389/feart.2022.1042477

Experimental and numerical model of anisotropic permeability and CO_2 injectivity of coal during CO_2 enhanced coalbed methane recovery process

Qinghe Niu[1,2,3]*, Mingwei Hu[1,2,3], Bing Leng[4], Xiang He[5], Wenjie Su[6], Wei Wang[1,2,3]*, Qizhi Wang[7†], Jiangfang Chang[1,2], Zhongmin Ji[8] and Xiaofei Qi[9]

[1]State Key Laboratory of Mechanical Behavior and System Safety of Traffic Engineering Structures, Shijiazhuang Tiedao University, Shijiazhuang, China, [2]Hebei Technology and Innovation Center on Safe and Efficient Mining of Metal Mines, Shijiazhuang, China, [3]Key Laboratory of Roads and Railway Engineering Safety Control (Shijiazhuang Tiedao University), Ministry of Education, Shijiazhuang, China, [4]The Second Drilling Engineering Branch of CNPC Bohai Drilling Engineering Co., Ltd., PetroChina, Renqiu, China, [5]Institute of Geology, The Fourth Oil Production Plant of Changqing Oilfield Company, PetroChina Company Limited., Jingbian, China, [6]Exploration Division of Changqing Oilfield Company, PetroChina Company Limited., Xi'an, China, [7]Innovation Center of Disaster Prevention and Mitigation Technology for Geotechnical and Structural Systems of Hebei Province (Preparation), Shijiazhuang, China, [8]School of Civil Engineering, Zhengzhou University of Technology, Zhengzhou, China, [9]The Second Geological Team of Hebei Coalfield Geology Bureau, Xingtai, China

Guaranteeing CO_2 injectivity has been the precondition for implementing the CO_2-enhanced coalbed methane recovery (CO_2-ECBM), however, it dramatically decreases during the CO_2 injection process because it is influenced by the dynamic change of the anisotropic permeability of coal. To reveal and evaluate the CO_2 injectivity of coal, the anisotropic permeability test and the CO_2 injectivity simulation test were first conducted, then the corresponding numerical models were established and verified by the experimental data. The results show that the permeability of coal in parallel face cleat direction is the largest, followed by the permeability of coal in parallel butt cleat direction and that in vertical bedding direction is the minimum. The peak value of the instantaneous injectivity rate is enhanced and the injection time is prolonged with the increase of the CO_2 injection pressure. The total CO_2 injectivity rate is nonlinearly increased from 13.61 to 311.87 cm^2/MPa min when the CO_2 injection pressure raises from 2 to 10 MPa. The anisotropic permeability model is appropriate to describe the dynamic evolution of permeability under different boundary conditions, the CO_2 injectivity prediction model can be used to evaluate the CO_2 injectivity during the CO_2 injection process. Increasing the CO_2 injection pressure may temporarily promote CO_2 injectivity, while the CO_2 injection increment is limited. The CO_2 fracturing by phase transition may be an available reservoir stimulation method for enhancing the CO_2 injection and should be focused on in the future.

KEYWORDS
CO_2-ECBM, adsorption swelling, injection pressure, cleat, CO_2 injectivity

Introduction

In 2018, China's total coal consumption has reached 2.74 billion tons. Although the Chinese government is adjusting its energy structure, it is predicted that the coal consumption demand is up to 50% of total energy consumption in 2025 (Xie et al., 2019). Coal burning has caused a lot of additional environmental problems, such as the sharp increase in greenhouse gas emissions and some heavily polluted weather (Rao and Rubin, 2002; Liu et al., 2021). The Chinese government pledges to reach a peak in its emissions by 2030 and strives to achieve carbon neutrality by 2,060, and a set of carbon emission reduction actions have been established. The carbon capture, utilization, and storage (CCUS) technology have been identified as the only option for substantially reducing GHG emission intensities while using fossil-fuel-based processes (Xu et al., 2019; Janzen et al., 2020). According to the differences in the geological reservoirs, the main CCUS forms are: utilizing CO_2 for enhanced oil recovery (CO_2-EOR) (Wei et al., 2019), gas recovery (CO_2-EGR) (Shi et al., 2017), coalbed methane (CO_2-ECBM) (Niu et al., 2017a; Niu et al., 2020a). As clean and efficient energy, the exploration and development of coalbed methane (CBM) can both relieve the energy crisis and improve the safety of coal mine operations (Wen et al., 2020; Niu et al., 2022). The Chinese government and related enterprises have advocated some technologies to improve the CBM extraction rate, among them, CO_2-ECBM is an effective and significant feasible way, and lots of pilot tests have been implemented all over the world (Godec et al., 2014; Pan et al., 2018). The theoretical basis of CO_2-ECBM is that the adsorption capacity of CO_2 on coal is stronger than that of CH_4, more CH_4 molecules are replaced and displaced out of the coal seam with the benefit of their competitive adsorption effect. However, the volumetric swelling induced by CO_2 adsorption is extremely serious, which compresses the space of fractures in coal seam and causes the significant attenuation of the reservoir permeability (Wang et al., 2020; Wang et al., 2021) and the CO_2 injectivity (Kumar et al., 2012), which has been confirmed by field tests (van Bergen et al., 2006; Shi et al., 2008). Guaranteeing CO_2 injectivity has been the precondition for implementing the CO_2-enhanced coalbed methane recovery (CO_2-ECBM) (Niu et al., 2021a).

For this issue, many researchers analyzed the evolution mechanism of coal permeability during the CO_2 injection process. Lin et al. found that the permeability reduction can reach 13 %–70% for the CO_2 exposure time in different testings (Lin et al., 2021), however, the permeability is also affected by many factors, for example, effective stress has a significant control effect on the permeability (Lv et al., 2022), when the CO_2 is injected into coal seams at high pressure, the decrease of effective stress has a dominated on permeability and can compensate the permeability loss induced by adsorption swelling (Anggara et al., 2016). Moreover, the moisture, temperature and coal rank are also related to the permeability, their positive and negative effects on the permeability of coal during CO_2 injection have been thoroughly studied (Niu et al., 2019a).

The coal has a complex pore-fracture structure, with the face cleat, butt cleat and bedding plane developing in it (Wang et al., 2018a; Jin et al., 2022; Liu et al., 2022), the permeability thus exhibits strong anisotropic characteristics. The fracture system is the medium to connect the wellbore and the pores in the coal matrix, the anisotropic characteristic of permeability should be emphasized because the permeability in any direction can affect the CO_2 injectivity of coal. To quantitatively describe the permeability of coal, Pan and Connell developed a model to predicate the behavior of anisotropic permeability for primary and enhanced coalbed methane recovery (Pan and Connell, 2011). And lots of investigators have improved the anisotropic permeability model by considering more conditions, such as the temperature (Zhou et al., 2020), the damaging effect (Cheng et al., 2022) and the gas slippage (Chen et al., 2020). However, the dynamic evolution of anisotropic permeability is complex and the evolution mechanism is not clear, meanwhile, the CO_2 injectivity model is lacking and causing the prediction of CO_2 injectivity to be difficult.

Therefore, in this paper, the anisotropic permeability and CO_2 injectivity experiments are first performed by a self-developed CO_2 injection and coalbed methane enhanced development model platform, then the anisotropic permeability evolution characteristics and mechanism are analyzed in depth, and finally, the anisotropic permeability and CO_2 injectivity models are established and verified by the experimental data. This research will provide technical guidance for the efficient CO_2 injection of coal seams and lay the theoretical foundation of CO_2-ECBM.

Experimental work

Sample preparation

The coal samples used in this paper were selected from the Chengzhuang coal mine and Sihe coal mine in Shanxi Province, China. The cubic sample (30 mm × 30 mm × 30 mm) was obtained by cutting from the block coal of Chengzhuang coal mine along the face cleat direction, the butt cleat direction and the bedding plane direction. The cylinder sample (50 mm × 100 mm) was obtained by core drilling rig from the block coal of Sihe coal mine along the vertical bedding direction. Then the

TABLE 1 The basic information of samples used in this work.

Sample source	$R_{o,max}$ (%)	Proximate analysis (wt%)					Ultimate analysis (wt%)			Maceral composition (vol%)		
		M_{ad}	A_{ad}	V_{daf}	FC_{ad}	O_{daf}	C_{daf}	H_{daf}	N_{daf}	Vit	Ine	Min
Chengzhuang coalmine	2.96	2.71	12.18	6.94	81.72	3.27	92.84	2.31	3.27	75.80	21.40	2.80
Sihe coalmine	3.33	1.48	13.12	6.32	81.39	2.98	93.45	2.15	1.00	79.84	18.36	1.80

Note: M_{ad}, moisture content of air-dried basis; A_{ad}, ash content of air-dried basis; V_{daf}, volatile content of dry ash-free basis; FC_{ad}, fixed carbon content of air-dried basis; O_{daf}, oxygen content of dry ash-free basis; C_{daf}, carbon content of dry ash-sfree basis; H_{daf}, hydrogen content of dry ash-free basis; N_{daf}, nitrogen content of dry ash-free basis; Vit, vitrinite; Ine, inertinite; Min, mineral.

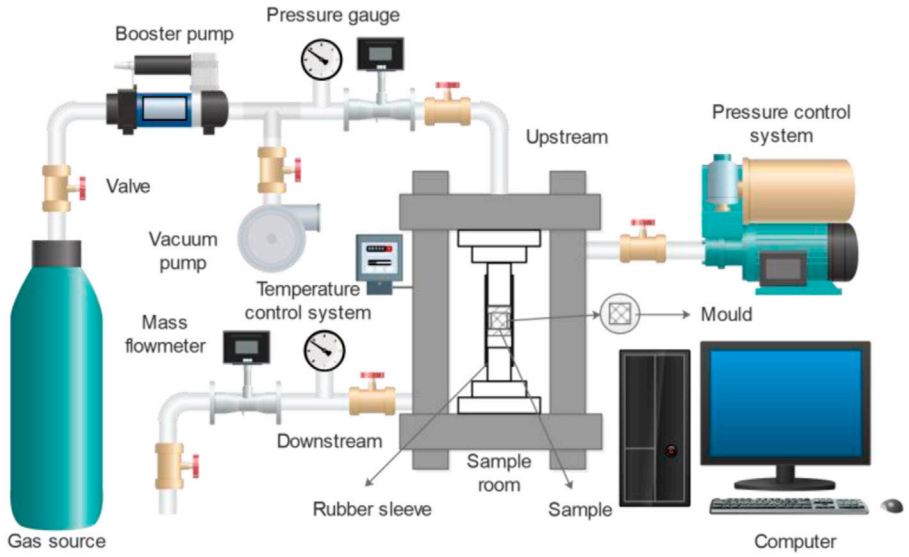

FIGURE 1
The anisotropic permeability testing system.

surfaces of the sample were polished with diamond sandpapers to ensure the accuracy of the experimental results. The proximate analysis, ultimate analysis and maceral composition were measured according to the standards suggested by International Standardization Organization (ISO 589, ISO 562, ISO 1171 and ISO 7404–3) (Table 1). The $R_{o,max}$ of coal samples from Chengzhuang coal mine and Sihe coal mine are 2.96% and 3.33%, respectively, and the fixed carbon, the carbon content and the inertinite are dominant in the results of proximate analysis, ultimate analysis and maceral composition.

Experimental setup

The anisotropic permeability was measured by the testing system shown in Figure 1. The CO_2 is stored in the gas tank and provides the gas source for the whole experimental setup. The booster pump is used to promote the gas pressure to the target value. The pressure gauge and the mass flowmeter are adopted to measure the gas real-time gas pressure and gas flow, with the accuracy of 0.01 MPa and 0.01 ml/min. The temperature control system is employed to guarantee that the experimental setup is still in a state of the constant target temperature. The pressure control system permits independent control of the axial stress and confining pressure of the sample, respectively. The monitored data is transmitted to the computer and the experimental process is operated by the control software installed on the computer. For the measurement of the permeability of the cubic sample, the sample is first installed in the homemade mould and then placed in the rubber sleeve with corrosion resistance, then the anisotropic permeability is tested by changing the sample orientation according to the method by Niu et al. (2018). For the measurement of the permeability of the cylinder sample, the sample is wrapped by

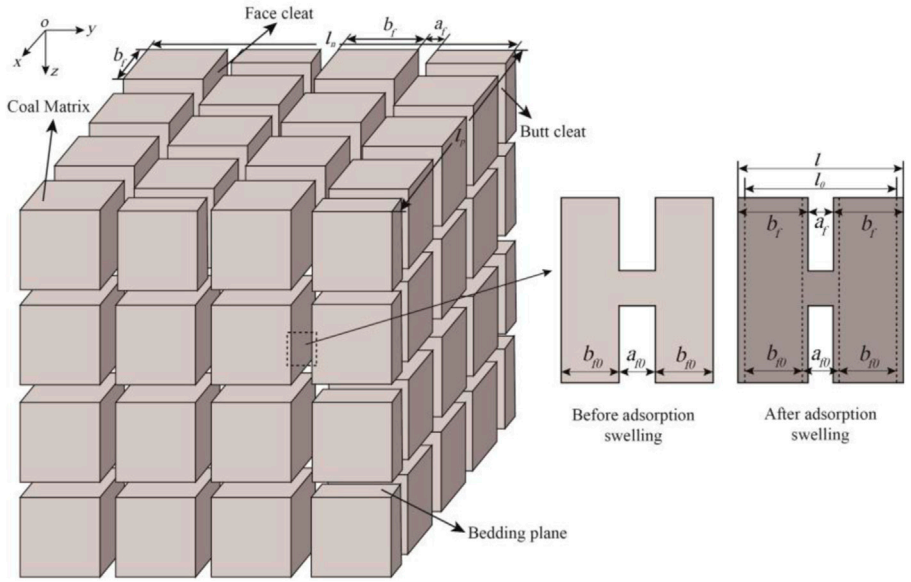

FIGURE 2
Schematic diagram of the representative elementary volume (REV) of coal and adsorption-induced swelling.

a rubber sleeve and placed in the sample room to measure the permeability.

Experimental scheme

The influence of the confining pressure and the gas pressure is analyzed and thus the permeability of coal is measured by alternately changing the confining pressure and the gas pressure. Referring to actual reservoir conditions, the confining pressure is set to 10, 12, 14 and 16 MPa, the gas pressure is set to 1, 2, 3 and 4 MPa, and the temperature is set to 35°C during the whole experimental process. The permeability of coal is calculated by the steady-state method based on the Darcy law, the principle has been introduced in previous research (Niu et al., 2019b; Niu et al., 2020b). For the simulation test of the CO_2 injection process, the confining pressure is 12 MPa, the injection pressure is increased from 2 MPa, 4 MPa, 6 MPa, 8–10 MPa, and the CO_2 injection flow is dynamically monitored by the inlet flowmeter and recorded in the computer.

Anisotropic permeability model of coal during the CO_2 injection process

Model establishment

A large number of studies show that the pores and fractures are widely regularly distributed in coal (Pan et al., 2016; Niu et al., 2017b; Niu et al., 2019a), i.e., the pores with different scales occur in the coal matrix (Jin et al., 2017; Jin et al., 2020), while the fractures occur between the coal matrix and cut coal into a system of matrix blocks. The fractures mainly include the face cleat, the butt cleat and the bedding plane fracture, they are vertically staggered with each other and distributed in the coal body (Rodrigues et al., 2014; Wang et al., 2018b; Jin et al., 2019). For the primary coal without geological structural fractures, the three-dimensional model of coal can be simplified to the representative elementary volume (Figure 2).

The cleats and bedding plane fractures are the main seepage channels, while the permeability of coal has a direct relationship with the porosity (Mckee et al., 1988):

$$\frac{k}{k_0} = \left(\frac{\phi}{\phi_0}\right)^3 \tag{1}$$

where the k and φ represent the permeability and porosity respectively, and the subscript 0 represents the initial value. For the REV, taking the oz direction as an example, the porosity in this direction is the plane porosity degree perpendicular to the oxy section:

$$\phi_f = \frac{A_f}{A_{rz}} \tag{2}$$

where the A_f represents the porosity in the oxy section, A_{rz} represents the area of oxy section. The oxy section is composed of several fractures. Assuming the fracture number is n_f, A_{rz} and A_f can be expressed as:

$$\begin{cases} A_f = n_f a_f l_p \\ A_{rz} = l_n l_p \end{cases} \tag{3}$$

where b_f represents the width of the coal matrix, the width of REV (l_n) is thus composed of fracture width (a_f) and coal matrix width:

$$l_n = (a_f + b_f) n_f \tag{4}$$

Substituting Eqs 3,4 into Eq. 2 to obtain:

$$\phi_f = \frac{A_f}{A_{rz}} = \frac{n_f a_f l_p}{l_n l_p} = \frac{n_f a_f}{(a_f + b_f) n_f} = \frac{a_f}{a_f + b_f} \tag{5}$$

Considering the anisotropic characteristics of coal, the porosity of the face cleat, butt cleat and bedding plane are respectively:

$$\begin{cases} \phi_x = \dfrac{a_x}{a_x + b_x} \\ \phi_y = \dfrac{a_y}{a_y + y} \\ \phi_z = \dfrac{a_z}{a_z + b_z} \end{cases} \tag{6}$$

Taking the face cleat as an example, the derivative of Eq. 6 can be obtained:

$$d\phi_x = d\left(\frac{a_x}{a_x + b_x}\right) = d\left(\frac{l - b_x}{a_x + b_x}\right) = \frac{b_x}{l_x}\left(\frac{dl_x}{l_x} - \frac{db_x}{b_x}\right) \tag{7}$$

Where:

$$\frac{b_x}{l_x} = 1 - \phi_x \tag{8}$$

Substituting Eq. 8 into Eq. 7 to obtain:

$$\frac{d\phi_x}{1 - \phi_x} = \frac{dl_x}{l_x} - \frac{db_x}{b_x} \tag{9}$$

It can also be written as:

$$\frac{\Delta\phi_x}{1 - \phi_x} = \frac{\Delta l_x}{l_x} - \frac{\Delta b_x}{b_x} \tag{10}$$

The porosity of coal is quite low. To simplify the formula, the 1-φ_x is approximated to 1. And the variation of face cleat width is caused by the strain in the direction of the butt cleat, then Eq. 10 can be converted into:

$$\Delta\phi_x = \Delta\varepsilon_y^b - \Delta\varepsilon_y^m \tag{11}$$

The strain of coal is composed of two parts, i.e., the strain caused by the change of effective stress ($\Delta\varepsilon_e$) and the strain caused by gas adsorption ($\Delta\varepsilon_a$), then the strain caused by the change of effective stress and gas adsorption in butt cleat direction are:

$$\begin{cases} \Delta\varepsilon_y^b = \Delta\varepsilon_{ay}^b + \Delta\varepsilon_{ey}^b \\ \Delta\varepsilon_y^m = \Delta\varepsilon_{ay}^m + \Delta\varepsilon_{ey}^m \end{cases} \tag{12}$$

According to Pan and Connell. (2011), for the anisotropic media, the strain caused by the effective stress in the face cleat direction under the action of three-dimensional stress can be expressed as:

$$\begin{cases} \Delta\varepsilon_{ey}^b = \dfrac{\Delta\sigma_{ey} - \nu_{xy}^b \sigma_{ex} - \nu_{zy}^b \sigma_{ez}}{E_y^b} \\ \Delta\varepsilon_{ey}^m = \dfrac{\Delta\sigma_{ey} - \nu_{xy}^m \sigma_{ex} - \nu_{zy}^m \sigma_{ez}}{E_y^m} \end{cases} \tag{13}$$

In this work, the compression is set as negative, the tension is set as positive, and the effective stress of coal is

$$\Delta\sigma_e = \alpha\Delta p - \Delta\sigma_t \tag{14}$$

Where the $\Delta\sigma_t$ represents the change of the external stress, α represents the Biot coefficient, Δp represents the change of the gas pressure. The deformation increment of coal due to gas adsorption is:

$$\begin{aligned} \Delta l &= l - l_0 = a_f + 2b_f - (a_{f0} + 2b_{f0}) \\ &= a_{f0} - 2\Delta\varepsilon_{ain}^m b_{f0} + 2b_{f0}(1 + \Delta\varepsilon_{at}^m) - (a_{f0} + 2b_{f0}) \\ &= 2b_{f0}(\Delta\varepsilon_{at}^m - \Delta\varepsilon_{ain}^m) \end{aligned} \tag{15}$$

Where $\Delta\varepsilon_{at}^m$ represents the total swelling strain change caused by the gas adsorption under limited conditions; $\Delta\varepsilon_{ain}^m$ represents the internal swelling strain change caused by the gas adsorption, which compresses the fractures in the coal and affects the permeability of the coal seam. In combination with Eq. 15, the swelling strain change of coal can be expressed as:

$$\Delta\varepsilon_{at}^b = \frac{\Delta l}{l_0} = \frac{2b_{f0}(\Delta\varepsilon_{at}^m - \Delta\varepsilon_{ain}^m)}{a_{f0} + 2b_{f0}} \tag{16}$$

Since the fracture width in coal is far smaller than the size of the coal matrix, i.e., $a_{f0} \ll b_{f0}$ Eq. 16 can be rewritten as:

$$\Delta\varepsilon_{at}^b = \frac{\Delta l}{l_0} = \frac{2b_{f0}(\Delta\varepsilon_{at}^m - \Delta\varepsilon_{ain}^m)}{a_{f0} + 2b_{f0}} \approx \Delta\varepsilon_{at}^m - \Delta\varepsilon_{ain}^m \tag{17}$$

The measured swelling strain change is $\Delta\varepsilon_{at}^b$ and the internal swelling strain is difficult to measure directly. Therefore, the internal swelling coefficient (f_{in}) is introduced in this paper, which is the ratio of internal swelling strain to total swelling strain. In addition to the influence of gas adsorption, the temperature and moisture will affect the permeability by affecting the internal swelling coefficient of coal. Therefore, assuming that f_{ina}, f_{inT} and f_{inw} are the internal swelling coefficients caused by gas adsorption, temperature and moisture respectively, the total internal swelling coefficient is:

$$f_{in} = f_{ina} + f_{inT} + f_{inw} \tag{18}$$

Then Eq. 17 can be converted into:

$$\Delta\varepsilon_{at}^{b} = \Delta\varepsilon_{at}^{m} - \Delta\varepsilon_{ain}^{m} = \varepsilon_{at}^{m} - \varepsilon_{ai0}^{m} - \left(\varepsilon_{ain}^{m} - \varepsilon_{ai0}^{m}\right) = \varepsilon_{at}^{m} - \varepsilon_{at0}^{m} - \left(f_{in}\varepsilon_{at}^{m} - f_{in0}\varepsilon_{at0}^{m}\right) = \varepsilon_{at}^{m}\left(1 - f_{in}\right) - \varepsilon_{at0}^{m}\left(1 - f_{in0}\right) \tag{19}$$

The change of swelling strain caused by gas adsorption in the face cleat can be expressed as:

$$\Delta\varepsilon_{ay}^{b} = \varepsilon_{ay}^{m}\left(1 - f_{in}\right) - \varepsilon_{ayo}^{m}\left(1 - f_{in0}\right) \tag{20}$$

The matrix swelling of coal conforms to the Langmuir-type equation, then the strain of matrix caused by gas adsorption of face cleat is:

$$\Delta\varepsilon_{ay}^{m} = \frac{\varepsilon_{Ly}P}{P + P_{Ly}} \tag{21}$$

Taking Eqs. 12, 13, 18, 20, and 21 with Eq. 11, the variation of porosity of face cleat is:

$$\Delta\phi_X = \frac{\Delta\sigma_{ey} - \nu_{xy}^{b}\sigma_{ex} - \nu_{zy}^{b}\sigma_{ez}}{E_y^{b}} - \frac{\Delta\sigma_{ey} - \nu_{xy}^{m}\sigma_{ex} - \nu_{zy}^{m}\sigma_{ez}}{E_y^{m}} - \varepsilon_{Ly}\left(\frac{\left(f_{ina} + f_{inT} + f_{inw}\right)_x P}{P + P_{Ly}} - \frac{\left(f_{ina} + f_{inT} + f_{inw}\right)_{x0} P_0}{P_0 + P_{Ly}}\right) \tag{22}$$

In the same way, the variation of porosity of the butt cleat and bedding plane is as follows:

$$\Delta\phi_y = \frac{\Delta\sigma_{ex} - \nu_{yx}^{b}\sigma_{ey} - \nu_{zx}^{b}\sigma_{ez}}{E_x^{b}} - \frac{\Delta\sigma_{ex} - \nu_{yx}^{m}\sigma_{ey} - \nu_{zx}^{m}\sigma_{ez}}{E_x^{m}} - \varepsilon_{Lx}\left(\frac{\left(f_{ina} + f_{inT} + f_{inw}\right)_y P}{P + P_{Lx}} - \frac{\left(f_{ina} + f_{inT} + f_{inw}\right)_{y0} P_0}{P_0 + P_{Lx}}\right) \tag{23}$$

$$\Delta\phi_z = \frac{\Delta\sigma_{ez} - \nu_{yz}^{b}\sigma_{ey} - \nu_{xz}^{b}\sigma_{ex}}{E_z^{b}} - \frac{\Delta\sigma_{ez} - \nu_{yz}^{m}\sigma_{ey} - \nu_{xz}^{m}\sigma_{ex}}{E_z^{m}} - \varepsilon_{Lz}\left(\frac{\left(f_{ina} + f_{inT} + f_{inw}\right)_x P}{P + P_{Lz}} - \frac{\left(f_{ina} + f_{inT} + f_{inw}\right)_{z0} P_0}{P_0 + P_{Lz}}\right) \tag{24}$$

Therefore, the porosity in any seepage direction is:

$$\phi_i = \phi_{i0} + \begin{bmatrix} \frac{\Delta\sigma_{ej} - \nu_{ij}^{b}\Delta\sigma_{ei} - \nu_{kj}^{b}\Delta\sigma_{ek}}{E_j^{b}} - \frac{\Delta\sigma_{ej} - \nu_{ij}^{m}\Delta\sigma_{ei} - \nu_{kj}^{m}\Delta\sigma_{ek}}{E_j^{m}} \\ + \frac{\Delta\sigma_{ek} - \nu_{ik}^{b}\Delta\sigma_{ei} - \nu_{jk}^{b}\Delta\sigma_{ej}}{E_k^{b}} - \frac{\Delta\sigma_{ek} - \nu_{ik}^{m}\Delta\sigma_{ei} - \nu_{jk}^{m}\Delta\sigma_{ej}}{E_k^{m}} \\ -\varepsilon_{Lj}\left(\frac{\left(f_{ina} + f_{inT} + f_{inw}\right)_j P}{P + P_{Lj}} - \frac{\left(f_{ina} + f_{inT} + f_{inw}\right)_{j0} P_0}{P + P_{Lj}}\right) \\ -\varepsilon_{Lk}\left(\frac{\left(f_{ina} + f_{inT} + f_{inw}\right)_k P}{P + P_{Lk}} - \frac{\left(f_{ina} + f_{inT} + f_{inw}\right)_{k0} P_0}{P_0 + P_{Lk}}\right) \end{bmatrix} \tag{25}$$

Substitute Eq. 25 into Eq. 1 to obtain:

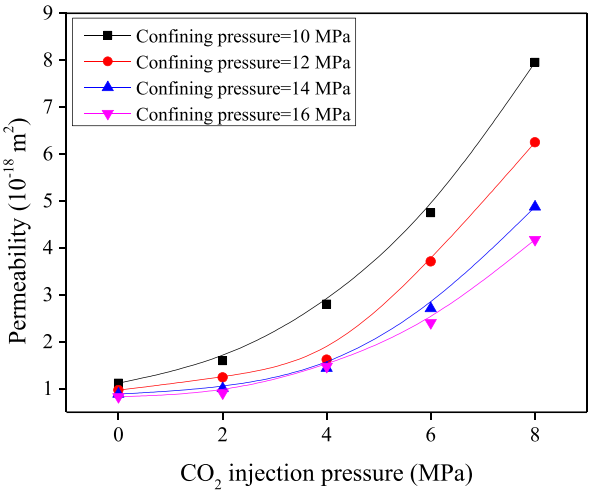

FIGURE 3
Changes in the permeability of cylinder sample with the increasing CO_2 injection pressure.

$$k_i = k_{i0}\left\{1 + \frac{1}{\phi_{i0}}\begin{bmatrix} \frac{\Delta\sigma_{ej} - \nu_{ij}^{b}\Delta\sigma_{ei} - \nu_{kj}^{b}\Delta\sigma_{ek}}{E_j^{b}} - \frac{\Delta\sigma_{ej} - \nu_{ij}^{m}\Delta\sigma_{ei} - \nu_{kj}^{m}\Delta\sigma_{ek}}{E_j^{m}} \\ + \frac{\Delta\sigma_{ek} - \nu_{ik}^{b}\Delta\sigma_{ei} - \nu_{jk}^{b}\Delta\sigma_{ej}}{E_k^{b}} - \frac{\Delta\sigma_{ek} - \nu_{ik}^{m}\Delta\sigma_{ei} - \nu_{jk}^{m}\Delta\sigma_{ej}}{E_k^{m}} \\ -\varepsilon_{Lj}\left(\frac{\left(f_{ina} + f_{inT} + f_{inw}\right)_j P}{P + P_{Lj}} - \frac{\left(f_{ina} + f_{inT} + f_{inw}\right)_{j0} P_0}{P + P_{Lj}}\right) \\ -\varepsilon_{Lk}\left(\frac{\left(f_{ina} + f_{inT} + f_{inw}\right)_k P}{P + P_{Lk}} - \frac{\left(f_{ina} + f_{inT} + f_{inw}\right)_{k0} P_0}{P_0 + P_{Lk}}\right) \end{bmatrix}^3\right\} \tag{26}$$

Where, $i \neq j \neq k$, for coal with a porous structure, the elastic modulus of the matrix is far greater than that of coal, i.e., $E_j^{m} \gg E_j^{b}$, Eq. 26 is converted into:

$$k_i = k_{i0}\left\{1 + \frac{1}{\phi_{i0}}\begin{bmatrix} \frac{\Delta\sigma_{ej} - \nu_{ij}^{b}\Delta\sigma_{ei} - \nu_{kj}^{b}\Delta\sigma_{ek}}{E_j^{b}} + \frac{\Delta\sigma_{ek} - \nu_{ik}^{m}\Delta\sigma_{ei} - \nu_{jk}^{m}\Delta\sigma_{ej}}{E_j^{m}} \\ -\varepsilon_{Lj}\left(\frac{\left(f_{ina} + f_{inT} + f_{inw}\right)_j P}{P + P_{Lj}} - \frac{\left(f_{ina} + f_{inT} + f_{inw}\right)_{j0} P_0}{P_0 + P_{Lj}}\right) \\ -\varepsilon_{Lk}\left(\frac{\left(f_{ina} + f_{inT} + f_{inw}\right)_k P}{P + P_{Lk}} - \frac{\left(f_{ina} + f_{inT} + f_{inw}\right)_{k0} P_0}{P_0 + P_{Lk}}\right) \end{bmatrix}^3\right\} \tag{27}$$

Boundary condition

(1) Constant confining pressure

Under this boundary condition, the pore pressure changes while the total stress remains unchanged:

$$\Delta\sigma_{tx} = \Delta\sigma_{ty} = \Delta\sigma_{tz} = 0 \tag{28}$$

The effective stress can be expressed as:

$$\Delta\sigma_{ex} = \Delta\sigma_{ey} = \Delta\sigma_{ez} = \Delta P \tag{29}$$

Substitute Eq. 29 into Eq. 27 to obtain the permeability model under the boundary condition of constant confining pressure:

$$k_i = k_{i0}\left\{1 + \frac{1}{\phi_{i0}}\left[\begin{array}{c} \frac{\left(1-V_{ij}^b-V_{kj}^b\right)\Delta P}{E_j^b} + \frac{\left(1-V_{ik}^b-V_{jk}^b\right)\Delta P}{E_k^b} \\ -\varepsilon_{Lj}\left(\frac{\left(f_{ina}+f_{inT}+f_{inw}\right)_j P}{P+P_{Lj}} - \frac{\left(f_{ina}+f_{inT}+f_{inw}\right)_{j0}P_0}{P_0+P_{Lj}}\right) \\ -\varepsilon_{Lk}\left(\frac{\left(f_{ina}+f_{inT}+f_{inw}\right)_k P}{P+P_{Lk}} - \frac{\left(f_{ina}+f_{inT}+f_{inw}\right)_{k0}P_0}{P_0+P_{Lk}}\right) \end{array}\right]\right\}^3 \tag{30}$$

(2) Constant effective stress

Under this boundary condition, the effective stress remains unchanged, i.e., the increment of the effective stress is always zero:

$$\Delta\sigma_{ex} = \Delta\sigma_{ey} = \Delta\sigma_{ez} = 0 \tag{31}$$

Substitute Eq. 31 into Eq. 27 to obtain the permeability model under the boundary condition of constant effective stress:

$$k_i = k_{i0}\left\{1 - \frac{1}{\phi_{i0}}\left[\begin{array}{c} -\varepsilon_{Lj}\left(\frac{\left(f_{ina}+f_{inT}+f_{inw}\right)_j P}{P+P_{Lj}} - \frac{\left(f_{ina}+f_{inT}+f_{inw}\right)_{j0}P_0}{P_0+P_{Lj}}\right) \\ +\varepsilon_{Lk}\left(\frac{\left(f_{ina}+f_{inT}+f_{inw}\right)_k P}{P+P_{Lk}} - \frac{\left(f_{ina}+f_{inT}+f_{inw}\right)_{k0}P_0}{P_0+P_{Lk}}\right) \end{array}\right]\right\}^3 \tag{32}$$

(3) Constant pore pressure

Under this boundary condition, the pore pressure remains unchanged, i.e., the increment of pore pressure is constant at zero:

$$\Delta P = 0 \tag{33}$$

The effective stress formula can be changed to:

$$\Delta\sigma_e = -\Delta\sigma_t \tag{34}$$

Substitute Eq. 34 into Eq. 27 to obtain the permeability model under the boundary condition of constant pore pressure:

$$k_i = k_{i0}\left\{1 - \frac{1}{\phi_{i0}}\left[\begin{array}{c} \frac{\Delta\sigma_{tj}-v_{ij}^b\Delta\sigma_{ti}-v_{kj}^b\Delta\sigma_{tk}}{E_j^b} + \frac{\Delta\sigma_{tk}-v_{ik}^b\Delta\sigma_{ti}-v_{jk}^b\Delta\sigma_{tj}}{E_j^m} \\ +\varepsilon_{Lj}\left(\frac{\left(f_{ina}+f_{inT}+f_{inw}\right)_j - \left(f_{ina}+f_{inT}+f_{inw}\right)_{j0}P_0}{P+P_{Lj}}\right) \\ +\varepsilon_{Lk}\left(\frac{\left(f_{ina}+f_{inT}+f_{inw}\right)_k - \left(f_{ina}+f_{inT}+f_{inw}\right)_{k0}P_0}{P_0+P_{Lk}}\right) \end{array}\right]\right\}^3 \tag{35}$$

Results and discussion

Permeability and model validation of cylinder sample

The permeability of the cylinder sample under different CO_2 injection pressures and confining pressures is shown in Figure 3. When the CO_2 injection pressure increases from 2 to 8 MPa, the permeability averagely increases from 0.95 $m^2 \times 10^{-18}$ m^2 to 5.81 $m^2 \times 10^{-18}$ m^2; when the confining pressure increases from 10 to 16 MPa, the permeability averagely decreases from 3.64 $m^2 \times 10^{-18}$ m^2 to 1.96 $m^2 \times 10^{-18}$ m^2. Apparently, the CO_2 permeability of coal is positively related to the injection pressure and negatively related to the confining pressure. Increasing the confining pressure will compress the fractures developed in coal and reduce the permeability while increasing the injection pressure will decrease the effective stress and promote the permeability.

For the cylinder sample, the permeability is assumed to be isotropic, hence, and Eq. 36 can be transformed into:

$$v_{ij}^b = v_{ik}^b = v_{ik}^b = v^b, E_j^b = E_k^b = E^b \tag{36}$$

$$k_i = k_{i0}\left\{1 - \frac{1}{\phi_{i0}}\left[\frac{2\left(1-2v^b\right)\Delta P}{E^b} - \varepsilon_L\left(\begin{array}{c} \frac{\left(f_{ina}+f_{inT}+f_{inw}\right)P}{P+P_{Lj}} \\ -\frac{\left(f_{ina}+f_{inT}+f_{inw}\right)_0 P_0}{P_0+P_{Lj}} \end{array}\right)\right]\right\}^3 \tag{37}$$

To verify the reliability of the proposed model, the relevant parameters are from the literature (Peng et al., 2017), as shown in Table 2. The experimental data for permeability were first converted to k/k_0 and then fitted by the permeability model (Figure 4). The experimental data has a high correlation with this model, the correlation coefficients are all greater than 0.99. It indicates that the anisotropic permeability model can be used to predict the change of isotropic permeability if the difference of mechanical parameters in different directions is ignored. It can be seen that the k/k_0 gradually increases with the increase of CO_2 injection pressure. This is because the CO_2 injection causes the closed fractures to reopen. At the same time, the coal matrix swells to the outside, resulting in the widening of the fractures and improving the permeability of coal.

Permeability and model validation of cubic sample

The permeability of the cubic sample under different CO_2 injection pressures and confining pressures is shown in Figure 5. As a whole, the variation trends of permeability in either direction with confining pressure and CO_2 injection pressure are coincident, this indicates that the influence of the effect stress on the seepage capacity of face cleat, butt cleat and bedding plane fracture is analogous. However, the permeability measured in different directions shows distinct anisotropic characteristics. The ratios of k_x:k_y:k_z are 1.53:1.35:1, 1.58:1.42:1, 1.58:1.33:1, and 1.61:1.43:1 respectively, e.g., the permeability of coal in parallel face cleat direction is the largest, followed by the permeability of coal in parallel butt cleat direction, and that in vertical bedding direction is the minimum. The k_x, k_y and k_z of coal are respectively

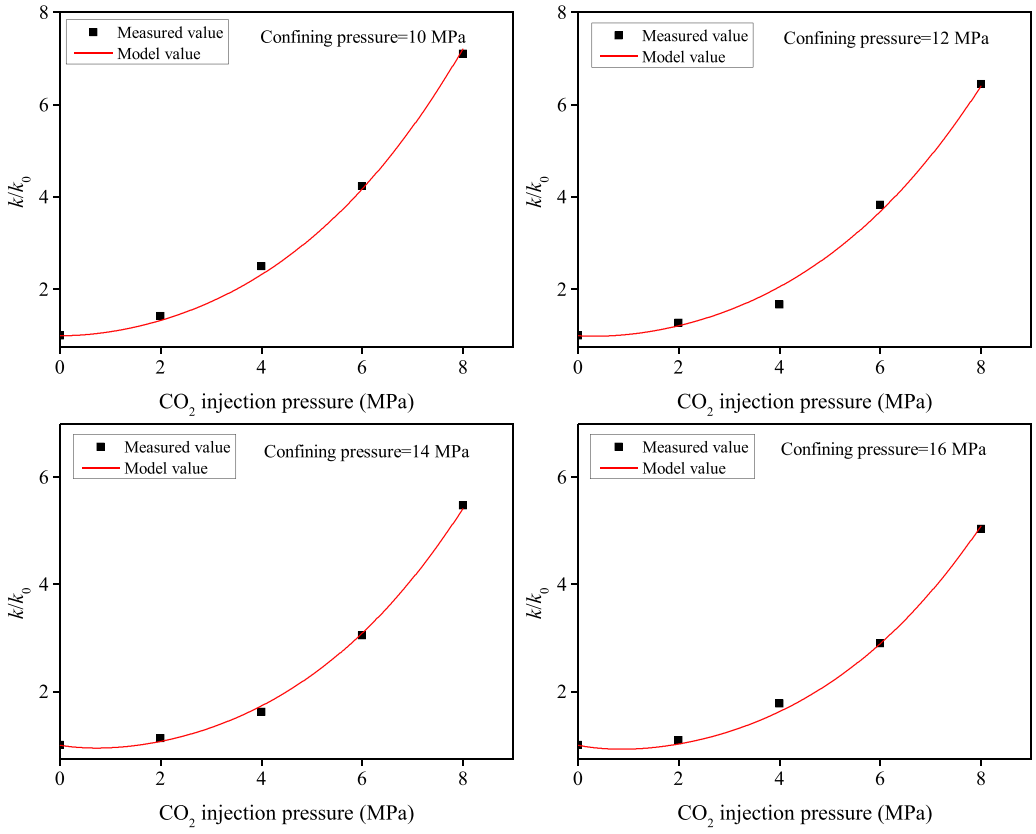

FIGURE 4
Fitting results of the permeability results of cylinder sample.

TABLE 2 Parameter values used for model validation of permeability of cylinder sample.

Parameter	Value	Unit
E^b	1,300	MPa
ν^b	0.3	—
ϕ_0	0.3	%
p_0	0	MPa
p_L	6	MPa
ε_L	0.025	—

contributed by the "face cleat + bedding plane fracture", the "butt cleat and bedding plane fracture" and the "bedding plane fracture", generally, the sequence of the average aperture from large to small is bedding plane fracture, face cleat and butt cleat (Busse et al., 2017; Shi et al., 2018; Wang et al., 2019). According to the parallel-plate law of fractures (Klimczak et al., 2010), it can be deduced that the permeability distribution in the different directions measured in this paper is reasonable and correct.

To verify the correctness of the anisotropic permeability model proposed in this paper, the parameters of elastic modulus, Poisson's ratio, Langmuir strain and Langmuir pressure were selected from the previous literatures and the porosity was the assumed value. The elastic modulus, Langmuir strain and Langmuir pressure are considered isotropic in the parallel bedding plane direction, while the Poisson's ratio is considered isotropic in three directions. The permeability results of the cubic sample are fitted by Eq. 38, it can be seen that the model value and the measured value show the same change trend (Figure 6), their correlation coefficients are higher than 0.96. Obviously, this anisotropic permeability model can be appropriate to evaluate the permeability evolution of heterogeneous coal reservoirs with CO_2 injection under *in situ* conditions.

CO_2 injectivity characteristic of coal

As analyzed above, CO_2 injectivity is the most critical factor restricting the implementation of CO_2-ECBM projects. To

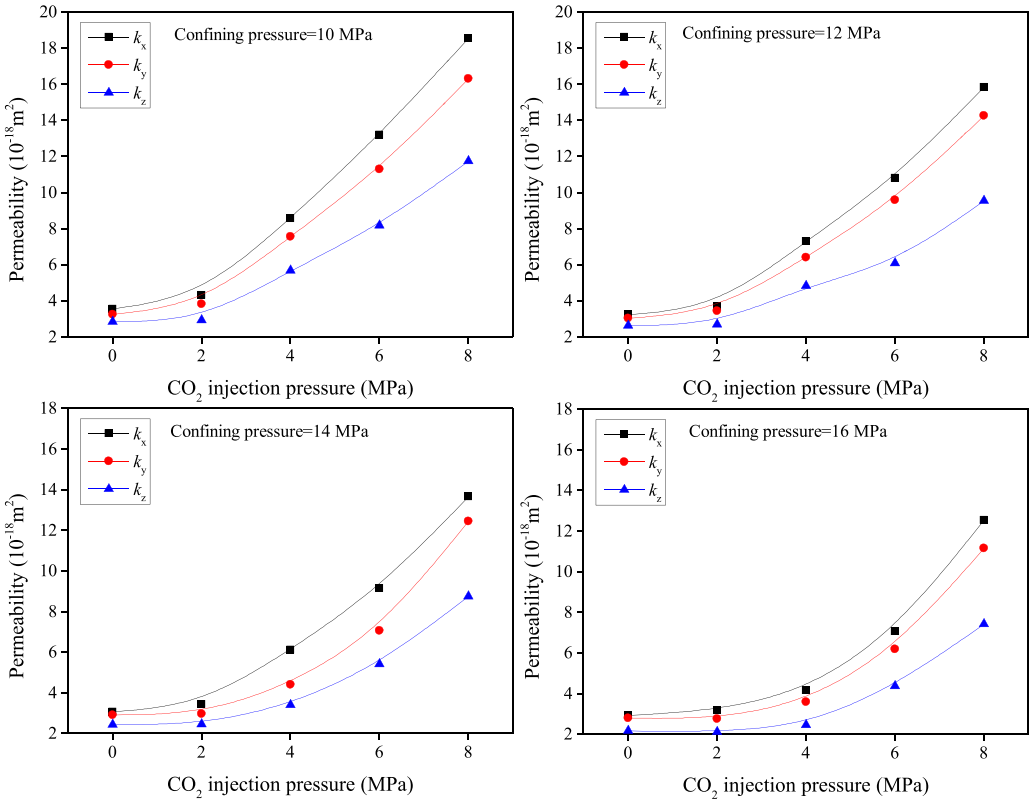

FIGURE 5
Changes in the permeability of cubic sample with the increasing CO_2 injection pressure.

investigate the CO_2 injectivity, the parameter of injectivity rate (J) is used to characterize the CO_2 injectivity of coal (Heddle et al., 2003):

$$J = \frac{Q_{in}}{h(P_{wf} - P)} \tag{38}$$

where h is the coal reservoir thickness, m; p_{wf} is the pressure at the wellbore, MPa; p is the reservoir pressure, MPa; Q_{in} is the injection flow, m^3/d.

The indoor permeability test formula is:

$$k = \frac{2Qp_a\mu L}{A(P_{in}^2 - P_{out}^2)} \tag{39}$$

Where k is the permeability, 10^{-15} m^2, Q is the volumetric rate of flow, cm^3/s; μ is the fluid viscosity, cp; L is the length of the sample, cm; A is the cross-section area of the sample, cm^2, p_{in} is the inlet gas pressure, Pa; p_{out} is the outlet gas pressure, Pa. Q=Q_{in}-V/t, V is the volume of pore in coal (cm^3) and t is the injection time (min).

Thus, the calculation formula for CO_2 injectivity of coal is:

$$J = \frac{kA(P_{in}^2 - P_{out}^2)}{h(P_{wf} - P)P_a\mu L} \tag{40}$$

The equivalent permeability can be expressed as:

$$k = \sqrt[3]{k_x k_y k_z} \tag{41}$$

Combining Eqs. 35, 39 the CO_2 injectivity evaluation model is obtained as follows:

$$J = \frac{A(P_{in}^2 - P_{out}^2)}{h(P_{wf} - P)P_a\mu L}\prod_{i\neq j\neq k}\left\{k_{i0} + \frac{k_{i0}}{\phi_{i0}}\begin{bmatrix} \frac{\Delta\sigma_{ej} - v_{ij}^b\Delta\sigma_{ei} - v_{kj}^b\Delta\sigma_{ek}}{E_j^b} + \frac{\Delta\sigma_{ek} - v_{ik}^b\Delta\sigma_{ei} - v_{jk}^b\Delta\sigma_{ej}}{E_k^b} \\ -\varepsilon_{Lj}\left(\frac{(f_{ina} + f_{inT} + f_{inw})_j}{P_{in} + P_{Lj}} - \frac{(f_{ina} + f_{inT} + f_{inw})_{j0}P_0}{P_0 + P_{Lj}}\right) \\ -\varepsilon_{Lk}\left(\frac{(f_{ina} + f_{inT} + f_{inw})_k P_{in}}{P_{in} + P_{Lk}} - \frac{(f_{ina} + f_{inT} + f_{inw})_{k0}P_0}{P_0 + P_{Lj}}\right) \end{bmatrix}\right\} \tag{42}$$

Then, the CO_2 injectivity evaluation model under the constant confining pressure condition can be converted to:

$$J = \frac{A(P_{in}^2 - P_{out}^2)}{h(P_{wf} - P)P_a\mu L}\prod_{i\neq j\neq k}\left\{k_{i0} + \frac{k_{i0}}{\phi_{i0}}\begin{bmatrix} \frac{(1 - v_{ij}^b - v_{kj}^b)\Delta P}{E_j^b} - \frac{(1 - v_{ik}^b - v_{jk}^b)\Delta P}{E_k^b} \\ -\varepsilon_{Lj}\left(\frac{(f_{ina} + f_{inT} + f_{inw})_j P_{in}}{P + P_{Lj}} - \frac{(f_{ina} + f_{inT} + f_{inw})_{j0}P_0}{P_0 + P_{Lj}}\right) \\ -\varepsilon_{Lk}\left(\frac{(f_{ina} + f_{inT} + f_{inw})_k P}{P + P_{Lk}} - \frac{(f_{ina} + f_{inT} + f_{inw})_{k0}P_0}{P_0 + P_{Lj}}\right) \end{bmatrix}\right\} \tag{43}$$

The changes in instantaneous injectivity rate with the time of coal under the confining pressure of 12 MPa are shown in

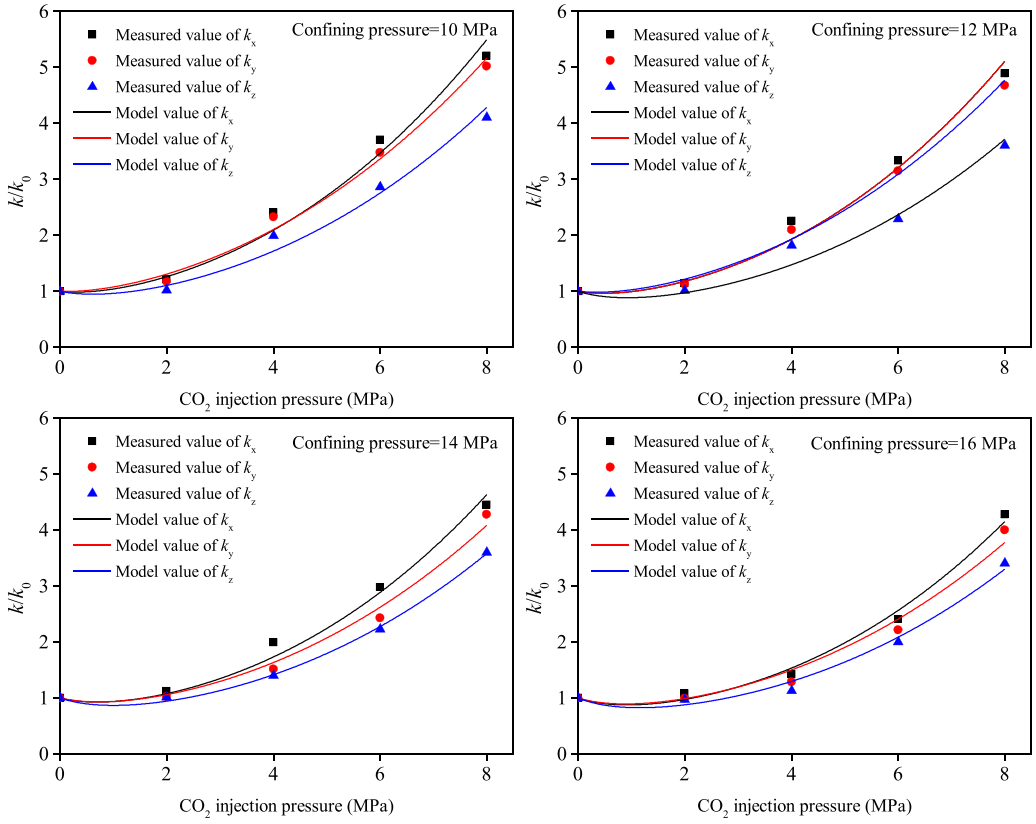

FIGURE 6
Fitting results of the permeability results of cubic sample.

Figure 7. When the CO_2 injection is injected into coal, the instantaneous injectivity rate is advanced immediately and shows several fluctuations. The maximum instantaneous injectivity rate for the subcritical CO_2 (CO_2 injection pressure < 7.4 MPa) can reach 1.8 cm^2/MPa min. The injection pressure is then reduced after 1 h and the CO_2 injectivity cannot recover during the subsequent monitoring process. Compared with the subcritical CO_2, there is no improvement in the instantaneous injectivity rate when the injection pressure reaches 8 MPa, while the maintenance time of the CO_2 injection process is promoted. In particular, two instantaneous injectivity rate peaks appear after 2 h of CO_2 injection. When the CO_2 injection pressure is equal to 10 MPa, the instantaneous injectivity rate increases dramatically, the maximum instantaneous injectivity rate is close to 5 cm^2/MPa min, and the injection process has the longest duration (3 h). It can be seen that the CO_2 injectivity of coal increases with the increase of injection pressure, which is because the closed fractures of coal are effectively supported and reopened under high injection pressure. At the same time, the high reservoir pressure drives more CO_2 molecules to migrate and diffuse into coal pores and further causes the injectivity increase of the coal seam.

Sum the instantaneous injectable rate at each injection pressure to obtain the total CO_2 injectivity rate, the relationship between the total CO_2 injectivity rate and the CO_2 injection pressure is shown in Figure 8 The total CO_2 injectivity rate is nonlinearly increased from 13.61 cm^2/MPa min to 311.87 cm^2/MPa min when the CO_2 injection pressure raises from 2 MPa to 10 MPa. The total CO_2 injectivity rate increases slowly during the subcritical CO_2 injection process and increase quickly during the supercritical CO_2 injection process.

The Formula (45) is used to fit the results between the total injectivity rate and the CO_2 injection pressure, the comparison results of the model value and the measured value are shown in Figure 8. The parameters used in the fitting process are from Table 3, the overall change trend of the CO_2 injectivity evaluation model is consistent with the experimental value. The main reason for the inconsistency depends on the selection of parameters and supposed conditions. Despite all this, the proposed CO_2 injectivity evaluation model is capable of predicting the CO_2 injectivity of a coal seam and will guide the favorable area optimization of CO_2-ECBM.

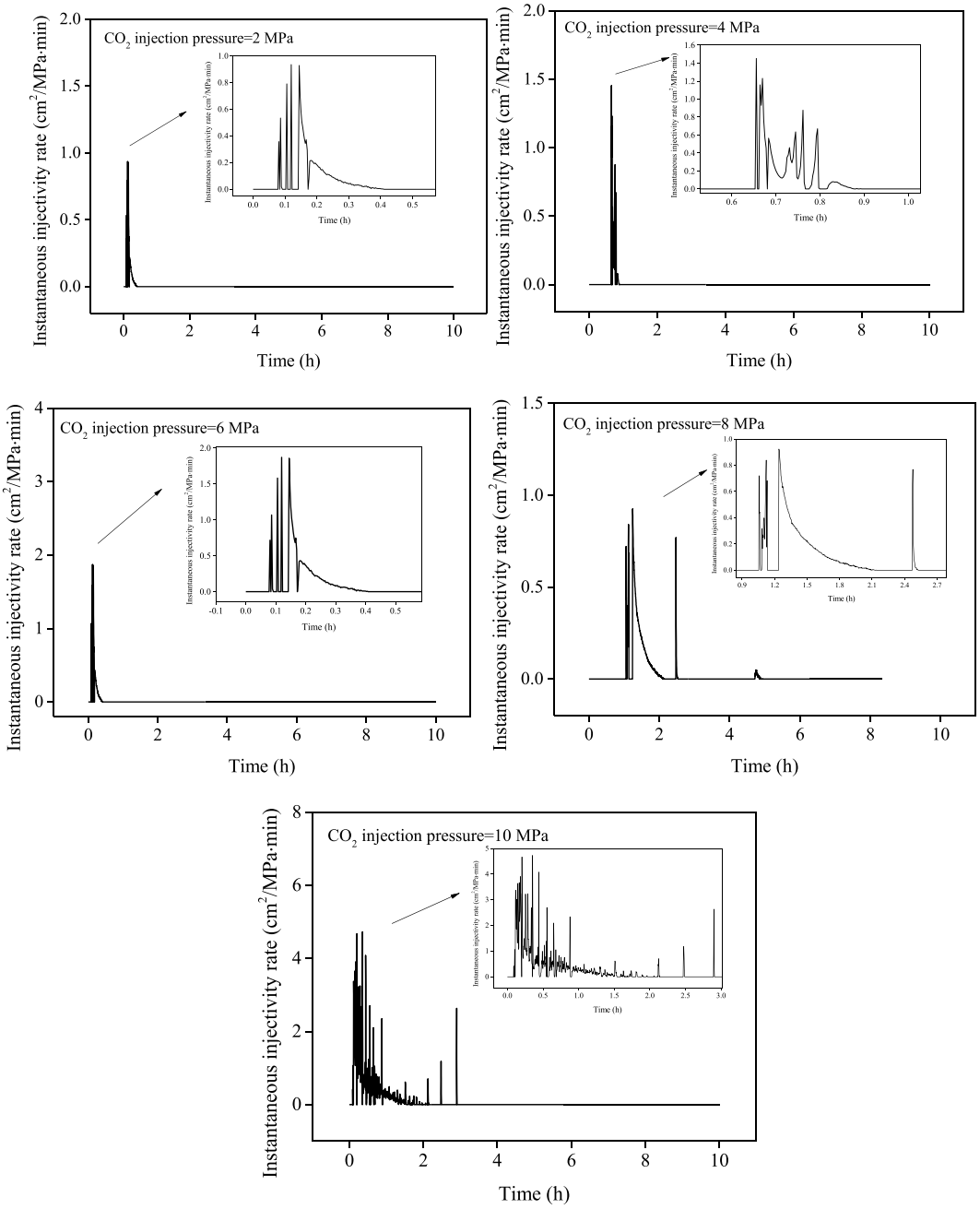

FIGURE 7
Changes in instantaneous injectivity rate with time.

Analysis of improving CO_2 injectivity of coal

CO_2 injectivity is the first requirement for evaluating the effectiveness of CO_2-ECBM, the main reason for CO_2-ECBM not being carried out on a large scale in China is that the CO_2 is difficult to be injected into coal seams. The key to restricting CO_2 injectivity is the permeability reduction induced by the adsorption swelling of the coal matrix. While the cleats are more susceptible to the swelling strain compared with the bedding plane fractures or other larger structural fractures (Niu et al., 2018), therefore, the narrowing or closing of the cleats intercepts the continuous injection process of CO_2 from the wellbores to the coal matrix pores. And both our experiment

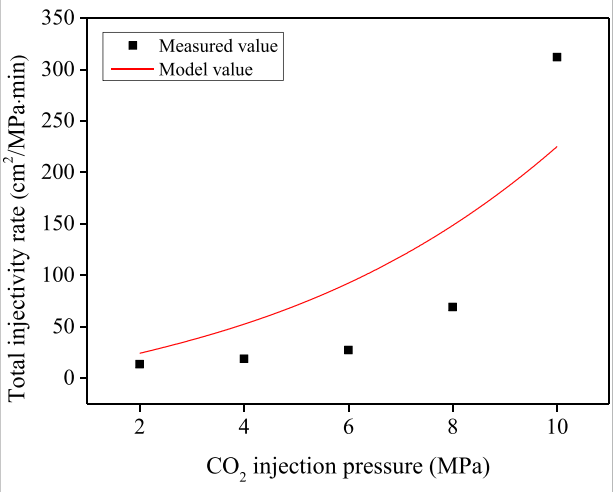

FIGURE 8
Fitting results of the total injectivity rate.

TABLE 3 Parameter values used for model validation of permeability of cubic sample.

Parameter	Value	Unit	Data source
$E_x^b = E_y^b$	2,800	MPa	Zhao et al. (2014)
E_z^b	2,120	MPa	
$\nu_x = \nu_y = \nu_z$	0.24	—	Jia, (2016)
ϕ_{x0}	0.340	%	Experimental value
ϕ_{y0}	0.350	%	
ϕ_{z0}	0.295	%	
$\varepsilon_{Lx}=\varepsilon_{Ly}$	0.634	%	Wang et al. (2013)
ε_{Lz}	1.063	%	
$p_{Lx}= p_{Ly}$	2.707	MPa	
p_{Lz}	2.582	MPa	

and numerical simulation confirm that increasing the CO_2 injection pressure can first offset the permeability decrease induced by adsorption swelling and then promote the permeability, this positive effect may be more favorable for the larger fractures and has little effect on the cleats (Zhang et al., 2019). Thus, increasing the CO_2 injection pressure may temporarily promote CO_2 injectivity, while the CO_2 injection increment is limited.

In the previous research, the intermittent CO_2 injection, N_2 displacing CO_2 and pre-fracturing for improving CO_2 injectivity were validated by the indoor experiment (Niu et al., 2021b), the reservoir stimulation may be the direct and effective measures to solve the problem of CO_2 injectivity attenuation. While traditional hydraulic fracturing can induce large-scale fractures and cannot connect the fractures on the cleat scale. The high-pressure CO_2 gas fracturing can damage the coal seams and promote the formation of the complex network of micro-fractures (Cao et al., 2022), which may promote the cleat seepage of coal during the CO_2 injection process and then increase the CO_2 injectivity. Thus, the CO_2 fracturing by phase transition may be available for enhancing the CO_2 injection and should be focused on in the future.

Conclusion

In this paper, the anisotropic permeability and CO_2 injectivity of coal during CO_2 enhanced coalbed methane recovery process were measured, and the corresponding numerical models were established and verified by the experimental data. Based on this, the dynamic evolution of CO_2 injectivity and methods of improving CO_2 injectivity was clarified. The major conclusions are drawn as follows:

(1) The anisotropic permeability of coal during the CO_2 injection process can be measured by the cubic coal samples. The permeability of coal in parallel face cleat direction is the largest, followed by the permeability of coal in parallel butt cleat direction, and that in vertical bedding direction is the minimum. The ratios of k_x:k_y:k_z are 1.53:1.35:1, 1.58:1.42:1, 1.58:1.33:1, and 1.61:1.43:1 respectively when the CO_2 injection pressure increases from 10 MPa to 16 MPa. The CO_2 injectivity is transformed from the data of CO_2 inlet flow, with the increase of the CO_2 injection pressure, the peak value of instantaneous injectivity rate is enhanced and the injection time is prolonged. The total CO_2 injectivity rate is nonlinearly increased from 13.61 cm^2/MPamin to 311.87 cm^2/MPamin when the CO_2 injection pressure raises from 2 to 10 MPa.

(2) The anisotropic permeability model of coal considering the influence of adsorption swelling, effective stress, water and temperature are established, the injectivity rate is proposed to describe the CO_2 injectivity of coal and the CO_2 injectivity prediction model is built based on the anisotropic permeability model. The validity of these models is confirmed by the experimental results in this paper.

(3) The narrowing or closing of the cleats during the CO_2 injection process intercept the continuous injection process of CO_2 from the wellbores to coal matrix pores. Increasing the CO_2 injection pressure may temporarily promote CO_2 injectivity, while the CO_2 injection increment is limited. The CO_2 fracturing by phase transition may be effective for connecting the cleats in coal, which is thus an available reservoir stimulation method for enhancing the CO_2 injection and should be focused on in the future.

Data availability statement

The datasets presented in this study can be found in online repositories. The names of the repository/repositories and accession number(s) can be found in the article/Supplementary Material.

Author contributions

Writing—original draft: QN; conceptualization: WW; methodology: MH and BL; validation: XH and WS; formal analysis: QW; visualization: JC; resources: ZJ; supervision: XQ.

Funding

This work was supported by the National Natural Science Foundation of China (U1967208, 51979170, and 11902208), the Hebei Natural Science Foundation (E2021210128, E2021210077, and E2020208071), the S&T Program of Hebei (22374102D and 216Z5403G), the Science and Technology Project of Hebei Education Department (QN2021129 and BJK2022010), the Autonomous Subject of State Key Laboratory of Mechanical Behavior and System Safety of Traffic Engineering Structures (KF2020-08), and the Natural Science Foundation of Henan (222300420366).

Conflict of interest

Author BL was employed by the company CNPC Bohai Drilling Engineering Co., Ltd., and PetroChina. Author XH was employed by the company Changqing Oilfield Company and PetroChina Company Limited. Author WS was employed by the company Exploration Division of Changqing Oilfield Company, PetroChina Company Limited.

The remaining authors declare that the research was conducted in the absence of any commercial or financial relationships that could be construed as a potential conflict of interest.

Publisher's note

References

Anggara, F., Sasaki, K., and Sugai, Y. (2016). The correlation between coal swelling and permeability during CO_2 sequestration: A case study using kushiro low rank coals. *Int. J. Coal Geol.* 166, 62–70. doi:10.1016/j.coal.2016.08.020

Busse, J., de Dreuzy, J. R., Galindo Torres, S., Bringemeier, D., and Scheuermann, A. (2017). Image processing based characterisation of coal cleat networks. *Int. J. Coal Geol.* 169, 1–21. doi:10.1016/j.coal.2016.11.010

Cao, Y., Zhang, J., Zhang, X., Liu, S., and Elsworth, D. (2022). Micro-fractures in coal induced by high pressure CO_2 gas fracturing. *Fuel* 311, 122148. doi:10.1016/j.fuel.2021.122148

Chen, Y., Jiang, C., Leung, J. Y., Wojtanowicz, A. K., and Zhang, D. (2020). Gas slippage in anisotropically-stressed shale: An experimental study. *J. Petroleum Sci. Eng.* 195, 107620. doi:10.1016/j.petrol.2020.107620

Cheng, X., Chen, L., Luan, H., Zhang, J., and Jiang, Y. (2022). Why coal permeability changes under unconstrained displacement boundary conditions: Considering damage effects. *J. Nat. Gas Sci. Eng.* 105, 104702. doi:10.1016/j.jngse.2022.104702

Godec, M., Koperna, G., and Gale, J. (2014). CO_2-ECBM: A review of its status and global potential. *Energy Procedia* 63, 5858–5869. doi:10.1016/j.egypro.2014.11.619

Heddle, G., Herzog, H., and Klett, M. (2003). *The economics of CO_2 storage*. Massachusetts Institute of Technology, Laboratory for Energy and the Environment.

Janzen, R., Davis, M., and Kumar, A. (2020). Evaluating long-term greenhouse gas mitigation opportunities through carbon capture, utilization, and storage in the oil sands. *Energy* 209, 118364. doi:10.1016/j.energy.2020.118364

Jia, J. L. (2016). *Experimental simulation on stress and StrainEffects as supercritical CO_2 being injected into deep anthracite reservoirs*. Xuzhou: China University of Mining and Technology.

Jin, Y., Dong, J., Zhang, X., Li, X., and Wu, Y. (2017). Scale and size effects on fluid flow through self-affine rough fractures. *Int. J. Heat Mass Transf.* 105, 443–451. doi:10.1016/j.ijheatmasstransfer.2016.10.010

Jin, Y., Wang, C., Liu, S., Quan, W., and Liu, X. (2020). Systematic definition of complexity assembly in fractal porous media. *Fractals* 28, 2050079. doi:10.1142/s0218348x20500796

Jin, Y., Zheng, J., Dong, J., Wang, Q., Liu, Y., Wang, B., et al. (2022). Fractal topography and complexity assembly in multifractals. *Fractals* 30, 529. doi:10.1142/s0218348x22500529

Jin, Y., Zheng, J., Liu, X., Pan, J., and Liu, S. (2019). Control mechanisms of self-affine, rough cleat networks on flow dynamics in coal reservoir. *Energy* 189, 116146. doi:10.1016/j.energy.2019.116146

Klimczak, C., Schultz, R. A., Parashar, R., and Reeves, D. M. (2010). Cubic law with aperture-length correlation: Implications for network scale fluid flow. *Hydrogeol. J.* 18, 851–862. doi:10.1007/s10040-009-0572-6

Kumar, H., Elsworth, D., Liu, J., Pone, D., and Mathews, J. P. (2012). Optimizing enhanced coalbed methane recovery for unhindered production and CO_2 injectivity. *Int. J. Greenh. Gas Control* 11, 86–97. doi:10.1016/j.ijggc.2012.07.028

Lin, J., Ren, T., Cheng, Y., and Nemcik, J. (2021). Laboratory quantification of coal permeability reduction effect during carbon dioxide injection process. *Process Saf. Environ. Prot.* 148, 638–649. doi:10.1016/j.psep.2021.01.038

Liu, X., Nie, B., Guo, K., Zhang, C., Wang, Z., and Wang, L. (2021). Permeability enhancement and porosity change of coal by liquid carbon dioxide phase change fracturing. *Eng. Geol.* 287, 106106. doi:10.1016/j.enggeo.2021.106106

Liu, X., Wang, L., Kong, X., Ma, Z., Nie, B., Song, D., et al. (2022). Role of pore irregularity in methane desorption capacity of coking coal. *Fuel* 314, 123037. doi:10.1016/j.fuel.2021.123037

Lv, A., Ali Aghighi, M., Masoumi, H., and Roshan, H. (2022). On swelling stress-strain of coal and their interaction with external stress. *Fuel* 311, 122534. doi:10.1016/j.fuel.2021.122534

Mckee, C. R., Bumb, A. C., and Koenig, R. A. (1988). Stress-Dependent permeability and porosity of coal and other geologic formations. *SPE Form. Eval.* 3, 81–91. doi:10.2118/12858-pa

Niu, Q., Cao, L., Sang, S., Wang, W., Yuan, W., Chang, J., et al. (2021b). A small-scale experimental study of CO_2 enhanced injectivity methods of the high-rank coal. *Petroleum Sci.* 18, 1427–1440. doi:10.1016/j.petsci.2021.08.006

Niu, Q., Cao, L., Sang, S., Wang, W., Zhou, X., Yuan, W., et al. (2021a). Experimental study on the softening effect and mechanism of anthracite with CO_2 injection. *Int. J. Rock Mech. Min. Sci.* 138, 104614. doi:10.1016/j.ijrmms.2021.104614

Niu, Q., Cao, L., Sang, S., Zhou, X., and Liu, S. (2019a). Experimental study of permeability changes and its influencing factors with CO_2 injection in coal. *J. Nat. Gas Sci. Eng.* 61, 215–225. doi:10.1016/j.jngse.2018.09.024

Niu, Q., Cao, L., Sang, S., Zhou, X., Wang, W., Yuan, W., et al. (2020a). Study on the anisotropic permeability in different rank coals under influences of supercritical CO_2 adsorption and effective stress and its enlightenment for CO_2 enhance coalbed methane recovery. *Fuel* 262, 116515. doi:10.1016/j.fuel.2019.116515

Niu, Q., Cao, L., Sang, S., Zhou, X., and Wang, Z. (2018). Anisotropic adsorption swelling and permeability characteristics with injecting CO_2 in coal. *Energy fuels.* 32, 1979–1991. doi:10.1021/acs.energyfuels.7b03087

Niu, Q., Cao, L., Sang, S., Zhou, X., Wang, Z., and Wu, Z. (2017a). The adsorption-swelling and permeability characteristics of natural and reconstituted anthracite coals. *Energy* 141, 2206–2217. doi:10.1016/j.energy.2017.11.095

Niu, Q., Pan, J., Cao, L., Ji, Z., Wang, H., Wang, K., et al. (2017b). The evolution and formation mechanisms of closed pores in coal. *Fuel* 200, 555–563. doi:10.1016/j.fuel.2017.03.084

Niu, Q., Pan, J., Jin, Y., Wang, H., Li, M., Ji, Z., et al. (2019b). Fractal study of adsorption-pores in pulverized coals with various metamorphism degrees using N_2 adsorption, X-ray scattering and image analysis methods. *J. Petroleum Sci. Eng.* 176, 584–593. doi:10.1016/j.petrol.2019.01.107

Niu, Q., Wang, Q., Wang, W., Chang, J., Chen, M., Wang, H., et al. (2022). Responses of multi-scale microstructures, physical-mechanical and hydraulic characteristics of roof rocks caused by the supercritical CO_2-water-rock reaction. *Energy* 238, 121727. doi:10.1016/j.energy.2021.121727

Niu, Q., Wang, W., Liang, J., Yuan, W., Wen, L., Chang, J., et al. (2020b). Investigation of the CO_2 flooding behavior and its collaborative controlling factors. *Energy fuels.* 34, 11194–11209. doi:10.1021/acs.energyfuels.0c01286

Pan, J., Niu, Q., Wang, K., Shi, X., and Li, M. (2016). The closed pores of tectonically deformed coal studied by small-angle X-ray scattering and liquid nitrogen adsorption. *Microporous Mesoporous Mater.* 224, 245–252. doi:10.1016/j.micromeso.2015.11.057

Pan, Z., and Connell, L. D. (2011). Modelling of anisotropic coal swelling and its impact on permeability behaviour for primary and enhanced coalbed methane recovery. *Int. J. Coal Geol.* 85, 257–267. doi:10.1016/j.coal.2010.12.003

Pan, Z., Ye, J., Zhou, F., Tan, Y., Connell, L. D., and Fan, J. (2018). CO_2 storage in coal to enhance coalbed methane recovery: A review of field experiments in China. *Int. Geol. Rev.* 60, 754–776. doi:10.1080/00206814.2017.1373607

Peng, Y., Liu, J., Pan, Z., Connell, L. D., Chen, Z., and Qu, H. (2017). Impact of coal matrix strains on the evolution of permeability. *Fuel* 189, 270–283. doi:10.1016/j.fuel.2016.10.086

Rao, A. B., and Rubin, E. S. (2002). A technical, economic, and environmental assessment of amine-based CO_2 capture technology for power plant greenhouse gas control. *Environ. Sci. Technol.* 36, 4467–4475. doi:10.1021/es0158861

Rodrigues, C. F., Laiginhas, C., Fernandes, M., Lemos De Sousa, M. J., and Dinis, M. A. P. (2014). The coal cleat system: A new approach to its study. *J. Rock Mech. Geotechnical Eng.* 6, 208–218. doi:10.1016/j.jrmge.2014.03.005

Shi, J., Durucan, S., and Fujioka, M. (2008). A reservoir simulation study of CO_2 injection and N_2 flooding at the Ishikari coalfield CO_2 storage pilot project. *Jpn. Int. J. Greenh. Gas. Con.* 2, 47–57. doi:10.1016/s1750-5836(07)00112-0

Shi, X., Pan, J., Hou, Q., Jin, Y., Wang, Z., Niu, Q., et al. (2018). Micrometer-scale fractures in coal related to coal rank based on micro-CT scanning and fractal theory. *Fuel* 212, 162–172. doi:10.1016/j.fuel.2017.09.115

Shi, Y., Jia, Y., Pan, W., Huang, L., Yan, J., and Zheng, R. (2017). Potential evaluation on CO_2-EGR in tight and low-permeability reservoirs. *Nat. Gas. Ind. B* 4, 311–318. doi:10.1016/j.ngib.2017.08.013

van Bergen, F., Pagnier, H., and Krzystolik, P. (2006). Field experiment of enhanced coalbed methane-CO_2 in the upper Silesian basin of Poland. *Environ. Geosci.* 13, 201–224. doi:10.1306/eg.02130605018

Wang, J. G., Liu, J., and Kabir, A. (2013). Combined effects of directional compaction, non-Darcy flow and anisotropic swelling on coal seam gas extraction. *Int. J. Coal Geol.* 109-110, 1–14. doi:10.1016/j.coal.2013.01.009

Wang, R., Wang, Q., Niu, Q., Pan, J., Wang, H., and Wang, Z. (2020). CO_2 adsorption and swelling of coal under constrained conditions and their stage-change relationship. *J. Nat. Gas Sci. Eng.* 76, 103205. doi:10.1016/j.jngse.2020.103205

Wang, Z., Fu, X., Hao, M., Li, G., Pan, J., Niu, Q., et al. (2021). Experimental insights into the adsorption-desorption of CH_4/N_2 and induced strain for medium-rank coals. *J. Petroleum Sci. Eng.* 204, 108705. doi:10.1016/j.petrol.2021.108705

Wang, Z., Fu, X., Pan, J., Niu, Q., Zhou, H., and Zhai, Y. (2019). The fracture anisotropic evolution of different ranking coals in Shanxi Province, China. *J. Petroleum Sci. Eng.* 182, 106281. doi:10.1016/j.petrol.2019.106281

Wang, Z., Pan, J., Hou, Q., Niu, Q., Tian, J., Wang, H., et al. (2018a). Changes in the anisotropic permeability of low-rank coal under varying effective stress in Fukang mining area, China. *Fuel* 234, 1481–1497. doi:10.1016/j.fuel.2018.08.013

Wang, Z., Pan, J., Hou, Q., Yu, B., Li, M., and Niu, Q. (2018b). Anisotropic characteristics of low-rank coal fractures in the Fukang mining area, China. *Fuel* 211, 182–193. doi:10.1016/j.fuel.2017.09.067

Wei, Q., Li, X., Hu, B., Zhang, X., Zhang, J., He, Y., et al. (2019). Reservoir characteristics and coalbed methane resource evaluation of deep-buried coals: A case study of the No.13–1 coal seam from the panji deep area in huainan coalfield, southern north China. *J. Petroleum Sci. Eng.* 179, 867–884. doi:10.1016/j.petrol.2019.04.100

Wen, H., Cheng, X., Chen, J., Zhang, C., Yu, Z., Li, Z., et al. (2020). Micro-pilot test for optimized pre-extraction boreholes and enhanced coalbed methane recovery by injection of liquid carbon dioxide in the Sangshuping coal mine. *Process Saf. Environ. Prot.* 136, 39–48. doi:10.1016/j.psep.2019.12.036

Xie, H. P., Wu, L. X., and Zheng, D. Z. (2019). Prediction on the energy consumption and coal demand of China in 2025. *J. China Coal Soc.* 44 (7), 1949–1960. doi:10.13225/j.cnki.jccs.2019.0585

Xu, L., Li, Q., Myers, M., Chen, Q., and Li, X. (2019). Application of nuclear magnetic resonance technology to carbon capture, utilization and storage: A review. *J. Rock Mech. Geotechnical Eng.* 11, 892–908. doi:10.1016/j.jrmge.2019.01.003

Zhang, G., Ranjith, P. G., Liang, W., Haque, A., Perera, M. S. A., and Li, D. (2019). Stress-dependent fracture porosity and permeability of fractured coal: An *in-situ* X-ray tomography study. *Int. J. Coal Geol.* 213, 103279. doi:10.1016/j.coal.2019.103279

Zhao, Y., Zhao, G., Jiang, Y., Elsworth, D., and Huang, Y. (2014). Effects of bedding on the dynamic indirect tensile strength of coal: Laboratory experiments and numerical simulation. *Int. J. Coal Geol.* 132, 81–93. doi:10.1016/j.coal.2014.08.007

Zhou, H. W., Rong, T. L., Wang, L. J., Mou, R. Y., and Ren, W. G. (2020). A new anisotropic coal permeability model under the influence of stress, gas sorption and temperature: Development and verification. *Int. J. Rock Mech. Min. Sci.* 132, 104407. doi:10.1016/j.ijrmms.2020.104407

frontiers | Frontiers in Earth Science

TYPE Original Research
PUBLISHED 23 January 2023
DOI 10.3389/feart.2022.1100951

OPEN ACCESS

EDITED BY
Junjian Zhang,
Shandong University of Science and Technology, China

REVIEWED BY
Junjian Zhang,
Shandong University of Science and Technology, China
Xiaoqi Wang,
Suzhou University, China

*CORRESPONDENCE
Yinghai Guo,
gyinghai@163.com

SPECIALTY SECTION
This article was submitted to Economic Geology, a section of the journal Frontiers in Earth Science

RECEIVED 17 November 2022
ACCEPTED 19 December 2022
PUBLISHED 23 January 2023

CITATION
Hu Y, Guo Y, Qing H and Hou Y (2023), Study on influencing factors and mechanism of pore compressibility of tight sandstone reservoir—A case study of upper carboniferous in ordos basin. *Front. Earth Sci.* 10:1100951. doi: 10.3389/feart.2022.1100951

Study on influencing factors and mechanism of pore compressibility of tight sandstone reservoir—A case study of upper carboniferous in ordos basin

Yunbing Hu[1,2,3], Yinghai Guo[2]*, Hairuo Qing[3] and Yundong Hou[4]

[1]Jiangsu Vocational Institute of Architectural Technology, Xuzhou, China, [2]School of Resources and Earth Science, China University of Mining and Technology, Xuzhou, China, [3]School of Science, University of Regina, Regina, SK, Canada, [4]Changqing Oilfield Exploration and Development Research Institute, Xi'an, China

A series of studies were carried out on 11 tight sandstone samples of Upper Carboniferous in Ordos Basin. Firstly, the deposit composition and pore structure characteristics are investigated based on analysis and experiments including cast thin section scanning electron microscope high-pressure mercury intrusion and nuclear magnetic resonance Then, combined with DP-P test, the stress-dependent permeability change and pore compressibility characteristics of sandstone reservoirs were studied to reveal the influencing factors and mechanism of reservoir pore compressibility. The detrital particles of the sandstone reservoir in the study area are mainly quartz (75.8%–89%), followed by fragments (3%–16.1%), and almost no feldspar. The content of interstitial materials is 6.5%–11.2%. The type I reservoirs mainly consist of mesopores and macropores, accounting for 60.57% and 32.84% respectively. Mesopores are dominated in Type II reservoirs, accounting for 78.98% of the total pore volume. There are almost no macropores, while a similar proportion of mesopores, micro mesopores and micropores in the type III reservoirs. The study of pore compressibility shows that the pore compressibility coefficient decreases with the increase of effective stress, and the reduction rate shows the two-stage characteristics of rapid in the early stage and slow in the later stage. The pressure turning point is between 3 and 10 MPa. The average pore compressibility coefficient increases from type I to type III reservoirs. The compressibility coefficient is directly proportional to the changing rate of the pore volume. The higher the content of rigid detrital particles, quartz and carbonate cement in sandstone, the smaller the pore compressibility coefficient, while the higher the content of ductile components such as soft rock fragments and clay minerals, the greater the pore compression coefficient. The pore-throat structure is closely related to the pore compressibility, reservoirs with low displacement pressure, T_{2glm} value, and large average pore-throat radius show lower compressibility coefficient. In addition, the compressibility coefficient of the reservoir is positively correlated with D_L (dimension of large pores such as mesopores and macropores), and negatively correlated with D_S (the fractal dimension of micropores and micro mesopores). It is considered the pore compression of sandstone including two stages, viscoplastic destructive deformation of ductile components for the first and then the small-scale non-ideal elastic deformation on rigid particles.

KEYWORDS

tight gas, pore compressibility, medium deformation, sandstone reservoirs, ordos basin

1 Introduction

Tight gas has become an important research field in worldwide exploration and development of oil and gas (Higgs et al., 2007; Guo et al., 2015; Wang et al., 2018; Hu et al., 2020a). The pore-throat structure characters, reflecting the pore-throat geometry, pore size distribution (PSD), and connectivity of tight sandstone reservoir, can affect the migration and accumulation of hydrocarbon, which thereby determines its subsequent efficient development (Lai et al., 2018; Jiang et al., 2020; Zong et al., 2020; You et al., 2021). The pore-throat structure of tight sandstone reservoir is mainly characterized by complexity and diversity appears as strong heterogeneity and disconnectivity, various types of pores in micron scaled and irregular forms of nano to submicron scaled throats, which all greatly destroy the seepage performance of the reservoir (Desbois et al., 2011; Zou et al., 2012a; Rezaee et al., 2012; Li et al., 2017; Wang et al., 2018). In addition, certain compressibility for pores of sandstone reservoir exists, and which can be characterized by compressibility coefficient. On the one hand, reservoir compression can provide a driving force for oil production, but at the same time, the reduction of pore pressure caused by reservoir exploitation will also increase the effective stress of the pores in the reservoir, which would get the complexity of pore throat structure increased, change the porosity and permeability, and thereby affect the natural gas productivity of the reservoir significantly (Vairogs et al., 1971; Jones and Owens, 1980; Lorenz, 1999; Dou et al., 2015; Zhang et al., 2015; Huang et al., 2021; Zhang et al., 2021). Therefore, the compression of reservoir pores needs to be carefully evaluated and utilized.

Reservoir pore compressibility coefficient, described as the changing rate of reservoir pore volume caused by the unit pressure added or unload, is a significant parameter in the calculation of dynamic geological reserves, the simulation of reservoir fluid flow, the prediction of petroleum productivity, and the evaluation of reservoir stress sensitivity (Zimmerman et al., 1986; Li et al., 2004; He et al., 2016; Yuan et al., 2018). The most intuitive calculation method for measuring the rock compressibility coefficient is to quantify the loss of pore volume caused by unit differential pressure (Seidle et al., 1992; Liu and Harpalani, 2014). However, due to the extremely low porosity of pores and fractures of samples in tight gas sandstone reservoirs, it is complicated to accurately measure the change of pore and fracture volume, and the measurement results are often of low confidence levels (Seidle et al., 1992; Liu and Harpalani, 2014). Under the action of effective stress, the compression of pore and fracture volume is bound to cause the change of reservoir permeability (Mckee et al., 1988; Seidle et al., 1992; Ross and Bustin, 2008; Dong et al., 2010; Ouyang et al., 2016; Yang et al., 2019). A large number of mathematical formulas and models have been established revealing the internal relationship between effective stress and reservoir permeability, among which the exponential relationship between the reservoir permeability and effective stress based on the pore-fracture compression coefficient is finally widely used (Seidle et al., 1992; Shi and Durucan, 2010; Chen et al., 2015; Yang et al., 2019). Therefore, the calculation method of deducing the pore compressibility coefficient by using the reservoir permeability changes obtained through laboratory experiment tests or logging numerical simulation is widely adopted (Li et al., 2013; Yao et al., 2021).

The compression of reservoir pores will cause a change in reservoir permeability to a certain extent. A large amount of research work has been brought into force on the stress sensitivity of reservoir permeability and its controlling factors. It is considered that the sensitivity of reservoir permeability is jointly controlled by the deposit composition and micro-pore structure (Kang et al., 2006; Sheng et al., 2016; Meng et al., 2019; Liu et al., 2020). However, there are limited studies on the characteristics, influencing factors, and mechanisms of the pore compressibility coefficient of tight sandstone reservoirs. Ordos Basin is an important petroliferous basin in China, which is rich in tight sandstone gas resources. In present study, sandstone samples from Benxi Formation, Upper Carboniferous of Ordos Basin, with different microstructures were selected for the measurement of porosity and permeability under different confining pressures. In addition tests and analyses such as CTS analysis, SEM observation, HPMI and NMR are carried out as well. On the basis of the study on reservoir material composition, micropore structure, and reservoir heterogeneity of samples, the discussion on the mechanism and influencing factors of reservoir pore compressibility were discussed subsequently, which will provide a theoretical basis for the evaluation of reservoir stress sensitivity in the process of drilling and production.

2 Experimental test and sample preparation

2.1 Sample collection

Ordos Basin with rich resources is one of the main natural gas-producing areas in China (Zou et al., 2012b). Benxi Formation in the basin is mainly filled with Lagoon-tidal flat, with lagoon iron aluminum mudstone at the bottom and tidal flat sandstone, mudstone, coal seam, thin limestone lens, barrier sand bar, and shallow water delta sediments upward. Its strata are widely distributed and the hydrocarbon source rocks with stable thickness generating here, which is an important gas source stratum in the Ordos basin. Meanwhile, two sets of large-scale sand bodies in the Pangou member and Jinci member also developed here (Figure 1C). The study area is located in the northeast of the Yishaan slope in Ordos Basin, as shown in Figure 1A, B

In the present study, a total of 11 tight sandstone reservoir column samples were drilled from different exploration wells for various tests and comprehensive analysis. The location distribution of sampling wells and their basic parameters are shown in Figure 1B and Table 1 respectively.

2.2 Experimental tests

11 column samples with a required size of 25 mm×50 mm were drilled from 11 sandstone samples, which were prepared for NMR and overburden permeability experiments. The remaining samples were broken into blocks of different sizes and prepared for CTS, SEM and, HPMI experiments.

The cast thin section (CTS) samples were prepared in the Langfang Branch of China Petrol. Explor. Dev+ Research Institute and then identified and analyzed *via* polarizing microscope technology in China University of Mining and Technology (CUMT), Xuzhou to investigate the petrological characteristics including reservoir deposit composition, characters of detrital particles, and pore-throat characters. The SEM observation was completed in the Advanced Analysis and Calculation Center of CUMT. In this study, all 11 samples about 0.5 cm long for each were gold-coated and dried and then the subsequent analysis was conducted with FEI quantatm

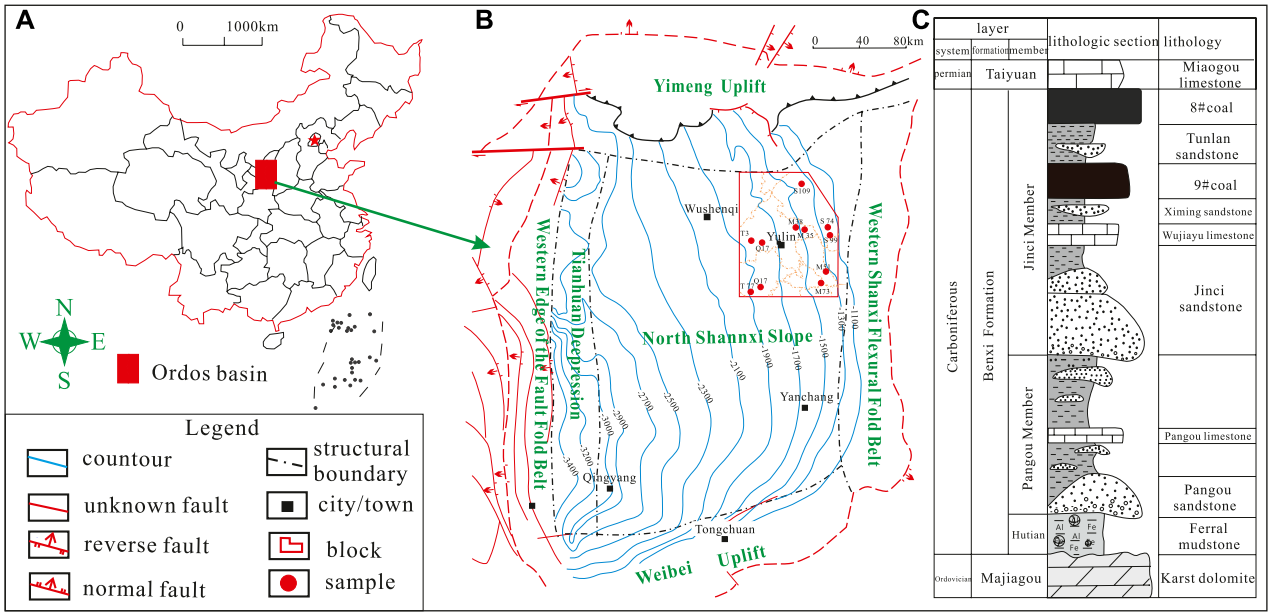

FIGURE 1
Sample information in the study area. **(A)** Location of Ordos Basin. **(B)** Location of the study area. **(C)** Stratigraphic characteristics of Benxi Formation in study area.

TABLE 1 The basic information and related parameters of selected experimental samples.

Number	Sample	Well	Depth (m)	Lithology	Permeability (mD)	Porosity (%)
1	22	Double 99	1966.4	Quartz arenite	1.2837	9.74
2	30	Tong 77	3326.27	Quartz arenite	1.2323	7.17
3	38	Shuang 74	2123.05	Sublitharenite	8.1069	10.91
4	69	Mi 35	2539.85	Sublitharenite	3.0147	9.70
5	18	Mi 51	2148.4	Quartz arenite	0.2424	6.44
6	21	Tong 3	2153.84	Sublitharenite	0.4775	7.26
7	37	Shuang 109	2381.44	Quartz arenite	0.2940	8.56
8	39	Shan 211	2129.13	Sublitharenite	0.1312	7.10
9	13	Qi 17	3026	Quartz arenite	0.0968	5.84
10	16	Mi 73	2298.85	Sublitharenite	0.0352	3.20
11	52	Mi 38	2773.77	Sublitharenite	0.0146	2.01

250 equipment to investigate the characteristics of mineral, pores, and reservoir morphology.

Sandstone samples with a size of about 4 mm were selected for high-pressure mercury intrusion experiments by using Micro metrics Auto pore IV9520 (0.1–60000 psi) according to the Chinese Standard SY/T5346-2005 to investigate the pore-throat structure characters. Firstly, the sample is dried in an oven at 70°C for 12 h, and then the test is carried out. A total of 108 pressure points were collected under the control of the computer during the whole experiment process. The upper-pressure limit was 200 MPa, as a result, the pore throat radium of 3 nm–1000 μm can be measured.

11 plunger samples were selected to conduct T_2 spectrum signal measurement under saturated centrifugal state by MacroMR12-150H-1 tester produced by Newmark testing company, Suzhou, China. The specific operation flow and parameter setting during the experiment are shown in Hu et al. (2020) (Lai et al., 2018).

Then, the AP-608 overlying pressure porosimeter produced by American core Temco Products Co., Ltd. was used to conduct pressure-sensitive experiments on column samples (Figure 2), aiming to measure the permeability of samples. The experimental method is called the unsteady-state pressure drop method, of which the experimental gas is high-purity nitrogen. The displacement pressure was provided by plunger pumps and the confining pressure was provided by separate confining pressure pumps. Under the condition of keeping the displacement pressure unchanged, the change of effective stress was simulated by

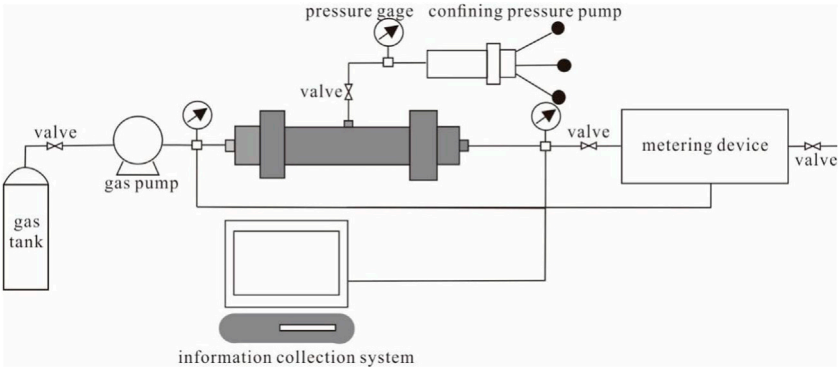

FIGURE 2
Schematic diagram of stress sensitivity experiment.

changing the confining pressure. In this way, the effective stress was increased to 3, 10, 15, 20, 25, 30, 40, and 50 MPa. At the same time, to avoid the influence of pressurization time and the change of total volume, it took 30 min to measure each pressure point, and the time interval of 30 s between the two pressure points was maintained.

2.3 Data processing method

2.3.1 Pore compressibility

Based on the data result of DP-P, Seidle et al. (1992) derived the typical formula on permeability and stress by using the matchstick model:

$$k = k_0 e^{-3c_f(\sigma-\sigma_0)} \tag{1}$$

Where C_f is the volume compressibility coefficient of pores and fractures under the effective horizontal stress in a changing state, Mpa^{-1}; K is the permeability measured under the changed stress, mD; K_0 is the initial permeability, mD.

Logarithmic operation on both sides of eq 1 can be further performed to obtain the calculation formula of compression coefficient C_f based on DC-P measurement:

$$c_f = \frac{-\ln(k/k_0)}{3(\sigma-\sigma_0)} \tag{2}$$

Equation 2 has become the most common method to solve C_f(Shi et al., 2014; Zhang et al., 2019). Therefore, the average compressibility coefficient C_{fi} under different effective stresses can be solved according to Eq 2.

$$c_{fi} = \frac{-\ln(k_i/k_0)}{3(\sigma_i-\sigma_0)} \tag{3}$$

Where C_{fi} is the average compression coefficient after the ith pressurization, MPa-1.

2.3.2 Fractal dimension

NMR fractal theories has showed its unique advantages in quantitatively characterizing the morphological and structural characteristics of pores and fractures in reservoirs (Harmer et al., 2001). When the fluid was placed in the environment where intergrated action of static magnetic field and radio frequency field exists, the spin hydrogen nuclei would performed NMR relaxation. Which could be expressed by transverse relaxation time T_2 (Cai et al., 2013). The formula is as follows.

$$\frac{1}{T_2} = \frac{1}{T_{2B}} + \frac{1}{T_{2S}} + \frac{1}{T_{2D}} \tag{4}$$

Where the T_{2B} and T_{2D} is the relaxation time caused by the fluid and pore surface interaction and diffusion, respectively, while the T_{2S} is surface relaxation time.

Taking the single fluid and well-distributed magnetic field into consideration, the T_{2b} and $T_{2D\ \mathrm{can\ be}}$ ignored (Cai et al., 2013). Then the T_2 formula can be rewritten as follows.

$$\frac{1}{T_2} \approx \frac{1}{T_{2S}} = \rho\frac{S}{V} = F_S\frac{\rho}{r} \tag{5}$$

Where F_S is the morphological factor. If the pore shape in the reservoir is regarded as spherical, the value of F_S would be 3. Then, the capillary pressure P_c can be calculated through the following formula 6.

$$P_c = C\frac{1}{T_2} \tag{6}$$

Where P_c represents capillary pressure, (MPa); and C is refer to the conversion factor and can be expressed as $C = |2\sigma\cos\theta/F_s\rho|$.

From Eq 6, we can conclude that there is an inverse relationship between capillary pressure P_c and transverse relaxation time T_2. Therefore, $P_{c\,\min} = C_{T2\,\max}{}^{-1}$.

Taking Washburn formula into consideration and then combining the derivation results of Ouyang et al. (2016), the formula describing the relationship between cumulative pore volume V_P and capillary pressure P_c can be concluded as follows

$$V_p = \left(\frac{P_c}{P_{c\,\min}}\right)^{D-3} \tag{7}$$

Combine Eq 6 and Eq 7, the formula of V_P can be rewritten as

$$V_p = \left(\frac{T_{2\,\max}}{T_2}\right)^{D-3} \tag{8}$$

Take logarithm on both sides of Eq 8, and then equation (8) is transformed into

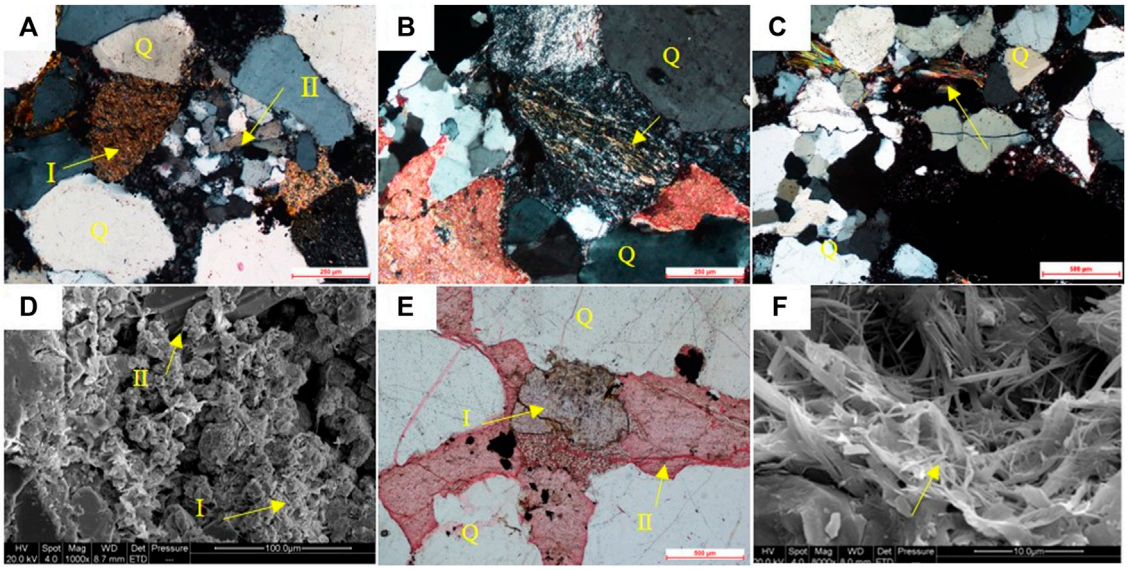

FIGURE 3
Material composition characteristics of tight sandstone reservoirs. **(A)**. Lgneous rock fragments (arrow II) slate fragments (arrow I), well Shuang74, 2123.05m, orthogonal polarization; **(B)**. Phyllite fragments, well Qi 17, 3026m, orthogonal polarization; **(C)**. Strongly deformed mica, well Mi 73, 2421.1m, orthogonally polarized; **(D)**. Kaolinite (arrow I), quartz (arrow II), well Tong 77, 3326.27m; **(E)**. Calcite (arrow II), iron calcite (arrow I), kaolinite, well Mi 38, 3480.45m, single polarized light; **(F)**. Illite, well Mi 73, 2421.1 m.

$$\lg\left(V_p\right) = (3 - D_w)\lg(T_2) + (D_w - 3)\lg T_{2\,\max} \quad (9)$$

Where V_p is the percentage of cumulative pore volume under saturated water state; D_w is the fractal dimension value based on NMR data under water-saturated state. T_{2max} is the maximum transverse relaxation time.

3 Results

3.1 Lithology characteristics

Through CTS and SEM analysis, it is found that the reservoir rocks are mainly quartz arenite and sublitharenite. quartz is mainly single crystal quartz (75.8%–89%, with an average of 81.79%). Almost free of feldspar. The content of rock fragments is low (3%–16.1%, with an average of 9.14%), and it mainly consists of rigid rock fragments such as magmatic rock and quartzite (Figure 3A) (with an average of 5.65%) and a small amount of ductile rock fragments such as slate, phyllite, and mica (Figure 3B,C) (with an average of 3.48%). The content of interstitial material ranges from 6.5% to 11.2%, with an average of 9.07%. It mainly consists of clay minerals (4.65%), quartz cement following (2.91%), and a small amount of carbonate and iron (average 1.13% and 0.47% respectively) (Figures 3D–F). The particles with good sorting are in subround-subangular shape and their size distribution of main particles range are different. The cement types are mainly poreed and enlarged pore type.

3.2 Pore type and structural characteristics

According to the analysis of CTS and SEM, various pores including residual primary intergranular pores, intergranular dissolved pores, intragranular dissolved pores, intergranular pores, and microfractures exist in the reservoir of the study area (Figure 3). Previous studies demonstrated that mercury injection parameter R_{50} of sandstone pore structure shows a significant correlation with reservoir porosity and permeability (Zhong et al., 2020). In the present study, based on the mercury injection experimental parameter R_{50} and the morphological characteristics of the capillary pressure curve of each sample, the pore structures are divided into three categories, type I, type II, and type III. The type I pore-throat structure reservoirs are composed of quartz arenite in coarse grain and giant grain size. The pore types appear in the form of multiple pore combinations, including residual intergranular pores, intergranular dissolved pores, intragranular dissolved pores, and intergranular pores, however, it is dominated by the intergranular pores and the throat is mainly necked and curved lamellar throat. The type II pore-throat structure reservoirs mainly consist of quartz arenite in medium-grained, with the pore types similar to the type I reservoir, however, the pores are mainly dissolution pores, with the curved lamellar throats. The type III pore-throat structure reservoirs are composed of quartz arenite and sublitharenite, fine-silt grained. The pores are mainly intragranular dissolved pores and intergranular pores, tubular throat. The pore structure characteristics of different types of reservoirs are shown in Table 2.

In terms of characterizing reservoir pore size and its distribution, The NMR technology shows higher accuracy than high-pressure mercury injection technology (Loucks et al., 2012; Li et al., 2019; Hu et al., 2020b). A large amount of research work has been conducted on pore classification based on pore size (Zou et al., 2012a; Zou et al., 2012b; Hu et al., 2020a). This research adopts the previous schemes of pore size division to divide pores into micropores, micro mesopores, mesopores, and macropores (Lai

10.3389/feart.2022.1100951

TABLE 2 Pore structure characteristic parameters of different types of tight sandstone reservoirs.

Type	I		II		III	
	Range	Average	Range	Average	Range	Average
Porrosity, %	8.2%–10.9	9.63	6.4–8.6	7.35	3.2–5.8	4.6
Permeability, mD	0.8–3.02	1.47	0.15–0.48	0.29	0.04–0.13	0.09
Threshold pressure, MPa	0.14–0.44	0.28	0.53–2.09	1.09	0.68–2.38	1.31
Sorting cofficient	0.28–0.94	0.59	0.06–0.24	0.13	0.05–3.04	1.08
Medium pressure, MPa	0.46–1.2	0.76	1.14–4.6	2.8	5.84–9.1	7.38
Medium Radius, μ m	0.62–1.64	1.11	0.26–0.56	0.41	0.02–0.14	0.1
Average pore throat radius, μ m	0.4–1.12	0.85	0.1–0.37	0.22	0.05–0.09	0.07
T2cutoff	20.8–51.3	38.8	16.9–57.6	31.7	0.5–34.3	3.8
Moverable water saturation,%	41.3–84.8	66.8	49.0–65.6	55.4	30.5–36.9	33.7

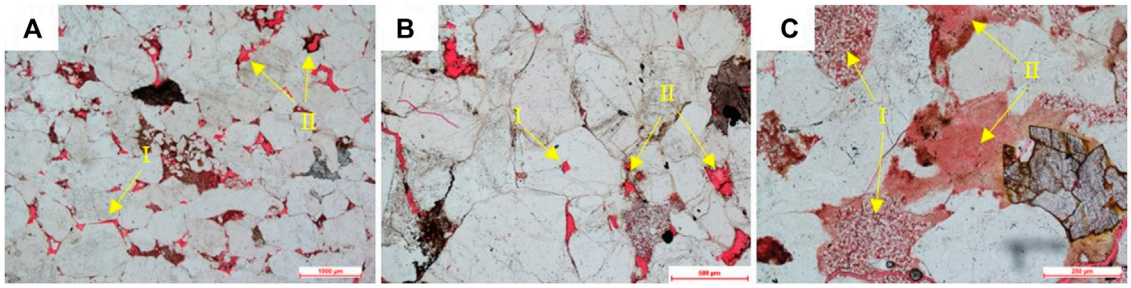

FIGURE 4
Pore types and pore characteristics of tight sandstone reservoirs **(A)**. Residual intergranular pore (arrow I), intergranular dissolved pore (arrow II), well Mi 35, 2539.85m, single polarized light; **(B)**. Intragranular dissolved pore (arrow I), intergranular dissolved pore (arrow II), well Mi 51, 2151.41m, single polarized light; **(C)**. Kaolinite intercrystalline pore (arrow I), illite intercrystalline pore (arrow II), well Mi38, 3480.45m, single polarized light.

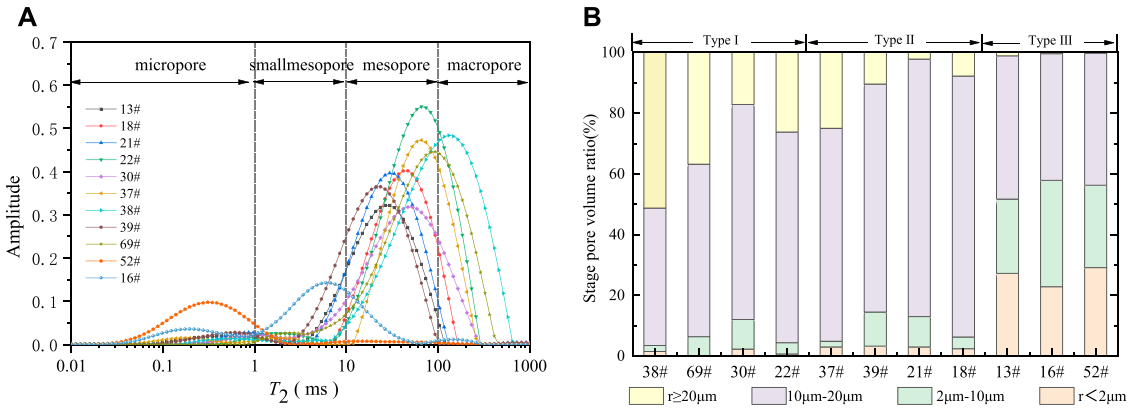

FIGURE 5
Reservoir **(A)** pore size division and **(B)** stage pore volume ratio of different types of pore structure reservoir.

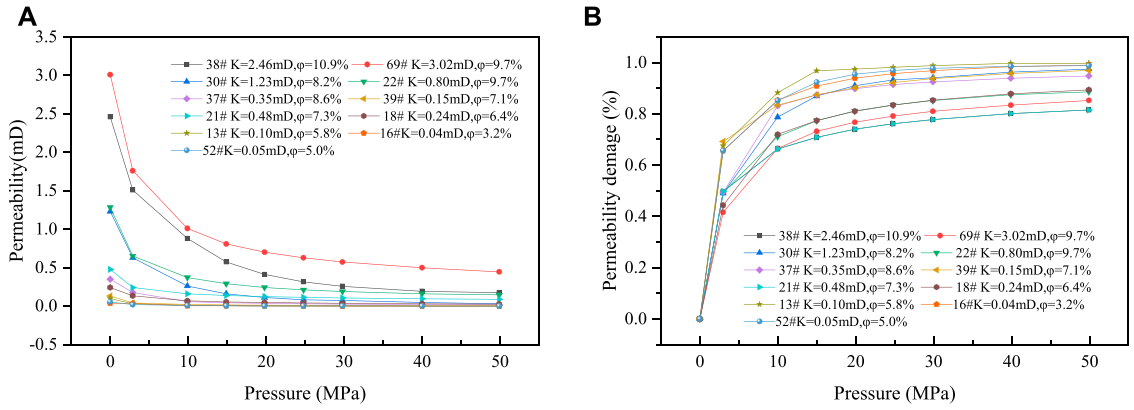

FIGURE 6
Variation of **(A)** permeability and **(B)** permeability damage rate of different samples under dynamic effective stress.

et al., 2016), and the corresponding T_2 values are ≤ 1 m, 1 ≤ T_2 ≤ 10 m, 10 ≤ T_2 ≤ 100 m and 100 ≤ T_2 ≤ 1000 m respectively (Figure 4A). By comparing the pore distribution characteristics of type I, II, and III reservoirs at different stages, it is founded that with the deterioration of reservoir physical properties, the proportion of reservoir pore volume at different stages changes significantly. The proportion of macro pores decreases sharply from the average of 32.84% of type I reservoirs to the average of 1.63% of type III reservoirs; The proportions of micro mesopores and micropores in type I and type II reservoirs are low, but they increase rapidly to an average of 25.16% and 36.77% respectively in type III reservoirs. The proportion of mesopores increases first and then decreases, and shows the highest proportion in type II reservoirs, accounting for 78.98%.

3.3 Change of reservoir permeability under effective stress state

The DP-P test result of 11 sandstone samples is shown in Figure 5A. It appears that as the effective stress increases from 0 MPa to 50MPa, the permeability shows a good exponential function decreasing trend. To investigate the influence of dynamic effective stress on permeability quantitatively, the dimensionless parameter D_K (permeability loss rat) was introduced to evaluate the permeability sensitivity caused by stress. The D_K can be calculated through the formula as follows:

$$D_k = \frac{k_0 - k_i}{k_0} \times 100\% \quad (10)$$

where k_0 is the permeability of sandstone samples under initial confining pressure, mD; K_i is the permeability of sandstone samples after applying confining pressure for i times, mD.

The variation of permeability damage rate of different samples with different effective stress is shown in Figure 5B. When effective stress reaches 50MPa, the permeability loss rate of samples ranges from 81.51% to 99.74%, with an average of 93.01%, which indicates that effective stress can compress reservoir pores, resulting in great changes in reservoir pore structure, and the permeability response of samples with different pore structures differs greatly to the same effective stress.

4 Discussion

4.1 Pore compressibility of tight sandstone reservoirs

The pore compression coefficients of 11 sandstone samples under different effective stress are calculated, as shown in Figure 6A. When effective stress is 3Mpa, the pore compression coefficients of sandstone samples are between 0.054 and 0.125, with an average of 0.084. When effective stress increases to 50MPa, the pore compression coefficients are between 0.013 and 0.040, with an average of 0.021. The pore compression coefficients decrease with the increase of the confining pressure. The comparison analysis of the pore compressibility characteristics among the three types of reservoirs (Figure 6B) indicates that under the same effective stress, the type III reservoir shows the largest average pore compressibility coefficient, and the type I reservoir has the smallest average pore compressibility coefficient, which indicates that the response sensitivity of pore compressibility to the change of effective stress increases from type I to type III reservoirs.

The effect of effective stress on pore compressibility among the tested samples shows obvious stages. During the stage of effective stress less than10MPa, with the increase of effective stress, the pore compressibility of samples decreases sharply. However, when effective stress reaches 10MPa, the change of pore compressibility coefficient to the increase of stress is not obvious. The unit stress-strain rate of reservoir pore volume decreases gradually and the pore compressibility coefficient tends to be stable, which reflects that pores are more difficult to be compressed in the later stage of compression. It is probably because pores and fractures of sandstone samples used to show high compressibility under the low-pressure stage, during that period, the large, medium-sized pores and micro-fractures tend to close firstly with the increasing effective pressure, thereby resulting in the obvious decrease of sandstone permeability (Figure 5A). However, with the continuous increase of the effective stress, the decreasing rate of pore-fracture

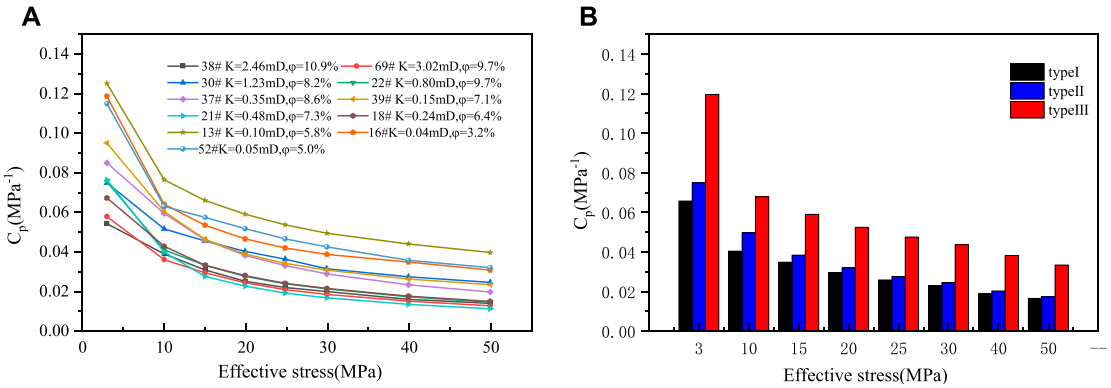

FIGURE 7
Pore compressibility characteristics of tight sandstone reservoirs **(A)** Distribution of pore compressibility coefficient of different samples under different effective stresses. **(B)** Pore compressibility of different types of reservoirs.

compressibility slows down to a very obvious extent. It is mainly because in this stage, the increase of stress can only cause the closure of some small pores, which leads to the slight change in the pore compressibility coefficient of sandstone during the later stage of stress increase (Figure 6A).

4.2 Influencing factors of pore compressibility

4.2.1 Porosity

The relationship between porosity and pore compressibility is analyzed, as shown in Figure 7, it is found that pore compressibility is negatively correlated to porosity. However, it is well known that loose rocks with high porosity are easier to be compressed than dense rocks. It should be pointed out that the compressibility coefficient is the rate of volume change under pressure. For rocks with the same volume, the higher the porosity, the less the skeleton volume, and the weaker level of support, therefore, the pore compressibility coefficient would be quite large. On the contrary, rocks with lower porosity show larger skeleton volume, stronger lever of support and smaller pore compressibility. The compressibility coefficient is not inversely proportional to the pore volume but directly proportional to the change rate of the pore volume. The smaller the pore volume is, the more difficult it is for the pores to be compressed. Therefore, compared with large pores, the change of small pore volume is smaller, however, the changing rate for pore volume is often greater than that of large pores.

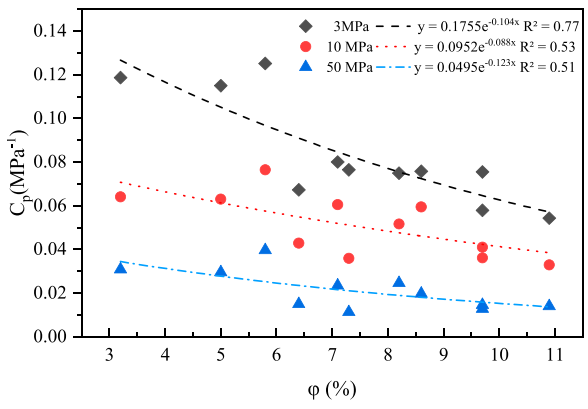

FIGURE 8
Relationship between reservoir porosity and pore compressibility under different stress states.

4.2.2 Lithology

Tight sandstone is composed of skeleton particles and interstitial materials that show a quite different compaction resistance properties. Skeleton particles of the tight sandstone reservoirs in the study area mainly consist of quartz and rock fragments. Quartzes and felspars with strong hardness and brittleness are not easy to be compressed, therefore the shape and size of skeleton particles are hardly get changed with the increase of effective stress (Zhang et al., 2004). The higher the relative content of quartz, the stronger the support of the reservoir rock skeleton and the more difficult it is for reservoir media to be compressed (Figure 8A). Therefore, the pore compression coefficient of type I reservoirs with higher quartz detrital particles is the smallest (Figure 6A). The type III reservoirs dominated by sublithiarenite are high in phyllite, slate fragments (Figures 9A, B), mica and other flexible components content. In addition, the abundant ductile clay mineral cement such as illite and kaolinite (Figures 9D, F) in type III reservoirs are easy to deform and break under external force. When effective stress increases, the ductile fragments and clay mineral particles are first compacted, deformed, and arranged more closely, and then the reservoir permeability gets reduced (He et al., 2012), At the same time, the loss of pore space makes the reservoir medium show strong pore compressibility. Therefore, the content of ductile material in sandstone is positively correlated with the pore compressibility coefficient (Figures 8B, C). Rigid cement existing among skeleton particles, such as over growth of quartz cement and continuous crystal cementation of carbonate cement (Figure 9E), can resist external stress and provide a strong supporting effect on pores and fractures, thus reducing the reservoir porosity compressibility (Bloch et al., 2002; Henares et al., 2016) (Figure 8D).

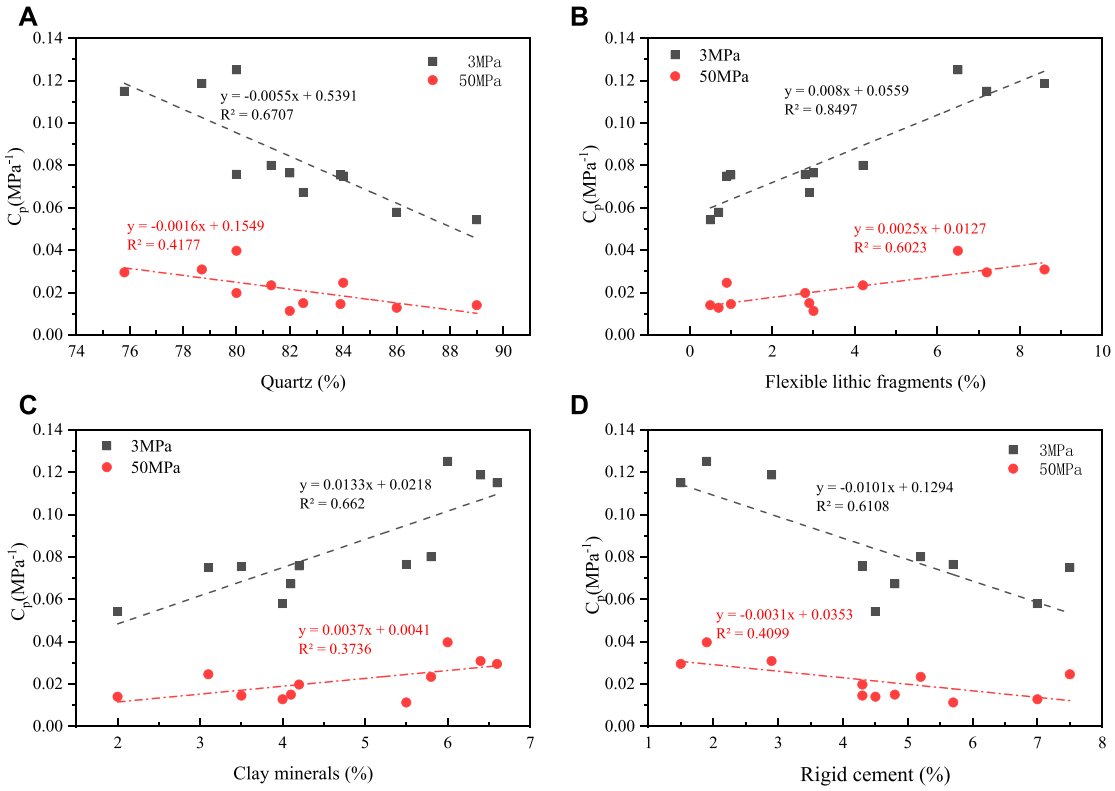

FIGURE 9
Relationship between reservoir material composition and pore compressibility: **(A)** Quartz, **(B)** Flexibe fragments, **(C)** Clay minerals, and **(D)** Rigid cement.

4.2.3 Pore structure characteristics

There is a close relationship between reservoir micropore structure and reservoir pore compressibility. Micro-pore structure of tight sandstone reservoirs differs greatly (Liu et al., 2019) (Table 2; Figure 6), resulting in the different compressibility in the different types of reservoirs. In general, type III reservoirs with high displacement pressure, irreducible water saturation, low median pore throat radius, and T_2 geometric average have high pore compressibility (Figure 10; Figure 6).

The distribution and variation trend of reservoir pore compressibility coefficient with different pore structure parameters under different effective stress is shown in Figures 10A–D. With the continuous increase of displacement pressure and irreducible water saturation, the continuous decrease of the median pore throat radius, and NMR T_{2glm}, the pore compression coefficient of sandstone reservoir samples keeps increasing, meanwhile, in the process of increasing effective stress, the pore compression coefficient of sandstone samples with higher displacement pressure, higher irreducible water saturation, lower median pore throat radius and NMR T_{2glm} shows a more obvious decrease trend. However, the final pore compression coefficient is still greater than that of sandstone samples with lower displacement pressure and lower irreducible water saturation (Figure 10; Figure 6B), which the reason is that the sandstone with lower displacement pressure and irreducible water saturation, large average pore throat radius and T_{2glm} are mainly type I reservoir sandstone and it is mostly pure and is of good physical property, low content of ductile rock fragments and clay minerals, high content of rigid cement and less content of compressible deformation materials among skeleton particles. When effective stress increases, the ductile rock fragments and clay minerals among quartz particles are compressed first. With the destruction and deformation of ductile materials, the support force of sandstone reservoir skeleton particles increases, the reservoir pore compression changes from the compression of ductile materials to that of rigid skeleton particles and the pore volume strain rate decreases greatly, resulting in the overall performance of the rapid decrease of pore compression coefficient before the effective stress reaches 10 MPa and the slow decrease after that. In addition, type I reservoirs mainly consist of large pores, and the proportion of small size pores is relatively low (Figure 4B). The reduction of the pore volume of large pores shows a very small changing rate. However, reservoirs with high displacement pressure, high irreducible water saturation, small average pore throat radius and T_{2glm} value, show a relatively high content of compressible deposit composition such as ductile fragments and fillings, and a relatively low pore space as well. The low stress resistance and small pore volume make these reservoirs show a higher pore compression coefficient.

4.2.4 Pore heterogeneity of the reservoir

Comparison and analysis of the relationship between stage pore volume and pore compressibility coefficient under different pressure. The results are shown in Figure 11. Pore compressibility coefficients is positively correlated with the volume of micropores and micro mesopores in sandstone reservoirs (Figures 11A, B), while it is negatively correlated with the volume of mesopores and macropores (Figures 11C, D), and the pore compressibility

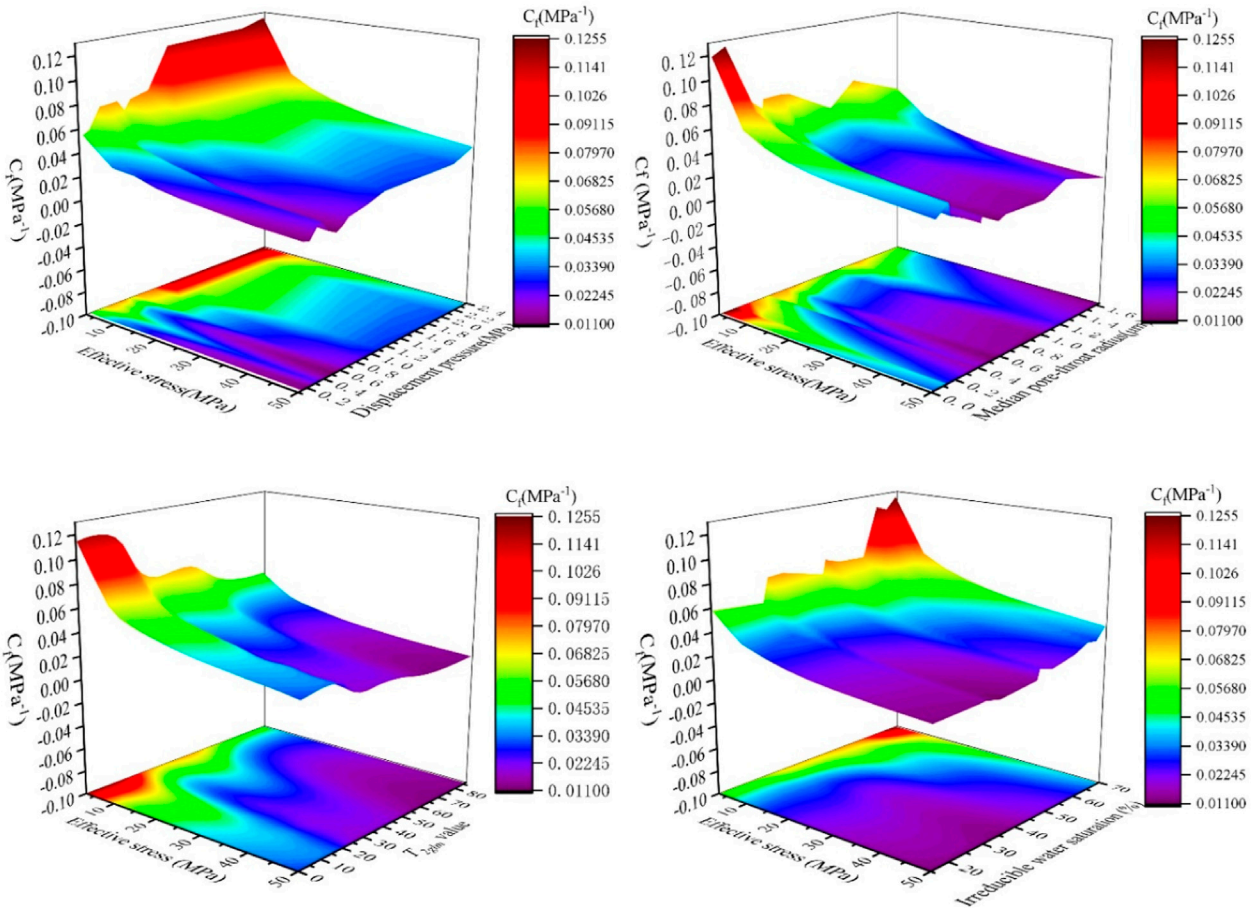

FIGURE 10
Variation trend of pore compressibility coefficient with different effective stress and pore structure parameters.

coefficient has a greater correlation coefficient with micropores and micro mesopores, which all indicate that the loss of pore space of micropores and micro mesopores, etc, caused by compression and destruction of clay minerals runs through the whole effective stress loading process, and the response of pore volume ratio of micropores and micro mesopores to the change of reservoir pore compressibility is more obvious. However, the correlation coefficient between pore compression coefficient and macropores, mesopores is lower, indicating that the compressibility of macropores and mesopores are jointly controlled by many factors, such as sorting, rounding, arrangement of rock fragments particles, and the mechanical properties of cement, which results in the difference of pore compression degree of different types of reservoir samples under changing stress state.

In the present study, the micropores and micro mesopores are regarded as small pores, correspondingly, the mesopores and macropores are considered macropores. On this basis, the stage fractal dimension of small pores and macropores of different samples are obtained (Zhang et al., 2022) (Figure 12A), In addition, the relationship between the stage pore fractal dimension and pore compressibility coefficient is analyzed (Figure 12B), It is found that reservoir pore compressibility coefficient has an obvious positive correlation with the fractal dimension D_L of mesopores and macropores, while a negative correlation with the fractal dimension D_s of micropores and micro mesopores. The pore fractal dimension is jointly controlled by the dispersion degree of reservoir pore size distribution and the complexity of the pore surface (Wu et al., 2019; Hu et al., 2020a). The Larger D_L indicates fewer large pores developing in reservoirs and the reservoir total porosity is small, resulting in a large change rate of pore volume under a stress state, to present a large pore compression coefficient, but it does not mean that reservoir medium is easier to be compressed. On the contrary, the larger the D_S, the higher the proportion of relatively large pores in reservoirs, corresponding to the large total porosity in the reservoir, which caused the smaller change rate of pore volume under dynamic stress.

4.3 Pore compressibility mechanism

The deformation of sandstone reservoir medium resulted from the deformation and destruction of skeleton particles and interstitial materials under effective stress can lead to the change of reservoir pore-throat morphology and loss of reservoir space, which is macroscopically reflected in the compressibility of reservoirs (Shan and Zhou, 2020). The compression deformation of sandstone

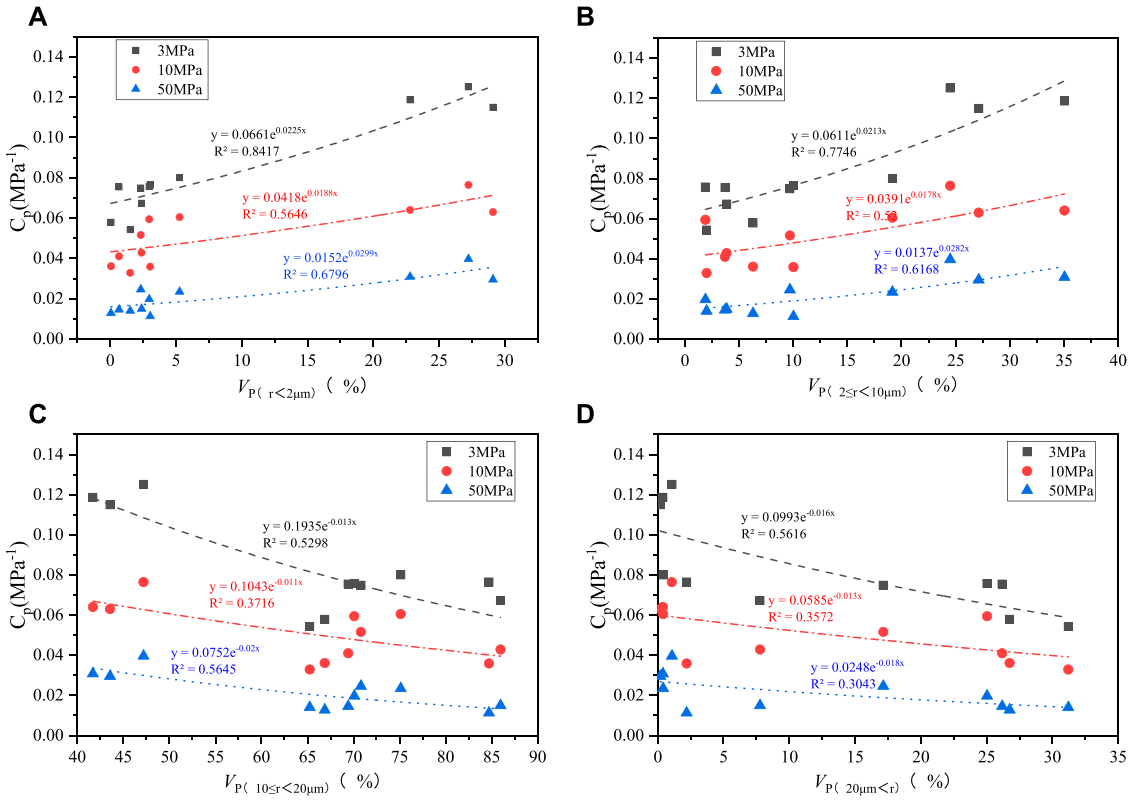

FIGURE 11
Relationship between stage pore volume and pore compressibility: **(A)** Volume of pores (r < 2 μm), **(B)** Volume of pores (2 μm ≤ r < 10 μm), **(C)** Volume of pores (10 μm ≤ r < 20 μm), and **(D)** Volume of pores (20 μm < r).

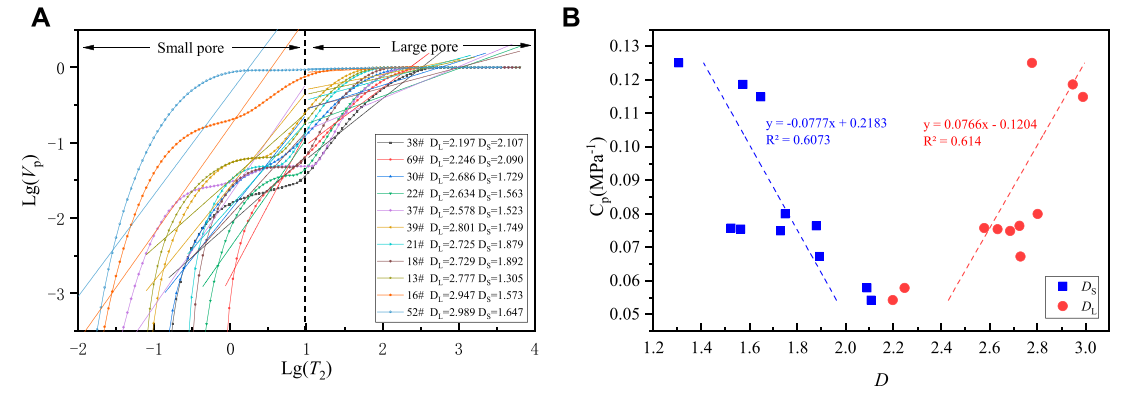

FIGURE 12
Relationship between pore distribution heterogeneity and pore compressibility. **(A)** Pore-throat fractal dimension based on NMR, **(B)** Relationship between pore fractal dimension and pore compressibility.

reservoirs is not a single complete elastic deformation or ductile deformation, but an extremely complex elastic-ductile deformation process, which is jointly controlled by the sandstone deposit composition, contact relationship of detrital particles, arrangement of the detrital particles, and the mode of cementation and type of cement.

When tight sandstone is compressed, deformation happens in the throat firstly (Ruan and Wang, 2002), and large and medium-sized pores and micro-fractures also close at first with the increase of pressure. Slate, phyllite soft rock fragments and kaolinite, illite, and other clay minerals filled in reservoir throat are deformed and damaged by compression, resulting in the occupancy of the pore space and the great reduction of the pore volume. All of those make the reservoirs more compact (Fjaer et al., 2008), and make the permeability of sandstone decrease significantly. At this stage (stage I), the sandstone reservoir is dominated by viscoplastic

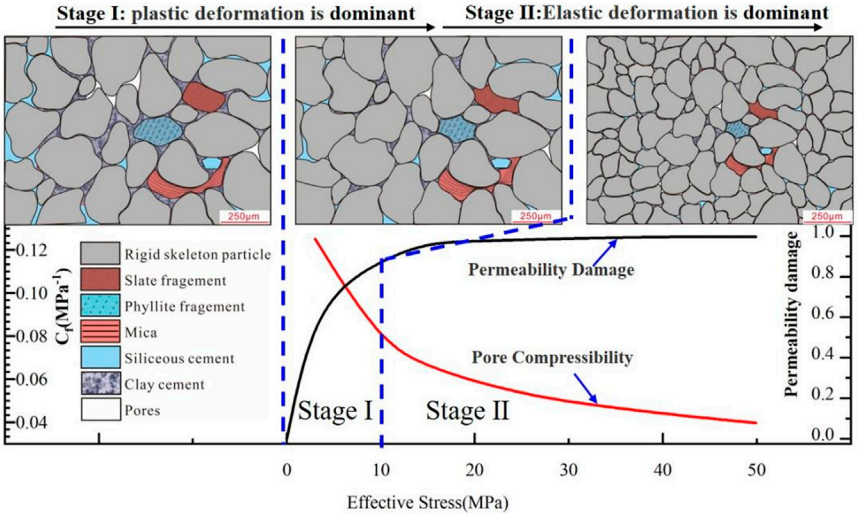

FIGURE 13
Schematic diagram of pore compression mode of tight sandstone reservoirs.

failure and deformation of ductile rock fragment and clay minerals. During this stage, the sandstone reservoir shows high permeability damage and pore compressibility. (Figure 13). After the compression of the first stage, reservoir rigid quartz particles are in close contact. With the further increase of effective stress, the closure of the reservoir throat will not continue, the damage increment of reservoir permeability decreases and small-scale non-ideal elastic deformation of rigid quartz particles occurs in sandstone reservoirs, which cause a small amount of loss of intergranular pore space (stage II) (Figure 13), thereby presenting a small pore compression coefficient. The compression deformation of sandstone reservoirs without ductile material mainly happens in stage II.

5 Conclusion

In this study, the characteristics, influencing factors and, mechanism of pore fracture compressibility of tight sandstone reservoir are analyzed and the main conclusions are as follows:

1) Sandstone in the study area are mainly quartz arenite and sublitharenite. The content of quartz detrital particles is 75.8%–89%, with an average of 81.79%. Fewer rock fragments, ranging from 3% to 16.1%, with an average of 9.14%, and almost free of feldspar. The content of interstitial materials is 6.5%–11.2%, with an average of 9.07%. The type I reservoirs mainly consist of mesopores and macropores, accounting for 60.57% and 32.84% respectively. Mesopores are dominated in Type II reservoirs, accounting for 78.98% of the total pore volume. There are almost no macropores, while a similar proportion of mesopores, micro mesopores and micropores in the type III reservoirs.
2) The study of pore compressibility shows that the pore compressibility coefficient decreases gradually with the increase of effective stress, and the reduction rate shows the two-stage characteristics of rapid in the early stage and slow in the later stage. The pressure turning point is between 3 and 10 MPa. The type III reservoir shows the largest average pore compression coefficient, however, type I for the lowest value.
3) The coefficient of pore compressibility is not inversely proportional to pore volume, but directly proportional to the change rate of pore volume. The higher the content of rigid detrital particles, quartz and carbonate cement in sandstone, the smaller the pore compressibility coefficient while the higher the content of ductile components such as soft rock fragments and clay minerals, the greater the pore compression coefficient. The pore structure of the reservoir is closely related to the pore compressibility, reservoir with low displacement pressure, large average pore throat radius, and small T_{2glm} value show a lower compressibility coefficient. Moreover, the compressibility coefficient of the reservoir is positively correlated with D_L (dimension of large pores such as mesopores and macropores) and negatively correlated with D_S (the fractal dimension of micropores and micro mesopores).
4) The compression deformation of sandstone reservoirs is jointly controlled by the material composition of skeleton particles, the contact relationship between skeleton particles, the arrangement of particles, the mode of cementation, and type of cement. It is considered the the pore compression of sandstone including two stages, viscoplastic destructive deformation of ductile components for the first and then the small-scale non-ideal elastic deformation on rigid particles.

Data availability statement

The original contributions presented in the study are included in the article/supplementary material, further inquiries can be directed to the corresponding author.

Author contributions

Conceptualization: YG Data curation: YH Formal analysis: YH; YH Funding acquisition:YH; YG Investigation: YH; YG; HQ Methodology: YH; HQ; Project administration: Key Laboratory of Coalbed Methane Resources and Reservoir Formation Process of the Ministry of Education (China University of Mining and Technology) Resources: YG; HQ Supervision: YG; HQ Roles/Writing–original draft:YH Writing–review and editing: YH; YG; HQ.

Acknowledgments

We acknowledge the support from the National Natural Science Foundation of China (No. 41772130) and the Jiangsu Graduate Student Scientific Research and Innovation Program (KYCX21_2325). The authors wish to acknowledge the Research Institute of Petroleum Exploration & Development of Changqing Oilfield Company for providing the cores and some geological data. We also thank the reviewers for constructive comments that improved the manuscript.

Conflict of interest

The authors declare that the research was conducted in the absence of any commercial or financial relationships that could be construed as a potential conflict of interest.

Publisher's note

References

Bloch, S., Lander, R. H., and Bonnell, L. (2002). Anomalously high porosity and permeability in deeply buried sandstone reservoirs: Origin and predictability. *AAPG Bulletin* 86, 301–328.doi:10.1306/61EEDABC-173E-11D7-8645000102C1865D

Cai, Y., Liu, D., Pan, Z., Yao, Y., Li, J., and Qiu, Y. (2013). Pore structure and its impact on CH4 adsorption capacity and flow capability of bituminous and subbituminous coals from Northeast China. *Fuel* 103, 258–268. doi:10.1016/j.fuel.2012.06.055

Chen, D., Pan, Z., and Ye, Z. (2015). Dependence of gas shale fracture permeability on effective stress and reservoir pressure: Model match and insights. *Fuel* 139, 383–392. doi:10.1016/j.fuel.2014.09.018

Desbois, G., Urai, J. L., Kukla, P. A., Konstanty, J., and Baerle, C. (2011). High-resolution 3D fabric and porosity model in a tight gas sandstone reservoir:A new approach to investigate microstructures from mm- to nm-scale combining argon beam cross-sectioning and SEM imaging. *Journal of Petroleum Science and Engineering*. 78 (2), 243–257. doi:10.1016/j.petrol.2011.06.004

Dong, J. J., Hsu, J. Y., Wu, W. J., Shimamoto, T., Hung, J. H., Yeh, E. C., et al. (2010). Stress-dependence of the permeability and porosity of sandstone and shale from TCDP Hole-A. *International Journal of Rock Mechanics and Mining Sciences*. 47 (7), 1141–1157. doi:10.1016/j.ijrmms.2010.06.019

Dou, X., Liao, X., Zhao, X., Wang, H., and Lv, S. (2015). Quantification of permeability stress-sensitivity in tight gas reservoir based on straight-line analysis. *Journal of Natural Gas Science and Engineering*. 22, 598–608. doi:10.1016/j.jngse.2015.01.011

Fjaer, E., Holt, R. M., Horsrud, P., Raaen, A. M., and Risnes, R. (2008). *Petroleum related rock mechanics*. Second. Amsterdam, Netherlands: Elsevier (isbn:978-0-44450260-5.

Guo, C., Xu, J., Wei, M., and Jiang, R. (2015). Experimental study and numerical simulation of hydraulic fracturing tightsandstone reservoirs. *Fuel* 159, 334–344. doi:10.1016/j.fuel.2015.06.057

Harmer, J., Callcott, T., Maeder, M., and Smith, B. E. (2001). A novel approach for coal characterization by NMR spectroscopy: Global analysis of proton T1 and T_2 relaxations. *Fuel* 80 (3), 417–425. doi:10.1016/s0016-2361(00)00103-4

He, J., Fu, Y., Shen, G., Zhu, X., and Wu, Q. (2012). Coupling relations between the petrologic characteristics and stress-sensitiveness in low-permeability sandstone reservoirs. *Petroleum Geology*. 33, 923–931.doi:10.11743/ogg20120614

He, J., Ling, K., Pei, P., and Ni, X. (2016). Calculation of rock compressibility by using the characteristics of downstream pressure change in permeability experiment. *Journal of Petroleum Science and Engineering*. 143, 121–127. doi:10.1016/j.petrol.2016.02.030

Henares, S., Caracciolo, L., Viseras, C., Fernandez, J., and Yeste, L. M. (2016). Diagenetic constraints on heterogeneous reservoir quality assessment: A triassic outcrop analog of meandering fluvial reservoirs. *AAPG Bulletin*. 100 (9), 1377–1398. doi:10.1306/04011615103

Higgs, K. E., Zwingmann, H., Reyes, A. G., and Funnell, R. H. (2007). Diagenesis, porosity evolution, and petroleum emplacement in tight gas reservoirs, Taranaki basin, New Zealand. *Journal of Sedimentary Research*. 77, 1003–1025. doi:10.2110/jsr.2007.095

Hu, Y., Guo, Y., Shangguan, J., Zhang, J., and Song, Y. (2020). Fractal characteristics and model applicability for pores in tight gas sandstone reservoirs: A case study of the upper paleozoic in Ordos Basin. *Energy & Fuels* 34 (12), 16059–16072. doi:10.1021/acs.energyfuels.0c03073

Hu, Y., Guo, Y., Zhang, J., Shangguan, J., Li, M., Quan, F., et al. (2020). A method to determine nuclear magnetic resonance T_2 cutoff value of tight sandstone reservoir based on multifractal analysis. *Energy Science & Engineering*. 8 (4), 1135–1148. doi:10.1002/ese3.574

Huang, Z., Gu, Q., Wu, Y., Wu, Y., Li, S., Zhao, K., et al. (2021). Effects of confining pressure on acoustic emission and failure characteristics of sandstone. *International Journal of Mining Science and Technology*. 31 (05), 963–974. doi:10.1016/j.ijmst.2021.08.003

Jiang, R., Liu, C., Zhang, J., Zeng, Q., He, P., Huang, J., et al. (2020). Quantitative reservoir characterization of tight sandstone using extended elastic impedance. *Natural Resources Research*. 30, 395–409. doi:10.1007/s11053-020-09711-6

Jones, F. O., and Owens, W. W. (1980). Alaboratory study of low-permeability gas sands. *Journal of Petroleum Exploration and Production Technology*. 32 (9), 1631–1640. doi:10.2118/7551-pa

Kang, Y., Zhang, H., Chen, Y., Li, Q., You, L., and Cheng, Q. (2006). Comprehensive research of tight sandstones gas reservoirs stress sensitivity in DaNiuDi gas field. *Nat. Gas Geosci*. 17 (3), 335–344. In Chinese. doi:10.3969/j.issn.1672-1926.2006.03.011

Lai, F., Li, Z., Wei, Q., Zhang, T., and Zhao, Q. (2016). Experimental investigation of spontaneous imbibition in a tight reservoir with nuclear magnetic resonance testing. *Energy & Fuels* 30 (11), 8932–8940. doi:10.1021/acs.energyfuels.6b01324

Lai, J., Wang, G., Wang, Z., Chen, J., Pang, X., Wang, S., et al. (2018). A review on pore structure characterization in tight sandstones. *Earth-Science Reviews*. 177, 436–457. doi:10.1016/j.earscirev.2017.12.003

Li, C., Liu, G., Cao, Z., Yuan, W., Wang, P., and You, Y. (2019). Analysis of petrophysical characteristics and water movability of tight sandstone using low-field nuclear magnetic resonance. *Natural Resources Research*. 29, 2547–2573. doi:10.1007/s11053-019-09582-6

Li, C., Wang, S., and Zhou, Y. (2004). Effect of rock compressibility on reservoir dynamic reserves determination. *Petrol. Geol. Oilfield Dev. in Daqing* 23 (6), 31–32. In Chinese. doi:10.3969/j.issn.1000-3754.2004.06.012

Li, P., Zheng, M., Bi, H., Wu, S., and Wang, X. (2017). Pore throat structure and fractal characteristics of tight oil sandstone: A case study in the Ordos Basin, China. *Journal of Petroleum Science and Engineering*. 149, 665–674. doi:10.1016/j.petrol.2016.11.015

Li, S., Tang, D., Pan, Z., Xu, H., and Huang, W. (2013). Characterization of the stress sensitivity of pores for different rank coals by nuclear magnetic resonance. *Fuel* 111, 746–754. doi:10.1016/j.fuel.2013.05.003

Liu, D., Sun, W., and Ren, D. (2019). Experimental investigation of pore structure and movable fluid traits in tight sandstone. *Processes* 7 (3), 149. doi:10.3390/pr7030149

Liu, G., Yin, H., Lan, Y., Fei, S., and Yang, D. (2020). Experimental determination of dynamic pore-throat structure characteristics in a tight gas sandstone formation with consideration of effective stress. *Marine and Petroleum Geology*. 113, 104170. doi:10.1016/j.marpetgeo.2019.104170

Liu, S., and Harpalani, S. (2014). Compressibility of sorptive porous media: Part 1. Background and theory. *AAPG Bulletin*. 98 (9), 1761–1772. doi:10.1306/03241413133

Lorenz, J. C. (1999). Stress-sensitive reservoirs. *Journal of Petroleum Technology*. 51 (01), 61–63. doi:10.2118/50977-ms

Loucks, R. G., Reed, R. M., Ruppel, S. C., and Hammes, U. (2012). Spectrum of pore types and networks in mudrocks and a descriptive classification for matrix-related mudrock pores. *AAPG Bulletin*. 96 (6), 1071–1098. doi:10.1306/08171111061

Mckee, C. R., Bumb, A. C., and Koenlg, R. A. (1988). Stress-dependent permeability and porosity of coal and other geologic formations. *SPE Formation Evaluation*. 3 (01), 81–91. doi:10.2118/12858-pa

Meng, Y., Luo, C., Li, G., and Liu, H. (2019). An experimental study on stress sensitivity of tight sandstone gas reservoirs during nitrogen drilling. *Arabian Journal of Geosciences*. 12 (18), 576. doi:10.1007/s12517-019-4779-0

Ouyang, Z., Liu, D., Cai, Y., and Yao, Y. (2016). Fractal analysis on heterogeneity of porefractures in middle-high rank coals with NMR. *Energy & Fuels* 30 (7), 5449–5458. doi:10.1021/acs.energyfuels.6b00563

Rezaee, R., Saeedi, A., and Clennell, B. (2012). Tight gas sands permeability estimation from mercury injection capillary pressure and nuclear magnetic resonance data. *Journal of Petroleum Science and Engineering*. 88, 92–99. doi:10.1016/j.petrol.2011.12.014

Ross, D. J. K., and Bustin, R. M. (2008). Characterizing the shale gas resource potential of Devonian–Mississippian strata in the Western Canada sedimentary basin: Application of an integrated formation evaluation. *AAPG Bulletin*. 92 (1), 87–125. doi:10.1306/09040707048

Ruan, M., and Wang, L. (2002). Low-permeability oilfield development and pressure-sensitive effect. *Acta Pet. Sin*. 23 (3), 73–76. In Chinese.doi:10.7623/syxb200203016

Seidle, J. P., Jeansonne, D. J., and Erickson, D. J. (1992). "Application of matchstick geometry to stress dependent permeability in coals," in In: Presented at SPE Rocky mountain regional meeting, Casper, Wyoming, Wyoming, United States, May 1992. SPE 24361. doi:10.2118/24361-MS18–21

Shan, J., and Zhou, X. (2020). Starting conditions of particle migration in tight sandstone reservoir development. *Processes* 8 (11), 1491. doi:10.3390/pr8111491

Sheng, Y., Hu, Q., Gao, H., Shi, Y., Dang, Y., Shao, F., et al. (2016). Evaluation on stress sensibility of low reservoir *in situ* conditions. *Acta Scientiarum Naturalium Universitatis Pekinensis*. 52 (6), 1025–1033. In Chinese.doi:10.13209/j.0479-8023.2016.050

Shi, J., and Durucan, S. (2010). Exponential growth in san juan basin fruitland coalbed permeability with reservoir drawdown: Model match and new insights. *SPE Reservoir Evaluation & Engineering*. 13, 914–925. doi:10.2118/123206-pa

Shi, J., Pan, Z., and Durucan, S. (2014). Analytical models for coal permeability changes during coalbed methane recovery: Model comparison and performance evaluation. *International Journal of Coal Geology*. 136, 17–24. doi:10.1016/j.coal.2014.10.004

Vairogs, J., Hearn, C. L., Dareing, D. W., and Rhoades, V. W. (1971). Effect of rock stress on gas production from lowpermeability reservoirs. *J. Pet. Techno*. 23 (09), 1161–1167. doi:10.2118/3001-pa

Wang, F., Liu, Y., Hu, C., Wang, Y., Shen, A., and Liang, S. (2018). Experimental study on feasibility of enhanced gas recovery through CO2 flooding in tight sandstone gas reservoirs. *Processes* 6 (11), 214. doi:10.3390/pr6110214

Wu, Y., Zhao, Y., and Li, P. (2019). Effect of the heterogeneity on sorptivity in sandstones with high and low permeability in water imbibition process. *Processes* 7 (5), 260. doi:10.3390/pr7050260

Yang, D., Wang, W., Li, K., Chen, W., Yang, J., and Wang, S. (2019). Experimental investigation on the stress sensitivity of permeability in naturally fractured shale. *Environ. Earth ScEnvironmental Earth Sciencesi*. 78, 55. doi:10.1007/s12665-019-8045-2

Yao, W., Xu, Y., Wang, C., Xia, K., and Hokka, M. (2021). Dynamic Mode II fracture behavior of rocks under hydrostatic pressure using the short core in compression(SCC) method. *International Journal of Mining Science and Technology*. 31 (05), 927–937. doi:10.1016/j.ijmst.2021.08.001

You, W., Dai, F., Liu, Y., Du, H., and Jiang, R. (2021). Investigation of the influence of intermediate principal stress on the dynamic responses of rocks subjected to true triaxial stress state. *International Journal of Mining Science and Technology*. 31 (05), 913–926. doi:10.1016/j.ijmst.2021.06.003

Yuan, J., Jiang, R., and Zhang, W. (2018). The workflow to analyze hydraulic fracture effect on hydraulic fractured horizontal well production in composite formation system. *Advances Geo-Energy ReAdvances in Geo-Energy Researchs*. 2 (3), 319–342. doi:10.26804/ager.2018.03.09

Zhang, H., Kang, Y., Chen, Y., Li, Q., You, L., and He, J. (2004). Deformation theory and stress sensitivity of tight sandstones reservoirs. *Nat. Gas Geosci*. 15, 482–486. doi:10.3969/j.issn.1672-1926.2004.05.008

Zhang, J., Chu, X., Wei, C., Zhang, P., Zou, M., Wang, B., et al. (2022). Review on the application of low-field nuclear magnetic resonance technology in coalbed methane production simulation. *ACS omega* 7, 26298–26307. doi:10.1021/acsomega.2c02112

Zhang, J., Wei, C., Zhao, J., Ju, W., Chen, Y., and Landry, S. T. (2019). Comparative evaluation of the compressibility of middle and high rank coals by different experimental methods. *Fuel* 245, 39–51. doi:10.1016/j.fuel.2019.01.052

Zhang, L., Huang, M., Xue, J., Li, M., and Li, J. (2021). Repetitive mining stress and pore pressure effects on permeability and pore pressure sensitivity of bituminous coal. *Natural Resources Research*. 30, 4457–4476. doi:10.1007/s11053-021-09902-9

Zhang, R., Ning, Z., Yang, F., Wang, X., Zhao, H., and Wang, Q. (2015). Impacts of nanopore structure and elastic properties on stress-dependent permeability of gas shales. *Journal of Natural Gas Science and Engineering*. 26, 1663–1672. doi:10.1016/j.jngse.2015.02.001

Zhong, X., Zhu, Y., Liu, L., Yang, H., Li, Y., Xie, Y., et al. (2020). The characteristics and influencing factors of permeability stress sensitivity of tight sandstone reservoirs. *Journal of Petroleum Science and Engineering*. 191, 107221. doi:10.1016/j.petrol.2020.107221

Zimmerman, R., Somerton, W., and King, M. (1986). Compressibility of porous rocks. *Journal of Geophysical Research: Solid Earth*. 91 (B12), 12765–12777. doi:10.1029/jb091ib12p12765

Zong, Y., Han, L., Meng, Q., and Wang, Y. (2020). Strength properties and evolution laws of cracked sandstone samples in re-loading tests. *International Journal of Mining Science and Technology*. 30 (02), 251–258. doi:10.1016/j.ijmst.2019.03.004

Zou, C., Yang, Z., Tao, S., Li, W., Wu, S., Hou, L., et al. (2012). Nano-hydrocarbon and the accumulation in coexisting source and reservoir. *Petroleum Exploration and Development+* 39, 15–32. doi:10.1016/s1876-3804(12)60011-1

Zou, C., Zhu, R., Liu, K., Su, L., Bai, B., Zhang, X., et al. (2012). Tight gas sandstone reservoirs in China: Characteristics and recognition criteria. *Journal of Petroleum Science and Engineering*. 88, 82–91. doi:10.1016/j.petrol.2012.02.001

frontiers | Frontiers in Earth Science

TYPE Original Research
PUBLISHED 25 January 2023
DOI 10.3389/feart.2022.1108520

OPEN ACCESS

EDITED BY
Junjian Zhang,
Shandong University of Science and Technology, China

REVIEWED BY
Zaitian Dong,
China University of Mining and Technology, China
Zheng Zhang,
China University of Mining and Technology, China

*CORRESPONDENCE
Yuan Bao,
y.bao@foxmail.com

SPECIALTY SECTION
This article was submitted to Economic Geology, a section of the journal Frontiers in Earth Science

RECEIVED 26 November 2022
ACCEPTED 06 December 2022
PUBLISHED 25 January 2023

CITATION
Guo Z, Bao Y, Wang Y, Yuan Y, Li Z, Wang Y, Xia L, Liu W and Ma J (2023), Hydrogeochemical characteristics and water-rock interaction mechanism of coalbed-produced water in the Linfen mining area, eastern margin of Ordos Basin, China.
Front. Earth Sci. 10:1108520.
doi: 10.3389/feart.2022.1108520

Hydrogeochemical characteristics and water-rock interaction mechanism of coalbed-produced water in the Linfen mining area, eastern margin of Ordos Basin, China

Zhidong Guo[1,2], Yuan Bao[3]*, Yubin Wang[2], Yang Yuan[2], Zhengyan Li[3], Yaya Wang[4], Lin Xia[2], Weibin Liu[2] and Jianli Ma[2]

[1]Petroleum Engineering School, Southwest Petroleum University, Chengdu, China, [2]Institute of Engineering and Technology, PetroChina Coalbed Methane Company Limited, Xi'an, China, [3]College of Geology and Environment, Xi'an University of Science and Technology, Xi'an, China, [4]College of Chemistry and Chemical Engineering, Xi'an University of Science and Technology, Xi'an, China

Linfen mining area is one of the main coalbed methane industrial bases in the eastern margin of Ordos Basin, China. However, there are few studies on the hydrogeochemical characteristics of coalbed-produced water in the area. This article collected water samples from 14 coalbed methane drainage wells and analyzed the ionic concentrations, hydrogen and oxygen isotopes, dissolved inorganic carbon isotopes ($\delta^{13}C_{DIC}$) and trace elements. The results showed that the water of Nos. Five and eight coal seams are both Cl-Na type. The total dissolved solids content was high, ranging from 5011.45 mg/L to 23405.39 mg/L. Hydrogen and oxygen isotope data indicated that the coalbed-produced water in the study area is recharged from atmospheric precipitation. In addition, the HCO_3^- in the produced water of No. Five coal seam and No. Eight coal seam was negatively correlated with $\delta^{13}C_{DIC.}$ The value $\delta^{13}C_{DIC}$ in the produced water of No. Five coal seam was heavier than that of No. Eight coal seam. These indicate that microbial degradation occurred more strongly in No. Five coal seam than in No. Eight coal seam. The water-rock interaction in the study area was found to be dominated by cation exchange and dissolution filtration through the relationships between anion and cation.

KEYWORDS

coalbed-produced water, hydrogen and oxygen isotopes, microbial action, water-rock interaction, Ordos Basin

1 Introduction

Coalbed methane (CBM) is mixture gases dominated by methane that is mainly adsorbed on the surface of coal matrix and partially free in the pores and fissures of coal, and has shown good development potential in recent years as an efficient and clean energy source (Zhang and Qin, 2018; Bao et al., 2020). China is rich in CBM resources. At present, two CBM development bases in the Qinshui Basin and the eastern edge of the Ordos Basin have been established and commercialized (Qin et al., 2012; Huang H. X. et al., 2018). Mining CBM not only relieves the pressure of conventional natural gas supply, but also greatly reduces the probability of accidents in coal mines through pre-pumping. While ensuring safety and improving economic efficiency, it is also conducive to environmental protection and provides a strong guarantee for clean energy. The principle of CBM drainage is to pump the groundwater into the coal seam and its surrounding rocks (Liu et al., 2013), reduce the pressure in the coal reservoir, desorb the gas adsorbed in the coal reservoir and diffuse, percolate and transport it into the wellbore through the pores and fractures, so that it can be exploited (Tao et al., 2011). The coalbed-produced water experienced a long-time contact with the coal seam and surrounding rocks underground, which contained rich geochemical information (Bao et al., 2021). As a direct product of CBM well drainage, coalbed-produced water has an important impact on CBM enrichment mechanism and exploration and development research (Bao et al., 2021).

In recent years, research on coalbed-produced water has received increasing attention from scholars at domestic and international (Bao et al., 2016; Guo et al., 2017; Guo et al., 2020). Previous studies have also done a lot of research around the geochemical characteristics of the coalbed-produced water (Bao et al., 2016; Guo et al., 2017; Zhang et al., 2018; Guo et al., 2020). Since Craig (1961) first proposed the global precipitation line (GMWL), hydrogen and oxygen isotopes have been widely used in hydrogeochemical studies (Zheng et al., 1983; Chen et al., 2011; Bao et al., 2021). Hydrogen and oxygen isotopes have played an important role in determining the source of water and the types and mechanisms of water-rock interactions (Bozau et al., 2017; Hao et al., 2019). Water-rock interaction refers to the physicochemical reaction between groundwater and surrounding rock during the geological action of coalbed-produced water, which generally includes cation exchange, rock dissolution and filtration, and evaporation and concentration (Li Q. G. et al., 2016; Li X. et al., 2016; Huang X. J. et al., 2018). Bao *et al.* (2021) investigated the hydrogeochemical characteristics of coalbed-produced water from the Dafosi biogas field on the southern margin of Ordos and found that cation exchange occurs in coalbed-produced water in this area. Qin *et al.* (2014) proposed a method to distinguish between the source resolution of the produced water and the mixed CBM feasibility discrimination based on the trace element concentration in the coalbed-produced water. Redwan *et al.* (2016) investigated the effect of water-rock interaction on the chemical elements of coal-bearing rocks and applied statistical methods to identify and evaluate water-rock reaction processes. Therefore, the geochemical index of coalbed-produced water is a good indicator of the water source and water-rock interaction process.

The Linfen mining area is located at the eastern margin of the Ordos Basin and is rich in CBM resources (Huang H. X. et al., 2018). Although the CBM in this area has undergone more than two decades of exploration and development, little research has been conducted on the mechanism of water-rock interaction in the coalbed-produced water in this area. The geochemical characteristics of the coalbed-produced water can predict the CBM enrichment area, which is important for drainage. Therefore, this article collected water samples from 14 CBM wells with single-layer discharge in the study area, and tested their pH, total dissolved solids (TDS), conventional ions, hydrogen and oxygen isotopes, dissolved inorganic carbon isotopes and trace elements to analyze the water chemistry types, ionic composition characteristics and sources of coalbed-produced water. The water-rock action types and mechanisms were also elucidated. The research results can provide theoretical support for the exploration and development of CBM in the study area and the selection of the sweet spot area.

2 Sample collection and test methods

2.1 Sample collection

There are 220 CBM extraction wells in Linfen mining area. The main CBM wells are developed in the No. Five coal seam of Shanxi Formation and No. Eight coal seam of Taiyuan Formation. The well types are straight wells and directional wells. According to the location of CBM wells and single layer drainage, a total of 14 representative coalbed-produced water samples were collected to cover the whole area as much as possible, including 10 samples from No. Five coal seam and four samples from No. Eight coal seam. Sample numbers were J5-1, J5-2, J5-3, J5-4, J5-5, J5-6, J5-7, J5-8, J5-9, J5-10, J8-1, J8-2, J8-3, J8-4, respectively. Before sample collection, polyethylene sampling bottles were sterilized in the laboratory under UV light. The water samples were collected using 2.5 L and 500 ml polyethylene sampling bottles at the drainage of CBM wells to collect coalbed-produced water. The 500 ml polyethylene sampling bottles were acidified to pH <3 with dilute hydrochloric acid on site for subsequent cation detection. The 2.5 L polyethylene sampling bottles were used to collect raw water samples for pH, anion, TDS, trace elements, hydroxide isotopes and dissolved inorganic carbon isotope composition. The water samples were collected in the field by rinsing the

TABLE 1 Geochemical parameters of coalbed-produced water in the Linfen mining area (unit, mg/L).

ID	pH	TDS	Na^+	K^+	Ca^{2+}	Mg^{2+}	CO_3^{2-}	HCO_3^-	Cl^-	SO_4^{2-}
J8-1	6.78	13093.97	5249.20	48.97	215.98	62.64	0.00	1333.52	6489.84	0.58
J8-2	7.07	16434.21	6386.60	87.15	186.57	73.30	0.00	1316.89	9042.14	<0.10
J8-3	7.50	7465.12	2930.80	44.64	74.83	25.42	0.00	1509.02	3632.02	2.90
J8-4	9.14	5011.45	2161.90	19.44	6.81	9.10	249.73	1279.54	2170.20	4.23
Ave	7.62	10501.19	4182.13	50.05	121.05	42.62	62.43	1359.74	5333.55	2.57
J5-1	7.72	5096.39	2134.10	41.23	30.91	7.68	0.00	1424.47	2170.09	0.14
J5-2	7.37	6484.87	2693.90	14.95	45.99	12.04	0.00	1004.55	3215.68	0.03
J5-3	7.54	6529.45	2651.60	44.82	45.79	11.23	0.00	1160.28	3195.87	<0.10
J5-4	7.29	9758.49	4013.60	19.66	72.78	17.43	0.00	1405.81	4932.11	<0.10
J5-5	7.85	5464.32	2231.20	24.43	41.42	8.87	0.00	1372.13	2472.33	<0.10
J5-6	7.63	7874.54	3262.80	18.25	66.67	17.28	0.00	1314.31	3852.38	<0.10
J5-7	6.91	23405.39	8506.80	53.73	618.43	105.61	0.00	671.24	13785.20	<0.10
J5-8	7.22	14999.15	5752.00	213.06	181.58	44.24	0.00	1255.38	8180.58	<0.10
J5-9	7.03	13719.69	5411.50	55.39	153.20	38.45	0.00	1329.68	7396.31	<0.10
J5-10	7.25	13648.50	5260.70	24.48	154.85	32.54	0.00	1045.24	7653.31	<0.10
Ave	7.38	10698.08	4191.82	51.00	141.16	29.54	0.00	1198.31	5685.39	0.09

polyethylene sampling bottle three times with the coalbed-produced water. Then filtered microorganisms, coal dust and suspended substances with 0.5 μm filter paper placed at the mouth of the bottle, and filled the bottle to remove the air from the bottle. Next sealed the bottle with the cap and checked whether it leaked. Finally marked the sampling time and place and sent it to the Guizhou Institute of Geochemistry, Chinese Academy of Sciences for testing.

2.2 Test methods

The water samples were tested for anions and cations, hydrogen and oxygen isotopes of water, dissolved inorganic carbon isotopes and trace elements. Among them, the instrument used for cation test is Vista MPX inductively coupled plasma - emission spectrometer of Varian, United States. The anion test used ion chromatography (Thermo Fisher ICS-90). The HCO_3^- and CO_3^{2-} ion test used acid titration method to detect. Anion and cation detection standards referred to GB/T 5750.6-2006 and DZ/T 0064.51-1993, respectively. The instrument used for hydrogen and oxygen isotope testing was the liquid isotope analyzer 912-0026, with a standard deviation of 0.6‰ for δD and 0.1‰ for $\delta^{18}O$. The isotopes of dissolved inorganic carbon were measured by gas isotope mass spectrometer MAT252 with an accuracy of ≤0.01‰. The isotopes of hydrogen, oxygen and inorganic carbon were measured according to DZ/T 0184.19-1997, DZ/T 0184.21-1997 and GB 13193-91, respectively.

The pH was measured by PP-50-p11 m and TDS was measured by DDSJ-308A conductivity meter. The testing standards were executed according to GB/T 6920-1986 and DZ/T 0064.9-1993, respectively.

3 Results and analysis

3.1 Produced water conventional ion

The results of water quality testing and analysis of coalbed-produced water in the Linfen mining area were shown in Table 1. The pH of the produced water of No. Five coal seam ranged from 6.91 to 7.85 with an average value of 7.38. The produced water of No. Five coal seam was weakly alkaline, which was favorable to the survival of methanogenic bacteria in the coalbed-produced water. The pH of the produced water of No. Eight coal seam ranged from 6.78 to 9.14 with an average value of 7.62. But the pH of No. Eight coal seam had a larger span and a higher average pH than that of No. Five coal seam. The cations of coalbed-produced water in the study area are mainly Na^+. The concentration of Na^+ ranges from 2134.10 to 8506.80 mg/L. In addition, they also contain certain concentrations of Ca^{2+}, Mg^{2+}

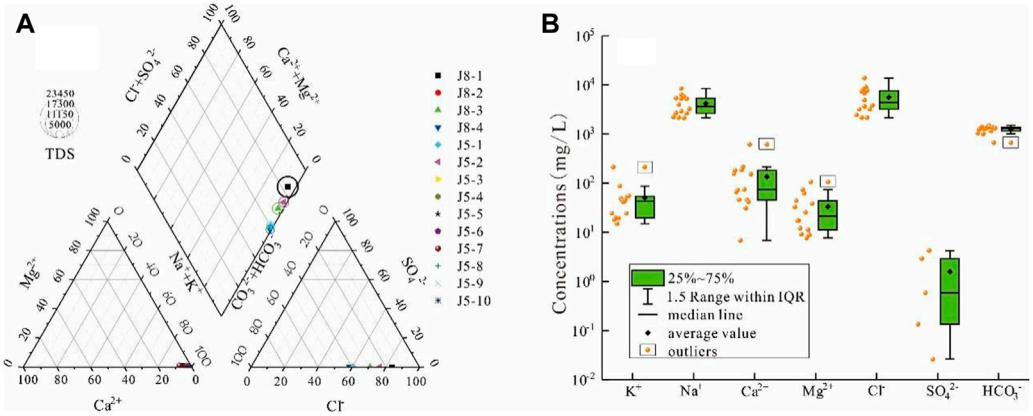

FIGURE 1
Piper diagram [**(A)**; Bao et al., 2021 and box chart of ion concentrations **(B)**; Guo et al., 2017] of coalbed-produced waters in the Linfen mining area.

and K^+. The anions were dominated by Cl^-. The concentration of Cl^- ranges from 2170.09 to 13,785.20 mg/L. In addition, they also contained CO_3^{2-}, HCO_3^- and SO_4^{2-}. Among them, CO_3^{2-} was only detected in J8-4 with a concentration of 249.73 mg/L. The concentration of HCO_3^- ranges from 671.24 to 1509.02 mg/L, and higher levels of HCO_3^- were detected in 10 CBM wells in No. Five coal seam and four CBM wells in No. Eight coal seam. The higher content of HCO_3^- suggested a higher degree of confinement in the groundwater environment. The SO_4^{2-} concentration ranges from <0.10 to 4.23 mg/L. The concentration of TDS in the study area ranges from 5011.45 mg/L to 23,405.39 mg/L. The TDS of J5-7, J5-8, J5-9, J5-10, J8-1 and J8-2 were all higher than 13,000 mg/L. The higher mineralization may be related to groundwater rock action.

The data of 14 sets of water samples from the Linfen mining area were plotted on a Piper trilinear graph (Figure 1A), showing that the water chemistry type in the study area is Cl-Na type. According to the box plot of ion concentrations in coalbed-produced water in the study area (Figure 1B), the concentrations of Na^+, Cl^- and HCO_3^- are much larger than other ions. The data are more concentrated, with the median line located almost half of the length of the square box, indicating that the concentrations of Na^+, Cl^- and HCO_3^- ions do not vary much. The concentration of SO_4^{2-} is lower and the data are scattered. The lower quantile line of Ca^{2+} and SO_4^{2-} box plots with the lower quantile line far from the square box imply that the Ca^{2+} and SO_4^{2-} concentration content of each individual well is low and varies more than most CBM wells. The anomalous data were marked by boxes in the graph. The presence of anomalous values of K^+, Ca^{2+}, Mg^{2+}, and HCO_3^- concentrations in the coalbed-produced water indicate that they are related to the groundwater environment and that groundwater-rock interactions need to be identified.

TABLE 2 Hydrogen and oxygen isotopic and DIC carbon isotopic compositions of coalbed-produced water in the Linfen mining area.

Sample ID	δD_{H2O} (‰)	$\delta^{18}O_{H2O}$ (‰)	$\delta^{13}C_{DIC}$ (‰)
J8-1	−74.95	−10.82	9.65
J8-2	−79.10	−11.32	11.12
J8-3	−78.02	−11.03	7.98
J8-4	−85.84	−12.14	12.68
Ave	−79.48	−11.33	10.36
J5-1	−79.87	−11.27	28.34
J5-2	−77.79	−10.92	31.58
J5-3	−80.32	−11.54	28.07
J5-4	−73.35	−10.46	26.94
J5-5	−76.88	−10.77	25.79
J5-6	−81.27	−11.61	29.49
J5-7	−64.31	−9.07	34.16
J5-8	−68.40	−9.91	29.57
J5-9	−67.13	−9.83	36.50
J5-10	−65.39	−9.63	35.48
Ave	−73.47	−10.50	30.59

3.2 Hydrogen, oxygen, and carbon isotopic signatures

Table 2 shows the hydrogen, oxygen and carbon isotope values of the coalbed-produced water in the Linfen mining area. As shown in, the hydrogen and oxygen isotopes of the produced

TABLE 3 Results of trace element concentration of coalbed-produced water in the Linfen mining area (unit, μg/L).

ID	Li	As	Ba	Co	Cr	Mn	Mo	Rb	Sr	Zn
J8-1	1119.52	7.83	30930.46	0.28	1.13	128.03	1.76	38.76	28799.65	5.01
J8-2	1923.32	9.48	47203.30	1.07	0.96	699.89	1.52	61.24	46215.72	4.87
J8-3	555.20	2.81	20694.38	0.12	0.86	131.24	1.55	41.70	17105.84	6.23
J8-4	398.79	1.84	4323.18	0.04	0.82	21.47	143.37	13.25	3996.26	0.75
J5-1	287.88	1.25	11832.31	0.22	0.65	223.18	19.28	22.81	8786.70	2.78
J5-2	323.97	2.31	13879.82	0.50	0.71	165.32	33.48	17.98	11797.50	3.26
J5-3	399.01	3.02	14784.00	5.02	0.67	991.65	21.01	32.55	13558.49	1.52
J5-4	703.56	3.28	25330.83	0.64	0.74	175.01	11.33	35.07	26896.25	3.82
J5-5	322.38	1.94	11139.32	0.10	0.73	165.86	6.18	33.58	7673.70	1.94
J5-6	408.78	3.14	16613.33	4.39	0.75	223.70	22.87	32.73	15896.56	2.70
J5-7	1162.15	9.82	137348.67	2.10	0.90	1116.92	3.35	59.06	107240.41	33.07
J5-8	970.06	5.02	69528.23	0.80	1.18	299.06	6.00	79.23	43521.63	16.89
J5-9	807.38	3.85	39979.54	2.43	1.01	1065.28	5.78	25.94	30316.57	8.66
J5-10	713.54	3.78	47319.29	0.67	0.77	680.79	2.56	28.32	34156.31	9.74
Ave	721.11	4.24	35064.76	1.31	0.85	434.81	20.00	37.30	28282.97	7.23

water from No. Five coal seam and No. Eight coal seam do not differ significantly. δD ranges from −85.84‰ to ⁻64.31‰, with an average value of −75.22‰. $\delta^{18}O$ ranges from −12.14‰ to −9.07‰, with an average value of −10.74‰. However, the inorganic carbon isotopes of the produced water from No. Five coal seam and No. Eight coal seam differed significantly. The dissolved inorganic carbon isotopes $\delta^{13}C_{DIC}$ of the produced water from No. Eight coal seam ranges from 7.98‰ to 12.68‰ with a mean value of 10.36‰. The dissolved inorganic carbon isotopes $\delta^{13}C_{DIC}$ of the produced water from No. Five coal seam ranges from 25.79‰ to 36.50‰ with a mean value of 30.59‰. All of the $\delta^{13}C_{DIC}$ in the study area exhibited positive values, indicating that dissolved CO_2 in groundwater is enriched in ^{13}C (Li et al., 2022).

3.3 Produced water trace elements

In this article, a total of 22 trace elements were detected in the coalbed-produced water of the Linfen mining area. The average content of Cd, Cu, Hg, Pb, Sb, Sn, Ti, Tl, U, and Zr elements below 0.10 μg/L were not analyzed, and the statistical results of other elements with stable distribution and high content were shown in Table 3. The trace elements in the produced water of No. Five coal seam and No. Eight coal seam do not vary much. The content of Li in this area ranges from 287.88 to 1923.32 μg/L, with an average value of 721.11 μg/L. The content of Al ranges from 1.60 to 61.57 μg/L, with an average value of 14.77 μg/L. The content of As ranges from 1.25 to 9.48 μg/L, with an average value of 4.24 μg/L. The content of Ba ranges from 4323.18 to 69,528.23 μg/L, with an average value of 35,064.76 μg/L. The content of Co ranges from 0.10 to 5.02 μg/L, with an average value of 1.31 μg/L. The contents of Ni ranges from 0.52 to 39.43 μg/L, with an average value of 15.28 μg/L; The contents of Cr ranges from 0.65 to 1.13 μg/L, with an average value of 0.85 μg/L; The contents of Zn ranges from 0.75 to 16.89 μg/L, with an average value of 7.23 μg/L; The contents of Sr ranges from 3996.26 to 107,240.41 μg/L, with an average value of 28,282.97 μg/L; The contents of Rb ranges from 13.25 to 79.23 μg/L, with an average value of 37.30 μg/L. The content of Mo ranged from 1.52 to 143.37 μg/L, with an average value of 20.00 μg/L. The content of Mn ranges from 21.47 to 1116.92 μg/L, with an average value of 434.81 μg/L. The concentrations of Li, Ba, Sr, Rb, Mo and Mn in the coalbed-produced water are relatively high, and the average values are all greater than 20 μg/L. Ba is the trace element with the highest content in the coalbed-produced water in this area. The average concentrations of trace elements in the coalbed-produced water in this area are Ba>Sr>Li>Mn>Rb>Mo>Zn>As>Co>Cr.

4 Discussions

4.1 Source of coalbed-produced water

The hydrogen-oxygen isotopic composition of coalbed-produced water can reflect the source of produced water.

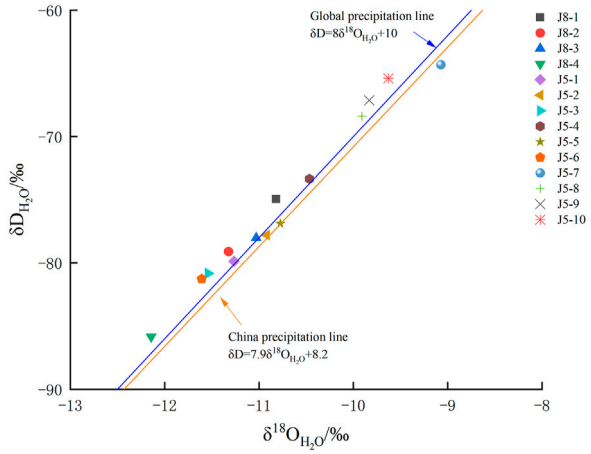

FIGURE 2
Relationship between $\delta D(H_2O)$ and $\delta^{18}O(H_2O)$ of coalbed-produced water in the Linfen mining area (modified from Bao et al., 2021).

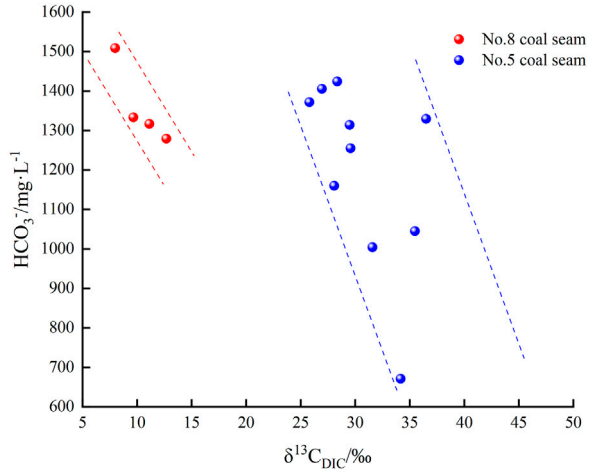

FIGURE 3
Relationship between $\delta^{13}C_{DIC}$ and HCO_3^- of coalbed-produced water in the Linfen mining area.

Craig (1961) obtained the global meteoric water line (GMWL) as: $\delta D = 8\delta^{18}O+10$. The Chinese meteoric water line (CMWL) first proposed by Zheng *et al.* (1983), expressed as: $\delta D = 7.9\delta^{18}O+8.2$. The hydrogen-oxygen isotope data in Table 2 were projected onto the $\delta^{18}O$-δD relationship diagram (Figure 2), it was found that the hydrogen-oxygen isotope projections of the produced water from 14 CBM wells in the study area were all located near the GMWL and CMWL. It showed that the coalbed-produced water in the study area originated from atmospheric precipitation and received recharge from atmospheric precipitation, providing a way to carry microorganisms into the coal seam for microbial degradation to occur.

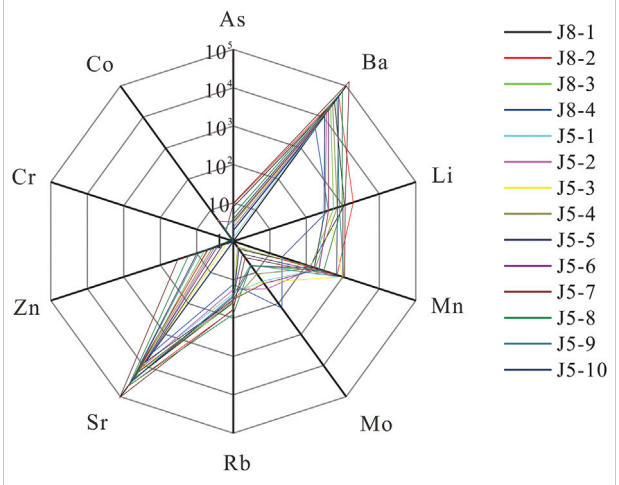

FIGURE 4
Radar map of trace elements concentration of coalbed-produced water in the Linfen mining area.

4.2 Microbial action

Dissolved inorganic carbon in coalbed-produced water is generally considered to originate from dissolution of carbonate minerals, dissolution of CO_2 in CBM, and microbial action (Lemay and Konhauser, 2006). Figure 3 showed the relationship between HCO_3^- and $\delta^{13}C_{DIC}$ in the coalbed-produced water in the study area. As shown in, both were positive and showed a significant negative correlation. This suggested that strong microbial action had occurred *in situ* in the coal seam in the study area. The positive $\delta^{13}C$ values indicate the occurrence of methanogenesis in groundwater environments because methanogens preferentially utilize $^{12}CH_4$, resulting in the remaining ^{13}C enriched in CO_2 and DIC (Meng et al., 2014; Li et al., 2022). The comparison shows that No. Five coal seam $\delta^{13}C_{DIC}$ is heavier than that of No. Eight coal seam, implying that microbial degradation occurs more strongly in No. Five coal seam than in No. Eight coal seam.

4.3 Water-rock interaction and mechanism

Figure 4 shows the radar map of trace element content distribution in coalbed-produced water. The content of Ba, Sr, Mn, Li and other elements are relatively high. On the one hand, these trace elements have their own active chemical properties and easily loss or gain electrons with existing in ion form in

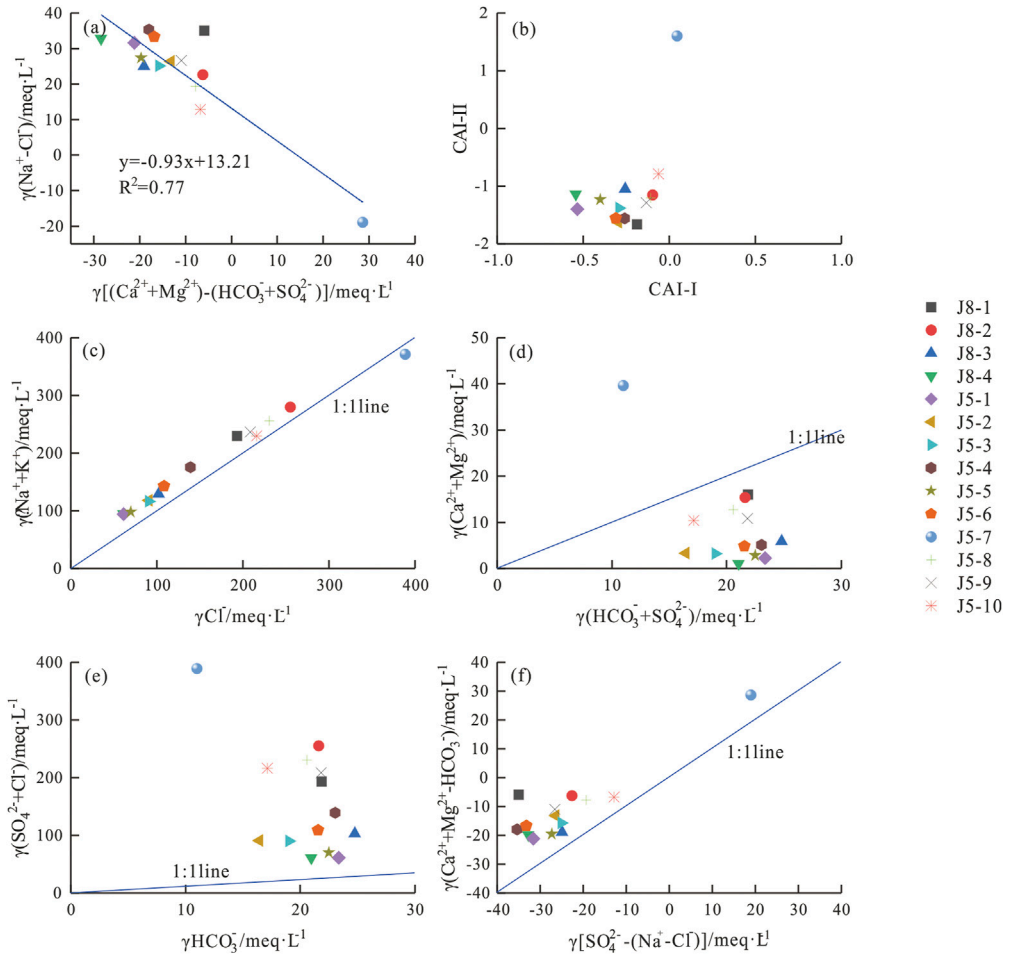

FIGURE 5
Relationship between hydrochemical compositions: **(A)** molar ratio of [(Ca^{2+}+Mg^{2+})-(HCO_3^-+SO_4^{2-})] vs. (Na^+-Cl^-); **(B)** chloro-alkaline indices (CAI); **(C)** molar ratio of (Cl^-) vs. (Na^++K^+); **(D)** molar ratio of (HCO_3^-+SO_4^{2-}) vs. (Ca^{2+}+Mg^{2+}); **(E)** molar ratio of (HCO_3^-) vs. (SO_4^{2-}+Cl^-); **(F)** molar ratio of [SO_4^{2-}-(Na^+-Cl^-)] vs. (Ca^{2+}+Mg^{2+}-HCO_3^-). The ionic unit is meq/L (modified from Bao et al., 2021).

produced water. On the other hand, Ba, Sr, and Mn elements have high affinity for silica-aluminates. Li element has carbonate affinity (Dai et al., 2005), and these properties result in different trace elements. During the contact between the coal seam and the surrounding rocks, a certain degree of enrichment of these trace elements will occur in the water through dissolution-precipitation, adsorption of substances such as iron-manganese oxides and hydroxides, carryover of organic matter and ion exchange of clay minerals, etc. In addition, the stronger the groundwater dynamic conditions, the stronger the water-rock interaction will be, and the higher the element dissolution will be. As a result, the coalbed-produced water contains higher concentrations of trace elements such as Ba, Sr, Mn and Li.

The source of ions and the process of water-rock action can be determined from the relationship between the content of major ions in water (Lakshmanan et al., 2003). The occurrence of cation exchange is usually reflected by the ratio relationship between γ(Na^+-Cl^-) and γ[(Ca^{2+}+Mg^{2+})-(HCO_3^-+SO_4^{2-})] (Tang et al., 2013). The relationship between the chloride base index (CAI-Ⅰ=[Cl^--(Na^++K^+)/Cl^-]) and (CAI-Ⅱ=[Cl^--(Na^++K^+)]/(SO_4^{2-}+HCO_3^-+CO_3^{2-})) relationships can characterize the direction and intensity of ion exchange (Li et al., 2013). The ratio relationship between γ(Na^++K^+) and γ(Cl^-) can reflect the source of Na^+ and K^+ (Li et al., 2015). The relationship between the ratio of γ(Ca^{2+}+Mg^{2+}) and γ(HCO_3^-+SO_4^{2-}) can determine the source of Ca^{2+} and Mg^{2+} in the produced water (Tang et al., 2013). The relationship between the ratio of γ(Ca^{2+}+Mg^{2+}-HCO_3^-) and γ[SO_4^{2-}-(Na^+-Cl^-)] can reflect the source of SO_4^{2-} in the produced water (Singh et al., 2015).

The relationship between γ(Na^+-Cl^-) and γ[(Ca^{2+}+Mg^{2+})-(HCO_3^-+SO_4^{2-})] of the coalbed-produced water in the study area is shown in (Figure 5A), which show a significant negative correlation (R^2=0.77), indicating that cation exchange is occurring in this mine. The chloride and alkali index of the

coalbed-produced in the Linfen mining area is almost less than 0 (Figure 5B), implying that positive cation exchange occurs mainly in the study area. Exchange Ca^{2+} and Mg^{2+} in the water with Na^{+} in the surrounding rocks, resulting in an increase in the Na^{+} content in the coalbed-produced water. The reaction mechanism is shown in Eq. 1 (Houatmia et al., 2016).

$$(Na^{+})(Rock) + (Ca^{2+} + Mg^{2+})(Water) = (Ca^{2+} + Mg^{2+})(Rock) + (Na^{+})(Water) \quad (1)$$

The sample points of the coalbed-produced water in the study area basically fall above the $\gamma(Na^{+}+K^{+})/\gamma(Cl^{-})$=1:1 line (Figure 5C), indicating that the main source of Na^{+} and K^{+} in the study area is the dissolution of silicate minerals such as potassium feldspar and sodium feldspar. The reaction mechanism is shown in Eqs 2, 3.

$$2NaAlSi_3O_8\,(\text{Sodium feldspar}) + 2CO_2 + 11H_2O \rightarrow Al_2Si_2O_5(OH)_4 + (2Na^{+}) + 4H_4SiO_4 + 2HCO_3^{-} \quad (2)$$

$$2KAlSi_3O_8\,(\text{potassium feldspar}) + 2CO_2 + 11H_2O \rightarrow Al_2Si_2O_5(OH)_{4^{+}} + 2K^{+} + 4H_4SiO_4 + 2HCO_3^{-} \quad (3)$$

The ratio of $\gamma(Ca^{2+}+Mg^{2+})$ to $\gamma(HCO_3^{-}+SO_4^{2-})$ in the coalbed-produced water in Linfen mining area is almost all less than 1 (Figure 5D), suggesting that the dissolution of silicate minerals and evaporite is the main source of Ca^{2+} and Mg^{2+} in the coalbed-produced water (Li et al., 2015). Figure 5E shows the scatter plot of $\gamma(SO_4^{2-}+Cl^{-})$ to $\gamma(HCO_3^{-})$ milligram equivalent ratio of coalbed-produced water, which can reflect the dissolved evaporite and carbonate rocks in the water column (Tang et al., 2013). The sample points of the coal seam produced water in the study area were mainly distributed above the 1:1 line, exhibiting that the dissolution of evaporite in the produced water mainly occurred in the study area. $\gamma(Ca^{2+}+Mg^{2+}\text{-}HCO_3^{-})$ can characterize the Ca^{2+} concentration and $\gamma[SO_4^{2-}\text{-}(Na^{+}\text{-}Cl^{-})]$ can characterize the SO_4^{2-} concentration of gypsum dissolution in the produced water. The sample points of coal seam output water in the study area were all distributed above the $\gamma(Ca^{2+}+Mg^{2+}\text{-}HCO_3^{-})/\gamma[SO_4^{2-}\text{-}(Na^{+}\text{-}Cl^{-})]$ = 1:1 line (Figure 5F), displaying that SO_4^{2-} in coalbed-produced water mainly originated from the dissolution of gypsum and mannite.

5 Conclusion

The water chemistry of the produced water from No. Five coal seam and No. Eight coal seam in the study area is of Cl-Na type and the TDS concentration is generally high. The degree of confinement of the groundwater environment is high, which is favorable to the generation of biogas. The hydrogen-oxygen isotope relationship indicates that the coalbed-produced water in Linfen mining area originates from atmospheric precipitation, which provides a way to carry microorganisms into the coal seam for microbial degradation. The pH value of the No. Five coalbed-produced water in the Shanxi Formation of the Linfen mining area is weakly alkaline and lower than that of the No. Eight coalbed-produced water, implying that the *in situ* water in the No. Five coal seam is favorable for the survival of methanogenic bacteria. Meanwhile, the $\delta^{13}C_{DIC}$ value of the produced water from No. Five coal seam is significantly heavier than that of No. Eight coal seam, indicating that microbial degradation occurs more strongly in No. Five coal seam than in No. Eight coal seam.

Water-rock interaction in the study area is dominated by cation exchange and dissolution filtration, resulting in relatively high contents of trace elements such as Li, Ba, Sr and Mn in the coalbed-produced water. The Na^{+} in the coalbed-produced water mainly comes from the dissolution of sodium feldspar minerals and the cation exchange of Ca^{2+} and Mg^{2+} in the water with Na^{+} in the surrounding rocks. The K^{+} mainly comes from the dissolution of potassium feldspar silicate minerals. The Ca^{2+} and Mg^{2+} mainly come from the dissolution of silicate minerals and evaporite. The SO_4^{2-} and Cl^{-} mainly come from the dissolution of evaporite (gypsum, mannite, etc.).

Data availability statement

The original contributions presented in the study are included in the article/Supplementary Material, further inquiries can be directed to the corresponding author.

Author contributions

All authors listed have made a substantial, direct, and intellectual contribution to the work and approved it for publication.

Funding

This work was supported by the National Natural Science Foundation of China (grant numbers: 42172200; 41972183).

Conflict of interest

Authors YW and YY are employed by PetroChina Coalbed Methane Company Limited, China.

The remaining authors declare that the research was conducted in the absence of any commercial or financial relationships that could be construed as a potential conflict of interest.

Publisher's note

References

Bao, Y., An, C., Wang, C. Y., Guo, C., and Wang, W. B. (2021). Hydrogeochemical characteristics and water–rock interactions of coalbed-produced water derived from the Dafosi biogenic gas field in the southern margin of Ordos Basin, China. *Geofluids* 2021, 1–13. doi:10.1155/2021/5972497

Bao, Y., Ju, Y. W., Yin, Z. S., Xiong, J. L., Wang, G. C., and Qi, Y. (2020). Influence of reservoir properties on the methane adsorption capacity and fractal features of coal and shale in the upper Permian coal measures of the south Sichuan coalfield, China. *Energy Explor. Exploitation* 38 (1), 57–78. doi:10.1177/0144598719877527

Bao, Y., Wei, C. T., and Neupane, B. (2016). Generation and accumulation characteristics of mixed coalbed methane controlled by tectonic evolution in Liulin CBM field, eastern Ordos Basin, China. *J. Nat. Gas Sci. Eng.* 28, 262–270. doi:10.1016/j.jngse.2015.11.033

Bozau, E., Licha, T., and Ließmann, W. (2017). Hydrogeochemical characteristics of mine water in the Harz Mountains, Germany. *Geochemistry* 77 (4), 614–624. doi:10.1016/j.chemer.2017.10.001

Chen, L. W., Gui, H. R., and Yin, X. X. (2011). Monitoring of flow field based on stable isotope geochemical characteristics in deep groundwater. *Environ. Monit. Assess.* 179, 487–498. doi:10.1007/s10661-010-1751-6

Craig, H. (1961). Isotopic variations in meteoric waters. *Science* 133 (3465), 1702–1703. doi:10.1126/science.133.3465.1702

Dai, J. X., Li, J., Luo, X., Zhang, W., Hu, G., Ma, C., et al. (2005). Stable carbon isotope compositions and source rock geochemistry of the giant gas accumulations in the Ordos Basin, China. *Org. Geochem.* 36 (12), 1617–1635. doi:10.1016/j.orggeochem.2005.08.017

Guo, C., Qin, Y., Wu, C. F., and Lu, L. L. (2020). Hydrogeological control and productivity modes of coalbed methane commingled production in multi-seam areas: A case study of the bide–santang basin, Western Guizhou, south China. *J. Petroleum Sci. Eng.* 189, 107039. doi:10.1016/j.petrol.2020.107039

Guo, C., Qin, Y., Xia, Y. C., Ma, D., Han, D., Chen, Y., et al. (2017). Geochemical characteristics of water produced from CBM wells and implications for commingling CBM production: A case study of the bide-santang basin, Western Guizhou, China. *J. Petroleum Sci. Eng.* 159, 666–678. doi:10.1016/j.petrol.2017.09.068

Hao, C. M., Huang, Y., He, P. Y., and Sun, W. (2019). Isotope drift characteristics in ordovician limestone karst water caused by coal mining in northern China. *Mine Water Environ.* 38 (3), 507–516. doi:10.1007/s10230-019-00606-4

Houatmia, F., Azouzi, R., Charef, A., and Bedir, M. (2016). Assessment of groundwater quality for irrigation and drinking purposes and identification of hydrogeochemical mechanisms evolution in Northeastern, Tunisia. *Environ. Earth Sci.* 75 (9), 746. doi:10.1007/s12665-016-5441-8

Huang, H. X., Nie, Z. H., Chao, H. Y., Chen, D., and Liu, Y. (2018). Discussion of the selection for producing layers of deep CBM wells in Linfen block. *J. China Coal Soc.* 43 (6), 1627–1633. doi:10.13225/j.cnki.jccs.2018.4041

Huang, X. J., Wang, G. C., Liang, X. Y., Cui, L. F., Ma, L., and Xu, Q. Y. (2018). Hydrochemical and stable isotope (δD and $\delta^{18}O$) characteristics of groundwater and hydrogeochemical processes in the ningtiaota coalfield, northwest China. *Mine Water Environ.* 37 (1), 119–136. doi:10.1007/s10230-017-0477-x

Lakshmanan, E., Kannan, R., and Kumar, M. S. (2003). Major ion chemistry and identification of hydrogeochemical processes of ground water in a part of Kancheepuram district, Tamil Nadu, India. *Environ. Geosci.* 10 (4), 157–166. doi:10.1306/eg100403011

Lemay, T. G., and Konhauser, K. (2006). *Water chemistry of coalbed methane reservoirs*. Canada: Alberta Energy and Utilities Board, EUB/AGS, Special Report.

Li, C. C., Gao, X. B., and Wang, Y. X. (2015). Hydrogeochemistry of high- fluoride groundwater at Yuncheng Basin, northern China. *Sci. Total Environ.* 508, 155–165. doi:10.1016/j.scitotenv.2014.11.045

Li, P. Y., Wu, J. H., and Qian, H. (2013). Assessment of groundwater quality for irrigation purposes and identification of hydrogeochemical evolution mechanisms in Pengyang County, China. *Environ. Earth Sci.* 69 (7), 2211–2225. doi:10.1007/s12665-012-2049-5

Li, Q. G., Ju, Y. W., Lu, W. Q., Wang, G. C., Neupame, B., and Sun, Y. (2016). Water rock interaction and methanogenesis in formation water in the southeast Huaibei coalfield, China. *Mar. Petroleum Geol.* 77, 435–447. doi:10.1016/j.marpetgeo.2016.06.021

Li, X., Fu, X. H., Ge, Y. Y., and Chang, X. X. (2016). Research on sequence stratigraphy, hydrogeological units and commingled drainage associated with coalbed methane production: A case study in zhuzang syncline of Guizhou province, China. *Hydrogeol. J.* 24 (8), 2171–2187. doi:10.1007/s10040-016-1448-1

Li, Y., Chen, J., Tang, S. H., Zhang, S. H., and Xi, Z. D. (2022). Biogeochemical assessment of the coalbed methane source, migration, and fate: A case study of the shizhuangnan block, southern Qinshui Basin. *ACS Omega* 7 (9), 7715–7724. doi:10.1021/ACSOMEGA.1C06496

Liu, H., Sang, S., Formolo, M., Li, M., Liu, S., Xu, H., et al. (2013). Production characteristics and drainage optimization of coalbed methane wells: A case study from low-permeability anthracite hosted reservoirs in southern Qinshui Basin, China. *Energy Sustain. Dev.* 17 (5), 412–423. doi:10.1016/j.esd.2013.04.005

Meng, Y. J., Tang, D. Z., Xu, H., and Gao, L. J. (2014). Coalbed methane produced water in China: Status and environmental issues. *Environ. Sci. Pollut. Res.* 21 (11), 6964–6974. doi:10.1007/s11356-014-2675-4

Qin, Y., Yuan, L., Hu, Q. T., et al. (2012). Status and development trend of coalbed methane exploration and development technology in China. *Coal Sci. Technol.* 40 (10), 1–6. doi:10.13199/j.cst.2012.10.7.qiny.007

Qin, Y., Zhang, Z., Bai, J. P., Liu, D. H., and Tian, Y. D. (2014). Source apportionment of produced-water and feasibility discrimination of commingling CBM production from wells in Southern Qinshui Basin. *J. China Coal Soc.* 39 (9), 1892–1898. doi:10.13225/j.cnki.jccs.2014.8012

Redwan, M., Abdel Moneim, A. A., and Amra, M. A. (2016). Effect of water–rock interaction processes on the hydrogeochemistry of groundwater west of Sohag area, Egypt. *Arab. J. Geosci.* 9 (2), 111. doi:10.1007/s12517-015-2042-x

Singh, N., Singh, R. P., Kamal, V., Sen, R., and Mukherjee, S. (2015). Assessment of hydrogeochemistry and the quality of groundwater in 24-Parganas districts, West Bengal. *Environ. Earth Sci.* 73, 375–386. doi:10.1007/s12665-014-3431-2

Tang, Q. F., Xu, Q., Zhang, F. C., Huang, Y. Y., Liu, J. C., Wang, X. C., et al. (2013). Geochemistry of iodine-rich groundwater in the taiyuan basin of central Shanxi province, north China. *J. Geochem. Explor.* 135, 117–123. doi:10.1016/j.gexplo.2012.08.019

Tao, S., Da, Z., Xu, H., Lv, Y. M., and Zhao, X. L. (2011). Analysis on influence factors of coalbed methane wells productivity and development proposals in southern Qinshui Basin. *J. China Coal Soc.* 36 (2), 194–198. doi:10.13225/j.cnki.jccs.2011.02.007

Zhang, Z., and Qin, Y. (2018). A preliminary investigation on water quality of coalbed natural gas produced water for beneficial uses: A case study in the southern Qinshui Basin, north China. *Environ. Sci. Pollut. Res.* 25 (22), 21589–21604. doi:10.1007/s11356-018-2298-2

Zhang, Z., Qin, Y., Bai, J. P., Li, G., Zhuang, X., and Wang, X. (2018). Hydrogeochemistry characteristics of produced waters from CBM wells in southern Qinshui Basin and implications for CBM commingled development. *J. Nat. Gas Sci. Eng.* 56, 428–443. doi:10.1016/j.jngse.2018.06.024

Zheng, S. H., Hou, F. G., and Ni, B. L. (1983). Study on hydrogen and oxygen stable isotopes of meteoric water in China. *Chin. Sci. Bull.* 13, 801–806. doi:10.1360/csb1983-28-13-801

frontiers | Frontiers in Earth Science

TYPE Original Research
PUBLISHED 25 January 2023
DOI 10.3389/feart.2022.1098035

OPEN ACCESS

EDITED BY
Junjian Zhang,
Shandong University of Science and Technology, China

REVIEWED BY
Kun Zhang,
Henan Polytechnic University, China
Jie Chi,
China University of Petroleum (Huadong), China

*CORRESPONDENCE
Shuxun Sang,
shxsang@cumt.edu.cn
Meng Wang,
wangm@cumt.edu.cn

SPECIALTY SECTION
This article was submitted to Economic Geology, a section of the journal Frontiers in Earth Science

RECEIVED 14 November 2022
ACCEPTED 05 December 2022
PUBLISHED 25 January 2023

CITATION
Zheng S, Sang S, Wang M, Liu S, Huang K, Feng G and Song Y (2023), Experimental investigations of CO_2 adsorption behavior in shales: Implication for CO_2 geological storage. *Front. Earth Sci.* 10:1098035. doi: 10.3389/feart.2022.1098035

Experimental investigations of CO_2 adsorption behavior in shales: Implication for CO_2 geological storage

Sijian Zheng[1,2], Shuxun Sang[1,2,3]*, Meng Wang[1,2]*, Shiqi Liu[1,2], Kai Huang[3], Guangjun Feng[3] and Yu Song[3]

[1]Jiangsu Key Laboratory of Coal-based Greenhouse Gas Control and Utilization, China University of Mining and Technology, Xuzhou, China, [2]Carbon Neutrality Institute, China University of Mining and Technology, Xuzhou, China, [3]School of Resources and Geosciences, China University of Mining and Technology, Xuzhou, China

Injecting CO_2 into shale reservoirs has dual benefits for enhancing gas recovery and CO_2 geological sequestration, which is of great significance to ensuring energy security and achieving the "Carbon Neutrality" for China. The CO_2 adsorption behavior in shales largely determined the geological sequestration potential but remained uncharted. In this study, the combination of isothermal adsorption measurement and basic petrophysical characterization methods were performed to investigate CO_2 adsorption mechanism in shales. Results show that the CO_2 sorption capacity increase gradually with injection pressure before reaching an asymptotic maximum magnitude, which can be described equally well by the Langmuir model. TOC content is the most significant control factor on CO_2 sorption capacity, and the other secondary factors include vitrinite reflectance, clay content, and brittle mineral content. The pore structure parameter of BET-specific surface area is a more direct factor affecting CO_2 adsorption of shale than BJH pore volume. Langmuir CO_2 adsorption capacity positive correlated with the surface fractal dimension (D_1), but a significant correlation is not found with pore structure fractal dimension (D_2). By introducing the Carbon Sequestration Leaders Forum and Department of Energy methods, the research results presented in this study can be extended to the future application for CO_2 geological storage potential evaluation in shales.

KEYWORDS

shale gas, adsorption capacity, pore structure, mineral composition, CO_2 geological storage

1 Introduction

Shale gas plays a crucial role in natural gas production in China because its great potential (recoverable reserves of ~3.12 × 10^{13} m^3) (Liu et al., 2019a; Li et al., 2019; Yao et al., 2019). The exploration and development of shale gas is the choice of fossil energy resource and national needs, which is of great significance to China's energy security (Xie et al., 2022). The methane content of shales is generally greater than 85%, even up to 99% (Howarth et al., 2011). The methane exists in shales in three strikingly different phases (Hazra et al., 2015; Zou et al., 2018; Yao et al., 2021): 1) Dissolving in the shale pore water as dissolved phase, which can be almost negligible. 2) Presenting in the form of movable fluid in shale pore-fracture system, defined as free phase methane. 3) Existing on the inner shale pore surface or in the shale matrix as an adsorbed state, defined as adsorbed phase methane.

The extremely low porosity and permeability of shale or coal reservoirs have significantly increased the difficulty of gas development (Zheng et al., 2018, 2019), and the initial fracturing engineering must be done to commercialize shale gas production (Liu et al., 2015; Ma et al., 2018; Dai et al., 2019). Currently, the hydraulic fracturing technology is a standard option for shale gas production (Gregory et al., 2011; Estrada and Bhamidimarri, 2016), but the high clay minerals content leads to poor stimulation–due to the expansion characteristics of shale clay minerals in contact with water (Ge et al., 2015; Zhou et al., 2022). In addition, additives in fracturing fluid can also pose a risk of environmental pollution (Vidic et al., 2013). CCUS (carbon capture, utilization, and storage) refers to the process of separating CO_2 from industrial processes or the atmosphere and then directly utilizing or injecting it into the stratum to achieve permanent CO_2 emission reduction (Liu et al., 2019b; Zheng et al., 2022). Injecting CO_2 into shales for enhancing shale gas recovery

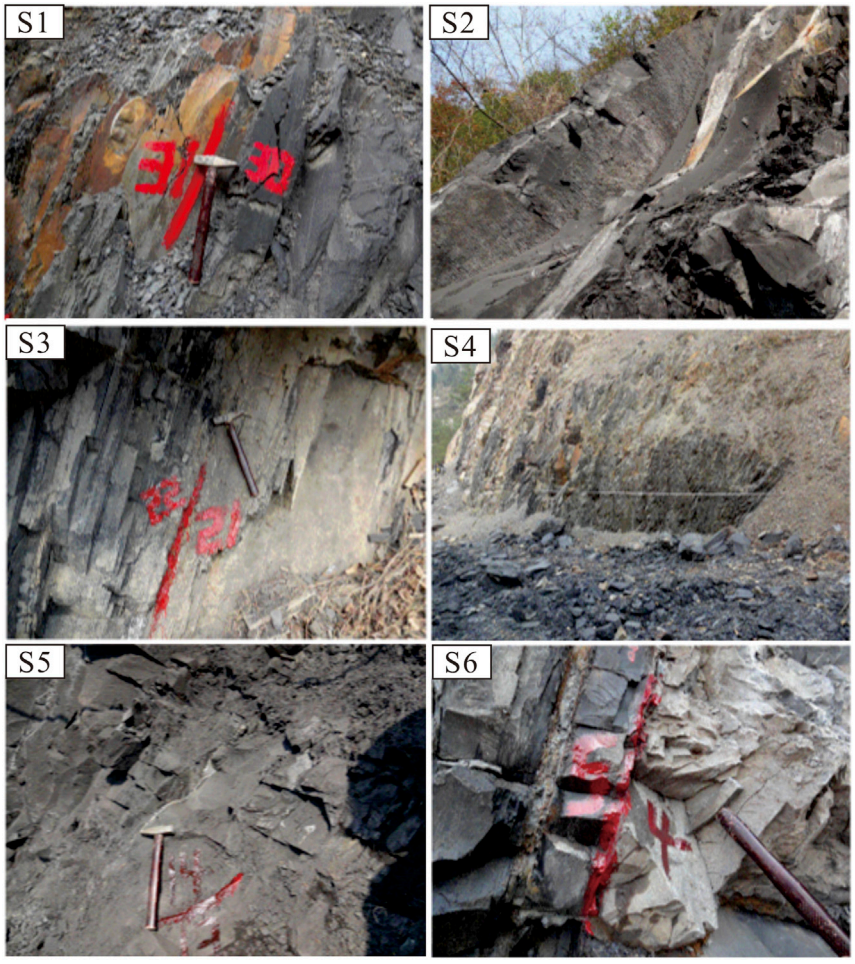

FIGURE 1
Field sampling photograph of the Longmaxi shale.

TABLE 1 Detailed basic physical properties of the selected shales.

id	Toc/%	Ro/%	Mineral content						
			Clay/%	Quartz/%	Plagioclase/%	Potassium feldspar/%	Calcite/%	Dolomite/%	Pyrite/%
S1	1.44	2.81	12.14	48.77	11.01	8.03	10.93	5.89	3.23
S2	2.59	2.90	8.11	48.93	7.03	3.04	—	29.86	3.03
S3	2.89	2.28	16.14	47.94	14.98	7.99	6.10	4.73	2.12
S4	2.97	2.00	16.95	54.04	6.84	6.17	5.97	4.18	5.85
S5	3.78	2.46	13.95	50.84	11.95	8.01	8.22	4.91	2.12
S6	4.97	2.00	13.92	51.94	8.27	5.83	13.15	4.89	2.00

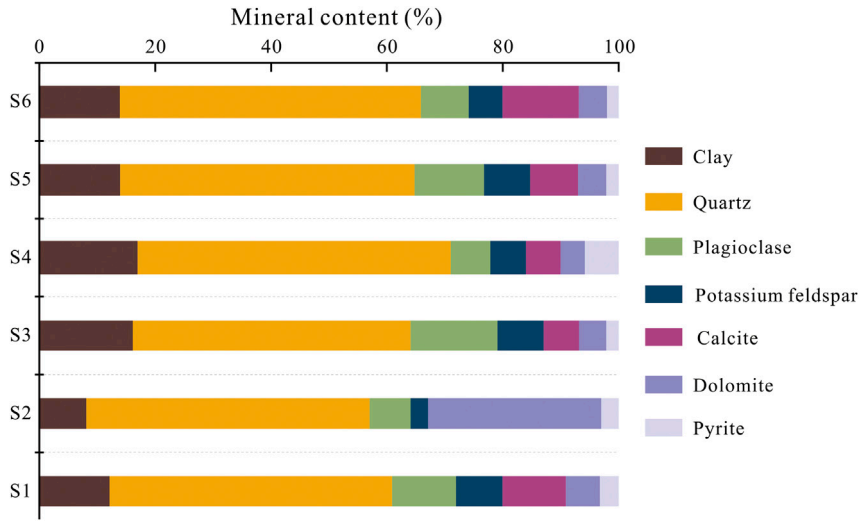

FIGURE 2
The mineral content of the shales identified by XRD measurement.

(abbreviated as CO_2-ESGR) has another unexpected benefits for CO_2 geological storage (Liu et al., 2017; Yang et al., 2018; Zheng et al., 2020). First, the CO_2 fracturing technology can reduce shale reservoir damage by comparing it with the fracturing fluid of water. In addition, the essence of CO_2-ESGR is the transformation of adsorbed methane to free phased–due to the CO_2-CH_4 competitive adsorption characterizations in shales. The characteristic of CO_2 adsorption in shales are essential for the CO_2-ESGR field application results and CO_2 geological storage safety.

Isothermal adsorption measurement is the most commonly used method for providing CO_2 adsorption characteristics in shales (Wang et al., 2016; Chen et al., 2021; Liu D et al., 2022). The analysis models to study CO_2 adsorption properties include the classical statistical mechanics-based Freundlich model, monolayer adsorption-based Langmuir model, multilayer adsorption BET model, and micro-pore filling adsorption D-R model (Du et al., 2021; Liu J et al., 2021; Shi et al., 2022). Weniger et al. (2010) estimated the CO_2 sorption capacity in shale samples from the Paraná Basin under an experimental temperature of ~35°C and ~45°C. They found CO_2 adsorption amount reached the maximum in the pressure range of 8.0–10.0 MPa. Kang et al. (2011) investigated the CO_2 storage potential in organic-rich-shales by performing CO_2 isothermal adsorption experiments. Experimental results in their study (Kang et al., 2011) indicated that pore-volume evaluation plays an essential role in shale reservoir CO_2 geological storage. By introducing the Monte Carlo and molecular dynamics simulation methods, CO_2 adsorption properties at modeled quartz were well described by the Langmuir model (Sun et al., 2016). In summary, the

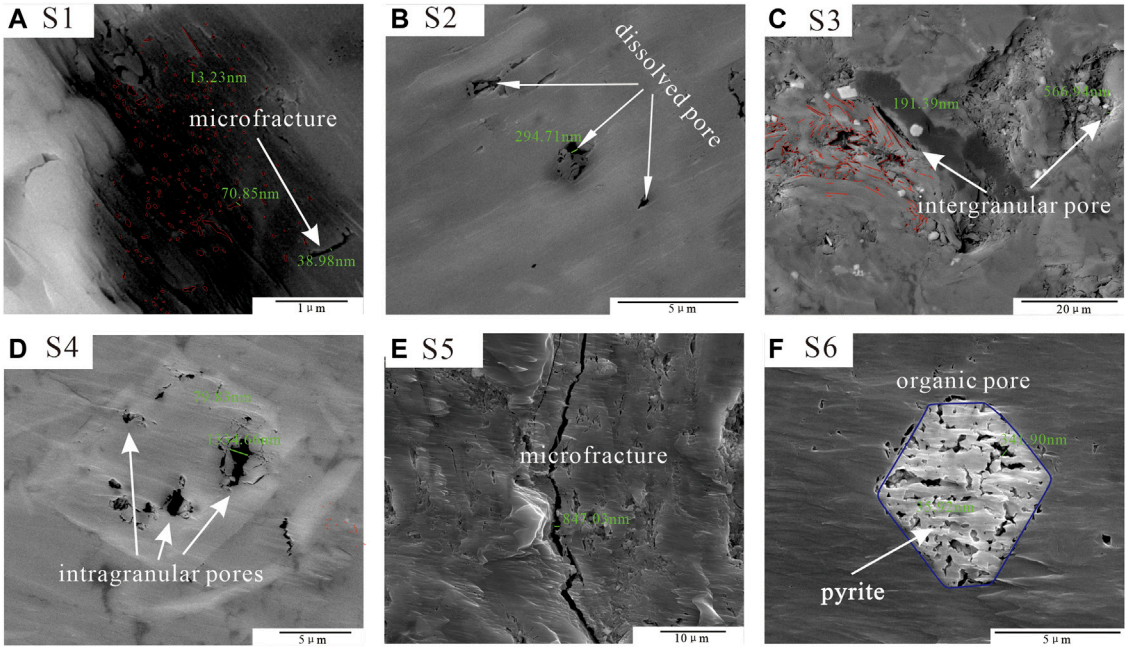

FIGURE 3
SEM results of the Longmaxi shale.

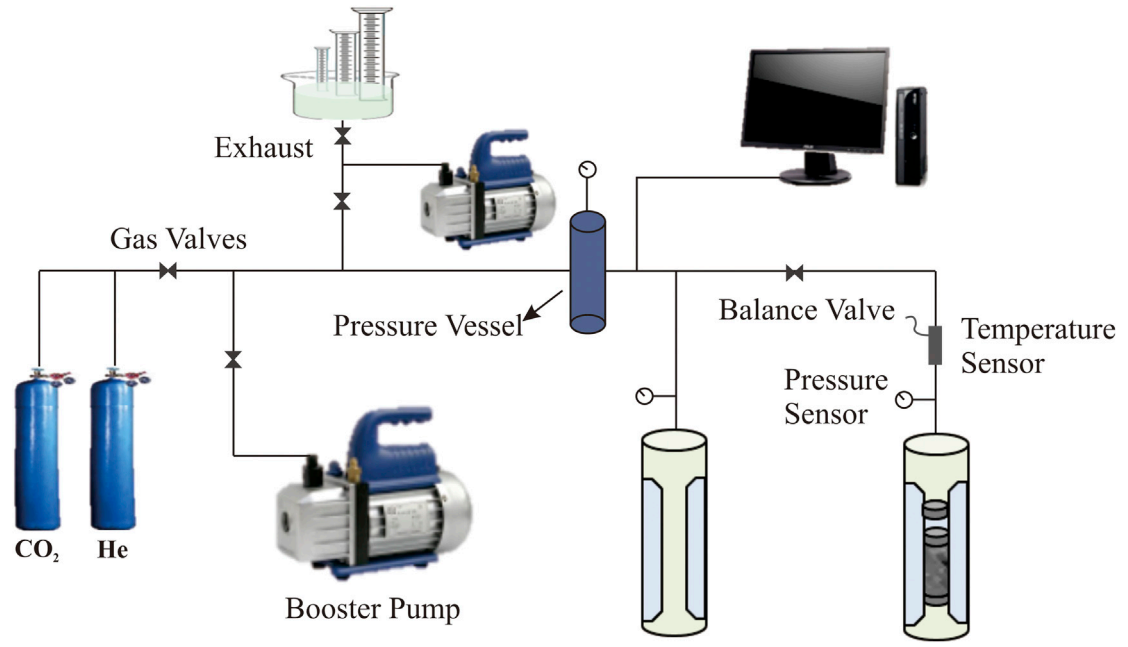

FIGURE 4
Schematic of the CO_2 adsorption isotherm measurement.

TABLE 2 Pore structure parameters on the selected shales identified by the LT-N_2GA measurement.

ID	BJH pore volume (cm^3/g)				BET specific surface area (m^2/g)			
	Total	Micro-pores	Meso-pores	Macro-pores	Total	Micro-pores	Meso-pores	Macro-pores
S1	0.0061	0.0020	0.0026	0.0015	7.94	6.48	1.39	0.07
S2	0.0144	0.0055	0.0061	0.0028	21.18	17.94	3.10	0.14
S3	0.0117	0.0045	0.0047	0.0025	16.95	14.18	2.64	0.12
S4	0.0157	0.0067	0.0069	0.0021	25.48	21.74	3.66	0.08
S5	0.0147	0.0069	0.0060	0.0018	66.02	21.84	44.11	0.07
S6	0.0163	0.0083	0.0058	0.0021	30.79	26.48	4.21	0.10

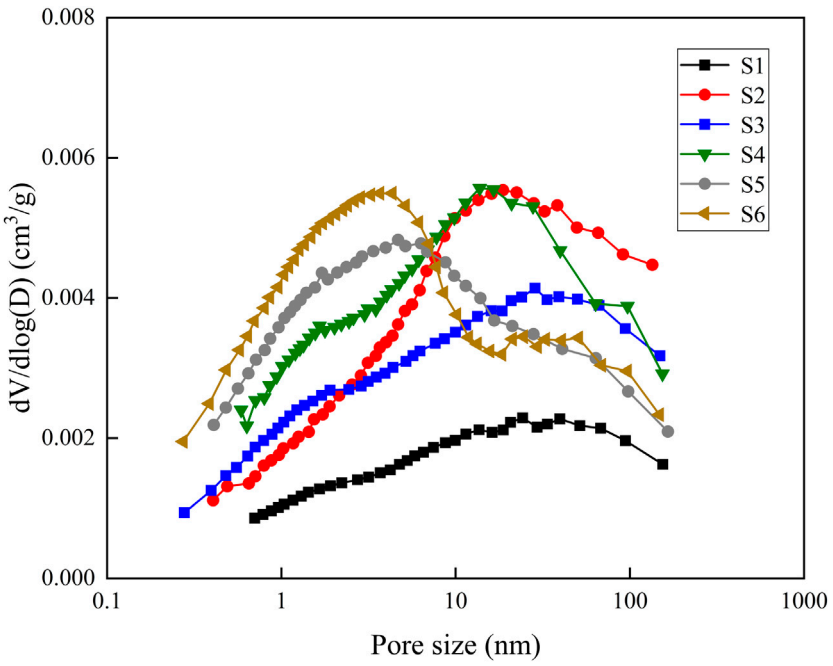

FIGURE 5
The pore size distribution of the shales identified by LT-N_2GA measurement.

contribution of shale internal compositions together with pore structures on its CO_2 adsorption characteristics still remains unclassified due to the complex multi-factor coupling factor.

In this paper, we first performed the sulfur-carbon test, organic matter measurement, and XRD measurement to investigate the shale's organic geochemical and mineralogical characteristics. Based on the combination of pore structure characterization method and single fractal theory, the heterogeneous features of shales are systematically estimated. The CO_2 adsorption characteristics in shale gas reservoirs are evaluated through isothermal adsorption experiments, and the control mechanisms and patterns are established to reveal CO_2 adsorption characteristics in shale gas reservoirs directly. The research results presented in this paper have great significance in estimating CO_2 sequestration storage potential in shales.

2 Sampling and experiments

2.1 Samples

In this study, six shales were obtained from the Longmaxi formation, Sichuan Basin. The shales of S1, S3, S5, and S6 were collected from the bottom to upper-middle Longmaxi formation

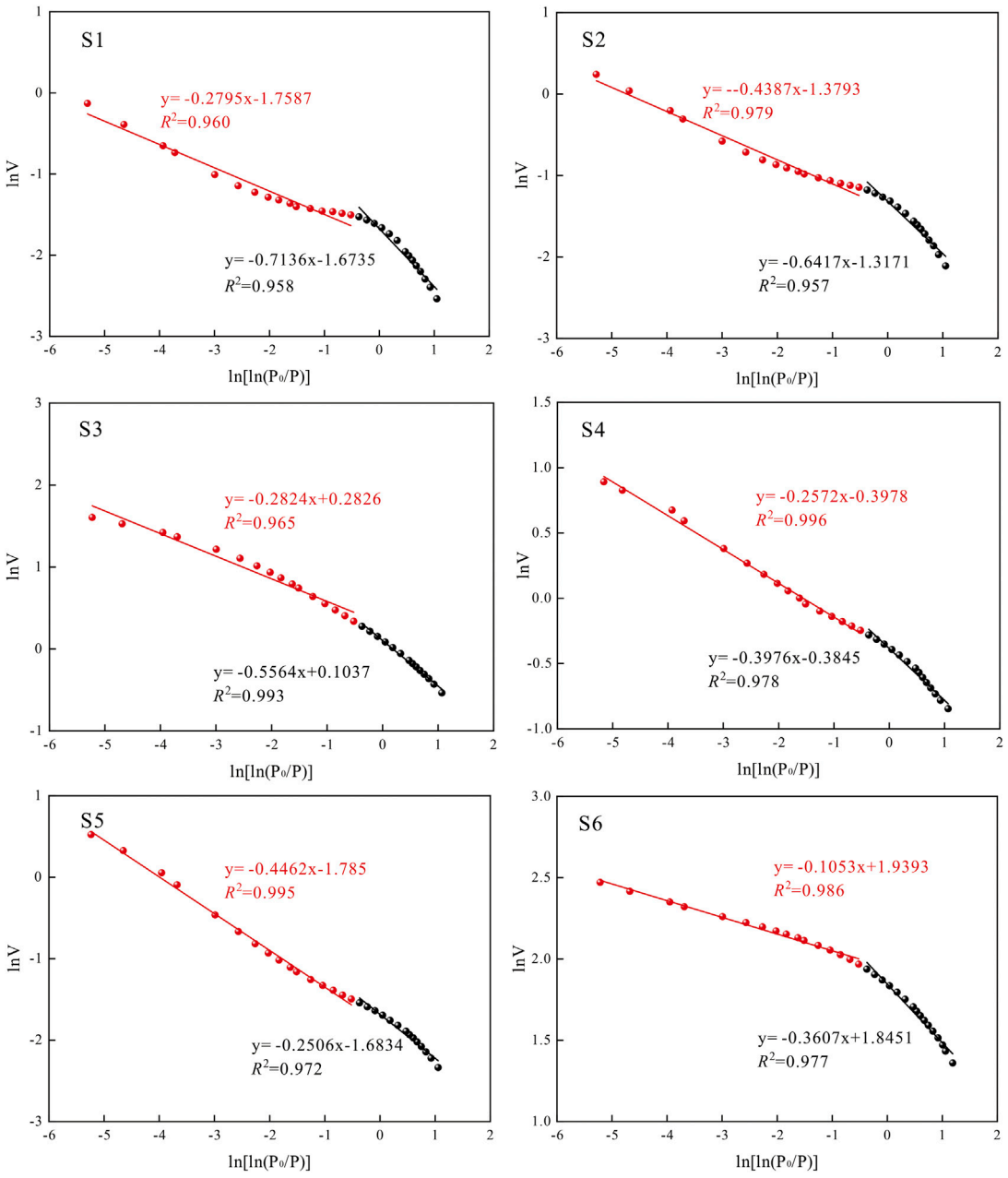

FIGURE 6
Scatterplots of ln*V* vs. ln (ln (P_0/*P*)) for six shales by LT-N_2GA measurement.

at the Chongqing Blackwater Section (Figure 1). In comparison, the S2 and S4 were gathered from the bottom Longmaxi formation located at Qiliao and Pengshui Sections, respectively (Figure 1). The detailed petro-physical, organic geochemical, and mineralogical information parameters are presented in Table 1. The TOC of the selected shales in the range of 1.44%–4.97%, estimated by the CS-800 Carbon sulfur analyzer. The R_o (vitrinite reflectance equivalent) of the selected shales averaged at ~2.41%, classifying to the over-mature stage. The XRD experimental results are listed in Table 1 and shown in Figure 2. Results indicated that the quartz content contributes the most significant mineral proportion of shales, ranging from 48.77% to 54.04%. The SEM results are displayed in Figure 3, the shale pore types include dissolved pore (Figure 3B), intergranular pore (Figures 3C,D), organic pore (Figure 3F), and microfracture (Figures 3A,E).

TABLE 3 The fractal dimension and Langmuir model fitting results of the shales.

ID	Fractal dimension		Langmuir model fitting results		
	D_1	D_2	V_L (cm^3/g)	P_L (MPa)	R^2
S1	2.29	2.72	3.26	3.05	0.9939
S2	2.36	2.56	3.85	1.43	0.9875
S3	2.44	2.72	4.73	2.28	0.9928
S4	2.60	2.74	5.48	0.99	0.9959
S5	2.75	2.55	5.91	1.33	0.9949
S6	2.64	2.89	6.95	1.49	0.9881

2.2 Pore structure characterization experiments

In this study, the low-temperature N_2 gas adsorption (LT-N_2GA) measurements were performed to investigate the pore structure properties of shales, following the Chinese standard of SY/T6154-1995. For the sample preparation, the large-sized shales were crushed to 60–80 mesh, then dried in an oven to remove impurity gas and internal bound-water. The LT-N_2GA procedures can be summarized as: 1) Subject a certain amount of powder shales to vacuum degassing. 2) Obtaining the N_2 adsorption/desorption properties under constant experimental conditions. 3) Estimating the pore structure parameters (e.g., specific surface area, pore volume). based on the BJH and BET models (Yao et al., 2008).

2.3 CO_2 isothermal adsorption measurements

CO_2 adsorption isotherm measurements were performed by the volumetric-based method (Figure 4). The principle of this method depends on the pressure changes in the sample and reference cells during CO_2 adsorption process. CO_2 adsorption isotherm experimental procedures were summarized as: 1) Grind the bulk shale into 60–80 mesh (0.02–0.03 cm) using a ball-mill instrument and then represent dry treatment for 72-h at a given temperature of 110°C to remove the moisture inside the sample. 2) Transfer the powder sample in to sample cell and then present vacuum treatment by a vacuum pump. 3) Calculate the free space volume based on the mass balance parameters before/after helium injection. 3) Inject the designed pressure of CO_2 into the sample cell for CO_2 adsorption. e) Estimate the CO_2 adsorption capacity on the basis of the ideal-gas equation.

3 Results and Discussion

3.1 Pore structure characterization of shales

Table 2 shows the pore structure parameters of the selected shales identified by the LT-N_2GA measurement. Results indicated that the BJH pore volume of shales range from 0.0117 to 0.0163 cm^3/g, the volume of micropores (pore radius <2 nm), mesopores (pore radius 2–50 nm), and macropores (pore radius >50 nm) contribute the total proportion as ~41.75%, ~41.05%, and ~17.2%, respectively. While the BET specific surface area in the range of 7.94–66.02 m^2/g, the specific surface area of micropores, mesopores and macropores contribute the total proportion as ~75.75%, ~23.75%, and ~0.5%. The low percentage of

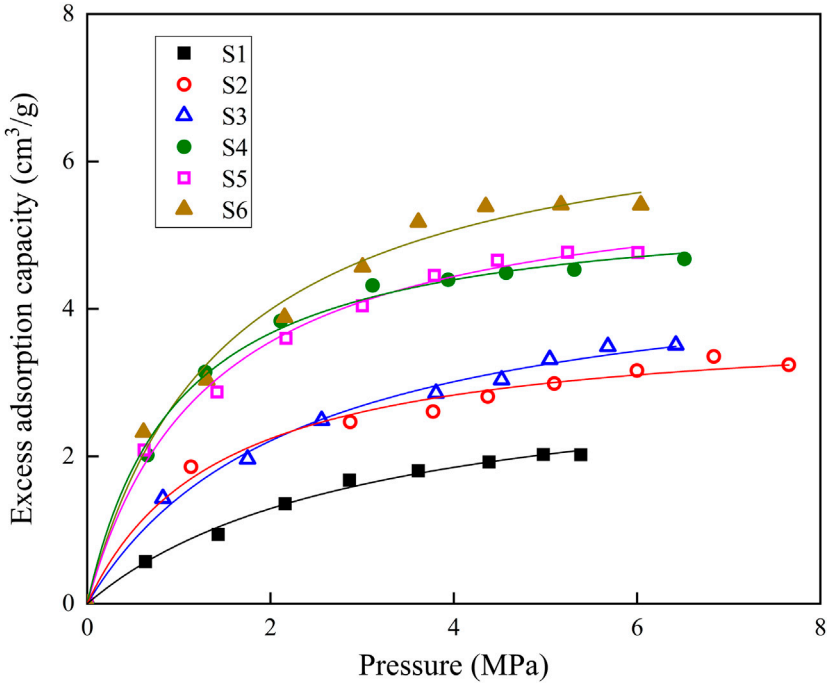

FIGURE 7
The CO_2 isothermal adsorption data with respect to different pressures for the shales.

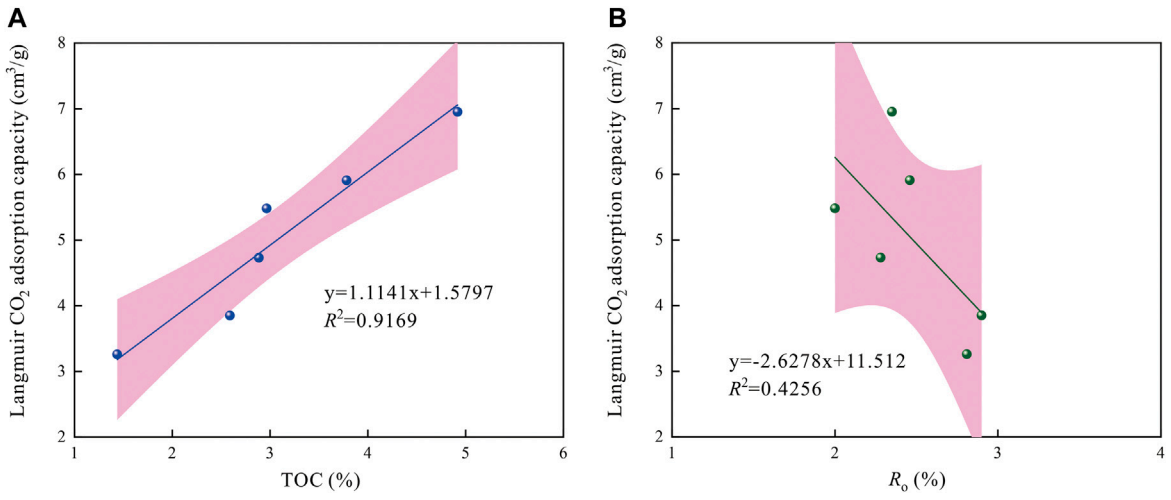

FIGURE 8
Relationships between TOC content, R_o value and Langmuir CO_2 adsorption capacity in shales.

macropores in BET specific surface area is mainly because the LT-N_2GA testing principle–limiting characterizes the pore size larger than 200 nm. As shown in Figure 5, the pore size distributions (PSD) of some shales (S6 and S5) emerge two significantly different peaks; from left to right, the peak locates at 2–3 and 10–20 nm, respectively. For the remaining shale samples, the PSD is characterized by a unimodal size distribution with a peak at approximately 8–20 nm.

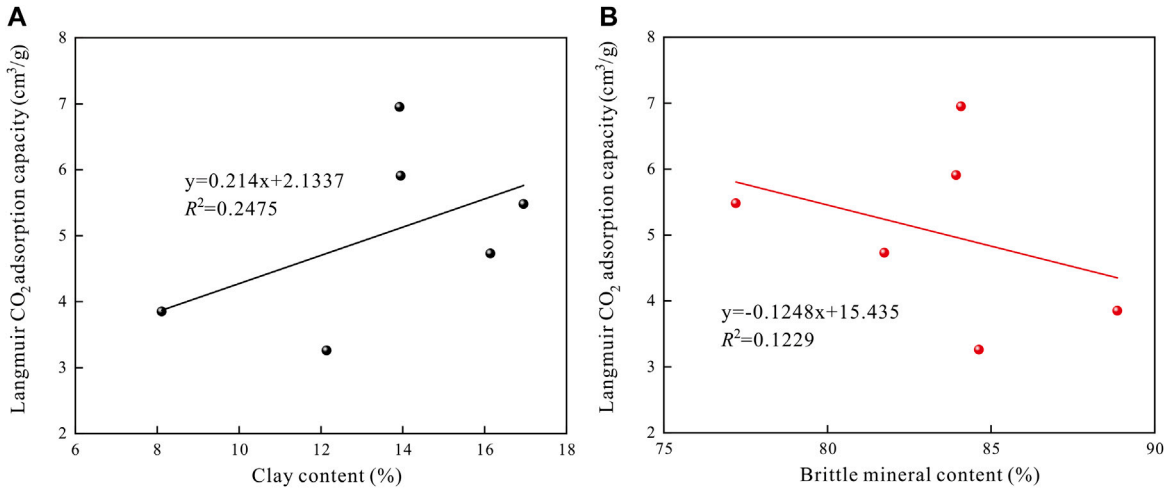

FIGURE 9
The relationships between clay content, brittle mineral content and Langmuir CO_2 adsorption capacity in shales.

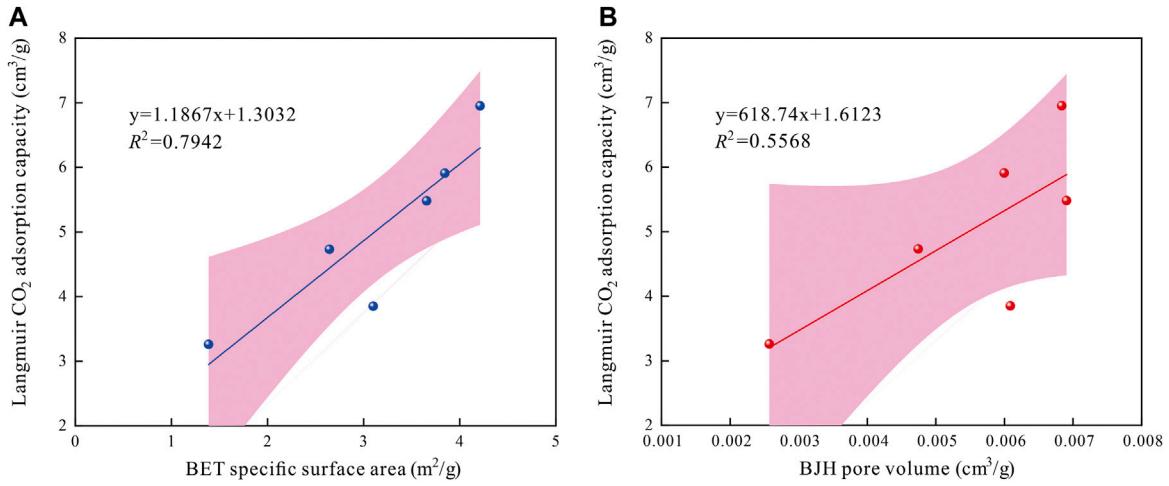

FIGURE 10
Relationships between pore structure parameters vs. Langmuir CO_2 adsorption capacity in shales.

Based on the LT-N_2GA experimental data and Frenkel-Halsey-Hil (FHH) model, the complexity and heterogeneity of shale were quantitatively characterized (He et al., 2021; Liu K et al., 2021). The greater fractal dimension is indicative of more heterogeneity pore structure. FHH fractal dimension calculation method was expressed as follows:

$$\ln\left(\frac{V}{V_0}\right) = K\left[\ln\left(\ln\left(\frac{P_0}{P}\right)\right)\right] + C \quad (1)$$

where V means the nitrogen adsorption volume under pressure P, mmol/g; P means the experimental equilibrium pressure, MPa; V_0 means the monolayer coverage volume, mmol/g; K and C are constant, dimensionless; P_0 is the nitrogen saturation pressure, MPa. According to Eq. 1, the slope of ln$V$ vs. ln (ln (P_0/P)) plots equals the constant C. While the fractal dimension D equals "C+3" value. Theoretically, fractal dimension D in the range of 2–3, the closest value to two indicates the more regular the pore space

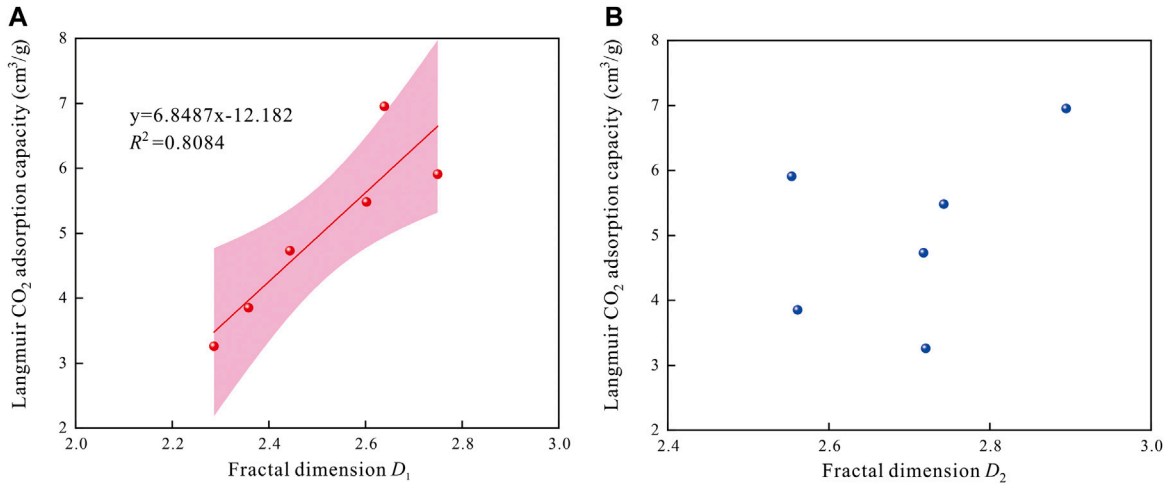

FIGURE 11
Relationships between fractal dimension and Langmuir CO_2 adsorption capacity in shales.

structures, and the closest value to three means the more complex and heterogeneity pore structures.

The scatterplot of ln$V$ vs. ln (ln (P_0/P)) for six shales are displayed in Figure 6. It can be found that there are two distinct linear segments, one at the P/P_0 intervals of 0–0.5 and the other one at the 0.5–1 region. In addition, these two linear segments show great linear relationships (R^2>0.95), indicating the different fractal characteristics. Here, the fractal dimension at P/P_0 intervals 0–0.5 and 0.5–1 as D_1 and D_2, respectively. Moreover, D_1 and D_2 represent the pore surface fractal and the pore structure fractal, dominated by Van der Waals forces and capillary condensation actions, respectively (Yao et al., 2008). As shown in Table 3, The fractal dimension D_1 of shales value as ~2.29–2.75, average at 2.51. While the fractal dimension D_2 ranges from 2.56 to 2.89, average at 2.70 (Table 3).

3.2 CO_2 isothermal adsorption of shales

Figure 7 represents the CO_2 isothermal adsorption data with respect to different pressures for the selected shales. The excess CO_2 adsorption capacity rapidly increases with pressure at low-pressure intervals, and slowly increases at high-pressure intervals. Additionally, the CO_2 adsorption capacities vary from region to region. The experimental determined maximum excess CO_2 adsorption capacity of shale S1 is ~2.02 cm^3/g, the smallest value among all the samples (Figure 7). In comparison, the experimental determined maximum excess CO_2 adsorption capacity of S6 is valued as ~5.41 cm^3/g (Figure 7). These differences probably arise because of the complex solid and heterogeneity in shales–resulting in the variation in internal composition and pore structure–leading to the different CO_2 adsorption capacities in different shales.

Langmuir model is the commonly used adsorption characterization model in coals, which can be extended to investigate the CO_2 adsorption capacity for shales. The Langmuir model was based on the following assumptions (Perera et al., 2011; Dutka, 2019; Liu Y et al., 2022): 1) The adsorbent surface was characterized as uniform; 2) A dynamic adsorption equilibrium state between adsorbent and adsorbate; 3) The adsorption behavior was monolayer molecular adsorption; 4) No interaction force among the adsorbent gas molecules. The Langmuir model can be deduced as follows:

$$V = \frac{V_L P}{P + P_L} \tag{2}$$

where V means the experimental measured adsorption capacity, cm^3/g; P means the experimental pressure, MPa. V_L means the Langmuir adsorption capacity, cm^3/g; P_L means Langmuir adsorption pressure, MPa.

The CO_2 isothermal adsorption data fitting results are listed as Table 3, and the fitting curves are displayed in Figure 7. Results indicate that the Langmuir model fitting curves are consistent with experimental excess CO_2 adsorption capacity changes. The CO_2 adsorption capacity rapidly increases with increasing pressure before reaches to a critical pressure; after that, the fitting curves rise smoothly and tend to saturate. As shown in Table 3, the Langmuir volumes of the CO_2 isothermal adsorption in the shale in the range of 3.26–6.95 cm^3/g (averaging ~5.03 cm^3/g). While, the Langmuir pressure of the CO_2 isothermal adsorption in the shale ranges from 0.99 MPa to 3.05 MPa (averaging ~1.76 MPa). It can be concluded that the Langmuir model is used equally well to investigate the CO_2 sorption behavior for shales, as evident by the high correlation coefficients >0.9875.

3.3 Effect of shale composition on CO_2 adsorption capacity

Figure 8 shows the relationships between TOC content, R_o value and Langmuir CO_2 adsorption capacity. Results indicate a perfect positive linear correlation between TOC content and Langmuir CO_2 adsorption capacity, with a high correlation coefficient as ~0.9169 (Figure 8A). The higher TOC content is indicative of greater CO_2 adsorption capacity. The above phenomenon can be attributed to the massive nanopore kerogen development in organic matter, which is the leading adsorption site of CO_2 in shales. In addition, the R_o presents a very weak negative correlation with the Langmuir CO_2 adsorption capacity (Figure 8B). Tang et al. (2016) investigated the adsorption behavior of the shales under the same conditions for organic matter and kerogen shale types, and found the adsorption capacities of over-mature shales were lower than these in high-maturity stages. The results presented in this section are consistent with the previous study (e.g., Chalmers and Bustin, 2008; Tang et al., 2016).

The effect of shale mineral composition on its CO_2 adsorption capacity is mainly reflected in the clay and brittle minerals. In this study, the relationships between clay content, brittle mineral content and Langmuir CO_2 adsorption capacity in shales are displayed in Figure 9. It can be found that there exists a positive correlation between the clay content and Langmuir CO_2 adsorption capacity (Figure 9A). While, the brittle mineral content was negative related with the Langmuir CO_2 adsorption capacity (Figure 9B), properly because the increase in brittle mineral content in the shale leads to relative decreases both in the clay and TOC content. The correlation coefficient of clay content and Langmuir CO_2 adsorption capacity was more significant than that with brittle mineral content, indicating clay content is the significant control factor on CO_2 adsorption.

3.4 Effect of pore structure properties on CO_2 adsorption capacity

Figure 10 presents the correlations between pore structure parameters (obtained from the LT-N_2GA measurements) and CO_2 adsorption capacity of shales. Results illustrate that both the specific surface area and pore volume positively affect the CO_2 adsorption capacity. The correlation coefficient of CO_2 adsorption capacity and specific surface area was greater than that with pore volume, indicating that the specific surface area is the most direct factor affecting the CO_2 adsorption of shale. The behavior of CO_2 adsorbing in shale pore surface is attributed to the physical adsorption of Vander Waals force. The larger specific surface area is indicative of more adsorption sites–more conducive to the CO_2 adsorption in shales.

The shale pore structures were characterized by heterogeneity (as discussed in Section 3.1), and the influence of these fractal characteristics on CO_2 adsorption behavior cannot be ignored. Generally, there are two conventional definitions for describing fractal characteristics of porous materials: the surface fractal dimension (D_1) and the pore structure fractal dimension (D_2). Thus, it is necessary to quantitatively investigate the effect of pore fractal characteristics on the adsorption and storage capacity. As shown in Figure 11, the two fractal dimensions have different influences on the CO_2 adsorption capacity of shales. Results show that the fractal dimension D_1 positively correlated with the Langmuir CO_2 adsorption capacity (Figure 11A). Because the higher fractal dimension D_1 values represent more rough surfaces of shales that offer more adsorption sites for CO_2 and lead to the higher adsorption capacity of shales. Additionally, there were no significant relationships between the fractal dimension D_2 and Langmuir CO_2 adsorption capacity (Figure 11B).

3.5 Potential application of this study in shale CO_2 geological storage

Shale reservoirs have considerable potential for large-scale CO_2 sequestration, and the sequestration mechanisms are mainly controlled by adsorption and mineralization reactions. CO_2-ESGR technology opens up a new way for the green and efficient development of domestic unconventional oil and gas and geothermal resources. It is conducive to realizing the strategic goal of "Carbon Peak" in 2030 and "Carbon Neutrality" in 2060 in China. In 2020, the shale gas proved geological reserves reached ~2×10^{12} m^3, providing a good application prospect in CO_2 geological storage. There are two classic methods to estimate the CO_2 geological storage potential in shales; one is the CSLF (Carbon Sequestration Leaders Forum) method (as described in Eq. 3), and the other one is the DOE (United States Department of Energy) method (as described in Eq. 4).

$$M_{co_2} = P_{PGI} \times \rho_g \times R_e \tag{3}$$

where M_{CO2} is the CO_2 geological storage volume in shales, m^3; ρ_g is the density of CO_2, kg/m^3; P_{PGI} is the available shale gas production, kg; R_e is replacement volume ration between CO_2 and CH_4, dimensionless.

$$M_{co_2} = A_{shale} \times \rho_g \times h \times \left(V_a + V_f\right) \times E \tag{4}$$

where M_{CO2} is the CO_2 geological storage volume in shales, m^3; A_{shale} is the target shale gas reservoir area, m^2; ρ_g is the density of CO_2, kg/m^3; h is the thickness of target shale gas reservoir, m; V_a is the CO_2 adsorption capacity, m^3/kg; V_f is the free phase CO_2 content, m^3/kg; E is the effective factor of shale CO_2 geological storage, which is influenced by the CO_2 adsorption capacity, buoyancy characteristics, and transport capacity. Based on the combination of CO_2 adsorption capacity and above parameters in Eq. 3 or Eq. 4, it is straightforward to calculate the CO_2 geological storage potential in shales.

4 Conclusion

In this study, the combination of isotherm adsorption measurement and basic petro-physical characterization methods were performed on six Longmaxi shales to investigate CO2 adsorption behavior and mechanism. The main conclusions are as follows.

(1) The fractal characteristics of shale pore structure were systematically analyzed by the FHH fractal model based on the LT-N_2GA experimental data. Two distinct linear segments at the P/P_0 intervals of 0–0.5 and 0.5–1 region correspond to the pore surface fractal (D_1) and the pore structure fractal (D_2) properties, respectively. The fractal dimensions D_1 and D_2 of shales are in the range of 2.29–2.75 and 2.56–2.89, indicating the complexity and heterogeneity of shale pore structures.
(2) The CO2 excess adsorption capacities increase gradually with increasing injection pressure before reaching an asymptotic maximum magnitude, which can be described equally well by the Langmuir model as evidenced by the high correlation coefficients.
(3) TOC content is the most significant control factor on shale CO2 sorption capacity, and a positive correlation exists between the surface fractal dimension D_1 and Langmuir CO2 adsorption capacity. By calculating the selective adsorption coefficient of CO_2/CH_4, the research results presented in this study can be extended to the prospective application of shale CO_2 geological storage potential evaluation.

Data availability statement

The raw data supporting the conclusion of this article will be made available by the authors, without undue reservation.

Author contributions

SS and MW provided the funding acquisition; SZ performed the experiments and wrote the paper; KH analyzed the data; GF and YS provided technical support.

Funding

We acknowledge financial support from the National Natural Science Foundation of China (42141012; 42030810; 41972168), the China Postdoctoral Science Foundation funded project (2022M723385), the Major research project of Jiangsu Key Laboratory of Coal-based Greenhouse Gas Control and Utilization (2020ZDZZ01B), the Peng Cheng Shang Xue Education Fund of CUMT Education Development Foundation (PCSX202204), and the Fundamental Research Funds for the Central Universities (2022QN1046).

Conflict of interest

The authors declare that the research was conducted in the absence of any commercial or financial relationships that could be construed as a potential conflict of interest.

Publisher's note

All claims expressed in this article are solely those of the authors and do not necessarily represent those of their affiliated organizations, or those of the publisher, the editors and the reviewers. Any product that may be evaluated in this article, or claim that may be made by its manufacturer, is not guaranteed or endorsed by the publisher.

References

Chalmers, G. R., and Bustin, R. M. (2008). Lower cretaceous gas shales in northeastern British columbia, Part I: Geological controls on methane sorption capacity. *Bull. Can. Petroleum Geol.* 56, 1–21. doi:10.2113/gscpgbull.56.1.1

Chen, L., Jiang, Z. X., Shu, J., Guo, S., and Tan, J. Q. (2021). Effect of pre-adsorbed water on methane adsorption capacity in shale-gas systems. *Front. Earth Sci.* 9, 757705. doi:10.3389/feart.2021.757705

Dai, C., Liu, H., Wang, Y. Y., Li, X., and Wang, W. H. (2019). A simulation approach for shale gas development in China with embedded discrete fracture modeling. *Mar. Pet. Geol.* 100, 519–529. doi:10.1016/j.marpetgeo.2018.09.028

Du, X. D., Cheng, Y. G., Liu, Z. J., Yin, H., We, T. F., Huo, L., et al. (2021). CO_2 and CH_4 adsorption on different rank coals: A thermodynamics study of surface potential, gibbs free energy change and entropy loss. *Fuel* 283, 118886. doi:10.1016/j.fuel.2020.118886

Dutka, B. (2019). CO_2 and CH_4 sorption properties of granular coal briquettes under *in situ* states. *Fuel* 247, 228–236. doi:10.1016/j.fuel.2019.03.037

Estrada, J. M., and Bhamidimarri, R. (2016). A review of the issues and treatment options for wastewater from shale gas extraction by hydraulic fracturing. *Fuel* 182, 292–303. doi:10.1016/j.fuel.2016.05.051

Ge, H. K., Yang, L., Shen, Y. H., Ren, K., Meng, F. B., Li, W. M., et al. (2015). Experimental investigation of shale imbibition capacity and the factors influencing loss of hydraulic fracturing fluids. *Pet. Sci.* 12, 636–650. doi:10.1007/s12182-015-0049-2

Gregory, K. B., Vidic, R. D., and Dzombak, D. A. (2011). Water management challenges associated with the production of shale gas by hydraulic fracturing. *Elements* 7, 181–186. doi:10.2113/gselements.7.3.181

Hazra, B., Varma, A. K., Bandopadhyay, A. K., Mendhe, V. A., Singh, B. D., Saxena, V. K., et al. (2015). Petrographic insights of organic matter conversion of Raniganj basin shales, India. *Int. J. Coal Geol.* 150–151, 193–209. doi:10.1016/j.coal.2015.09.001

He, H. F., Liu, P. C., Xu, L., Hao, S. Y., Qiu, X. Y., Shan, C., et al. (2021). Pore structure representations based on nitrogen adsorption experiments and an FHH fractal model: Case study of the block Z shales in the Ordos Basin, China. *J. Pet. Sci. Eng.* 203, 108661. doi:10.1016/j.petrol.2021.108661

Howarth, R. W., Santoro, R., and Ingraffea, A. (2011). Methane and the greenhouse-gas footprint of natural gas from shale formations. *Clim. Change* 106, 679–690. doi:10.1007/s10584-011-0061-5

Kang, S. M., Fathi, E., Ambrose, R. J., Akkutlu, I. Y., and Sigal, R. F. (2011). Carbon dioxide storage capacity of organic-rich shales. *SPE J.* 16 (04), 842–855. doi:10.2118/134583-pa

Li, J. Q., Wang, S. Y., Lu, S. F., Zhang, P. F., Cai, J. C., Zhao, J. H., et al. (2019). Microdistribution and mobility of water in gas shale: A theoretical and experimental study. *Mar. Pet. Geol.* 102, 496–507. doi:10.1016/j.marpetgeo.2019.01.012

Liu, D. M., Yao, Y. B., and Chang, Y. H. (2022). Measurement of adsorption phase densities with respect to different pressure: Potential application for determination of free and adsorbed methane in coalbed methane reservoir. *Chem. Eng. J.* 446, 137103. doi:10.1016/j.cej.2022.137103

Liu, J., Xie, L. Z., Elsworth, D., and Gan, Q. (2019b). CO_2/CH_4 competitive adsorption in shale: Implications for enhancement in gas production and reduction in carbon emissions. *Environ. Sci. Technol.* 53 (15), 9328–9336. doi:10.1021/acs.est.9b02432

Liu, J., Xie, L. Z., He, B., Gan, Q., and Zhao, P. (2021). Influence of anisotropic and heterogeneous permeability coupled with *in-situ* stress on CO_2 sequestration with simultaneous enhanced gas recovery in shale: Quantitative modeling and case study. *Int. J. Greenh. Gas Control* 104, 103208. doi:10.1016/j.ijggc.2020.103208

Liu, J., Xie, L. Z., Yao, Y. B., Gan, Q., Zhao, P., and Du, L. H. (2019a). Preliminary study of influence factors and estimation model of the enhanced gas recovery stimulated by carbon dioxide utilization in shale. *ACS Sustain. Chem. Eng.* 7, 20114–20125. doi:10.1021/acssuschemeng.9b06005

Liu, J., Yao, Y. B., Liu, D. M., and Elsworth, D. (2017). Experimental evaluation of CO_2 enhanced recovery of adsorbed-gas from shale. *Int. J. Coal Geol.* 179, 211–218. doi:10.1016/j.coal.2017.06.006

Liu, K. Q., Ostadhassan, M., Jiang, H. W., Zakharova, N. V., and Shokouhimehr, M. (2021). Comparison of fractal dimensions from nitrogen adsorption data in shale via different models. *RSC Adv.* 11, 2298–2306. doi:10.1039/d0ra09052b

Liu, P. L., Feng, Y. S., Zhao, L. Q., Li, N. Y., and Luo, Z. F. (2015). Technical status and challenges of shale gas development in Sichuan Basin, China. *Petroleum* 1, 1–7. doi:10.1016/j.petlm.2015.03.001

Liu, Y., Cao, Q., Ye, X., and Dong, L. (2022). Adsorption characteristics and pore structure of organic-rich shale with different moisture contents. *Front. Earth Sci.* 10, 863691. doi:10.3389/feart.2022.863691

Ma, Y. S., Cai, X. Y., and Zhao, P. R. (2018). China's shale gas exploration and development: Understanding and practice. *Petroleum Explor. Dev.* 45, 589–603. doi:10.1016/s1876-3804(18)30065-x

Perera, M. S. A., Ranjith, P. G., Choi, S. K., and Airey, D. (2011). The effects of sub-critical and super-critical carbon dioxide adsorption-induced coal matrix swelling on the permeability of naturally fractured black coal. *Energy* 36, 6442–6450. doi:10.1016/j.energy.2011.09.023

Shi, Q. M., Cui, S. D., Wang, S. M., Mi, Y. C., Sun, Q., Wang, S. Q., et al. (2022). Experiment study on CO_2 adsorption performance of thermal treated coal: Inspiration for CO_2 storage after underground coal thermal treatment. *Energy* 254, 124392. doi:10.1016/j.energy.2022.124392

Sun, H. Y., Sun, W. C., Zhao, H., Sun, Y. G., Zhang, D. R., Qi, X. Q., et al. (2016). Adsorption properties of CH_4 and CO_2 in quartz nanopores studied by molecular simulation. *RSC Adv.* 6, 32770–32778. doi:10.1039/c6ra05083b

Tang, X. L., Jiang, Z. X., Jiang, S., Wang, P. F., and Xiang, C. F. (2016). Effect of organic matter and maturity on pore size distribution and gas storage capacity in high-mature to post-mature shales. *Energy fuels.* 30, 8985–8996. doi:10.1021/acs.energyfuels.6b01499

Vidic, R. D., Brantley, S. L., Vandenbossche, J. M., Yoxtheimer, D., and Abad, J. D. (2013). Impact of shale gas development on regional water quality. *Science* 340, 1235009. doi:10.1126/science.1235009

Wang, Y., Zhu, Y. M., Liu, S. M., and Zhang, R. (2016). Pore characterization and its impact on methane adsorption capacity for organic-rich marine shales. *Fuel* 181, 227–237. doi:10.1016/j.fuel.2016.04.082

Weniger, P., Kalkreuth, W., Busch, A., and Krooss, B. M. (2010). High-pressure methane and carbon dioxide sorption on coal and shale samples from the Paraná Basin, Brazil. *Int. J. Coal Geol.* 84, 190–205. doi:10.1016/j.coal.2010.08.003

Xie, W. D., Wang, M., Vandeginste, V., Chen, S., Yu, Z. H., Wang, J. Y., et al. (2022). Adsorption behavior and mechanism of CO_2 in the Longmaxi shale gas reservoir. *RSC Adv.* 12, 25947–25954. doi:10.1039/d2ra03632k

Yang, S., Li, Y. L., Zhu, Y., and Liu, D. Q. (2018). Effect of fracture on gas migration, leakage and CO_2 enhanced shale gas recovery in Ordos Basin. *Energy Procedia* 154, 139–144. doi:10.1016/j.egypro.2018.11.023

Yao, Y. B., Liu, D. M., Tang, D. Z., Tang, S. H., and Huang, W. H. (2008). Fractal characterization of adsorption-pores of coals from North China: An investigation on CH_4 adsorption capacity of coals. *Int. J. Coal Geol.* 7, 27–42. doi:10.1016/j.coal.2007.07.003

Yao, Y. B., Liu, J., Liu, D. M., Chen, J. Y., and Pan, Z. J. (2019). A new application of NMR in characterization of multiphase methane and adsorption capacity of shale. *Int. J. Coal Geol.* 201, 76–85. doi:10.1016/j.coal.2018.11.018

Yao, Y. B., Sun, X. X., Zheng, S. J., Wu, H., Zhang, C., Liu, Y., et al. (2021). Methods for petrological and petrophysical characterization of gas shales. *Energy fuels.* 35, 11061–11088. doi:10.1021/acs.energyfuels.1c01475

Zheng, S. J., Yao, Y. B., Elsworth, D., Liu, D. M., and Cai, Y. D. (2020). Dynamic fluid interactions during CO_2-ECBM and CO_2 sequestration in coal seams. Part 2: CO_2-H_2O wettability. *Fuel* 279, 118560. doi:10.1016/j.fuel.2020.118560

Zheng, S. J., Yao, Y. B., Liu, D. M., Cai, Y. D., and Liu, Y. (2018). Characterizations of full-scale pore size distribution, porosity and permeability of coals: A novel methodology by nuclear magnetic resonance and fractal analysis theory. *Int. J. Coal Geol.* 196, 148–158. doi:10.1016/j.coal.2018.07.008

Zheng, S. J., Yao, Y. B., Liu, D. M., Cai, Y. D., Liu, Y., and Li, X. W. (2019). Nuclear magnetic resonance T_2 cutoffs of coals: A novel method by multifractal analysis theory. *Fuel* 241, 715–724. doi:10.1016/j.fuel.2018.12.044

Zheng, S. J., Yao, Y. B., Sang, S. X., Liu, D. M., Wang, M., and Liu, S. Q. (2022). Dynamic characterization of multiphase methane during CO_2-ECBM: An NMR relaxation method. *Fuel* 324, 124526. doi:10.1016/j.fuel.2022.124526

Zhou, Y., You, L. J., Kang, Y. L., Jia, C. G., and Xiao, B. (2022). Influencing factors and application of spontaneous imbibition of fracturing fluids in lacustrine and marine shale gas reservoir. *Energy fuels.* 36, 3606–3618. doi:10.1021/acs.energyfuels.2c00153

Zou, J., Rezaee, Z., Xie, Q., You, L. J., Liu, K. Q., and Saeedi, A. (2018). Investigation of moisture effect on methane adsorption capacity of shale samples. *Fuel* 15, 323–332. doi:10.1016/j.fuel.2018.05.167

frontiers | Frontiers in Earth Science

TYPE Original Research
PUBLISHED 27 January 2023
DOI 10.3389/feart.2023.1122109

OPEN ACCESS

EDITED BY
Zhenzhi Wang,
Henan Polytechnic University, China

REVIEWED BY
Decheng Zhang,
Hebei University of Technology, China
Qiang Chen,
Chongqing University, China
Jun Liu,
Sichuan University, China

*CORRESPONDENCE
Run Chen,
chenrun@cumt.edu.cn

SPECIALTY SECTION
This article was submitted to Economic Geology, a section of the journal Frontiers in Earth Science

RECEIVED 12 December 2022
ACCEPTED 13 January 2023
PUBLISHED 27 January 2023

CITATION
Chen R, Hu K, Lv F and Zhang Y (2023), Effect of supercritical CO_2 extraction on pore characteristics of coal and its mechanism.
Front. Earth Sci. 11:1122109.
doi: 10.3389/feart.2023.1122109

Effect of supercritical CO_2 extraction on pore characteristics of coal and its mechanism

Run Chen[1,2]*, Kunpeng Hu[1,2], Fengrong Lv[1,2] and Yajun Zhang[1,2]

[1]Jiangsu Key Laboratory of Coal-based Greenhouse Gas Control and Utilization (Carbon Neutrality Institute), China University of Mining and Technology, Xuzhou, China, [2]School of Resources and Geosciences, China University of Mining and Technology, Xuzhou, China

Abundant pore space in coal is not only the place for the accumulation of coalbed methane (CBM), but also the tunnel for gas migration. In this study, five sets of coal samples before and after the second coalification were selected from the eastern margin of Ordos Basin to simulate supercritical CO_2 (Sc-CO_2) extraction in supercritical extraction equipment. The evolutions of pore structure and porosity were tested by mercury intrusion porosimetry and nuclear magnetic resonance spectroscopy to compare the changes of pore structure and porosity due to the Sc-CO_2 extraction, and to explain the related mechanism. The results show that: (1) Pore volume, pore specific surface area, and connectivity characteristics changed significantly due to Sc-CO_2 extraction, and the increment of pore volume and pore specific surface area presented a law of increase–decrease–increase with the increase in the coal rank, and the turning point was near the second coalification. (2) The porosity increment change trend due to Sc-CO_2 extraction was increase–decrease–increase with increasing coal rank, and the turning point was again near the second coalification, which supports the mercury intrusion porosimetry results. (3) The changes were observed in the porosity characteristics due to Sc-CO_2 extraction through pore-increasing and expanding effects. Before the second coalification, the pore-increasing and expanding effects co-existed in the micropores, and after the second coalification, the pore-expanding effect mainly existed in the transitional pores and above. (4) The variation model for the pore structure of coal due to Sc-CO_2 extraction was established. The conclusions offer not only important theoretical significance for the CO_2-enhanced CBM (CO_2-ECBM) mechanism but also important significance for CO_2-ECBM engineering.

KEYWORDS

SC-CO2 extraction, pore structure, porosity, mechanism, coal rank

1 Introduction

Coal is a heterogeneous porous medium, in which the structure is characterized as a dual pore system that includes original porosity and secondary porosity (Wang et al., 2018). The original porosity includes microspores, transitional pores, and mesopores in the coal matrix, the gas adsorbs/desorbs on/from the coal matrix, and undergoes diffusion. The secondary porosity is composed of non-uniformly distributed macropores and microfractures, and gas diffuses and seeps in it (Fu et al., 2005; Chen et al., 2021; Liu et al., 2022; Xu and Qin, 2022).

In recent decades, extensive research efforts have been devoted to the study of the pore structure of coal for systematic exploration of the causes and influencing factors of pore structure. The pores were found to be formed during the process of coalification (Wang and Chen, 1995; Zhang, 2001; Wu et al., 2016). Tang et al. (2008) found that the porosity, pore structure, and specific surface area of coal were controlled by the degree of coal metamorphism

based on the results of mercury intrusion porosimetry and nitrogen adsorption test. Liu Y. W. et al. (2020) found that the Brunauer–Emmett–Teller (BET) specific surface area of coal increased and then decreased with the increase of coal rank, the micropores decreased and then increased, and the small pores and mesopores increased, and then decreased as indicated by low-temperature nitrogen adsorption test. Yang et al. (2021) found that the proportion of micropores and small pores gradually increased and that of mesopores and macropores gradually decreased with the increase of coal rank by low-field nuclear magnetic resonance (NMR) spectroscopy test. Zhao et al. (2010) found that the coal porosity, micropore volume, and BET surface area of coal showed high–low–high variation pattern with the increase of coal rank through vitrinite reflectance test, mercury intrusion porosimetry, and low-temperature nitrogen adsorption test. Liu H. F. et al. (2020) studied the surface pore morphology of coal by scanning electron microscopy (SEM) and found that the surface porosity of coal samples increased with the increase in the degree of coalification. Zhu et al. (2019) studied the pore characteristics of coal by NMR spectroscopy and found that the total porosity first decreased and then increased with the increase of coal rank. Moreover, it has been found that the pore structure of coal is affected by many geological factors and their coupling, such as mineral content, maceral composition, coal structure type, and tectonic stress (Lv et al., 1991; Fu et al., 2007; Du et al., 2018).

Notably, some techniques and approaches are available to change the pore structure of coal. For example, injecting CO_2 into coal reservoirs can dissolve carbon rock salt minerals present in coal, destroy the macromolecular structure, and extract functional groups, which leads to an increase in the specific surface area, total pore volume, and porosity of coal (Guo et al., 2018; Zhang et al., 2019; Zhang et al., 2020; Wang et al., 2021). Moreover, Yuan et al. (2022) found that the pore structure of coal samples changed after the freeze-thaw cycle, and the number of large pores and medium pores increased. Di et al. (2022) found that microbial participation in coal reservoir degradation could stabilize pore size, make pores smoother, reduce specific surface area, and increase pore volume. Si et al. (2021) observed that the intrusion of water reduced the type and content of minerals in coal, resulting in an increase in pore volume.

The above-mentioned studies indicate that the characteristics of the pore structure of coal and its influencing factors have been extensively explored. However, supercritical (Sc)-CO_2 that offers a better ability to transform the pore structure of coal, resulting in significant changes in pore structure, has not been extensively investigated to date. Notably, Sc-CO_2 can extract small organic molecules from the coal matrix, change the pore structure characteristics of coal, and affect the recovery and storage effect of CO_2-enhanced coal bed recovery (CO_2-ECBM) (Wang, 2018; Zhang, 2019; Sampath et al., 2020; Wang et al., 2022). In this study, five sets of coal samples before and after the second coalification ($R_{o,max}$ = 1.3%) were selected from the eastern margin of Ordos Basin to simulate the process of Sc-CO_2 extraction of small organic molecules from coal under geological conditions. The mercury intrusion porosimetry and NMR spectroscopy were used to analyze the transformation of coal pore structure and porosity by Sc-CO_2 extraction, and the evolving relationship with coal rank was discussed. The mechanism was revealed and the geological model was constructed, in order to provide a basis for theoretical research and engineering implementation of replacement CBM extraction and CO_2-ECBM.

2 Experimental

2.1 Collection of coal samples

The Ordos basin is a large stable craton basin, which is rich in fossil energy. The geological structure of the basin is relatively simple. It is distributed in a north-south direction, showing the structural characteristics of north-south zonation and east-west zonation, and has experienced the evolution of a multi-stage tectonic cycle (Zhang, 2019).

The main coal-bearing strata are the Upper Carboniferous-Lower Permian Taiyuan Formation and Lower Permian Shanxi Formation. The formations of Benxi, Taiyuan, Shanxi, Lower Shihezi, Upper Shihezi, and Shiqianfeng are the main coal-bearing formations, which consist principally of coal, limestone, siltstone, and sandstone (Chen et al., 2017). Hedong coalfield is one of the six major coalfields in Shanxi Province and is a typical Carboniferous-Permian coalfield. There are 6–15 layers of coal, among which 6 to 8 layers can be mined, with an average thickness of 7–28 m. The coal rank gradually increases from north to south.

In order to investigate the influence of coal rank on Sc-CO_2 extraction and avoid the influence of geological structure, five undeformed coal samples distributed around the second coalification were collected from the Hedong Coalfield of the eastern edge of the Ordos Basin (Figure 1). The physical properties of the coals investigated in this study are listed in Table 1. The maximum vitrinite reflectance under oil immersion ($R_{o,max}$) of the coals varies from 0.76% to 2.01%. The proximate analysis result shows that the equilibrated moisture varies from 0.18% to 1.54%, the ash yield varies from 6.70% to 21.07%, and the volatile matter varies from 14.29% to 29.49% for the five coal samples. The ultimate analysis result shows that the carbon content varies from 82.50% to 89.36%, the hydrogen content varies from 4.21% to 4.81%, and the oxygen content varies from 1.74% to 10.96% for the five coal samples.

To avoid oxidation during the transportation of specimens and also during the time required to carry out Sc-CO_2 extraction, the coal samples were stored *via* vacuum packaging and sealed in plastic bags. A cylinder with dimensions of 25 mm × 25 mm was prepared in the laboratory for the NMR test and the square coal block with a side length of 1.5 cm was used for the mercury intrusion porosimetry. The prepared coal samples were divided into two parts, one for Sc-CO_2 extraction experiments and the other for comparative analysis. In order to reduce the mineralization reaction between CO_2 in the water environment and minerals in the coal matrix, the necessary drying treatment of the coal pillar was carried out before the experiment.

2.2 Experimental methods

2.2.1 Sc-CO_2 extraction experiment

A high-temperature and pressure reaction kettle (TC-2, Jiangsu Tuochuang Scientific Instrument Limited Liability Company, Nantong, China) was used as the experimental equipment. The experimental temperature was adjusted to ~45°C, the pressure was adjusted to ~10 MPa, and the extraction time was 96 h. The flow chart

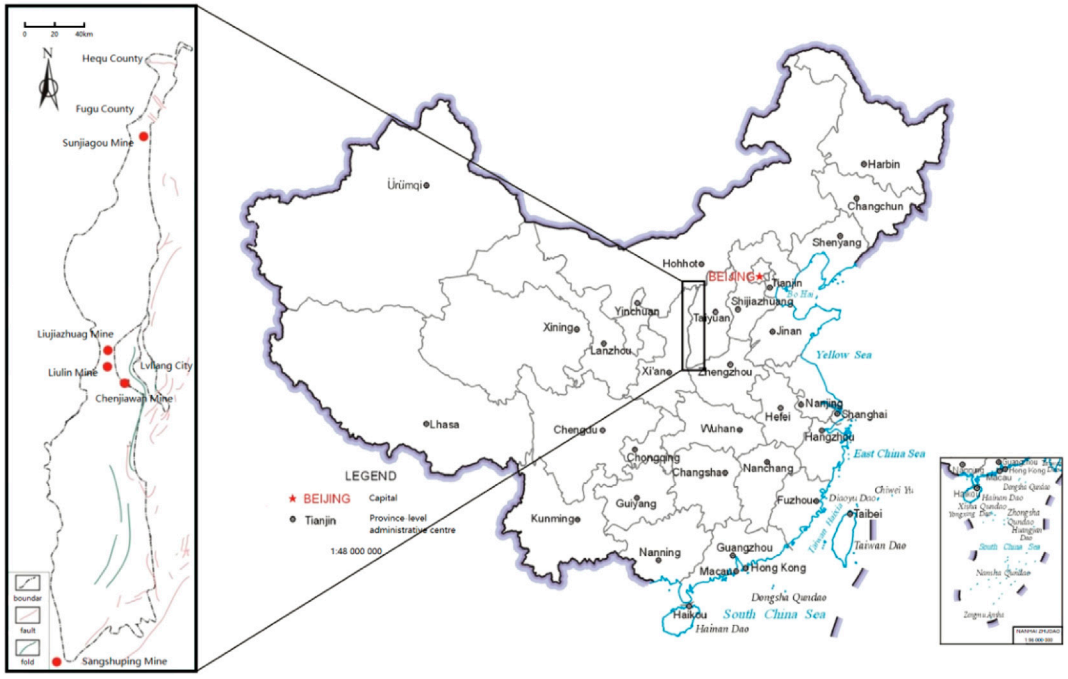

FIGURE 1
Location of coal samples collected.

TABLE 1 The results of $R_{o,max}$ proximate analysis and ultimate analysis.

Sample	$R_{o,max}$	Proximate analysis (%)				Ultimate analysis (%)				
		M_{ad}	A_d	V_{daf}	FC_d	$S_{t,d}$	C_{daf}	H_{daf}	O_{daf}	N_{daf}
SJG coal	0.76	1.54	11.05	29.49	62.72	0.63	82.50	4.41	10.96	1.43
LJZ coal	1.00	0.94	17.56	26.85	60.31	0.38	85.42	4.81	7.86	1.44
LL coal	1.20	0.77	21.07	19.88	63.24	0.52	86.53	4.21	7.32	1.28
CJW coal	1.56	0.45	6.70	18.94	75.63	1.07	89.36	4.46	3.48	1.55
SSP coal	2.01	0.18	9.60	14.29	77.48	5.79	86.66	4.23	1.74	0.96

of Sc-CO_2 extraction is shown in Figure 2. The operating steps are as follows.

1) The extraction cell was opened and the coal pillar was placed in the supercritical extraction cell, which was then covered with a cauldron and the screws were tightened to ensure a good seal.
2) The CO_2 gas cylinder valve was opened to allow the CO_2 gas to flow through the purifier and the cooling system, after which it was eventually compressed into the extraction cell. After the pressure and temperature of the cell were adjusted to ~10 MPa and 45°C, respectively, the CO_2 gas cylinder valve was closed to ensure that the extraction cell remained under the designed condition. The temperature and pressure were monitored throughout the process.
3) After 96 h of Sc-CO_2 extraction, the supercritical equipment was shut down, the gas was released to bring the pressure of the extraction cell to the atmospheric pressure, and the coal sample was collected after the extraction cell was cooled down to room temperature, the separation cells were washed with a solvent, and the waste liquid was collected for testing.

2.2.2 Mercury intrusion porosimetry

In this study, pore size distribution, surface area, and pore connectivity were investigated by mercury intrusion porosimetry (AutoPore IV9500, Micromeritics Instrument Crop, Norss, GA, United States). Mercury intrusion porosimetry is based on the capillary flow governing liquid penetration in small pores. This law, in the case of a non-wetting liquid such as mercury, is expressed by using the Washburn equation (Washburn, 1921):

$$D = \left(\frac{1}{P}\right)4\gamma \cos\varphi \quad (1)$$

where D is the diameter of the pore, P is the applied pressure, γ is the surface tension of mercury, and φ is the contact angle between the mercury and the sample, all in consistent units. In this study, the

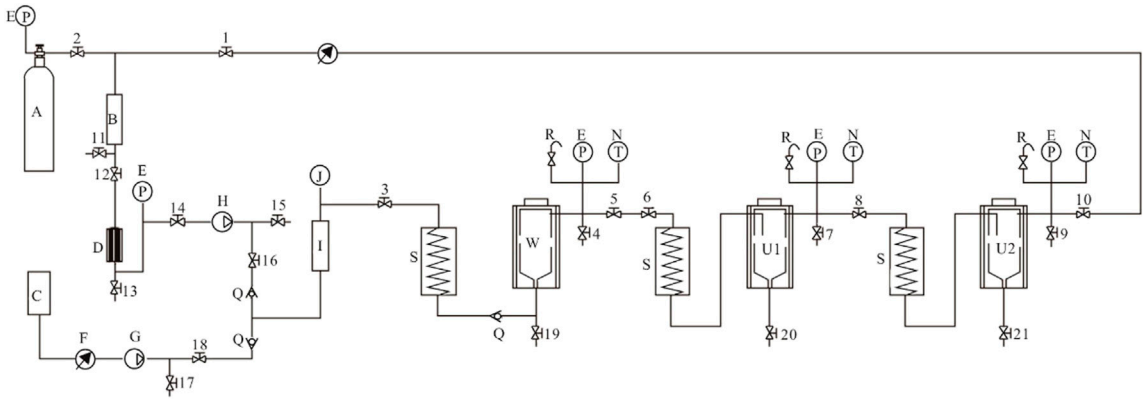

FIGURE 2
The flow chart of SC-CO_2 extraction experiment. **(A)** CO_2 cylinder; **(B)** Purifier; **(C)** Carry dose bucket; **(D)** Cold condenser; **(E)** Pressure gauge; **(F)** Carrier flowmeter; **(G)** Carrier pump; **(H)** High pressure CO_2 pump; **(I)** Mixer; **(J)** Electric contact pressure gauge; **(N)** Thermometer; **(P)** CO_2 flowmeter; **(Q)** Check valve; **(R)** Safety valve; **(S)** Pre-heater; U1: Separation kettle; **(W)** Extraction kettle; 1–5, 7–21: Stop valve; 6: Regulating valve.

TABLE 2 Pore volumes of the samples before and after the Sc-CO_2 extraction.

Coal sample		Volume ($cm^3 \cdot g^{-1}$)					Proportion (%)			
		V_{mi}	V_{tr}	V_{me}	V_{ma}	V_t	V_{mi}/V_t	V_{tr}/V_t	V_{mei}/V_t	V_{ma}/V_t
SJG	Raw coal	0.0115	0.0211	0.0026	0.0041	0.0395	29.26	53.58	6.69	10.47
	Sc-CO_2 extracted coal	0.0145	0.0173	0.0030	0.0054	0.0401	36.09	43.11	7.40	13.40
LJZ	Raw coal	0.0042	0.0055	0.0009	0.0025	0.0132	32.16	41.86	6.78	19.20
	Sc-CO_2 extracted coal	0.0053	0.0070	0.0024	0.0065	0.0211	24.90	33.00	11.14	30.96
LL	Raw coal	0.0028	0.0032	0.0010	0.0025	0.0096	29.47	33.24	10.79	26.50
	Sc-CO_2 extracted coal	0.0038	0.0048	0.0010	0.0018	0.0114	32.96	42.23	8.86	15.95
CJW	Raw coal	0.0060	0.0075	0.0016	0.0064	0.0216	27.85	34.91	7.57	29.66
	Sc-CO_2 extracted coal	0.0066	0.0083	0.0036	0.0087	0.0273	24.17	30.53	13.25	32.05
SSP	Raw coal	0.0064	0.0079	0.0021	0.0070	0.0234	27.16	33.80	9.03	30.01
	Sc-CO_2 extracted coal	0.0069	0.0089	0.0021	0.0123	0.0303	22.87	29.29	7.03	40.82

V_{mi}: Micropore volume; V_{tr}: Transitional pore volume; V_{me}: Mesopore volume; V_{ma}: Macropore volume; V_t: Total pore volume.

surface tension was 485 $dyn \cdot cm^{-1}$, the contact angle between the mercury and coal sample was 130°, and the density of mercury was 13.5335 $g \cdot mL^{-1}$.

2.2.3 Nuclear magnetic resonance test

In this study, porosity was investigated using a cabinet NMR low-temperature porosity analyzer (NMRC12-010V, Suzhou Niumag analytical instrument Limited Liability Company, Suzhou, China). Notably, the NMR signal is proportional to the water content of the sample for the same test parameters (Zheng et al., 2018). The pores of the sample were filled with water, and a set of standard samples with known water content was first tested to fit with a curve of water content and NMR signal volume. Then, the measured NMR signal volume of the sample was substituted into the curve equation to find the water content in the sample. Pore volume was calculated according to moisture content and porosity was derived by combining sample volume (Liu et al., 2019; Zheng et al., 2019; Xiong et al., 2022; Zhao et al., 2022).

The NMR experiments were performed using 25 mm coils, the experimental temperature was 32°C, and the resonance frequency was 12 MHz. Besides, in the NMR test, the sample signal was collected according to the Carr–Purcell–Meiboom–Gill (CPMG) sequence, echo spacing (T_E) was 0.35 m, waiting time (T_W) was 6000 m, echo number (NECH) was 4096, and scan time (N_S) was doubled.

3 Results and discussion

In this study, the Чодот В. В. (Чодот, 1966). decimal classification method was used to classify the pore structure types in coal. That is micropore (<10 nm), transitional pore (10–100 nm), mesopore (100–1000 nm), and macropore (>1000 nm).

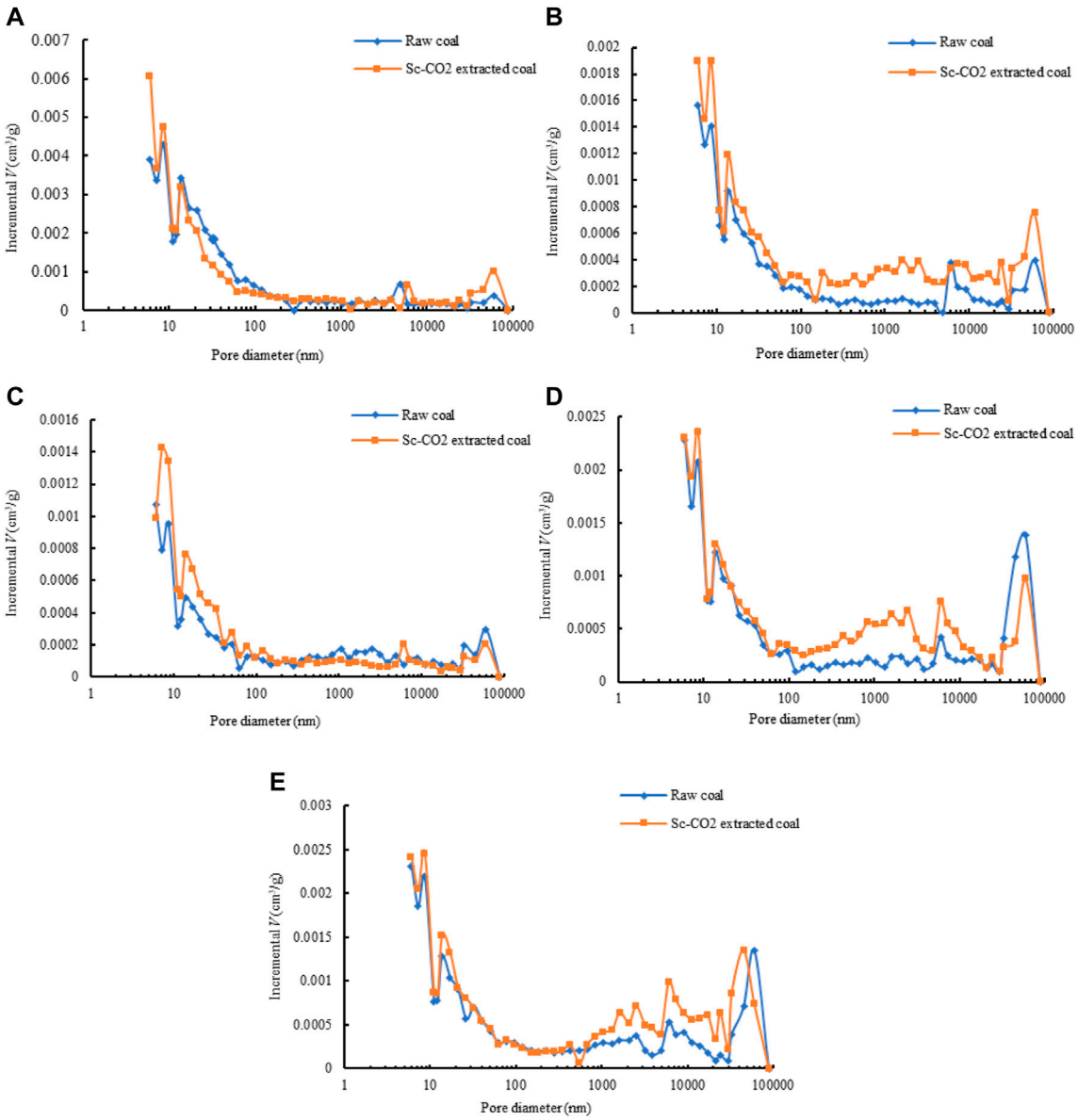

FIGURE 3
Pore volume distribution of the coal samples before and after Sc-CO_2 extraction **(A)** SJG coal; **(B)** LJZ coal; **(C)** LL coal; **(D)** CJW coal; and **(E)** SSP coal.

3.1 Pore structure change and its evolution

3.1.1 Pore volume change and its evolution

Table 2 presents the mercury injection pore volume test results of coal samples before and after Sc-CO_2 extraction, and the pore volume distributions of raw and Sc-CO_2 extracted coal are shown in Figure 3. The total pore volume of coal samples increased to different degrees after Sc-CO_2 extraction, and it was most significant for LJZ coal and SSP coal (Table 2). The pore volume of micropores and macropores increased more obviously after the Sc-CO_2 extraction of coal samples, and the increase of transitional pores and mesopores was smaller (Figure 3). After Sc-CO_2 extraction, the proportion of micropore and transitional pore volume decreased and that of the mesopore and macropore volume increased (Table 2).

In summary, the changes in pore volume and proportion of coal samples indicate that Sc-CO_2 extraction can increase the pore volume of coal, which is achieved by the increase in the number of pores and expansion of the pore diameter.

To determine the changes in pore volumes due to Sc-CO_2 extraction, ΔV can be defined by using the following equation:

$$\Delta V = V_B - V_A \tag{2}$$

where ΔV is the pore volume change due to Sc-CO_2 extraction, $cm^3 \cdot g^{-1}$; V_B is the pore volume of the sample after the Sc-CO_2 extraction, $cm^3 \cdot g^{-1}$; and V_A is the pore volume of the sample before the Sc-CO_2 extraction, $cm^3 \cdot g^{-1}$.

Figure 4 shows that the ΔV_{mi} and ΔV_{me} of coal are positive, and most of ΔV_{tr} and ΔV_{ma} are positive, indicating that Sc-CO_2 extraction causes the incremental pore volume to increase, and the incremental macropore volume makes up most of the total

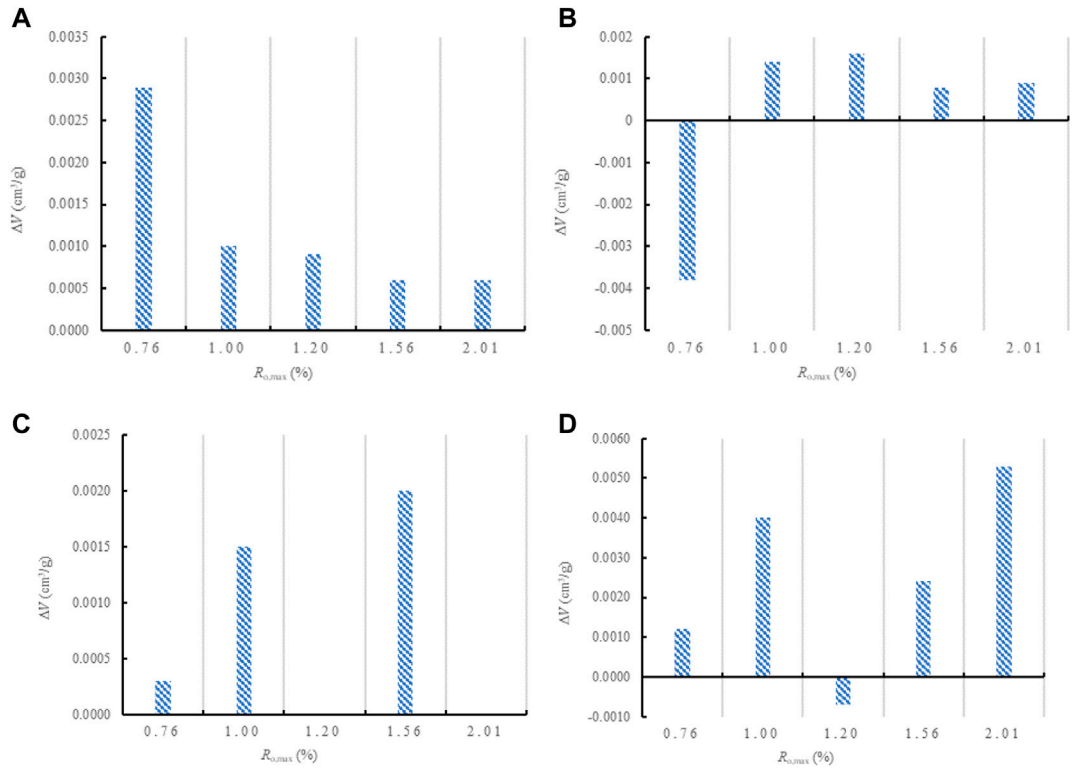

FIGURE 4
The changes in incremental pore volume of coal samples due to Sc-CO_2 extraction **(A)** Micropore; **(B)** Transitional pore; **(C)** Mesopore; and **(D)** Macropore.

TABLE 3 Pore-specific surface area of the samples before and after the Sc-CO_2 extraction.

Coal sample		Pore specific surface area ($m_2 \cdot g^{-1}$)					Proportion (%)			
		S_{mi}	S_{tr}	S_{me}	S_{ma}	S_t	S_{mi}/S_t	S_{tr}/S_t	S_{me}/S_t	S_{ma}/S_t
SJG	Raw coal	5.7888	3.8959	0.0432	0.0037	9.7316	59.49	40.03	0.44	0.04
	Sc-CO_2 extracted coal	6.2344	3.5285	0.0434	0.0032	9.8096	63.55	35.97	0.44	0.03
LJZ	Raw coal	2.1526	1.0716	0.0133	0.0017	3.2393	66.45	33.08	0.41	0.05
	Sc-CO_2 extracted coal	2.6499	1.3157	0.0297	0.0056	4.0008	66.23	32.88	0.74	0.14
LL	Raw coal	1.4347	0.6070	0.0129	0.0024	2.0570	69.75	29.51	0.63	0.12
	Sc-CO_2 extracted coal	1.8576	0.9348	0.0150	0.0015	2.8090	66.13	33.28	0.53	0.05
CJW	Raw coal	3.0500	1.4270	0.0200	0.0037	4.5007	67.77	31.71	0.44	0.08
	Sc-CO_2 extracted coal	3.3230	1.5519	0.0432	0.0089	4.9270	67.45	31.50	0.88	0.18
SSP	Raw coal	3.2190	1.4797	0.0286	0.0052	4.7325	68.02	31.27	0.60	0.11
	Sc-CO_2 extracted coal	3.4879	1.6981	0.0274	0.0097	5.2232	66.78	32.51	0.53	0.19

S_{mi}: Micropore specific surface area; S_{tr}: Transitional pore specific surface area; S_{me}: Mesopore specific surface area; S_{ma}: Macropore specific surface area; S_t: Total specific surface area.

pore volume. The relationship between incremental pore volume and coal rank was analyzed, and it was found that Sc-CO_2 extraction caused incremental pore volume to show an increasing–decreasing–increasing pattern with the increase of coal rank. The turning point is near the second coalification. Before the turning point, the incremental pore volume increases and then decreases with coal rank. After the turning point, the incremental pore volume increases gradually with coal rank. It is most significant in macropores.

3.1.2 Pore-specific surface area change and its evolution

Table 3 presents the mercury injection test results of the specific surface area of pores of coal samples before and after Sc-CO_2

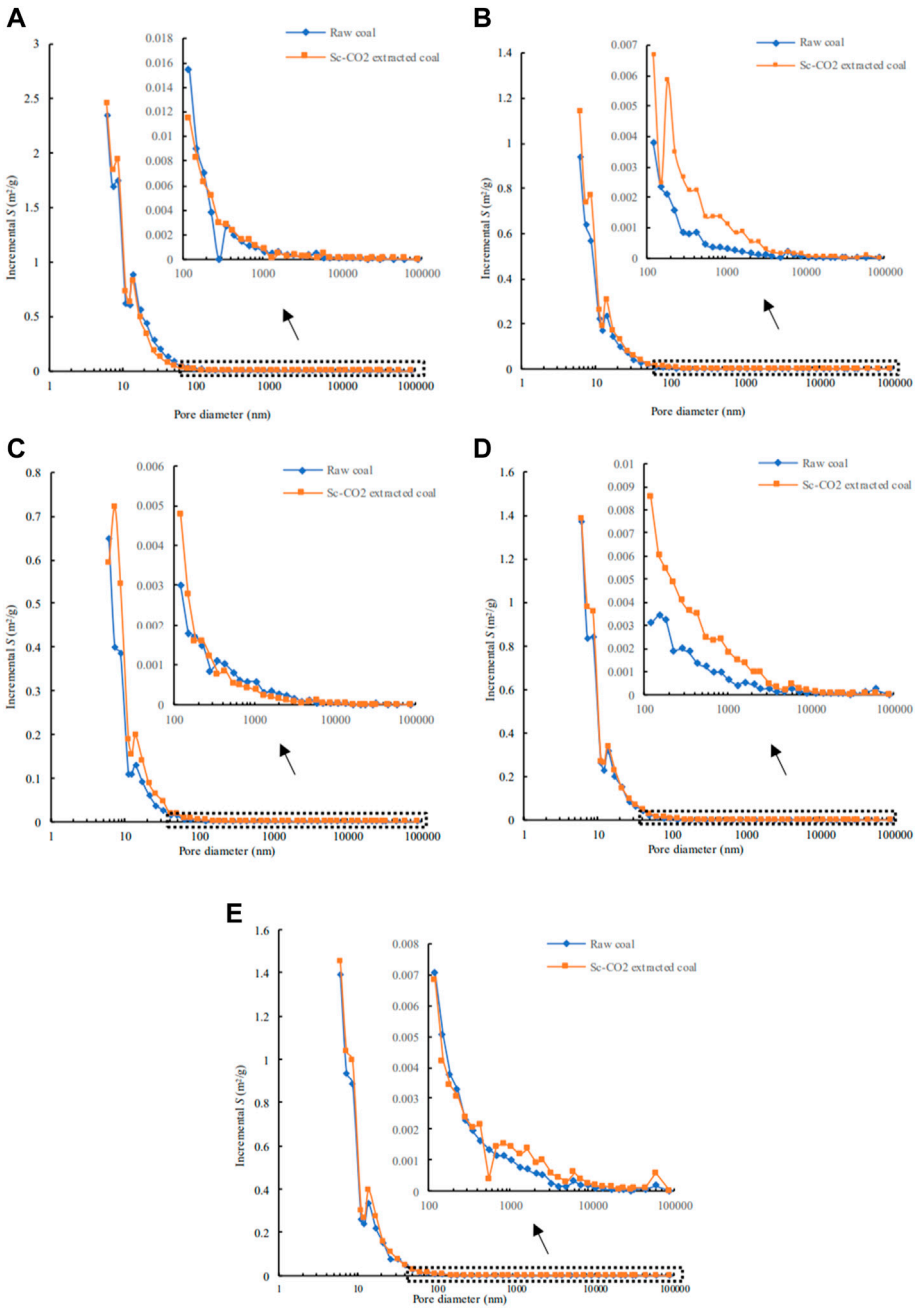

FIGURE 5
Pore-specific surface area distribution of the coal samples before and after Sc-CO_2 extraction **(A)** SJG coal; **(B)** LJZ coal; **(C)** LL coal; **(D)** CJW coal; and **(E)** SSP coal.

extraction, and the pore-specific surface area distributions of raw and Sc-CO_2 extracted coal are shown in Figure 5. The total specific surface area of pores of coal samples increased to different degrees after Sc-CO_2 extraction, and it was the most significant for LJZ coal and LL coal (Table 3). The specific surface area of micropores and transitional pores increased more obviously after the Sc-CO_2 extraction of coal samples, and the increase of mesopores and macropores was smaller (Figure 5). After Sc-CO_2 extraction, the proportion of micropores and transitional pore-specific surface area decreased, and a tendency was observed for the increase in the pore-specific surface area of mesopores and macropores (Table 3).

To determine the changes in pore-specific surface area due to Sc-CO_2 extraction, ΔS can be defined by using the following equation:

$$\Delta S = S_B - S_A \tag{3}$$

where ΔS is the pore-specific surface area change due to Sc-CO_2 extraction, $m_2 \cdot g^{-1}$; S_B is the pore-specific surface area of the coal sample after the Sc-CO_2 extraction, $m_2 \cdot g^{-1}$; and S_A is the pore-specific surface area of the coal sample before the Sc-CO_2 extraction, $m^2 \cdot g^{-1}$.

Figure 6 shows that the ΔS_{mi} values of coal are positive, and most of ΔS_{tr}, ΔS_{me}, and ΔS_{ma} are positive, indicating that the Sc-CO_2

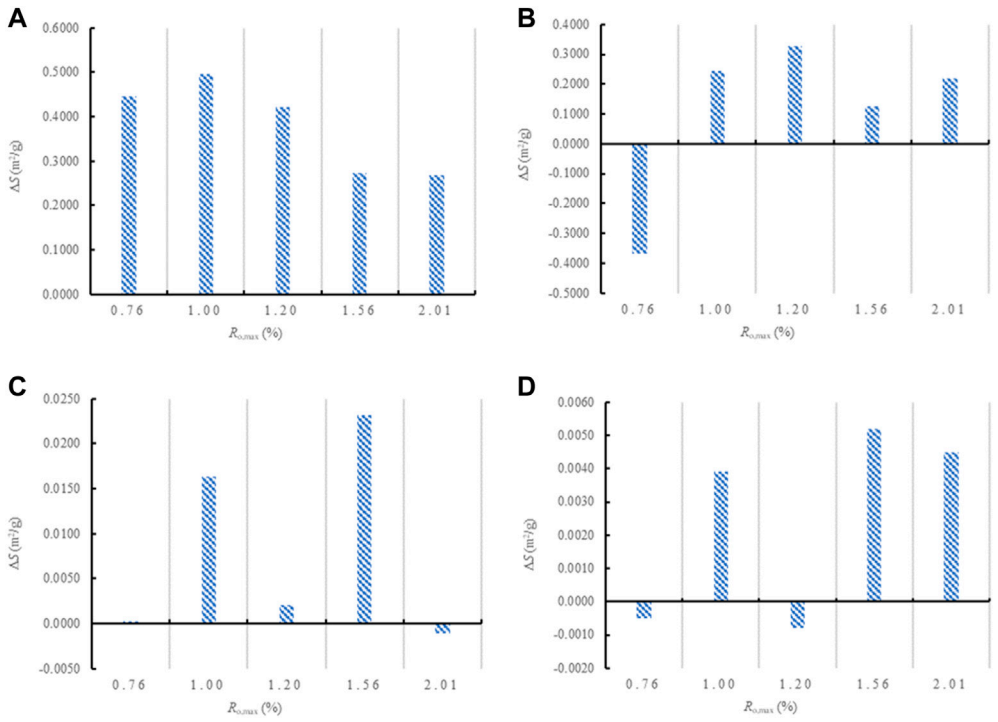

FIGURE 6
The changes of incremental pore-specific surface area of coal due to Sc-CO_2 extraction **(A)** Micropore; **(B)** Transitional pore; **(C)** Mesopore; and **(D)** Macropore.

extraction causes the incremental pore-specific surface area to increase and that the incremental micropore-specific surface area is the main contributor to the total pore-specific surface area. The relationship between incremental pore-specific surface area and coal rank was analyzed, and the results indicate that Sc-CO_2 extraction caused incremental pore-specific surface area to show an increasing–decreasing–increasing pattern with the increase of coal rank. The turning point was near the second coalification. Before the turning point, the incremental pore-specific surface area increased and then decreased with coal rank. After the turning point, the incremental pore-specific surface area increased gradually with coal rank. It is the most significant in transitional pores.

In summary, Sc-CO_2 extraction can not only increase the number of pores but also expand the pore volume. The analysis indicates that the main reason for this change is the precipitation of small organic molecules out of the coal by Sc-CO_2 extraction (Chen et al., 2017; Liu et al., 2018), which increases the number of open pores and also opens partially closed pores, acting as a pore increasing/expanding effect. Moreover, the evolution of pore volume and specific surface area increment with coal rank indicates that the pore volume and specific surface area of coal samples before and after Sc-CO_2 extraction change significantly near the second coalification. It indicates that the changes in pore structure during Sc-CO_2 extraction are controlled by coalification.

3.1.3 Pore morphology and its connectivity

Based on the experimental measurement data of mercury injection porosimetry, the mercury injection and ejection curves of coal samples were obtained (Figure 7). The volume of mercury withdrawn from the pores is less than the volume of mercury entering the pores at the same pressure; therefore, the mercury entering the coal pores cannot be completely discharged, which forms a hysteresis (Wu et al., 1991; Li and Zhou, 2021; Qi et al., 2022).

Figure 7 demonstrates that the maximum mercury injection of SJG coal slightly increased after Sc-CO_2 extraction, and the maximum mercury injection of LJZ, LL, CJW, and SSP coals significantly increased. The difference in the volume of mercury injection and ejection from coal samples before and after Sc-CO_2 extraction reveals that: (1) when small organic molecules present in open pores or pore throats are extracted and dissolved, the pores in coal get enlarged and pore throats are opened, resulting in the migration of mercury in the coal. (2) When small organic molecules present in closed pores or ink bottle pores in coal are partially precipitated after Sc-CO_2 extraction, some pores can be opened or converted into new ink bottle-shaped pores. With the conversion of the sealed pores into new ink bottle-shaped pores, mercury trapped in coal increases.

Sc-CO_2 extraction dissolves small organic molecules present in coal, making the closed and semi-closed pores in coal transit to open pores, and some micron-sized pores are opened, which plays a role in increasing coal pores and improving porosity.

3.2 Porosity change and its evolution

The results of the transverse relaxation time T_2 spectrum of the coal samples before and after Sc-CO_2 extraction are shown in Figure 8. The amplitude and area of the T_2 spectrum of coal samples increased gradually after Sc-CO_2 extraction, indicating that Sc-CO_2 extraction

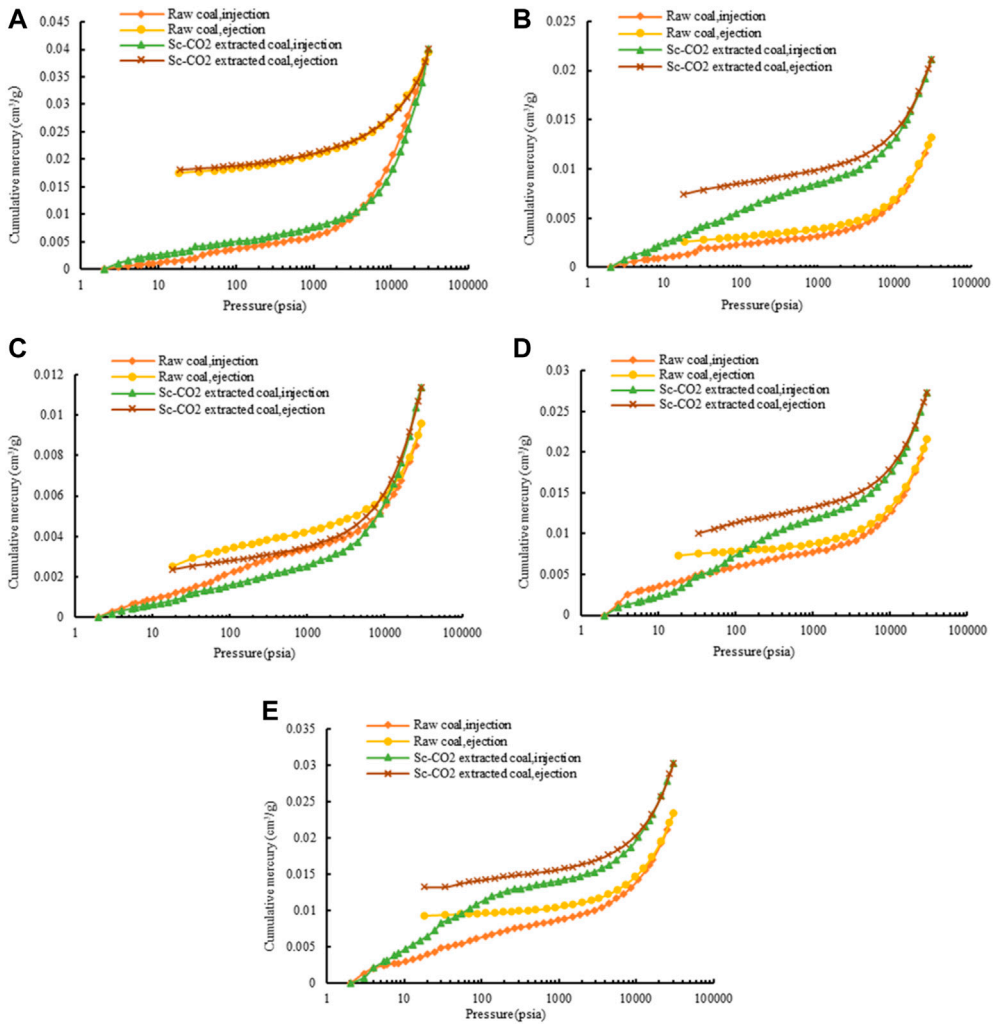

FIGURE 7
Mercury injection and ejection of coal samples **(A)** SJG coal; **(B)** LJZ coal **(C)** LL coal; **(D)** CJW coal; and **(E)** SSP coal.

could transform the pore structure of coal and promote the development of pores.

Based on the NMR spectroscopy principle, the T_2 peaks corresponding to each pore segment were identified by the NMR test results. The T_2 peaks corresponding to microporous and transitional pores are located in the range of 0.1–0.15 m, those corresponding to mesopores are present in the range of 5–55 m, and the T_2 peaks corresponding to large pores are located in the segment greater than 80 m.

The porosity of the coal sample can be obtained by using the T_2 spectrum of coal samples obtained under saturated water conditions. The specific implementation methods are as follows: (1) Measurement of the porosity of a certain volume of known samples, and establishment of a relationship equation between the NMR unit volume signal and porosity, as shown in Figure 9; (2) The test coal samples are measured by NMR spectroscopy, and the NMR unit signal of coal samples under saturated water and bound water conditions is substituted into the relationship equation with porosity (see equation in Figure 9) for calculation.

Table 4 lists the porosity test results of the coal sample before and after Sc-CO_2. The total porosity of coal samples increased to different degrees after Sc-CO_2 extraction, and it was the most significant for SSP coal. The porosity of micropore and macropore increased significantly, and that of transitional pore and mesopore increased or decreased. After Sc-CO_2 extraction, the proportion of micropore and transitional pore porosity decreased, while the proportion of mesopore and macropore porosity increased.

To determine the changes in porosity due to Sc-CO_2 extraction, ΔP can be defined by using the following equation:

$$\Delta P = P_B - P_A \tag{4}$$

where ΔP is the porosity change due to Sc-CO_2 extraction, %; P_B is the porosity of the coal sample after the Sc-CO_2 extraction, %; and P_A is the porosity of the coal sample before the Sc-CO_2 extraction, %.

Figure 10 exhibits that the ΔP_{ma} values of coal are positive, and most of ΔP_{mi}, ΔP_{tr}, and ΔP_{me} are positive, indicating that the Sc-CO_2 extraction leads to an increase in incremental porosity, and incremental macropore porosity is the main contributor to total porosity. The relationship between incremental porosity and coal rank was analyzed, and it was found that Sc-CO_2 extraction caused

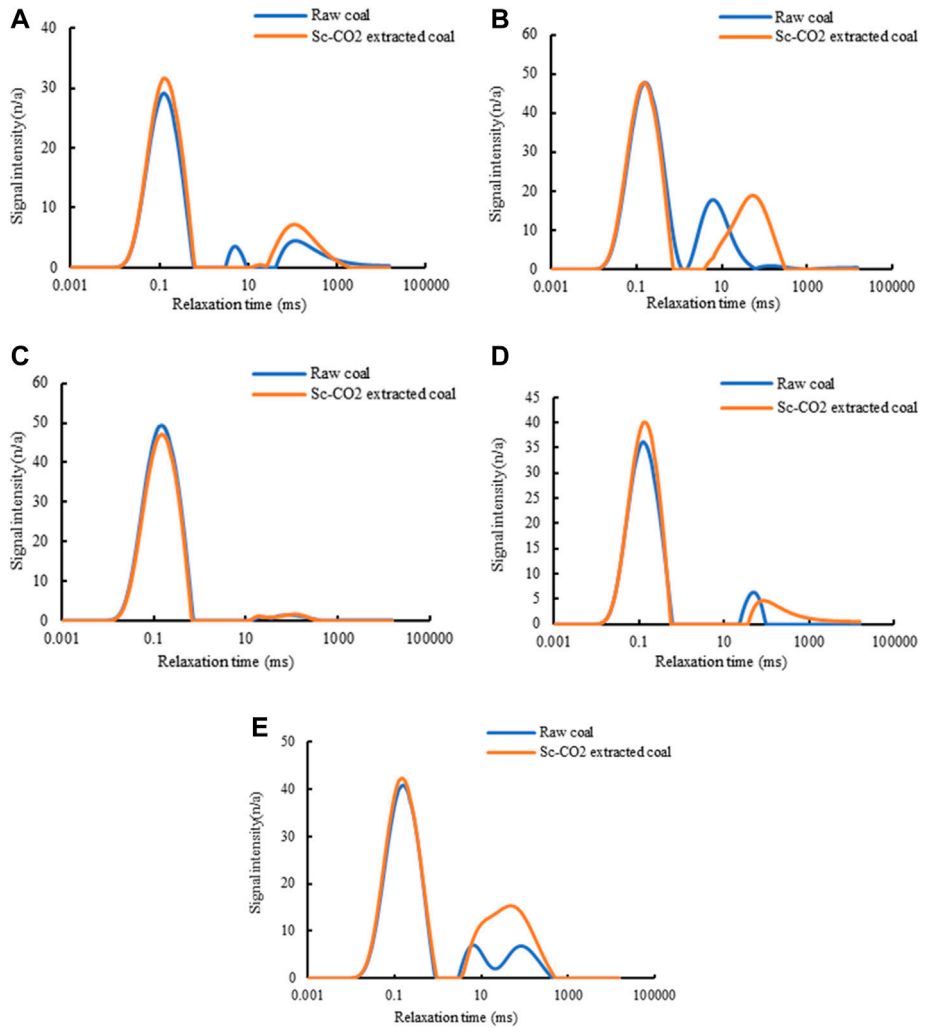

FIGURE 8
Transverse relaxation time T_2 spectrum of coal sample **(A)** SJG coal; **(B)** LJZ coal; **(C)** LL coal; **(D)** CJW coal; and **(E)** SSP coal.

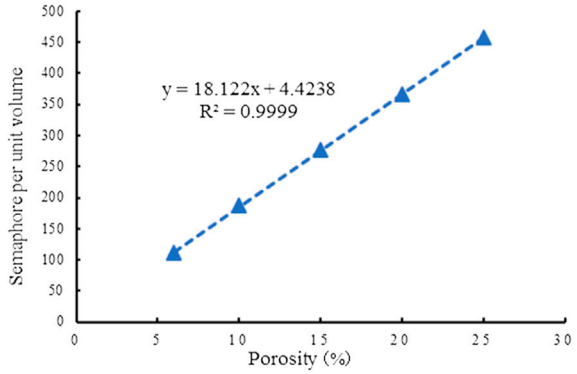

FIGURE 9
Calibration curve.

incremental porosity to present an increasing–decreasing–increasing trend with the increase of coal rank. The turning point was near the second coalification. Before the turning point, incremental porosity increases and then decreases with coal rank. After the turning point, incremental porosity increases gradually with coal rank. It is the most significant in micropore and mesopore porosity.

In summary, the variation of porosity increment with coal rank under Sc-CO_2 extraction is similar to that of pore volume and pore-specific surface area. The results of the NMR test and mercury intrusion porosimetry test are mutually corroborated, which proves again that Sc-CO_2 extraction exhibits an obvious transformation effect on pore structure in coal.

3.3 Pore structure evolution model

According to the previous discussion, Sc-CO_2 extraction exhibits a dual effect of increasing and expanding pores on the transformation of the pore structure of coal. The increasing pore effect mainly occurs in the micropores, and the expanding pore effect mainly occurs in the transitional pores and the above-mentioned pores. The change of pore structure of coal by Sc-CO_2 extraction is controlled by coalification.

TABLE 4 The porosity of coal samples before and after Sc-CO_2 extraction.

Coal sample		Porosity (%)					Proportion (%)			
		P_{mi}	P_{tr}	P_{mc}	P_{ma}	P_t	P_{mi}/P_t	P_{tr}/P_t	P_{mc}/P_t	P_{ma}/P_t
SJG	Raw coal	0.8256	0.0074	0.0415	0.0283	0.9028	91.45	0.82	4.60	3.13
	Sc-CO_2 extracted coal	0.7832	0.0031	0.0071	0.1125	0.9059	86.46	0.34	0.78	12.42
LJZ	Raw coal	0.7371	0.0203	0.0203	0.1397	0.9174	80.35	2.21	2.21	15.23
	Sc-CO_2 extracted coal	1.0529	0.0148	0.0346	0.2465	1.3488	78.06	1.10	2.57	18.28
LL	Raw coal	1.0864	0.0348	0.0109	0.0248	1.1569	93.91	3.01	0.94	2.14
	Sc-CO_2 extracted coal	1.1070	0.0266	0.0167	0.0289	1.1792	93.88	2.26	1.42	2.45
CJW	Raw coal	1.6223	0.3052	0.3717	0.0437	2.3429	69.24	13.03	15.86	1.87
	Sc-CO_2 extracted coal	1.6859	0.0594	0.4425	0.3546	2.5424	66.31	2.34	17.40	13.95
SSP	Raw coal	1.1298	0.0882	0.1376	0.1317	1.4873	75.96	5.93	9.25	8.85
	Sc-CO_2 extracted coal	1.4258	0.1051	0.4751	0.3256	2.3316	61.15	4.51	20.38	13.96

P_{mi}: Micropore porosity; P_{tr}: Transitional porosity; P_{mc}: Mesopore porosity; P_{ma}: Macropore porosity; P_t: Total porosity.

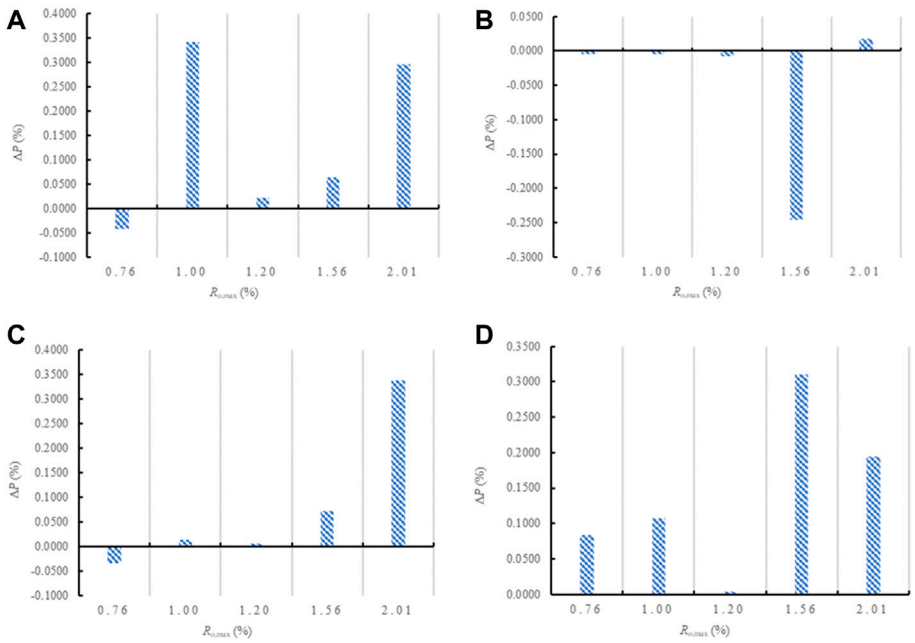

FIGURE 10
The changes in incremental porosity of coal due to Sc-CO_2 extraction **(A)** Micropore; **(B)** Transitional pore; **(C)** Mesopore; and **(D)** Macropore.

The mechanisms of Sc-CO_2 extraction affecting coal pore structure are attributed to the dissolution of small organic molecules in Sc-CO_2 fluid. In order to describe the pore structure evolution characteristics of coal based on Sc-CO_2 extraction, according to the related previous research results (Chen et al., 2017; Su et al., 2018; Wang et al., 2022) and the analysis of results of this study, the evolution model of pore structure of coal by Sc-CO_2 extraction was established (Figure 11). In the process of coalification, under the influence of coalification, temperature, and pressure, the branches and side chains in the macromolecular structure of organic matter present in coal continuously fall off to form small organic molecules in coal, which get filled in the pore structure of coal to form closed or semi-closed organic filling pores (Figure 11A). After Sc-CO_2 extraction, the small organic molecules present in the pore structure of filled coal are partially extracted, resulting in the increase of pore volume, specific surface area, and porosity of coal to varying degrees. Owing to the short extraction time, some organic small molecules still do not get extracted completely (Figure 11B). At the same time, the pore throats originally filled with small organic molecules (Figure 11C) are likely to be opened from open pores (Figure 11D) after Sc-CO_2 extraction, and the porosity of coal pores becomes better.

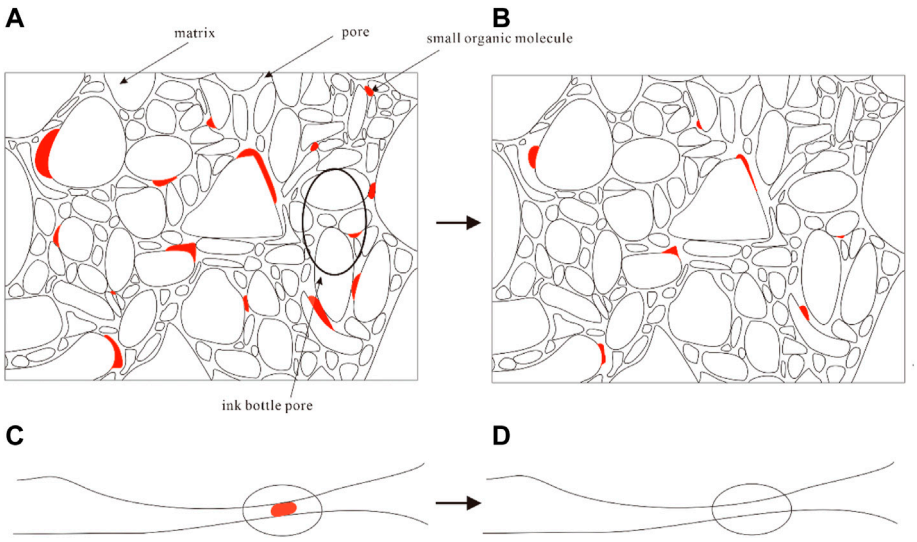

FIGURE 11
Hypothetical model of sample pore structure evolution **(A)** Pore structure of raw coal; **(B)** Pore structure of Sc-CO_2 extraction coal **(C)** Raw coal throat; **(D)** and Sc-CO_2 extraction coal throat.

4 Conclusion

The Sc-CO_2 extraction device was used to simulate the extraction process of CO_2-ECBM under geological conditions, and the mercury intrusion porosimetry and NMR spectroscopy tests were conducted to test the pore structure and porosity of coal before and after CO_2 extraction. Based on the results, the following conclusions can be drawn.

1) Pore volume, pore-specific surface area, and connectivity characteristics changed significantly by Sc-CO_2 extraction, and the increment of pore volume and pore-specific surface area presented an increasing–decreasing–increasing trend with the increase in the coal rank, and the turning point was found to be near the second coalification.
2) The porosity change due to Sc-CO_2 extraction increased–decreased–increased with increasing coal rank, the turning point was also near the second coalification, which supports the mercury intrusion porosimetry results.
3) The changes were observed in the porosity characteristics due to Sc-CO_2 extraction through pore-increasing and expanding effects. Before the second coalification, the pore-increasing and expanding effects co-existed in the micropores; however, after the second coalification, the pore-expanding effect mainly existed in transitional pores and above.
4) Based on the research, the pore structure evolution model of Sc-CO_2 extraction of coal was established.
5) The extraction time of this study was short, which may be different from the effect of Sc-CO_2 extraction on coal pores under geological conditions. Undeniably, a lot more systematic explorations are further demanded to investigate the time effect of Sc-CO_2 extraction on coal pore characteristics, which will be pursued in the future.

Data availability statement

The raw data supporting the conclusions of this article will be made available by the authors, without undue reservation.

Author contributions

RC designed the facilities and experiments; RC, KH, and FL performed the experiment and analyzed the data; RC, KH, and YZ compiled the data and plotted the graphs; RC wrote the paper.

Funding

This research was funded by the Fundamental Research Funds for the Central Universities (2019XKQYMS24). The authors express their appreciation to by the Fundamental Research Funds for the Central Universities (2019XKQYMS24) for the financial support of this work. Experiments were conducted at China University of Mining and Technology.

Acknowledgments

We would like to thank a number of research students from China University of Ming and Technology for their assistance in the coal sampling and some experiments.

Conflict of interest

The authors declare that the research was conducted in the absence of any commercial or financial relationships that could be construed as a potential conflict of interest.

Publisher's note

References

Chen, R., Qin, Y., Wei, C. T., Wang, L. L., Wang, Y. Y., and Zhang, P. F. (2017). Changes in pore structure of coal associated with Sc-CO_2 extraction during CO_2-ECBM. *Appl. Sci.* 7, 931. doi:10.3390/app7090931

Chen, Y. P., Jiang, W. Z., Qin, Y. J., and Su, W. W. (2021). Review on research theory and methods of pore distribution characteristics of coal. *Saf. Coal Mines* 52, 190–196. doi:10.13347/j.cnki.mkaq.2021.03.035

Di, G., Guo, H. L., Guo, B. Q., Kaili, T., and Ren, H. X. (2022). Impact of microbially enhanced coalbed methane on the pore structure of coal. *Front. Earth Sci.* 10. doi:10.3389/feart.2022.869917

Du, Y., Sang, S. X., Wang, W. F., Liu, S. Q., Wang, T., and Fang, H. H. (2018). Experimental study of the reactionsa of supercritiacal CO_2 and minerals in high-rank under formation conditions. *Energy Fuels* 32, 1115–1125. doi:10.1021/acs.energyfuels.7b02650

Fu, X. H., Qin, Y., Zhang, W. H., Wei, C. T., and Zhou, R. F. (2005). Study on fractal classification and natural classification of coal pores based on coalbed methane transport. *Sci. Bull.* 50, 51–55. doi:10.3321/j.issn:0023-074X.2005.z1.009

Fu, X. H., Qin, Y., and Wei, C. T. (2007). *Coal bed methane geology*. Xuzhou: China university of mining and technology press.

Guo, H., Ni, X. M., Wang, Y. B., Du, X. M., Yu, T. T., and Feng, R. M. (2018). Expeimental study of CO_2-water-mineral interactions and their influence on the permeability of coking coal and implications for CO_2-ECBM. *Minerals* 8, 117. doi:10.3390/min8030117

Li, J. R., and Zhou, Q. Z. (2021). "Characterization of the pore structure of coal samples based on mercury-pressure experiments," in Proceedings of the 27th annual academic conference of the Beijing Mechanics Society, 1299–1302. doi:10.26914/c.cnkihy.2021.001964

Liu, S. Q., Ma, J. S., Sang, S. X., Wang, T., Du, Y., and Fang, H. H. (2018). The effects of supercritical CO_2 on mesopore and macropore structure in bituminous and anthracite coal. *Fuel* 233, 32–43. doi:10.1016/j.fuel.2018.03.036

Liu, J., Xie, L. Z., Elsworth, D., and Gan, Q. (2019). CO_2/CH_4 competitive adsorption in shale: Implications for enhancement in gas production and reduction in carbon emissions. *Environ. Sci. Technol.* 15, 9328–9336. doi:10.1021/acs.est.9b02432

Liu, H. F., Song, D. Z., He, X. Q., Tian, X. H., Lou, Q., and Wang, W. X. (2020). Influence of coalification on microstructure characteristics of coal surface. *China Saf. Sci. J.* 30, 121–127. doi:10.16265/j.cnki.issn1003-3033.2020.01.019

Liu, Y. W., Zhang, X. M., and Miao, J. (2020). Study on evolution of pore structure of medium and high rank coals. *Saf. Coal Mines* 51, 7–13. doi:10.13347/j.cnki.mkaq.2020.11.003

Liu, H. Q., Wang, L., Xie, G. X., Yuan, Q. P., Zhu, C. Q., and Jiao, Z. H. (2022). Comprehensive characterization anf full pore size fractal characteristics of coal pore structure. *J. Min. Saf. Eng.* 39, 458–469. doi:10.13545/j.cnki.jmse.2021.0630

Lv, Z. F., Zhang, X. M., Zhong, L. W., Zhang, S. A., Zhu, Z. Y., and Li, J. (1991). Pore characteristics of lump coal and its influencing factors. *J. China Univ. Ming Technol.* 20, 48–57.

Qi, L. L., Zhou, X. Q., Peng, X. S., Wang, Z. F., and Dai, J. H. (2022). Study on pore structure of coking coal based on low-temperature nitrogen adsorption and mercury intrusion method. *Saf. Coal Mines* 53, 1–6. doi:10.13347/j.cnki.mkaq.2022.07.002

Sampath, K. H. S. M., Sin, I., Perera, M. S. A., Matthai, S. K., Ranjith, P. G., and Li, D. Y. (2020). Effect of supercritical CO_2 interaction time on the alterations in coal pore structure. *J. Nat. Gas Sci. Eng.* 76, 103214. doi:10.1016/j.jngse.2020.103214

Si, L. L., Ping, J., Xi, Y. J., Wang, H. Y., Wen, Z. H., Li, B., et al. (2021). The influence of long-time water intrusion on the mineral and pore structure of coal. *Fuel* 290, 119848. doi:10.1016/J.fuel.2020.119848

Su, E. L., Liang, Y. P., Li, L., Zou, Q. L., and Niu, F. F. (2018). Laboratory study on changes in the pore structures and gas desorption properties of intact and tectonic coals after supercritical CO_2 treatment: Implications for coalbed methane recovery. *Energies* 11, 3419. doi:10.3390/en11123419

Tang, S. H., Cai, C., Zhu, B. C., Duan, L. J., and Zhang, J. Z. (2008). The control of the degree of coal metamorphism on the physical properties of coal reservoirs. *Nat. Gas. Ind.* 28, 30–33. doi:10.3787/j.issn.1000-0976.2008.12.007

Wang, S. W., and Chen, Z. H. (1995). Progress in the study of pore and fracture systems in coal reservoirs. *Geol. Sci. Technol. Inf.* 14, 53–59.

Wang, Z. Z., Pan, J. N., Hou, Q. L., Yu, B. S., Li, M., and Niu, Q. H. (2018). Anisotropic characteristics of low-rank coal fractures in the Fukang mining area, China. *Fuel* 211, 182–193. doi:10.1016/j.fuel.2017.09.067

Wang, Z. Z., Fu, X. H., Hao, M., Li, G. F., Pan, J. N., Niu, Q. H., et al. (2021). Experimental insights into the adsorption-desorption of CH_4/N_2 and induced strain for medium-rank coals. *J. Petroleum Sci. Eng.* 204, 108705. doi:10.1016/J.petrol.2021.108705

Wang, X. L., Geng, J. B., Zhang, D. M., Xiao, W. J., Chen, Y., and Zhang, H. (2022). Influence of sub-supercritical CO_2 on pore structure and fractal characteristics of anthracite: An experimental study. *Energy* 261, 125115. doi:10.1016/J.energy.2022.125115

Wang, Y. Y. (2018). *Supercritical CO_2 extraction coal adsorption characteristics and its mechanism*. China: China University of Mining and Technology.

Washburn, E. W. (1921). The dynamics of capillary flow. *Am. Phys. Soc.* 17, 273–283. doi:10.1103/physrev.17.273

Wu, J., Jin, K. L., Tong, Y. D., and Qian, R. D. (1991). Coal pore theory and its application in gas protrusion and extraction evaluation. *J. China Coal Soc.* 86, 95.

Wu, S., Tang, D. Z., Xu, H., and Li, S. (2016). Characeristics of pore development in medium-high rank coal. *Coal Geol. Explor.* 44, 69–74. doi:10.3969/j.issn.1001-1986.2016.06.013

Xiong, J. L., Wang, K., Du, Q. X., Meng, X. C., and Guo, B. B. (2022). Study on pore characteristics of acidified coal samples based on low field nuclear magnetic resonance technology. *Min. Saf. Environ. Prot.* 49, 47–52. doi:10.19835/j.issn.1008-4495.2022.01.008

Xu, H. G., and Qin, X. G. (2022). Study on the influence of cooking coal pore structure on meathane desorption in Xishan coalfield. *Saf. Coal Mines* 53, 7–12. doi:10.13347/j.cnki.mkaq.2022.05.002

Yang, M., Liu, L., Zhang, X. B., Mao, J. R., and Cai, P. (2021). Nucler magnetic resonance experimental study on pore structure and fluid characteristics of coal at different ranks. *China Saf. Sci. J.* 31, 81–88. doi:10.16265/j.cnki.issn1003-3033.2021.01.012

Yuan, J. W., Xia, J. Y., Wang, Y., Chen, M., and Chen, J. X. (2022). Effect of freeze-thaw cycles on coal pore structure and gas emission characteristics. *Acs Omega* 7, 16087–16096. doi:10.1021/acsomega.2C01413

Zhang, K., Sang, S. X., Liu, C. J., Ma, M. Y., and Zhou, X. Z. (2019). Experimental study the influences of geochemical reaction on coal structure during the CO_2 geological storage in deep coal seam. *J. Petroleum Sci. Eng.* 178, 1006–1017. doi:10.1016/j.petrol.2019.03.082

Zhang, D. F., Li, C., Li, Y. H., and Jiang, W. P. (2020). Progress in the study of the relationship between CO_2 fluids and mineral interaction in coal during sequestration. *J. Saf. Environ.* 20, 297–309. doi:10.13637/j.issn.1009-6094.2019.0568

Zhang, H. (2001). Genesis types of coal pore space and its study. *J. China Coal Soc.* 26, 40–44. doi:10.3321/j.issn:0253-9993.2001.01.009

Zhang, P. F. (2019). *Study on the characteristics of pore permeation changes of supercritical CO_2 extracted coal*. China: China University of Mining and Technology.

Zhao, X. L., Tang, D. Z., Xu, H., Tao, S., and Chen, Z. L. (2010). Effect of coal matamorphic process on pore system of coal resevoirs. *J. China Coal Soc.* 35, 1506–1511. doi:10.13225/j.cnki.jccs.2010.09.009

Zhao, P., He, B., Zhang, B., and Liu, J. (2022). Porosity of gas shale: Is the NMR-based measurement reliable? *Petroleum Sci.* 19, 509–517. doi:10.1016/j.petsci.2021.12.013

Zheng, S. J., Yao, Y. B., Liu, D. M., Cai, Y. D., and Liu, Y. (2018). Characterizations of full-scale pore size distribution, porosity and permeability of coals: A novel methodology by nuclear magnetic resonance and fractal analysis theory. *Int. J. Coal Geol.* 196, 148–158. doi:10.1016/j.coal.2018.07.008

Zheng, S. J., Yao, Y. B., Liu, D. M., Cai, Y. D., Liu, Y., and Li, X. W. (2019). Nuclear magnetic resonance T_2 cutoffs of coals: A novel method by multifractal analysis theory. *Fuel* 241, 715–724. doi:10.1016/j.fuel.2018.12.044

Zhu, Q. Z., Yang, Y. H., Lu, X. Q., Liu, D. M., Li, X. W., Zhang, Q. Q., et al. (2019). Pore structure of coals by mercury intrusion, N_2 adsorption and NMR: A comparative study. *Appl. Sci.* 9, 1680. doi:10.3390/app9081680

Чодот, B. B. (1966). *Coal and gas outburst*. Beijing: China industry press. Wang Y A. translation.

frontiers | Frontiers in Earth Science

TYPE Original Research
PUBLISHED 09 February 2023
DOI 10.3389/feart.2023.1104418

OPEN ACCESS

EDITED BY
Mingjun Zou,
North China University of Water Resources and Electric Power, China

REVIEWED BY
Wei Jiang,
Suzhou University, China
Yu Qi,
Yanshan University, China
Cheng Huang,
Luoyang Institute of Science and Technology, China

*CORRESPONDENCE
Yubao Shao,
yubshao@163.com
Yinghai Guo,
gyhai@163.com

SPECIALTY SECTION
This article was submitted to Economic Geology, a section of the journal Frontiers in Earth Science

RECEIVED 21 November 2022
ACCEPTED 30 January 2023
PUBLISHED 09 February 2023

CITATION
Shao Y, Wang H, Guo Y, Huang X, Wang Y, Zhao S, Zhu Y, Shen L, Huang X, Song Y, Wang M, Cui K and Yang Q (2023), Geological characteristics and gas-bearing evaluation of coal-measure gas reservoirs in the Huanghebei coalfield. *Front. Earth Sci.* 11:1104418. doi: 10.3389/feart.2023.1104418

Geological characteristics and gas-bearing evaluation of coal-measure gas reservoirs in the Huanghebei coalfield

Yubao Shao[1,2,3]*, Huaihong Wang[2,4], Yinghai Guo[1,5]*, Xinglong Huang[2,3,6,4], Yongjun Wang[2,3,6,4], Shushan Zhao[2,3,6,4], Yuzhen Zhu[2,3,6,4], Lijun Shen[2,3,6,4], Xin Huang[2,3,6,4], Yu Song[2,3,6,4], Ming Wang[2,3,6,4], Kai Cui[2,3,6,4] and Qidong Yang[2,3,6,4]

[1]School of Resources and Geosciences, China University of Mining and Technology, Xuzhou, China, [2]Shandong Provincial Research Institute of Coal Geology Planning and Exploration, Jinan, China, [3]Shandong Research Center for Accident Prevention Technology in Key Industries (Non coal Mines), Jinan, China, [4]Key Laboratory of Coal Geophysics, Chinese Geophysical Society, Jinan, China, [5]Key Laboratory of Coalbed Methane Resources and Reservoir Formation Process, Ministry of Education, China University of Mining and Technology, Xuzhou, China, [6]Technical Innovation Platform for Unconventional Energy Exploration in Shandong Province, Jinan, China

Bystudying the source reservoir geochemical characteristics, reservoir cap physical properties, gas-bearing characteristics and reservoir-forming types of the coal-measure gas (CMG) accumulation system, the potential of CMG resources in the Huanghebei Coalfield was determined, and the sedimentary reservoir control mechanism was analyzed, which is of great significance for the orderly development of CMG reservoirs. CMG in the Huanghebei Coalfield mainly includes abundant shale gas (SG; 2100.45 × 10^8 m^3), coalbed methane (CBM; 137.89 × 10^8 m^3) and a small amount of tight sandstone gas, limestone gas and magmatic rock gas. CMG rocks mainly include shale and coal seams of the marine–terrestrial transitional facies Taiyuan Formation and continental facies Shanxi Formation, providing a favorable material basis for CMG enrichment. The coal seams are largely mature to highly mature, with satisfactory hydrocarbon generation potential and reservoir connectivity. They are low-porosity, low-permeability, underpressurized and undersaturated reservoirs. The shale organic matter is primarily Type II, with a moderate organic matter abundance. The material is at the middle-to high-maturity stage, provides a suitable hydrocarbon generation potential, belongs to low-porosity and low-permeability reservoirs, and exhibits favorable fracturing properties. There are several stable and independent gas-bearing systems among the coal measures. The CMG accumulation combination types are mostly self-sourced gas reservoirs and self-sourced+other-source near-source gas reservoirs, followed by other-source gas reservoirs. CBM and SG play the role of vertical regulation and horizontal regulation, respectively.

KEYWORDS

Huanghebei Coalfield, coal-measure gas, Taiyuan Formation, Shanxi Formation, reservoir feature, gas-bearing evaluation, gas reservoir assemblage

1 Introduction

Coal-measure gas (CMG) refers to natural gas generated from coal, carbonaceous shale and dark shale in coal measures, including shale gas (SG), coalbed methane (CBM) and tight gas (TG) (Law and Curtis, 2002; Clarkson, 2013; Dai, 2018; Hou et al., 2018; Zou et al., 2019; Shen et al., 2021; Li et al., 2022). In recent years, due to progress in exploration and development technology, CMG has changed the global natural gas pattern and plays an important role in ensuring the world energy supply and reducing air pollution. The typical CMG basins worldwide mainly include the San Juan Basin in the United States, the Surat Basin in Australia, the Western Siberian Basin in Russia and the Ordos Basin in China, but there is no independent resource evaluation of CMG abroad (Zou et al., 2019). Based on the spatial ranges and vertical extents of CMG overlap, the analysis of CMG as a unified gas-bearing system has therefore become a key research direction (Qin, 2021).

CMG constitutes an important guarantee for increasing reserves and producing natural gas in China (Qin, 2021). According to a recent prediction of the China Geological Survey, the CMG resources in China total approximately 82×10^{12} m^3 (Bi, 2019). China has become the sixth largest gas-producing country globally, evolving from being a gas-poor country (Dai, 2018). By the end of 2016, the discovered coal-measure fields in China accounted for 66% of the national gas fields, mainly distributed in the Ordos, Qinshui, Sichuan and other Carboniferous–Permian basins and Jurassic–Cretaceous coal-bearing basins, such as Tarim and Qaidam, as well as the Yinggehai-Qiongdongnan and Donghai Cenozoic coal-bearing basins (Zou et al., 2019). CMG is derived from the same origin and coexists in multiple layers, and it is generally associated with strong hydrocarbon generation, high continuous filling capacity, coexistence of multiphase gas, multiple types of gas reservoirs, source reservoir facies dependence, reservoir cap interaction, multiple seals, complex gas–water distribution relationships, and fragile dynamic balance between systems (Fu et al., 2013; Yang et al., 2013; 2015; Cao et al., 2014; Yuan, 2014; Qin et al., 2016; Zheng, 2016; Qin, 2018; 2021; Bi et al., 2020; Liu et al., 2020; Bi et al., 2021). The accumulation of CMG mainly depends on four aspects: hydrocarbon generation intensity, migration mode and transport system, formation fluid energy, and regional effective caprock. The accumulation effect of superimposed gas-bearing systems has become a leading direction of coal-measure gas geological research (Qin, 2018), which can provide a theoretical basis for large-scale exploration and development.

The exploration of upper Paleozoic coal-formed gas reservoirs in the Bohai Bay Basin adjacent to the northern Huanghe North coalfield has made great breakthroughs (Jin et al., 2009; Liang et al., 2016), indicating that the study area has good exploration potential. The Huanghebei area is a typical coal-bearing basin east of the coal accumulation area in North China, which is affected by intrusions associated with Yanshanian magmatism. It shows the unique characteristics of coalbed methane, shale gas and a skarn-rich iron ore pool (ore) (Wang et al., 2021). The abundance of organic matter in the Carboniferous-Permian coal measure source rocks in the study area is poor to medium (Cui, 2001; Chen et al., 2003; Yu, 2003; Mu, 2008). The peak period of gas generation was mainly in the Early Triassic and Jurassic-Cretaceous, and the abnormally high thermal geothermal field in the Yanshanian played a key role in the hydrocarbon generation of the source rocks (He et al., 2005; Zhao, 2005; Li, 2006; Zhou, 2015; Yang et al., 2018). These source rocks still retain a high hydrocarbon generation potential (Xu et al., 2005). The occurrence of coal-measure gas is mainly affected by factors such as faults, sedimentary environment, inorganic minerals, caprock conditions, burial depth, overburden thickness, hydrogeological conditions and magma (Fan et al., 2001; Liu and Guo, 2003; Zhao, 2007; Zhao et al., 2016; Huang et al., 2018; Li, 2019). Shallow CBM has been pumped and utilized in the study area. In 2010, the Zhaoguan Coal Mine used the gas pumped during coal mining for power generation for the first time in this area, which indicates that CMG here could yield a certain development prospect. With the support of the Shandong Provincial Geological Exploration Fund, survey and evaluation studies of CBM and SG resources in the research area have been conducted. A number of gas-bearing strata have been found in the Upper Paleozoic Taiyuan Formation and Shanxi Formation. CMG is dominated by CBM and SG, demonstrating the characteristics of source reservoir facies dependence, reservoir cap interaction and multiple seals. In this paper, the coal seams and shale of the upper Paleozoic Shanxi Formation and Taiyuan Formation were adopted as research objects, and a systematic study of the reservoir formation and exploration potential of the Huanghebei Coalfield is of great significance to understanding the CMG reservoir formation mechanism and to the collaborative exploration and efficient development and utilization of multiple mineral resources.

2 Geological setting

2.1 Regional structure and stratigraphic characteristics

The Huanghebei Coalfield is located in the western regions of the Luxi uplift in the North China Plate (Figure 1). It starts from the Woniushan fault in the east, reaches the Liuji fault in the west, is bounded by the outcrop of the bottom (hidden) of the coal-bearing stratum in the south, and ends at the Qiguang fault in the north (Figure 1). This area is rich in coal resources and is an important coal production base in western Shandong Province. The study area generally comprises a wide and gentle monocline trending northeast–northwest, which is shallow in the south and deep in the north. The dip angle of the monocline is generally low, with wide and gentle northeast-trending folds developed. The regional structure is dominated by fault structures. In general, there are three groups of fault structures distributed along the NE–NNE, NW–NNW, and near-E–W directions, and the former two groups are relatively well developed, while SN-directed faults are not very developed in this area. These groups of large faults intersect each other, controlling the generation and development of uplift and depression in the region.

The stratigraphic division of the study area is classified as the western Shandong stratigraphic division of the North China stratigraphic area. Only a small range of Cambrian Ordovician strata is exposed in the south (south of the Huanghebei Coalfield), and the remaining area is covered by Quaternary strata. The strata from old to new include the Taishan Group and Cambrian, Ordovician, Carboniferous, Permian, Triassic, Neogene and Quaternary strata, lacking Upper Ordovician to Lower Carboniferous, Jurassic and Cretaceous strata. Paleogene rocks are not developed to the south of the Qiguang fault, and they are mainly distributed to the north of the Qiguang fault.

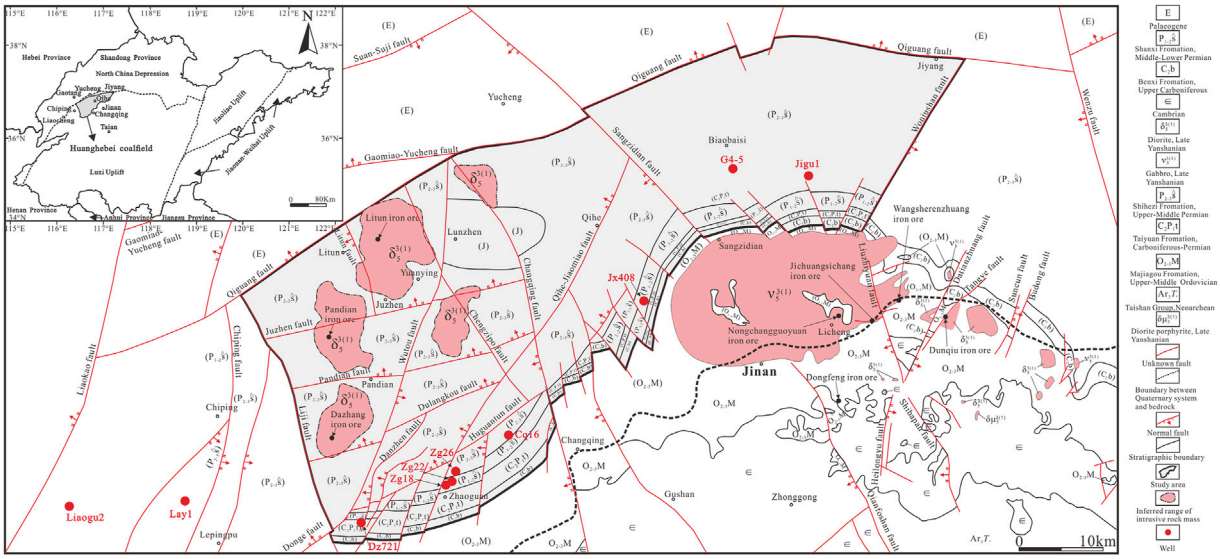

FIGURE 1
Geological map of the pre-Neogene bedrock in the study area. The area north of the dotted line at the lower right is the Quaternary coverage area. The overview map at the upper left shows the location of the study area, and the gray area within the black line denotes the Huanghebei Coalfield.

Magmatic rocks are widely distributed in the region, mainly including Neoarchean, Mesoproterozoic and Mesozoic intrusive rocks. Among them, Neoarchean intrusive rocks are the most developed and are distributed in the southern part of the Zhangqiu–Changqing area. Ultrabasic, basic, and acidic intrusive rocks occur, with intermediate–acidic intrusive rocks being the most common. The distribution of Mesozoic intrusive rocks is limited, and these rocks are mainly distributed in the Yucheng - Jinan area and are mainly composed of intermediate–basic rocks (Figure 1). Magmatic rocks of other ages are not developed. The Mesozoic intrusive rocks, such as the Jinan gabbro (Yang et al., 2005; Huang et al., 2012; Yang, 2012; Ning et al., 2013; Xie et al., 2015), Tai'an gabbro and diorite (Ning et al., 2013), and Qihe—Yucheng diabase (Zhu et al., 2021), mainly formed in the Early Cretaceous (100 ~ 135 Ma). The intrusive rocks in the study area are mainly diabase, diorite, quartz monzodiorite, quartz monzonite and granite. Among them, the Litun rock mass contains all the above rock types (Shen et al., 2020; Shen et al., 2021; Zhu et al., 2021), while the Dazhang rock mass and Pandian rock mass mainly contain quartz monzonite (Zhang et al., 2022). Except for the Litun rock mass, which exhibits a narrow range of direct contact with the overlying Neogene strata, the known rock groups in the west are capped by residual Permian strata, and the Jinan rock mass occurs in direct contact with Quaternary strata except for a small amount of Ordovician limestone. At the same time, three layers of Mesozoic magmatic rocks intruded the Shanxi Formation and Taiyuan Formation, and these magmatic rocks are present in the form of bedrock or dikes. The upper and lower layers are acidic magmatic rocks, and the middle layer comprises medium-basic magmatic rocks. The layers intruded by the upper magmatic rock are mainly coal seams three and four overlying strata of the Shanxi Formation. The middle magmatic rock mainly intruded coal seam five of the Shanxi Formation to coal seam nine of the Taiyuan Formation and severely damaged coal seam seven of the Taiyuan Formation. The lower magmatic rock mainly damaged coal seams 11 and 13 of the Taiyuan Formation.

2.2 Sequence stratigraphic characteristics

CMG in China exhibits the characteristics of large-scale vertical and horizontal distributions, an unclear gas-water boundary, a complex pressure system, diverse reservoir rock types, interbedded occurrence, notable cyclicity, and variable source–reservoir–cap associations (Qin, 2021). The CMG characteristics in the study area are consistent with the basic geological characteristics of China. The proposal of an unconnected multiple superimposed CBM system explains the highly consistent relationship and genetic mechanism between sequence division and independent segmentation of the gas content gradient in the sequence stratigraphic framework (Qin et al., 2008; Shen et al., 2012) and further extends to the superimposed CMG-bearing system. The sequence stratigraphic framework explains the development of key layers and establishes a coal measure reservoir (production) combination model constrained by these key layers. High-resolution identification of fluid and energy under the cell framework of three-layer sequence stratigraphy was carried out (Qin et al., 2016; Shen et al., 2017). The logging data of wells Zg18, Zg22 and Zg26 demonstrate that SG, CBM and a small amount of TG, carbonate rock gas and magmatic rock gas occur in the Shanxi Formation and Taiyuan Formation (Figure 2), which are constrained by the sequence stratigraphic framework and contain multiple relatively independent gas-bearing units.

The isochronous sequence stratigraphic framework is helpful for predicting the distribution of coal measure source rocks (Shao et al., 2008). For the offshore coal-bearing rock series of the North China platform, three third-order sequences can be identified in the Benxi Formation, Taiyuan Formation and Shanxi Formation (Shao et al., 2014). There are two scales of the sequence stratigraphic division

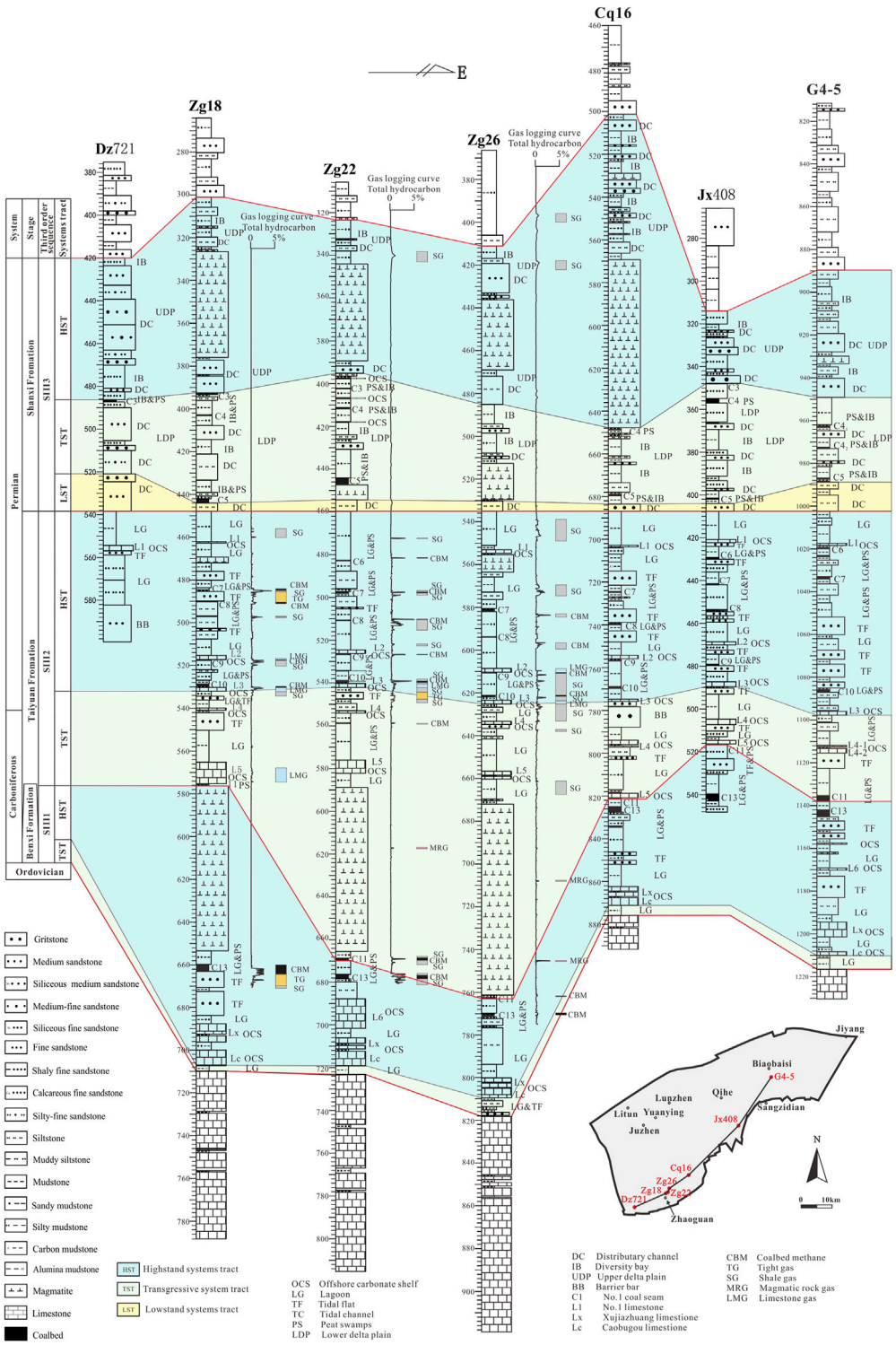

FIGURE 2
Correlation diagram of the sedimentary facies and sequence stratigraphy (SW–NE).

scheme of the Benxi Formation, Taiyuan Formation and Shanxi Formation in Shandong Province, including three third-order sequences (Wang et al., 2003; Li et al., 2005; Zhang et al., 2010; Li et al., 2021) and four third-order sequences (Jia and Lv, 2009). According to the regional unconformity surface and the regional tectonic stress transformation surface, the Permian Shanxi Formation, upper Carboniferous–lower Permian Taiyuan Formation and Carboniferous Benxi Formation in the study area are divided into three third-order sequences (SIII1-SIII3) and eight fourth-order sequences (SIV1-SIV8) (Figure 2). The Shanxi Formation corresponds to sequence SIII3, the Taiyuan Formation corresponds to the highstand systems tract (HST) of sequence

SIII1 and sequence SIII2, and the Benxi Formation corresponds to the transgressive systems tract (TST) of sequence SIII1. The bottom boundary of sequence SIII1 is a regional unconformity surface, namely, the interface between Ordovician and Carboniferous strata. The maximum flooding surface is the boundary between the Taiyuan and Benxi Formations, which is located at the bottom of the Xuhui Formation. Thirteen coal seams are mainly developed in the TST. The bottom boundary of sequence SIII2 mainly comprises the floor of the No. 11 coal seam below the L5 limestone formed in a lagoon and swamp environment. The maximum flooding surface is located at the bottom of the L3 limestone. The No. 6, 7, 8, 9, 10 and 11 coal seams of the Taiyuan Formation are well developed. The initial flooding surface of sequence SIII3 is located near the floor of the No. 5 coal seam, and the maximum flooding surface is located at the top of the No. 3 coal seam. The bottom boundary of the sequence mainly encompasses the incised valley of the distributary channel in the lower delta plain, which is the boundary between the Shanxi Formation and Taiyuan Formation. The No. 3, 4, and 5 coal seams of the Shanxi Formation are well developed.

2.3 Evolution of the sedimentary system

The Carboniferous–Permian coal accumulation basin in North China mainly developed in the paleogeographic background of sea–land interaction (Liu et al., 1987; Ma and Tian, 2006). The western Shandong region mainly featured carbonate platform, lagoon tidal flat, and shallow water delta sedimentary systems from Benxi to Shanxi (Wang et al., 2003; Jia and Lv, 2009; Zhang et al., 2010; Shao et al., 2014). In the late Paleozoic, namely, from the Carboniferous to the Permian, barrier lagoon, tidal flat, river-controlled shallow-water delta and river–lake sedimentary systems were mainly developed in the study area (Wang et al., 2021). Along with the North China Depression, the study area has experienced large-scale transgression since the late Carboniferous, formed coal-bearing rock series represented by sand–mud interbeds, and developed favorable gas reservoirs. During the Benxi period, with seawater intrusion, the TST of sequence SIII1 formed lagoon tidal flat deposits dominated by gray–white bauxite and gray or gray–black mudstone with thin bedded limestone interbedded residues, accompanied by small-scale transgression. During the Taiyuan period, at the end of the late Carboniferous, the North China Depression experienced a movement entailing a rise in the north and a descent in the south. By this time, the epicontinental sea environment had reached its peak. The HST of sequence SIII1 and sequence SIII2 developed an offshore shelf barrier lagoon tidal flat sedimentary system. The lithology mainly includes dark mudstone, fine siltstone, thin limestone and coal seams. The biological species are rich, and the organic content is high. During the Shanxi period, with tectonic uplift and seawater retreat, a fluvial-dominated shallow delta depositional system was widely developed in sequence SIII3, with distributary channels and interdistributary bays occupying the main part, in which the lowstand systems tract (LST) and TST mainly comprise a set of shallow delta–lower delta plain deposits, while the HST mainly includes shallow water delta–upper delta plain and meandering river deposits. During the Shihezi period, the Huanghebei Coalfield completely transformed from epicontinental sea deposits to continental deposits, and seawater was withdrawn. At this time, a set of very thick silicate clastic materials were deposited. The Huanghebei Coalfield experienced the complete process of the formation, development, prosperity, shrinkage and transformation of the epicontinental sea basin during the late Paleozoic and experienced multiple transgression regression cycles. The lithofacies paleogeographic pattern accordingly changed and was subjected to the evolution process of the tidal flat–barrier lagoon system–delta system–river system. During this period, a complete set of coal-measure source rocks in the Shanxi Formation and Taiyuan Formation with large thicknesses and high organic contents were developed, and this sequence comprises a vertical succession of shale, coal seam, clastic rock and carbonate rock strata and provides the basic geological conditions for a CMG source, reservoir and cap.

3 Samples and experiments

3.1 Samples

Our samples were mainly collected from five wells, Zg18, Zg22, Zg26, Cq16 and Lay1, constructed in 2011–2016. Three coal samples and 12 shale samples were collected from Well Zg18. Three coal samples and five shale samples were collected from Well Zg22. Four coal samples and 12 shale samples were collected from Well Zg26. Thirty-six shale and six coal seam samples were collected from Well Cq16. Twenty-two shale and 11 coal seam samples were collected from Well Lay1. Field tests and laboratory analyses were carried out immediately after sample collection.

3.2 Experimental approaches

Maceral identification, macroscale coal rock type identification, microfracture statistics, gas content analysis, isothermal adsorption tests, and total organic carbon analysis of coal seam samples were performed at the Shandong Taishan Mineral Resources Detection and Research Institute.

The coal macerals were determined according to the determination of coal group composition and minerals in coal (GB/T 8899-2013). The volume fraction of various macerals was determined by using the number point method under axio scope. A1 microscope (Carl Zeiss, Germany) and under single polarized light or incomplete orthogonal polarized light to determine the type of organic matter. The macroscopic coal rock type as mainly determined by axio scope. A1 microscopy based on the classification of macrolithotype for bituminous coal (GB/T 18023-2000). Refer to the description methodology of fractures in coal (MT/T 968-2005) for information on the observation and statistics of coal microfractures.

The coal seam gas content was determined according to the method of determining coalbed gas content (GB/T 19559-2008). The time from drilling to coring is required to be no more than 2 min for core lifting every 100 m. An 800 g sample of core was canned within 10 min after the core reached the wellhead, and the desorption capacity was tested in a thermostatic water bath. Natural desorption ended after the daily desorption capacity was less than 10 cm^3 for seven consecutive days. The desorbed sample was pressed to 2-3 cm, and 500 g was placed into a ball mill for residual gas measurement. At the time of rapid gas measurement, a 500 g sample of coal core was loaded into the ball mill tank. First, it was naturally desorbed for 8 h

and then crushed by ball milling for 30 min. Then, it was put into the thermostatic device for natural desorption. The process of crushing and desorption was repeated until the amount of desorbed gas over two consecutive times was less than 10 cm^3. The measured gas volume of natural desorption and residual gas was converted into the total gas content at a temperature of 0°C and a pressure of 101.325 kPa, with correction for gas loss. The gas components mainly include CH_4, CO_2, N_2 and heavy hydrocarbons, using GC-7820 gas chromatograph (Shandong Huifen Instrument Co., Ltd., China). The analysis of natural gas by gas chromatography (GB/T 13610-2003) was used for the test process. Three gas component analysis samples were collected for each desorption sample during the test on the first, third and fifth days of desorption. Samples with a low coalbed methane content were collected appropriately in advance.

The coal seam isothermal adsorption test used the WX-VI high-pressure isothermal adsorption apparatus (Qingdao Ruihai Xinda Instrument Co., Ltd., China). According to the method of determining microscopically the reflectance of vitrinite in coal (GB/T 19560-2008) and determination of equilibrium moisture in coal isothermal adsorption method (MT/T 1157-2011), 200 g coal samples with particle sizes of 0.25–0.18 mm were prepared, and a sample mass of 40 g was weighed for equilibrium moisture measurement. Six test pressures (0.5, 1.0, 2.0, 4.0, 6.0, and 8.0 Mpa) were applied. Then, the Langmuir pressure (P_L) and Langmuir volume (V_L) were obtained.

The reflectance of coal seam vitrinite was measured by axio scope. A1 microscope (Carl Zeiss, Germany) at the Shandong Taishan Mineral Resources Testing and Research Institute and the laboratory of the Guizhou Coalfield Geology Bureau. Referring to the method of determining microscopically the reflectance of vitrinite in coal (GB/T 6948-2008) (λ= 546 nm) measured by a photoelectric converter, more than 50 points were measured for single coal seam coal samples when the maximum reflectance of vitrinite was 0.45%–2.00%, and more than 100 points were measured when the maximum reflectance of vitrinite was 2.00% to ensure sufficient accuracy.

Coal seam permeability and reservoir pressure were determined by the Xi'an Research Institute of China Coal Research Institute with reference to the method of injection/falloff well test for coalbed methane well (GB/T 24504-2009). After drilling to the floor of the tested coal seam, the test string was inserted at the roof of the coal seam, and a microfracture test was conducted to obtain the maximum injection pressure value. Then, an injection/pressure drop test was performed. The water injection time was 18 h, and the well shut-in time was 36 h; then, *in situ* stress tests were carried out.

The gas content, porosity, permeability, pyrolysis analysis, total organic carbon, and mechanical properties of shale were measured at the Shandong Taishan Mineral Resources Detection and Research Institute.

The gas content of shale was determined according to the measurement method of shale gas content (SY/T 6940-2013). The time from drilling to coring was required to be less than 12 h. A core sample with a height of 20 cm–30 cm was canned within 10 min after the core reached the wellhead. The desorption was tested in a thermostatic water bath until the daily desorption volume was less than 5 cm^3 for three consecutive days. Three samples after desorption, 100 g each, were placed into the sealed tank of the residual gas volume tester for crushing, and the residual gas volume was taken as the mean value of the measurement results of the three samples. The measured gas volume of natural desorption and residual gas was converted into the total gas content at a temperature is 0°C and a pressure of 101.325 kPa, with correction for gas loss.

The porosity and permeability of shale were measured by a CMS-300 automatic core overburden porosity-permeability tester (Beijing Aotao Science & Technology Co., Ltd., China) with reference to porosity and permeability measurement under overburden pressure (SY/T6385-1999). The overburden pressure was applied to the rock sample by means of hydrostatic pressure to ensure that the stress in all directions of the rock sample was balanced and the pore pressure remained unchanged. The overburden pressure was gradually increased to measure the porosity and permeability. The accuracy of the pressure sensor and the relative error of the helium pore meter are both less than 0.1%.

The pyrolysis analysis of shale was measured by YY-3000A oil shale comprehensive evaluator (Lunan Ruihong Chemical Instrument Co., Ltd., China) according to the reference standard rock pyrolysis analysis (GB/T18602-2012). The sample was crushed to a particle size of 0.07–0.15 mm, an analytical balance with an accuracy of 0.1 mg was used to weigh 0.1 g, and the sample was placed into the instrument for heating. The sample was pyrolyzed in a nitrogen environment with a purity of >99.99% at 90°C, 300°C, and >300°C–600°C. The measured parameters include the hydrocarbon content (S_0) measured at 90°C, the hydrocarbon content (S_1) measured at 300°C, the hydrocarbon content (S_2) measured at >300°C–600°C, and the temperature at the highest point of the corresponding *S2* peak (T_{max}).

The compressive strength, elastic modulus, Poisson's ratio and tensile strength of shale was determined by a YAW-300D microcomputer controlled compression and bending tester, WAW-600F microcomputer controlled electro-hydraulic servo rock testing machine and YAW-1000D microcomputer controlled compression shear testing machine (Jinan Xinshijin Test Machine Co., Ltd., China). The compressive strength was tested according to methods for determining the physical and mechanical properties of coal and rock-Part 7: methods for determining the uniaxial compressive strength and counting softening coefficient (GB/T 23561.7-2009). Elastic modulus and Poisson's ratio was determined according to methods for determining the physical and mechanical properties of coal and rock-Part 8: methods for determining the deformation parameters of coal and rock (GB/T 23561.8-2009). Refer to methods for determining the physical and mechanical properties of coal and rock-Part 10: methods for determining tensile strength of coal and rock (GB/T 23561.10-2010).

The determination of total organic carbon in coal seams and shale was based on the specification for determination of total organic carbon in sedimentary rock (GB/T18602-2012), using CS230 carbon sulfur analyzer (LECO, United States). The sample was ground until the particle size was less than 0.2 mm. An analytical balance with an accuracy of 0.1 mg was used to weigh 1 g of the sample. The inorganic carbon in the sample was removed with dilute hydrochloric acid, and the sample was burned under a high-temperature oxygen flow to convert the total organic carbon into carbon dioxide. The content of total organic carbon was determined by infrared detection.

The shale kerogen macerals were determined in the laboratory of Guizhou coalfield geology bureau using a axio scope. A1 microscope (Carl Zeiss, Germany). According to method of identification microscopically the macerals of kerogen and indivision the kerogen type by transmitted-light and fluorescence (SY/T 5125-2014), each maceral was identified according to optical characteristics under

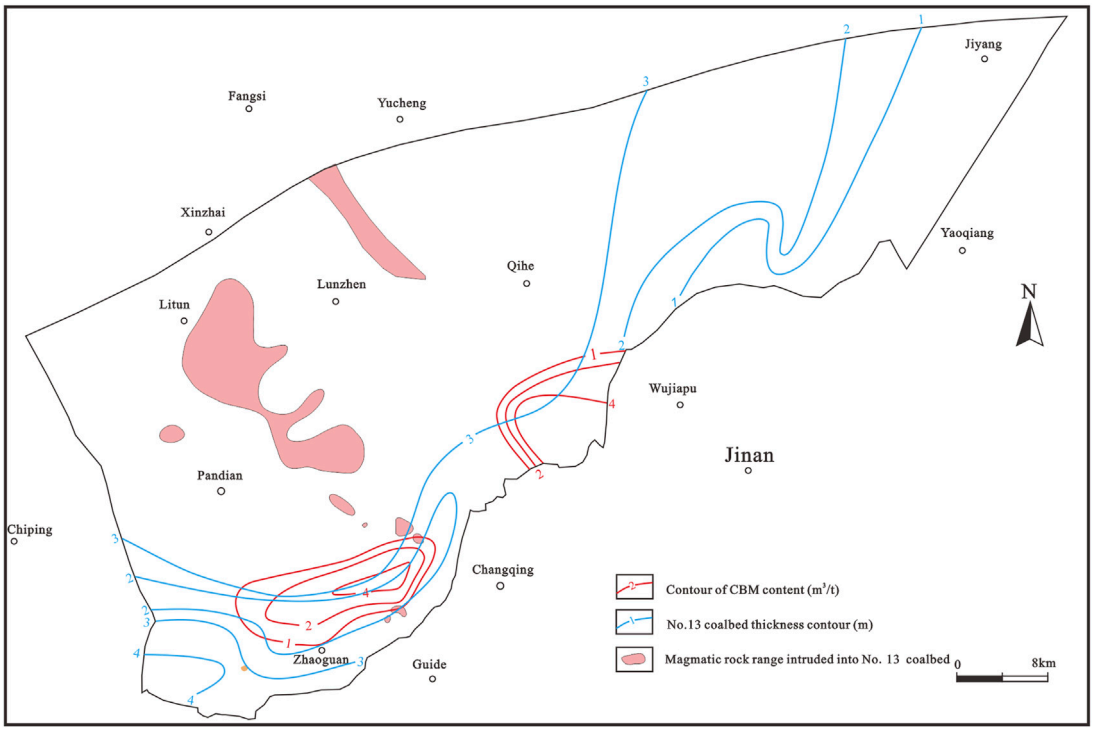

FIGURE 3
No. 13 coalbed thickness and gas content distribution.

transmitted light and emission fluorescence, and the contents of the sapropel group, chitin group, vitrinite group and inertinite group were obtained. The type index (*TI*) was calculated, and the types of kerogen were classified.

The vitrinite reflectance of shale was measured in the laboratory of the Guizhou coalfield geology bureau with a axio scope. A1 microscope (Carl Zeiss, Germany). According to method of determining microscopically the reflectance of vitrinite in sedimentary (SY/T5124-2012), for the optical sheet of the same sample, when the average reflectivity is greater than 2.0%, the number of measured points should greater than 30; when the average emissivity is between 0.5% and 2.0%, the number of measured points should greater than 20 to ensure the representativeness of the measured results.

4 CMG accumulation system

4.1 Development characteristics of the coal-measure source rocks

The shale and coal seams of the Taiyuan Formation and Shanxi Formation are the main coal-bearing gas source rocks in the study area, which exhibit the characteristics of extensive deposition. The total thickness of the coal-bearing strata of the Taiyuan Formation and Shanxi Formation in the study area is approximately 245 m. There are 14 coal seams in the coal-bearing strata, of which the No. 1 to 5 coal seams occur in the Shanxi Formation, and the No. 6 to 14 coal seams occur in the Taiyuan Formation. The minable and partially minable coal seams are the No. 5, 6, 7, 8, 10, 11 and 13 coal seams. The total thickness of the coal seams varies between 4 and 9 m, with an average of 5.5 m. The coal-bearing coefficient of the minable coal seams is 2.2%, revealing thin characteristics in the eastern and northern parts and thick characteristics in the western and southern parts in the study area. For example, the thickness center of the No. 13 coal seam is mainly located in the southwest of the Huanghebei Coalfield (Figure 3). The spatial distribution of each coal seam is deep in the north and shallow in the south, ranging from −200 to −2500 m.

Among them, sandstone is mainly developed above the No. 4 coal seam in the Shanxi Formation and is greatly affected by the intrusion of upper magmatic rock. Under the influence of lower magmatic rocks, shale below the No. 11 coal seam in the Taiyuan Formation is damaged to varying degrees, which is unfavorable for CMG accumulation. There are favorable SG intervals with large cumulative thicknesses in the strata between the No. 4 coal seam of the Shanxi Formation and the No. 10 coal seam of the Taiyuan Formation. The gas logging results for the corresponding intervals in Wells Zg18, Zg22 and Zg26 are satisfactory. The accumulated thickness of dark shale in the area ranges from 52.83 to 97.1 m, with an average of 84.8 m. The thickness in the south–central part of the area is small, mostly less than 60 m, while the thickness in the northwestern part is large, mostly greater than 90 m. The burial depth ranges from 414.05 to 1290.55 m, which is deep in the north and shallow in the south.

4.2 Organic geochemical characteristics of the coal-measure source rocks

Organic matter in source rock is the main factor determining the hydrocarbon generation ability. The organic matter abundance

TABLE 1 Evaluation results of the organic matter abundance of marine terrestrial interactive shale.

Well number	Layer	Number of samples	Hydrocarbon source rock evaluation results (the evaluation parameters refer to Huang et al. (1996)			
			Good-excellent	Medium	Poor	Non
			TOC: 3%–40%	TOC: 1.5%–3%	TOC: 0.6%–1.5%	TOC:<0.6%
Cq16	Shanxi Formation	7	1	4	1	1
	Taiyuan Formation	28	4	12	18	1
Lay1	Shanxi Formation	3	2	0	0	1
	Taiyuan Formation	19	3	14	2	0
Well	Stratum	Number of samples	S_1+S_2: 6.0–200 mg/g	S_1+S_2: 2.0–6.0 mg/g	S_1+S_2: 0.5–2.0 mg/g	S_1+S_2: <0.50 mg/g
Cq16	Shanxi Formation	7	0	0	1	6
	Taiyuan Formation	29	2	5	19	3
Lay1	Shanxi Formation	3	2	0	0	1
	Taiyuan Formation	18	1	6	10	1

indexes of marine-terrigenous source rocks widely recognized by the academic community mainly include the total organic carbon (TOC) content and hydrocarbon generation potential (S_1+S_2) (Huang et al., 1996). Based on the above indicators, the organic matter abundance of shale in the study area was evaluated (Table 1).

4.2.1 Abundance of organic matter

In the study area, the S_1+S_2 value of the coal seams of the Shanxi Formation and Taiyuan Formations in Well Jigu one varied between 80.93 and 173.68 mg/g, with an average of 132.95 mg/g, and the hydrogen index (HI) ranged from 133.84 to 188.00 mg/g, with an average of 161.67 mg/g (Chen et al., 2003; Yu et al., 2003). The TOC mainly refers to the data of adjacent Well Lay1, in which the TOC content in the Shanxi Formation ranged from 62.4% to 73.65%, with an average of 67.00%. The TOC content in the Taiyuan Group varied between 58.3% and 76.65%, with a mean of 67.34%.

The TOC content in the shale of the Shanxi Formation in Well Cq16 varied between 0.43% and 3.25%, with an average of 2.03%; S_1+S_2 varied between 0.1 and 0.78 mg/g, with an average of 0.27 mg/g; the TOC content in the shale of the Taiyuan Formation ranged from 0.55% to 17.65%, with an average of 2.82%; and S_1+S_2 ranged from 0.3 to 17.45 mg/g, with an average of 2.44 mg/g. Moreover, the TOC content in the Shanxi Formation shale in Well Lay1 in the adjacent area ranged from 0.57% to 18.25%, with an average of 9.49%, and S_1+S_2 ranged from 0.3 to 31.10 mg/g, with an average of 16.93 mg/g. The TOC content in the shale of the Taiyuan Formation varied between 1.11% and 21.95%, with an average of 3.98%, and the S_1+S_2 value ranged from 0.35 to 8.72 mg/g, with an average of 2.02 mg/g. As indicated by the statistical results (Table 1), the shales of the Shanxi Formation and Taiyuan Formation in Wells Cq16 and Lay1 mainly included poor to medium hydrocarbon source rocks. Combined with the inversion data of coal exploration well logging in the area, the TOC content in the shale of the Shanxi Formation and Taiyuan Formation in the study area ranged from 1.78% to 2.74%, with an average of 2.09%. The overall assessment of the organic matter abundance suggested a moderate abundance. The central area is a high-value area, with a TOC content higher than 2.6%, and the value gradually decreases toward the surroundings.

Both coal and shale seams are the main gas-generating layers of hydrocarbon source rocks, in which coal seams, as accumulated organic matter, contribute more to hydrocarbon generation and fulfill a decisive role in CMG reservoirs, while shale rich in organic matter remains stable during development, and the thickness advantage compensates for the lack of organic matter. It has been found that the hydrocarbon generation capacity of exinite source rocks with a certain content is higher (Qin et al., 2005). In general, the Huanghebei coalfield exhibits favorable hydrocarbon generation conditions.

4.2.2 Maturity of organic matter

Affected by magmatic intrusion, the vitrinite reflectance (R_o) values in the coal reservoirs of the Shanxi Formation and Taiyuan Formation in the area ranged from 0.61% to 6.35%, which suggests the mature to highly mature stage, and were higher than those of Well Lay1 in the adjacent area not affected by magmatic intrusion (with R_o ranging from 0.70% to 0.74%).

The shale R_o value of the Shanxi Formation in Well Cq16 ranged from 2.11% to 2.44%, T_{max} ranged from 471.9°C to 476.4°C, the shale R_o value of the Taiyuan Formation ranged from 1.34% to 2.13%, and T_{max} reached 476.40°C. The shale mainly occurred at the medium–to high-maturity stage, with a satisfactory hydrocarbon generation potential. Figure 4 shows that a very thick magmatic rock was developed in the Shanxi Formation in Well Cq16. The maturity of shale significantly increased within 75 m from the top and bottom of the magmatic rock, and no obvious abnormality was found in TOC and S_1+S_2. The shale of the Shanxi Formation and Taiyuan Formation in Well Jigu1 was not affected by magmatism, with R_o ranging from 0.75% to 1.02% (Chen et al., 2003; Yu et al., 2003). T_{max} of the shale of the Shanxi Formation in Well Lay1 ranged from 432.5°C to 477.5°C, the R_o value of the shale in the Taiyuan Formation ranged from 0.74% to 1.76%, and T_{max} ranged from 435.1°C to 475.8°C, mainly at the low-to medium-maturity stage.

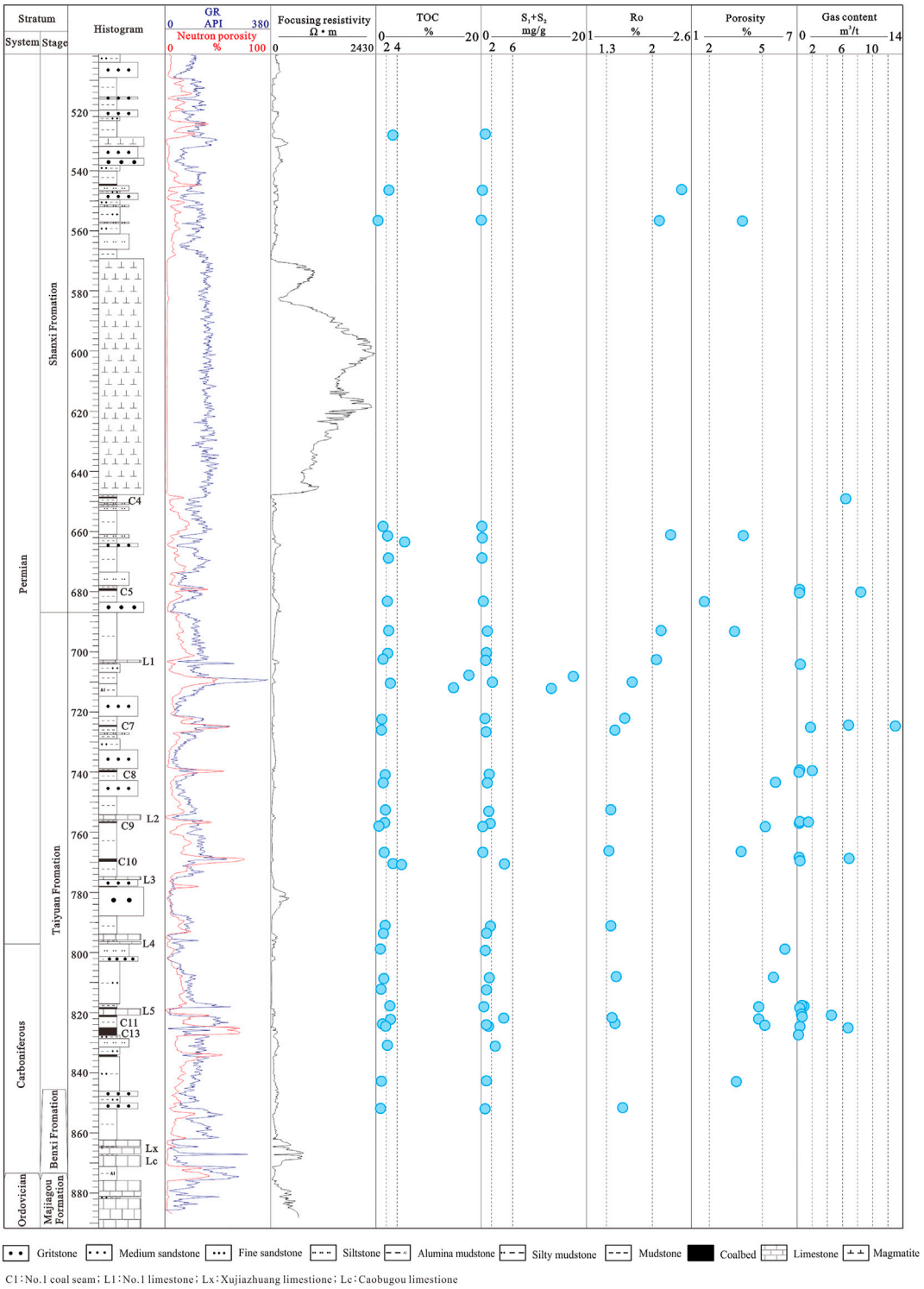

FIGURE 4
Geochemical and physical characteristics of the coal-measure source rock in Well Cq16.

Combined with the maximum reflectance data of shale vitrinite retrieved from the coalfield boreholes in the area, most shales of the Shanxi Formation and Taiyuan Formation in the whole study area occurred at the medium-mature stage and had entered the favorable area for SG generation. The organic matter maturity in the south was relatively low, mostly between 0.7% and 0.9%, followed by that in the east, while the maturity of the magmatic rock intrusion zone at the center was the highest.

4.2.3 Kerogen type

The sapropel, exinite, vitrinite, and inertinite contents in the coal seam of the Taiyuan Formation in adjacent Well Lay1 ranged

TABLE 2 Maceral content of shale in Wells Cq16 and Lay1.

Well number	Layer	Depth/m	Sapropelite/%	Exinite/%	Vitrinite/%	Inertinite/%	Type of organic matter
CQ16	Shanxi Formation	545.03	0	29	65	6	III
		660.51	0	60	22	18	III
	Taiyuan Formation	692.25	0	62	32	6	II2
		709.6	8	72	15	5	II2
		721.71	11	80	7	2	II1
		752.22	64	25	8	3	II1
		790.94	82	12	5	1	I
		807.88	90	5	4	1	I
		824.0	75	15	7	3	II1
		851.72	93	3	3	1	I
Lay1	Taiyuan Formation	1685.6	4	20	68	8	III
		1686.6	2	17	69	12	III
		1687.6	1	21	72	6	III
		1688.6	3	19	70	8	III
		1689.6	4	25	61	10	III
		1690.6	5	26	61	8	III
		1691.35	2	15	68	15	III
		1694.3	0	4	81	15	III
		1694.8	3	12	69	16	III
		1739.6	20	20	54	6	III
		1742.3	15	12	63	10	III
		1741.33	11	10	69	10	III
		1743.3	4	12	76	8	III
		1744.3	0	3	82	15	III
		1745.4	0	2	85	13	III

from 0% to 4%, 0% to 23%, 69% to 82% and 4% to 22%, respectively. The type of organic matter was Type III, which is consistent with the type of organic matter in the coal seam of the Taiyuan Formation in Well Liaogu2 (Hu et al., 2015). Since there are no measured data regarding the type of organic matter in the coal seams of the Shanxi Formation and Taiyuan Formation in the area, the type of organic matter in the coal seams in Wells Lay1 and Liaogu2 was determined to be Type III.

The sapropel content of shale in the Shanxi Formation in Well Cq16 reached 0, the exinite content ranged from 29% to 60%, the vitrinite content ranged from 22% to 65%, the inertinite content ranged from 6% to 18%, the TI value ranged from −40 to −5, and the organic matter type was Type III. The shale sapropel content in the Taiyuan Formation ranged from 0% to 93%, the exinite content ranged from 3% to 80%, the vitrinite content ranged from 3% to 32%, and the inertinite content ranged from 1% to 6% (Table 2). The organic matter type mainly included Type II, followed by Type I. The shale sapropel content in the Taiyuan Formation in Well Lay1 ranged from 0% to 20%, the exinite content ranged from 2% to 26%, the vitrinite content ranged from 54% to 85%, the inertinite content ranged from 6% to 16%, and the organic matter type was Type III.

4.3 Physical characteristics of the reservoir cap

4.3.1 Pore and fracture characteristics

The mercury injection porosity test results for the coal samples indicated that with increasing coal rank, the porosity of medium-rank coal seams first decreased from 4.29% to 2.72% and then increased to 4.56%, and the average porosity of the high-rank coal seams reached 5.38% (Meng, 2011). The pores of the coal reservoirs in the area were dominated by micropores (Meng, 2011). In Wells Zg18, Zg22 and Zg26, the permeability of each coal seam measured *via* the injection/pressure drop method exhibited a wide range and high heterogeneity. The permeability of the No. 7 coal seam ranged from 0.30 to 5.56 mD, that of the No. 10 coal seam was 0.53 mD, and that of the No. 13 coal

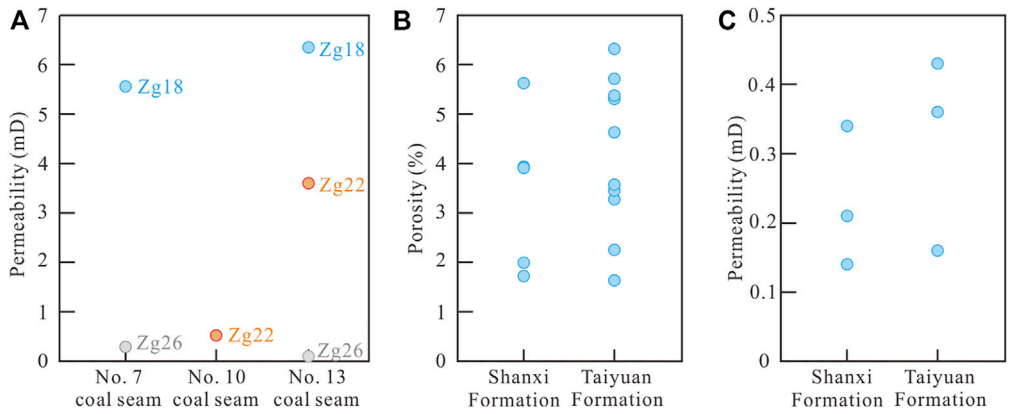

FIGURE 5
Permeability **(A)** of the No. 7, 10 and 13 coal seams in Wells Zg18, Zg22 and Zg26, and porosity **(B)** and permeability **(C)** of shale in the Shanxi Formation and Taiyuan Formation of Well Cq16.

seam ranged from 0.12 to 6.35 mD (Figure 5). In summary, the coal seams could be classified as a low-porosity and low-permeability reservoir.

The macrofractures in the coal reservoirs were more well developed than the microfractures. Fracture development was obviously affected by tectonic movement stress. The macrofractures could further connect several independently developed microfracture groups into a larger fracture system, thus generating an important seepage channel facilitating CBM diffusion, which more favorably affects the permeability of coal reservoirs. The microcracks are difficult to identify with the naked eye and can only be observed with a microscope or scanning electron microscope. The length of the microcracks is tens of microns to several millimeters, the height is hundreds of microns, and the width is on the scale of micrometers (Fu et al., 2007).

Microfractures were more developed in bright and semibright coal rock strata. The macroscale coal body structures of the No. 7, 10 and 13 coal seams mainly comprised primary and cataclastic structures. The macroscale coal rock types included semibright and semidark coal, with a largely moderate connectivity. Fractures were well developed. The main fractures ranged from 0.3 cm to 6.0 cm in length, the height ranged from 0.2 cm to 4.5 cm, the density ranged from 4 to 25 every 10 cm, and secondary fractures were not developed. The microscale coal rock type comprised semidark coal, with poor to moderate connectivity, slightly developed fractures and a slight overall fracture density difference, among which the No. 10 coal seam contained the most well-developed fractures (Table 3). The microscopic type in the area exhibited a crack width of >5 μm, and fractures with a length of 10 mm≥L≥1 mm constituted the main part. Compared to the Ordos Basin, Qinshui Basin and Lianghuai Coalfields in the North China Craton (Yao, 2006; 2007; Hu, 2016; Zhang, 2017), the width and length of the microfractures in the Huanghebei Coalfield were larger, but the spatial density was slightly lower.

The porosity of the shale of the Shanxi Formation in Well Cq16 ranged from 1.73% to 5.63%, and the permeability ranged from 0.14 to 0.34 mD (Figure 5). The porosity of the shale of the Taiyuan Formation ranged from 1.63% to 6.32%, and the shale permeability ranged from 0.16 to 0.43 mD (Figure 5). The shale of the Taiyuan Formation and Shanxi Formation revealed similar porosity and permeability conditions, both belonging to low-porosity and low-permeability reservoirs.

4.3.2 Mechanical properties

Rocks with a high elastic modulus and low Poisson's ratio are relatively more brittle and are more likely to form natural and pressure-induced fractures (Yan et al., 2015). The compressive strength of rocks with natural fractures is lower (Miao et al., 2021). The rock mechanical property test results of Wells Zg18, Zg22, Zg26 and Cq16 indicated that the elastic modulus of the shale of the Shanxi Formation was 9.6 GPa, Poisson's ratio was 0.18. Moreover, the elastic modulus of the shale of the Taiyuan Formation ranged from 6.7 to 18.3 GPa, with an average of 10.19 GPa, and Poisson's ratio ranged from 0.09 to 0.19, with an average of 0.15. The elastic modulus and Poisson's ratio of the shale above were lower than those of the Bakken, Marcellus, Woodford, Eagle Ford, Haynesville, Barnett, Jiaoshiba and other typical SG reservoirs in China and elsewhere (Sheng et al., 2016). The tensile strength of the shale of the Shanxi Formation in Wells Zg18, Zg22, Zg26 and Cq16 was 2.51 MPa, and the compressive strength reached 32.1 MPa. The tensile strength of the shale of the Taiyuan Formation ranged from 0.66 to 5.13 MPa, with an average of 1.61 MPa, and the compressive strength ranged from 12.6 to 74.9 MPa, with an average of 31.08 MPa (Figure 6). The tensile and compressive strengths of the shale were low. The above mechanical parameters comprehensively indicate that the shale in this area exhibited favorable fracturing properties.

4.4 Gas occurrence trend and gas-bearing characteristics

The Langmuir volume (V_L) represents the maximum adsorption capacity of the reservoir, and the Langmuir pressure (P_L) reflects the difficulty of reservoir analysis (Fu, 2007). The isothermal adsorption

10.3389/feart.2023.1104418

TABLE 3 Microfracture characteristics of the coal seams in the Huanghebei Coalfield.

Coal seam	Coal petrographic type	Connectivity	Fracture development degree	Main fissure				Secondary fissure			
				Length (cm) min-max/average	Height (cm) min-max/average	Width (μm) min-max/average	Density (strip/10 cm)	Length (cm) min-max/average	Height (cm) min-max/average	Width (μm) min-max/average	Density (strip/10 cm)
7	Semidark coal	Poor-Medium	Relatively developed	0.01–3.3/0.54	0.04–1.5/0.44	1–90/11	28	0.04–0.8/0.21	0.03–0.6/0.21	1–20/7	1.2
10	Semidark coal	Medium	Developed	0.005–1.2/0.28	0.005–1.2/0.22	1–50/10	84	0.005–0.5/0.09	0.005–0.8/0.16	1–30/6	5.4
13	Semidark coal	Poor-Medium	Relatively developed	0.01–1.8/0.33	0.01–2.3/0.51	1–40/8	21–39	0.01–2.1/0.33	0.005–1.3/0.32	1–40/7	1.3–3.2

test results for the coal seams in the southern part of the study area demonstrate (Table 4) that the V_L of the No. 7 and 10 coal seams was large, indicating a high adsorption capacity, while the adsorption capacity of the No. 11 and 13 coal seams subjected to magmatic erosion was lower. The P_L values of the No. 11 and 13 coal seams were higher than those of the No. 7 and 10 coal seams, and desorption was relatively difficult. The coal reservoir pressure increased with increasing burial depth, among which the maximum pressure of the No. 13 coal seam reached 7.04 MPa, while the pressure gradient and gas saturation parameters of the No. 7, 10 and 13 coal seams generally indicated underpressurized and undersaturated reservoirs, respectively.

The total gas contents in the No. 5, 7 and 10 coal seams were higher than those in the No. 11 and 13 coal seams, which was mainly caused by the notable escape of coal seam gas from the No. 11 and 13 coal seams due to lower magmatic rock intrusion. The molecular diameter of N_2 is small, which easily diffuses and migrates over a long distance and gradually becomes enriched along the direction of CMG transport (Shen et al., 2021). CBM in the No. 5, 7 and 10 coal seams in the study area was dominated by CH_4, followed by N_2, while the CBM occurring in the No. 4, 11 and 13 coal seams was dominated by N_2, followed by CH_4, which confirms that CBM near magmatic rocks had migrated throughout the transport system.

The measured data of the SG content were all retrieved from Well Cq16. The gas content in the two shale samples of the Shanxi Formation ranged from 0.25 to 0.34 m^3/t, with an average of 0.30 m^3/t. The gas content in the 14 shale samples of the Taiyuan Formation ranged from 0.17 to 6.80 m^3/t, with an average of 0.93 m^3/t. According to the gas logging data of Wells Zg18, Zg22 and Zg26, gas logging anomalies were observed in the shale section, fine sandstone section, limestone section and a small range of the magmatic rock section between the No. 5 coal seam and No. 13 coal seam floor; notably, SG, TG, carbonate rock gas and magmatic rock gas occurred, respectively. The measured data of SG in the study area were relatively limited, but a large amount of TOC data was available. Because the TOC content is positively correlated with the gas content (Zou et al., 2014), a linear relationship model (Li et al., 2021) could be established between the SG and TOC contents in the Luxi uplift area (Figure 7), and the SG content in the area was thus estimated to vary between 0.25 and 0.53 m^3/t according to the TOC content.

4.5 Creation of several independent gas-bearing systems by the key gas barrier

The coal-measure hydrocarbon source rock exhibited a moderate organic matter abundance, satisfactory hydrocarbon generation potential and wide-covering sedimentary characteristics. The source rock was mainly developed in the TST and HST of sequence SIII2 and the TST of sequence SIII3. The source rock comprised a lagoon tidal flat and lower delta plain deposit. The CMG reservoir forming characteristics, such as source reservoir dependency, reservoir cap interaction, and multiple seals, yield a complex gas–water distribution relationship in coal measures, and multifluid pressurized systems are often developed vertically (Yang et al., 2021). Figure 2 shows that each gas-bearing interval was stably developed. There occurred lagoon facies of the Taiyuan Formation and thick fine sediments of the interdistributary bay of the Shanxi Formation between the intervals, which could be regarded as regional cap rocks and were

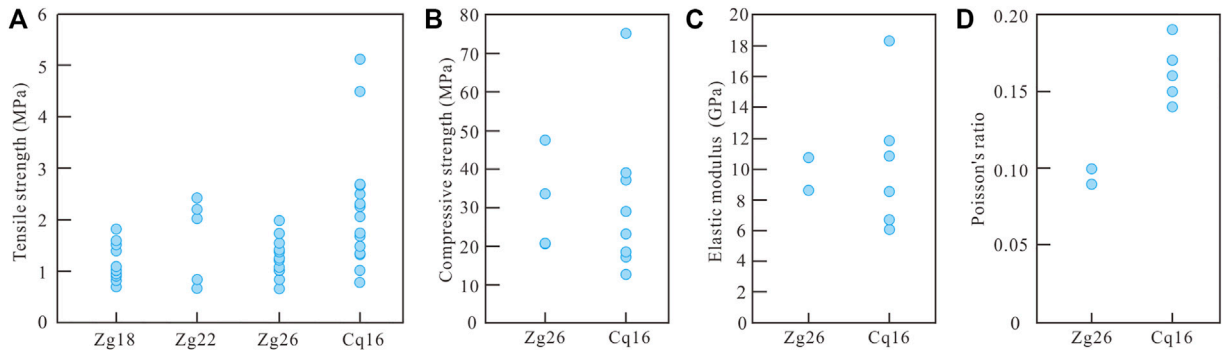

FIGURE 6
Mechanical parameters of shale rock in the Taiyuan Formation of Wells Zg18, Zg22, Zg26 and Cq16, including tensile strength **(A)**, compressive strength **(B)**, elastic modulus **(C)** and Poisson's ratio **(D)**.

relatively independent gas-bearing units. The siderite mudstone layer was characterized by a low porosity and permeability and high breakthrough pressure. As a key layer of water and gas resistance developed near the most extensive flooding surface, it formed the boundary of the coal series superimposed gas-bearing system (Shen et al., 2017). The main Carboniferous-Permian SG layers in western Shandong generally contain siderite (Zhang et al., 2020). The distribution of the siderite mudstone layer plays an important role in the development of independent gas-bearing units.

The discovery of carbonate gas indicates that the marine limestone marker bed is a reservoir rather than a gas barrier. Due to the influence of multistage transgression, for example, coal-measure limestone can develop into a suitable reservoir with many fractures/fractures or even karst caves, which can form a carbonate gas reservoir after receiving external CMG (Fu, 2018; Shi et al., 2020). The Taiyuan Formation in this area contains multiple well-developed marine marker beds with well-developed fractures and a certain gas storage space. The gas logging data for Wells Zg18, Zg22 and Zg26 indicated gas logging anomalies in the L2, L3 and L5 limestone marker beds, which were mainly caused by the migration of received near-source CMG.

The Ordos Basin and Bohai Bay Basin generally develop weathering crust karst reservoir paleogeomorphic gas reservoirs atop the Ordovician System, forming a reservoir cap combined with the bauxite mudstone of the Benxi Formation (Liang et al., 2016; Chi et al., 2021). There are many cases of high-angle normal faults cutting the Ordovician limestone roof in the study area. Against the structural background of the regional gentle monocline and NW-trending stepped normal faults, deep CMG migrates vertically and laterally along the fault to the top of the Ordovician to form near-source gas reservoirs. The sandstone reservoirs in the study area mainly include tidal flat facies sand bodies of the Taiyuan Formation, distributary channel sand bodies of the Shanxi Formation and fluvial facies of the Shihezi Formation. The sand bodies exhibited favorable physical properties and high heterogeneity. They were superimposed and inlaid in the coal measures during many periods. The vertical thickness was large, and they provided the basis for the development of large areas of multilayer high-quality reservoirs. Under the condition of satisfactory wall rock capping, coal measures are mostly developed in low-abundance gas field areas with notable small-scale segmentation and a large number of gas reservoirs (Li et al., 2021). At present, only shallow tight sandstone gas has been found in the Taiyuan Formation in the southern part of the study area. It is believed that with the further development of deep exploration in the north, CMG originating from magmatic rocks, fault systems, microfractures and hydrodynamic transport systems can be found in the sand bodies of the Shanxi Formation and Shihezi Formation. Therefore, the deep Ordovician top boundary weathering crust, Shanxi Formation and Shihezi Formation sand bodies in the study area should be the focus of CMG exploration in this area.

4.6 Types of CMG reservoirs

The types of CMG reservoirs can be divided into unconventional continuous-type (source coalbed gas, source SG and near-source TG) and conventional trap-type reservoirs (Zou et al., 2019). Gas reservoirs often repeatedly overlap, and there are multiple types of gas reservoir combinations (Zhu et al., 2016). At present, Carboniferous–Permian CMG reservoirs are found in the southern part of the study area and are mainly near-source and source reservoirs. Due to the relatively large burial depth of the main hydrocarbon source rocks in the northern part of the study area, no targeted drilling has been performed. However, according to the current geological understanding, it is believed that there exists a higher possibility of remote source gas reservoirs or conventional trap-type gas reservoirs in the north. Coal seams are prone to vertical migration due to the presence of numerous developed vertical fractures. Moreover, shale fractures are not developed, the bedding direction permeability is obviously higher than the vertical direction permeability, and lateral migration easily occurs. CMG mainly undergoes rapid overpressure flow migration driven by hydrocarbon generation pressurization and molecular diffusion flow migration driven by the hydrocarbon concentration gradient under the effect of the residual pressure difference with the source reservoir.

According to the spatial combination type of source, reservoir and cap rock, the CMG reservoirs in the Huanghebei Coalfield can be divided into three types (Figure 8), namely, heterogeneous gas reservoirs, self-sourced gas reservoirs and self-sourced+heterogeneous near-source superimposed gas reservoirs. The Shanxi Formation mainly contains SG reservoirs, namely, self-sourced gas reservoirs. There are many types of gas reservoir combinations in the Taiyuan Formation, including coalbed gas, SG,

TABLE 4 Analysis results of the CBM content in each coal seam.

Coal seam	Total gas content (m^3/t)	CH_4 concentration (m^3/t)	Gas composition (%)			Langmuir volume (m^3/t)		Langmuir pressure (MPa)	Reservoir pressure (MPa)	Pressure gradient (MPa/100 m)	Gas saturation (%)	Permeability (mD)	R_o (%)
			CH_4	CO_2	N_2	Air dried basis	Dry ash free base						
4	6.44 (1)	1.24 (1)	21.73 (1)	0.15 (1)	73.46 (1)	—	—	—	—	—	—	—	—
5	8.42 (1)	3.84 (1)	58.20 (1)	6.65 (1)	33.30 (1)	—	—	—	—	—	—		0.78–2.26/1.08 (6)
7	0.32–12.99/6.32 (8)	0.23–10.55/5.05 (8)	5.47–95.68/56.13 (8)	0.58–10.03/3.84 (8)	1.05–90.70/39.88 (8)	24.81–28.22/26.21 (3)	34.93–37.40/36.11 (3)	3.26–3.51/3.34 (3)	0.49–5.52/3.00 (2)	0.10–0.97/0.54 (2)	26–73	0.30–5.56/2.93 (2)	0.66–3.72/1.28 (38)
10	0.35–16.54/6.76 (10)	0.12–16.29/5.77 (10)	9.86–98.58/63.15 (10)	0.40–16.66/4.20 (10)	0.40–73.48/32.53 (10)	29.46–30.57/30.02 (2)	37.12–38.17/37.65 (2)	3.04–3.40/3.22 (2)	4.20 (1)	0.80 (1)	59	0.53 (1)	0.61–4.52/1.51 (42)
11	0.35–4.55/2.01 (3)	0.11–1.09/0.54 (3)	32.82–39.92/36.57 (3)	0.47–4.23/2.44 (3)	54.00–66.70/59.83 (3)	19.09 (1)	21.94 (1)	5.92 (1)	—	—	—	—	0.62–6.35/2.22 (69)
13	0.13–6.73/1.78 (11)	0.03–3.66/1.19 (11)	0.64–76.07/35.28 (11)	0.16–16.20/6.18 (11)	4.90–96.48/55.21 (11)	25.19–29.33/26.97 (2)	32.13–40.87/36.05 (2)	4.03–4.21/4.13 (2)	6.02–7.04/6.46 (3)	0.85–0.93/0.89 (2)	1–4	0.12–6.35/3.36 (3)	0.62–5.87/1.49 (117)

CBM, content analysis was conducted for Well Cq16 at the No. 4, 5, 7, 10, 11 and 13 coal seams, for Well Zg18 at the No. 7, 10 and 13 coal seams, for Well Zg22 at the No. 7, 10 and 11 coal seams, and for Well Zg26 at the No. 7, 10, 11 and 13 coal seams. Isothermal adsorption tests were carried out for nine layers of coal in Wells Zg18, Zg22 and Zg26, and injection/pressure drop tests were carried out for six layers of coal. In addition, the following data were obtained from the previous exploration report: six vitrinite reflectance values for the No. 5 coal seam, 4 gas contents and 35 vitrinite reflectance values for the No. 7 coal seam, 6 gas contents and 40 vitrinite reflectance values for the No. 10 coal seam, 68 vitrinite reflectance values for the No. 11 coal seam, and 8 gas contents and 114 vitrinite reflectance values for the No. 13 coal seam. Similar data structure 0.32-12.99/6.32 (8) represented min-max/average (number of data).

10.3389/feart.2023.1104418

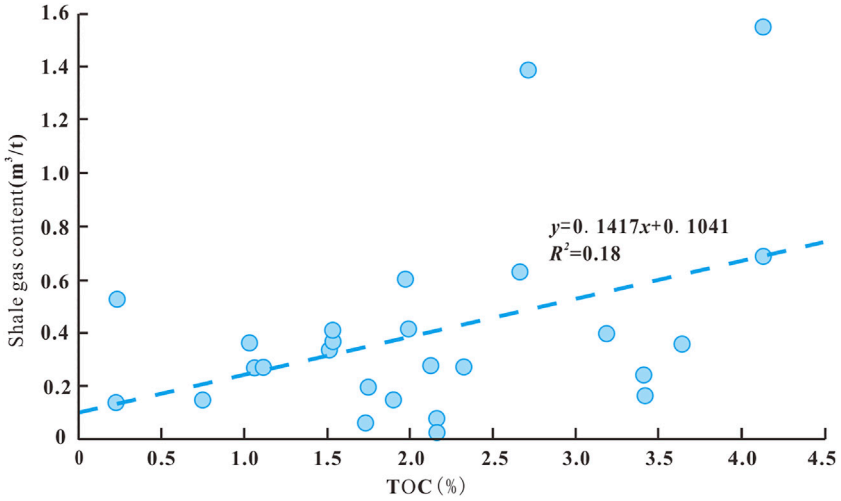

FIGURE 7
Linear relationship between the SG and TOC contents in the western Shandong coal-bearing area Li et al., 2021.

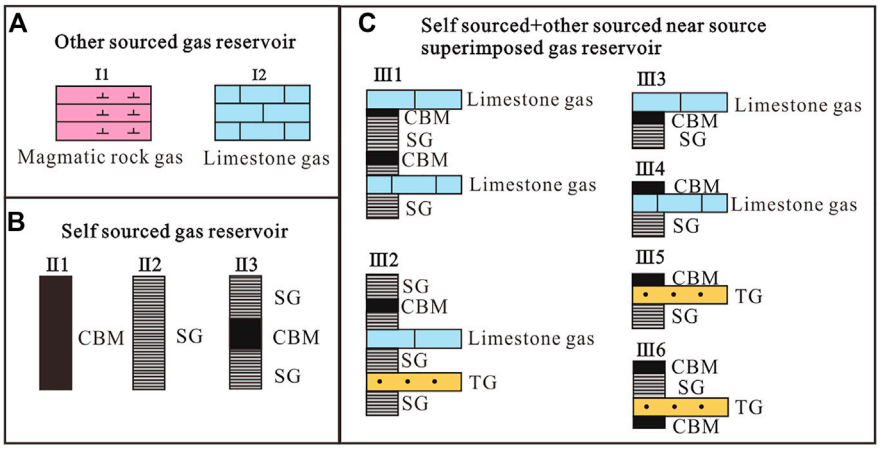

FIGURE 8
Three types of CMG reservoirs, namely, other-source gas reservoirs **(A)**, self-sourced gas reservoirs **(B)** and self-sourced+other-source near-source superimposed gas reservoirs **(C)**.

tight sandstone gas, carbonate rock gas and magmatic rock gas reservoirs. Self-sourced gas reservoirs and self-sourced+other-source near-source gas reservoirs dominate, followed by other-source gas reservoirs. Among them, self-sourced gas reservoirs and self-sourced+other-source near-source gas reservoirs exhibit the highest gas content and the most obvious gas logging anomalies.

(1) Type I: Other-source gas reservoir.

This type of gas reservoir contains independent magmatic rock gas and carbonate rock gas units (I1-I2), which is mainly a fracture-type reservoir, and the gas source encompasses near-source coalbed gas and SG. Deep natural gas vertically and laterally migrated and accumulated in the fractures of limestone and magmatic rock and was sealed by the overlying thick fine sediment for preservation. The abnormal section of limestone gas logging was obviously wider than that of magmatic rock, indicating that the reservoir space was more notably developed.

(2) Type II: Self-sourced gas reservoir.

This type of gas reservoir mainly exists independently or in combination with CBM and SG reservoirs and can be divided into three combinations (II1-II3). In combination II3, CBM mainly migrates vertically into the SG reservoir, and the overall gas content gradually decreases from the center of the coal seam toward the shale at the top and bottom.

(3) Type III: Self-sourced + other-source near-source superimposed gas reservoir.

CBM, SG, TG and carbonate rock gas reservoirs overlap, and there are six combinations (III1-III6). CBM mainly play the role of vertical interbed migration paths, supplying gas to adjacent limestone and tight sandstone reservoirs. SG is mainly transported along transverse layers to balance the gas energy.

Figure 2 shows that when the roof and floor of the coal seam solely comprise shale or silty mudstone, the overpressure peak pointing

TABLE 5 Overview of CBM resources.

Coal seam	Medium-rank CBM (10^8 m^3)	High-rank CBM (10^8 m^3)	Total (10^8 m^3)
5	36.19	6.70	42.89
7	39.48	5.67	45.15
10	34.08	4.76	38.84
13	6.82	4.19	11.01
Total	116.57	21.32	137.89

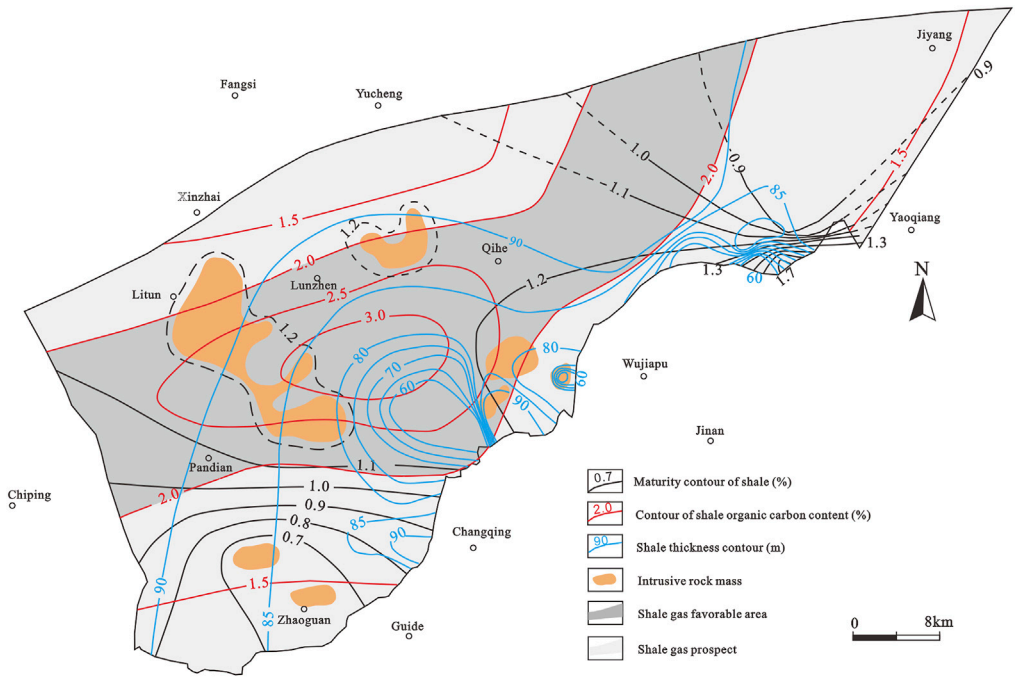

FIGURE 9
Distribution of shale thickness, TOC, maturity and favorable areas in the Shanxi Formation and Taiyuan Formation.

TABLE 6 Reference standard for SG area selection in the Huanghebei Coalfield.

Constituency	Thickness of the shale series	TOC (%)	Ro (%)	Burial depth (m)	Surface conditions	Preservation conditions	Magmatic rock development
Favorable area	Ratio of the effective shale series to the stratum thickness: >60%; the thickness of a single layer mudstone: >6 m; and the continuous thickness: ≥30 m	Average not less than 2.0%	Type II kerogen ≥0.9%; Type III kerogen ≥0.7%	500 ~ 4500	Preferably	Medium structure, continuous stratigraphic development, and a traceable correlation	Close to the target stratum series, without intruding into the effective rock stratum
Prospective area	No requirement	Average not less than 0.5%	Not less than 0.4%	100 ~ 4500	Preferably	There is development and a certain distribution of regional shale series, with general preservation conditions	No requirement

phenomenon easily occurs, such as in the II3 and III2 combinations. The reason is that when the coal seam and shale function as cap rocks, the hydrocarbon generation capacity of the coal seam is better than that of shale, which plays a role in inhibiting and preventing the escape of shale hydrocarbons, and the shale sealing capacity is notable. Self-generated gas can mitigate the concentration sealing effect of CBM

migration (Zhu et al., 2016). When the top or bottom of the coal seam comprises limestone, the limestone provides poor porosity and permeability conditions, but fissures are relatively well developed, CBM escapes into the limestone under the sealing effect of mudstone, and the peak amplitude of the coal seam is reduced to a certain extent. The shale limits the gas escape process due to the high hydrocarbon generation intensity of the coal seam, such as the III1, III3, and III4 combinations. When the roof of the coal seam comprises argillaceous shale or silty mudstone and the floor comprises fine sandstone, as CBM can diffuse along the underlying stratum through fine sandstone with relatively favorable porosity and permeability conditions, the amplitude of the CBM peak is reduced to a certain extent, such as the III5 combination. When the roof of the coal seam comprises fine sandstone, due to the poor sealing conditions of the fine sandstone, the peak pointing phenomenon of CBM is not obvious. For example, in combination III6, CBM at the bottom escapes into the fine sandstone to form tight sandstone gas. At the same time, CBM enters the overlying shale and coalbed through the fine sandstone migration medium, thus enhancing the peak pointing phenomenon of overpressure in the upper coal seam. In general, the interbedded combination of coal seams and shale is the most conducive to CMG preservation, and the overall gas content is high.

5 Resources and evaluation of the CMG accumulation system

The No. 5, 7, 10 and 13 coal seams are the main CBM reservoirs in this area and are also the target reservoirs in this paper. According to the regulation of coalbed methane reserve estimation (DZ/T 0216-2020), the methods for estimating CBM resources are the volume method and analogy method. The volume method is the basic method for estimating the geological reserves of CBM, which is applicable to the calculation of CBM reserves at all levels. Its accuracy depends on the understanding of the extent of block exploration, geological conditions and reservoir conditions. The analogy method is mainly based on comparison of the geological parameters and engineering parameters of the developed CBM fields or adjacent CBM fields and is often used when the exploration degree of the block is low. Therefore, the volume method is used to estimate the CBM resource quantity. The estimation formula is

$$G_i = 0.01AhDC_{ad} \quad (1)$$

where G_i is the geological reserves of coalbed methane, 10^8 m^3; A is the coal seam gas bearing area, km^2; h is the net thickness of the coal seam, m; D is the apparent density of coal on an air-dried basis, t/m^3; and C_{ad} is the air content of coal on an air-dried basis, m^3/t.

The shallow area with an elevation of −500 m belongs to the wind oxidation zone, and the resource quantity is thus not estimated. Based on the data of 569 coalfield boreholes and 4 CBM boreholes in 20 exploration areas within the Huanghebei Coalfield and relevant test data, the CBM resource quantity at an elevation ranging from approximately −500 to −2000 m was evaluated using the volume method (Table 5). The estimated area was 2267 km^2, the initial thickness of the coal seam was 0.50 m, and the initial standard of the CBM content was 1 m^3/t (air-dried basis). The CBM resources of the No. 5, 7, 10 and 13 coal seams amounted to 42.89 × 10^8 m^3, 45.15 × 10^8 m^3, 38.84 × 10^8 m^3 and 11.01 × 10^8 m^3, respectively, with total resources of 137.89 × 10^8 m^3. Among them, the resource amount of medium-rank CBM was 116.57 × 10^8 m^3, and the high-rank CBM resource amount reached 21.32 × 10^8 m^3.

To reflect the current situation of SG resource exploration in the study area more accurately, based on Zhang et al.'s (2012) optimal conditions for favorable and prospective areas of SG in China, the criteria for the selection of favorable areas were adjusted according to the control degree in this SG survey. Please refer to Table 6 for specific criteria for area selection. As such, favorable and prospective areas for the development of SG resources in the Carboniferous–Permian system could be identified in the Huanghebei Coalfield (Figure 9). According to the standard for shale gas resources and reserves estimation (DZ/T 0254-2020), the analogy method, volumetric method and volumetric method can be used for shale gas resource estimation. Different from the other two methods, the analogy method is applicable to the estimation unit without measured gas content and gas saturation data. If the shale section does not contain crude oil, the volume method can be used to estimate the total shale gas resources.

$$Q = 0.01A_g h\rho_y C_Z \quad (2)$$

where Q is the total resources, 10^8 m^3; A_g is the gas bearing area, km^2; h is the effective thickness, m; ρ_y is the shale mass density, t/m^3; and C_z is the total gas content in the shale interval, m^3/t.

Since the measured total shale gas content in the area is limited, the total shale gas content in each block can be estimated using TOC data through the linear relationship model of shale gas content and TOC content (Figure 7). The total amount of SG resources was estimated at 2100.45×10^8 m^3 *via* the volumetric method. Among them, the resource amount in the favorable area reached 1075.77×10^8 m^3, with a resource amount of 1024.68×10^8 m^3 in the prospective area.

6 Conclusion

Based on source reservoir geochemical characteristics, reservoir cap physical properties and gas-bearing properties, the reservoir-forming effect of the CMG accumulation system in the Huanghebei Coalfield was analyzed, and the potential of CMG resources was evaluated. The following three main conclusions could be obtained:

(1) The CMG source rocks mainly included the shale and coal seams of the Taiyuan Formation and Shanxi Formation, providing a favorable material basis for CMG enrichment. The coal seams were mainly mature to highly mature coal seams, with a satisfactory hydrocarbon generation potential. They belonged to low-porosity, low-permeability, underpressurized and undersaturated reservoirs. The N_2 content among the CBM components greatly affected by faults, magma and other transport systems exceeded the CH_4 content. The shale organic matter was mainly Type II, with a moderate organic matter abundance. The material reached the middle-to high-maturity stage, provided satisfactory hydrocarbon generation potential, belonged to a low-porosity and low-permeability reservoir, and exhibited favorable fracturing properties.

(2) As regional caprocks, the thick fine sediments of the lagoon facies of the Taiyuan Formation and the interdistributary bay of the Shanxi Formation, combined with the sideritic mudstone of the

key gas barrier, created several stable and independent gas-bearing systems. The combination types of CMG reservoirs mainly included self-sourced gas reservoirs and self-sourced+heterogeneous near-source gas reservoirs, followed by heterogeneous gas reservoirs. CBM and SG play vertical and horizontal regulatory roles, respectively. Sand bodies, magmatic rocks, fault systems, microfractures and hydrodynamic forces, as macroscale transport systems, expand the development space of heterogeneous gas reservoirs.

(3) CMG in the Huanghebei Coalfield mainly includes SG, coalbed gas and a small amount of tight sandstone gas, carbonate rock gas and magmatic rock gas. The SG and CBM resources are abundant, and the CBM resource amount is $137.89 \times 10^8\ m^3$, while the coal SG resource amount reaches $2100.45 \times 10^8\ m^3$.

Data availability statement

The original contributions presented in the study are included in the article/supplementary material, further inquiries can be directed to the corresponding authors.

Author contributions

YSH and YG: Contributed equally to this research. YSH, XH, YW, SZ, YZ, and LS: Field investigation. XH, YSO, MW, KC, and QY: Data analysis. YSO: Writing—original draft preparation. YSO, HW, YG, and XH: Writing—review and editing. All authors listed have made substantial, direct, and intellectual contributions to the work and approved it for publication.

Funding

This study was carried out in the financial support of the 2022-2023 key scientific research project of Shandong Coalfield Geology Bureau (2022-17, 2022-18 and 2022-55), Natural Science Foundation of Shandong Province (ZR2020MD031), and the special fund project of geological exploration in Shandong Province Exploration Prospect (2013-6 and 2013-144). We thank our scientific research team for their help and guidance in the field investigation.

Conflict of interest

The authors declare that the research was conducted in the absence of any commercial or financial relationships that could be construed as a potential conflict of interest.

Publisher's note

All claims expressed in this article are solely those of the authors and do not necessarily represent those of their affiliated organizations, or those of the publisher, the editors and the reviewers. Any product that may be evaluated in this article, or claim that may be made by its manufacturer, is not guaranteed or endorsed by the publisher.

References

Bi, C. Q., Hu, Z. F., Tang, D. Z., Tao, S., Zhang, J. Q., Tang, S. L., et al. (2021). Research progress of coal-measure gas and some important scientific problems. *Geol. China* 48 (2), 402–423. (in Chinese with English Abstract). doi:10.12029/gc20210205

Bi, C. Q., Zhang, J. Q., Shan, Y. S., Hu, Z. F., Wang, F. G., Chi, H. P., et al. (2020). Geological characteristics and co-exploration and co-production methods of Upper Permian Longtan coal measure gas in Yangmeishu syncline, Western Guizhou Province, China. *China Geol.* 3 (1), 38–51. doi:10.31035/cg2020020

Cao, D. Y., Yao, Z., and Li, J. (2014). Evaluation status and development trend of unconventional gas in coal measure. *Coal Sci. Technol.* 42 (1), 89–105. (in Chinese with English Abstract). doi:10.13199/j.cnki.cst.2014.01.021

Chen, Y. H., Lin, Y. X., and Jiang, H. C. (2003). The potential of gas generation from coal bearing formation in Huimin Sag. *Coal Geol. Explor.* 31 (03), 26–29. (in Chinese with English Abstract).

Chi, X. Q., Feng, Q. H., Xu, S. M., and Shu, P. (2021). Facies control of weathering crust reservoir in mawu1-4 sub-members of Ordos Basin: Case study of tao 2 block in sulige gas field. *Nat. Gas. Geosci.* 32 (09), 1358–1371. (in Chinese with English Abstract). doi:10.11764/j.issn.1672-1926.2021.03.013

Clarkson, C. R. (2013). Production data analysis of unconventional gas wells: Workflow. *Int. J. Coal Geol.* 109-110, 147–157. doi:10.1016/j.coal.2012.11.016

Cui, X. C. (2004). *Evaluating on coal gas source rock of Carboniferous-Permian in Huanghebei coalfield and Jiyang basin*. Qingdao: Shandong University of Science and Technology. (in Chinese with English Abstract).

Dai, J. X., and Gong, J. M. (2018). Establishment of coal-derived gas geological theory and its strategic significance to the development of natural gas industry in China. *China Pet. Explor.* 23 (04), 1–10. (in Chinese with English Abstract). doi:10.3969/j.issn.1672-7703.2018.04.001

Fan, S. Y., Wu, X. R., and Guo, J. P. (2001). Evaluation of coal gas resource in Huanghebei coal field, Shandong Province. *Geol. China* 28 (6), 28–30. (in Chinese with English Abstract). doi:10.3969/j.issn.1000-3657.2001.06.005

Fu, X. H., Chen, Z. S., Song, R., and Zhang, Q. H. (2018). Discovery of coal measures limestone gas and its significance. *Coal Geol. China* 30 (06), 59–63. (in Chinese with English Abstract). doi:10.3969/j.issn.1674-1803.2018.06.12

Fu, X. H., Ge, Y. Y., Liang, W. Q., and Li, S. (2013). Pressure control and fluid effect of progressive drainage of multiple superposed CBM systems. *Nat. Gas. Ind.* 33 (11), 35–39. (in Chinese with English Abstract). doi:10.3787/j.issn.1000-0976.2013.11.006

Fu, X. H., Qin, Y., and Wei, C. T. (2007). *Coalbed gas geology*. Xuzhou: China University of Mining and Technology Press. (in Chinese with English Abstract).

He, R. W., Du, Y. M., Liu, J., and Liu, Y. L. (2005). Gas generation model of Permo-Carboniferous coal in south slope of Huimin Sag. *Coal Geol. Explor.* 33 (4), 42–44. (in Chinese with English Abstract). doi:10.3969/j.issn.1001-1986.2005.04.011

Hou, X. W., Zhu, Y. M., and Yao, H. P. (2018). Coupled accumulation characteristics of Carboniferous-Permian coal measure gases in the Northern Ordos Basin, China. *Arab. J. Geosci.* 11, 156–169. doi:10.1007/s12517-018-3512-8

Hu, X. C., Zhou, Y. Q., and Zhang, F. X. (2015). The characteristics of coal source rock in Taiyuan Formation of eastern linqing depression and its main controlling factors. *Sci. Technol. Eng.* 15 (06), 41–47. (in Chinese with English Abstract).

Hu, Z. Z., Huang, W. H., Liu, S. P., Zhang, Q., Xu, Q. L., and Feng, X. L. (2016). Study on the influencing factors of the microfracture development in coal reservoir in southern Qinshui basin. *Coal Geol. Explor.* 44 (05), 63–70. (in Chinese with English Abstract).

Huang, D. F., and Xiong, C. W. (1996). Generation, migration and evaluation of hydrocarbon generation potential of oil formed in coal-bearing strata. *Explorationist* 1 (2), 6–11. (in Chinese with English Abstract).

Huang, X. L. (2018). Study on occurrence characteristics and controlling factors of coalbed methane in Zhaoguan Coalfield. *Coal Sci. Technol.* 46 (4), 196–201. (in Chinese with English Abstract). doi:10.13199/j.cnki.cst.2018.04.031

Huang, X. L., Zhong, J. W., and Xu, Y. G. (2012). Two tales of the continental lithospheric mantle prior to the destruction of the North China Craton: Insights from Early Cretaceous mafic intrusions in Western Shandong, East China. *Geochimica Cosmochimica Acta* 96, 193–214. doi:10.1016/j.gca.2012.08.014

Jia, Q., and Lv, D. W. (2009). Sequence division and eustatic area level change of Carberours-Permian systems in Liaocheng, Shandong Province. *North West. Geol.* 42 (2), 108–115. (in Chinese with English Abstract).

Jin, Q., Song, G. Q., Liang, H. B., Cheng, F. Q., and Wang, L. (2009). Characteristics of carboniferous -permian coal-derived gas in the Bohai Bay Basin and their implication to exploration potential. *Acta Geol. Sin.* 83 (06), 861–867. (in Chinese with English Abstract).

Law, B. E., and Curtis, J. B. (2002). Introduction to unconventional petroleum systems. *AAPG Am. Assoc. Pet. Geol.) Bull.* 86, 1851–1852. doi:10.1306/61eedda0-173e-11d7-8645000102c1865d

Li, C. F., Huang, X. L., Shao, Y. B., and Dou, F. K. (2021). Shale gas exploration potential in southwestern Shandong Province of eastern China. *Front. Earth Sci.* 9, 1–17. doi:10.3389/feart.2021.702902

Li, G., Yang, Z. B., Gao, W., Zhang, Z. G., Jiang, B. R., and Lu, B. J. (2022). Characteristics of coal-measure gas reservoirs in thin interbedded marine–continental transitional facies and optimization of combined production: Examples from the tucheng syncline in western Guizhou. *Nat. Resour. Res.* 31 (3), 1503–1522. doi:10.1007/s11053-022-10053-8

Li, J. T., Li, Z. X., Yu, J. F., Guo, J. B., Liu, X. L., and Liu, H. F. (2022). Stratigraphic sequence correlation based on wavelet transform of well - logging data: Taking the coal-bearing strata of permian - carboniferous system in Luxi and jiyang area as an example. *Acta sedimentol. sin.* 23 (4), 639–645. (in Chinese with English Abstract).

Li, Y. G. (2019). Research on coalbed methane geological characteristics and exploration direction of No.7 coal seam in Huanghebei coalfield. *China Coalbed Methane* 16 (5), 2441. (in Chinese with English Abstract).

Li, Y., Xu, W. K., Gao, J. X., Wu, P., Tao, C. Q., Tian, Y., et al. (2021). Mechanism of coal-measure gas accumulation under integrated control of "source reservoir-transport system": A case study from east margin of Ordos Basin. *J. China Coal Soc.* 46 (08), 2440–2453. (in Chinese with English Abstract). doi:10.13225/j.cnki.jccs.CB21.0765

Li, Z. (2006). Hydrocarbon-generation evolution of permian-carboniferous source rock in jiyang depression. *Acta Pet. Sin.* 27 (4), 29–35. (in Chinese with English Abstract). doi:10.3321/j.issn:0253-2697.2006.04.006

Liang, Z., Zhou, Y. Q., Wang, R., Liu, C. G., Zhu, Z. J., and Zhang, D. B. (2016). Hydrocarbon accumulation characteristics of well Gaogu 4 coal-derived gas reservoir in eastern Linqing Depression. *Coal Geol. Explor.* 44 (04), 46–53. (in Chinese with English Abstract).

Liu, D. M., Liu, Z. S., and Cai, Y. D. (2020). Research progress on accumulation mechanism and formation geological conditions of coalbed methane. *Coal Sci. Technol.* 48 (10), 1–16. (in Chinese with English Abstract). doi:10.13199/j.cnki.cst.2020.10.001

Liu, H. J., Jia, Y. R., Long, Y. Z., and Wang, H. W. (1987). The features of the barrier island systems of the epeiric sea and their event deposits of coal bearing formations in Carboniferous of North China. *Acta Geol. Sin.* 5 (3), 73–80. (in Chinese with English Abstract).

Liu, S. L., and Guo, J. P. (2003). Igneous rock features and its influence on coal seam and coal quality of Huanghebei coalfield,Shandong Province. *Coal Geol. China* 15 (6), 14–15. (in Chinese with English Abstract). doi:10.3969/j.issn.1674-1803.2003.06.005

Ma, Y. S., and Tian, H. Q. (2006). *A comprehensive study of deep sequence paleogeography and petroleum geology in the northern part of North China basin*. Beijing: Geological publishing house. (in Chinese with English Abstract).

Meng, Y. R. (2011). *Existent features and resource assessment of coalbed methane in Shandong Province – take Huanghebei and adjacent region for example*. Qingdao, China: Shandong University of Science and Technology, 42. (in Chinese with English Abstract).

Miao, F. B., Peng, Z. Q., Wang, Z. X., Zhang, B. M., Wang, C. S., and Gong, L. (2021). Brittleness characteristics and influencing factors of marine shale of niutitang Formation in xuefeng region: A case study of well XZD-1. *Geol. China* 2021, 1–18. (in Chinese with English Abstract). Available at: http://kns.cnki.net/kcms/detail/11.1167.P.20210913.1540.010.html.

Miu, J. J. (2008). *Analysis of the secondary hydrocarbon-generation mechanism and potential of the Carboniferous-Permian coal-measure source rocks in Jiyang-Linqing Depression*. Chengdu: Chengdu University of Technology. (in Chinese with English Abstract).

Ni, P. S., Long, Q., Cheng, T., Hu, Z. P., and Chen, F. K. (2013). Geochemistry and Sr-Nd-Pb isotopic composition of late mesozoic intermediate-basic rock in western Shandong block. *J. Earth Sci. Environ.* 35 (4), 62–76. (in Chinese with English Abstract).

Qin, J. Z., Li, Z. M., and Zhang, Z. R. (2005). Contribution of various coal measures source rocks to oil and gas reservoir formation. *Petroleum Explor. Dev.* 32 (04), 131–141. (in Chinese with English Abstract).

Qin, Y. (2021). Research progress and strategic thinking of coal-measure gas accumulation system and development geology. *J. China Coal Soc.* 46 (08), 2387–2399. (in Chinese with English Abstract). doi:10.13225/j.cnki.jccs.CB21.0719

Qin, Y. (2018). Research progress of symbiotic accumulation of coal-measure gas in China. *Nat. Gas. Ind.* 38 (4), 26–36. (in Chinese with English Abstract). doi:10.3787/j.issn.1000-0976.2018.04.003

Qin, Y., Shen, J., and Shen, Y. L. (2016). Joint mining compatibility of superposed gas-bearing systems: A general geological problem for extraction of three natural gases and deep CBM in coal series. *J. China Coal Soc.* 41 (1), 14–23. (in Chinese with English Abstract). doi:10.13225/j.cnki.jccs.2015.9032

Qin, Y., Xiong, M. H., Yi, T. S., Yang, Z. B., and Wu, C. F. (2008). On unattached multiple superposed coalbed-methane system: In a case of the shuigonghe syncline, zhijin-nayong coalfield, Guizhou. *Geol. Rev.* 54 (1), 65–70. (in Chinese with English Abstract). doi:10.16509/j.georeview.2008.01.015

Shao, L. Y., Dong, D. X., Li, M. P., Wang, H. S., Wang, D. D., Lu, J., et al. (2014). Sequence-paleogeography and coal accumulation of the Carboniferous-Permian in the North China basin. *J. China Coal Soc.* 39 (8), 1725–1734. (in Chinese with English Abstract). doi:10.13225/j.cnki.jccs.2013.9033

Shao, L. Y., He, Z. P., and Lu, J. (2008). *Study on sequence stratigraphy and coal accumulation of Carboniferous - Permian in the west of circum bohai bay*. Beijing: Geological publishing house. (in Chinese with English Abstract).

Shen, J., Li, K. X., Zhang, H. W., Shabbiri, K., Hu, Q. J., and Zhang, C. (2021). The geochemical characteristics, origin, migration and accumulation modes of deep coal-measure gas in the west of Linxing block at the eastern margin of Ordos Basin. *J. Nat. Gas Sci. Eng.* 91, 103965. doi:10.1016/j.jngse.2021.103965

Shen, L. J., Zhu, Y. Z., and Gao, Z. J. (2020). Paimary study on geological characteristics of Litun rock mass in Qihe-Yucheng rich iron ore area in Shandong Province. *Shandong Land Resour.* 36 (2), 23–29. (in Chinese with English Abstract). doi:10.12128/j.issn.1672-6979.2020.02.004

Shen, L. J., Zhu, Y. Z., Wang, H. H., Li, S., Gao, Z. J., Zhang, X. B., et al. (2021). Geochemical characteristics and geological significance of Litun iron ore deposit in Qihe - Yucheng area, Shandong Province. *Geol. Rev.* 67 (1), 84–98. doi:10.16509/j/georeview.2021.01.007

Shen, Y. L., Qin, Y., Guo, Y. H., Yi, T. S., Shao, Y. B., and Jin, H. B. (2012). Sedimentary controlling factor of unattached multiple superimposed coalbed-methane system formation. *Earth Sci. – J. China Univ. Geosciences* 37 (3), 573–579. (in Chinese with English Abstract). doi:10.3799/dqkx.2012.064

Shen, Y. L., Qin, Y., Shen, J., and Gu, J. Y. (2017). Sedimentary control mechanism of the superimposed gas bearing system development in the Upper Palaeozoic coal measures along the eastern margin of the Ordos Basin. *Nat. Gas. Ind.* 37 (11), 29–35. (in Chinese with English Abstract). doi:10.3787/j.issn.1000-0976.2017.11.004

Sheng, Q. H., and Li, W. C. (2016). Evaluation method of shale fracability and its application in Jiaoshiba area. *Prog. Geophys. (in Chinese)* 31 (4), 1473–1479. (in Chinese with English Abstract). doi:10.6038/pg20160409

Shi, L. Q., Liu, T. H., Zhang, X. Y., Huang, J. Y., Zhang, W., and Zhao, S. Q. (2020). Origin type and generating mechanism of coal measure limestone gas: A case study of L1 limestone gas in the Taiyuan Formation of the shenzhou coal mine, eastern edge of the Ordos Basin, China. *Enery & Fuels* 34, 10904–10914. doi:10.1021/acs.energyfuels.0c02127

Wang, H. H., Shen, L. J., Wang, D. D., Zhu, Y. Z., Li, Z. X., Wang, Y. J., et al. (2021a). Study on mesozoic magmatic intrusion and paleozoic multi-mineral Genesis mechanism in Huanghebei coalfield, Shandong Province. *Coal Geology & Exploration* 49 (2), 83–92. (in Chinese with English Abstract). doi:10.3969/j.issn.1001-1986.2021.02.011

Wang, H. H., Yin, L. S., Zhu, Y. Z., Wang, D. D., Zhou, M. L., Zhang, X. B., et al. (2021b). Paleozoic lithofacies, paleogeography and coal measures source rock development in Huanghebei region. *Coal Geology of China* 33 (1), 13–21. (in Chinese with English Abstract). doi:10.3969/j.issn.1674-1803.2021.01.03

Wang, Z. Z., Li, Z. X., and Yu, J. F. (2003). Stratigraphic sequence correlation of Permo-Carboniferous system in Luxi and Jiyang area. *Coal geology & exploration* 31 (5), 1–3. (in Chinese with English Abstract).

Xie, Q. H., Zhang, Z. C., Hou, T., Santosh, M., Jin, Z. L., Han, L., et al. (2015). Petrogenesis of the Zhangmatun gabbro in the Ji'nan complex, North China Craton: Implications for skarn-type iron mineralization. *Journal of Asian Earth Sciences* 113, 1197–1217. doi:10.1016/j.jseaes.2015.03.040

Xu, H. Z., Zhou, X. K., Gao, J. H., and Wang, X. W. (2005). Reconstruction of early-middle triassic basin in north China and hydrocarbon generation in palaeozoic. *Oil & Gas Geology* 26 (3), 329–336. (in Chinese with English Abstract). doi:10.3321/j.issn:0253-9985.2005.03.011

Yan, J. P., Yan, Y., Si, M. L. Q., Wen, D. N., Wen, X. F., and Geng, B. (2015). Relationship between fracture characteristics and "five-property" of shale reservoir. *Lithologic Reservoirs* 27 (03), 87–93+132. (in Chinese with English Abstract).

Yang, C. H., Xu, W. L., Yang, D. B., Liu, C. C., Liu, X. M., and Hu, Z. C. (2005). Chronology of the jinan gabbro in Western Shandong: Evidence from LA-ICP-MS zircon U-Pb dating. *Acta Geologica Sinica* 26 (4), 321–325. (in Chinese with English Abstract).

Yang, Q. L. (2012). *A geochemical study of Early Cretaceous mafic intrusions in the southeastern North China Block*. Hefei: University of Science and Technology of China. (in Chinese with English Abstract).

Yang, Y., Yang, C., Zhang, C. Z., Tang, W. Q., and Li, Y. (2018). Evaluation and potential analysis of coal measures source rocks in huimin sag. *Journal of Xi'an Shiyou University (Natural Science)* 33 (3), 2350. (in Chinese with English Abstract). doi:10.3969/j.issn.1673-064X.2018.03.004

Yang, Z. B., Qin, Y., Chen, S. Y., and Liu, C. J. (2013). Controlling mechanism and vertical distribution characteristics of reservoir energy of multi-coalbeds. *Acta Geologica Sinica* 87 (1), 139–144. (in Chinese with English Abstract). doi:10.3969/j.issn.0001-5717.2013.01.014

Yang, Z. B., Yi, T. S., Li, G., Yan, Z. H., Geng, D. Y., Gao, W., et al. (2021). Reservoir-forming characteristic of marine coal-measure gas and its favorable development segments: Taking the carboniferous xiangbai Formation in well longcan 1 in weining,

north Guizhou as an example. *Journal of China Coal Society* 46 (08), 2454–2465. (in Chinese with English Abstract). doi:10.13225/j.cnki.jccs.CB21.0797

Yao, Y. B., Liu, D. M., Tang, D. Z., Tang, S. H., and Huang, W. H. (2007). Preservation and deliverability characteristics of coalbed methane, North China. *Petroleum Exploration and Development* 34 (06), 664–668. (in Chinese with English Abstract).

Yu, L. P., Cao, Z. X., and Li, Z. X. (2003). Organic geochemical characteristics of carboniferous-permian hydrocarbon source rocks in jiyang depression. *Geology-Geochemistry* 31 (04), 68–73. (in Chinese with English Abstract).

Yuan, X. X. (2014). *Recognition of multi-coalbed methane bearing system: A case study of coal-bearing strata of upper permian in western Guizhou*. Xuzhou: University of Mining and Technology, 89–126. (in Chinese with English Abstract).

Zhang, C. C., Peng, W. Q., Hu, C. Q., Li, Z., Gao, B. Y., Li, Z. M., et al. (2020). Characteristics and resource potential of main shale gas reservoirs in Shandong Province. *Acta Geologica Sinica* 94 (11), 3421–3435. (in Chinese with English Abstract).

Zhang, D. W., Li, Y. X., and Zhang, J. C. (2012). *Investigation and evaluation of shale gas resource potential in China*. Beijing: Geological Publishing House, 10–138. (in Chinese with English Abstract).

Zhang, K. (2017). *Study on physical properties of differentrank coal reservoir in the eastern margin of Ordos basin (dissertation)*. Beijing: China University of Geosciences, 24–25. (in Chinese with English Abstract).

Zhang, W., Lu, J., Li, Y. J., Wang, J. Y., and Shao, L. Y. (2010). Sequence stratigraphy and coal accumulation of the Carboniferous and Permian coal measures in southwestern Shandong Province. *Journal of Palaeogeography* 12 (1), 90–96. (in Chinese with English Abstract).

Zhang, Z. N., Cao, Y., Zhu, Y. Z., Pang, Z. S., Shen, L. J., Guan, J. Y., et al. (2022). Enrichment mechanism of iron in Dazhang skarn iron deposit, Shandong Province: Evidence from fluid inclusions and hydrogen-oxygen isotopes. *Mineral Deposits* 41 (1), 91–105. (in Chinese with English Abstract). doi:10.16111/j.0258-7106.2022.01.006

Zhao, Q. F. (2005). *On the thermal evolution and kinetics of hydrocarbon generation of late Paleozoic coal measure source rocks in Huimin Depression*. Guangzhou: The Graduate School of the Chinese Academy of Sciences. (in Chinese with English Abstract).

Zhao, X. G. (2007). *Analysis on existent condition of coal-bed methane in Huanghebei coalfield and adjacent region*. Qingdao: Shandong University of Science and Technology. (in Chinese with English Abstract).

Zhao, Y., Ma, M. Y., and Qu, Z. L. (2016). Analysis of main control factors and estimation of resource of coal bed gas in the Huanghebei coalfield, Shandong Province. *Shandong Coal Science and Technology* 177 (8), 173–174. (in Chinese with English Abstract). doi:10.3969/j.issn.1005-2801.2016.08.074

Zheng, S. J. (2016). *Source-reservoir-cap rock assemblages and sequence sratigraphic framework control in coal measures of Linxing area*. Xuzhou: China University of Mining and Technology. (in Chinese with English Abstract).

Zhou, P. M. (2015). *Research on forming mechanism of the primary gas reserviors of the C-P coal-bearing sequence in Jiyang Depression*. Xuzhou: China University of Mining and Technology. (in Chinese with English Abstract).

Zhu, Y. M., Hou, X. W., Cui, Z. B., and Liu, G. (2016). Resources and reservoir formation of unconventional gas in coal measure, Hebei Province. *Journal of China Coal Society* 41 (01), 202–211. (in Chinese with English Abstract). doi:10.13225/j.cnki.jccs.2015.9013

Zhu, Y. Z., Zhang, Z. N., Shen, L. J., Wang, H. H., Zhou, M. L., Zhang, X. B., et al. (2021). Geochronology and geochemistry of late mesozoic diabase in the Litun ore district, north China Craton. *Geological Journal* 56 (9), 4735–4746. doi:10.1002/gj.4211

Zou, C. N., Tao, S. Z., and Hou, L. H. (2014). *Unconventional oil and gas geology*. Beijng: Geological Publishing House, 274–306. (in Chinese with English Abstract).

Zou, C. N., Yang, Z., Huang, S. P., Ma, F., Sun, Q. P., Li, F. H., et al. (2019). Resource types, formation, distribution and prospects of coal-measure gas. *Petrol. Explor. Develop.* 46 (3), 451–462. doi:10.1016/S1876-3804(19)60026-1

Frontiers in Earth Science

Investigates the processes operating within the major spheres of our planet

Advances our understanding across the earth sciences, providing a theoretical background for better use of our planet's resources and equipping us to face major environmental challenges.

Discover the latest Research Topics

See more →

Frontiers

Avenue du Tribunal-Fédéral 34
1005 Lausanne, Switzerland
frontiersin.org

Contact us

+41 (0)21 510 17 00
frontiersin.org/about/contact